THE JOURNAL OF
PHYSICAL CHEMISTRY
Registered in U. S. Patent Office

VOLUME 72, NUMBER 4 APRIL 15, 1968

Pyrex Membrane Potential in Binary Nitrate Melts[1]

by A. G. Keenan, K. Notz, and F. L. Wilcox

Department of Chemistry, University of Miami, Coral Gables, Florida 33124 *(Received November 13, 1967)*

Electromotive force measurements at 350° are reported for cells with a Pyrex membrane and containing binary nitrate melts of the type MNO_3–$AgNO_3$. M is Li, Na, or K varying in concentration from 0 to 90 mol %. The ion-exchange model fits the data, whereas the liquid-junction model does not. This result agrees with a previous fused-salt system involving an inert solvent and a lower concentration range but constitutes a more stringent test of the ion-exchange model, since both cations are potential determining and present over essentially the whole concentration range. Selectivity constants have the same rank order in the two systems as well as in aqueous solutions. The significance of this is discussed.

Membrane potentials have commonly been interpreted on the basis of either the liquid-junction[2] or ion-exchange[3] models. The physical basis of the liquid-junction model consists simply of a diffusion potential integrated from one liquid phase to the other according to the equation

$$E = -(RT/F)\int_1^2 \Sigma(t_i/Z_i)\ \mathrm{d}\ln a_i \qquad (1)$$

where t_i is the transference number, Z_i is the charge, a_i is the activity, and the summation includes all ions which carry current. Thus the model is clearly inapplicable, in principle, to glass membranes, since the phase-boundary discontinuities, and the ion-exchange equilibrium which is known to occur at them, are completely neglected. Nevertheless, the model has been widely used to correlate emf data for glass membranes by invoking transference numbers (or relative ionic mobilities) with properties suitable for obtaining agreement with the experimental data. The moderately successful application of the liquid-junction model to glass-membrane potentials has been possible, in short, by use of the transference member as an adjustable parameter.

In a recent publication,[4] a system was described in which the liquid-junction model failed completely to fit the data, whereas the ion-exchange model gave an excellent fit and meaningful values for the parameters. The system in question consisted of a Pyrex membrane immersed in a solution of alkali metal or silver nitrates, singly or mixed, in fused ammonium nitrate solvent at 190°. The recent elegant derivation of the ion-exchange equation by Conti and Eisenman[5] reduces, for the case where one side of the membrane is exposed to a reference solution of constant composition, to

$$E = E' + (RT/F)\ln \Sigma k_i a_i \qquad (2)$$

where

$$k_i = (u_i/u_1)K_{1i} \qquad (3)$$

The u_i are mobilities in the membrane and the K_{1i} ion-exchange equilibrium constants at the surface, relative to a reference ion numbered 1. The order of the cation selectivity constants, k_i, was found to be the same as for aqueous solutions, indicating that the potential-determining ion-exchange processes at the

(1) This work was supported by the Office of Naval Research under Contract Nonr-4008(07). It comprises parts of the Ph.D. Dissertation of K. Notz and the M.S. Thesis of F. L. Wilcox.

(2) D. A. McInnes, "The Principles of Electrochemistry," Reinhold Publishing Corp., New York, N. Y., 1939, p 220.

(3) R. H. Doremus in "Glass Electrodes for Hydrogen and Other Cations," G. Eisenman, Ed., Marcel Dekker, Inc., New York, N. Y., 1967, p 101.

(4) K. Notz and A. G. Keenan, *J. Phys. Chem.*, **70**, 662 (1966).

(5) F. Conti and G. Eisenman, *Biophys. J.*, **5**, 247 (1965).

glass interface involve unsolvated ions in both the aqueous system and in a fused salt.

The ammonium nitrate system was probably the first clear-cut case in fused salts to distinguish between the liquid-junction and ion-exchange models. However, the potential-determining ions were diluted by an inert solvent, and concentrations never exceeded 30 mol %. In the present article, a more exacting case is examined, namely, binary nitrate melts ranging over essentially the whole concentration range and with both cations potential determining. It is again found that the ion-exchange model provides the correct functional form for fitting the data, whereas the liquid-junction model does not.

The cell used in this research may be formulated as

$$\text{Ag} \;\Big|\; \begin{matrix}\text{AgNO}_3\\ \\ \text{MNO}_3\end{matrix} \;\Big|\; \text{Pyrex} \;\Big|\; \begin{matrix}\text{Ag}^+ \text{ in}\\ \text{nitrate}\\ \text{eutectic}\end{matrix} \;\text{Ag}$$

M was Li, Na, or K. The reference electrode is on the right.

Experimental Section

The apparatus, procedures, and Pyrex bulbs were essentially the same as previously reported,[4] except that a Leeds and Northrup Type K-3 potentiometer was used for most of the measurements. The temperature for all runs was 350.0 ± 0.1°. The asymmetry potential of the bulb was measured before each run and the correction applied to the data. The reference solution inside the bulb for the first two columns of data for the $NaNO_3$–$AgNO_3$ system was an equimolar solution of these two constituents. In all the other cases, the reference solution was 0.1 m $AgNO_3$ in an equimolar mixture of KNO_3 and $NaNO_3$.

Results and Discussion

Cell-potential data are given in the first four columns of Table I. Activity coefficients have recently been reported[6] for $AgNO_3$ in the systems in question. These are given in column 5 of Table I. It is to be noted that the activity corrections are far from negligible, an assumption frequently made in discussing fused-salt emf. Graphs of cell emf against the logarithm of the silver activity, plotted according to the Nernst equation for the electrode potential, showed pronounced curvature in all cases, indicating the presence of a membrane potential varying with concentration.

If the liquid-junction model is used for the membrane potential, making the usual assumption of only cation mobility in the membrane, then the total cell potential will be of the form[7]

$$E = E' + (RT/F)t_{\text{Na}} \ln (a_2/a_1) \qquad (4)$$

where a_2 and a_1 are the activities of MNO_3 and $AgNO_3$, respectively. A standard Gibbs–Duhem calculation[8] was applied to the $AgNO_3$ activity coefficients to produce the values for the other nitrates shown in Table I. The data, now plotted according to eq 4, again showed pronounced curvature. Some representative graphs are shown in Figure 1. Thus the liquid-junction model does not apply to these systems.

Table I: Emf Data for Pyrex Membrane Cells Containing the Binary Nitrate Melts MNO_3–$AgNO_3$ at 350°

$AgNO_3$, mol %	Cell potential for replicate runs on different bulbs, mV			Activity coefficients $AgNO_3$[a]	Activity coefficients MNO_3
		$LiNO_3$–$AgNO_3$			
100.0	−213.7[b]	−214.7	−219.4	1.00	...
79.8	−212.1	−204.7	−209.3	1.04	1.61
60.0	−200.5	−195.0	−199.7	1.14	1.28
40.0	−181.0	−182.9	−184.8	1.30	1.12
19.6	−155.7	−157.2	−157.4	1.59	1.03
10.0	−126.4	−129.4	−126.9	1.75	1.02
		$NaNO_3$–$AgNO_3$			
100.0	−39.0	−38.8	−219.4[b]	1.00	...
90.4	−29.5	−30.7	...	1.01	1.79
80.3	−20.3	−23.8	−200.9	1.03	1.59
70.5	−15.3	−16.1	...	1.08	1.38
60.0	...	...	−184.3	1.12	1.29
50.3	0.0	0.0	...	1.18	1.20
39.9	9.5	9.4	−166.8	1.27	1.14
30.4	17.9	21.2	...	1.37	1.08
20.0	36.6	37.0	−137.8	1.50	1.05
10.4	64.0	68.6	−109.3	1.68	1.03
		KNO_3–$AgNO_3$			
100.0	...	−214.1[b]	−218.0	1.00	...
80.0	−211.6	−214.9	−217.9	1.02	0.989
60.0	−211.5	−215.2	−218.6	1.03	0.948
40.1	−209.7	−212.5	−214.6	0.99	0.992
20.0	−199.4	−201.3	−201.4	0.98	0.998
10.0	−179.5	−178.0	−178.0	0.97	0.999

[a] Reference 6. [b] These data are shown in Figures 1 and 2.

Combining the usual Nernst expression for electrode potentials with the ion-exchange equation (eq 2) for membrane potential gives

$$E_{\text{cell}} = E' + (RT/F) \ln \frac{k_1 a_1 + k_2 a_2}{a_1} \qquad (5)$$

Since silver is the common ion in these systems, it is convenient at first to standardize the selectivity ratio scale relative to silver by putting $k_1 = 1$. E' then is evaluated at $a_2 = 0$ and eq 5 may be recast in the form

$$\log^{-1} Y = \log^{-1}\left[\frac{F(E_{\text{cell}} - E')}{2.3RT}\right] = 1 + k_2 \frac{a_2}{a_1} \qquad (6)$$

When plotted according to eq 6, all the data gave excellent straight lines, some representative examples

(6) M. Bakes, J. Guion, and J. P. Brenet, *Electrochim. Acta*, **10**, 1001 (1965).

(7) R. W. Laity, *J. Amer. Chem. Soc.*, **79**, 1849 (1957).

(8) I. M. Klotz, "Chemical Thermodynamics," W. A. Benjamin, Inc., New York, N. Y., 1964.

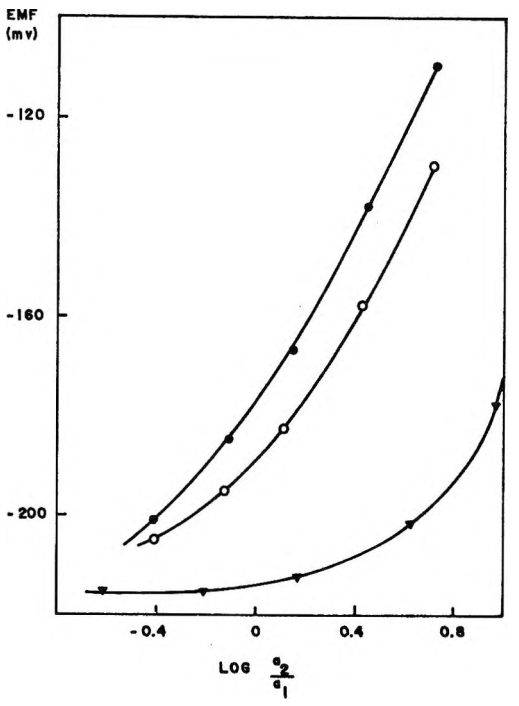

Figure 1. Cell emf at 350° *vs.* log of activity ratio, according to liquid-junction model: ●, Na–$AgNO_3$ (bulb 26); ○, Li–$AgNO_3$ (bulb 29); ▼, K–$AgNO_3$ (bulb 31). $AgNO_3$ is component 1.

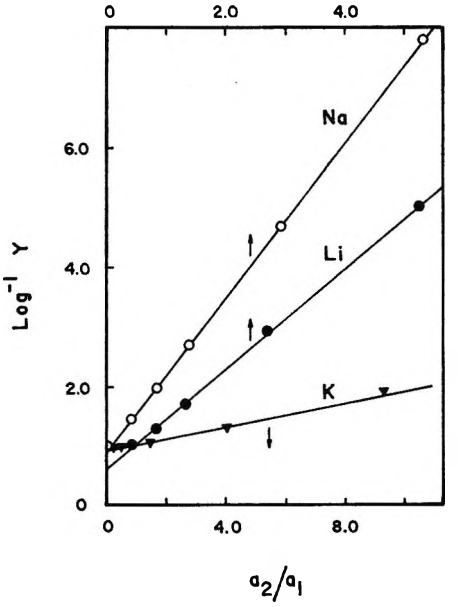

Figure 2. Emf data at 350° *vs.* activity ratio, according to ion-exchange model.

being shown in Figure 2. All except the lithium lines passed through unity on the ordinate axis.

The lithium lines could also be made to pass through unit intercept by making a correction of about −6 mV to E'. Since E' was evaluated from a pure silver nitrate solution, it seems probable that this correction represents a bias which is introduced by an initial etching of the glass surface by lithium ion below 10 mol % concentration. The anomalous behavior of lithium on glass is well known.[4] Although emf readings were taken between 0 and 10 mol % MNO_3, it was not possible to study this phenomenon further because the activity coefficient data could not be read sufficiently accurately in this range from the published values.[6] In any case, the selectivity constants discussed below are calculated from the slope and are not affected appreciably by the variation in E'.

The agreement of the data in functional form with eq 5 thus demonstrates that the ion-exchange model applies to the binary melts used. Selectivity constants calculated from the slope of eq 6 and converted to a basis of $k_{Na} = 1$ are given in Table II. It is seen that the rank order of selectivity constants is the same in fused ammonium nitrate solvent at 190° and in binary nitrate melts at 350°. The values for the other ions relative to sodium are, however, an order of magnitude larger at the higher temperature, presumably due to the increased mobility in glass.

Table II: Selectivity Constants (k) for Pyrex in Nitrate Melts

Ion	Binary nitrates[a] (350°)	NH_4NO_3[b] (190°)
Na^+	1.00	1.00
Ag^+	0.78	0.32
Li^+	0.63	0.065
K^+	0.070	0.007

[a] This research. [b] Reference 4.

It was pointed out in the previous work[4] that the rank order of selectivity constants in Table II, for fused salts, is the same as found by Eisenman[9] for aqueous solutions. This might at first appear unlikely, considering the large variation in extent of hydration and, therefore, effective size of the ions in question. These data have been interpreted[10] recently to indicate that in fused salts the whole glass membrane takes on the transport and exchange functions of the hydrated gel layer in aqueous systems at room temperature. Since in most cases the gel layer occupies only a small fraction of the transport path, an alternative explanation of these data is that in aqueous systems the hydrated ion on entering the gel layer prior to adsorption loses its hydration sphere in a preequilibrium which does not influence the membrane potential. The potential-determining ion-exchange equilibrium constant at the lattice adsorption site, which enters into the selectivity constant according to eq 3, then corresponds to that in fused salts.

(9) G. Eisenman, *Biophys. J.*, **2**, 259 (1962).
(10) G. A. Rechnitz, *Chem. Eng. News*, **45**, 146 (1967).

An X-Ray Study of Formamide and Solutions of Potassium Iodide in Formamide

by R. J. DeSando[1] and G. H. Brown

Department of Chemistry, University of Cincinnati, Cincinnati, Ohio 45200 *(Received March 27, 1967)*

X-ray diffraction patterns at 23° have been recorded for liquid formamide and four solutions of potassium iodide in formamide in the concentration range 0.714–4.019 *m*. The interpretation of the radial distribution curve and physical properties of liquid formamide suggest that this highly associated liquid possesses a short-range structure paralleling that of the crystalline state. The radial distribution curves of the solutions exhibit evidence of ion-pair formation at all concentrations with the mean K^+–I^- distance being 3.7 Å. Maxima in the distribution curves at about 3.0 Å are due, in part, to the presence of potassium ion interaction with the carbonyl oxygen of the solvent; solvation numbers range from 4 in the most dilute solution to 2 in the most concentrated solution.

Introduction

A suitable understanding of the nature of ionic solutions requires a knowledge of the extent of association or ion interactions of oppositely charged species. Because of the interesting properties of formamide as a solvent, it seemed desirable to conduct a study by X-ray diffraction of formamide and of a series of solutions of an ionic salt in formamide. The salt selected for this investigation was potassium iodide; this salt is fairly soluble in formamide, making available a range of concentrations for study and thereby diminishing the uncertainty that often accompanies the interpretation of an electron-distribution curve of a single solution.

The component ions have such high atomic numbers that a large fraction of the total X-ray scattering at the concentrations used should be due to the solute rather than to the solvent. Consequently, the K^+–I^- and I^-–I^- interactions predominate in the diffraction patterns.

Experimental Procedure and Calculations

Formamide, reagent grade, obtained from Eastman Kodak Chemicals, was refluxed for several hours over calcium oxide and then doubly distilled at a pressure of approximately 2 mm. The fraction selected for study had a boiling point of 76° and density of 1.130 g/ml, in good agreement with the literature.[2,3] The solutions were prepared by direct weight of reagent grade potassium iodide (Baker and Adamson) and the purified formamide. The densities of the solutions were determined with a calibrated 10-ml pycnometer.

The samples for X-ray exposure were immediately placed in Pyrex glass capillaries (inside radius 0.023 cm and wall thickness 0.0024 cm); the uniform fabrication of these capillaries is described by Ritter.[4] After sealing, the meniscus of the liquid was checked under a microscope before and after each X-ray exposure to verify that there was no loss of solvent. None of the solutions became colored after irradiation. All data were taken at 23°.

Since diffractometric equipment was not available, X-ray diffraction patterns were obtained with a Debye–Scherrer camera having an effective diameter of 114.6 mm; the camera was modified slightly to permit the introduction of a helium atmosphere in order to diminish air scattering. Monochromatic Mo $K\alpha$ radiation was obtained by reflection from a well-developed (002) face of a urea nitrate crystal. In order to ensure linearity of the film, exposure times were limited to keep the optical densities below 1.5. The relatively low intensity of the (004) reflection, about $^1/_{60}$ that of the (002) reflection,[5] permits the X-ray tube to be operated well above the excitation potential without fear of introducing parasitic harmonic wavelengths such as $\lambda/2$. Each exposure was immediately preceded and followed by calibration exposures on separate film, in order to measure the X-ray flux delivered by the monochromator. An estimate of this flux was necessary in order to correct for absorption in the glass capillary. The average of six readings was used to establish the flux value.

The microphotometer readings of each film were divided by its flux and the time of exposure, thus affording a set of normalized intensity data for each sample. The intensity curves, obtained by averaging four sets of values from two photographs, were cor-

(1) Mound Laboratory (operated by Monsanto Research Corp. for the Atomic Energy Commission), Miamisburg, Ohio.

(2) R. A. Kromhout and G. W. Moulton, *J. Chem. Phys.*, **25**, 35 (1956).

(3) L. R. Dawson, E. D. Wilhort, and P. G. Sears, *J. Amer. Chem. Soc.*, **79**, 5906 (1957).

(4) H. L. Ritter, OSR-TV-55-297, Chemistry Division, Air Force Office of Scientific Research, Washington, D.C., Sept 1955.

(5) R. L. Harris, R. E. Wood, and H. L. Ritter, *J. Amer. Chem. Soc.*, **73**, 3152 (1951).

rected for absorption due to the glass container, for self-absorption due to the liquid, for diffraction due to the glass container, and for polarization. It should be pointed out that one cannot simply subtract the intensity curve of the empty capillary from the intensity curve of the solution and capillary, since the total intensity curve is affected by both self-absorption of the glass and absorption in the sample; that is, the contribution of the sample holder to the total intensity is not the same as the intensity of the empty sample holder. The method of computing the absorption corrections has been nicely explained by Ritter.[4,6]

The corrected experimental intensity data were normalized according to the procedure of Krogh-Moe[7] and Norman;[8] a convergence factor e^{-as^2} was included in the normalization procedure in order to suppress the uncertainty in the experimental and total independent intensity data at a large s value.

Figure 1 shows the observed intensity curve for formamide corrected for absorption and polarization and normalized (curve 1); the total calculated independent intensity is represented in curve 2. The observed and calculated intensities for the four solutions are shown in Figure 2 (see Table I for concentrations).

The reduced intensity function used is

$$si(s) = s\left\{KI_{\text{rel}}(s) - \left(\sum_i x_i f_i^2(s) + \sum_i x_i F_{\text{inc}}(s)\right)\right\}$$

where $\sum_i x_i f_i^2(s)$ and $\sum_i x_i F_{\text{inc}}$ are the calculated coherent and incoherent scattering factors,[9-12] respectively; x_i is the atom fraction; I_{rel} is the intensity in relative units corrected for absorption and polarization; K is the normalization factor; and $s = 4\pi \sin\theta/\lambda$.

The modification function $M(s)$ developed by Waser and Schomaker[13] was employed in order to sharpen the distribution function and is given by

$$M(s) = \left[\sum_i x_i Z_i \Big/ \sum_i x_i f_i(s)\right]^2$$

with the summations being over all the atoms in the stoichiometric unit; Z_i represents the atomic numbers. The same modification function was used in the computation of each distribution curve. The Fourier transform of the product of $si(s)$ and $M(s)$ is

$$4\pi r^2 g(r) = 4\pi r^2 g_0 + \frac{2r}{\pi}\int_0^{s_m} si(s)M(s) \sin rs \, ds$$

where $4\pi r^2 g(r)$ is a superposition of modified pair-distribution functions for the different kinds of atom pairs, that is

$$4\pi r^2 g(r) = \sum_i \sum_j 4\pi r^2 g_{ij}(r)$$

The modification of a pair-distribution function g_{ij} is given by[13,14]

$$4\pi r^2 g_{ij}(r) = 4\pi r \int_{-\infty}^{\infty} \mu g_{ij}(\mu) T_{ij}(\mu - r) \, d\mu$$

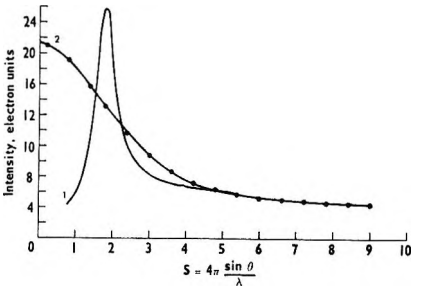

Figure 1. Curve 1 represents the observed intensity for formamide corrected and normalized. Curve 2 shows the total calculated independent-atom intensity. The dots in curve 2 represent values of s for which independent intensities are calculated.

Table I: Solution Compositions

Solution no.	Molality	Unit composition
1	0.714	$(CH_3NO)_{0.165}(KI)_{0.0053}$
2	1.963	$(CH_3NO)_{0.162}(KI)_{0.0143}$
3	3.083	$(CH_3NO)_{0.159}(KI)_{0.0221}$
4	4.019 (satd)	$(CH_3NO)_{0.157}(KI)_{0.0274}$

where $T_{ij}(r)$ is the peak-shape function which modifies the sharp pair-distribution function and is given by

$$T_{ij}(r) = \frac{1}{\pi}\int_0^{s_m} f_i f_j M(s) \cos rs \, ds$$

Results and Discussion

The electron-pair distribution curve for formamide shown in Figure 3 exhibits maxima at 1.45, 2.30, 3.05, 3.75, and 5.0 Å. The crystal structure analysis of formamide by Ladell and Post[15] shows there are puckered sheets of molecules. Within these sheets, pairs of formamide molecules are associated through hydrogen bonding at 2.935 Å to form nearly coplanar "bimolecular" units, and each pair of molecules, in turn, is hydrogen bonded in a stronger fashion to four other bimolecular units at 2.88 Å. The crystal study shows the C–O and C–N distances to be approximately 1.3 Å.

(6) H. L. Ritter, R. L. Harris, and R. E. Wood, *J. Appl. Phys.*, **22**, 169 (1951).

(7) J. Krogh-Moe, *Acta Crystallogr.*, **9**, 951 (1956).

(8) N. Norman, *ibid.*, **10**, 370 (1957).

(9) J. Berghuis, I. M. Haanappel, M. Potters, B. O. Loopstra, C. H. MacGillavry, and A. L. Veenendaal, *Acta Crystallogr.*, **8**, 478 (1955).

(10) L. H. Thomas and K. Umeda, *J. Chem. Phys.*, **26**, 293 (1957).

(11) A. J. Freeman, *Acta Crystallogr.*, **12**, 261 (1959).

(12) A. H. Compton and S. K. Allison, "X-Rays in Theory and Experiment," D. van Nostrand Co., New York, N. Y., 1935, p 782.

(13) J. Waser and V. Schomaker, *Rev. Mod. Phys.*, **25**, 671 (1953).

(14) H. A. Levy, M. D. Danford, and P. A. Agron, *J. Chem Phys.*, **31**, 1458 (1959).

(15) J. Ladell and B. Post, *Acta Crystallogr.*, **7**, 559 (1954).

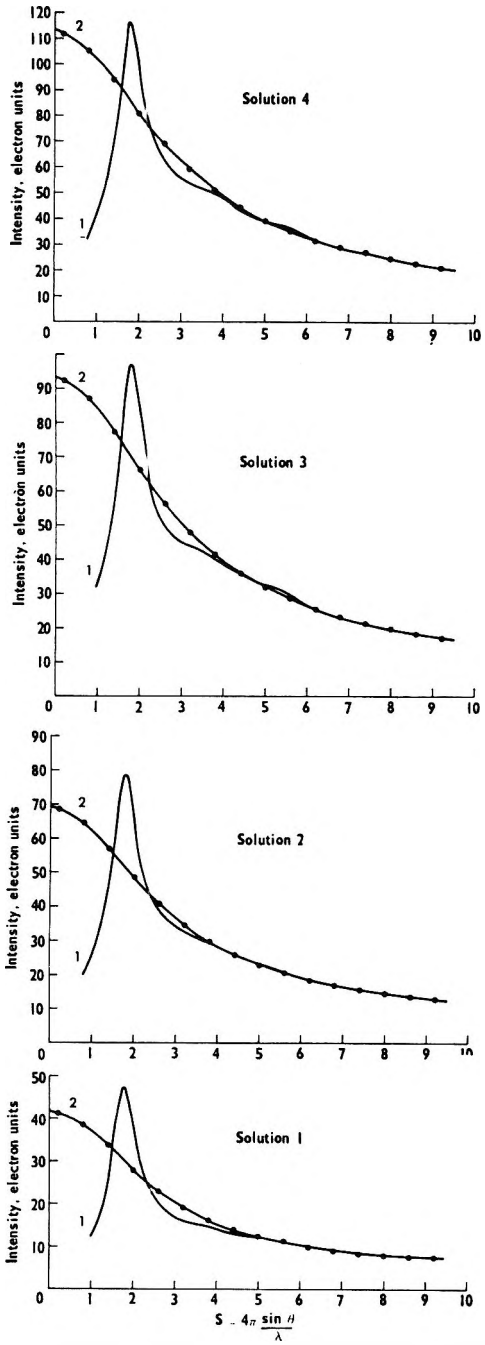

Figure 2. Curve 1 in each figure represents the observed intensity for potassium iodide in formamide corrected and normalized. Curve 2 in each figure shows the total calculated independent intensity. The dots in curve 2 represent values of s for which independent intensities are calculated. See Table I for composition of the solution.

The peak at 1.45 Å (Figure 3) in the distribution curve can be attributed to a coalescence of the peaks due to the intramolecular distances for C–O and C–N. The total electron concentration under the peak corresponds to the interactions proposed. The peak at 2.30 Å is attributed to the intramolecular O–N distance (2.27 Å in the solid). The area under this peak corresponds to exactly 1 oxygen/nitrogen, agreeing with the atomic arrangement in a formamide molecule.

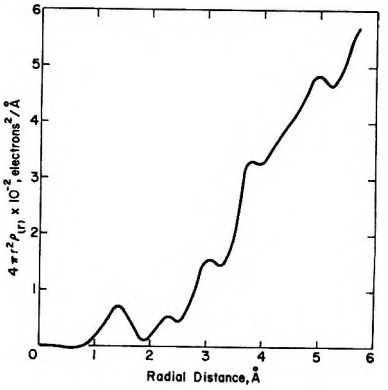

Figure 3. Radial distribution curve for liquid formamide at 23° for the stoichiometric unit of $C_{0.167}$, $H_{0.500}$, $H_{0.167}$, $O_{0.167}$.

We assign the maximum at 3.05 Å principally to intermolecular N···O interactions through hydrogen bonding and to other intermolecular interactions. Of the two types of hydrogen bonds observed in the crystal, the longer of the two utilized in the formation of bimolecular units would be expected to be broken on melting; consequently, the retention of the stronger hydrogen bond interactions could result in the existence of chains or polymeric species of formamide molecules. The prominence of the peak attests to the existence of hydrogen bonding in the liquid. Peaks at 3.75 and 5.0 Å undoubtedly result from a variety of intermolecular interactions and no attempt was made to interpret them. From the data presented in this paper, the authors conclude that formamide in the liquid state possesses a short range order which resembles that of the crystalline state.

Radial distribution functions for the solutions of potassium iodide in formamide (see Table I) are traced in Figure 4. Each of the distribution curves exhibits a resolved peak at 1.6 Å and maxima at 2.3, 3.0, 3.7, 4.4, and 5.1 Å. For these concentrated solutions, the K^+–I^- and I^-–I^- interactions would be expected to predominate over the weakly scattering solvent and also over the scattering from the ion–solvent interactions. The interactions in the neighborhood of 3.7 Å may be assigned to K^+–I^- separations. These distances, in order, beginning with the most dilute solution are 3.72, 3.70, 3.70, and 3.65 Å, respectively, and compare favorably with crystallographic data.[16] Information concerning the number of interactions may be obtained from the peak areas above a suitably chosen base line; for the most dilute solution the electron density of the solvent was subtracted from that of the total solution. The area under the peak at 3.72 Å corresponds to 4.1 K^+–I^- interactions or 2.0 iodides/potassium ion in the 0.714 m solution. The areas under the same peak for the 1.963, 3.083, and 4.019 m solutions correspond to 4.1, 4.1, and 4.6 K^+–I^- interactions, respectively, or an average of two K^+–I^-

(16) P. G. Hambling, *Acta Crystallogr.*, 6, 98 (1953).

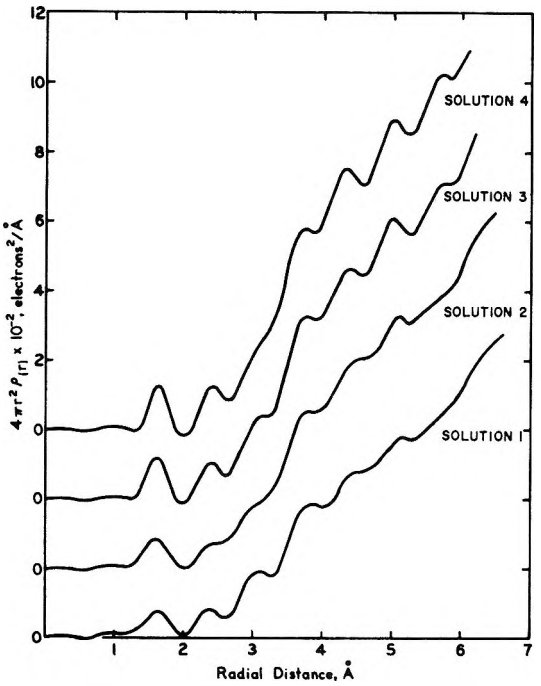

Figure 4. Radial distribution curves for solutions of potassium iodide in formamide at 23°. The curves are displaced vertically to preserve clarity of the contours. See Table I for composition of the solutions.

pairs per potassium. As there is no apparent change in coordination number with concentration, the average coordination may be taken to be 2 iodides/potassium ion.

Another maximum in the radial curve for each of the solutions is seen to occur at about 5.0 Å; it is most prominent for the two more concentrated solutions. This peak is attributed principally to I^-–I^- interactions, although contributions from ion–solvent–ion interactions as well as interactions from secondary coordination shells are undoubtedly present. The ratio of the distances of I^-–I^- to K^+–I^- occurs at nearly 1.414, which is suggestive of octahedral geometry.

The maximum at about 3.0 Å is due principally to intermolecular N···O interactions through hydrogen bonding and the presence of potassium–solvent interactions, namely, metal ion–ligand interactions with the carbonyl oxygen as the electron-donor species. Raman studies[17] support this observation of solvent–ion interaction. Cations cause a vibrational frequency decrease and an intensity lowering of the C–O stretching band as the mole ratio of solute to solvent increases. Further support of the observation is represented by the work of Uno, *et al.*[18] They attributed anomalous infrared spectra of amides dissolved in alkali metal halide pellets to ion–dipole interactions between the carbonyl oxygen and the alkali metal cation and to interactions between the anion and N–H group. It might be mentioned also that the hydration distance K–O in various crystalline hydrates of potassium salts[19,20] has been determined as lying between 2.8 and 3.3 Å.

As an approximation, the area under the peak at 3.0 Å in order of increasing concentration of the solutions corresponds to 4.6, 2.5, 2.1, and 2.1 potassium ion–formamide pairs/potassium ion, respectively. These solvation numbers appear to be reasonable, since in the most dilute solution there are approximately 15 formamide molecules/potassium ion. In the remaining solutions the solvent to potassium ion ratio decreases in the order 5.6:1, 3.6:1, and 2.7:1, respectively, with increasing concentration. However, because of lack of good resolution of this peak the area assignments under the peak make these values approximate.

Each of the solutions exhibits a maximum at about 4.4 Å, just discernible in the most dilute solution and becoming quite prominent in the two most concentrated solutions. Although overlapping contributions exist at this distance, a major contribution is ascribed to I^-–I^- contact distances. The peak at 1.6 Å for each of the solutions is attributed to the coalescence of the intramolecular C–O and C–N distances.

The radial distribution curves exhibit evidence of ion-pair formation at all concentrations and also cation solvation, greatest for the most dilute solution and approaching on the average 2 formamide molecules/potassium ion for the most concentrated solution.

(17) Z. Kecki, *Spectrochim. Acta*, **18**, 1165 (1962).

(18) T. Uno, K. Machida, and I. Hamanaka, *Bull. Chem. Soc. Jap.*, **34**, 1448 (1961).

(19) R. W. G. Wyckoff, "Crystal Structures," Vol. 3, 2nd ed, Interscience Publishers, Inc., New York, N. Y., 1965, p 733.

(20) D. J. Haas, *Acta Crystallogr.*, **17**, 1516 (1964).

A Sessile Drop Study of Liquid–Solid Adhesion for the System Indium(l)–Aluminum Using Ultrahigh Vacuum Techniques

by R. G. Aldrich[1a] and D. V. Keller, Jr.[1b]

Department of Chemical Engineering and Metallurgy, Syracuse University, Syracuse, New York *(Received May 1, 1967)*

A sessile drop study was conducted to examine the wetting and adhesion behavior for the system indium–aluminum in the region of bulk immiscibility near the solidification temperature of indium. Ultrahigh purity materials and ultrahigh vacuum techniques were employed to establish contacting surfaces of near atomic cleanliness. The effects of oxygen, nitrogen, and hydrogen on this system over periods of time to 65 hr were observed from ambient pressures of 10^{-10} to 1 torr. The surface tension of liquid indium on a polycrystalline aluminum substrate at 160° in a vacuum of 10^{-10} torr was observed to be 658 (±10%) dynes/cm. The rather large error was presumably caused by the different degrees of liquid interaction with the different crystallographic orientations of the substrate as reflected in the rather large variations in the average contact angle of 120°. The presence of the contaminating gases hydrogen and nitrogen did not significantly affect the observed surface tension of the liquid indium. Oxygen contamination appeared to form an oxide cover on the liquid such that the surface tension of indium appeared to vary with exposure time. The observed adhesion strengths in tension of the indium(s)–aluminum composite at room temperature fell into two distinct and separate classes, *e.g.*, strengths greater than the tensile strength of indium and strengths approaching zero. The former was observed when the interface was formed in ultrahigh vacuum or in an oxygen atmosphere, and the latter was observed when the interface was formed in a hydrogen or nitrogen atmosphere.

Introduction

The behavior of a sessile or immobile liquid drop resting on a solid substrate has long been utilized to interpret the extent of the interfacial reaction[2,3] and to measure the surface tension or specific surface free energy of the liquid component.[4] Extensive reviews of these investigations and the underlying principles have been presented for organic systems[5,6] and liquid metal–inorganic systems,[7–9] but little work has been conducted for liquid metal–solid metal systems in which the nature of the reacting surfaces was restricted to a two- or three-component system. Under atmospheric conditions, in the presence of inert gases or even moderate vacuum environments, a metal surface consists of a stable oxide layer and a layer of physically adsorbed gases, principally water, which inhibit intimate metal–metal interactions between the sessile drop and the metal substrate atoms. Furthermore, there have been presented conflicting experimental data regarding the inability of immiscible metal–metal surfaces to form a wetting type configuration.[10]

The purpose of this investigation was twofold. The first was to investigate the spreading and adhesion behavior of liquid indium on a solid aliminum substrate in the thermal region of bulk immiscibility near the melting point of liquid indium under conditions of ultrahigh vacuum (UHV) and extreme surface cleanliness. Secondly, it was felt that the modification in this system, as induced by controlled additions of specific gaseous contaminants, ought to provide some insight into the extent of interfacial interactions.

The system indium–aluminum was chosen for study on the basis that the mutual bulk solubility of indium and aluminum over the temperature range immediately above the melting point of indium is virtually nil, as indicated by Davis and Rowe.[11] Furthermore, the melting point of indium is low enough, *i.e.*, 155°,[12] to permit simple liquid metal manipulation, and the vapor pressure of both components[13] over the experimental temperature range (<450°) is sufficiently low

(1) (a) Presented as partial fulfillment of Ph.D. requirements, Department of Chemical Engineering and Metallurgy, Syracuse University, Syracuse, N. Y. (b) Address correspondence to this author.

(2) (a) J. T. Davies and E. K. Rideal, "Interfacial Phenomena," Academic Press, New York, N. Y., 1963; (b) S. J. Gregg, "The Surface Chemistry of Solids," Reinhold Publishing Corp., New York, N. Y., 1961.

(3) D. D. Eley, "Adhesion," Oxford University Press, London, 1961.

(4) N. K. Adam, "The Physics and Chemistry of Surfaces," Oxford University Press, London, 1941.

(5) W. A. Zisman, "Contact Angle," R. F. Gould, Ed., American Chemical Society, Washington, D. C., 1964, pp 1–51.

(6) L. H. Sharpe and H. Schonhorn, ref 5, p 189.

(7) W. D. Kingery, "Property Measurements at High Temperatures," John Wiley and Sons, Inc., New York, N. Y., 1959, p 362.

(8) J. E. McDonald and J. G. Eberhart, *Trans. Met. Soc. AIME*, **233**, 512 (1965).

(9) V. N. Yeremenko and Y. V. Naydich, "Wetting of Refractory Compounds With Liquid Metals," OTS, Washington, D. C., 60-11-873 (1960).

(10) K. J. B. McEwan and D. R. Milner, *Brit. Welding J.*, **9**, 406 (1962).

(11) M. T. Ledwick, "Indium," The Indium Corp. of America, Utica, N. Y., 1950, p 28.

(12) Reference 11, p 15.

(13) R. E. Honig, *RCA Review*, **23** (4) (1962).

such that excessive mass transport effects can be neglected. Neither indium nor aluminum experiences any magnetic or phase change effects and both may be obtained in ultrahigh purity, *i.e.*, 99.9999%.

In addition to the use of air as a contaminant, the gases hydrogen, nitrogen, and oxygen of assayed reagent grade quality were chosen for this study. Although extensive data are not available, it appears that hydrogen is relatively inert toward bulk indium[14] and aluminum[15] under the conditions of these experiments. Nitrogen, however, reacts with indium to form a stable indium nitride, having a wurtzite structure,[16] but it does not react appreciably with aluminum[15] under these conditions. Oxygen reacts readily with both elements to form the respective sesquioxides (M_2O_3).

Experiments were also conducted using a sapphire (Al_2O_3) substrate in ultrahigh vacuum to compare the difference between the indium(l) interaction with a well-formed crystalline oxide sapphire and that of a sorbed oxide layer as would be expected to appear on the clean aluminum substrate exposed to oxygen. Similar comparative studies were carried out in air.

Experimental Section

To accomplish such an investigation, an apparatus was designed which was capable of supporting ambient pressures of the order of 10^{-10} torr and withstanding bakeout temperatures to 450° in the test cell area for periods of 15–24 hr. Also incorporated in the experimental consideration was a means for producing a very nearly contaminant-free solid aluminum surface and a means for ejecting onto this surface controlled amounts of the liquid metal constituent. A photographic technique was utilized to record the liquid metal configuration such that the necessary parameters could be obtained for the determination of the surface tension of the liquid by the technique of Bashforth and Adams[17] as well as the contact angle measurement for later correlation to the adhesion data.

The ultrahigh vacuum (UHV) test cell, shown schematically in Figure 1, consisted of a 60 × 120-mm Pyrex tube sealed at both ends with 60-mm Pyrex optical plates. Three 25-mm side arms were sealed to the main tube normal to its major axis: one side arm supported the indium ejection tube in the vertical position, a second side arm supported the aluminum evaporator which was used to deposit an ultraclean aluminum film on the oxide-covered aluminum substrate, and the third side arm led to the substrate support, Redhead gauge (NRC-752), contaminant gas leak valve, titanium sublimation pump, and 25-mm main vacuum system valve.

The test cell and appendages were evacuated through the isolation valves by an 80-l./sec three-stage mercury diffusion pump in series with a 10-l./sec three-stage mercury diffusion pump, and a Welch Duo-Seal mechanical pump. The high-speed diffusion pump was separated from the isolation valves by two bakeable liquid nitrogen traps and two nonbakeable traps; further, each pumping stage was isolated by a liquid nitrogen trap. A cold cathode gauge was utilized to monitor the fore-pressure to the large diffusion pump during the bakeout cycle. The main cell and appendages with the exception of the argon bulb, which was isolated through a break-off tip, was capable of an extended bakeout to 450° since all valves were of the ultrahigh vacuum bakeable type (Granville-Phillips Co.).

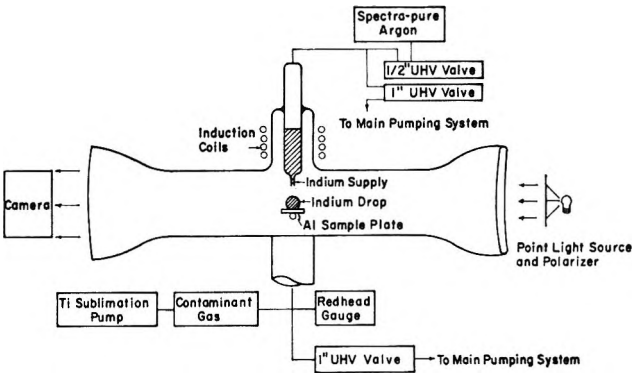

Figure 1. Ultrahigh vacuum cell.

The re-entrant seal assembly used to support a liquid indium source consisted of a 19-mm Pyrex tube tapered to a 0.5-mm i.d. capillary tip and sealed to the UHV cell by means of a 25-mm tube. Surface tension held the liquid metal in place until ejection was desired. The indium charge was heated prior to ejection by means of an induction coil as shown in the figure. By simultaneous manipulation of the 13- and 25-mm valves in the liquid metal section the pressure over the surface of the liquid indium could be increased with reagent grade argon such that the liquid indium was ejected in controlled amounts to the substrate.

The aluminum substrate assembly was supported on a portion of a three-lead nickel through-seal such that a Pt—Pt–10% Rh heater and chromel–alumel thermocouple were mounted adjacent to the substrate. The heater was used to elevate the substrate temperature (~330° or $0.65T_m$) during the vapor deposition of the aluminum film, such that the film would deposit in an annealed condition. Furthermore, the plate temperature after vapor deposition and immediately prior to the placement of the drop on the substrate could readily be controlled to about 160°.

(14) S. Dushman and S. M. Lafferty, "Scientific Formulations of Vacuum Technique," John Wiley and Sons, Inc., New York, N. Y., 1962, p 517.

(15) J. R. Dafler, *J. Amer. Chem. Soc.*, **88**, 5667 (1966).

(16) M. Hansen, "Constitution of Binary Alloys," McGraw-Hill Book Co., Inc., New York, N. Y., 1958, p 852.

(17) F. Bashforth and J. C. Adams, "An Attempt to Test the Theories of Capillary Action," Cambridge University Press, London, 1883.

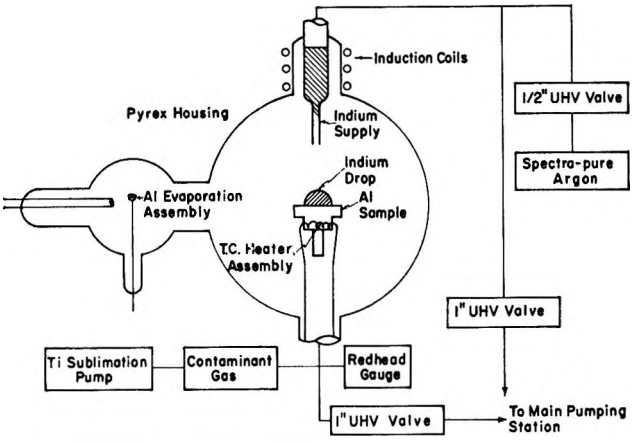

Figure 2. Photographic assembly.

The aluminum evaporator assembly used to deposit a clean aluminum surface on the aluminum substrate consisted of a helically wound 15-mil tungsten wire basket mounted on a through-seal and heated by means of electron bombardment from a 6-mil filament, mounted on a separate seal, by application of a dc potential between the two. The 0.5-g charge of spectrographically pure aluminum (Materials Research Corp.; major impurities Si 4 ppm, Zn 1–2 ppm) was stored in an 8-mm side arm of the evaporator cell until the basket was thoroughly degassed. The pellet was then moved by magnetic means into the basket, thoroughly degassed, and heated to the vapor point.

All aluminum substrates (99.9999%) were polycrystalline and metallurgically polished using an etch–polish technique which left the substrate in a hill–valley structure; the average distance between hills was about 25 μ and the maximum depth of the valleys was about 0.25 μ as determined by section metallographic analysis. A similar structure was observed on the unwetted regions of the plate after a sessile drop study was performed.

Several small Pyrex tubes were fitted with break-off tips and filled with an assayed reagent grade gas in order to provide a means for admitting contaminant gases to the UHV system. These were then sealed with magnetic plungers in an assembly of larger tubes connected in turn to one side of a 6-mm variable leak valve, the other side of which led directly to the ultra-high vacuum cell. Each tube was capable of establishing a pressure in the test cell of 1–10 torr.

Figure 2 provides an alternate view of the test cell and a schematic illustration of the photographic arrangement. The object to be photographed represented the meridional outline of the sessile drop located centrally in the field of view of the Pyrex flats as shown in Figure 1. Lighting was supplied through one of these flats by means of a photoflood lamp equipped with a polarizer shield. Photographs were taken through the second flat using a 35-mm single lens reflex camera with a bellows-mounted 105-mm lens. A shutter speed of $^1/_{125}$ sec was used in conjunction with a lens setting of f5.6 for each sequence. To ensure that the horizontal substrate was properly aligned normal to the focal plane, the camera was mounted on a leveled optical bench using a stripped microscope stage to position the camera.

At the onset of each operational cycle the system was evacuated to at least 10^{-6} torr, and the bakeable portions were heated to a temperature of about 450° for a period of 15–24 hr. A preliminary degassing of all heater components in the cell was conducted with the cell at bakeout temperature to minimize readsorption. Following this brief period the bakeable traps were cooled to liquid nitrogen temperature and the cell to room temperature. A complete degassing of all components at temperatures well above their operating temperatures was conducted until the peak pressure was below 10^{-9} torr. The test cell was then isolated from the main pumping system and allowed to stand under the combined pumping action of the Redhead gauge and the small titanium sublimation pump[18] until a pressure of 10^{-10} torr was attained. Upon adjusting the substrate temperature, a heavy film (~1000 Å) of aluminum was deposited on the substrate. The total time of vapor deposition was approximately 2 min, and the peak pressure during this period was less than 10^{-8} torr; immediately thereafter, the pressure decreased to below 10^{-9} torr. The substrate and the indium reservoir temperatures were then adjusted to 160° and one of two procedures was followed for each contaminant gas.

1. The liquid indium was immediately ejected onto the plate and photographs of the drop profile were taken every quarter hour for a period of 1 hr. After 1 hr, one of the assayed reagent grade gases was admitted to various pressure levels from 10^{-8} to 1 torr. A series of photographs was taken at each system variation.

2. The contaminant gas was admitted to its maximum pressure (<1 torr) and the indium drop formed. Photographs of the profile were taken at regular intervals over a period of at least 5 hr.

Upon solidification and removal of the drop and plate from the UHV cell, the solidified indium–aluminum couple was then subjected to a fracture test in tension in an effort to estimate qualitatively the junction strength of the composite. The substrate plate was mounted in an inverted position in a rigid bracket and a small hook fastened to the drop by means of a self-curing plastic such that the longitudinal axis of the hook shank was coincident with the axis of symmetry of the drop. The plastic mount was always

(18) D. V. Keller, Jr., and T. Spalvins, "Adhesion Between Atomically Clean Metallic Surfaces," in Transactions, Vacuum Metallurgy Conference, R. F. Bunshah, Ed., American Vacuum Society, 1962, p 49.

affixed to the indium such that the major diameter of the drop was included in the plastic matrix, or in the few cases when the contact angle was less than 90°, to a plane representing at least half of the drop height. Since the contact angles were a minimum of 80° and more usually greater than 100°, the maximum stress concentration was in the interfacial zone. A cup was then placed on the hook and continuously filled with mercury until fracture took place. Metallographic examinations of the plate surface, meridional section, and fracture surfaces were conducted after each test. Samples were analyzed using spectrographic and electron probe techniques in an attempt to detect mass transfer.

Results and Discussion

The experiments conducted during the course of this study may be classified by the following configurations: I, a liquid indium drop resting on a freshly deposited solid aluminum surface under conditions of ultrahigh vacuum with no contamination at the indium–aluminum interface or at either of the free surfaces; II, a liquid indium drop resting on a freshly prepared solid surface of aluminum with a surrounding atmosphere consisting of a single contaminant gas added to condition I; the gas, at pressures ranging from 10^{-8} to 1 torr, can establish immediate contact only with the free surfaces, and access of this gas to the interface region is available only by diffusion mechanisms; III, a liquid indium drop resting on a specifically contaminated solid surface of freshly deposited aluminum, the drop being formed in the presence of the contaminant; the contaminant gas interacted at all surfaces and interfaces; IV, a liquid indium drop resting on a previously outgassed sapphire (Al_2O_3) surface under conditions of ultrahigh vacuum.

Table I summarizes the average liquid indium surface tension, contact angle values, and solidified couple joint tensile strengths observed for two or more separate runs under each of the conditions and over ten measurements per run.

Due to the momentum imparted to the indium during the process of ejection, the liquid was forced to establish a larger than equilibrium contact area at the moment of impact. As the "equilibrium" shape of the drop developed, the outer periphery of the interface *receded* to its "equilibrium" position. This was observed using high-speed movie film taken during the ejection process and was further observed metallographically as a delineating indium ridge extending over the aluminum surface slightly beyond the three-phase boundary of the massive indium drop. The contact angles observed were, therefore, regarded as receding angles.

Metallographic examination of the aluminum substrate material following a typical cycle of bakeout and outgassing indicated the occurrence of considerable grain growth to equiaxed grains corresponding to an ASTM grain size of (−1) to (−2) (~0.4–1.0 mm). X-Ray examination of the deposited aluminum film indicated a slight (220) preferred orientation, but no conclusive evidence was obtained to this effect due to the large grain size. The anisotropy of the polycrystalline substrate and its inherent heterogeneity, *e.g.*, grain boundaries, steps, ledges, etc., was manifested in a significant irregular variation (±20°) in contact angle around each drop periphery. Metallographic examination of substrate surface near the indium indicated that the variations could best be correlated with the individual grain boundaries. The sessile drops were approximately 0.7 cm in diameter; hence each drop covered several randomly oriented grains. As discussed by Butler and Bloom[19] and made evident from these data, the errors in surface tension (specific surface free energy) calculations induced by this variation for drops of this size undoubtedly exceeded the random errors of measurements. Although it was difficult to calculate the absolute error under these conditions, it was estimated that a sensitivity of 10–20% was achieved.

Experiments conducted for the sessile drop systems indium–aluminum or sapphire in UHV and the modified systems in the presence of hydrogen and nitrogen to 1 torr indicated no observable time dependence in the establishment of a constant value of surface tension and contact angle. Each configuration was recorded photographically for a minimum period of 1 hr with most being observed for a period of 5 hr and some being observed intermittently for as long as 65 hr. The average value for the surface tension of liquid indium resting on a freshly prepared surface of polycrystalline aluminum was found to be 658 (±10%) dynes/cm, which compares favorably with the value of 600 dynes/cm previously stated[20] by the authors using a less pure (99.99%) form of indium. Timofeevicheva and Pugachevich[21] have reported a value of 556.0 dynes/cm for indium using high-vacuum techniques, and the surface tension of indium in air has been reported as 340 dynes/cm. A value of 595 (±10%) dynes/cm was observed for indium resting on a previously outgassed sapphire plaque in UHV.

As noted in Table I, oxygen contamination in levels to 10^{-6} torr produced no apparent changes in liquid indium surface tension or contact angle. With increasing oxygen content, however, a film, most probably of indium oxide, was observed over the entire free surface of the indium drop. Since oxygen combines quite readily with both indium and aluminum to form the respective oxides which are solid at the tempera-

(19) J. N. Butler and B. H. Bloom, *Surface Sci.*, **4**, 1 (1966).

(20) R. G. Aldrich and D. V. Keller, Jr., *J. Appl. Phys.*, **36** (11) 3546 (1965).

(21) D. A. Timofeevicheva and P. P. Pugachevich, *Dokl. Akad. Nauk SSSR*, **124**, 1093 (1959).

Table I: Sessile Drop System Indium(l)–Aluminum Exposed to Various Contaminants[a]

Interface	$(\gamma_{LV})_{av}$, dynes/cm	θ_{av}, deg	Pressure, torr	Joint strength
Indium–Vacuum (I)	658	118 ± 10	10^{-10}	> Bulk In
Indium–Oxygen (II)	652	118 ± 7	10^{-6}	...
Indium–Oxygen (II)	80–500	Variable	1	> Bulk In
Indium–Oxygen (III)	80–300	Variable	1	> Bulk In
Indium–Nitrogen (II)	620*	80 ± 4	10^{-7}	> Bulk In
Indium–Nitrogen (II)	620*	80 ± 3	1	> Bulk In
Indium–Nitrogen (III)	620*	85 ± 5	1	< Bulk In
Indium–Hydrogen (II)	671	114 ± 5	10^{-7}	> Bulk In
Indium–Hydrogen (II)	627	117 ± 4	1	> Bulk In
Indium–Hydrogen (III)	631	118 ± 3	1	< Bulk In
Indium–Air (II, III)	80–200	Variable	760	> Bulk In
Vacuum (IV)	595	130	10^{-10}	> Bulk In

[a] Experimental conditions: I, Al substrate formed in UHV; II, gas admitted after drop formed; III, gas admitted before drop formed; IV, sapphire substrate outgassed in UHV; *, large errors due to proximity of drop to hemisphere; <, less than; >, greater than.

tures near the melting point of indium, the solid envelope acted to constrain the drop. Light vibration of the cell housing resulted in the fracturing of this envelope and eventually the almost complete spreading of the drop over the substrate. In an effort to determine whether the interaction In–Al_2O_3 or In_2O_3–Al_2O_3 promoted spreading, an experiment was conducted in UHV using an outgassed sapphire substrate. This configuration resulted in nearly the same contact angle and liquid indium surface tension values as was observed for the configuration indium–aluminum in UHV. The presence of an oxide–oxide interaction was concluded to be the primary agent for the spreading in the indium–aluminum system.

The adhesive strength of a solidified sessile drop substrate system is dependent both on the nature of the interfacial interaction and the true area of intimate contact as well as the form and distribution of stress concentrations along the interface. Since plastic failure or failure by rupture of a joint is a kinetic process whereas classical thermodynamics is restricted to systems at equilibrium, there is little to be gained in comparing the adhesive strength of solidified couples with measurable thermodynamic properties such as that work of adhesion equation suggested by Dupré.[22] Furthermore, factors such as contact angle, thermal strain, interfacial misfit, enclosed contaminants (gas bubbles), chemical reactions, and plastic flow induce a very complex stress system which acts significantly to modify the tensile behavior of such solidified sessile drop systems. The observed adhesive strength in tension, however, for those solidified sessile drop configurations formed under UHV conditions (I, II, IV) for both the aluminum and sapphire substrates, indicated a joint strength in excess of the bulk tensile strength (28 kg/cm², 388 psi) of pure indium, failure occurring in each case within the bulk indium. Although it is felt by the authors that quantitative value of joint strength are most difficult to interrupt due to the difficulties outlined above, the values calculated on the basis of the macroscopic area fell reasonably close (25%) to the observed tensile strength of indium.

The lack of composite strength in those cases in which the original interface was contaminated with hydrogen and nitrogen prior to drop formation seems significant in that the degree of surface contamination by these gases would not be expected to exceed, and may be less than, a few monolayers at the temperatures (~160°) and exposure time (<5 hr) cited. However, even this small degree of contamination, a layer readily penetrated by electronic tunnelling, is sufficient to reduce the macro-junction strength to near zero without grossly affecting either the contact angle or liquid surface tension of the systems. Such appears to be most inconsistent with the normal pattern of liquid–solid interfacial analysis techniques as set forth for low surface energy systems.

Since the interface of the pure In–Al system demonstrated a rather high degree of strength, it is reasonable to assume that some atomic Al–In interaction existed; the presence of a contaminant layer of H_2 or N_2 presented an interruption to this interaction. The presence of contaminant molecules on the two free surfaces prior to contact was either by physi- or chemisorption. If the physisorbed state is assumed as the stable configuration, then it would have been energetically favorable for the highly mobile indium atoms to exchange with the weakly sorbed gas molecules in forming the more stable Al–In system. In this event, it would be expected that the excess gas would have been removed by dissolution and that a strong junction strength

(22) A. Dupré, "Theorie Mechanique de la Chaleur," Gantheir-Villars, Paris, 1869, p 369.

similar to that in the uncontaminated case would have been observed. Such was not the case, however, even after a nitrogen-contaminated interface was held *in situ* for 65 hr. In the case of chemisorption of the contaminant gases, such displacement mechanisms would not be expected and the interface would remain as a metal–compound–metal complex with low strength properties due to the brittleness of the intermediate phase. This provides a reasonable explanation for the lack of strength in these contaminated systems. No explanation, however, exists as to why in these systems the contact angle and surface tension values remained almost invariant, even though the other free surfaces were also exposed to the chemisorbed species. Such variations may not be within the detectable limits of this study, but such gross modifications of interfacial behavior would be expected to be similarly reflected in the liquid surface parameters.

The presentation of these data appears also to develop two other points of inconsistency with analysis based on the usual Young–Dupré technique. In the first case, the interfacial tension is estimated from the observed UHV contact angle, the liquid surface tension data, and the estimated[23] value of the surface tension value of solid aluminum (1890 dynes/cm) as 2083 dynes/cm, then one would suspect from the standard arguments[5] that the composite strength (Dupré) would be less than the bulk strength of indium. Such was *not* the case in any of the studies in which the interface could be considered as pure In–Al. Secondly, when the same interfacial tension is estimated by the Girifalco and Good[24] technique utilizing the same data, one finds the interfacial tension to be quite unrealistic, −9050 dynes/cm, which is doubly inconsistent. These points of inconsistency exist even though there seems to be a strong degree of overall self-consistency within the experimental data and even though a great deal of refinement could be expected in the absolute values of the data presented.

The variable which is almost always neglected in the investigation of low-surface energy systems, and more often than not in high-energy system investigations, is the presence of adsorbed gases which are forever present on all surfaces and interfaces in systems outside of ultrahigh vacuum, or those which are very specifically controlled. Although this omission may not be significant in certain low energy systems, this is not the case for those involving metals since the heat of sorption of most active gases on metals far exceeds the actual interfacial bonding energy which is under investigation. The consequence of this is that most wetting phenomena studied under impure conditions involve exchange reaction systems between the liquid and the atomically bound contaminant layers separating the liquid and the metal rather than a direct interaction study. Since a monolayer is formed by most gases on most metals, possibly with the exception of some of the platinum metals, in about 1 Langmuir ($= 10^{-6}$ torr sec), extreme care must be exercised to maintain the partial pressure of all reactive gas molecules at extremely low concentrations during the course of the experiment.

Even under the conditions of extreme atmosphere control, the purity of surfaces may still be in question due to the ability of certain very low bulk concentration components to selectively deposit on the surface by diffusion mechanisms. Through the careful selection of materials and extreme care in UHV control over the samples in this investigation, the probability of the existence of unknown contaminant layers was reduced to a minimum.

Although the presence of extraneous contamination may be cited in any experiment as a source of inconsistency, the authors feel that a number of other experiments presented in the past few years support the observed phenomena and suggest a direction for further intepretation of the behavior which is not dependent on the Young–Dupreé analytical approach. The generally accepted derivation of the Young equation from classical Gibbsian thermodynamics, as discussed by Johnson,[25] is directly dependent on two basic assumptions: (a) the liquid and solid must be immiscible with each other with respect to interfacial reactions; and (b) adsorption reactions and other chemical interactions, *e.g.*, diffusion of liquid along solid surface, etc., must also be neglected. In effect, the contact angle equation is only a statement of mechanical equilibrium and does not regard the two-component, liquid–solid, equilibrium at all. Metal interfaces consist of monatomic species interacting with nearest neighbors and their adjacent atoms with covalent and electrostatic atomic bonding forces, which are much more energetic than those observed between molecules in molecular crystals. Based on these electron-exchange interactions and those establishing the contact potential across the interface due to the equilibration of the Fermi levels, the weak dispersion forces often considered in molecular solids are of little consequence in a metallic interface. The heat of adsorption of cesium on tungsten being 64 kcal/mole[26] may be cited as an example of the driving force for interface formation. Due possibly to these interacting forces with their inherent low directionality in metallic systems and the forces resulting in surface impurity and/or self-diffusion, there is a reasonably high probability of atomic position exchange across the interface positions such that the interfacial region attains a finite continuous concentration gradient over some

(23) A. Bondi, *Chem. Rev.*, **52**, 417 (1953).
(24) L. A. Girifalco and R. J. Good, *J. Phys. Chem.*, **61**, 904 (1957).
(25) R. E. Johnson, Jr., *ibid.*, **63**, 1655 (1959).
(26) G. Ehrlich, *Ann. N. Y. Acad. Sci.*, **101**, 583 (1963).

normal distance, which is a function of the interacting species and temperature.

Such a model has been carefully considered by Cahn and Hilliard[27] in a general analysis of interfaces based on thermodynamics and regular solution theories, and many others in the recent literature.[28-30] The conclusions of the Cahn study indicated that interfaces with high chemical gradients would involve a zone through which the gradient varied continuously, the thickness of which was related to the interatomic forces between the atomic species and a reduced temperature which is based on the critical solution temperature of the species. Since all multicomponent metallic systems may be regarded as having a critical temperature, *e.g.*, a temperature at which complete miscibility exists, the term "immiscibility" becomes unnecessary.

In effect, the indium–aluminum interface may be considered as a region of continuous concentration gradient in both aluminum and indium over some finite distance, which is a function of temperature. Such a model would provide the necessary composite strength to warrant that which was observed in the In–Al experiment; however, metallographic analysis of the interface region of the indium–sapphire and electron micro-probe analysis of the interface of the In–Al systems did not indicate gross exchange within their respective limits of analysis. Other experiments indicate the nature of this interfacial zone in immiscible metal systems: for example, a low-energy electron diffraction investigation of copper epitaxy on pure surfaces of a (110) face of tungsten crystal by Taylor.[31] At temperatures below 200° copper was found to form a solution with tungsten to a depth of about *five* atomic layers and thereafter epitaxial layers of copper were formed above the interface. Exposure of this system to minute quantities of oxygen removed the dissolved copper from the tungsten layers and prevented further dissolution and epitaxy. Due to the preciseness of this investigation and the extreme value of a Cu–W critical temperature, one is led to suspect that the Cahn–Hilliard model is consistent with experiment. Other LEED epitaxial studies[32-34] of miscible metals and semimetals at temperatures well below the critical temperature also support this model. However, with the mounting evidence in support of the Cahn–Hilliard model, it becomes increasingly evident that the "immiscibility" assumption necessary for the derivation of the contact angle equation relative to metallic systems must be reconsidered. Certainly, a clear distinction must now be made between bulk immiscibility and surface phase immiscibility.

The Cahn–Hilliard model adequately explains the interface configuration and the relationship of this system to components of low miscibility; however, it does not explain the relationship of the line of three-phase equilibrium, *i.e.*, apex of contact angle in three dimensions, nor the tangent to liquid contour of the meridional section in this region. It appears evident that the substrate and sessile drop are not entirely independent of one another as assumed in the classical approach and that the observed values of contact angle and surface tension should be considered after the attainment of complete equilibrium as relative values. The availability of considerably more contact angle data between liquid and solid metals under ultraclean and various controlled contaminant conditions is required to clarify these relationships.

Conclusions

A technique was developed which permits the investigation of the interaction of a liquid metal in the form of a sessile drop and a substrate under conditions of extreme surface cleanliness in ultrahigh vacuum. The technique was further extended to investigate the effect of very small concentrations of gaseous contaminants on the spreading and adhesion behavior of the indium(l)–aluminum system.

The surface tension of liquid indium resting on an ultraclean surface of polycrystalline aluminum was found to be 658 dynes/cm (160°). The solidified sessile-drop substrate couple was found to exhibit a joint strength in tension in excess of the bulk strength of indium.

No detectable variation in surface tension or contact angle was observed for H_2 or N_2 contamination levels to 1 torr. The joint strength of this system was identical with the UHV case if the gas was admitted after the drop was established, whereas fracture occurred at extremely light loads when the gas was admitted prior to drop formation.

The presence of oxygen to levels greater than 10^{-6} torr caused the sessile drop to spread in a discontinuous manner. Joint strengths in excess of the bulk strength of indium were attributed to oxide–oxide interaction based on a UHV analysis of the indium drop on sapphire.

A general examination of these data, based on recent theoretical models, suggests that a reexamination of the

(27) J. W. Cahn and J. E. Hilliard, *J. Chem. Phys.*, **28**, 258 (1958).
(28) J. C. Eriksson, *Advan. Chem. Phys.*, **6**, 145 (1964).
(29) L. Ter-Minassian-Sarage, *J. Colloid Interface Sci.*, **22**, 311 (1966).
(30) P. L. de Bruyn, "Some Aspects of Classical Surface Thermo," in "Fundamental Phenomena in the Natural Sciences," L. J. Bonis, P. L. de Bruyn, and J. J. Duga, Ed., Phenum Press, New York, N. Y., 1966, p 1.
(31) N. J. Taylor, *Surface Sci.*, **4**, 161 (1966).
(32) P. J. Estrup and J. Morrison, *ibid.*, **2**, 465 (1964).
(33) J. J. Lander, *ibid.*, **1**, 125 (1964).
(34) J. J. Lander and J. Morrison, *ibid.*, **2**, 553 (1964).

applicability of classical thermodynamics to the interpretation of spreading and adhesion phenomena of high energy systems ought to be undertaken.

Acknowledgment. The authors gratefully acknowledge the Sandia Corporation for the support of this research program.

Mass Spectrometric Studies at High Temperatures. XXII. The Stabilities of Tantalum Pentafluoride and Tantalum Oxytrifluoride

by K. F. Zmbov and J. L. Margrave

Department of Chemistry, Rice University, Houston, Texas 77001 *(Received June 1, 1967)*

A mass spectrometer was used to study equilibria among vapor species produced by reactions between tantalum and MnF_2, between tantalum and mixtures of MnF_2 and MnO, and between Ta_2O_5 and MnF_2 in a Knudsen effusion cell. TaF_5 and Mn, MnF, and MnF_2 were identified in the Ta–MnF_2 system, while TaF_5, $TaOF_3$, and Mn, MnF, and MnF_2 were found in the Ta–MnO–MnF_2 and Ta_2O_5–MnF_2 systems. Heats of reactions involving these molecules were evaluated and used to calculate the heats of atomization of $TaF_5(g)$ and $TaOF_3(g)$.

Oxyfluorides of the transition metals are well known compounds, but their thermodynamic properties have been little investigated. Mass spectrometric electron impact studies of VOF_3[1,2] and CrO_2F_2[2,3] were made in an attempt to determine the bond strengths in these molecules, but straightforward conclusions were not obtained because of secondary processes in the ion source.

In the present work, a mass spectrometric study of high-temperature equilibria involving gaseous tantalum oxytrifluoride was utilized to determine the stability of this molecule. In an auxiliary experiment, the stability of tantalum pentafluoride was measured.

Experimental Section

The experiments were carried out on a single-focusing, 12-in. radius, 60° magnetic sector mass spectrometer[4] with a tantalum Knudsen cell containing appropriate reaction mixtures at high temperatures serving as the source of vapor species. Temperatures were measured by a Pt—Pt–10% Rh thermocouple, calibrated against a standard NBS thermocouple.

Results

Tantalum Pentafluoride. Equilibria involving TaF_5 were studied by heating a mixture of elemental tantalum and MnF_2 in the Knudsen cell. The ions showing a shutter effect and their appearance potentials are shown in Table I. The approximate appearance potentials of Mn-containing ions were close to those observed for the Mn–MnF_2 system[5] and indicated the presence of neutral Mn, MnF, and MnF_2 in the vapor.

Ta-containing ions were assumed to be produced by dissociative ionization of TaF_5 molecules, and this was confirmed by recording the mass spectrum of a pure TaF_5 sample.

Table I: Appearance Potentials of Ions over the MnF_2–Ta System

Ion	Appearance potential, eV	Neutral precursor
Mn^+	7.0 ± 0.5	Mn
MnF^+	8.1 ± 0.5	MnF
	14.5 ± 0.5	MnF_2
MnF_2^+	11.7 ± 0.5	MnF_2
Ta^+	39.5 ± 1.0	
TaF^+	36.5 ± 1.0	
TaF_2^+	27.3 ± 0.8	TaF_5
TaF_2^+	22.5 ± 0.5	
TaF_4^+	14.8 ± 0.3	

The equilibrium constant for the heterogeneous reaction (eq 1)

(1) R. Baldock and T. Sites, U. S. Atomic Energy Commission Report No. Y-759, Oak Ridge, Tenn., 1951.

(2) G. D. Flesch and H. J. Svec, *J. Amer. Chem. Soc.*, **81**, 178 (1959).

(3) H. J. Svec in "Mass Spectrometry," R. I. Reed, Ed., Academic Press Inc., New York, N. Y., 1965.

(4) G. D. Blue, J. W. Green, R. G. Bautista, and J. L. Margrave, *J. Phys. Chem.*, **67**, 877 (1963).

(5) R. A. Kent, T. C. Ehlert, and J. L. Margrave, *J. Amer. Chem. Soc.*, **86**, 5090 (1964).

$$2.5MnF_2(g) + Ta(s) = 2.5Mn(g) + TaF_5(g) \quad (1)$$

was determined at a series of temperatures from the ion-current measurements at low-electron voltages.

The ion currents, I^+, are related to the partial pressures, P, by the expression[6]

$$P = \left(\frac{I^+T}{s\sigma\gamma}\right)\left(\frac{A}{E - A}\right)$$

where A is the appearance potential of the ion; E is the electron energy at which the measurement is made; σ and γ are ionization cross sections and multiplier efficiency, respectively, for the ion; T is the absolute temperature; and s is the sensitivity of the mass spectrometer. The σ values used here were those given by Otvos and Stevenson,[7] while the secondary-electron efficiencies were estimated from the calibration data for a similar type of multiplier.[8] The instrumental sensitivity, s, was evaluated by evaporating silver at a fixed temperature. The results were used to calculate the heat of reaction (eq 1) by the third-law method, according to the equation

$$\Delta H^\circ_{298} = -RT \ln K_{eq} - T\Delta[(G^\circ_T - H^\circ_{298})/T] \quad (2)$$

Free-energy functions for Mn(g) and Ta(s) are tabulated by Stull and Sinke,[9] and those for $MnF_2(g)$ by Brewer, Somayajulu, and Brackett.[10]

Since no thermodynamic data are available for tantalum pentafluoride, an attempt was made to estimate the free-energy functions for this molecule by analogy with other pentahalides.[11] This yielded a value of -96 ± 4 cal deg^{-1} mol^{-1} for the free-energy function of $TaF_5(g)$ at 1200°K, and $\Delta(fef) = -4 \pm 5$ cal deg^{-1} mol^{-1} for the reaction (eq 1). From the measured equilibrium constants and the free-energy functions, one obtains 26 ± 6 kcal mol^{-1} for the enthalpy of reaction (eq 1) at 298°K. The uncertainty of ± 6 kcal mol^{-1} reflects the assumed uncertainty of ± 4 cal deg^{-1} mol^{-1} in the estimation of the free-energy functions of $TaF_5(g)$.

With the heat of atomization of $MnF_2(g)$, $\Delta H_a^0 = 220.1 \pm 5.5$ kcal mol^{-1},[5] and the heat of sublimation of Ta, $\Delta H_s^0(Ta) = 186.8$ kcal mol^{-1},[9] one obtains 711 ± 10 kcal mol^{-1} for the heat of atomization of TaF_5.

Appearance-potential measurements can also be used for approximate evaluation of the heat of atomization of TaF_5. If one considers the process

$$TaF_5(g) + e = Ta^+(g) + 5F(g) + 2e \quad (3)$$

the appearance potential of Ta^+ ion is given by I.P.(Ta) + $\Delta H_a^0[TaF_5(g)]$.

By using the experimental value as A.P.(Ta^+/TaF_5) = 39.5 ± 1 eV and the spectroscopic value for the ionization potential, I.P.(Ta) = 7.88 eV,[12] and assuming that no ion-pair process is involved, $\Delta H_a[TaF_5(g)] = 729 \pm 23$ kcal mol^{-1} is obtained in reasonable agreement, within the limits of experimental error, with the thermochemical value. For comparison, the heat of atomization of $TaF_5(g)$ as calculated from the available data on the heat of formation of $TaF_5(s)$, $\Delta H_f^\circ[TaF_5(s)] = -455.1 \pm 0.3$ kcal mol^{-1},[13] and the heat of sublimation,[14] $\Delta H_s^\circ(TaF_5) = 17.4$ kcal mol^{-1}, is $\Delta H_a[TaF_5(g)] = 719 \pm 2$ kcal mol^{-1} (31.2 eV). Thus the average bond energy in $TaF_5(g)$ is 144 ± 2 kcal mol^{-1}.

$TaOF_3$. Tantalum oxytrifluoride was produced both by heating a mixture of MnO and MnF_2 in a tantalum cell, and by treating MnF_2 with Ta_2O_5.

The mass spectrum and appearance potentials of ions from effusing vapors in the MnO–MnF_2–Ta system revealed the presence of neutral Mn, MnF, MnF_2, TaF_5, and $TaOF_3$ species. The appearance potentials of MnF_n^+ and TaF_n^+ ions were the same as those in the MnF_2–Ta system. Appearance potentials of ions from $TaOF_3$ are presented in Table II.

Table II: Mass Spectrum of $TaOF_3$ at 1200°K

Ion	Appearance potential, eV
Ta^+	...
TaO^+	...
$TaOF^+$	20.5 ± 0.5
$TaOF_2^+$	14.8 ± 0.3
$TaOF_3^+$	12.7 ± 0.3

The ion currents in the Mn–O–F–Ta system, measured at 5 eV above the thresholds and converted into absolute pressures of the corresponding gaseous components by the procedure already described for MnF_2–Ta system, were used to calculate the equilibrium constants and heat for the reaction

$$MnO(s) + TaF_5(g) = MnF_2(g) + TaOF_3(g) \quad (4)$$

Thermodynamic data for MnO(s) and $MnF_2(g)$ are available in the literature.[10,15] The free-energy function for $TaF_5(g)$ at 1200°K, -96 ± 4 cal deg^{-1}

(6) R. Collin and J. Drowart, *J. Chem. Phys.*, **37**, 1120 (1962).

(7) J. W. Otvos and D. P. Stevenson, *J. Amer. Chem. Soc.*, **78**, 546 (1956).

(8) M. G. Inghram, R. J. Hayden, and D. C. Hess, National Bureau of Standards Circular 522, U. S. Government Printing Office, Washington, D. C., 1953, p 257.

(9) D. R. Stull and G. C. Sinke, *Advan. Chem. Ser.*, **18** (1956).

(10) L. Brewer, R. G. Somayajulu, and E. Brackett, *Chem. Rev.*, **63**, 111 (1963).

(11) "JANAF Thermochemical Tables," D. R. Stull, Ed., Clearinghouse for Federal Scientific and Technical Information, Springfield, Va., Aug 1965, Document No. PB-168, 370.

(12) C. E. Moore, National Bureau of Standards Circular 467, Vol. 3, U. S. Government Printing Office, Washington, D. C., 1958.

(13) E. Greenberg, C. A. Natke, and W. N. Hubbard, *J. Phys. Chem.*, **69**, 2089 (1965).

(14) R. C. Feber, U. S. AEC Report LA-3164, Los Alamos Scientific Laboratory, Los Alamos, N. M., 1964, p 135.

(15) K. K. Kelley, Bureau of Mines Bulletin No. 584, 1962, p 121.

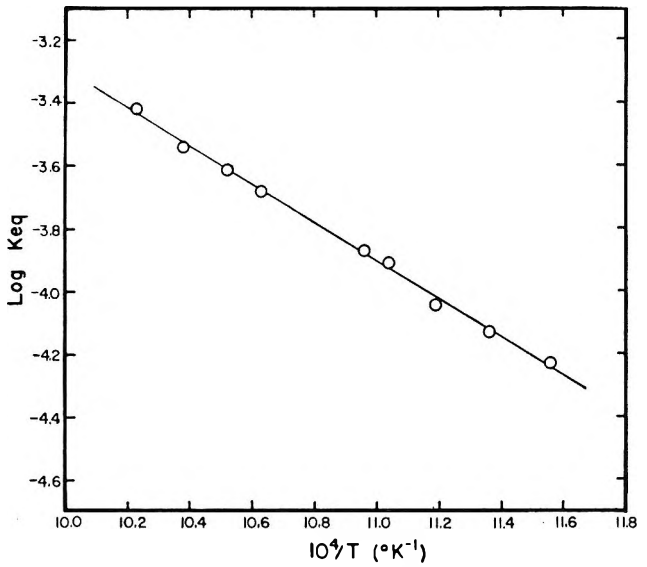

Figure 1. Second-law plot of the equilibrium constants for the reaction $^1/_5Ta_2O_5(s) + {}^3/_5TaF_5(g) = TaOF_3(g)$.

mol^{-1}, estimated previously, and a value of -99 ± 5 cal deg^{-1} mol^{-1} estimated for the free energy function of $TaOF_3$ by analogy with other oxyhalide molecules[11] were used in this calculation. This procedure yielded $\Delta H°_{298} = 75 \pm 10$ kcal mol^{-1} for the heat of reaction (eq 4). The rather large uncertainty of ± 10 kcal mol^{-1} attached is to allow for the errors in the estimation of the free-energy functions of TaF_5 and $TaOF_3$.

By using the heat of reaction (eq 4) and the heat of atomization of $TaF_5(g)$, $\Delta H_a° = 719 \pm 2$ kcal mol^{-1},[14] as well as the data for $\Delta H_f°(MnO) = -92.5$ kcal mol^{-1},[11] $\Delta H_{subl}(Mn) = 67.0$ kcal mol^{-1},[9] and $D°(O_2) = 118$ kcal mol^{-1},[11] one obtains 642 ± 10 kcal mol^{-1} for the heat of atomization of $TaOF_3(g)$.

The vapor over the Ta_2O_5–MnF_2 system had the same composition as that in the MnO–MnF_2–Ta system. The reaction to be considered is

$$^1/_5Ta_2O_5(s) + {}^3/_5TaF_5(g) = TaOF_3(g) \qquad (5)$$

Both second- and third-law methods were employed to calculate the heat of reaction. The second-law plot of log K *vs.* $1/T$ is presented in Figure 1. The least-square analysis of the data gave $\Delta H°_{920°K} = 28.7 \pm 1.1$ kcal mol^{-1}. With heat-content data for $Ta_2O_5(s)$[12] and estimated values for $TaF_5(g)$ and $TaOF_3(g)$, one calculates $\Delta H°_{298} = 31 \pm 5$ kcal mol^{-1}.

Third-law analysis of the data in Table III gave an average value of 32 kcal mole^{-1} for the heat of reaction[5] at 298°K. The absolute uncertainty is estimated to be ± 8 kcal mol^{-1}. Thus, this is reasonable agreement between the second- and third-law heats of the reaction (eq 5).

Table III: Equilibrium Constants and Heat for the Reaction $^1/_5Ta_2O_5(s) + {}^3/_5TaF_5(g) = TaOF_3(g)$

Temp, °K	Log K_{eq}	$-\Delta\left(\frac{G° - H°_{298}}{T}\right)$, cal deg^{-1} mol^{-1}	$\Delta H°_{298}$, kcal mol^{-1}
977	−3.42	17	32
963	−3.54	17	32
951	−3.61	17	32
941	−3.68	17	32
923	−3.80	17	32
912	−3.87	18	32
894	−4.04	18	32
880	−4.13	18	32
865	−4.23	18	32
906	−3.91	18	32
		Avg	32

The heat of atomization of $TaOF_3(g)$ as calculated from the heat for reaction (eq 5), the known heat of formation of $Ta_2O_5(s)$,[16] and $\Delta H_s(Ta)$, $D(O_2)$, and $\Delta H_a(TaF_5)$, as mentioned above, is $\Delta H_a[TaOF_3(g)] = 630 \pm 16$ kcal mol^{-1}. From the two measurements, one concludes that $\Delta H_a[TaOF_3(g)] = 638 \pm 10$ kcal mol^{-1}. If there are three "average" Ta–F bonds of 144 ± 2 kcal mol^{-1} each, then the Ta–O bond energy in $TaOF_3$ is 204 ± 10 kcal mol^{-1}. Previous studies have shown D(Ta–O) = 193 ± 5 kcal mol^{-1}.[17]

One can thus derive atomization energies for $TaOF_2$-(g) and TaOF(g) as 496 ± 10 and 352 ± 10 kcal mol^{-1}, respectively, and the thermodynamic data as presented in Table IV.

Table IV: Heats of Formation of Gaseous Ta–F and Ta–O–F Species

Molecule	$\Delta H_f°$, kcal mol^{-1}
TaF_5	-437.7 ± 1.0
TaF_4	-313 ± 10
TaF_3	-188 ± 10
TaF_2	-63 ± 10
TaF	$+62 \pm 10$
$TaOF_3$	-337 ± 10
$TaOF_2$	-212 ± 10
TaOF	-87 ± 10

Acknowledgment. This work was supported by the National Aeronautics and Space Administration.

(16) C. E. Wicks and F. E. Block, U. S. Bureau of Mines Bulletin 605, U. S. Government Printing Office, Washington, D. C., 1963.

(17) M. G. Inghram, W. A. Chupka, and J. Berkowitz, *J. Chem. Phys.*, **27**, 569 (1957).

Vaporization Studies on Arsenic[1]

by C. C. Herrick and Roy C. Feber

Los Alamos Scientific Laboratory, University of California, Los Alamos, New Mexico 87544 *(Received June 12, 1967)*

Angular-displacement studies of the vaporization of solid arsenic have been made to 700°K using cylindrical effusion cells, free-vaporizing surfaces, and an effusion cell fabricated from sintered arsenic powder. An automated recording system was used. Arsenic samples were prepared and handled in such a manner as to minimize the effect of impurities. Effusion pressures did not vary as the orifice diameter ranged from 0.005 to 0.040 in. From the effusion measurements, the heat of sublimation of solid arsenic to $As_4(g)$ at 298.15°K was found to be 38.54 ± 0.10 kcal/mol of $As_4(g)$, whereas the free-vaporization measurements gave 44.23 ± 0.3 kcal/mol. For the calculation of these quantities, previously available thermodynamic functions for As(s) and $As_4(g)$ were replaced by recomputed values. A comparison of pressures resulting from these measurements suggests a temperature dependence of the condensation coefficient, which was confirmed by the angular displacement measurements on the arsenic effusion cell.

I. Introduction

A study of the vapor pressure and vaporization rates of arsenic is desirable for at least two reasons. First, of course, a knowledge of the equilibrium vapor pressure and the thermodynamic quantities derived therefrom is of interest. These quantities are not well established. Also, such a study can add to an understanding of the extent to which complex vapor species can influence simple condensation and evaporation processes. Over the range of temperatures accessible to the usual experimental techniques as applied to this system, the vapor is essentially all $As_4(g)$,[2] and a very small condensation coefficient has been reported.[3] Therefore, kinetic considerations of the evaporation and condensation processes become important. The discussions by Stranski and coworkers[4,5] of situations of this sort are especially useful.

Several methods have been used to measure the vapor pressure of arsenic. The data have been reviewed by Stull and Sinke[6] and by Nesmeyanov.[2] Stull and Sinke estimated the thermodynamic functions for $As_4(g)$ necessary for their computation of the thermodynamic properties of the system. Nesmeyanov gave an equation to represent his selected vapor pressures as a function of temperature. Vapor pressures tabulated as "best" in the two reviews are very similar. The vapor-density measurements of Preuner and Brockmöller[7] showed that saturated arsenic vapor contains essentially all As_4 molecules up to 500°, and that dissociation of As_4 can be disregarded up to 800°. From an examination of the vapor flux from a Langmuir-type experiment in a mass spectrometer (530–620°K), Kane and Reynolds[8] agreed that the vapor is predominantly As_4. Other mass spectrometric studies leading to the same conclusion include those of Drowart and Goldfinger,[9] Westmore, Mann, and Tickner,[10] and Gutbier.[11] Ruff and Bergdahl[12] determined the vapor pressure by a boiling point method, and later Ruff and Mugdan[13] repeated the experiments. The remainder of the data were obtained by static methods, with the exception of the more recent measurements of Nesmeyanov,[2] and Brewer and Kane.[3] These authors used versions of the Knudsen method. Nesmeyanov rejected his data in his selection of the best values of the vapor pressure, and Brewer and Kane did not list their experimental results. Rosenblatt[14] used the experiments of Brewer and Kane to formulate meaningful suggestions for the interpretation of Knudsen measurements on porous materials.

Klemm, *et al.*,[15,16] reported anomalies in the temperature dependencies of the crystallographic axes, the enthalpy, the diamagnetism, and the electrical resistivity of crystalline arsenic at about 500°K. These observations were not confirmed by Taylor, Bennett,

(1) Work performed under the auspices of the United States Atomic Energy Commission.

(2) A. N. Nesmeyanov, "Vapor Pressure of the Chemical Elements," Elsevier Publishing Co., New York, N. Y., 1963.

(3) L. Brewer and J. S. Kane, *J. Phys. Chem.*, **59**, 105 (1955).

(4) I. N. Stranski and G. Wolff, *Research*, **4**, 15 (1951).

(5) W. Hirschwald and I. N. Stranski, "Condensation and Evaporation of Solids," E. Rutner, P. Goldfinger, and J. P. Hirth, Ed., Gordon and Breach, New York, N. Y., 1964.

(6) D. R. Stull and G. C. Sinke, "Thermodynamic Properties of the Elements," Advances in Chemistry Series, No. 18, American Chemical Society, Washington, D. C., 1956.

(7) G. Preuner and I. Brockmöller, *Z. Phys. Chem.* (Leipzeig), **81**, 129 (1912).

(8) J. S. Kane and J. H. Reynolds, *J. Chem. Phys.*, **25**, 342 (1956).

(9) J. Drowart and P. Goldfinger, *J. Chim. Phys.*, **55**, 721 (1958).

(10) J. B. Westmore, K. H. Mann, and A. W. Tickner, *J. Phys. Chem.*, **68**, 606 (1964).

(11) H. B. Gutbier, *Z. Naturforsch.*, **14a**, 32 (1959).

(12) O. Ruff and B. Bergdahl, *Z. Anorg. Chem.*, **106**, 76 (1919).

(13) O. Ruff and S. Mugdan, *ibid.*, **117**, 147 (1921).

(14) G. Rosenblatt, *J. Electrochem. Soc.*, **110**, 563 (1963).

(15) W. Klemm, H. Spitzer, and H. Niermann, *Agnew. Chem.*, **72**, 985 (1963).

(16) W. Klemm and H. Niermann, *Agnew. Chem. Intern. Ed.*, **2**, 523 (1963).

and Heyding.[17] Similar problems arise, although on a more complicated scale, in studies on graphite.

The present work was undertaken because the relatively few measurements of the vapor pressure were not in good agreement. Applying the third-law check to the vapor pressures selected in the two reviews mentioned above gave very temperature dependent heats of sublimation at 298.15°K. The two most obvious potential sources of difficulty are the presence of arsenic oxide as an impurity and the impossibility of attaining near-equilibrium conditions in an effusion system due to the low condensation coefficient. Therefore, in addition to special care to remove oxide impurities from the effusion-cell samples, confirmation was sought for the magnitude of the condensation coefficient by free-vaporization studies. From measurements of pressures using effusion cells with orifice diameters ranging from 0.005 to 0.040 in., the possible effect of a low condensation coefficient on the determination of vapor pressures by an effusion technique could be studied.

Measurements of the effusion fluxes were made in CaF_2, Y_2O_3, and Al_2O_3 cylindrical cells. The free-vaporization studies used TaC-coated graphite holders. A continuously monitoring device was used in conjunction with an electronic computer to evaluate these angular-displacement studies. Condensation-coefficient data were obtained from the results of the effusion and free-vaporization experiments and from an effusion cell made of sintered arsenic powder.

II. Experimental Section

Materials. Arsenic, stated to be 99.999% pure with respect to total metallic impurities, was obtained in lump, crystalline, and powder forms. The first two forms were received in 25-g lots, and the powder was received in a 100-g lot. All were sealed under vacuum. The powder, on analysis, was found to contain 8% by weight of oxygen. Before using the powder for the effusion measurements, oxygen was removed by a two-step process. Samples of the powder were mixed with zirconium powder which had been previously heated to 1000° under vacuum, $\sim 10^{-6}$ torr. The mixture was sealed in a quartz cylinder 3 in. long and 2 in. in diameter which was provided along its axis with a 10-mm tube extending from within 0.25 in. of the cylinder to 6 in. below its base. Arsenic was distilled from the mixture at about 600°, and the distilled fraction was removed by sealing off the condensate tube. Further purification was accomplished by repeated sublimations in a split-tube furnace. The number of such sublimations depended on the amount of waxlike, light-yellow flakes of As_2O_3 which appeared on quenching. X-Ray analysis of the flakes showed them to be primarily As_2O_3 with lesser amounts of an unidentified cubic phase. Because one section of the furnace was held at about 650° and the other section was some 100° cooler, the cubic phase may have been one of the solid arsenic phases reported to form on quenching from the vapor phase.

The crystalline arsenic was subjected only to sublimation in the gradient furnace. One sublimation was usually sufficient for this material.

For the free-vaporization experiments, 0.120 in. thick slices were initially cut from the lump material with a small diamond wheel. The slices were subsequently ground to 0.060-in. thickness on silicon carbide paper. Immediately prior to an experiment, any surface oxide present was removed with an S. S. White dental unit.

The arsenic effusion cell was fabricated from as-received arsenic by first pressing a 1.5 × 1.5-in. slug at 340° under 15,000 lb of pressure in a graphite die. The desired internal cell dimensions were then obtained by a combination of electrical and mechanical machining.

Crucibles and Holders. Crucibles for this work, illustrated in Figure 1, were slip cast from Al_2O_3, Y_2O_3, and CaF_2 powders of at least 99.9% purity. Small orifices were drilled in the "green" state. The larger orifices were made with a diamond drill after firing. The oxide crucibles were fired in air at 1750° for 16 hr, and the fluoride crucibles were fired at 960° for 4 hr. Lids were ground and lapped to fit.

Holders for the free-vaporization studies, shown in Figure 2, were fabricated from high-density graphite. The center section, mask, and screws were coated to a depth of 0.002 in. with TaC and heat treated to 1900°.[18]

Furnace–Torsion System. The furnace–torsion system has been described in an earlier report.[19]

Data-Taking System. Because a complete description of the continuously monitoring data-acquisition system has also been given elsewhere,[20] only a brief outline follows.

The system is based on the properties of the ellipse. The mirror, sensing the angular displacement due to the vaporizing flux, is suspended inside the vacuum system at one focal point. A unifaced mirror rotating at 1800 rpm is located outside the vacuum system at the second focal point. A light beam reflected from the suspended mirror defines an angle θ, which is a measure of the angular position of interest. The beam is then reflected from an elliptical surface and, because of the properties of an ellipse, onto the rotating mirror at the second focal point and finally onto a photodiode. A second angle, α, the one actually measured, is defined as the angle between a normal to the rotating mirror when that mirror sees the beam reflected from the ellipse and a reference line established

(17) J. B. Taylor, S. L. Bennett, and R. D. Heyding, *J. Phys. Chem. Solids*, **26**, 69 (1965).

(18) M. Bowman, personal communication, Los Alamos Scientific Laboratory, 1966.

(19) C. C. Herrick, *Trans. Met. Soc. AIME*, **230**, 1439 (1964).

(20) D. Peters and C. C. Herrick, *Rev. Sci. Instrum.*, in print.

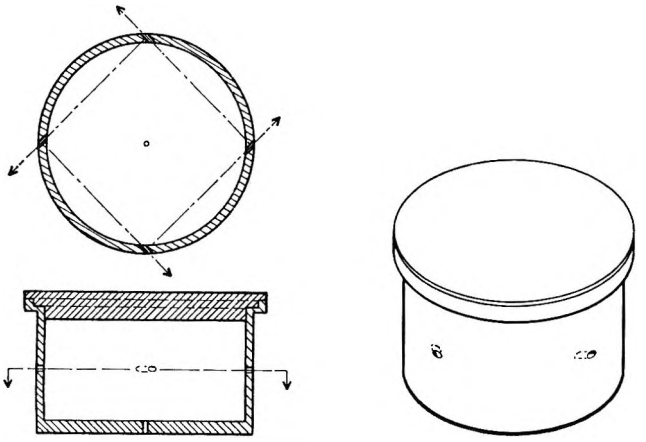

Figure 1. Ceramic effusion cells.

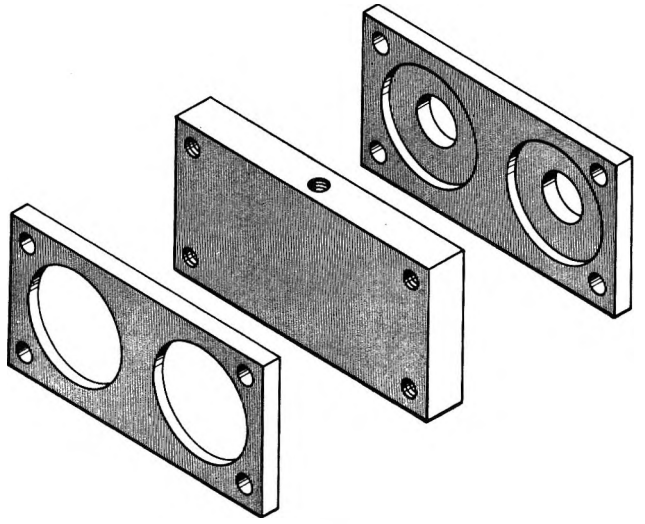

Figure 2. Free-vaporization holders.

by the reflection of a fixed beam from the rotating mirror onto a second photodiode. The magnitude of α is proportional to the time between the two pulses, which is measured by an electric counter. An integrating circuit is used to produce a voltage to operate a recorder and a digital voltmeter. The digital voltmeter readings are also punched on paper tape. The thermocouple voltage is simultaneously monitored by a recorder and punched on the tape. Records are made on the paper tape every 2 min.

A measured angle, α_i, is related to the corresponding angular position, θ_i, by the relation

$$\theta_i = \arctan\left[-\sin 2\alpha_i/(k_1 + k_2 \cos 2\alpha_i)\right] \quad (1)$$

where $k_1 = 2ac/b$, $k_2 = c^2a^2/b^2$, a = semimajor axis = 10.250 in., b = semiminor axis = 7.125 in., $c = (a^2 - b^2)^{1/2}$.

Procedure. Cells for the effusion experiments were cleaned before adding the samples by heating to 900° under vacuum, 10^{-7} torr. They were calibrated by measuring the vapor pressure of distilled zinc supplied by the National Bureau of Standards as a freezing point standard. For each calibration, about 5 g of zinc was cut into small chips and cleaned with a magnet while in a glove box filled with nitrogen. After was added to the cell, the lid was positioned and the cell was transferred to the torsion system. During this period, the apparatus was flushed with nitrogen gas first passed through a liquid nitrogen trap. The torsion system was then evacuated, heated to about 200°, and allowed to stand overnight to permit cell oscillations to cease.

A sequence of data points was obtained with increasing or decreasing temperatures over the interval 425–700°K. About 4–8 hr was required to cover this temperature range. An analogous procedure was used for the arsenic measurements.

The proxy thermocouple, which was shaped in the form of a fish hook, was calibrated by replacing the effusion cell with a dummy cell containing a standard Pt–Pt–10% Rh thermocouple previously calibrated against the freezing points of Sn, Zn, Al, and Ag.

Furnace temperatures were on occasion increased beyond the experimental range to clean out the cells and redistribute condensed material to a cold zone of the furnace tube.

III. Calculations

Because no effect of orifice size was detected in the torsion–effusion measurements, the process studied is assumed to be

$$4\mathrm{As(s,}\ T,\ p) \underset{k_{-1}}{\overset{k_1}{\rightleftharpoons}} \mathrm{As_4(g,}\ T,\ p) \quad (2)$$

The process taking place in the free-vaporization studies was taken to be

$$4\mathrm{As(s,}\ T,\ 10^{-7}\ \mathrm{torr}) \xrightarrow{k_1} \mathrm{As_4(g,}\ T,\ 10^{-7}\ \mathrm{torr}) \quad (3)$$

We thus assumed that the primary subliming species in eq 3 is the tetramer. Data obtained from the studies of these processes were treated in two steps. First, data from the paper tapes were transferred to magnetic tape. As a part of this step, the data were plotted on an oscilloscope and bad points due to scanner failure in reading the paper tapes or due to worn hammers on the paper punch were given a weight of zero with a pen light. A modified version of a computer program for a nonlinear least-squares method[21] (hereafter referred to as a nonlinear analysis) was used to evaluate the data in its natural plane.

The equation of Volmer describes the dependence of the pressure on the angular position.

$$P_i = \frac{2D}{\sum_j a_j r_j f_j}(\theta_i - \theta_0) \quad (4)$$

(21) R. Moore and R. Zeigler, Los Alamos Scientific Laboratory Report LA-2367, Los Alamos, N. M., 1959.

where $\theta_0 = \theta_i$ when the vaporizing force is negligible, D = torsion constant of the wire = 2.899 dyn cm, a_j = geometrical area of the j orifice, r_j = lever arm of the j orifice, f_j = transmittance of the j orifice.

If it is assumed that the cell geometry is not affected by temperature over the experimental range, eq 4 can be written

$$P_i = K'(\theta_i - \theta_0) \quad (5)$$

From thermodynamics the pressure is given by

$$P_i = \exp(-\Delta H_{s,298}/RT) \exp(\Delta(\text{fef})/R) \quad (6)$$

where $\Delta H_{s,298}$ is the heat of sublimation at 298.15°K, and Δ(fef) is the difference between a polynomial representing the free energy function of the products and one representing that of the reactants over the temperature range of the experiments. By combining eq 5 and 6 and substituting for θ_i from eq 1, the following working relation is obtained.

$$\theta_i = \arctan[-\sin 2\alpha_i/(k_1 + k_2 \cos 2\alpha_i)] = K[\exp(-\Delta H_{s,298}/RT + \Delta(\text{fef})/R)] + \theta_0 \quad (7)$$

This relation contains the three parameters: K, $\Delta H_s°_{298}$, and θ_0, and the two independent variables, temperature and Δ(fef). In principle, it should be possible to evaluate all three parameters from the effusion data for arsenic alone with a nonlinear analysis. However, to allow an unambiguous interpretation of data in a potentially nonequilibrium situation, the parameter K was determined for each cell by calibration with zinc. This, of course, is possible because K is a function only of the cell and its suspension. Calibration with zinc is appropriate because its vapor pressure is well established and measurements can be made over the same temperature range as that used with arsenic.

The parameter K for the apparatus used in the free-vaporization studies was determined by evaluating D with a known moment of inertia and measuring the orifice geometrical areas and lever arms. The area of the sample was taken to be the geometrical area, and f was assumed to be unity.

The derivation of thermodynamic data from the experimental observations could proceed by several alternate techniques.

1. Either the angular-position differences, $\theta_i - \theta_0$, or their vapor pressure equivalents as determined by calibration of the apparatus may be transformed to the logarithmic plane and plotted against reciprocal temperature. From the slope at each point a second-law heat of sublimation at temperature may be determined, although over moderate temperature ranges which do not include any phase changes in the condensed phase the plot is commonly a straight line within the precision of the measurements. If pressures are used and heat capacity equations for the reactants and products are available, a Σ calculation may be used to produce a straight-line plot for those systems for which a plot of log p *vs.* $1/T$ is curved.

2. If absolute entropies are known and the experimental data expressed as pressures are transformed to the logarithmic plane, two additional procedures can be used.

(a) With appropriate free-energy functions, values of $\Delta H_s°_{298}$ may be calculated for each experimental point and an average taken of all of these values. This procedure is usually referred to as the third-law method. If only a few experimental points with relatively large scatter are available, it may be the only practicable procedure. The third-law method may be expressed as

$$-R \ln p + \Delta(\text{fef}) = \Delta H_{s,298}/T \quad (8)$$

Thus the method may be regarded as a plot of the left-hand side of eq 8 *vs.* $1/T$, and the individual values of $\Delta H_{s,298}$ as slopes of lines between individual experimental points and the origin. This constraint limits the sensitivity of the method as an internal check on the reliability of the experimental data. Such a check is frequently sought from the agreement between third-law values from various investigations or from the agreement between second- and third-law values of a particular investigation.

(b) Another procedure, which has been called the "slope–third-law" method,[19] may be used to provide an internal check of data reliability. This procedure, which removes the constraint noted above in the usual third-law method, is formulated by assuming that the uncertainty of an observed pressure may be expressed as

$$p_{\text{equil}} = z p_{\text{calcd}} \quad (9)$$

In the logarithmic plane, eq 6 then becomes

$$-R \ln p_{\text{calcd}} + \Delta(\text{fef}) = \Delta H_{s,298}/T + R \ln z \quad (10)$$

A single value of $\Delta H_{s,298}$ will be obtained from the slope of a plot of the left-hand side of eq 10 *vs.* $1/T$. If the free-energy functions are reliable, a constant deviation of z from unity will indicate a constant systematic error in p_{calcd}. In such a situation $\Delta H_{s,298}$ will correspond to a second-law heat and $R \ln z$ will be the difference between calculated and observed entropies of vaporization. If $R \ln z$ is 0, second- and third-law values are identical. The value $\Delta H_s°_{298}$ Zn(s) = 31.204 kcal/mol was derived from a slope–third-law analysis of vapor pressure data in the literature. The free-energy functions used were essentially the same as those tabulated by Hultgren, *et al.*[21]

3. A nonlinear regression analysis[21-23] may be used

(22) T. G. Strand, D. A. Kohl, and R. A. Bonham, *J. Chem. Phys.*, 39, 1307 (1963).

(23) N. R. Draper and H. Smith, "Applied Regression Analysis," John Wiley and Sons Inc., New York, N. Y., 1966, Chapter 10.

to fit observed angular positions in their natural plane to the relation defined by eq 7. As noted above, one has the option of deriving the three parameters: K, $\Delta H_{s,298}$, and θ_0, or previously evaluating K by calibration with a material of known vapor pressure. It should be noted that in the other procedures the selection of θ_0 is likely to be somewhat subjective, but it is maintained as a parameter in the nonlinear analysis.

We chose to apply a nonlinear analysis to the vapor pressure data for arsenic. The choice was dictated by the fact that the uncertainty in the experimental observables, θ_i is additive, whereas if the observables had been transformed to the logarithmic plane, the uncertainties would have been assumed to be multiplicative. The two approaches may or may not give the same values for the thermodynamic parameters, depending on how well the data fit the assumed functional representation. McWilliams, Furchner, and Richmond[24] have illustrated some situations in which the distinction is not trivial. Because in the present situation the measurement extends to relatively small values of $\theta_i - \theta_0$, the data are most appropriately treated by insisting on the additivity of uncertainties.

Thus for both the effusion and free-vaporization data, two parameters were optimized by the nonlinear analysis. Error analysis was as described by Moore and Zeigler.[21]

The thermodynamic functions for solid arsenic given in Table I are slightly different from those given by Stull and Sinke[6] and Hultgren, *et al.*[25] Most of the difference is due to the value $S°_{298}$As(s) = 8.534 eu calculated from the low-temperature heat-capacity data of Anderson (57 - 291°K)[26] and the recent data of Nogteva, Paukov, and Strelkov (13.9–289°K).[27] In addition to the older data, thermodynamic functions for the solid above 298.15°K take into account the high-temperature heat-content data of Klemm, Spitzer, and Niermann.[15]

The regular tetrahedral structure of As_4(g) has been recently confirmed by the gas electron-diffraction studies of Morino, Ukaji, and Ito,[28] who have given a more accurate value of the interatomic distance than previously available. From their values of the mean amplitude and the anharmonicity parameter, they estimated vibrational frequencies. The estimated frequencies have been used to calculate the thermodynamic functions for As_4(g) given in Table II. The uncertainty in free-energy functions corresponding to the uncertainties in the estimated frequencies is ±1.3 eu. The calculated value of $S°_{298}As_4$(g) is some 3.8 eu greater than that tabulated by Stull and Sinke[6] and

Table I: Thermodynamic Functions for Solid Arsenic[a]

Temp, °K	$-(G°_T - H°_{298.15})/T$, cal/gfw/deg	$H°_T - H°_{298.15}$, kcal gfw	$S°_T$, cal/gfw deg	$C°_p$, cal/gfw deg
298.15	8.534	0.000	8.534	5.892
300.00	8.534	0.011	8.571	5.896
310.00	8.539	0.070	8.764	5.930
320.00	8.549	0.129	8.953	5.956
330.00	8.564	0.189	9.137	5.975
340.00	8.583	0.249	9.315	5.989
350.00	8.607	0.309	9.489	6.002
400.00	8.768	0.611	10.295	6.068
450.00	8.979	0.916	11.013	6.135
500.00	9.215	1.224	11.664	6.201
550.00	9.465	1.536	12.258	6.268
600.00	9.721	1.851	12.806	6.334
650.00	9.978	2.169	13.316	6.400
700.00	10.234	2.491	13.792	6.466
750.00	10.486	2.816	14.240	6.533
800.00	10.734	3.144	14.664	6.599
850.00	10.977	3.476	15.067	6.666
900.00	11.215	3.811	15.449	6.732
950.00	11.448	4.149	15.815	6.798
1000.00	11.675	4.491	16.166	6.865
1050.00	11.897	4.835	16.502	6.931
1090.00	12.071	5.114	16.762	6.984

[a] $H°_{298.15} - H°_0$ = 1.223 cal/gfw.

Table II: Thermodynamic Functions for As_4(g)[a]

Temp, °K	$-(G°_T - H°_{298.15})/T$, cal/gfw deg	$H°_T - H°_{298.15}$, kcal/gfw	$S°_T$, cal/gfw deg	$C°_p$, cal/gfw deg
298.15	78.834	0.000	78.834	18.546
300.00	78.834	0.034	78.948	18.561
350.00	79.061	0.971	81.836	18.887
400.00	79.570	1.921	84.373	19.107
450.00	80.231	2.881	86.633	19.261
500.00	80.975	3.847	88.668	19.374
550.00	81.760	4.818	90.519	19.458
600.00	82.561	5.792	92.215	19.522
650.00	83.365	6.770	93.780	19.573
700.00	84.161	7.749	95.232	19.614
750.00	84.945	8.731	96.586	19.646
800.00	85.713	9.714	97.855	19.673
850.00	86.462	10.698	99.048	19.696
900.00	87.193	11.683	100.175	19.715
950.00	87.905	12.670	101.241	19.730
1000.00	88.597	13.656	102.253	19.744
1050.00	89.270	14.644	103.217	19.756
1100.00	89.926	15.632	104.136	19.766
1150.00	90.563	16.620	105.015	19.775
1200.00	91.182	17.609	105.857	19.783
1250.00	91.786	18.599	106.665	19.790
1300.00	92.373	19.588	107.441	19.796

[a] $H°_{298.15} - H°_0$ = 4.256 kcal/gfw.

(24) P. McWilliams, *et al.*, *Health Phys.*, **10**, 817 (1964).

(25) R. Hultgren, *et al.*, "Selected Values of Thermodynamic Properties of Metals and Alloys, John Wiley and Sons, Inc., New York, N. Y., 1963, and subsequent loose leaf revisions and additions.

(26) C. T. Anderson, *J. Amer. Chem. Soc.*, **52**, 2296 (1930).

(27) V. V. Nogteva, I. E. Paukov, and P. G. Strelkov, *Soviet Phys.-Solid State*, **7**, 1884 (1965).

(28) Y. Morino, T. Ukaji, and T. Ito, *Bull. Chem. Soc. Jap.*, **39**, 71 (1966).

Table III: Experimental Data for Arsenic

Run no.	Crucible orifices, in., and material	$\Delta H_{s,298}$ nonlinear	$\Delta H_{s,298}$ third law	θ_0, radians	K (torsion constant)	ΔT, °K	No. of data points[a]	Weighted variance	Unweighted sum of squares of deviations
1	0.020, Y_2O_3	38,516 ± 2	38,409	−0.177674 ± 2.44 × 10^{-4}	538	525–645[b]	827	1.991 × 10^{-5}	1.503 × 10^{-2}
2	0.20, Y_2O_3	38,555 ± 2	38,489	−0.174706 ± 1.61 × 10^{-4}	538	525–643	422	5.125 × 10^{-6}	2.255 × 10^{-3}
3	0.20, Y_2O_3	38,620 ± 4	38,648	−0.114155 ± 2.85 × 10^{-4}	538	635–475	298	8.495 × 10^{-6}	2.225 × 10^{-3}
4	0.20, Y_2O_3	38,536 ± 6	38,216	−0.12229 ± 5.97 × 10^{-4}	538	526–636	369	6.091 × 10^{-5}	2.235 × 10^{-2}
5	0.20, Y_2O_3	38,482 ± 3	38,267	−0.18138 ± 4.14 × 10^{-4}	538	640–526	316	2.156 × 10^{-5}	6.770 × 10^{-3}
6	0.20, Y_2O_3	38,646 ± 4	38,634	−0.18172 ± 1.14 × 10^{-4}	538	614–573	494	1.401 × 10^{-6}	6.893 × 10^{-4}
7	0.20, Y_2O_3	38,562 ± 2	38,564	−0.17336 ± 1.74 × 10^{-3}		586–629[b]	703	1.633 × 10^{-6}	1.145 × 10^{-3}
8	0.020, Al_2O_3	38,454 ± 14	38,533	0.13976 ± 2.12 × 10^{-3}	−518	529–648	219	3.548 × 10^{-4}	7.699 × 10^{-2}
9	0.005, CaF_2	38,284 ± 13	37,745	−0.36778 ± 1.94 × 10^{-3}	45	528–714	248	4.727 × 10^{-4}	1.163 × 10^{-1}
10	0.005, CaF_2	38,382 ± 11	37,876	−0.45713 ± 1.61 × 10^{-3}	45	522–656	102	1.464 × 10^{-6}	1.464 × 10^{-4}
11	0.040, Y_2O_3	38,741 ± 11	38,906	−0.37125 ± 1.22 × 10^{-3}	1085	552–620[b]	766	1.397 × 10^{-4}	1.067 × 10^{-1}
12	0.04, Y_2O_3	38,382 ± 8	38,151	−0.46250 ± 1.89 × 10^{-3}	1085	539–645	317	5.216 × 10^{-4}	1.643 × 10^{-1}
13	0.04, Y_2O_3	37,891 ± 58	37,839	−0.39231 ± 6.75 × 10^{-4}	1085	525–611	605	9.84 × 10^{-5}	5.934 × 10^{-2}
		38,465[c]	38,321[c]				5686[d]		

[a] Data points taken every 2 min. [b] Data taken with increasing and decreasing temperature. [c] Average value. [d] Total number of points.

accounts for about one-half of the difference between the standard heat of sublimation reported here and that given by Stull and Sinke[6] or Hultgren, *et al.*[25]

IV. Results and Discussion

The results of our experiments using effusion cells are contained in Table III. In the second column the crucible material and diameter, in inches, of an individual orifice are presented. The fifth column indicates θ_0, the arbitrary initial, angular position, and since it like $\Delta H_{s,298}$ is a parameter, the standard deviations are also listed. A negative value occurs when the initial position of the light beam lies to the right of the major axis of the ellipse and the cell direction is clockwise. The next to the last column contains the weighted variance, which was computed from the individual variances. These values were required to assure us that the points with the largest variances will have the least influence on the final fit.[21] The weighted variance can be looked upon as an average deviation of a data point. The final column lists the total sum of the squares of the deviations. With the large number of data points taken, the reliability of the data can be judged from the indices.

Figure 3 illustrates the result given in Table IV as run no. 3. The solid line is the best fit. Figures 4 and 5 illustrate a slope–third law ($\Delta H_{s,298}$ = 38,597) and a Clausius–Clayperon (ΔH = 36.467 ± 0.241) plot utilizing the data of run no. 7. In order to obtain meaningful results with these types of plots, it is essential that the smallest angular position difference be sufficiently large that experimental uncertainties do not produce a tailing off of the data. Such a tailing off results when the data shown in Figure 3 are plotted as differences.

Table IV: Comparison of Effusion and Free-Vaporization Pressures

Temp, °K	$P_{\text{free vaporization}}/P_{\text{effusion}}$
523.5	9.22 × 10^{-4}
531.6	1.04 × 10^{-3}
540.0	1.14 × 10^{-3}
550.4	1.28 × 10^{-3}
560.9	1.45 × 10^{-3}
570.6	1.63 × 10^{-3}
580.2	1.83 × 10^{-3}
590.3	2.01 × 10^{-3}

We were unable to distinguish any meaningful variation due to orifice area, nor were we able to find evidence for the development of sample porosity. An attempt was made to find a dependence on evaporating surface area. For this purpose two resublimed samples were used. The first sample was condensed at 550° and formed a single piece with many crystalline facets

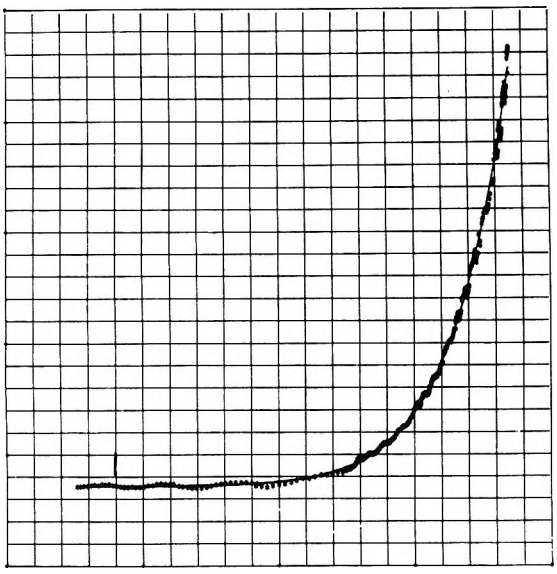

Figure 3. Angular displacement of arsenic.

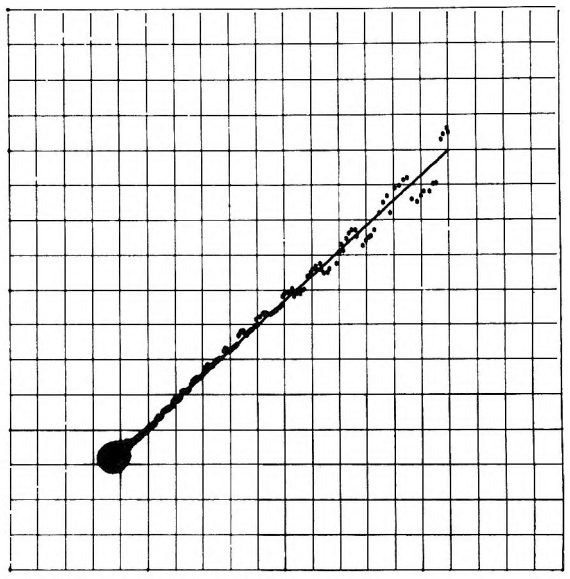

Figure 5. Second-law plot for arsenic.

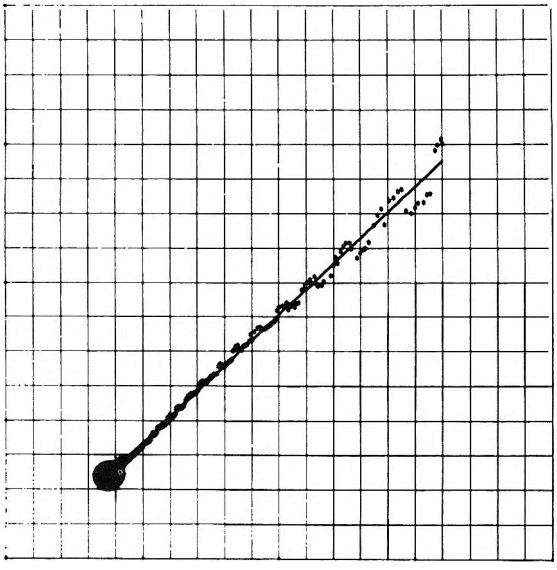

Figure 4. Slope third-law plot for arsenic.

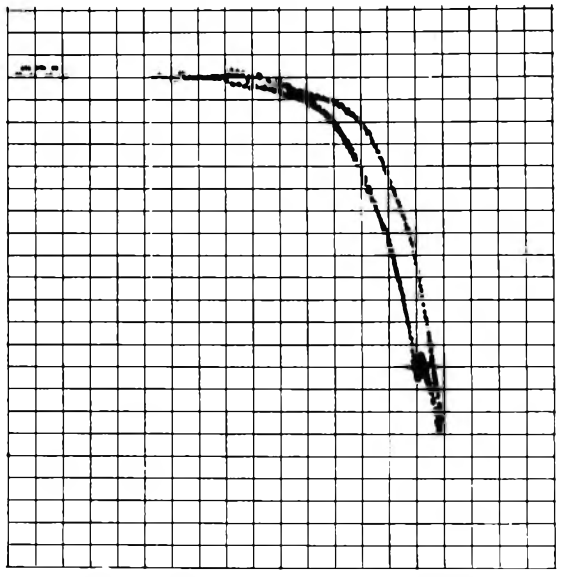

Figure 6. Angular displacement for free vaporization of arsenic

(run no. 2). The second sample (run no. 4) was condensed at room temperature and produced a thin tube which was easily crumbled into tiny fragments of large surface area. Standard heats of sublimation for these two samples, calculated from data taken in a Y_2O_3 cell of 0.020-in. orifice diameter, were 38,555 and 38,536 cal/mol, respectively.

Figure 6 illustrates the results of a free-vaporization experiment with $^3/_8$-in. masks and a counterclockwise rotation. A prior experiment was made with 0.25-in. masks and a clockwise rotation. The combination of experiments should minimize any effect due to imperfections in the mirrors. In the experiment with the 0.25-in. masks we found a "knee" in the angular position at about 600°K with increasing temperature and a "spike" at the same temperature with decreasing temperature. In the experiment with the $^3/_8$-in. masks only the spike with decreasing temperature was observed. Although the cause for the gross effect is not known, the different character with increasing and decreasing temperature is probably due to a change in the product of the condensation coefficient times the area of the vaporizing surface. During the course of the second experiment, a small portion of the sample was placed at one end of an evacuated quartz tube, and the temperature was increased at the same rate as in the angular-displacement experiment. The other end of the quartz tube was at room temperature. Thermal etching was not noticeable to the naked eye until the highest temperature was reached, at which point a dendrite-like surface became evident.

A quantitative analysis of the free-vaporization experiments is complicated by the appearance of the knees or spikes. However, an analysis which treated

portions of the results separately gave the values 44,048 and 44,228 cal/mol for the heat of sublimation to $As_4(g)$. This is in agreement with a previously reported result of 43 ± 3 kcal/mol obtained from Langmuir studies.[3]

The free-vaporization samples were removed from the TaC holder and run in an Al_2O_3 effusion cell. The ratios of the free-vaporization pressures to the effusion cell pressures are given in Table IV.

A simple demonstration of the existence of a condensation coefficient for arsenic can be made by constructing an effusion cell of the vaporizing material. This type of experiment has been previously made by Wessel.[29] Unfortunately, the arsenic cell, constructed as described above, was fabricated before the large amount of oxide impurity in the powder was known. Although the temperature and reducing conditions would reduce the oxygen content, exposure during the machining operations would tend to increase it.

For an uncontaminated cell of this type, the free-vaporization relation for the external exposed surfaces is

$$P_1 = K_1'(\theta_1 - \theta_0) \tag{11}$$

For the contribution from the interior surfaces

$$P_2 = K_2'(\theta_2 - \theta_0) \tag{12}$$

If P_2 can be equated to P_{eq}, the condensation coefficient becomes

$$\alpha = P_1/P_{eq} \sim P_1/P_2 \tag{13}$$

The symmetry of the cell permits the angular displacement to be written as

$$\Delta\theta = \theta_2 - \theta_1 = P_{eq}\frac{(1 - \alpha)}{K} \tag{14}$$

If the condensation coefficient, α, is unity, the angular displacement is zero. The results of this experiment are shown in Figure 7, in which only points for increasing temperature are plotted. Large oscillations terminated the run at about 600°K, the same temperature at which knees or spikes were observed in the free-vaporization experiments. Although the almost certain presence of oxide limits the conclusions that can be drawn, the observation of an angular displacement is taken to confirm the existence of a small condensation coefficient. Visual inspection of the cell showed the surface to be porous.

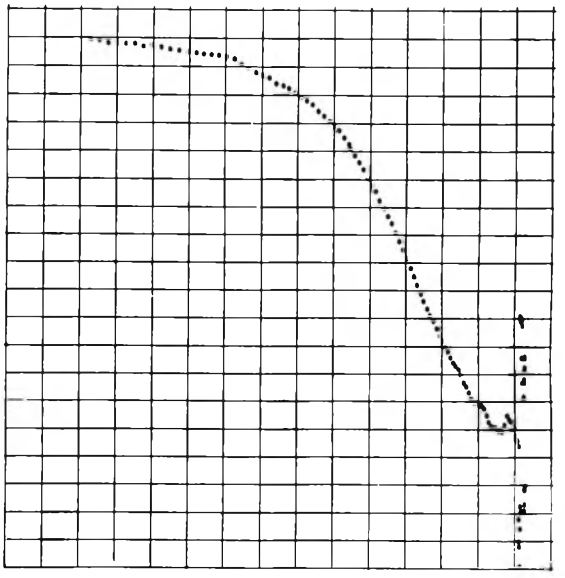

Figure 7. Condensation-coefficient effect for arsenic.

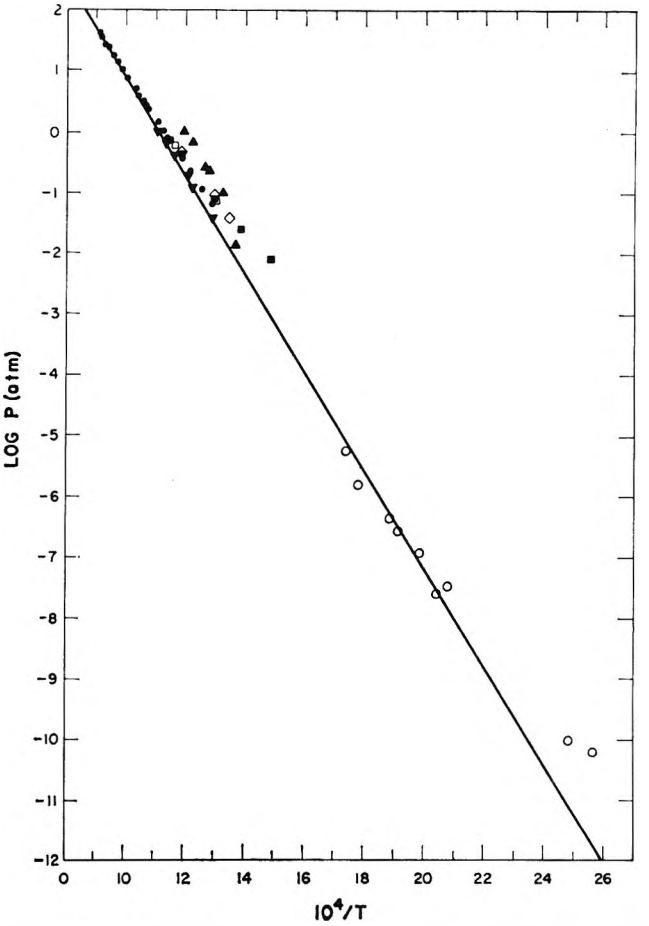

Figure 8. Vapor pressure of arsenic: ▲, Ruff and Bergdall; ▼, Ruff and Mugdan; ■, Preuner and Grockmöller; □, Weichmann and Heimburg; ◇, Gibson; ●, Horbia; ○, Nesmeyanov; —, these authors.

Table V: Vaporization Studies on Arsenic (Selected Data)

Temp, °K	Vapor pressure, atm: Stull and Sinke	Nesmeyanov	This work
300	8.28×10^{-17}		4.92×10^{-19}
400	1.43×10^{-10}	1.72×10^{-10}	4.65×10^{-12}
500	6.98×10^{-7}	8.20×10^{-7}	6.24×10^{-8}
600	1.77×10^{-4}	2.01×10^{-4}	3.22×10^{-5}
700	8.67×10^{-3}	9.57×10^{-3}	2.60×10^{-3}
800	1.47×10^{-1}	1.59×10^{-1}	6.61×10^{-2}

(29) G. Wessel, *Z. Phys.*, **130**, 539 (1951).

The vapor pressures selected by Nesmeyanov[2] and Stull and Sinke[6] and those selected from this study are listed in Table V.

The results obtained in this study and the experimental results of previous investigators are plotted in Figure 8. If conventional third-law calculations are made using the data of individual investigations directly, temperature dependencies of the standard heats of sublimation are found from the data of Weichmann and Heimburg[30] and Preuner and Brockmöller.[7] The data of Ruff and Mugdan[13] do not show such a dependence. Both the data of Horbita[31] and the experiments of Nesmeyanov[2] have a temperature dependence, mostly at low pressures. It is clear that the data of Ruff and Mugdan, the authors, and most of the data of Horbita along with the experimental data of Nesmeyanov, form a consistent set. Because four different experimental techniques are represented: boiling point, static, Knudsen effusion, and torsion–effusion, the consistency is quite satisfying.

The use of effusion for the determination of the vapor pressure of arsenic has been justifiably questioned by Nesmeyanov.[2] The problem of molecular flow from a torsion–effusion cell, in which the vaporizing surface cannot "see" outside the cell, has not yet been solved.[32] Such a solution would enable one to predict cell dimensions necessary to obtain near-equilibrium conditions within the effusion cell. As a first approximation, the relation of Rossman and Yarwood[33] for the coaxial-effusion case may be applied to the present situation. We write

$$\frac{P_{eq}}{P_2} = 1 + \frac{\sum_j r_j a_j f_j}{\alpha S} \qquad (15)$$

where S is the area of the vaporizing surface and the other quantities have their previously assigned meanings. S is calculated from the internal diameter of the cells, or 1.5 in., α is taken from Table III, and f_j is from the results of a Monte Carlo calculation,[34] *e.g.*, 0.1094 for a cell with a 0.020-in. orifice. The expected ratios of pressures then become 1.00, 1.07, and 1.54 for cells with orifice diameters of 0.005, 0.020, and 0.040 in., respectively. Because no dependence on orifice diameter was observed experimentally, the use of eq 15 may be questionable. Its application here involves the assumptions that the cells may be considered spherical, that the condensation coefficient is independent of pressure, and that the geometrical area is equal to the area of the vaporizing surface. The first assumption is probably reasonable, the second is suspect, the third is likely to be valid only for liquids or a solid for which faceting is unimportant. Also, samples prepared under varying conditions could have different vaporization–condensation rates.

V. Conclusions

The experimental results of this study confirm the existence of a small condensation coefficient for the sublimation of polycrystalline arsenic. A standard heat of sublimation at 298.15°K of 38.540 ± 0.100 kcal/mol of $As_4(g)$ was selected for arsenic samples prepared by resublimation. This value is consistent with some, but not all, of the previous investigations using boiling point, static, and Knudsen effusion techniques.

(30) F. Weichmann and M. Heimburg, *Z. Anorg. Chem.*, **240**, 129 (1938).

(31) S. Horbita, *Z. Phys. Chem.* (Leipzeig), **106**, 295 (1923).

(32) V. I. Lozgachev, *Soviet Phys.-Tech. Phys.*, **7**, 827 (1963).

(33) M. G. Rossman and J. Yarwood, *J. Chem. Phys.*, **21**, 1406 (1953).

(34) M. Frazer, R. C. Feber, and C. C. Herrick, Regional Meeting, American Chemical Society, Albuquerque, N. M., Dec 1966.

Spectroscopy of Alkali Metals in Fused Alkali Metal Salts

by J. F. Rounsaville and J. J. Lagowski

Department of Chemistry, The University of Texas, Austin, Texas 78712 *(Received June 12, 1967)*

The optical spectra from 5000 to 20,000 Å of several alkali metals in the corresponding alkali halides and mixtures of alkali halides have been determined. A single, broad absorption band occurs in these spectra; the position of the band depends upon the size and the mole fraction of the cation and anions in the salt mixture serving as the solvent. The results suggest that the spectroscopically important species in these solutions is the solvated electron.

Introduction

The alkali metals dissolve in fused alkali halides to give true solutions in which weak interactions occur between the dissolved metal and the salt serving as solvent. Although these solutions have received periodic attention,[1] the relatively recent investigations are the only sources for useful quantitative data because of the high temperatures required. Also, the very reactive nature of the solutions leads to considerable experimental difficulties.

Phase diagrams for most of the alkali metal–alkali metal halide systems have been determined using an all-metal apparatus.[2] In general, the phase diagrams show a depression of the freezing point of the salt as the metal concentration increases to the solubility limit of the metal; at greater metal concentrations, two phases, a salt-rich phase and a metal-rich phase, arise below the consolute temperature. The conductivity of metal-fused salt solutions has been determined for the sodium and potassium systems using sapphire and magnesium oxide conductivity cells.[2a] The atomic conductivity of the metal at infinite dilution is 30–100 times greater than the conductivity of the solvent salt. Although the results of an esr study[3] and one magnetic susceptibility study[4] on these systems were inconclusive, another magnetic susceptibility investigation indicated that the metal–molten salt systems are paramagnetic.[5]

Spectrophotometric studies using molten salts as solvents have been reported frequently during the last decade, and the techniques, primarily used to investigate the spectra of transition metal ions, are highly developed.[1] The spectra of the systems Na–NaX (X = Cl, Br, I);[6] K–KX (X = Br, I);[6] M–LiCl,[7] M in LiF–NaF–KF eutectic,[7] and M in LiCl–KCl eutectic[8] (M = Li, Na, K); and Na–NaI[9] have been reported to show one band, the position of which varies in the range 5300–9800 Å, depending upon the solvent. Apparently, the alkali metals also dissolve in the corresponding amides and hydroxides to give colored solutions.[10, 11]

The properties of these solutions are similar to those of the more thoroughly investigated metal–ammonia solutions.[12] Since the properties of metal–salt solutions have been discussed in terms of the solvated electron as an important species in these systems,[13] and because of our interest in the nature of metal–ammonia solutions, a systematic spectrophotometric investigation of the dilute alkali metal–alkali metal halide solutions was undertaken in an attempt to elucidate the nature of the species present.

Experimental Section

Spectra of the molten salt solutions were obtained in Pyrex or quartz cells maintained at the appropriate temperature using a furnace especially designed to fit into the cell compartment of a Cary Model 14 spectrophotometer. The furnace,[14] a cross section of which is shown in Figure 1, was constructed of brass and the block was nickel plated. The furnace block was heated by four 600-W heaters (Watlow Electric Manu-

(1) (a) M. Blander, "Molten Salt Chemistry," John Wiley and Sons, Inc., New York, N. Y., 1964; (b) B. R. Sundheim, "Fused Salts," McGraw-Hill Book Co., Inc., New York, N. Y., 1964.

(2) (a) M. Bredig, U. S. Atomic Energy Commission, Washington, D. C., ORNL-3391, 1963; (b) M. Bredig, H. Bronstein, and W. Smith, *J. Amer. Chem. Soc.*, **77**, 1454 (1955); (c) M. Bredig, J. Johnson, and W. Smith, *ibid.*, **77**, 307 (1955); (d) M. Bredig and H. Bronstein, *J. Phys. Chem.*, **64**, 64 (1960); (e) M. Bredig and J. Johnson, *ibid.*, **64**, 1899 (1960); (f) J. Johnson and M. Bredig, *ibid.*, **62**, 604 (1958); (g) A. Dworkin, H. Bronstein, and M. Bredig, *ibid.*, **66**, 572 (1962).

(3) J. Brown, U. S. Atomic Energy Commission, Washington, D. C., UCRL-9944, 1961.

(4) N. H. Nachtrieb, *J. Phys. Chem.*, **66**, 1163 (1962).

(5) M. Bettmann, *J. Chem. Phys.*, **44**, 3255 (1966).

(6) E. Mollwo, *Nachr. Ges. Wiss. Göettingen Jahresber. Geschaftsjähr Math.-Physik. Kl. Fachgruppen II*, **1**, 203 (1935).

(7) (a) J. Young, *J. Phys. Chem.*, **67**, 2507 (1963); (b) J. Young, U. S. Atomic Energy Commission, Washington, D. C., ORNL-P-403, 1964.

(8) J. Greenberg and I. Warshawsky, *J. Amer. Chem. Soc.*, **86**, 3572 (1964).

(9) J. Greenberg and I. Warshawsky, *ibid.*, **86**, 5351 (1964).

(10) C. Fernelius and F. Bergstrom, *J. Phys. Chem.*, **35**, 740 (1931).

(11) A. Titherly, *J. Chem. Soc.*, **65**, 504 (1894).

(12) J. C. Thompson in "The Chemistry of Non-Aqueous Solvents," Vol. 2, J. J. Lagowski, Ed., Academic Press Inc., New York, N. Y., 1967.

(13) K. Pitzer, *J. Amer. Chem. Soc.*, **84**, 2025 (1962).

(14) J. Morrey and A. Madsen, *Rev. Sci. Inst.*, **32**, 799 (1961).

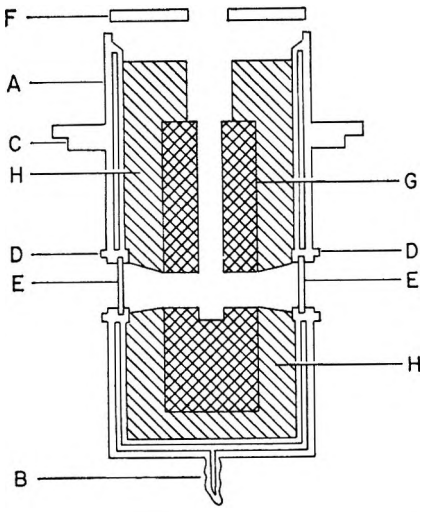

Figure 1. Cross section of the furnace used to maintain a constant temperature for the optical cell: A, water jacket; B, water inlet; C, plate; D, light port; E, quartz disk; F, lid; G, furnace block; H, insulation.

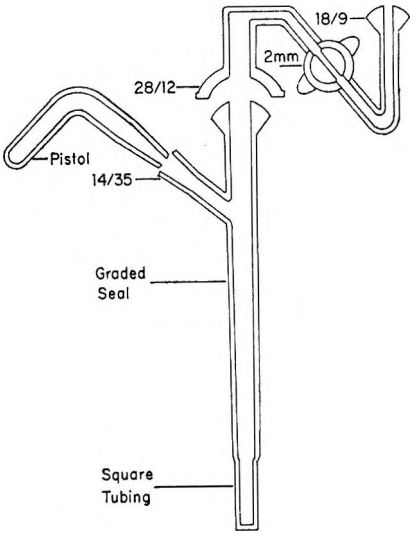

Figure 2. Glass optical cell and vacuum line adapter.

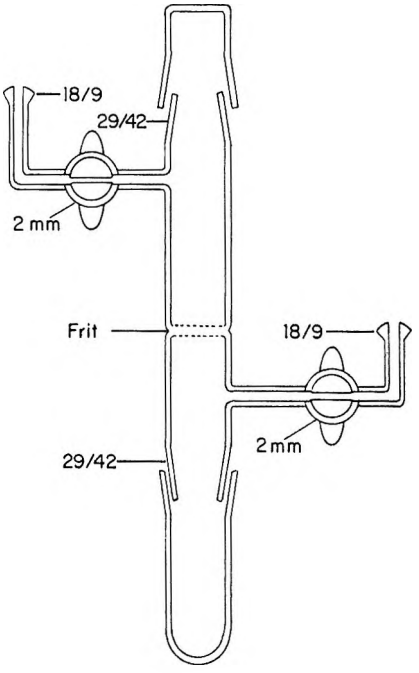

Figure 3. Salt purification apparatus.

facturing Co.) controlled with two powerstats, the temperature at the cell position in the furnace being determined with a calibrated thermocouple and potentiometer. Alignment of the furnace block aperture in the light path of the spectrometer was fixed by cementing the block into the water jacket with cast Firecrete (Johns-Manville) and asbestos cement. Optical cells which could be loaded in a drybox or attached to a vacuum system were constructed of either 1.00-cm precision bore square Pyrex (Ace Glass, Inc.) or quartz tubing (Thermal American Fused Quartz Co.) (Figure 2).

Potassium (J. T. Baker Chemical Co., purified) and sodium (B. & A. Allied Chemicals, reagent) were distilled *in vacuo* into glass ampoules. Lithium (Foote Mineral Co., 99.99%), cesium (Fairmount Chemical Co., CP, double distilled), barium (K & K Laboratories, 99.5%), and calcium (Fischer Chemical Co., 98%), as well as the ampoules containing potassium and sodium, were stored and manipulated in a drybox, the atmosphere of which was equilibrated with the liquid Na–K eutectic.

Commercially available salts of the highest purity were dried and freed from hydrolysis products before use as solvents by one of two procedures. Where there was little danger of hydrolysis, *e.g.*, KI or KBr, drying at 500° *in vacuo* was employed. For KCl, LiCl, and KCl–LiCl mixtures, the salts were placed in the upper portion of the apparatus shown in Figure 3, were fused, and chlorine gas was passed through the melt to remove water and/or hydrolysis products.[15] Argon (Matheson Chemical Co., 99.998%) was then passed through the melt to remove excess chlorine, and the system was evacuated. Liquid argon was then condensed in the lower portion of the apparatus, and the molten salt was allowed to pass through the frit, dropping into liquid argon. The apparatus was then evacuated and transferred to the drybox, where the apparatus was stored. All operations were conducted in a conventional high-vacuum gas-handling system, using the usual precautions.[16] Thus, using this treatment, the salt was never exposed to the atmosphere after it had been purified.

The potassium amide used as a solvent was prepared by the reaction of anhydrous ammonia with potassium at 350°. On the other hand, potassium amide used as an additive was prepared by the reaction of potassium with anhydrous liquid ammonia using iron oxide as a

(15) D. Maricle and D. Hume, *J. Electrochem. Soc.*, **107**, 354 (1960).

(16) For detailed procedures, see J. F. Rounsaville, Ph.D. Dissertation, The University of Texas, Austin, Texas, 1966.

catalyst. Potassium hydroxide (Mallinckrodt Chemical Works, analyzed reagent) was purified by vacuum sublimation at 500°, while Li_2O was prepared by the method of Bravo.[17]

In general, a molten salt solution was prepared and its spectrum recorded using the following procedure. Weighed amounts of the salt and any additives were placed in the bottom of the optical cell, and several weighed pieces of metal were placed in the side arm, all manipulations being conducted in a drybox. The optical cell was then transferred from the drybox to the vacuum system, evacuated, and filled with about 250 mm of dry argon. The salt was then melted in the optical furnace and the spectrum of the solvent salt recorded. After adding the metal, incrementally, until the solution developed a color, the spectrum was recorded again. The metal concentration in the salt solution was in the range 10^{-2} to 10^{-3} M when the spectrum was recorded; accurate values for extinction coefficients were difficult to obtain because the color faded. A typical spectrum is shown in Figure 4; discontinuities caused by using different light sources or attenuation as well as the background spectrum of the solvent have been removed.[16] During the course of these experiments, there was no indication of alkali metal distilling from the melts.

For calibration purposes, the experimental technique and equipment were used to determine the spectrum of $CoCl_2$ in the LiCl–KCl eutectic mixture at 400°. Absorption bands at 15,500, 6980, 6650, and 6100 Å were observed with molar extinction coefficients of 20, 340, 335, and 215, respectively. These results are in good agreement with those reported in earlier investigations.[18]

Results

Spectra of LiCl–KCl Solutions. The spectrum of potassium in a molten LiCl–KCl eutectic mixture (400–500°) is featureless in the region 3500–25,000 Å; in spite of repeated attempts using pure components, colored solutions could not be obtained. However, if basic species (*e.g.*, KOH, Li_2O, or KNH_2 at about 0.1 M) were present in the molten solvent, potassium metal gave a blue color; the spectra of these solutions consists of a single, broad unsymmetrical band centered at about 7200 Å (Figure 4). Melts containing KOH or KNH_2 did not develop an immediate color upon the addition of potassium, but a color invariably developed after a certain increment of metal had been added. The stoichiometry suggests that sufficient metal must be added to melts containing KOH or KNH_2 to convert these compounds into the corresponding oxide or nitride (eq 1 and 2). The spectra of melts

$$KOH + K \longrightarrow K_2O + {}^1/_2H_2 \quad (1)$$

$$KNH_2 + 2K \longrightarrow K_3N + H_2 \quad (2)$$

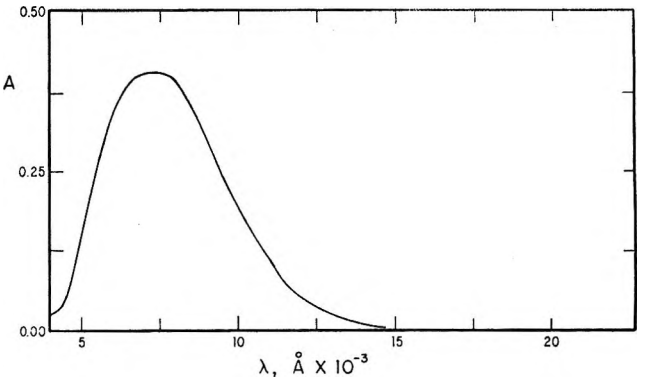

Figure 4. The spectrum of potassium at 500° in the eutectic KCl–LiCl mixture containing 0.1 M Li_2O.

containing 0.1 M KOH show absorption bands at 19,100 and 14,100 Å which correspond in relative intensity to the two predominant bands observed for liquid water at 14,500 and 19,200 Å.[19] If a larger concentration of KOH is present in the melt ($\simeq$0.5 M), water condenses on the walls of the optical cell above the heated zone. The bands at 19,100 and 14,100 Å decreased as potassium metal was added to melts containing KOH and disappeared when the blue color developed. These observations suggest that the over-all process described in eq 1 occurs by dehydration of the hydroxide ion to form water, which then reacts with potassium. Similar observations were made on the melts containing KNH_2; the spectra of these melts exhibit a band at 20,600 Å which disappears when sufficient potassium is added to form a blue solution. Ammonia contains several bands in this region, the band at 20,000 Å being the most intense.[20] Thus it would appear that eq 2 represents the over-all process which occurs in melts containing KNH_2, but the reaction probably involves ammonia which is formed from the decomposition of amide ions. These results suggest that the species which stabilizes the blue solutions in LiCl–KCl melts is the oxide or the nitride ion. An attempt to verify this observation was made by investigating the formation of blue solutions in LiCl–KCl melts containing Li_2O.[21] Lithium oxide dissolves slowly in these melts; however, solutions containing this substance did not develop a color when the first portions of potassium metal were added. It was necessary to add about 0.5 mol of potassium for every mole

(17) J. Bravo, *Inorg. Syn.*, **7**, 1 (1963).

(18) (a) D. Gruen and R. McBeth, *Pure Appl. Chem.*, **6**, 23 (1963); (b) B. Sundheim and M. Kukk, *Discussions Faraday Soc.*, **32**, 49 (1961); (c) G. Harrington and B. R. Sundheim, *Ann. N. Y. Acad. Sci.*, **79**, 950 (1960).

(19) H. Yamatera, B. Fitzpatrick, and G. Gordon, *J. Mol. Spectrosc.*, **14**, 268 (1964).

(20) D. F. Burow and J. J. Lagowski, *Advan. Chem. Ser.*, **50**, 125 (1965).

(21) Under the conditions of these experiments the most stable oxide is Li_2O: J. Bockris, "Physiochemical Measurements at High Temperatures," Butterworth and Co. Ltd., London, 1959.

of Li_2O present before the characteristic blue color was observed. Invariably, the optical cells used with melts containing basic substances were noticeably etched. These observations suggest that silicates formed by the interaction of oxide ions with the optical cells are reduced by potassium metal to reform oxide ions and either elemental silicon or lower silicon oxides. Since oxide ions are reformed in this process, attack on the cell walls can continue, the net result being a slow fading of the blue color characteristic of potassium solutions. The cells were also attacked, but to a lesser extent, by the alkali metals yielding reduction products that colored the optical surfaces.

The spectra of a series of LiCl–KCl melts containing alkali metals were recorded under various conditions to determine the effect of the temperature, solvent composition, and concentration of the stabilizing basic component on the characteristics of the absorption band. The position of the band maximum is not appreciably sensitive to temperature. Solutions of potassium in LiCl–KCl (46% KCl) mixtures containing 0.1 *M* KOH show a shift of the band center to lower energies with increasing temperature at a rate of about 2 Å/deg (Figure 5); similar results are observed using different salt mixtures as solvents, basic stabilizing species, or alkali metals.[16] An increase in the concentration of KCl in the solvent (at a constant concentration of basic stabilizer) also causes the band center to move to lower energies in a regular manner (Table I); similar results are obtained for solutions of sodium in NaI–KI mixtures (Table II). In addition, neither the nature of the basic additive present in solution nor its concentration seems to influence the position of the absorption band, as long as sufficient additive is present to give a colored solution (Table III). Higher concentrations of the additive gave more stable solutions, in the sense that the fading was less rapid. This was reflected in a large initial absorbance for solutions containing higher concentrations of additives. The alkali and alkaline earth metals which dissolve in LiCl–KCl melts containing basic stabilizers give spectra that are indis-

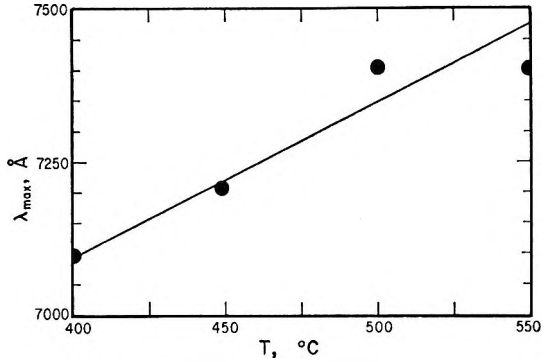

Figure 5. The temperature variation of the absorption band for potassium in LiCl–KCl (46% KCl) mixtures containing 0.1 *M* KOH.

Table I: Position of the Absorption Maximum for Potassium Dissolved in Various LiCl–KCl Mixtures (mol %) Containing 0.1 *M* KOH at 500°

X_{KCl}	λ_{max}, Å	$\bar{\nu}_{1/2}$, cm^{-1}
0[a]	5200	...
36	7000	8500
41[b]	7100	8400
46	7400	8400
70	8500[c]	7900
100	8800[d]	6400

[a] Data for pure LiCl at 650° taken from ref 7a and corrected for temperature difference (2 Å/deg, *cf.* Figure 5). [b] Eutectic mixture. [c] Spectrum determined in a quartz cell at 650° (*cf.* Table IV) and corrected for temperature difference (2 Å/deg, *cf.* Figure 5). [d] Spectrum determined in a quartz cell at 800° (*cf.* Table IV) and corrected for temperature difference (2 Å/deg, *cf.* Figure 5).

Table II: Position of the Absorption Maximum for Sodium Dissolved in Various KI–NaI Mixtures (mol %) Containing 0.1 *M* KOH at 675°

X_{KI}	λ_{max}, Å	$\bar{\nu}_{1/2}$, cm^{-1}
0[a]	8,000 ± 300	5100
25	7,000 ± 500	...
50	8,000 ± 500	6000
75	8,500 ± 500	7000
100	10,600 ± 300	6500

[a] Spectrum determined at 750° (*cf.* Table IV) and corrected for temperature difference (2 Å/deg, *cf.* Figure 5).

Table III: Positions of Absorption Bands for Solutions of Alkali Metals in LiCl–KCl Eutectic Mixtures[a] at 500°

Metal	Additive[b]	λ_{max}, Å	$\bar{\nu}_{1/2}$, cm^{-1}
K	...	...[c,d]	...
K	KOH (0.01)	...[c]	...
K	KOH (0.07)	7300	7000
K	KOH (0.1)	7100	8400
K	KOH (0.6)	7400	8000
K	KNH_2 (0.1)	7200	4800
K	KNH_2 (0.25)	7000	6600
K	Li_2O (0.06)	...[c]	...
K	Li_2O (0.12)	7200	8200
K	Li_2O (0.24)	7100	9600
Li	KOH (0.1)	7200	7600
Ba	KOH (0.1)	7200	7800
Na	KOH (0.1)	...[c]	...
Ca	KOH (0.1)	...[c]	...
K	Li_2O (0.12)	7200	8200
Na	Li_2O (0.11)	...[c]	...

[a] The eutectic mixture contains 41 mol % KCl. [b] Molarity of additive given in parentheses. [c] Spectrum is featureless. [d] Similar results were obtained using a stainless steel cell with Al_2O_3 windows; see ref 16.

tinguishable from each other. However, in some instances the solvent does not appear to dissolve the active metal (Table III).

Alkali Metal–Metal Halide Solutions. Solutions of alkali metals in the corresponding alkali halide were also studied spectrophotometrically. It was unnecessary to add the alkali metal oxide to the K–KX (X = Cl, Br, I) and Cs–CsCl systems to obtain blue solutions; Na_2O was added to the Na–NaI system. Since these salts melted at higher temperatures than the LiCl–KCl mixtures, fused quartz optical cells were employed to determine their spectra. The results for the systems K–KCl, K–KBr, K–KI, Cs–CsCl, Na–NaI, and Li–LiCl are summarized in Table IV. Lithium did not give a colored solution in LiCl, even though in some experiments the melt contained 0.4 *M* Li_2O. The system Na–NaI exhibited the characteristic blue color, but it faded very rapidly compared to that observed for the other systems, and the data were acquired with a very rapid scanning rate (500 Å/sec). Accordingly, the band position is less accurately known for Na–NaI than for the other systems.

Table IV: Spectra of Alkali Metals Dissolved in Molten Salts

Solvent	Metal	Temp, °C	λ_{max}, Å	$\bar{\nu}_{1/2}$, cm^{-1}
CsCl	Cs	700	11,700 ± 300	5100
KI	K	750	11,100 ± 300	6400
KBr	K	775	10,500 ± 200	7300
KCl	K	800	9,400 ± 200	6400
NaI[a]	Na	750	8,100 ± 300	5100
LiCl	Li	650	...[b]	...
KNH_2	K	350	11,000 ± 300	6000

[a] Sodium oxide present. [b] No band observed. However, a broad absorption band at 5500 Å has been reported for the system Li–LiCl at 650° using a windowless cell (ref 7).

Molten potassium amide at 350° is green, and its spectrum exhibits bands at 20,900, 15,900, 12,600, and 11,000 Å. The positions and relative intensities of the first three bands correspond to those of the bands observed for ammonia.[19] The band at 11,000 Å increases in intensity when potassium is added to the melt (at which point the melt becomes deep blue) while the intensities of the other bands decrease. In this process the glass optical cell was only slightly etched and not discolored; it could be used repeatedly, in contrast to the cells used for the other experiments described here. In general, all metal solutions reacted with the glass optical cells; the higher the energy of the band maximum in the spectrum the more pronounced was this reaction. In the case of the Li–LiCl system, a stable solution could not be obtained under the conditions of these experiments, although the spectrum for this system has been obtained with a windowless cell.[7]

Discussion

Relatively few data are available for direct comparison with the results obtained in this investigation. The data for KCl and NaI solutions (Table IV) are in reasonable agreement with those reported previously by Mollwo,[6] but the variation in the position of the absorption band with the nature of the anion, as shown in Table IV for potassium salts, has not been observed previously. The spectra of potassium dissolved in either KCl, KBr, or KI have been reported to consist of only one broad absorption band at 9800 Å, whereas the spectra of sodium solutions in the corresponding sodium halides have been reported to exhibit a band at 7900 Å.[6] The greater success in obtaining spectra in molten sodium salts without added oxide in the earlier work[6] is probably due to the greater alkalinity of the glass (Supremax) used for the cells. In contrast with Mollwo's findings and the results reported here, a band at 5700 Å has been observed for the Na–NaI system at 675° using a quartz optical cell.[9] A band at 5500 Å has been observed for the Li–LiCl system,[7] which correlates well with the data given in Table I on the variation of the band maximum in LiCl–KCl mixtures with the composition of the melt. In addition, a band at 5300 Å has been reported[8] for solutions of Li, Na, or K in the LiCl–KCl eutectic at 400°; this band occurs at higher energy than the bands observed for any of the systems investigated here (Tables I and III) or for pure LiCl melts.[7]

The spectral results on alkali metal–molten salt systems that appear to form a consistent pattern give rise to several conclusions. A single, broad unsymmetrical absorption band was observed in the spectrum of all systems studied. The temperature coefficient of the position of the band maximum is small, being no more than ~2 Å/deg. The position of the band is also dependent upon the relative sizes of the ions which constitute the melt (Tables I, II, and IV), the larger anions and cations giving lower band energies and, qualitatively, more stable solutions. The data in Table IV can be represented analytically by eq 3, where r^+ and r^- are the ionic radii of the cation and

$$\lambda_{max} = 1130(r^+ + r^-)^{1.84} \quad (3)$$

anion, respectively. The form of eq 3 is suggested by a similar empirical expression developed for F centers.[22] Mixtures of alkali halides form colored solutions with alkali metals, the spectra of which also contain a single, broad unsymmetrical band. The position of the band maximum is a smoothly varying function of the composition of the salt (Tables I and II) and may be

$$(\lambda_{max})^{1/2} = 31\sum_i X_i r_i^+ + 24\sum_i X_i r_i^- + 13 \quad (4)$$

represented analytically by eq 4, where X_i represents the mole fraction of the ith species.

(22) H. Ivey, *Phys. Rev.*, **72**, 341 (1947).

The spectral properties of dilute metal–molten salt solutions might be attributed to colloidal metal particles,[2b] metal atoms (M),[2c,6] diatomic metal molecules (M_2),[2d,f,4] "subhalide cations" (M_2^+),[2e] or solvated electrons (M_x^{x-1}),[4,23a] all species except the first being understood as solvated. For solutions containing basic stabilizers (*e.g.*, KOH, KNH_2), there is also the possibility that the spectral bands could arise from discrete oxide species of the type $M_nO_y^{2y-}$. The presence of colloidal matter in the metal–molten salt solutions can be immediately excluded on the basis of freezing point depression data,[2] and conductivity data[23] eliminate the presence of significant concentrations of diatomic metal molecules.

The species M, M_2^+, and e^- are conceptually related, in the sense that they represent different degrees of delocalization of an electron: the electron is associated with one ion in the species M, with two ions in M_2^+, and with several ions in the case of e^-. The formation of any of these species corresponds to the introduction of a new particle into the melt, as is reflected in the colligative properties of these systems. A study of the vapor pressure of alkaline earth metals over their solutions in alkaline earth halides suggests that the species M or M_2^+ are probably not important in these systems.[24] Similar conclusions were reached in a study of the electrochemical cell $Li|LiCl|Cl_2$.[25] Although these do not appear to be particularly strong arguments for the existence of the solvated electron in metal–molten salt systems, the presence of this species could account for the previous observations[2,23-25] on dilute solutions.

In contrast to other data, the spectroscopic observations present a more direct indication of the nature of dilute metal–molten salt solutions. If the species present in a mixture of molten salts (such as LiCl and KCl) were metal atoms (M), the spectrum should consist of one band (for either Li or K), or at most two bands, the positions of which should be solvent independent; however, the intensities would be dependent upon the solvent composition. A similar argument can be formulated for the M_2^+ or M_2 species, except that three bands corresponding to Li_2^+ (Li_2), LiK^+ (LiK), and K_2^+ (K_2) might be anticipated. The possibility also exists that the bands might arise from the reactions of a metal atom with a different metal ion to form an atom of the second metal (eq 5). The experimental

$$M^0 + M'^+ \longrightarrow M'^0 + M^+ \qquad (5)$$

results do not corroborate either of these arguments. If either M or M_2 were present, it would be necessary to account for the fact that the band positions in solutions are considerably displaced from the positions of either the $^2S_{1/2} \rightarrow {}^2P_{3/2,1/2}$ doublet for the atomic systems (Li, 6708; Na, 5890, 5896; K, 7665, 7699; Cs, 8521, 8944 Å)[26] or the $\Sigma_g \rightarrow \Sigma_u$ transition for the diatomic systems (Li_2, 7132; Na_2, 6821; NaK, 8252; K_2, 8568; Cs_2, 9100–11,300 Å).[26] Indeed, any arguments on this basis would require that the absorption maximum in the Li–LiCl system be increased in energy with respect to the band observed in the gas phase spectra, while that for the other alkali metal–alkali halide systems is decreased. If a common metal atom were present in all systems, we would expect to observe the same spectrum.

The existence of the solvated electron as the predominant species in dilute solutions of metals in molten salts has been suggested previously[3,5,13] and presumably it is similar in nature to the F centers, which occur in alkali halide crystals when electrons occupy vacant anion sites. The positions of the band maxima for F centers in alkali halide crystals, which have been attributed to an S → P type transition,[23] show a regular progression with interatomic distances.[22] If the solvated electron in dilute molten salt solutions is delocalized on a cluster composed of cations and anions or occupies a cavity, the size of the unit constraining the electron is no longer directly determined by the dimensions of the crystal lattice (*i.e.*, by the size of the anion site), but rather by the size of the cavities or clusters available in the liquid state, which is consistent with the observed decrease in the energy of the band maximum with an increase in cation size. In the case of the LiCl–KCl eutectic mixtures containing stabilizers, the clusters or cavities presumably involve oxide or nitride ions together with the halide ions present in the solvent melt.

Acknowledgment. We gratefully acknowledge the financial assistance of the Robert A. Welch Foundation and a Fellowship from the National Science Foundation (to J. F. R.).

(23) (a) H. R. Bronstein and M. Bredig, *J. Phys. Chem.*, **65**, 1220 (1961); (b) H. R. Bronstein and M. A. Bredig, *J. Amer. Chem. Soc.*, **80**, 2077 (1958).

(24) J. Van Westenburg, *Dissertation Abstr.*, **25**, 1129 (1964).

(25) R. Snyder and J. Lander, *Electrochem. Technol.*, **4**, 179 (1966).

(26) (a) "Handbook of Chemistry and Physics," 46th ed, Chemical Rubber Publishing Co., Cleveland, Ohio, 1965; (b) G. Herzberg, "Spectra of Diatomic Molecules," 2nd ed, D. Van Nostrand Co. Inc., New York, N. Y., 1950.

Dielectric Properties of Polycrystalline Barium Trititanate and Barium Tetratitanate

by G. W. Marks and C. E. Antoniak

Naval Undersea Warfare Center, San Diego Division, San Diego, California 92152 *(Received June 15, 1967)*

An investigation was made of the dielectric properties of polycrystalline barium trititanate ($BaTi_3O_7$) and tetratitanate ($BaTi_4O_9$) in the frequency range 100 cps–10 Mcps, within the temperature range 0–250°. The variation of permittivity with temperature at constant frequency is linear, or nearly so, with the exception that dielectric dispersion occurs in the tetratitanate at lower frequencies above about 130°. Permittivity values lie within the range from 40 to 60. Log tan δ rises nearly linearly with temperature in the high-temperature range for frequencies from 10^2 to 10^5 cps, indicating that maxima occur at still higher temperatures. In both compounds, the direct current resistivity varies linearly with the reciprocal of the Kelvin temperature, whereas the 1-kcps resistivity has a minimum. This shows that the loss tangent is not determined alone by direct current conductivity, particularly at lower temperatures. No evidence of ferroelectricity was found for either of these dielectrics within the range 0–425°.

From their study of phase equilibria in the system BaO–TiO_2, Rase and Roy[1] concluded that there are five intermediate compounds of these oxides. These are barium orthotitanate (Ba_2TiO_4), barium metatitanate ($BaTiO_3$), barium dititanate ($BaTi_2O_5$), barium trititanate ($BaTi_3O_7$), and barium tetratitanate ($BaTi_4O_9$). An examination of the phase equilibrium diagram of Rase and Roy shows that Ba_2TiO_4, $BaTiO_3$, $BaTi_3O_7$, and $BaTi_4O_9$ can be obtained pure by firing corresponding stoichiometric mixtures of baria and titania.[1] However, the last two of these oxides melt incongruently and so the maximum firing temperatures for the preparation of these compounds in a pure state are limited to temperatures below the incongruent melting point.

Some previous work on the dielectric properties of certain of these oxides was done by Skanavi[2] and by Lipaeva.[3]

It is our purpose to discuss briefly results that were obtained from an experimental investigation of polycrystalline $BaTi_3O_7$ and polycrystalline $BaTi_4O_9$.

Experimental Section

Preparation of Specimens. Well-blended mixtures (−200 mesh) of dried (500°) reagent grade barium carbonate ($BaCO_3$) and titanium dioxide (TiO_2) were prepared in stoichiometric proportions for the synthesis of $BaTi_3O_7$ and $BaTi_4O_9$. These mixtures were fired at 1250–1300° for about 5 hr, powdered in a diamond mortar to −200 mesh after cooling, and again fired. X-Ray diffraction powder diagrams of these products, using Mo Kα radiation (Zr filter), showed the respective patterns for $BaTi_3O_7$ and $BaTi_4O_9$ as previously described.[1]

Samples of about 8–10 g of these titanates containing a binder of 5% starch solution were pressed into 1 in. diameter disks at 6000–8000 psi and fired for 2 hr at 1200–1230°. Preliminary tests of specimens after firing showed that the loss tangent lay within the range 0.1–0.4, which was much too high if $BaTiO_3$ is taken as a criterion. The samples were reground, 0.02% ferric oxide introduced, and disks were again prepared and fired. Subsequent tests at 1 kcps show the loss tangent to be about 0.001, which is the low order of magnitude to be expected.[4,5]

Microscopic examination of polished specimens etched with 6 N HCl containing 3% HF showed that the crystallite size ranged from about 1 to 15 μ. Disks for experimentation were cut to a thickness of about 0.1 in., faces were machined plane parallel to within 1 mil, and the densities were then determined. After electroding with silver, measurements were made on two samples of each compound. Replicate tests were made at each frequency.

Densities and porosities of representative samples are given in Table I. Porosity x, which is defined as the volume fraction of pore space, is found from the relation

$$x = (p_x - p_a)/p_x \qquad (1)$$

p_x is the maximum ideal density, ordinarily as deduced from crystal structure data; p_a is the density of the specimen. p_x for $BaTi_4O_9$ was calculated from crystal structure data whereas p_x for $BaTi_3O_7$ is the measurement of Rase and Roy by the pycnometer method.[1,6]

(1) D. E. Rase and R. Roy, *J. Amer. Ceram. Soc.*, **38**, 102 (1955).
(2) G. I. Skanavi, *Dokl. Akad. Nauk SSSR*, **59**, 41 (1948).
(3) G. A. Lipaeva, *Soviet Phys.-Solid State*, **4**, 1183 (1962).
(4) J. P. Remeika, *J. Amer. Chem. Soc.*, **76**, 940 (1954).
(5) G. Shirane, F. Jona, and R. Pepinsky, *Proc. Inst. Radio Engr.*, **43**, 1238 (1955).
(6) D. H. Templeton and C. A. Dauben, *J. Chem. Phys.*, **32**, 1515 (1960).

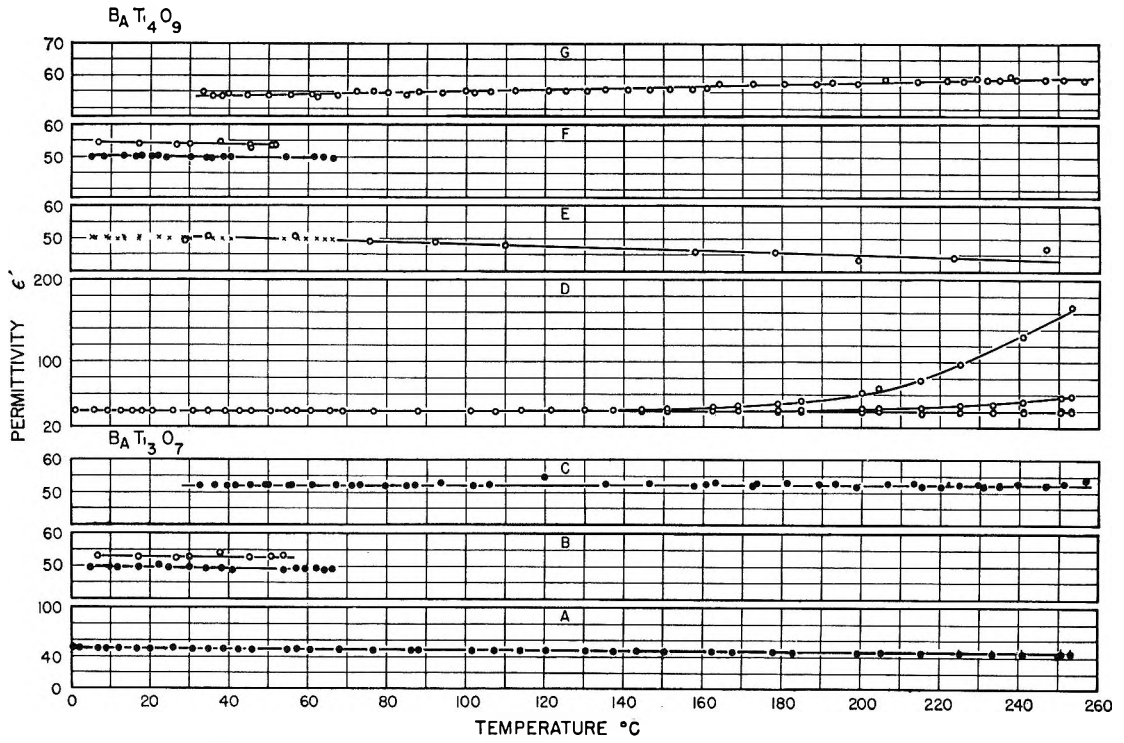

Figure 1. Variation of permittivity with temperature ($BaTi_3O_7$, density 4.08 g/cm³): (A) 100 cps and 1, 10, and 100 kcps; (B) lower curve, 500 kcps and 1 Mcps, upper curve, 5 Mcps; (C) 10 Mcps, $BaTi_4O_9$; (D) 100 cps (high curve), 1, 10, and 100 kcps are nearly the same; (E) ×, 500 kcps; O, 3 Mcps; (F) O, 1 Mcps; ●, 5 Mcps; (G) 10 Mcps.

Table I: Density and Porosity Data Concerning $BaTi_3O_7$ and $BaTi_4O_9$

Dielectric	Density, g/cm³ ρ_x	Density, g/cm³ ρ_a	Porosity, % x
$BaTi_3O_7$	4.7	4.08	13.4
		4.06	13.6
$BaTi_4O_9$	4.54	4.10	8.9
		4.16	8.4

Electrical Measurements. Measurements of capacitance and loss tangent were made within the temperature range 0–250° and of direct current resistance within the range 10–450°. Specimens were maintained at constant temperature to within ±0.5° in a pot furnace for temperatures above ambient and within ±0.1° in a chamber in an oil bath for those below. Corrections for capacitance of leads and supports were made when it was deemed necessary.

Measuring instruments employed were the following General Radio bridges: Types 716C, 1608A, 1615A, 916A, and 544B. Frequencies up to 10 Mcps were generated with a Hewlett-Packard Model 650A.

Results and Discussion

Permittivity and Loss Tangent. The variation of permittivity, ϵ', with temperature for polycrystalline $BaTi_3O_7$ and $BaTi_4O_9$, within the temperature range 0–210° and 100 cps–10 Mcps, is shown in Figure 1. The estimated accuracy of these results is ±5%. Upper temperature limits at which capacitance measurements could be made by the methods employed were determined by the rise in loss tangent of the samples.

Change of permittivity with temperature for $BaTi_3O_7$ at given frequencies is linear or nearly so (Figure 1). Separation of curves at 100 cps and 1, 10, and 100 kcps lay within the limits of experimental error, except above about 220° where a small displacement of the curve for 100 cps occurred. Curves for the tetratitanate are quite similar to those for the trititanate, except that above about 130° dielectric dispersion was found at the lower frequencies. It is observed that at any chosen temperature in the linear interval the permittivity rises with frequency to a maximum which lies between 5 and 10 Mcps.

Representative data showing the variation of tan δ with temperature and frequency at lower frequencies for $BaTi_3O_7$ are plotted in Figure 2. Similar results were obtained for $BaTi_4O_9$.

Log tan δ rises nearly linearly in the high-temperature range of the curves for frequencies from 10^2 to 10^5 cps. In the megacycle region the loss tangent tends to increase with increase in frequency. The rough constancy of tan δ with frequency change in the low-frequency region indicates a wide distribution of relaxation times. The presence of a relaxation of large size is suggested by the gradual rise of the loss tangent curves.

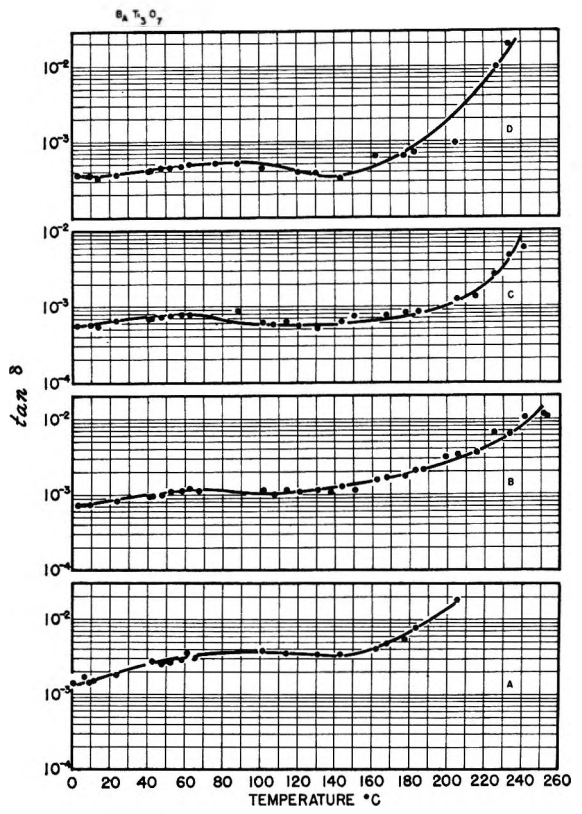

Figure 2. Variation of tan δ with temperature and frequency for $BaTi_3O_7$: (A) 100 cps, (B) 1 kcps; (C) 10 kcps; and (D) 100 kcps.

Such a relaxation is probably due to interfacial and space-charge polarization. Since the direct current conductivity was found to be rather low at ambient temperature, the contribution of the conductance to tan δ was then necessarily low.

It is customary[7] to represent the simultaneous occurrence of loss current and charging current by the introduction of a complex permittivity $\epsilon = \epsilon' - j\epsilon''$, where $\epsilon'' = \epsilon' \tan \delta$. The dependence of ϵ'' on temperature at stated frequencies is given in Table II. ϵ'' tends to rise with temperature. At lower frequencies marked changes occur only above about 150°. In the megacycle region, current conduction losses have increased by a factor of 10^2 or more.

Direct Current Conductivity. To learn what fraction of the loss tangent was due to direct current conductivity, measurements were made of the direct current resistance and of capacitance and tan δ at 1 kcps from room temperature to about 400°. Measurements were also made, by way of comparison, on disks of technical grade ceramic barium titanate (97% $BaTiO_3$) having a density of 5.733 g/cm^3. Results are plotted in Figures 3 and 4. Examination of these figures shows that, at low temperatures, the direct current conductivity represents only a small fraction of the total conductivity in each compound, whereas at higher temperatures it is the greater part of it. That is, the contribution of the direct current conductance to the

Table II: Change of Loss Factor, ϵ'', with Frequency and with Temperature for Polycrystalline $BaTi_3O_7$ and $BaTi_4O_9$

Frequency, cps	Temp, °C	$BaTi_3O_7$ loss index (ϵ'')	$BaTi_4O_9$ loss index (ϵ'')
10^2	20	0.089	0.0066
	50	...	0.0086
	100	...	0.039
	150	...	0.34
	200	...	...
10^3	20	0.042	0.039
	50	0.054	0.047
	100	0.048	0.12
	150	0.065	0.53
	200	0.12	4.2
	250	0.58	...
10^4	20	0.032	0.019
	50	0.039	0.020
	100	0.029	0.027
	150	0.028	0.12
	200	0.046	0.66
	240	0.36	...
10^5	20	0.035	0.018
	50	0.022	0.016
	100	0.024	0.012
	150	0.018	0.043
	200	0.078	...
	240	1.5	...
5×10^5	20	0.59	0.50
	40	0.47	0.45
10^6	20	2.9	2.00
	50	2.9	1.97
10^7	30	6.5	0.74
	50	3.2	0.86
	100	2.7	1.3
	150	5.6	6.4
	200	3.7	8.9
	250	2.9	5.5

experimentally determined tan δ is significant at higher temperatures. For example, in $BaTi_4O_9$ the ratio of the 1-kcps conductivity to the direct current conductivity is 4×10^{-8} at 60°.

Temperature Coefficient of Permittivity. Temperature coefficients of permittivity $(1/\epsilon')(d\epsilon'/dt)$ were evaluated from the plots of permittivity *vs.* temperature at the frequencies shown in Figure 1. Values at 20° are given in Table III. These coefficients do not change much in magnitude with rising temperature until the region of temperature dispersion appears; thereafter they become large and positive.

Piercy[8] has discussed the factors which contribute to the sign and magnitude of the temperature coefficient: (a) the coefficient of linear expansion, β, and

(7) H. Frölich, "Theory of Dielectrics," 2nd ed, Oxford University Press, Fair Lawn, N. J., 1958, Chapter I, p 192.

(8) B. Piercy, *Trans. Faraday Soc.*, 55, 39 (1959).

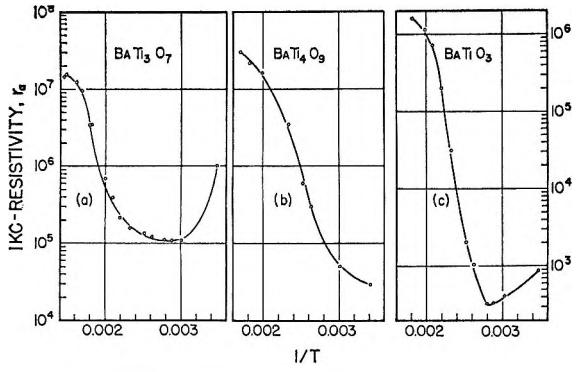

Figure 3. Variation of 1 kcps resistivity, r_a, in ohm centimeters with reciprocal of the Kelvin temperature, T, for ceramic: (a) $BaTi_3O_7$; (b) $BaTi_4O_9$; and (c) $BaTiO_3$.

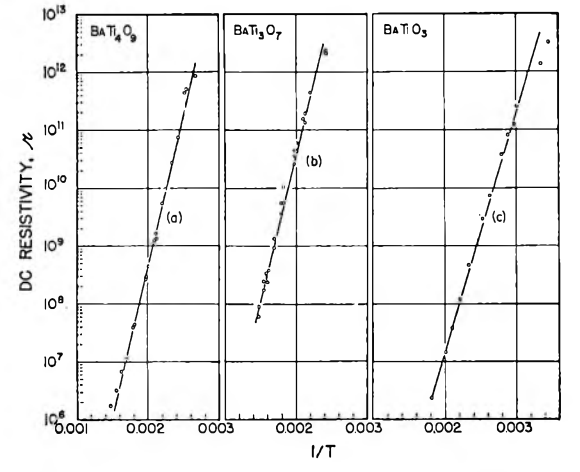

Figure 4. Variation of dc resistivity, r, in ohm centimeters with reciprocal of the Kelvin temperature, T, for ceramic: (a) $BaTi_4O_9$; (b) $BaTi_3O_7$; and (c) $BaTiO_3$.

Table III: Temperature Coefficient of Permittivity $(1/\epsilon')(d\epsilon'/dt)$ and Numerical Values of $A = (1/\epsilon')(d\epsilon'/dt)/\tan\delta$ at 20° for Ceramic $BaTi_3O_7$ and $BaTi_4O_9$

Ceramic	Frequency	$(1/\epsilon')d\epsilon'/dt$	$\lvert A\rvert$
$BaTi_3O_7$	100 cps–100 kcps	-4.5×10^{-4}	0.02
	500 kcps and 1 Mcps	-3.4×10^{-4}	0.62
	5 Mcps	-2.0×10^{-4}	0.009
	10 Mcps	0	0
$BaTi_4O_9$	100 cps–100 kcps	0	0
	500 kcps	-2.0×10^{-4}	0.04
	1 Mcps	-2.0×10^{-4}	0.04
	3 Mcps	-2.0×10^{-4}	...
	5 Mcps	-1.9×10^{-4}	0.01
	10 Mcps	4.7×10^{-4}	0.06

the temperature coefficient of electronic and ionic polarizabilities $(1/\alpha)(d\alpha/dt)$ result in the contribution $(1/\epsilon_\infty)(d\epsilon_\infty/dt)$, and (b) a contribution which is the result of dielectric relaxations.

The equation derived by Piercy[8] can be written in the form of eq 2.

$$(1/\epsilon)(d\epsilon/dt) = (\epsilon_\infty - 1)(\epsilon_\infty + 2)\left(\frac{1}{\alpha}\frac{d\alpha}{dt} - 3\beta\right)\frac{1}{3\epsilon_\infty} + (\epsilon/\epsilon_\infty)\frac{2}{\pi}\ln\left(\frac{1}{\omega\tau_0}\right)\frac{d}{dt}\tan\delta \quad (2)$$

The volume coefficient $(1/v)(dv/dt)$ is taken equal to 3β; α is the sum of the electronic and ionic polarizabilities. The derivation of this equation is partly based on the differentiation of the Clausius–Mossotti equation and strictly speaking is applicable only to those dielectrics to which this relationship applies. It is assumed that tan δ is independent of frequency. Examination of the loss tangent *vs.* temperature curves at fixed frequencies up to 10^5 cps for $BaTi_3O_7$ and $BaTi_4O_9$ showed that the loss tangent is essentially constant at any chosen temperature within the range investigated. It is seen that the temperature coefficient of permittivity will be negative only if the volume coefficient of expansion (3β) is the predominating factor when $(1/\alpha)(d\alpha/dt)$, β, and d tan δ/dt are positive.

Negative values of $(1/\epsilon)(d\epsilon/dt)$ for $BaTi_3O_7$ and $BaTi_4O_9$ in the low-frequency and low-temperature regions indicate that the polarizability coefficient $(1/\alpha)(d\alpha/dt)$ is smaller than 3β and that tan δ is negligible. There is a marked increase in d tan δ/dt at higher temperatures for $BaTi_4O_9$ with the result that the slope of the temperature coefficient of permittivity becomes positive. Any value of d tan δ/dt occurring in the temperature dispersion region at a low frequency shifts to higher temperatures with increase in frequency.

The entropy change (in electrostatic cgs units) per cubic centimeter of a dielectric, on the application of a static field E, is given by the relationship

$$S - S_0(T) = (\partial\epsilon_s/\partial T)E^2/8\pi \quad (3)$$

where T is the Kelvin temperature, $S_0(T)$ is the entropy per unit volume in the absence of the field E, and ϵ_s is the static permittivity which is essentially the same as the low-frequency permittivity.[7] The slope of the 100-cps curve for $BaTi_3O_7$ (Figure 1) is -0.022 deg^{-1}, whereas that for $BaTi_4O_9$ at the same frequency was taken to be zero. In the case of $BaTi_3O_7$, at a field strength of 30 V/cm ($E = 0.1$) the entropy decrease, as found from eq 3 is -8.8×10^{-6} esu/cm^3, indicating a slight ordering in the presence of the field.

Activation Energies. A comparison of the activation energy for the large dispersion in the high-temperature region with that for direct current conduction yields further knowledge concerning this particular relaxation process. We follow the procedure in which the approximation is made that there is but a single relaxation time and that $\epsilon_0' - \epsilon_\infty'$ is not temperature dependent.[8] If f_i and T_i, and f_j and T_j are any two frequencies and Kelvin temperatures, respectively, at which the capac-

ities of the sample are the same, the activation energy E_1 of the relaxation is given by

$$E_1 = 2.303\frac{kT_iT_j}{T_i - T_j}\log\frac{f_i}{f_j} \quad (4)$$

where k is the Boltzmann constant.

Examination of the Debye equations, which refer to a dispersion mechanism with but a single relaxation time τ, shows that tan δ also remains constant when $\omega\tau$ is constant.[7] Equation 4 is then applied by first choosing a value of tan δ for the region under study and reading temperatures off the tan δ *vs.* temperature curves and recording the frequencies.

Activation energies obtained by use of the two above given procedures for this large dispersion are given in columns 2 and 3 of Table IV. Frequencies chosen were in the range 10^2–10^5 cps and temperatures were in the neighborhood of 200°. In the case of $BaTi_3O_7$, dielectric dispersion had not occurred sufficiently at the higher temperatures to permit the evaluation of E_1.

The activation energy E_2 for dc conduction was evaluated from the log (resistivity) *vs.* $1/T$ plot (Figure 3). For $BaTi_3O_7$ and $BaTi_4O_9$ these resistivity curves lie well across the region of the large dielectric dispersion. Values for E_2 are given in Table IV.

Table IV: Activation Energies, E, by Different Procedures

	Activation energy, E, from		
Ceramic	Dielectric dispersion, eV	Tan δ, eV	Direct current conduction, eV
$BaTiO_3$	...	...	0.85
$BaTi_3O_7$	...	0.88	1.05
$BaTi_4O_9$	0.80	0.74	1.03

Tests for Ferroelectricity. An examination of Figure 1 shows that marked changes in permittivity with temperature rise were not observed for either dielectric in the temperature range 0–260°. Thus no phase changes are indicated in this region.

To determine whether or not these compounds are ferroelectric, respective disks of each were mounted in a 60-cps display circuit.[9] The hysteresis loop, characteristic of ferroelectrics, was not observed in the temperature range 0–425°. Also the maximum polarization was low and roughly 0.01 that for ceramic barium titanate under like conditions.[9] Examples are shown in Figure 5. The ratio of the polarizations at 10 kV/cm, $P_M(BaTi_3O_7)/P_M(BaTiO_3)$, was about 0.005.

Structure and Ferroelectricity. The atomic arrangement at ambient temperatures of the five intermediate compounds in the BaO–TiO_2 system has been determined with the exception of $BaTi_3O_7$. Only the metatitanate, $BaTiO_3$, displays ferroelectricity. The reasons

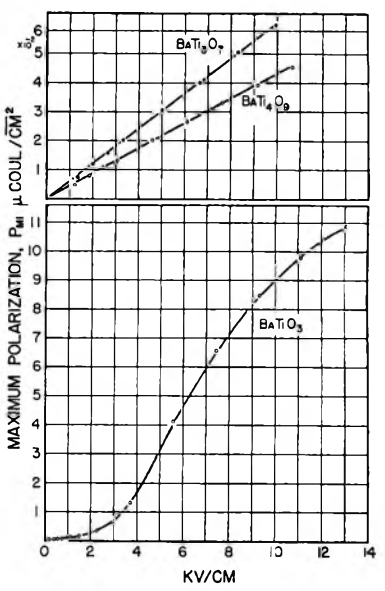

Figure 5. Evidence of lack of ferroelectricity in $BaTi_3O_7$ and $BaTi_4O_9$ at 25°. Upper curves, linear variation of the maximum polarization with peak field strength; lower curve, unpolarized ceramic $BaTiO_3$.

for this will now be pointed out. The orthotitanate, Ba_2TiO_4, has the monoclinic space group $P2_1/m$ and thus belongs to the point groups 2/m, which is a nonpolar crystal class, and so at least at room temperature this titanate is not ferroelectric.[10] The environment of the titanium site is not the usual octahedral arrangement so characteristic of perovskite-type titanates, but rather a more nearly tetrahedral arrangement of oxygen sites about the titanium ion, thus resembling a sulfate ion. In barium dititanate, $BaTi_2O_5$, the titanium atoms lie in a distorted structure of octahedra of oxygen atoms.[11] The space group is A2/m, which is also one of the nonpolar crystal class 2/m. Barium tetratitanate, $BaTi_4O_9$, has the symmetry of the nonpolar orthorhombic class (mmm) at room temperature.[6] The titanium sites lie in distorted octahedra which share edges and corners three dimensionally. The titanium atoms are not at the centers of these octahedra so that polarized octahedra are the result, but the over-all structure is a centric one, so that this titanate is not ferroelectric either. In barium metatitanate the titanium atoms lie within octahedra of oxygen atoms which share their corners with those of neighboring octahedra. At ordinary temperatures this compound belongs to the tetragonal space group P4/mm, which implies that the fourfold symmetry axis is polar, and hence this material is ferroelectric.[12]

(9) G. W. Marks, D. L. Waidelich, and L. A. Monson, *Commun. Electron.*, **26**, 469 (1956).

(10) J. A. Bland, *Acta Cryst.*, **14**, 875 (1961).

(11) F. W. Harrison, *ibid.*, **9**, 495 (1956).

(12) H. D. Megaw, "Ferroelectricity in Crystals," Methuen and Co., London, 1957, Chapter 4.

Summary

1. Within the temperature range 0–260° and the frequency range 100 cps–10 Mcps, the permittivity, ϵ', of ceramic $BaTi_3O_7$ and ceramic $BaTi_4O_9$ varies linearly with temperature.

2. The loss tangent of both dielectrics at any chosen temperature within the range 0–150° remains essentially constant with increase in frequency up to 10^5 cps.

3. Activation energies from direct current conduction measurements are 1.05 eV for $BaTi_3O_7$ and 1.03 eV for $BaTi_4O_9$.

4. No evidence of ferroelectricity was found for either of these dielectrics within the range 0–425°.

Properties of Ethylene–Methacrylic Acid Copolymers and Their Sodium Salts: Infrared Studies

by W. J. MacKnight,[1] L. W. McKenna, B. E. Read, and R. S. Stein

Department of Chemistry and Polymer Science and Engineering Program, University of Massachusetts, Amherst, Massachusetts 01002 *(Received June 20, 1967)*

An infrared spectroscopic investigation of ethylene–methacrylic acid copolymers and their sodium salts has been carried out. All the copolymers studied were based on a parent copolymer containing 4.1 mol % of methacrylic acid groups. This was then neutralized to various extents (from 0 to 78%) with sodium hydroxide. The per cent ionization was determined from the integrated absorbance of the 1700 cm^{-1} un-ionized carbonyl stretching band. Temperature-dependent infrared studies showed that the behavior of the un-ionized acid groups over the entire range of ionization is quantitatively comparable to that of low molecular weight carboxylic acids in nonpolar solvents. A monomer–dimer equilibrium exists among the acid groups and they are almost completely in the form of hydrogen-bonded dimers at room temperature. The heat of dissociation of the dimers was found to be 11.6 kcal mol^{-1}. Thus each hydrogen-bond has a bond strength of 5.8 kcal mol^{-1}. Infrared dichroism studies established that there is a significant amount of crystallinity even at the highest degree of ionization, that the hydrogen bonds are intermolecular in nature, and that the ionized carboxylate groups have a preferred orientation out of the plane of the main chain of the copolymer.

Introduction

This work represents part of a continuing study of the role of intermolecular forces on the physical and mechanical properties of polymers. The ethylene–methacrylic acid copolymers and their sodium salts provide an interesting system for such investigations. It has been established[2] that the ionization of these acid copolymers results in a significant enhancement of their tensile strengths and melt viscosities. These findings were explained on the basis of the introduction of strong interchain ionic links.[2] The validity of this interpretation is somewhat doubtful, however, and alternative explanations have recently been proposed.[3]

In this paper are reported the results of an infrared study on films of ethylene–methacrylic acid copolymers, ionized to various extents with sodium. The per cent ionization was determined by analysis of the infrared spectra. The equilibrium constant for the dissociation of carboxylic acid dimers and their heat of dissociation were obtained from temperature-dependent infrared studies. Infrared dichroism indicated that the hydrogen bonds formed between un-ionized carboxyl groups are intermolecular.

The implications of these findings concerning the mechanical properties of the materials are discussed elsewhere.[3]

Experimental Section

The starting material was a partially ionized copolymer of ethylene and methacrylic acid kindly supplied by the Du Pont Co. Its structure may be represented schematically as

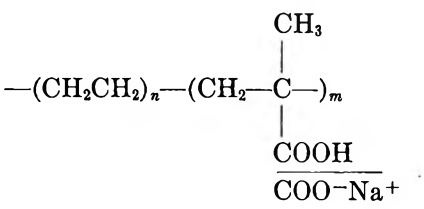

(1) To whom correspondence should be addressed.

The methacrylic acid content of the copolymer was 4.1 mol %. For a random distribution of methacrylic acid groups, this would yield an average value of n of about 25 for $m = 1$. As pointed out in the Discussion section, however, there may be some tendency for the methacrylic acid units to exist in blocks ($m > 1$). In this case the sequence lengths of many of the ethylene units would be much greater than 25.

The finely divided starting material was refluxed in tetrahydrofuran with dilute hydrochloric acid in order to produce the ionized copolymer. This was in turn neutralized to various extents by refluxing in tetrahydrofuran with sodium hydroxide for varying periods of time and at different base concentrations. After this treatment, the ionized copolymers were precipitated twice in a methanol–water mixture, washed thoroughly several times, and dried *in vacuo* at 100°. Samples were compression molded into thin films at 180° and 20,000 lb of pressure.

Infrared spectra of the films were obtained on a Beckman spectrophotometer, Model IR-10. This instrument was operated on the fast-scan setting with the gain control at position 5. The spectral accuracy of the IR-10 is given as 8 cm^{-1} from 4000 to 2000 cm^{-1} and as 4 cm^{-1} from 2000 to 300 cm^{-1}.[4] Temperature-dependent infrared studies were made using a temperature enclosure constructed for this purpose. Temperatures were measured using a calibrated copper–constantan thermocouple which rested against the polymer film surface.

Results and Discussion

Figure 1 shows the infrared spectra of the four samples investigated. The following points are of interest. First, there is strong evidence for hydrogen bonding in all cases as shown by the shoulder appearing at 2650 cm^{-1}. This shoulder is characteristic of the stretching mode of the hydrogen bonded hydroxyl group. Second, the un-ionized carbonyl stretching frequency appears at 1700 cm^{-1} and remains at the same position throughout the entire range of ionization. Finally, the absorption due to the asymmetric stretching mode of the carboxylate ion occurs at 1560 cm^{-1} and, of course, increases in magnitude with increasing ionization.

The integrated absorbance per centimeter sample thickness of the 1700-cm^{-1} carbonyl band was used to determine the degree of ionization. The absorbance, A, is defined as $\log I_0/I$, where I_0 is the incident and I is the transmitted intensity. The integrated absorbance corresponds to the area beneath plots of A against wave number (cm^{-1}). For the 1700-cm^{-1} band, the ratio $S:\Delta\nu_{1/2}$, where S is the spectral slit width and $\Delta\nu_{1/2}$ is the absorption band halfwidth, was found to vary from a value of about 0.13 for the acid copolymer to a value of about 0.06 for the most highly ionized copolymer. Since the peak absorbances did not exceed 0.8, the correction for instrument resolving power (about 1 %) was considered negligible.[5] The success of the present technique for measuring the degree of ionization depends on the lack of overlap of neighboring bands and on accurate film-thickness measurements. The intensity of the carbonyl absorption for the un-ionized acid copolymer is such that it is necessary to use a film of approximately 1.27×10^{-3} cm thickness in order to get this absorption on scale. The following procedure was developed to measure the thickness accurately. A band was selected with an absorbance that could be measured from film thicknesses of about 2.54×10^{-2} cm to thicknesses of less than 1.27×10^{-3} cm. An appropriate band for this is the 935-cm^{-1} band in the case of the un-ionized acid copolymer. This band is assigned to the out-of-plane deformation modes of the hydroxyl groups. Its absorbance should thus be proportional to the number of acid groups within the beam and should be independent of the thermal history of the sample. A plot was made of peak absorbance (A_{max}) *vs.* thickness for this band. Thicknesses in the range from 2.54×10^{-2} to $7.62 \times$

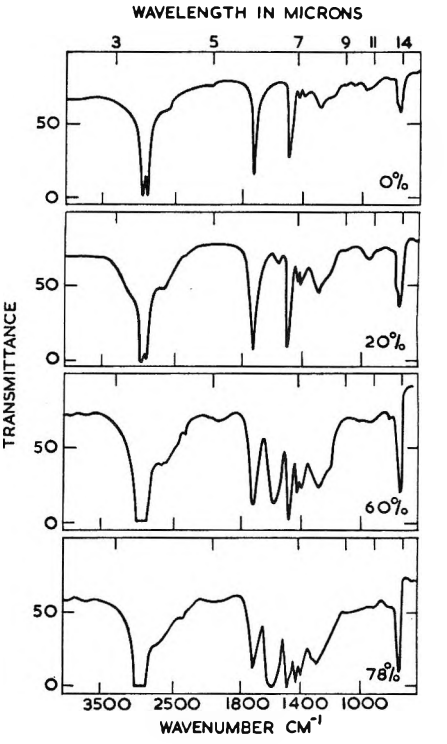

Figure 1. Infrared spectra of ethylene–methacrylic acid copolymer films ionized to different extents with sodium. Thickness: 0%, 1.2×10^{-3} cm; 20%, 2.5×10^{-3} cm; 60%, 6.1×10^{-3} cm; 78%, 9.4×10^{-3} cm.

(2) R. W. Rees and D. J. Vaughn, *Polym. Preprints*, 6, 296 (1965).

(3) W. J. MacKnight, L. W. McKenna, and B. E. Read, *J. Appl. Phys.*, 38, 4208 (1967).

(4) Beckman Instructions 1383-A (available from Beckman Instruments Inc., Scientific and Process Instruments Division, Fullerton, Calif. 92634).

(5) D. P. Ramsay, *J. Amer. Chem. Soc.*, 74, 72 (1952).

10^{-3} cm could be satisfactorily measured by a micrometer. This plot yielded a straight line which extrapolated through the origin. Thus it was established that Beer's law was obeyed. From this plot, the thickness of the films was determined, thus enabling the evaluation of the integrated absorbance of the 1700-cm^{-1} band/unit sample thickness. In the case of the ionized samples a similar procedure was followed, except that at the higher degrees of ionization it was not necessary to employ very thin films and the thicknesses could be measured directly by the micrometer. The per cent ionization was then calculated using the relationship

$$\% \text{ ionization} = \left[1 - \frac{\text{integrated absorbance/cm (ionized)}}{\text{integrated absorbance/cm (un-ionized)}}\right]100 \quad (1)$$

Table I lists the integrated absorbances and the per cent ionization for the four samples investigated.

Table I

Integrated absorbance of 1700-cm^{-1} peak/cm sample thickness, $cm^{-2} \times 10^{-3}$	% ionization
18.32	0
14.71	19.7
7.26	60.4
4.10	77.6

The results of the temperature-dependent infrared studies on the un-ionized copolymer are shown in Figure 2. Of interest are the appearance of a band at 3540 cm^{-1} which increases in magnitude with increasing temperature, and the appearance of a shoulder at 1750 cm^{-1} on the main 1700-cm^{-1} carbonyl band which also increases with increasing temperature. Such behavior is characteristic of low molecular weight carboxylic acids in nonpolar solvents and is interpreted on the basis of a monomer–dimer equilibrium.[6] Thus the 3540-cm^{-1} band is attributed to the free hydroxyl stretching vibration, the 1750-cm^{-1} band to the monomeric carbonyl stretching vibration, and the 1700-cm^{-1} band to the dimerized carbonyl stretching vibration. Figure 3 shows the peak absorbance film thickness for the 3540-cm^{-1} absorption as a function of temperature. From this plot it is evident that free hydroxyl groups are first detected by infrared at about 30°. The above results lead to a structure for the copolymer in which the acid groups are dimerized to form interchain links. The dimerization is essentially complete at room temperature. This structure may be schematically represented as

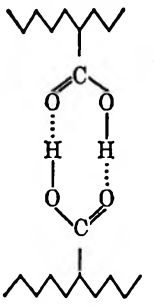

The dissociation constant, K, is defined by

$$K = \frac{[\text{-COOH}]^2}{[(\text{-COOH})_2]} \quad (2)$$

where [-COOH] is the concentration of monomeric carboxyl groups and $[(\text{-COOH})_2]$ is the concentration of dimerized carboxyl groups. K was evaluated from the spectra in Figure 2. This was accomplished by measuring the peak absorbances of the 1700- and 3540-cm^{-1} bands at each temperature (54–99°). At 99° the 1750-cm^{-1} band was sufficiently well resolved so that its peak absorbance could be measured using a base line determined as indicated in Figure 2. The ratio of this absorbance to that of the 3540 cm^{-1} free hydroxyl band was obtained at 99°. This ratio was assumed indepen-

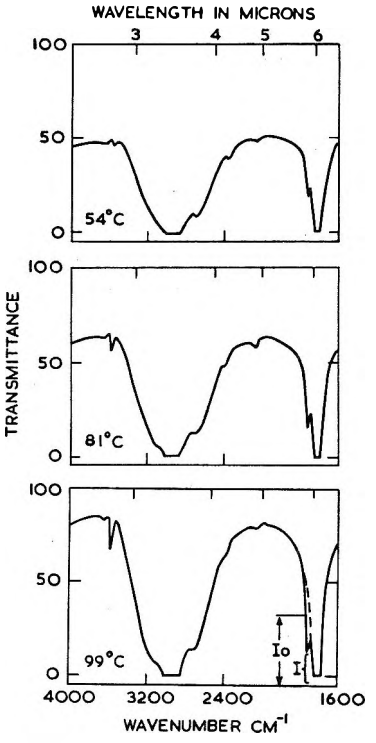

Figure 2. Temperature dependence of the infrared spectrum of the un-ionized ethylene–methacrylic acid copolymer. The dotted line on the 1750-cm^{-1} band at 99° was used to determine the base line for the peak-absorbance measurement of the band.

(6) C. N. R. Rao, "Chemical Applications of Infrared Spectroscopy," Academic Press, Inc., New York, N. Y., 1963, Chapter III.

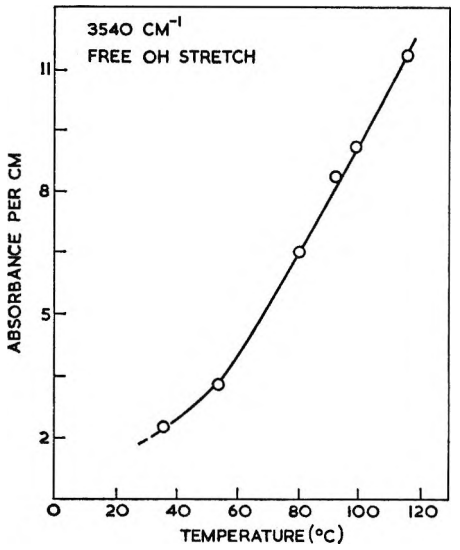

Figure 3. Temperature dependence of the peak absorbance per centimeter of the 3540-cm^{-1} free hydroxyl stretching band.

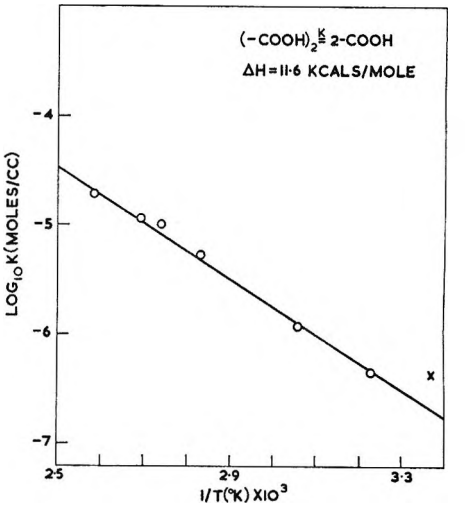

Figure 4. van't Hoff plot (log K *vs.* $1/T$) of the dissociation constant for the acid monomer–dimer equilibrium. The open circles are the experimental points. The cross (×) is the literature value for low molecular weight carboxylic acids in nonpolar solvents.

dent of temperature and thus the absorbances of the 1750-cm^{-1} band at the other temperatures could be derived from the measured absorbances of the 3540-cm^{-1} band at these temperatures. If the peak absorbances are expressed as absorbances per centimeter, the following relationships can reasonably be assumed to apply.

$$A_{1,\max} = \epsilon_1 C_1 \tag{3}$$

$$A_{2,\max} = \epsilon_2 C_2 \tag{4}$$

$$\epsilon_2 = 2\epsilon_1 \tag{5}$$

where $A_{1,\max}$ is the peak absorbance per centimeter of the 1750-cm^{-1} band, ϵ_1 is the molar extinction coefficient of the 1750-cm^{-1} band in square centimeters per mole, C_1 is the concentration in moles per cubic centimeter of the monomeric carboxyl groups, $A_{2,\max}$ is the peak absorbance per centimeter of the 1700-cm^{-1} band, ϵ_2 is the molar extinction coefficient of the 1700-cm^{-1} band in square centimeters per mole, and C_2 is the concentration in moles per cubic centimeter of the dimerized carboxyl groups. Equation 5 is justified by the work of Chang on the model system pivalic acid in benzene. It was found that the molar extinction coefficient for the dimer in this system is almost exactly twice the molar extinction coefficient for the monomer.[7] Using eq 3–5, the expression for the dissociation constant becomes

$$K \text{ (mol/cm}^3\text{)} = \frac{(A_{1,\max})^2 4}{(A_{2,\max})\epsilon_2} \tag{6}$$

ϵ_2 can be determined using eq 4, substituting in the value of the peak absorbance per centimeter of the 1700-cm^{-1} band at room temperature and the known concentration of the methacrylic acid groups in the copolymer. It is interesting to note that the value thus obtained, 9.14 × 10^5 cm^2 mol^{-1}, compares quite favorably with the value of 12.6 × 10^5 cm^2 mol^{-1} obtained for the pivalic acid–benzene system. Small differences would be expected, of course, between values obtained from different spectrometers owing to differences in resolving power, scanning speed, etc.

The logarithms of the dissociation constants are plotted as a function of reciprocal temperature in Figure 4. The open circles are the experimental points while the cross represents the value for the dissociation constant of unconjugated carboxylic acids in carbon tetrachloride measured by Wenograd and Spurr.[8] The heat of dissociation of 11.6 kcal mol^{-1} obtained from the slope of the van't Hoff plot in Figure 4 also agrees well with literature values for low molecular weight carboxylic acids in nonpolar solvents. Thus it may be concluded that the association of the acid groups of the copolymer is quantitatively comparable to the dimerization of low molecular weight carboxylic acids in nonpolar solvents. It was further established that the peak absorbance of the 3540 cm^{-1} free hydroxyl band is inversely proportional to the degree of ionization. This means that the monomer–dimer equilibrium of the remaining carboxyl groups is unaffected by ionization of a portion of the carboxyl groups.

The results of the infrared dichroism studies are presented in Figure 5. Attention is directed to the 720–730-cm^{-1} region. In the case of the un-ionized copolymer, the unpolarized band in this region consists of a doublet with absorption maxima at 720 and 730 cm^{-1}. Such behavior is characteristic of polyethylene

(7) L. C-Y. Chang, Ph.D. Thesis, Polytechnic Institute of Brooklyn, Brooklyn, N. Y., 1955.

(8) J. Wenograd and R. A. Spurr, *J. Amer. Chem. Soc.*, **79**, 5844 (1957).

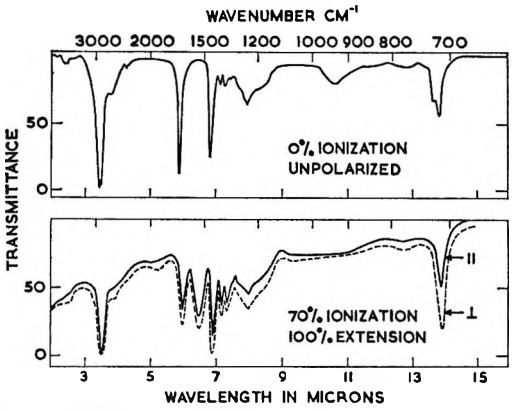

Figure 5. Polarized infrared spectra for the 70% ionized copolymer.

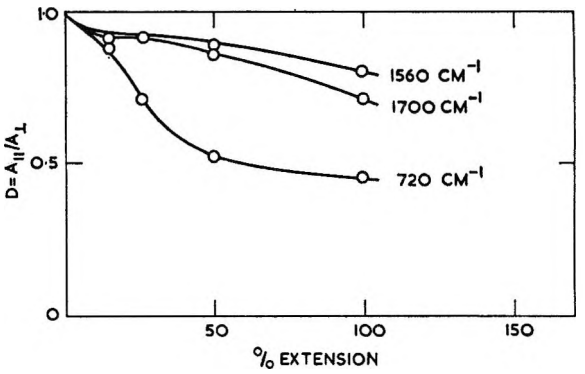

Figure 6. Dichroic ratio *vs.* per cent extension for three bands of the 70% ionized copolymer.

and it has been shown[9] that the 720-cm^{-1} band is due to both the amorphous and crystalline phases, the crystalline component being polarized along the *a* crystallographic axis. On the other hand, the 730-cm^{-1} band is due entirely to the crystalline phase and is polarized along the *b* crystal axis. Both the 720- and 730-cm^{-1} bands thus show perpendicular dichroism when the polymer is extended. Turning to the 70% ionized copolymer, it can be seen that the 730-cm^{-1} band has entirely disappeared in the parallel polarized spectrum but appears as a shoulder on the main 720-cm^{-1} band in the perpendicularly polarized spectrum. It is thus apparent that even at 70% ionization, a significant amount of crystallinity remains. It can also be seen that the shoulder around 2650 cm^{-1}, characteristic of the hydrogen bonded hydroxyl group, shows perpendicular polarization. This indicates that the transition moment of the hydrogen bonded hydroxyl group is perpendicular to the main chain and is thus evidence for the presence of intermolecular hydrogen bonds in the acid dimers present. In this connection it is interesting to note that the parallel dichroism of the hydrogen-bonded 3350-cm^{-1} hydroxyl band in isotactic polyvinyl alcohol has been cited as evidence for intramolecular hydrogen bonding in this polymer.[10]

Figure 6 shows a plot of the dichroic ratio (defined as $D = A_{\parallel}/A_{\perp}$ *vs.* per cent extension for three bands of the 70% ionized copolymer. The 720-cm^{-1} band shows relatively large perpendicular dichroism, again emphasizing the significant crystalline contribution to this band. Both the 1700- and 1560-cm^{-1} bands show relatively small perpendicular dichroism. This is consistent with the presence of the carboxyl groups and carboxylate ions in the amorphous phase, since they would be expected to be too large to be incorporated into the polyethylene crystal lattice. The perpendicular dichroism of the 1560-cm^{-1} band indicates that the carboxylate ions have a preferred orientation out of the plane of the main chain. This can be seen schematically as

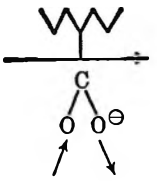

As shown, the transition moment direction for the asymmetric stretching mode would be parallel to the main chain if the carboxylate groups were in the plane of the main chain. The out-of-plane orientation of the carboxylate ions may be due to steric hindrance arising from neighboring carboxylate or carboxyl groups. Such steric hindrance would be expected to occur if the methacrylic acid units have a tendency to be in blocks.

Acknowledgments. We are grateful to the National Science Foundation for partial support of this research under Grants GP 5840 and GP 5372X. We are also indebted to Dr. W. F. Brondyke of the Plastics Department of the Du Pont Co. for supplying the starting material.

(9) R. S. Stein and G. B. B. M. Sutherland, *J. Chem. Phys.*, **21**, 371 (1953); **22**, 1993 (1954).

(10) S. Murahashi, H. Yuki, T. Sano, U. Yonemura, H. Tadokoro, and Y. Chatane, *J. Polymer Sci.*, **62**, 577 (1962).

A Spectroscopic Study of Binuclear Copper Complexes in Aqueous Poly(methacrylic acid) Solutions

by J. C. Leyte, L. H. Zuiderweg, and M. van Reisen

Laboratory of Physical Chemistry, The University of Leyden, The Netherlands

Accepted and Transmitted by The Faraday Society (July 3, 1967)

The changes in the ir, visible, and uv spectra and the static magnetism of aqueous solutions of the PMA–Cu(II) system as a function of the degree of neutralization of the polyacid have been recorded. It is concluded that at low polyelectrolyte charge a binuclear copper complex exists which dissociates, yielding mononuclear complexes, on increasing the charge of the polyion. It is shown that the ir intensities of the carboxylate groups may be of considerable use in the identification of binuclear carboxylates.

Introduction

The existence of a complex of Cu(II) and poly(methacrylic acid) (PMA) was established some time ago[1] and this complex has been the subject of several publications since.[2,3] The binding of copper ions by PMA is conveniently discussed in terms of the ratio f = [equivalent concentration of ionized PMA]/[equivalent concentration of Cu(II)].

With the help of several experimental methods (potentiometry, viscosity, electrophoresis, and spectrophotometry) it was shown that Cu(II) ions are chelated by two carboxylate groups per metal ion for $f \leqq 1.2$.[3] At higher charge densities of the polyelectrolyte ($f > 1.2$), a decrease was observed in the intensities of the visible and uv spectrum characteristic of the complex. As was done in the case of the Cu(II)–poly(acrylic acid) complex,[4] this was interpreted in terms of a partial disintegration of the complex and possible competition between site binding and interaction with the over-all electrostatic field of the polymer.

The nonspectroscopic methods mentioned before do not admit a definite interpretation of this phenomenon. We have, therefore, investigated this system using spectroscopic methods directed at the binding sites (ir) and the chelated ions (visible region) directly.

In this way it is possible to gain information about the environment of the Cu(II) ion while the changes in the ir spectrum associated with the carboxylate group yield quantitative information on the amount of these groups involved in binding Cu(II) ions.

Experimental Part

The measurements in the visible and uv regions were performed using Unicam SP700 and Zeiss PMQII spectrophotometers. The spectra of the PMA–Cu(II) system at different f values were obtained by spectrophotometric titration of aqueous PMA–Cu(II) solutions with NaOH. Although the same results are obtained at different Cu(II) concentrations, it proved experimentally convenient to work with solutions containing 30% equiv of $Cu(ClO_4)_2$ with respect to PMA. The titrations were performed with a variable-pathlength titration cell. As the spectral changes in the region f = 1.3–3.3 occur smoothly throughout this range, we have only represented the extremes in Figures 1 and 2.

The infrared region was studied with a Unicam SP100 instrument equipped with a rock salt prism and grating. Because of the low-energy conditions in the region studied in D_2O solution, large slit widths had to be used. Although no influence of the slit width on the peak height could be detected on decreasing the slit width by 50%, the quantitative measurements were carefully performed at the same slit width for a given wave number in a series of solutions. The solutions in the concentration range of 0.07–0.16 equiv/l. with respect to PMA were measured in cells with CaF_2 windows at pathlengths of about 0.01 cm. Compensation for the solvent was carried out with variable pathlength cells at 1310 cm^{-1}. Transmission values were determined by the base line method. For the absorptions at 1610 and 1550 cm^{-1} the same base line was used. From the copper-free solutions we verified that at 1600–1610 cm^{-1} the absorption due to the 1550-cm^{-1} peak is negligible.

PMA of molecular weight 7.5×10^5 was synthesized and fractionated as described before.[5] Solution of PMA in D_2O and subsequent evaporation of D_2O was repeated five times before the final solution for ir work was prepared. Analytical grade $CuCl_2 \cdot 2H_2O$ was

(1) H. P. Gregor, L. B. Luttinger, and E. M. Loeble, *J. Phys. Chem.*, **59**, 366 (1955).

(2) A. M. Kotliar and H. Morawetz, *J. Amer. Chem. Soc.*, **77**, 3692 (1955).

(3) M. Mandel and J. C. Leyte, *J. Polym. Sci., Part A-2*, 2883, 3771 (1964).

(4) F. T. Wall and S. J. Gill, *J. Phys. Chem.*, **58**, 1128 (1954).

(5) J. C. Leyte and M. Mandel, *J. Polym. Sci., Part A-2*, 1879 (1964).

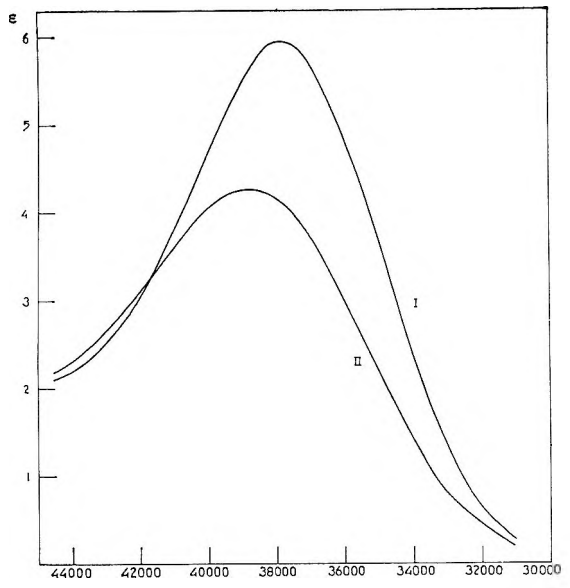

Figure 1. Ultraviolet spectrum of the PMA–Cu(II) system at $f = 1.3$ (I) and at $f = 3.3$(II): PMA, 3.00×10^{-3} equiv/l.; $Cu(C10_4)_2$, 9.00×10^{-4} equiv/l.

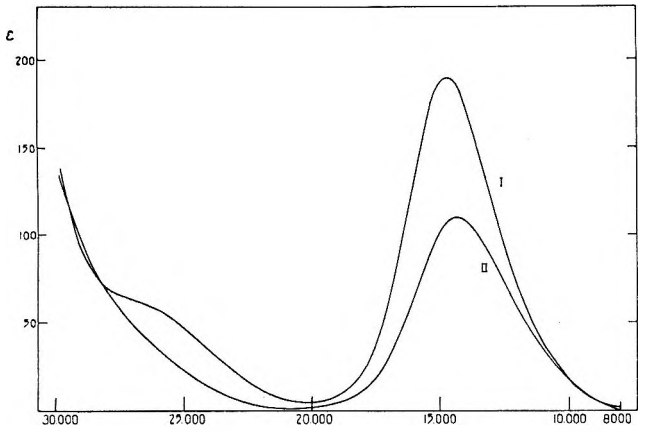

Figure 2. Visible and near-uv spectrum of the PMA–Cu(II) system at $f = 1.3$ (I) and at $f = 3.3$ (II): PMA, 3.00×10^{-2} equiv/l.; $Cu(C10_4)_2$, 9.00×10^{-3} equiv/l.

recrystallized four times from D_2O to exchange the water. NaOD solutions were prepared by dissolving freshly cut sodium in D_2O in a nitrogen atmosphere. D_2O of 99.8% was obtained from the Dutch Reactor Center.

Solutions of PMA containing 30% $CuCl_2$ (equivalent with respect to PMA) were mixed in varying proportions with identical solutions in which PMA was fully neutralized with NaOD to obtain PMA–$CuCl_2$ solutions at the degrees of neutralization wanted. Below $f = 1.3$, the complex is insoluble at the PMA concentrations used for ir work. All operations involving the D_2O solutions were performed in a drybox.

The magnetic measurements on the aqueous PMA–Cu system were performed at room temperature according to the Gouy principle. The authors are

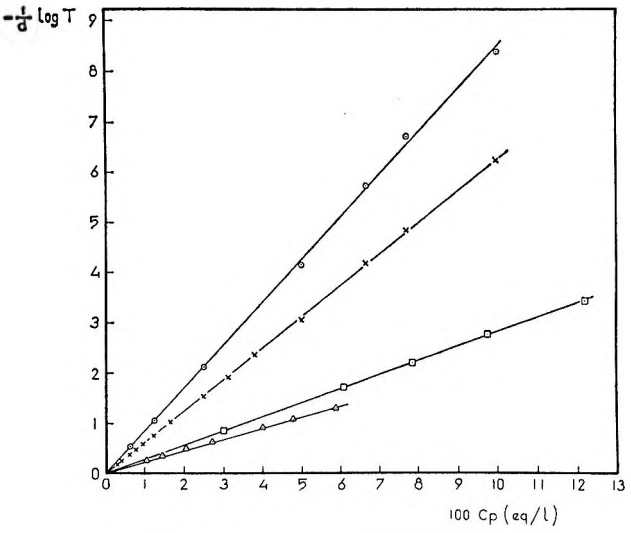

Figure 3. Lambert–Beer plots for the PMA–Cu(II) system: O, 38,000 cm^{-1} ($f = 1.5$); ×, 38,000 cm^{-1} ($f = 3.0$); □, 14,500 cm^{-1} ($f = 1.3$); △, 14,500 cm^{-1} ($f = 2.3$).

indebted to Dr. J. W. Roelofsen, who kindly obtained the results for them.

Results and Discussion

In Figure 1 and Figure 2, the visible and uv spectra of the Cu(II)–PMA system are shown for two f values. At $f = 1.3$ absorptions are observed at 37,800 and 14,500 cm^{-1}. A shoulder may be seen at 26,000 cm^{-1}, while symmetrical analysis of the absorption at 14,500 cm^{-1} reveals another maximum at 11,250 cm^{-1} ($\epsilon \approx 25$). At $f = 3.3$, the band at 26,000 cm^{-1} has disappeared and the uv maximum shifts to 38,750 cm^{-1} while its intensity decreases. The intensity decrease in the visible region is accompanied by a shift to 14,250 cm^{-1}. The absorption at 11,250 cm^{-1} decreases some 20%. When at $f = 3.3$ the solvent was replaced by dioxane, the band at 26,000 cm^{-1} reappeared. The magnetic moment shows an interesting dependence on f. From 1.91 μB at $f \approx 0$, it drops to 1.54 μB at $f = 1.3$. At $f = 3.0$ the moment has increased to 1.66 μB.

The application of both ir and uv spectroscopy to the same system often meets some experimental difficulties, as the concentrations that have to be used for convenient work in these regions generally differ by a factor of 100. Figure 3 shows that Lambert–Beer's law is obeyed (for $1.3 < f < 3$) in a concentration range that connects the regions in which the ir (0.1 equiv/l.) and uv (0.01–0.003 equiv/l.) results were obtained. A discussion of these results in terms of the same complex at a given value of f is, therefore, permitted.

An important conclusion which was tentatively reached earlier[3] may be confirmed from Figure 1: the ligands around a given Cu(II) ion are situated on one polymer molecule only. This explains the insensitivity of the relative complex concentration to dilution.

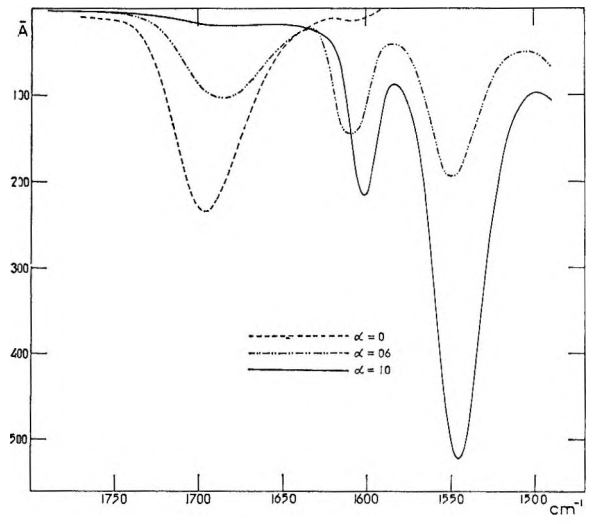

Figure 4. Infrared spectra of the aqueous PMA–Cu(II) system at three different α values. The solutions contain 30.0% equiv $CuCl_2$ with respect to PMA.

In Figure 4 the ir spectra are shown of the PMA–Cu(II) system at several degrees of neutralization. The identification in the region from 1500 to 1750 cm^{-1} presents no difficulties. The peaks at 1550 and 1700 cm^{-1} may be assigned to the antisymmetric stretching mode of the carboxylate group (ν_1) and the carbonyl stretching mode (ν_2), respectively.

An absorption at about 1600 cm^{-1} has been observed in the spectra of many Cu(II)–carboxylate complexes[6,7] and as there is no absorption of PMA in this region in the absence of cupric ions this peak may be identified with the antisymmetric stretching mode of the chelating carboxylate groups (ν_3).

The negligible intensity of ν_3 at $\alpha = 0$ shows that the unneutralized polyacid binds practically no Cu(II) ions. This is in agreement with previous results.[3]

Figure 5 shows the absorbance $\bar{A} = c_p^{-1} d^{-1} \log T^{-1}$ (c_p is the polymer concentration in equiv/l., d is the cell length in centimeters, and T is the transmission) plotted against the degree of neutralization α for ν_1, ν_2, and ν_3. The values plotted here were determined by the base line method and refer to the absorption maxima. Extinction coefficients determined from plots will be designated $\bar{\epsilon}$ to emphasize that they were not obtained from integrated intensities.

First the titration of PMA will be discussed. Whereas $\bar{A}(\nu_1)$ follows an intramolecular Beer's law, this is not true for $\bar{A}(\nu_2)$. In the region where $\bar{A}(\nu_2)$ deviates from the straight line, PMA is well known to exhibit a conformational transition from densely coiled to extended conformations.[5,8] As $\bar{A}(\nu_1)/\alpha = \bar{\epsilon}(\nu_1)$ does not change in this region, we may conclude that the first hydration sphere of the carboxylate groups is the same in both groups of conformations. From the validity of Beer's law for $\bar{A}(\nu_1)$, the important conclusion may be drawn that the carboxylate groups along the

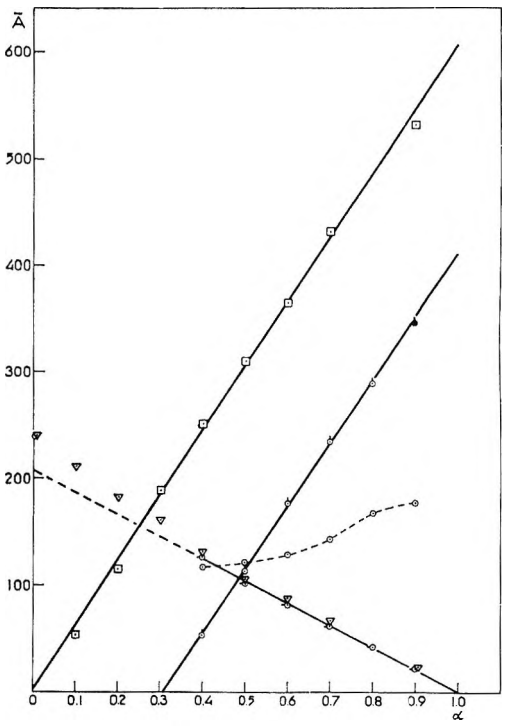

Figure 5. Absorbance, $\bar{A}$ (see text) from ir spectrophotometric titrations: PMA: ν_1 (□), ν_2 (▽), PMA + 30.0% equiv Cu(II): ν_1 (⊙), ν_2 (·⊙), ν_3 (⊙).

polymer chain are optically independent, even at high degrees of ionization of the polyacid.

In Figure 5, the plot of $\bar{A}(\nu_1)$ for the PMA–Cu(II) system is shifted 0.3 unit parallel to the α axis with respect to the copper-free system. As in the former case, 30.0% equiv of Cu(II) is present (referred to PMA); it is confirmed[3] that two carboxylate ions are bound per copper ion.

The equality of the slopes of the two lines ($\bar{\epsilon}_{\nu,1}$ = 597 l. mol^{-1} cm^{-1} for the titration of pure PMA and $\bar{\epsilon}_{\nu,1}$ = 600 l. mol^{-1} cm^{-1} in the other case) proves that once the point of equivalence with respect to Cu(II) has been reached ($\alpha = 0.3$) the number of bound carboxylate ions is constant. The original explanation of the intensity decrease of the electronic spectrum for $f > 1.2$ in terms of a dissociation producing copper ions and carboxylate ions is therefore abandoned (in Figure 5, $\alpha = 0.3f$). As pointed out before,[9] the band at 26,000 cm^{-1} and its disappearence on increasing f is important in the interpretation of the binding phenomena in the present system. Starting with the work of Tsuchida, *et al.*,[10] evidence has been presented that an absorption in this region and of the strength observed

(6) K. Nakamoto, "Infrared Spectra of Inorganic and Coordination Compounds," John Wiley and Sons, Inc., New York, N. Y., 1963.

(7) L. L. Shevchenko, *Ukr. Khim. Zh.*, 29, 1247 (1963).

(8) J. C. Lyte, *Polym. Letters*, 4, 245 (1966); M. Mandel, J. C. Leyte, and M. G. Stadhouder, *J. Phys. Chem.*, 71, 603 (1967).

(9) J. C. Leyte, *Kolloid-Z.*, 212, 168 (1966).

(10) R. Tsuchida and S. Yamada, *Nature*, 176, 1171 (1955).

here is characteristic of the formation of binuclear copper carboxylates both in the solid state and in solution.

As was discussed in a review[11] of the early results, the 26,000-cm^{-1} band is no proof of Cu–Cu interaction in complexes. Still, for the carboxylates the subnormal magnetic moments that are found when this band is observed indicate that its appearance is characteristic for copper acetate type dimeric structures. Recently, this was confirmed for a series of copper complexes of unsaturated acids by Edmondson and Lever.[12]

In connection with the present polyacid $(-CH_2C(CH_3)(COOH)-)_n$ especially, the results on the α,ω-dicarboxylic acids are of interest. Dubicki, *et al.*,[13] and Figgis and Martin[14] found that the copper complexes of these acids from the succinate upward in the homologous series behave as magnetically isolated dimers. For these complexes the 26,000-cm^{-1} band is present in the spectrum. In the spectra of the oxalate and the malonate, the band is absent and the magnetic behavior excludes the acetate type dimer structure.

It is suggestive that in PMA the number of C atoms between neighboring carboxylate groups equals that in the glutarate. In view of these results, the optical spectrum and the low magnetic moment of the present system strongly suggest the presence of binuclear copper complexes at $f = 1.3$. At $f = 3.3$ the characteristics of the dimer are absent and, from the ir results, it is seen that each copper ion still binds two carboxylate groups. Therefore, the explanation for the spectral changes seems to be a dissociation of the dimers into monomer complexes. This dissociation is probably due to the greater accessibility of water molecules to the interior of the polyelectrolyte molecule as a result of the expansion of the polymer on increasing its charge. This is confirmed by the reappearance of the 26,000-cm^{-1} band on replacing the solvent by dioxane. In this connection, it is of interest that 30 vol % of water in acetic acid solutions of cupric acetate completely destroys the dimer.[15]

A detailed discussion of the general decrease of extinction coefficients in the electronic spectrum is hampered by the absence of dependable term schemes, especially in the case of the dimer. From general considerations the observed decrease is, however, quite consistent with the dissociation of the dimer complexes. It is now accepted[16–18] that in the dimer the copper–copper interaction is weak and that the d manifold is probably only slightly disturbed if compared to mononuclear complexes.

The absorption in the 10.000–15.000-cm^{-1} region may, therefore, still be related to d–d transitions in the dimer. In the dimer carboxylates the Cu ions are bridged by four carboxylate groups, forming a structure of approximately D_{4h} symmetry with two additional solvent ligands on the C_4 axis. The symmetry center is halfway between the metal ions and the ligand charge distribution is, therefore, asymmetrical for a given Cu(II) ion. In this situation d–d transitions are allowed, resulting in an intense visible spectrum. In monomeric complexes the Cu(II) ions tend to surround themselves with a deformed octahedron of negative ligand charge. As the metal ion is in the symmetry center d–d transitions are in principle forbidden here, resulting in low visible intensities. For the uv region, analogous considerations hold.

It will now be shown that the ir spectra yield additional information in connection with the discussion just presented. In the same range of f values where the changes in the electronic spectrum occur, the intensity $\bar{A}(\nu_3)$ due to the chelated carboxylate ions increases considerably (Figure 5). Integration of some of the bands involving correction for the neighboring ν_1 obtained from spectra of Cu(II)-free solutions confirms this. Considering the insensitivity of $\bar{\epsilon}(\nu_1)$ (and of $\bar{\epsilon}(\nu_2)$ outside the conformational transition region) with respect to the electrostatic charge of the polymer and the fact that the number of bound carboxylate groups is constant (as shown by the absorption of the free ions), it is concluded that the behavior of $\bar{A}(\nu_3)$ is due to a change in the nature of the complex. It should be noted that a considerable change in the nature of the copper carboxylate bonding does not seem to occur, as the shift in ν_3 is small if existent at all (see discussion below).

The conservation of the number of bound carboxylates per Cu(II) ion, therefore, suggests a rearrangement of ligands: a structure in which the contributions of the individual ligands to the transition moment partially cancel is replaced by a structure in which this happens to a lesser degree. First, starting from the assumption that at $f = 1.3$ only mononuclear complex is present, any rearrangement reducing the symmetry of the orientation of the carboxylate groups with respect to each other necessarily reduces the symmetry of the orientation of these ions with respect to the central ion. This reduces the symmetry of the distribution of negative charge around this ion. Even without consideration of the 26,000-cm^{-1} band, this is quite in conflict with the general decrease of intensity in the visible and uv region as this, in view of the invariance of the number of bound carboxylate ions per

(11) M. Kato, H. B. Jonassen, and J. C. Fanning, *Chem. Rev.*, **64**, 99 (1964).

(12) B. J. Edmondson and A. B. P. Lever, *Inorg. Chem.*, **4**, 1608 (1965).

(13) L. Dubicki, C. M. Harris, E. Kokot, and R. L. Martin, *ibid.*, **5**, 93 (1966).

(14) B. N. Figgis and D. J. Martin, *ibid.*, **5**, 100 (1966).

(15) J. K. Kochi and R. V. Subramanian, *ibid.*, **4**, 1527 (1965).

(16) A. E. Hansen and C. J. Ballhauser, *Trans. Faraday Soc.*, **61**, 631 (1965).

(17) L. Dubicki and R. L. Martin, *Inorg. Chem.*, **5**, 2203 (1966).

(18) G. F. Kokoszka, H. C. Allen, and G. Gordon, *J. Chem. Phys.*, **46**, 3013 (1967).

copper ion, clearly indicates an increase of the symmetry of the charge distribution around the metal ion. Also, the low magnetic moment at $f = 1.3$ cannot be explained this way. Therefore, the consequences for $A(\nu_3)$ will be considered for the dissociation of a binuclear copper carboxylate with the well-known acetate structure into mononuclear complexes. The binuclear complex will be represented by a model consisting of 16 point masses: two Cu(II) ions and two solvent particles on the C_4 axis and four carboxylate ions (consisting of 3 point masses each) with the carbon atoms in σ_h of D_{4h}. Standard symmetry analysis yields the ir active vibrations: $4A_{2u} + 6E_u$. Using the C–O distance of the carboxylate ion as an internal coordinate,[19] it is found that the ir-active vibrations involving this coordinate are A_{2u} and E_u.

From the behavior under σ_h it is clear that the A_{2u} vibration stems from the antisymmetric stretching vibration of the free carboxylate ions, while the E_u vibrations arise from a combination of symmetric stretching vibrations of carboxylate groups. In other words, when four carboxylate ions react to form the binuclear complex, the antisymmetric vibrations of the free ions combine in different ways to yield $A_{2u} + E_g + B_{2u}$. Of these only A_{2u} is ir active, and this is only one of the four possible combinations. As these combinations are about equally probable (the ground states will not show energy differences which are appreciable with respect to kT) the intensity of ν_3 will be sharply reduced relative to the free ion if no large increase of the transition moment occurs as a result of the electronic interaction with the Cu(II) ion. As this is improbable, the extinction coefficient of ν_3 in a binuclear copper carboxylate with a structure analogous to that of the acetate should be some 25% of the extinction coefficient of ν_1 of the free carboxylate ion.

For the present system a value of 33% is found at $f = 1.3$ from integration of the bands. As at this f value part of the binuclear complexes are probably dissociated already (the intensities in the uv and visible spectrum start to decrease at $f = 1.2$), this result is satisfactory.

For the mononuclear complex we will first consider a structure of symmetry D_{2h} in which both carboxylate ions and the central ion are in σ_h. The same analysis that was applied to the dimer shows that in the monomer only one of the two possible combinations of the antisymmetric stretching vibrations of the carboxylate group is active. At $f = 3.3$ the extinction coefficient of ν_3 is found to be 47% relative to the free ion while roughly 50% should be expected. It should be stressed that any other model for the monomer is necessarily of lower symmetry with respect to the relative carboxylate orientation. Even higher extinction coefficients for the ligands are then expected. An increase of $A(\nu_3)$ is, therefore, expected for the dissociation of a dimer irrespective of the type of the resulting monomer.

It is concluded that the dissociation of binuclear complexes existing to some extent at $f = 1.3$ into monomers is responsible both for the changes in the spectrum of the complex and its magnetic behavior on increasing f.

Several attempts have been made to correlate the position of ν_3 with the type of interaction between metal ions and the carboxylate groups.[20] It has been established that for some metal ions the frequency order is more or less independent of the physical state of the compounds. It is assumed that the position of ν_3 with respect to ν_1 and ν_2 is a measure of the covalence of the metal–carboxylate bond.

The principle is of little use, however, in the interpretation of the spectrum of an isolated compound. Still a shift in ν_3 would be expected in our case if the type of bonding of the carboxylate groups changes when the binuclear complex dissociates. From Table I, it is seen that ν_1, ν_2, and ν_3 shift to lower frequencies on increasing α. This effect also occurs in the absence of Cu(II) ions for ν_1 and ν_2 and has been discussed previously for that case.[21] These shifts are connected with the expansion of the polyelectrolyte molecule upon increase of its charge density. Any small change in ν_3 due to a change in the nature of the copper complex will be superimposed on the shifts mentioned and it must be concluded that the small displacement of ν_3 cannot be used as an indication for a transformation of the complex. It is of interest to note that the poly(glutamic acid)–Cu(II) system shows an analogous behavior to the system treated here.[22]

Table I

α	ν_1	ν_2	ν_3
0	...	1698	1612
0.4	1554	1692	1611
0.7	1552	1685	1608
1.0	1550	...	1604

The authors mainly investigated the influence of Cu(II)-ion binding on the helix–coil transition, and for an explanation of the spectral phenomena, they leave the choice open between exciton interaction (disappearing when the copper ions become more widely spaced along the polymer chain) and direct copper–

(19) E. B. Wilson, J. C. Decius, and P. C. Cross, "Molecular Vibrations," McGraw-Hill Book Co., Inc., New York, N. Y., 1955.

(20) J. D. Donaldson, J. F. Knifton, and S. D. Ross, *Spectrochim. Acta*, **20**, 847 (1964).

(21) J. C. Leyte, L. H. Zuiderweg, and H. J. Vledder, *ibid.*, **23A**, 1397 (1967).

(22) H. Takesada and H. Yamazaki, *Biopolymers*, **4**, 713 (1966).

copper interaction. Our results on PMA, especially those from the vibrational spectrum, favor the latter explanation.

Acknowledgment. The authors wish to thank Professor M. Mandel and Professor G. Gordon for their comments and interest.

Acid–Base Reactions in Concentrated Aqueous Quaternary Ammonium Salt Solutions. III. Dicarboxylic Acids

by Joseph Steigman, Richard De Iasi,[1] Harvey Lilenfeld, and Donald Sussman

Department of Chemistry, Polytechnic Institute of Brooklyn, Brooklyn, New York *(Received July 11, 1967)*

A number of dicarboxylic acids were titrated with KOH in aqueous 7.75 *m* tetra-*n*-butylammonium bromide solutions at 25°. The ratio of the two dissociation constants was greater than in water for the following acids: maleic, *o*-phthalic, malonic, dimethyl- and di-*n*-propylmalonic, and succinic. The maleic acid ratio was greater than in water by more than 4×10^3. That for succinic acid was five times greater. The ratios for oxalic acid, for *m*- and *p*-phthalic acids, for fumaric acid, and for the longer-chain aliphatic dicarboxylic acids from glutaric to suberic were almost unchanged. Infrared spectra of some of these acids, their acid salts, and their fully neutralized salts were made in D_2O and in 7.75 *m* tetra-*n*-butylammonium bromide solutions in D_2O. With the exception of oxalic acid, those compounds which showed small changes in their dissociation constant ratios on transfer from water to the quaternary ammonium salt solution had monoacid salt spectra which were simple composites of those of the free acid and the fully neutralized salt. Acids which showed large changes in their ratios had monoacid anion spectra in which the carbonyl frequency of the acid moved to a lower frequency and the asymmetric carboxylate stretching frequency of the fully neutralized salt moved to a higher frequency, an effect which became larger in the quaternary ammonium salt solution. It was concluded that an internally hydrogen-bonded monoacid anion was formed by the latter acids and that water was a part of this structure. Since such a structure was not possible for the acid oxalate anion and since a dimer of this ion does not appear to exist in aqueous solution, it was concluded that the effects observed in the oxalic acid system are probably due to electrostatic forces.

Introduction

On statistical grounds, the ratio of the first to the second dissociation constant of a diprotic acid should be 4. In water, the first three members of the homologous aliphatic series—oxalic, malonic, and succinic acids—possess ratios which are much greater than 4, and the theoretical statistical value is not reached even for long-chain dicarboxylic acids. Bjerrum attributed these high ratios to the electrical work which is required to remove the second proton from the negatively charged monoanion, an approach which was further developed by other workers.[2,3] An alternative explanation for the first three members of the homologous series was put forth by Jones and Soper, who suggested that an internal hydrogen bond would stabilize the acid salt.[4] This would result in an increase in the value of the first dissociation constant and a decrease in the second constant, producing the high ratios which are observed. Eberson found that α,α'-disubstituted racemic succinic acids had dissociation constant ratios which were very much larger than those of the corresponding meso compounds and he concluded that the difference between them was due to a hydrogen-bonded intermediate for the acid salt in the preferred conformation of the racemic compound.[5] Miles and his coworkers further supported the hypothesis of an internally hydrogen-bonded intermediate by a potentiometric and kinetic study of the dissociation of disubstituted malonic acids in water.[6] On the other hand, Chapman, Lloyd, and Prince concluded from an examination of the infrared spectra of D_2O solutions of a number of dicarboxylic acids and their salts that the hydrogen malonate ion, the hydrogen maleate ion, and

(1) Taken from a thesis submitted by R. De Iasi to the Graduate School of the Polytechnic Institute of Brooklyn in partial fulfillment of the requirements for the degree of Doctor of Philosophy.

(2) N. Bjerrum, *Z. Phys. Chem.* (Leipzig), **106**, 219 (1923).

(3) J. G. Kirkwood and F. H. Westheimer, *J. Chem. Phys.*, **6**, 508 (1938).

(4) I. Jones and F. G. Soper, *J. Chem. Soc.*, 133 (1936).

(5) L. Eberson, *Acta Chem. Scand.*, **13**, 211 (1959).

(6) M. H. Miles, E. M. Eyring, W. W. Epstein, and R. E. Ostlund, *J. Phys. Chem.*, **69**, 467 (1965).

the hydrogen *o*-phthalate ion were not internally hydrogen bonded.[7]

This paper describes the results of the potentiometric titration of a number of dibasic acids with KOH in aqueous 7.75 *m* tetra-*n*-butylammonium bromide solution (*n*-Bu_4NBr) at 25.0°. In addition, measurements of the principal frequencies between 1800 and 1300 cm^{-1}, which are observed in the infrared absorption spectra of a number of these acids and their salts, were made in D_2O and in 7.75 *m* *n*-Bu_4NBr solution (in D_2O). Marked changes in the ratio of the two dissociation constants of a number of dicarboxylic acids in *n*-Bu_4NBr solution compared to water were correlated with shifts in the infrared spectra and the correlation led us to the conclusion that some type of internally hydrogen-bonded monoacid anion was formed.

Experimental Section

A. Chemicals. The acids were reagent grade products of Brothers, Matheson Coleman and Bell, Eastman Kodak, or K & K. Oxalic acid was purified according to Kolthoff and Sandell.[8] Adipic acid was recrystallized once from 1 *M* nitric acid and twice from distilled water. The other acids were recrystallized two or more times from either water or ethanol. Deuterated acids were prepared by recrystallization of purified acids from D_2O. The monoacid salts were prepared by potentiometric neutralization of an aqueous solution of the acid with NaOH at the second equivalence point, addition of an equivalent quantity of acid, evaporation *in vacuo*, and recrystallization from D_2O. A few experiments were performed with acid salts recrystallized from H_2O, since there was not enough dilution of the D_2O by the protons of the salt to interfere with the infrared measurements. The disodium salts were prepared by neutralization, were recrystallized from water, and were dried *in vacuo*. Potassium hydrogen phthalate was of reagent grade (Fisher Scientific) and was recrystallized from D_2O. Other chemicals were described in the preceding articles of this series.[9,10]

B. Potentiometric Titrations. The acids (approximately 0.02 *M*) were titrated with 1 *M* KOH at 25.00 ± 0.05° in 7.75 *m* *n*-Bu_4NBr. A Beckman Model G pH meter and ordinary glass and calomel electrodes were used. The negative logarithms of the dissociation constants recorded are not thermodynamic values, but are mixed acidity constants.[9] They were calculated according to Noyes' method,[11] using a computer program drawn up in Fortran IV language.

C. Spectrophotometric Measurements. Infrared spectra were measured on a Perkin–Elmer Model 521 spectrophotometer. The scanning rate was 10 cm^{-1} sec^{-1}, and the wave-number scale was expanded by a factor of 2; water-vapor peaks were used for calibration in the region of interest. Each run was checked against the wave-number scale. The frequencies which are reported are probably accurate to within 1–2 wave numbers. The sample solutions were held in a 0.1-mm pathlength demountable liquid cell (Barnes Engineering Co.). The reference solution was held in a Limit Corp. variable-thickness cell. Both cells were equipped with calcium fluoride windows. Path lengths were matched by adjusting the path length of the reference cell until all solvent bands were eliminated between 1800 and 1300 cm^{-1}.

Results and Discussion

Table I shows the values at 25° of the thermodynamic dissociation constants (called $pK_{A,1}$ and $pK_{A,2}$) in water of the dibasic acids under study, together with their mixed acidity constants called pK'_1 and pK'_2 in 7.75 *m* *n*-Bu_4NBr. The table shows the values of the ratios $K_{A,1}/K_{A,2}$ and K'_1/K'_2, as well as the ratio of the ratios $(K'_1/K'_2)/(K_{A,1}/K_{A,2})$. The constants for propionic acid and benzoic acid have been added[9] in order to show the behavior of typical carboxylic acids in this medium.

The results shown in Table I must be viewed in the light of the effect of quaternary ammonium salts on the structure of liquid water. Unlike most inorganic electrolytes, these compounds cause an increase in the hydrogen bonding of the water surrounding them.[12] This is evident from such properties as the high positive viscosity *B* coefficients of their aqueous solutions,[13] the high positive heat capacities of these solutions,[12] and their increased molar dielectric relaxation times.[14] Previous investigations of some chemical reactions in 7.75 *m* *n*-Bu_4NBr at 25° showed that the mixed acidity constants of aliphatic carboxylic acids were approximately 2.2 units greater than their thermodynamic pK_A values in water.[9] Benzoic acid behaved similarly. *Meta*- and *para*-substituted benzoic acids showed somewhat smaller increases.[10] In this medium the *ortho* effect in monosubstituted benzoic acids was not observed, and the *ortho* isomers showed larger increases in pK' (about 2.7 units).

Table I shows that in 7.75 *m* *n*-Bu_4NBr the mixed acidity constants of the longer-chain aliphatic dicarboxylic acids (from glutaric to suberic) are numerically

(7) D. Chapman, D. R. Lloyd, and R. H. Prince, *J. Chem. Soc.*, 550 (1964).

(8) I. M. Kolthoff and E. B. Sandell, "Textbook of Qualitative Inorganic Analysis," The Macmillan Co., New York, N. Y., 1952, p 529.

(9) J. Steigman and D. Sussman, *J. Amer. Chem. Soc.*, in press.

(10) J. Steigman and D. Sussman, *ibid.*, in press.

(11) Described in A. Albert and E. P. Serjeant, "Ionization Constants of Acids and Bases," Methuen and Co., Ltd., London, 1962, p 52.

(12) H. S. Frank and W. Y. Wen, *Discussions Faraday Soc.*, **24**, 133 (1957).

(13) E. R. Nightingale, Jr., *J. Phys. Chem.*, **66**, 894 (1962).

(14) G. H. Haggis, J. B. Hasted, and T. J. Buchanan, *J. Chem. Phys.*, **20**, 1452 (1952).

Table I: pK_A and pK' Values of Dibasic Acids in Water and in 7.75 *m* *n*-Bu_4NBr Solution at 25 ± 0.05°, and Values of $K_{A,1}/K_{A,2}$, K'_1/K'_2, and $(K'_1/K'_2)/(K_{A,1}/K_{A,2})$

Acid	$pK_{A,1}$[a,b,c] (H_2O)	$pK_{A,2}$[a,b,c] (H_2O)	pK'_1 (*n*-Bu_4NBr)	pK'_2 (*n*-Bu_4NBr)	$K_{A,1}/K_{A,2}$ (H_2O)	K'_1/K'_2 (*n*-Bu_4NBr)	$(K'_1/K'_2)/(K_{A,1}/K_{A,2})$
Oxalic	1.27	4.27	2.91 ± 0.02	6.09 ± 0.03	1,000	1,510	1.51
Malonic	2.86	5.70	3.43 ± 0.03	8.39 ± 0.03	690	92,500	134
Succinic	4.21	5.64	5.59 ± 0.07	7.71 ± 0.02	26.9	132	4.9
Glutaric	4.34	5.27	6.47 ± 0.02	7.22 ± 0.09	8.50	5.61	0.67
Adipic	4.41	5.28	6.70 ± 0.05	7.48 ± 0.04	7.42	6.02	0.81
Pimelic	4.51	5.31	6.59 ± 0.02	7.25 + 0.01	6.31	4.52	0.72
Suberic	4.52	5.33	6.83 ± 0.10	7.44 ± 0.05	6.30	4.09	0.65
Dimethylmalonic	3.15	6.20	4.52 ± 0.03	9.52 ± 0.05	1,120	102,000	91
Di-*n*-propylmalonic	2.15	7.34	3.34 ± 0.03	11.19 ± 0.01	316,000	72,000,000	228
Maleic	1.92	6.23	1.93 ± 0.03	9.86 ± 0.06	20,000	85,600,000	4280
Fumaric	3.02	4.38	4.95 ± 0.03	6.50 ± 0.03	23.0	36.2	1.57
Phthalic (*ortho*)	2.95	5.41	2.87 ± 0.09	8.25 ± 0.04	290	240,000	827
Isophthalic (*meta*)	3.62	4.60	5.17 ± 0.02	5.95 ± 0.03	9.56	6.2	0.65
Terephthalic (*para*)	3.54	4.46	5.27 ± 0.03	6.58 ± 0.03	8.3	20.4	2.46
Propionic	4.87		7.04 ± 0.03				
Benzoic	4.20		6.30 ± 0.01				

[a] Reference 11, p 134. [b] H. C. Brown, D. H. McDaniel, and O. Haflinger in "Determination of Organic Structures by Physical Methods," E. A. Braude and F. C. Nachod, Ed., Academic Press Inc., New York, N. Y., 1955. [c] G. Kortum, W. Vogel, and K. Andrussow, "Dissociation Constants of Organic Acids in Aqueous Solution," Butterworth and Co. Ltd., London, 1961.

greater than the thermodynamic pK_A values in water by 2.0–2.3 units for both dissociations. They are behaving like normal aliphatic acids. The same change is evident in fumaric acid. Isophthalic and terephthalic acids show changes which are only several tenths of a pK' unit from other benzoic acids. Oxalic acid, which shows a change of about 1.6 pK' units for both dissociations,, represents a special case which is discussed below.

On the other hand, malonic acid, the substituted malonic acids, maleic acid, and *o*-phthalic acid show abnormal differences between the pK_A values in water and the pK' values in the quaternary ammonium salt solution. In each case the first mixed acidity constant (pK') is much smaller than that found for a normal aliphatic acid in this solvent, and the second constant (pK'_2) is much larger. Thus the value of pK'_1 for maleic acid is 2.2 units less than the expected value for the first dissociation process, and the value of pK'_2 is 1.5 units greater than expected. Phthalic acid shows similar behavior if one takes into account the disappearance of the *ortho* effect for other monosubstituted benzoic acids. Succinic acid is tentatively included in this group; here the effect is small and is limited to the first dissociation. These results suggest that in this strongly organized solvent the monoprotic anion is being stabilized in some fashion, perhaps by incorporation into an organized cluster of water molecules. However, this explanation is insufficient to account for the difference between malonic and glutaric acids. It is necessary to attribute some specific structural effect to the monoacid malonate anion as well. This could be the internally hydrogen-bonded anion described earlier,[4-6] which is evidently much more stable in the quaternary ammonium salt solution than in water.

In order to examine this hypothesis by another method, infrared studies of solutions of a number of the acids of Table I, their acid salts, and their fully neutralized salts were made at room temperature in D_2O and in 7.75 *m* *n*-Bu_4NBr in D_2O. The solute concentrations were 1 *M* or less (depending on solubility). The results are shown in Table II, together with those of acetic acid and benzoic acid. The state of the acid refers to the solute: D_2A stands for the dicarboxylic acid, DA^- for the monoacid anion, and A^{2-} for the fully neutralized salt. The symbols $\nu_{CO(D_2A)}$ and $\nu_{CO(DA^-)}$ represent the carbonyl stretching wave numbers of the D_2A and DA^- forms, respectively; $\nu_{COO^-(asym)(DA^-)}$ and $\nu_{COO^-(sym)(A_2^-)}$ stand for the asymmetric carboxylate stretches of the DA^- and A^{2-} forms, and $\nu_{COO^-(sym)(DA^-)}$ and $\nu_{COO^-(sym)(A_2^-)}$ stand for the symmetric carboxylate stretches of the same two forms.

The infrared spectra of some of these acids in D_2O solution were previously measured by Chapman, Lloyd, and Prince.[7] There are some numerical differences between their values and those reported here. In general we believe that the present values are more accurate because of the difference in resolution between the Perkin–Elmer Model 21 (which they used) and the Model 521 used by us. With a sodium chloride prism the resolution of the Model 21 is approximately ±5 cm^{-1} in the region of interest. That of the Model 521 is ±1 cm^{-1}. In addition, our spectra were recorded with a slow scan on an expanded wave-number scale.

Table II: Wave Numbers of Dicarboxylic Acids and Salts in D_2O and in 7.75 *m* *n*-Bu_4NBr in D_2O at Room Temperature

Acid	State	$\nu_{C=O}$, cm^{-1}		$\nu_{COO^-(asym)}$, cm^{-1}		$\nu_{COO^-(sym)}$, cm^{-1}	
		D_2O	*n*-Bu_4NBr	D_2O	*n*-Bu_4NBr	D_2O	*n*-Bu_4NBr
Oxalic	D_2O	1733	1741				
	DA^-	1718, 1700	1736 (1766), 1711	1634	1643	1418	1400
	A^{2-}			1573	1573	1308	1305
Malonic	D_2A	1705	1722				
	DA^-	1696	1706	1583	1600	1410	1398
	A^{2-}			1571	1573	1433	1433
Di-*n*-propyl-malonic	D_2A	1688	1705				
	DA^-	1676	1693	1582	1611	1409	1401
	A^{2-}			1549	1562	1410	1404
Succinic	D_2A	1706	1717				
	DA^-	1700	1701	1560	1565	1397	1398
	A^{2-}			1559	1563	1394	1388
Glutaric	D_2A	1699	1713				
	DA^-	1695	1711	1554	1564	1405	1394
	A^{2-}			1559	1561	1400	1396
Adipic	D_2A	1695	1714				
	DA^-	1694	1710	1550	1563	1406	1400
	A^{2-}			1547	1563	1405	1397
Fumaric	D_2A	1695	1700				
	DA^-	1693	1698	1570	1582	1353	1333
	A^{2-}			1565	1569	1375	1367
Maleic	D_2A	1698	1708				
	DA^-	1683	1683	1574	1599	1420	1401
	A^{2-}			1559	1564	1431	1427
o-Phthalic	D_2A	1693	1705				
	DA^-	1693	1640	1583	1590	1402	1391
	A^{2-}			1559	1565	1403	1399
Acetic	DA	1710	1721				
	A^-			1560	1568	1415	1407
Benzoic	DA	1680	1695				
	A^-			1545	1557	1388	1373

Table II shows that the spectra of the DA^- forms of glutaric and adipic acids are almost exact superpositions of the spectra of the D_2A and A^{2-} species, both in D_2O and in the quaternary ammonium salt solution. It can be concluded that these monoprotic anions possess a carboxylic acid group and a carboxylate group which do not interact with each other. This is further confirmed by the observation that the differences between the carboxylate asymmetric frequencies in the DA^- states and the carbonyl stretches in the D_2A states of these acids are almost the same as the difference between the acetate carboxylate frequency and the acetic acid carbonyl stretch (145–150 cm^{-1}).

At the other extreme, the spectra of the acid oxalate anion in both media are very different from those of oxalic acid and oxalate ion. The differences in the asymmetric carboxylate modes between the DA^- and A^{2-} are particularly striking. The other acids in Table II fall between glutaric acid on the one hand and oxalic acid on the other. Table III represents an appropriate reorganization of the data of Table II. The symbol $\Delta\nu_{COO^-(DA^- - A^{2-})}$ stands for the difference in the asymmetric carboxylate stretching frequencies of the two ions.

Table III: Differences in Carbonyl and Carboxylate Stretching Frequencies of Dicarboxylic Acids in D_2O and in 7.75 *m* *n*-Bu_4NBr in D_2O at Room Temperature

Acid	$\Delta\nu_{CO(D_2A - DA^-)}$, cm^{-1}		$\Delta\nu_{COO^-(asym)(DA^- - A^{2-})}$, cm^{-1}	
	D_2O	*n*-Bu_4NBr	D_2O	*n*-Bu_4NBr
Glutaric	4	2	3	3
Adipic	1	4	3	0
Succinic	6	16	1	2
Malonic	9	16	12	27
Di-*n*-propyl-malonic	12	12	33	49
Maleic	15	25	15	35
Fumaric	2	2	5	13
Phthalic	0	65	24	25
Oxalic	15, 33	5, 31	61	70

Our interpretation of these results is based on the analysis of Chapman, *et al.*,[7] who pointed out that a hydrogen-bonded carboxyl group shows a lower carbonyl frequency than a nonhydrogen-bonded group, and that the asymmetric carboxylate frequency is raised by hydrogen bonding. They quote Eberson, who found that substituted succinic acids in D_2O

showed 35 cm^{-1} increases in the carboxylate asymmetric stretch and 30 cm^{-1} decreases in the carbonyl frequencies of COOH groups on hydrogen bonding.[15] Malonic acid, di-*n*-propylmalonic acid, *o*-phthalic acid, and maleic acid show differences in both sets of frequencies which become larger in the quaternary ammonium salt solution. Since the ratios of the dissociation constants of these acids are very much larger in 7.75 *m* *n*-Bu_4NBr than in water, the solvent is clearly involved in the stabilization of the acid anions. Both observations are consistent with an internally hydrogen-bonded monoacid anion in which one or more water molecules are hydrogen bonded to the carboxylate and carboxylic acid groups (a proposal originally advanced by Ives[16]). Such a hydrogen bond would be weaker than a simple hydrogen bond, because it would be subjected to collision and exchange with solvent molecules, but unlike a normal internal hydrogen bond it would be strengthened by the increased organization of the solvent in the *n*-Bu_4NBr solution.

Succinic acid shows these spectral shifts only in its carbonyl frequencies, and the ratio of its dissociation constants shows a small change on transfer to the quaternary ammonium salt solution. It is tentatively included in the preceding group of acids, but it probably forms a very weakly hydrogen-bonded acid anion.

Glutaric acid and the longer-chain dicarboxylic acids form acid anions in which there is no longer any interaction between the carboxylic acid group and the carboxylate anion. This is borne out by both the potentiometric and the spectroscopic results.

The spectroscopic behavior of fumaric acid is difficult to explain. It is impossible for it to form a simple internally hydrogen-bonded DA^- anion for geometrical reasons.[7] At the same time, the ratio of its dissociation constants shows very little change on transfer to *n*-Bu_4NBr solution, pointing to little or no solvent incorporation into the acid anion. In any event, the changes in its absorption band frequencies are much smaller than those of maleic acid. It is concluded that whereas maleic acid forms an internally hydrogen-bonded acid anion with solvent participation, fumaric acid does not do so.

The monoacid oxalate anion presents a special case. The ratio of the dissociation constants of the acid is practically the same in water and in 7.75 *m* *n*-Bu_4NBr. The differences in the carbonyl frequency between the D_2A and DA^- forms and in the asymmetric carboxylate frequency between the DA^- and A^{2-} forms are the largest shown in Table III. These results could be explained by the formation in the acid anion of a strong intramolecular hydrogen bond which is unaffected by the extent of organization of the solvent around it. However, there is reason to believe that such a hydrogen bond cannot be formed in the ion. The crystal structure of KHC_2O_4 was partly elucidated by Hendricks.[17] From his data it was possible to calculate the various distances and angles in the anion, which is planar. The two oxygen atoms between which an intramolecular hydrogen bond must be formed are about 2.9 Å apart, which is a little beyond the upper limit of known O–H–O linear distances.[18] However, the bond cannot be formed in a straight line between them. If it is assumed that there is a normal O–H bond distance on one carbon atom at a C–O–H angle of 120°, the distance between the hydrogen atom and the oxygen atom of the second carbon atom is 2.5 Å (the expected van der Waals distance) and, furthermore, the angle between them does not permit any interaction with the appropriate oxygen orbital. The situation is not improved by placing the hydrogen midway between the two oxygen atoms in a bent hydrogen bond. The O–H–O angle is then 120°, and in addition the contour length of the hydrogen bond is at least 3.5 Å. A final decision cannot be made until a more precisely measured anion structure is made, but certainly an intramolecular hydrogen bond is not possible in the light of presently available knowledge. The difficulty could be resolved by the formation of a stable dimeric acid anion in solution with two internal hydrogen bonds. However, an analysis of the electrical conductivity of sodium hydrogen oxalate in water shows, after appropriate corrections, that it behaves like a 1:1 electrolyte, and not like a 2:1 electrolyte.[19] Further, the molal freezing-point depression of aqueous potassium acid oxalate solutions is quite close to that of potassium bicarbonate at almost equivalent concentrations, and it is markedly different from those of $K_2C_2O_4$ and K_2CO_3 (which in turn are almost the same).[20] It can be concluded that the acid oxalate ion is predominantly or entirely monomeric in water. It is possible that the carbonyl frequency differences between oxalic acid and the acid oxalate ion and the asymmetric carboxylate frequency difference between the acid oxalate and the oxalate ions are due to electrostatic forces. If so, these forces would also explain the value of the ratio of the dissociation constants in water.

Acknowledgments. This work was supported in part by Research Grant AT (30-1)-2544 of the U. S. Atomic Energy Commission. We acknowledge additional support from the Science Development Program of the National Science Foundation, and from its summer undergraduate research participation program. Also,

(15) L. Eberson, *Acta Chem. Scand.*, **13**, 224 (1959).

(16) D. Chapman, D. R. Lloyd, and R. H. Prince, *J. Chem. Soc.*, 555 (1964).

(17) S. B. Hendricks, *Z. Kristallogr.*, **91**, 48 (1935).

(18) S. C. Nyburg, "X-Ray Analysis of Organic Structures," Academic Press Inc., New York, N. Y., 1961, p 306.

(19) E. E. Chandler, *J. Amer. Chem. Soc.*, **30**, 694 (1908).

(20) International Critical Tables, Vol. IV, McGraw-Hill Book Co., Inc., New York, N. Y., 1926, p 259.

J. S. wishes particularly to thank Professor M. Mammi of the Center of Structural Chemistry of the University of Padua for his enlightening analyses of the structure of the oxalate group.

Volume Changes on Mixing Solutions of Alkali Halides and Symmetrical Tetraalkylammonium Halides. II. Effects of Deuterium Oxide and Temperature

by Wen-Yang Wen and Kenichi Nara

Chemistry Department, Clark University, Worcester, Massachusetts 01610 *(Received July 24, 1967)*

Volume changes on mixing aqueous solutions of potassium bromide and some tetraalkylammonium bromides have been measured at constant total ionic strength in D_2O at 25° and in H_2O at 15 and 25°. In addition, the volume changes on mixing solutions of Pr_4NBr and CsBr, as well as Pr_4NBr and Me_4NBr, have been determined at 25°. The results are explicable in terms of the solvent structural changes induced by the ion–ion and ion–solvent interaction.

Introduction

In a previous paper we have reported a study on volume changes on mixing aqueous solutions of potassium bromide and symmetrical tetraalkylammonium bromides at 25°.[1] The results obtained were analyzed in terms of the ionic solution theory of Friedman,[2] and evidence for the cation–cation interaction has been presented. To gain further understanding of the ion–ion and ion–solvent interaction, we have carried out the measurements of D_2O solutions at 25° and H_2O solutions at 15 and 25°. In addition, the volume changes on mixing solutions of Pr_4NBr and CsBr, as well as Pr_4NBr and Me_4NBr, have been determined at 25°.

Experimental Section

Fisher Certified potassium bromide was recrystallized twice from water and dried carefully before use. The bromide was analyzed gravimetrically and found to be 99.9% or better in agreement with the calculated value. Three tetraalkylammonium salts (Me_4NBr, Et_4NBr, and Pr_4NBr) were obtained from the Distillation Products Industries and each recrystallized twice or more from the suitable solvents[3] and dried at proper temperatures[4] before use. The gravimetric analyses of the cations[5] and the anions indicated their purities to be at least 99.9%. Deuterium oxide (99.8%) obtained from the Stohler Isotope Chemicals and cesium bromide (99.9%) obtained from the Chemicals Procurement Laboratories were used without further purification.

Volume changes on mixing solutions of equal molal ionic strength were measured by use of a dilatometer similar to that reported by Wirth, Lindstrom, and Johnson.[6] The details of the apparatus and procedure for measurements have been described in paper I. The precision for values of $\Delta_m V^{ex}$ obtained in our experiments at $y = 0.5$ is ± 0.008 ml at $I = 0.5$, ± 0.004 ml at $I = 1.0$, and ± 0.002 ml at $I = 2.0$.

Results and Discussion

We define the excess function on mixing as follows

$$\Delta_m V^{ex}(y, I) = V^{ex}(y, I) - yV^{ex}(1, I) - (1 - y)V^{ex}(0, I) \quad (1)$$

where I is the total ionic strength, y is the fraction of the molal ionic strength due to AX in a mixture of AX and BX, and $V^{ex}(y, I)$ is the excess volume of the

(1) Paper I: W.-Y. Wen and K. Nara, *J. Phys. Chem.*, **71**, 3907 (1967).

(2) H. L. Friedman, *J. Chem. Phys.*, **32**, 1134 (1960); H. L. Friedman, "Ionic Solution Theory," Interscience Publishers, Inc., New York, N. Y., 1962.

(3) R. E. Verrall, Ph.D. Thesis, University of Ottawa, 1966, p 111.

(4) A. K. R. Unni, Ph.D. Thesis, McGill University, Montreal, 1958.

(5) Tetraalkylammonium cations were precipitated as tetraalkylammonium tetraphenylboride using the procedure of H. Flaschka and A. J. Barnard, Jr., *Advan. Anal. Chem. Instr.*, **1**, 24 (1960).

(6) H. E. Wirth, R. E. Lindstrom, and J. N. Johnson, *J. Phys. Chem.*, **67**, 2339 (1963).

solution whose composition is specified by y and I. For systems under consideration, A denotes R_4N^+, B denotes K^+, and X denotes Br^-.[7]

From the experimentally determined values of $\Delta_m V^{ex}$, a quantity Z, defined by eq 2, can be calculated.

$$Z = \Delta_m V^{ex}(y, I)/[I^2 y(1 - y)] = v_0 + v_1(1 - 2y) + v_2(1 - 2y)^2 + \ldots \quad (2)$$

According to Friedman the leading term, v_0, is the major term for 1:1 common-ion mixtures, and the major interactions contributing to v_0, are those of like-charged ion pairs as expressed in eq 3

$$v_0 = 2\bar{v}_{AB}^* - \bar{v}_{AA}^* - \bar{v}_{BB}^* \quad (3)$$

where $\bar{v}_{ij}^*$ is the part of the volume changes on mixing due to the structural effects when ion i is in the neighborhood of ion j.

For each value of I, we have determined $\Delta_m V^{ex}$ and Z at 16 different values of y and found that Z is nearly independent of y. For this reason and also for the reason of saving space, only the mean values of Z are reported and discussed in this article. The data are summarized in Tables I–III. In Table I the mean Z values obtained from mixing R_4NBr and KBr in D_2O are compared with the corresponding values in H_2O at unit aquamolality at 25°. The aquamolality expresses the number of moles of salts dissolved in 55.51 mol of solvent. As can be seen from Table I, the Z value in D_2O is greater than that in H_2O for the Pr_4NBr–KBr system. In paper I we were able to arrive at a clear-cut interpretation concerning the Pr_4N^+–Pr_4N^+ interaction owing to the fact that, for the Pr_4NBr–KBr system, $\bar{v}_{AA}^*$ was so much larger in absolute value than $\bar{v}_{AB}^*$ or $\bar{v}_{BB}^*$, with the result that Z came out to be a sizeable number (9 ml/mol) at I = 0.50. Since $Z(D_2O)$ is greater than $Z(H_2O)$ at I = 1.0, it is to be expected that $Z(D_2O)$ is also greater than $Z(H_2O)$ at I = 0.50, and our previous interpretation in H_2O is even more applicable to the same system in D_2O.

Table I: Comparison of Mean Z Values (ml/mol) Obtained from Mixing R_4NBr and KBr in D_2O and in H_2O at Unit Aquamolality at 25°

	Pr_4NBr–KBr		Et_4NBr–KBr		Me_4NBr–KBr	
	D_2O	H_2O	D_2O	H_2O	D_2O	H_2O
Z^a	3.75	3.44	1.69	1.88	0.22	0.37
$Z(D_2O) - Z(H_2O)$	0.31		−0.19		−0.15	
$Z(D_2O)/Z(H_2O)$	1.09		0.90		0.59	

[a] $Z = \Delta_m V^{ex}/[I^2 y(1 - y)]$.

For systems not involving Pr_4NBr the interpretation will be highly qualitative, since it is based on correlations and trends. Z values in D_2O are found to be smaller than those in H_2O for Et_4NBr–KBr and Me_4NBr–KBr systems. As shown in Table I, values for the ratio $Z(D_2O)/Z(H_2O)$ are 1.09, 0.90, and 0.59 for the three systems, respectively. Since the experimental conditions are kept identical for each system, except for the solvent, the data can be taken to reflect the solvent structural properties of the ions.

Table II: Comparison of Mean Z Values (ml/mol) Obtained from Mixing Pr_4NBr and KBr in H_2O at 15 and 25°

	I = 0.50		I = 1.0		I = 2.0	
	15°	25°	15°	25°	15°	25°
Z	9.30	8.79	3.77	3.44	1.52	1.31
$Z(15°) - Z(25°)$	0.51		0.33		0.21	
$Z(15°)/Z(25°)$	1.06		1.10		1.16	

Table III: Mean Z Values (ml/mol) Obtained from Mixing H_2O Solutions of Pr_4NBr and CsBr and of Pr_4NBr and Me_4NBr at I = 1.0 at 25°

	Pr_4NBr–CsBr	Pr_4NBr–Me_4NBr
Z	3.71	0.91

Since D_2O is known to possess more structure than H_2O,[8] a structure breaker should break more structure of the former than that of the latter, leading to a smaller volume in D_2O than in H_2O.[9] The fact that the ratio $Z(D_2O)/Z(H_2O)$ for Me_4NBr–KBr system is considerably less than unity may be taken to imply that both Me_4NBr and KBr are structure breakers. The Z ratio for the Pr_4NBr–KBr system is, on the other hand, very slightly above unity, indicating the structure-promoting effect of Pr_4N^+ ions. The Et_4NBr–KBr system has a value of 0.90 for the Z ratio, which may be taken to imply a slightly structure-breaking effect of KBr and very little structural influence of the Et_4N^+ ion.

The above structural interpretation is in accord with the results of Kay and Evans.[10] They measured the conductance of R_4N^+ ions in D_2O and compared the ratio R of the Walden product in D_2O to its value in H_2O, both at 25°. The value of R less than unity was taken as an indication of the solvent structure-promoting influence of the ion, while the value greater than unity was taken as indicative of the structure-breaking effect. The R values they obtained are 0.998 for Pr_4N^+, 1.008 for Et_4N^+, and 1.012 for Me_4N^+.

(7) For two systems to be discussed later, B denotes Cs^+ or Me_4N^+.

(8) See, for example, Y. C. Wu and H. L. Friedman, *J. Phys. Chem.*, **70**, 166 (1966).

(9) H. S. Frank reported that the virtual V_2^0 of KCl, or of CsCl in D_2O, is smaller by over 1 ml/mol than in H_2O. (See Saline Water Conversion Report, U. S. Department of the Interior, Washington, D. C., 1965, p 19.)

(10) R. L. Kay and D. F. Evans, *J. Phys. Chem.*, **69**, 4216 (1965).

In Table II mean values of Z obtained from mixing Pr_4NBr and KBr in H_2O at 15 and 25° are compared at constant total ionic strengths of 0.5, 1.0, and 2.0. As the temperature is lowered by 10°, the Z values increase in all cases. On the average, Z values increase about 6% at $I = 0.50$, about 10% at $I = 1.0$, and about 16% at $I = 2.0$. The increase of Z values with the lowering of temperature for this system clearly indicates the existence of more structure at lower temperature, in agreement with our expectation.

Mean Z values obtained from mixing H_2O solutions of Pr_4NBr and CsBr and of Pr_4NBr and Me_4NBr at $I = 1.0$ and at 25° are given in Table III. The Z values for the Pr_4NBr–CsBr system are about 8% greater than the corresponding values for the Pr_4NBr–KBr system. The interpretation may be as follows. The Cs^+ ion is known to be a stronger structure breaker than the K^+ ion and the mixing of Cs^+ ions into Pr_4NBr solution will disrupt the caging effect[11-14] to a greater extent than when K^+ ions are mixed, thus causing the greater increase of volume. As shown in Table III, the volume change due to mixing of Pr_4NBr and Me_4NBr is quite small, with a mean Z value of about only 0.9. This is quite surprising, since the Me_4N^+ ion is a structure breaker by many criteria and might be expected to act like the Cs^+ ion when mixing with Pr_4N^+. For example, Wood and Anderson[15] reported heats of mixing of CsCl and Pr_4NCl and of Me_4NCl and Pr_4NCl at $I = y = 0.5$ as -109.6 and -153.6 cal/kg of solvent, respectively, and concluded that the Me_4N^+ ion is a structure breaker.

As far as the volume change is concerned, the cation–cation effects are highly specific, so that the triplet Pr_4N^+–K^+–Me_4N^+ does not display "triangle additivity." The smallness of the volume change on mixing Pr_4N^+ may be ascribed to the similarity of the hydrophobic surface and to the mutual geometrical compatibility on packing these ions with water molecules. The difference in results of the heat of mixing and the volume of mixing on this system points out the basic fact that $\Delta_m H$ is largely a measure of the change in the number of hydrogen bonds of water in the solution, while $\Delta_m V$ is a measure of the change in the geometrical arrangement of water and ions.

Acknowledgments. This research was supported by the U. S. Department of the Interior, Office of Saline Water, through Grant No. 14-01-0001-456.

(11) The caging effect denotes the tendency of water molecules to form cagelike structure to "hide" the hydrocarbon tails of the R_4N^+ ion inside. When two cations approach to a suitable distance, their cage systems will tend to link up and stabilize each other, leading to a smaller total volume.

(12) W.-Y. Wen and S. Saito, *J. Phys. Chem.*, **68**, 2639 (1964).

(13) H. S. Frank, *Z. Phys. Chem.* (Leipzig), **228**, 364 (1965).

(14) H. S. Frank, "Chemical Physics of Ionic Solutions," B. E. Conway and R. G. Barradas, Ed., John Wiley and Sons, Inc., New York, N. Y., 1966, p 59.

(15) R. H. Wood and H. L. Anderson, *J. Phys. Chem.*, **71**, 1871 (1967).

The Effect of Impurities on the Spin-Lattice Relaxation of Ammonium Chloride

by D. E. Woessner and B. S. Snowden, Jr.

Mobil Oil Corporation, Field Research Laboratory, Dallas, Texas 75221 *(Received July 26, 1967)*

The effects of two types of foreign species in the ordered and disordered ammonium chloride lattice were investigated by spin-lattice relaxation temperature dependence measurements. Three major effects are caused by substitution of rubidium for ammonium ions in the ordered crystalline phase. These are: (1) the order–disorder transition occurs at a lower temperature, (2) the reorientation rate of the ammonium ions is enhanced, and (3) the temperature at which the T_1 minimum value occurs is decreased. Also, it was found that the substitution of water in the crystalline lattice decreases significantly the T_1 values of the disordered phase but does not appreciably affect the relaxation phenomena in the ordered phase.

Introduction

Previously,[1] we have made a temperature dependence study of the protonated and deuterated ammonium chloride spin-lattice relaxation rates using pulsed nmr techniques. A λ transition was observed at 242.8°K. In the temperature range above and below the transition region an apparent activation energy of 4.7 kcal/mol was obtained from the temperature dependence of the correlation time (τ_c). Comparison of this ammonium chloride study and similar studies on

(1) D. E. Woessner and B. S. Snowden, Jr., *J. Phys. Chem.*, **71**, 952 (1967).

ammonium bromide[2,3] reveals that for a particular compound the apparent activation energy is dependent only on the type of lattice structure, provided that the degree of lattice order is not changing.

The purpose of this work is to examine the effect of impurities on the apparent activation energy of the ammonium chloride lattice and on the λ transition. Two types of impurities are considered: first, the spherically symmetric rubidium ion; and second, the water molecule which has similar electrostatic properties to the ammonium ion.

Experimental Section

Two solid solutions of RbCl and NH_4Cl were prepared.[4] Sublimational analysis revealed the two samples to contain 2.18 and 4.71 mol % RbCl. Also, a sample of ammonium chloride was prepared by evaporation of a saturated ammonium chloride solution in a closed container using moist sodium chlorate as a desiccant. The moist sodium chlorate provided for evaporation of the water from ammonium chloride solution at 75% relative humidity.

The spin-lattice relaxation rate measurements are made using the previously described[2] nmr pulse apparatus and techniques at the resonance frequency of 25.0 MHz. The basic data are computer processed to obtain the relaxation time temperature dependences given in Figures 1 and 2 and numerically in Tables I–IV. Using a statistical 95% confidence index, the errors in T_1 are computed for each measurement. The average errors (given in Table V) are between 0.9 and 1.7%. The careful determination of errors is necessary to establish the relatively small relaxation time differences between samples.

Discussion

There are several interesting aspects of the temperture dependences of the relaxation times. First, the

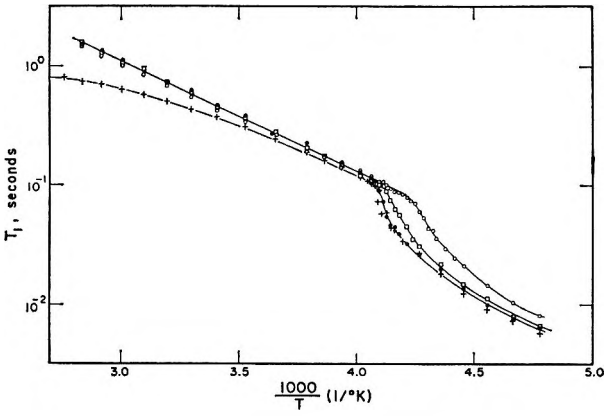

Figure 1. The temperature dependence in the upper temperature range of the proton T_1 values in ammonium chloride samples: ○, 95.29 mol % NH_4Cl and 4.71 mol % RbCl; □, 97.82 mol % NH_4Cl and 2.18 mol % RbCl; ●, sublimed NH_4Cl; +, NH_4Cl crystallized at 75% relative humidity.

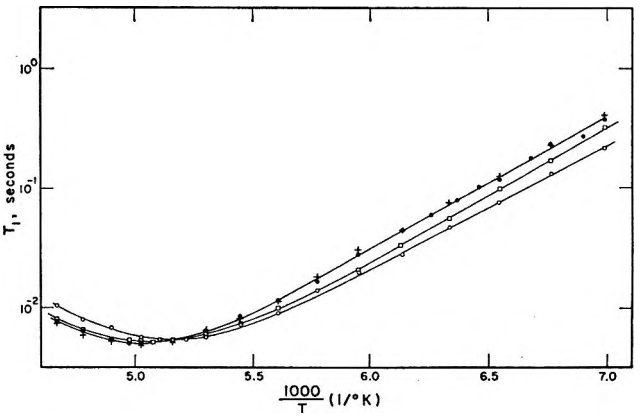

Figure 2. The temperature dependence in the lower temperature range of the proton T_1 values in ammonium chloride samples. (The same symbols as for Figure 1.)

temperature of the λ transition of the ammonium chloride is lowered with increasing rubidium content. The lowering of this transition increases with an increase in the mole fraction of rubidium chloride. The λ transition for the 2.18 mol % RbCl in NH_4Cl occurs 1.9°K lower than for the pure NH_4Cl. The corresponding shift is 8.6°K for the 4.71 mol % RbCl solid solution. It is interesting to note that within our experimental accuracy no discernible hysteresis is observed.

The λ transition of pure ammonium chloride was reported[5] to shift 9°K/1000 atm increase in pressure. The introduction of Rb^+ ions into the lattice seems to have an effect on lattice structural parameters similar to that of decreasing the external pressure.

The λ transition is less sharp at high pressure and relatively large concentrations of rubidium ions in the lattice. This decrease in abruptness of the transition may be attributed to a greater width of the distribution of correlation times in the ordered phase as conditions are varied from the pure sample at atmospheric pressure. The width of distribution of correlation times increases with rubidium content. This is reflected in an increase in the T_1 minimum value from 5.0 msec for the pure NH_4Cl to 5.2 msec for the 2.18 mol % RbCl–NH_4Cl, and to 5.3 msec for the 4.71 mol % RbCl–NH_4Cl sample.

Below the λ transition, RbCl seems to shift the T_1 temperature dependence curve. This shift is toward lower temperatures and increases with increasing RbCl content. Therefore, the T_1 minimum occurs at 194°K for the 4.71 mol % RbCl–NH_4Cl solid solution, 197°K for the 2.18 mol % RbCl–NH_4Cl, and 199°K for pure

(2) D. E. Woessner and B. S. Snowden, Jr., *J. Chem. Phys.*, **47**, 378 (1967).

(3) D. E. Woessner and B. S. Snowden, Jr., *ibid.*, **47**, 2361 (1967).

(4) R. J. Havighurst, E. Mack, Jr., and F. C. Blake, *J. Amer. Chem. Soc.*, **47**, 29 (1925).

(5) N. J. Trappeniers and W. Mandema, *Physica*, **32**, 1170 (1966).

Table I: The Temperature Dependence of the Proton T_1 in 97.82 mol % NH_4Cl and 2.18 mol % RbCl

Temp, °K	T_1, msec	ΔT_1, msec[a]	% Error[b]
352.8	1574.13	28.30	1.79
342.8	1314.65	13.10	0.99
332.9	1080.45	18.36	1.69
323.0	951.93	14.35	1.50
313.1	747.95	6.61	0.88
303.3	614.20	6.09	0.99
293.6	462.00	5.28	1.14
283.5	367.09	4.23	1.15
273.7	283.01	2.77	0.98
263.9	206.92	1.09	0.52
259.0	175.38	1.83	1.04
254.1	145.23	1.17	0.81
249.1	119.12	0.60	0.51
246.2	110.87	0.59	0.54
244.2	101.55	0.52	0.51
243.2	99.64	0.67	0.67
242.3	89.86	0.66	0.74
241.3	74.41	0.67	0.90
240.3	63.22	0.47	0.74
239.3	56.48	1.15	2.04
237.3	45.63	0.87	1.92
235.9	35.42	0.45	1.27
234.4	30.80	0.13	0.43
229.5	21.61	0.31	1.47
224.6	14.73	0.10	0.72
219.6	11.09	0.12	1.09
214.5	8.36	0.05	0.59
209.4	6.55	0.07	1.11
204.2	5.56	0.02	0.45
201.1	5.35	0.02	0.53
199.0	5.29	0.03	0.68
197.0	5.17	0.03	0.70
193.9	5.37	0.05	0.99
188.7	6.05	0.05	0.89
183.6	7.42	0.06	0.81
178.4	10.00	0.03	0.32
173.2	13.72	0.08	0.62
168.1	20.65	0.13	0.67
163.2	33.03	0.15	0.46
157.9	55.41	0.37	0.67
152.8	99.26	0.81	0.82
147.9	167.00	0.89	0.53
143.1	321.79	4.23	1.31

[a] ΔT_1 are the limits on T_1 statistically computed to give a 95% confidence index. [b] Per cent error defined as $100\Delta T_1/T_1$.

Table II: The Temperature Dependence of the Proton T_1 in 95.29 mol % NH_4Cl and 4.71 mol % RbCl

Temp, °K	T_1, msec	ΔT_1, msec	% Error
352.8	1450.42	22.49	1.55
342.9	1222.57	21.14	1.72
332.9	1017.42	11.76	1.15
323.0	859.59	15.60	1.81
313.1	691.66	11.94	1.72
303.3	552.73	8.22	1.48
293.6	424.48	10.15	2.39
283.5	344.95	5.23	1.51
273.2	267.33	3.09	1.15
263.9	199.42	3.28	1.64
259.0	171.12	2.40	1.40
254.1	141.78	1.44	1.02
249.1	132.76	1.98	1.49
246.2	117.21	2.40	2.05
244.2	108.00	1.38	1.28
243.2	102.91	1.21	1.18
242.3	100.85	0.90	0.89
241.3	95.64	1.14	1.19
240.3	87.94	0.60	0.68
239.3	87.67	0.88	1.00
238.3	84.43	0.94	1.12
237.3	78.35	0.49	0.63
236.4	73.92	0.57	0.77
235.4	70.17	0.50	0.71
234.4	60.62	0.63	1.04
233.4	53.88	0.45	0.84
232.4	44.07	0.69	1.58
231.4	41.61	0.49	1.19
230.5	36.32	0.68	1.88
228.5	29.47	0.34	1.17
226.5	24.77	0.35	1.44
224.5	20.83	0.35	1.68
219.6	14.45	0.15	1.07
214.5	10.33	0.12	1.22
209.4	7.94	0.07	0.99
204.2	6.72	0.09	1.34
199.0	5.61	0.04	0.84
193.9	5.29	0.05	1.03
191.8	5.34	0.04	0.78
188.7	5.82	0.09	1.61
183.6	7.09	0.07	0.99
178.4	9.26	0.07	0.85
173.2	14.21	0.08	0.62
168.1	20.19	0.25	1.25
163.0	29.34	0.23	0.79
157.9	46.76	0.67	1.45
152.8	78.18	1.51	1.93
147.9	133.50	2.05	1.54
143.1	218.06	1.94	0.89

NH_4Cl. With increasing applied pressure the T_1 minimum was observed[5] to shift +2°K/1000 atm. This shift is consistent with the predicted[1] results of pressure–volume changes on the potential energy barrier to reorientation of ammonium ions. The shift in the T_1 minimum temperature with rubidium ion concentration is much too large to follow this simple theory. The change in the T_1 minimum temperature for the RbCl–NH_4Cl solid solutions is ten times too large to be accounted for by the predicted change in lattice parameters. This shift results from a decrease in the correlation time with increasing RbCl content. This is expected since the presence of the spherical Rb^+ ions in place of the ammonium tetrahedra in the ordered lattice effectively reduces the dependence of the electrostatic energy of an ammonium ion on its orientation in the crystalline lattice. It should be noted that the effect of the rubidium ions is felt only in the ordered phase. Above the λ transition in the disordered phase the two RbCl–NH_4Cl solid solutions have the same correlation times as the pure NH_4Cl. The magnitude of

Table III: The Temperature Dependence of the Proton T_1 in Sublimed NH_4Cl

Temp, °K	T_1, msec	ΔT_1, msec	% Error
352.8	1593.31	50.34	3.16
342.8	1343.25	23.12	1.72
332.9	1113.10	17.98	1.61
323.0	890.59	11.17	1.25
313.1	750.21	15.58	2.07
303.3	621.94	15.02	2.41
293.6	475.70	13.14	2.76
283.5	376.41	7.91	2.10
274.7	269.68	4.63	1.71
263.9	214.06	3.00	1.40
259.0	179.39	2.33	1.30
254.1	155.77	2.77	1.78
249.1	127.70	1.66	1.30
246.2	115.00	1.11	0.97
245.2	109.41	2.48	2.27
244.2	90.01	1.35	1.50
243.2	72.68	1.45	2.00
242.3	55.51	1.34	2.42
241.3	46.42	0.92	1.98
240.3	44.22	0.97	2.20
239.3	38.73	0.54	1.40
237.3	32.56	0.38	1.19
234.4	25.64	0.48	1.89
229.5	19.78	0.39	1.97
224.6	13.45	0.20	1.49
219.6	9.96	0.11	1.11
214.5	7.46	0.08	1.07
209.4	6.24	0.10	1.75
204.2	5.39	0.12	2.35
201.1	4.95	0.08	1.67
199.0	5.18	0.09	1.86
197.0	5.26	0.14	2.76
193.9	5.44	0.10	1.85
188.7	6.22	0.10	1.60
183.6	8.29	0.10	1.22
178.4	11.35	0.13	1.23
173.2	16.61	0.21	1.27
168.1	28.26	0.70	2.50
163.0	43.21	0.43	1.00
159.9	59.00	0.63	1.07
157.0	77.55	0.82	1.06
154.8	98.71	1.20	1.21
152.8	119.14	1.24	1.04
149.8	178.65	3.16	1.77
147.9	237.13	3.37	1.42
145.0	274.02	6.51	2.37
143.1	380.01	4.02	1.06

Table IV: The Temperature Dependence of the Proton T_1 in NH_4Cl Crystallized at 75% Relative Humidity

Temp, °K	T_1, msec	ΔT_1, msec	% Error
362.7	843.58	24.80	2.94
352.8	802.59	18.21	2.27
342.9	729.18	11.59	1.59
332.9	664.03	8.34	1.25
323.0	586.33	5.92	1.01
313.0	534.23	11.29	2.11
303.3	447.72	4.81	1.07
293.6	377.06	3.31	0.87
283.5	330.02	7.47	2.26
273.7	250.48	2.36	0.94
263.9	193.16	2.84	1.47
259.0	164.52	1.90	1.15
254.1	138.53	1.04	0.75
249.1	118.20	1.44	1.22
247.2	109.19	0.76	0.69
246.2	103.01	0.61	0.60
245.2	101.08	1.09	1.08
244.2	97.07	0.57	0.59
244.2	90.88	0.93	1.02
244.2	74.09	0.93	1.26
243.2	63.80	0.70	1.10
242.3	50.91	0.43	0.85
241.3	43.19	0.37	0.87
240.3	40.17	0.29	0.73
238.3	33.63	0.37	1.12
234.4	26.71	0.46	1.75
229.5	18.09	0.19	1.07
224.5	10.84	0.37	3.49
219.6	9.08	0.15	1.65
214.5	6.92	0.08	1.19
209.3	5.74	0.05	1.01
204.2	5.25	0.08	1.65
199.0	4.77	0.05	1.12
193.9	5.21	0.10	2.04
188.7	6.27	0.09	1.44
183.6	7.85	0.09	1.25
178.4	11.11	0.09	0.89
173.2	17.25	0.13	0.76
173.2	18.51	0.23	1.28
168.1	30.52	0.36	1.20
163.0	44.43	0.56	1.27
157.9	74.77	0.61	0.82
152.8	125.41	1.75	1.39
147.9	232.12	2.67	1.15
143.1	407.55	4.68	1.15
138.1	671.71	15.73	2.34
133.1	1079.17	28.80	2.66

the anisotropic electrostatic energy contributed by positive ions in the ammonium chloride lattice is sufficiently small so that it has an insignificant effect on the over-all potential energy barrier to reorientation of an ammonium ion.[1] Therefore, the electrostatic effect of the rubidium ions is unimportant in the determination of the correlation times found for the disordered state. We would also expect this electrostatic effect to be equally small in the ordered state. This apparent contradiction can be resolved only if the electrostatic effect of the Rb^+ ions in the ordered state effectively decreases

Table V: Average Per Cent Error in T_1 Measurements

Sample	Average % error in T_1
97.82 mol % NH_4Cl and 2.18 mol % RbCl	0.91
95.29 mol % NH_4Cl and 4.71 mol % RbCl	1.26
Sublimed NH_4Cl	1.71
NH_4Cl crystallized at 75% relative humidity	1.33

the degree of order which, in turn, shortens the correlation time at a given temperature.

Unlike the RbCl impurities in the NH_4Cl lattice, the presence of water molecules appears only to have a significant effect on the relaxation time in the temperature region above the λ point. The failure of the water molecules in the moist ammonium chloride sample, prepared by evaporation at 75% relative humidity, to affect the relaxation times in the ordered phase may be partially attributed to the structural and electrostatic similarities[6] of water and the ammonium ion. However, it is mainly due to the small amount of H_2O present in the ammonium chloride lattice. It can be seen from Figure 1 that the presence of the water molecules does not appreciably shift the λ transition. Above the λ point the relaxation times of the moist sample are much shorter than those of the dry NH_4Cl. For the deuterated moist sample, similarly prepared, the relaxation times of the dry and moist deuterated samples are essentially the same for *all* temperature ranges studied.

If we assume that the moist $ND_4Cl \cdot xD_2O$ sample and the moist $NH_4Cl \cdot xH_2O$ samples have the same content and disposition of water in the ammonium chloride lattice, the observed depression of T_1 in the disordered phase of $NH_4Cl \cdot xH_2O$ must be caused by magnetic dipole–dipole interactions between protons of the water molecules and the protons of the ammonium ions. Such an interaction is much smaller for the deuterated sample because the deuteron magnetic dipole moment is much smaller than the proton magnetic dipole moment.

This interaction is observed only in the disordered phase for the following reason. The correlation times of the ammonium ions vary directly with reciprocal temperature. Only at the higher temperatures does the effective correlation time of this interaction appreciably influence the over-all relaxation time of the $NH_4Cl \cdot xH_2O$ sample.

Although the above explanation gives a consistent interpretation of our observed phenomena, it is completely dependent on the assumption that the protonated and deuterated samples are completely analogous. This assumption is supported by nmr line width temperature dependence measurements.[7] These measurements revealed a narrow-line component in the middle of the deuteron magnetic resonance line for ND_4Cl crystals which were exposed to atmospheric moisture. This was attributed to the existence of a water–ammonium chloride eutectic solution.

Summary

From our studies of doped ammonium chloride samples, we can make the following statements about the effect of foreign species in a crystalline lattice. First, the substitution of ammonium ions by spherical ions only affects the ordered crystalline phase. Three major effects are observed in this phase: (1) the order–disorder transition occurs at a lower temperature; (2) the reorientation rate of the ammonium ions is enhanced; and (3) the temperature at which the T_1 minimum value occurs is decreased. All three effects increase with increasing spherical ion concentration.

Next, the inclusion of small amounts of water molecules in the crystalline lattice does not have a marked effect on the ordered phase or on the λ transition. However, there is a pronounced decrease in the T_1 values of the disordered phase due to the magnetic dipole–dipole interaction of H_2O molecules and NH_4^+ ions. This effect is not seen in the ordered phase where the relaxation rate is predominantly determined by the interaction within the ion itself.

Except for the $NH_4Cl \cdot xH_2O$ sample in the disordered phase, the activation energies seem to be affected only to a minor extent by the presence of small impurities. This is consistent with our interpretation[1] that the activation energy of a crystalline phase is unaffected by the lattice order, provided that this order is constant.

Acknowledgments. The authors wish to thank P. H. Haagen and J. S. Grisham, Jr., for performing the pulse nmr measurements and E. D. Evans for analyzing the NH_4Cl–RbCl samples. We are also grateful to Mobil Oil Corp. for permission to publish this work.

(6) P. M. Vollmar, *J. Chem. Phys.*, **39**, 2236 (1963).

(7) V. Hovi and P. Pyykko, *Phys. Kondensierten Materie*, **5**, 1 (1966).

Internal Reflection Spectroscopy at Optically Transparent Electrodes

by V. S. Srinivasan and T. Kuwana

Department of Chemistry, Case Western Reserve University, Cleveland, Ohio 44106 *(Received July 28, 1967)*

The type of spectrum obtained by internal reflection spectroscopy[1] (IRS) at optically transparent electrodes is theoretically and experimentally examined. It is found that the thin conducting film used as the electrode surface on the transparent substrate greatly affects the character of the spectrum. General formulas applicable to this problem are derived from concepts of physical optics.

Introduction

Recently, IRS in the visible region of the spectrum was applied following the concentration of electrogenerated species essentially at the surface of an optically transparent electrode (OTE).[2] The electrode in this work was glass which was coated with a thin film of "doped" tin oxide. Such a film, as probably will be the case with most conductive films, has a high refractive index which influences the experimental IRS spectra. That is, the "background" IRS spectrum with the thin-film surface in contact with the background solution (*e.g.*, aqueous solution containing a supporting electrolyte which is transparent in the visible region) has an absorbance which fluctuates as a function of wavelength. This fluctuation is reminiscent of an interference phenomenon. If an absorbing species is present in solution, as it would be when one generates it electrolytically at the surface, the absorbance due to the species is not superimposed on the background spectrum proportionally to its molar absorptivity, the molar absorptivity being evaluated from normal transmission spectroscopy. If IRS is to serve as a qualitative and quantitative tool for investigating surface reactions in electrochemistry, it is important to understand the factors which are responsible for determining the character of an IRS spectrum. Thus theoretical and experimental analyses were undertaken. These analyses are a further elaboration of a previous work,[2] and particular emphasis will be on IRS using these tin oxide coated glasses.

The general formulas applicable to this problem are derived from concepts of physical optics. Similar conclusions are obtained from Maxwell's equations using suitable boundary conditions.[3,4]

Experimental Section

Antimony-doped, tin oxide coated glasses were obtained from Corning Glass Co. (Corning, N. Y.) Details of surface properties, electrical contacts, and cell designs have been discussed.[2,5] Thin films of gold were deposited on glass plates by vacuum evaporation method. Spectral measurements were performed using the Cary 15 spectrometer. An Eastman Kodak polascreen was used for polarizing the light beam. Doubly distilled water and reagent grade chemicals were employed for solutions. Computations were performed on a Univac 1107 computer using ALGOL language.

Theory

The light ray (as shown in Figure 1) enters the conducting film (hereafter referred to as a film) through the transparent glass substrate and undergoes multiple reflections in the film. These reflections give rise to an interference phenomenon which, of course, means that the light intensity emerging from the glass plate is wavelength dependent. A spectrum of a species at the surface of the film obtained by IRS would be, in some manner, superimposed on this interference pattern. For normal incidence of the light, an expression relating the reflection from thin films has been derived by Murmann and Forsterling.[6] The derivation in this paper is a generalized formula valid for any angle of incidence.

The problem is divided into two parts. First, the Fresnel reflective coefficients are calculated for reflections at the interface of two media, either one or both absorbing the radiation. These values are used next in the general formula first derived by Forsterling for normal incidence for reflection from thin films, but now modified to include any angle of incidence. Secondly, an approximate method to calculate the attenuation index of the material of the thin film from a single transmission experiment will be shown.

The complex Fresnel reflective coefficient, $\bar{r}_2$, at the interface (see Figure 1) of the two absorbing media, film and solution, for light polarized perpendicular to the plane of incidence is given by

$$\bar{r}_2 = \frac{\bar{n}_2 \cos \phi_2 - \bar{n}_3 \cos \phi_3}{\bar{n}_2 \cos \phi_2 + \bar{n}_3 \cos \phi_3} \qquad (1)$$

(1) Also referred to as attenuated total reflectance, ATR.

(2) W. N. Hansen, T. Kuwana, and R. A. Osteryoung, *Anal. Chem.*, **38**, 1809 (1966).

(3) W. N. Hansen, personal communication.

(4) M. Born and E. Wolf, "Principles of Optics," The Macmillan Co., New York, N. Y., 1966.

(5) J. W. Strojek and T. Kuwana, *J. Electroanal. Chem.*, in press.

(6) A. Vasicek, "Optics of Thin Films," North-Holland Publishing Co., Amsterdam, The Netherlands, 1960, pp 323–327.

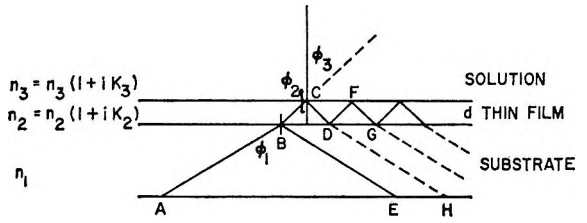

Figure 1. Multiple reflections in the thin film.

where $\bar{n}_2$ and $\bar{n}_3$ are the complex refractive indices which are equal to $n_2(1 + ik_2)$ and $n_3(1 + ik_3)$, respectively. The refractive indices n_2 and n_3 and the attenuation indices k_2 and k_3 are for the film and for the solution, respectively. The angle of incidence ϕ_2 and the angle of refraction ϕ_3 are for the light ray entering at the interface. In the above equation the angles are also complex, but they can be replaced in terms of the experimental quantities of angle of incidence ϕ_1 of the light beam at the substrate–film interface and of refractive index n_1 of the transparent substrate. These terms are interrelated through Snell's law as follows, assuming the media are isotopic

$$n_1 \sin \phi_1 = \bar{n}_2 \sin \phi_2 = \bar{n}_3 \sin \phi_3 \tag{2}$$

Equation 1 can be simplified by the usual complex algebraic method, and one obtains

$$\bar{r}_2 = \rho_2 \exp(i\beta) \tag{3}$$

with the amplitude ρ_2 of $\bar{r}_2$ given by

$$\rho_2 = \sqrt{\frac{\xi - \eta}{\xi + \eta}} \tag{4}$$

where

$$\xi = x^2 + y^2 + p^2 + q^2 \tag{5}$$

$$\eta = 2(px + qy) \tag{6}$$

$$x = (1/\sqrt{2})[(N_2^2 - N_2^2k_2^2 - \sin^2\phi_1) + \sqrt{(N_2^2 - N_2^2k_2^2 - \sin^2\phi_1)^2 + (2N_2^2k_2)^2}]^{-2} \tag{7}$$

$$y = (1/\sqrt{2})[-(N_2^2 - N_2^2k_2^2 - \sin^2\phi_1) + \sqrt{(N_2^2 - N_2^2k_2^2 - \sin^2\phi_1)^2 + (2N_2^2k_2)^2}]^{-2} \tag{8}$$

Similar functions can be written for p and q with N_3 replacing N_2 and k_3 replacing k_2, where $N_2 = n_2/n_1$ and $N_3 = n_3/n_1$. The phase angle β associated with the above electric vector is then given by

$$\sin \beta = 2(py - qx)/\sqrt{(\xi^2 - \eta^2)} \tag{9}$$

For each reflection, the amplitude and the phase angle can be evaluated from the above equations with the corresponding numerical values. The complex refractive index could have been defined in the form $\bar{n} = n(1 - ik)$ and the same results could have been obtained. The electric vector evaluated using this complex refractive index would be the conjugate value. The magnitude and the phase angle of the electric vector were calculated on the computer. It should be pointed out that since the phase angle is obtained only between the angles $-\pi/2$ and $+\pi/2$ from the arctan computations, the proper quadrant is chosen by examination of the sign of the real part of the solution.

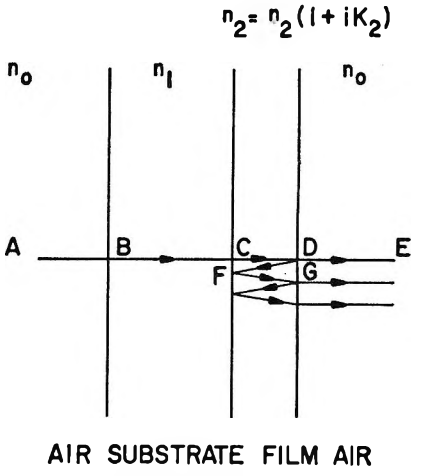

Figure 2. Near-normal incidence of light on the thin-film and multiple reflections.

Murmann–Forsterling Formula. For completeness, a brief account of the derivation for the reflectivity from thin films on glass substrates will be given here. In Figure 1, the light ray is refracted in the substrate at an angle ϕ_1 and is partially reflected with a Fresnel coefficient $\bar{r}_1 = \rho_1 \exp(i\gamma)$. It is partly transmitted through the film of thickness d with a coefficient $\bar{t}_1$. This transmitted part is reflected at the film–solution interface at C with a coefficient $\bar{r}_2 = \rho_2 \exp(i\beta)$, the refracted angle being ϕ_2 in the film. The light ray CD is once again partly reflected at D with a coefficient $\bar{r}_3$, which is equal to $-\bar{r}_1$, and transmitted at the film–substrate interface (point D) with a coefficient $\bar{t}_2$. The progressively attenuated rays thus undergo multiple reflections in thin films with the attenuation indices of solution and thin film determining the character of the rays. The emergent ray DH is out of phase by $\bar{\delta} = 4\pi n_2 d \cos \phi_2/\lambda$ due to the path difference of $2d\bar{n}_2 \cos \phi_2$ in the film. These partly emergent electric vectors may constructively or destructively interfere with the first reflected ray. The ratio of the resultant to the incident amplitude of the electric vectors is then given by the summation of all these

$$E = (E_0/E_i) = \bar{r}_1 + \bar{t}_1\bar{t}_2(1 + \bar{r}_2\bar{r}_3 \exp(i\bar{\delta}) + \bar{r}_2^2\bar{r}_3^2 \exp(2i\bar{\delta}) \ldots \tag{10}$$

Making use of the relationship $\bar{r}_1 = -\bar{r}_3$ and $\bar{r}_1^2 = 1 - \bar{t}_1\bar{t}_2$, the geometric summation gives

$$E = \bar{r}_1 + \bar{r}_2 \exp(i\bar{\delta})/1 + \bar{r}_1\bar{r}_2 \exp(i\bar{\delta}) \tag{11}$$

and the reflectivity is then given by EE^*. On simplifying, one obtains for reflectivity

$$R = \frac{\rho_1^2 + (\alpha\rho_2)^2 + 2\rho_1\rho_2\alpha \cos(\gamma - (\beta + \delta))}{1 + (\alpha\rho_1\rho_2)^2 + 2\rho_1\rho_2\alpha \cos[\gamma + (\beta + \delta)]} \quad (12)$$

with $\alpha = \exp(-\bar{\delta}_{im})$ and $\delta = \delta_{re}$ (im = imaginary, re = real). The reflections from thin films can be simulated through calculations using this equation.

Determination of Attenuation Index from Transmission Measurements. In Figure 2 the light ray is near normal incident to the air–glass interface with a transmission coefficient of $\bar{t}_{ag}$ (the subscripts a = air, g = glass, f = film). Part of this ray is further transmitted at the glass–film interface with a coefficient of $\bar{t}_{gf}$. This ray travels through the thin film of thickness d, and the refractive index $\bar{n}_2$ of the film is

$$\bar{n}_2 = n_2(1 + ik_2) \quad (13)$$

The film introduces a phase shift $\bar{\delta}$, and with incident angle θ very small ($\cos\theta \cong 1$), the phase shift is given by

$$\bar{\delta} = \frac{2\pi}{\lambda}\bar{n}_2 d \quad (14)$$

Part of the ray in path BC is then reflected at the film–air interface with a coefficient $\bar{r}_{fa}$ which is reflected again at the film–glass interface with a coefficient of $\bar{r}_{fg}$. All of these partly emerging electric vectors can constructively or destructively interfere. The resultant ratio of amplitude of these electric vectors is then

$$E = \left[\frac{E_t}{E_r}\right] = \bar{t}_{ag}\bar{t}_{gf}[\bar{t}_{fa} \exp(i\bar{\delta}) + \bar{t}_{fa}\bar{r}_{fa}\bar{r}_{fg} \exp(3i\bar{\delta}) + \ldots\ldots] \quad (15)$$

$$= \bar{t}_{ag}\bar{t}_{gf}\bar{t}_{fa} \exp(i\bar{\delta})/[1 + \bar{r}_{fa}\bar{r}_{fg} \exp(i2\bar{\delta})] \quad (16)$$

The ratio of the intensities is obtained by multiplying eq 13 by its conjugate. The corresponding magnitudes of the complex quantities are t_{ag}, t_{gf}, t_{fa}, r_{fa}, and r_{fg}. It is easy to see that the function has a cosine term in the denominator and is capable of having a maximum and minimum value for the extreme values of 1 or −1 for the cosine function. In terms of the magnitudes, the extreme values are then evaluated by using

$$\frac{I}{I_0} = t_{gf}^2 t_{ag}^2 t_{fa}^2 \alpha/[1 \pm \alpha^2 r_{fa} r_{fg}] \quad (17)$$

where

$$\alpha = \exp\left(\frac{-4\pi}{\lambda} n_2 k_2 d\right) \quad (18)$$

Both t_{gf} and t_{fa} can be obtained from the transmittance equations, where

$$\bar{t}_{gf} = \frac{2n_1}{n_1 + \bar{n}_2} \quad (19)$$

with n_1 equal to the refractive index of glass. The magnitudes of the other transmission and reflection coefficients can be evaluated by eq 19 and

$$t_{fa} = 2n_2\sqrt{1 + k_2^2}/\sqrt{(n_0 + n_2)^2 + n_2^2 k_2^2} \quad (20)$$

$$r_{gf} = \sqrt{\frac{(n_1 - n_2)^2 + n_2^2 k_2^2}{(n_1 + n_2)^2 + n_2^2 k_2^2}} \quad (21)$$

and

$$r_{fa} = \sqrt{\frac{(n_2 - n_0)^2 + n_2^2 k_2^2}{(n_2 + n_0)^2 + n_2^2 k_2^2}} \quad (22)$$

The experimentally obtained quantity is the absorbance which is equal to $-\log(I/I_0)$. Using different values of the attenuation index k_2 for the film, tin oxide in the present case, the absorbance at various wavelengths is evaluated. The k_2 which produces a calculated interference-type spectrum with the magnitude of minimum and maximum of absorbance at various wavelengths corresponding to the experimentally observed spectrum is taken as the best value of k_2. The assumption is made that k_2 is independent of wavelength. The value of $k_2 = 0.0035$ is found and is in reasonable agreement with the value of 0.004 reported by Hansen.[3]

Results and Discussion

The experimental reflection spectra of glass coated with a tin oxide film in contact with air and with water for light polarized normal to the plane of incidence is shown in Figure 3, where the absorbance A is defined as −log (reflectivity). The index of refraction of the borosilicate glass was 1.49 and the angle of incidence, ϕ, was 72°. The optical constants of the tin oxide film n_2, k_2, and the thickness, d, were determined from the transmission experiments to be 1.88, 0.0035 and 960 mμ, respectively. The value of d is near the 1 μ thickness suggested by the supplier of these coated glasses. Using the above values, theoretical spectra were reconstructed from computer calculations which were in fair agreement with the experimental ones, although agreement at all wavelengths is not expected since the

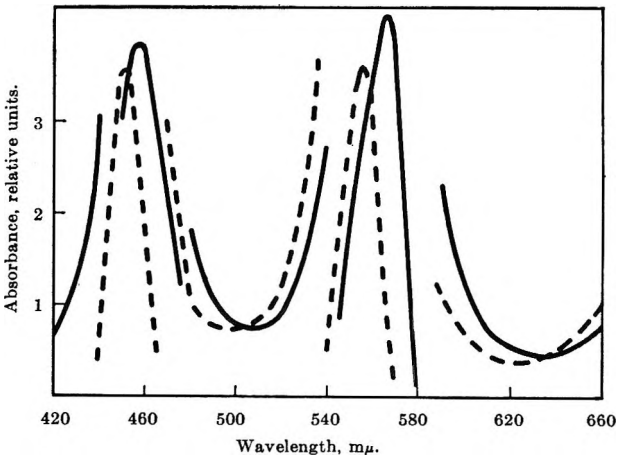

Figure 3. Reflection spectra of SnO_2 glass: - - - -, air; ———, solution. Discontinuities of curves due to changing absorbance scale of spectrometer.

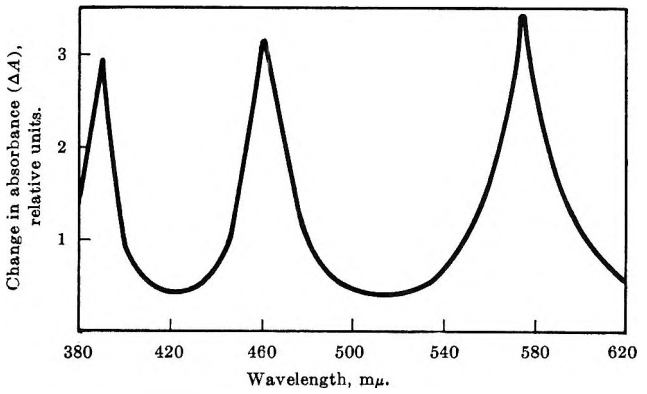

Figure 4. IRS of eosin-Y dye under various conditions. Effect of k_3 on absorbance.

assumed independence of refractive indices on wavelength is not completely valid. The results, as confirmed by both the experimental and simulated spectra, clearly show that changes in the position and the magnitude of the interference maxima are caused entirely by a change in the index of refraction of the third phase from 1.00 (air) to 1.33 (water).

If the absorbance of a species is independent of wavelength and the film is absent, the IRS spectrum would be a straight line parallel to the wavelength axis. The presence of the tin oxide film causes the usual interference pattern, but the absorbing species superimposed on this spectra would not be a straight line. A maximum absorbance due to the species would be observed and would coincide with the maximum of the interference peaks, assuming a constant value of k_3. The experimental absorption spectra is determined as the difference between a solution with k_3 equal to zero, *i.e.*, water, and the test solution where k_3 is greater than zero. In Figure 4 the relative change in absorbance is plotted as a function of wavelength with $k_3 = 0.005$. Notice that as long as the index of refraction of the reference base line is the same as the index of refraction of the test solution, concentration of the absorbing species will be proportional to k_3 at a constant wavelength. The shape of the spectrum for a species at the solution–film interface is greatly dependent on the index of refraction n_2 of the tin oxide film and on the thickness of the film, but as can be seen from eq 7 and 8, k_2, since it is much less than 1, does not affect the spectrum to the first order.

To study the IRS of an absorbing species with and without the tin oxide film, aqueous solutions of eosin-Y and sodium indigo sulfonate were examined. Figure 5A shows a spectrum of eosin-Y using a plastic plate for the cell. This plate was used rather than a glass plate because there was evidence of less surface adsorption by eosin-Y. By use of eq 1 and 3, the k_3 value for the dye was calculated. With this value, a simulated spectrum for a glass plate coated with the tin oxide film was found from eq 12. This spectrum,

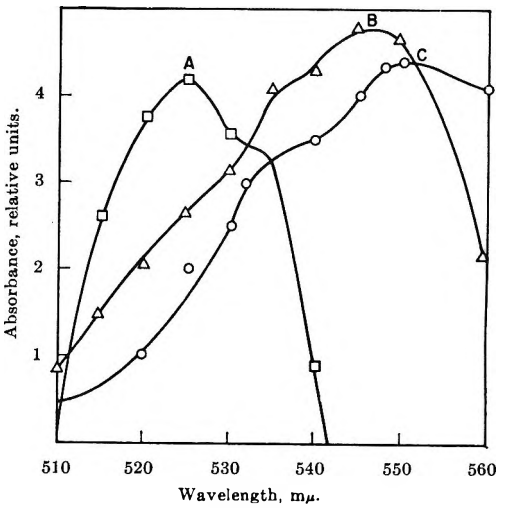

Figure 5. IRS of sodium indigo sulfonate under various conditions: A, ATR; B, simulated; C, experimental.

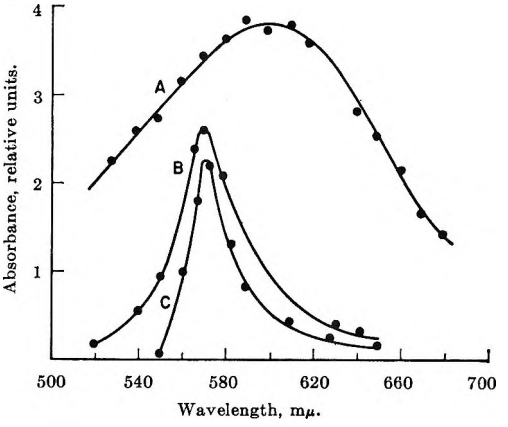

Figure 6. Effect of k_2 on absorbance: A, ATR; B, simulated; C, experimental.

Figure 5B, is compared to the experimentally determined one, Figure 5C, for eosin-Y in the cell with a tin oxide coated glass plate. Sodium indigo sulfonate was studied in the same manner, and these results are shown in Figure 6.

Of particular interest is the relationship between the position of the absorption maximum with and without the tin oxide film. For eosin-Y without the film, the absorption maximum occurs near 520 mμ, and for sodium indigo sulfonate, it occurs near 610 mμ. When the tin oxide film is introduced, however, the eosin-Y peak shifts to 550 mμ, while the sodium indigo sulfonate peak shifts in the opposite direction to 570 mμ. Thus compounds with well separated absorption maxima absorb at nearly the same wavelength when studied at a tin oxide film. It is evident from these results that without a thorough knowledge of the absorption properties of a species produced by an electrochemical reaction, an investigator may conclude erroneously about its spectral characteristics.

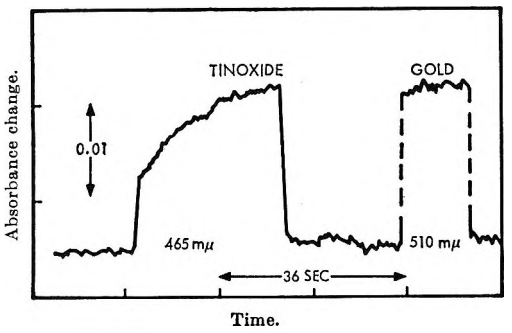

Figure 7. Change in absorbance for supporting electrolytes at applied potentials.

An additional interesting phenomenon is observed when these thin films are used as electrodes in contact with electrolytic solutions. That is, the IRS absorbance changes with applied potential in the absence of any electrolysis of electroactive species. For example, a change, similar to that noted previously for tin oxide films,[2] is shown in Figure 7 for a tin oxide film in contact with an acetate buffer solution when a square-wave potential pulse of +0.6 V *vs.* reference saturated calomel electrode is applied. The rate of change of absorbance lags considerably behind the rise and fall of the potential. The maximum absorbance change again occurs at the maximum of the "interference" peaks. Similar changes also occur with glass coated with vapor-deposited gold films, with the only difference being that the absorbance changes are much faster than with tin oxide. It is important that these changes affect the magnitude of the absorbance only and not the wavelength of the "interference" maximum. This suggests that the refractive index is not being changed in the immediate vicinity of the film surface. Perhaps optical rotation of the penetrating electric vector at the film solution interface due to the applied potential can explain these observations. Further work is necessary to understand these results.

Acknowledgment. The fruitful discussions with W. N. Hansen of the North American Aviation Science Center are greatly appreciated. The assistance of R. Chang during the early part of this work is acknowledged. The authors gratefully acknowledge the support of this work by Grant No. GM 14036 from the Research Grant Branch of National Institutes of General Medical Sciences, National Institutes of Health, and by Navy Ordnance Laboratory Contract N123-(62738)56006A.

Electrolytic Hydrogen Evolution Reaction on Aluminum in Acidic Solutions

by A. K. Vijh

R & D Laboratories, Sprague Electric Company, North Adams, Massachusetts 01247 *(Received July 31, 1967)*

The mechanism of the electrolytic hydrogen evolution reaction (h.e.r.) has been studied on aluminum in several acidic solutions. Experimental measurements consist of galvanostatic current–potential relationships, open-circuit decay from initial cathodic potentials, cathodic-charging curves, and determination of apparent heat of activation. Mechanistic conclusions are based on Tafel slopes, exchange current densities, reaction orders, apparent heat of activation, absence of arrests in the charging curves and potential-decay profiles, nature of capacity–potential curves calculated from open-circuit decay profiles, and some general considerations, *e.g.*, melting point and heat of atomization of aluminum. Significance of other approaches for determination of mechanism of h.e.r. in relation to aluminum is briefly discussed. Initial discharge step is suggested as the likely rate-determining stage (rds) in the over-all reaction; this inference, however, is not entirely conclusive, owing to the difficulties involved in distinguishing initial discharge step from the electrochemical desorption step as the probable rds.

I. Introduction

In the present investigations, an attempt has been made to examine the mechanism of the hydrogen evolution reaction (h.e.r.) on aluminum in acidic solutions. The solutions in which the h.e.r. has been studied are 0.2 *N* H_2SO_4, 0.5 *N* H_2SO_4, 0.86 *N* H_2SO_4, 1.7 *N* H_2SO_4, 1 *N* CH_3COOH, and (2 *N* CH_3COOH + 1 *N* $NH_4CO-OCH_3$). The only previous results available in the literature are the galvanostatic evaluation of the Tafel slopes for the h.e.r. on aluminum in 1 *N* HCl[1] and in 2 *N* H_2SO_4.[2] These studies, however, were carried out

(1) A. Hickling and F. W. Salt, *Trans. Faraday Soc.*, **36**, 1126 (1940).

before the germination[3,4] of modern procedures of solution purification, electrode preparation, luggin probes, etc. The quantitative significance of these reports,[1,2] therefore, is rather limited. Aluminum is a typical example of corrodible metals on which not many investigations involving h.e.r. have been carried out.

II. Experimental Section

A conventional three-compartment Pyrex cell and the circuits usually involved in the electrochemical measurements were used.[5-7] The cell was custom-made by the Kontes Glass Co., Vineland, N. J. The three compartments of the cell could be isolated by means of solution-sealed stopcocks. The cell was sealed off from the atmosphere by means of Tru-bore tubing and standard joints. The cell was provided with appropriate gas inlets and outlets. It was cleaned with chromic acid and rinsed several times in deionized, distilled water.

Solutions were made up of water which had been deionized and then distilled and CP sulfuric acid or ACS acetic acid, or ACS acetic acid plus ACS ammonium acetate. Purification of the sulfuric acid solutions was carried out by preelectrolysis for 16 hr at the highest current density used in the experiment on a sacrificial platinized-platinum electrode. Preelectrolysis of the acetic acid solutions, however, was carried out only for about 2 hr, since prolonged preelectrolysis seemed to introduce some impurities, as manifested by very irreproducible results, unsteady potentials (at constant current), anomalous Tafel slopes, and increased unsteadiness of potentials with increased rate of bubbling. These impurities, in acetic acid solutions, could arise during preelectrolysis in the anodic compartment and then migrate to the working compartment, since the stopcock between the two compartments had to be slightly open in order to pass the high currents desired during preelectrolysis. Shorter preelectrolysis or even no preelectrolysis at all seemed to give reproducible and steady results in acetic acid solutions. All solutions were also preelectrolyzed on large platinized platinum electrodes (at very low current densities of course) for about 3–5 hr in order to purge the solution of any organic impurities through chemisorption on the large electrode surface. Prepurified hydrogen was bubbled through the working compartment throughout preelectrolyses. No special claims are made regarding the purity of solutions, except that the residual steady-state contamination, if any, seemed not to interfere with the reproducibility and steadiness of the results; also, there was no effect of the rate of bubbling on the values of potential (at constant current) observed. This purification procedure when coupled with proper electrode surface preparation (to be described below) seemed to give reproducible Tafel plots over several decades of current density and without anomalously high Tafel slopes.

All experiments except those for the determination of the apparent heat of activation were carried out at room temperature (25 ± 1.5°). The apparent heat of activation was determined in 1 *N* CH_3COOH solutions from the exchange current densities obtained at 1, 12.5, 30.5, 38.5, and 55.5°. The entire cell was suspended in a large water bath with all the three compartments and the solution-sealed stopcocks dipping in the bath well above the level of the solution within the cell. No elaborate apparatus for temperature control of the bath was used. The temperature was controlled manually and the temperature stayed well within ±0.25° of the stated values during measurement of a given Tafel relation.

Before the commencement of the runs, the solution was thoroughly purged of oxygen and saturated with prepurified hydrogen. The working electrodes were prepared by engaging an aluminum wire (99.98%) into a glass tube by means of a joint made up of a special Teflon tubing, Flotite, manufactured by Pope Scientific, Inc. Such a joint is mechanically sound, leakproof and chemically inert toward strongly acidic polishing baths and degreasing organic solvents. A mechanical seal between glass–Teflon–aluminum[7] was also found to be satisfactory, except for the awkward electrode size in some runs in which very high current densities were desired for a given current.

All working electrodes were chemipolished for 2 min at 90° in a "bright-dip" bath (85% H_3PO_4 and 15% HNO_3) and were subsequently washed with deionized, distilled water, dipped in 1 *N* NaOH (10 min) and then washed again several times in deionized, distilled water. This procedure was carried out just before the commencement of the run and seems to give reproducible Tafel slopes over several decades of current densities.

The counterelectrodes were made up of smooth platinum wire. Hydrogen reference electrodes were used in all experiments. During all experiments, the three compartments were isolated by wet but closed solution-sealed stopcocks.

III. Results

A. Steady-State Current–Potential Relationships. In Figure 1, results are presented for potential–log (current density) relationships for h.e.r. on aluminum in 0.2 *N* H_2SO_4 (pH 0.94), 0.5 *N* H_2SO_4 (pH 0.59), 0.86 *N* H_2SO_4 (pH 0.37), and 1.7 H_2SO_4 (pH 0.1); the results are compared with some previous ones[2] in 2 *N* H_2SO_4 (pH 0.04). Tafel slope, b, and exchange current density, i_0, have the values equal to 0.11 V and $10^{-7.7}$ A cm^{-2}, respec-

(2) A. G. Pecherskaya and V. V. Stender, *Zh. Prikl. Khim.*, **19**, 1302 (1946).

(3) J. O'M. Bockris, *Chem. Rev.*, **43**, 525 (1948).

(4) J. O'M. Bockris, *Trans. Faraday Soc.*, **43**, 417 (1947).

(5) B. E. Conway and M. Dzieciuch, *Can. J. Chem.*, **41**, 21 (1963).

(6) J. J. MacDonald and B. E. Conway, *Proc. Roy. Soc.* (London), **A269**, 419 (1962).

(7) N. D. Greene, "Experimental Electrode Kinetics," Rensselaer Polytechnic Institute, Troy, N. Y., 1965

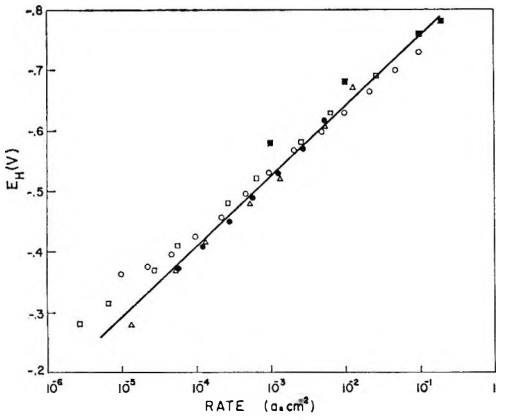

Figure 1. Tafel plots for h.e.r. on Al in H_2SO_4: ●, 0.2 *N*; ○, 0.5 *N*; △, 0.86 *N*; □, 1.7 *N*; and ■, results of Pecherskaya and Stender[2] in 2 *N* H_2SO_4. Values of *b* and log i_0 are 0.11 and −7.7, respectively.

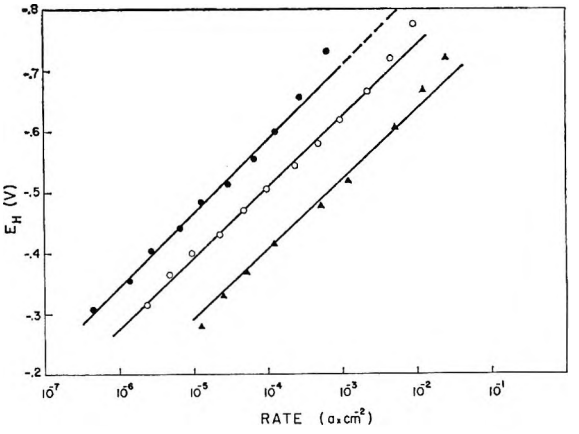

Figure 2. Tafel plots for h.e.r. on Al in acidic solutions of different pH values: ●, pH 4.4, *b* = 0.122 V (2 *N* CH_3COOH + 1 *N* NH_4COOCH_3); ○, pH 2.4, *b* = 0.117 V (1 *N* CH_3COOH); ▲, pH 0.37, *b* = 0.114 V (0.86 *N* H_2SO_4).

tively. It may be pointed out that the rate at a given potential seems to be independent of pH in the pH range 0.1–0.94. However, the scatter in this graph is almost comparable to the changes in rate, at a given overpotential, expected in going from pH 0.1 to 0.94. Increased scatter at lower cathodic potentials probably arises from complications due to "chemical" corrosion reaction[8] or from the presence of trace impurities in the solution. Some data of Pecherskaya and Stender,[2] also shown in Figure 1, seem to depart noticeably from the Tafel line drawn through our results for the four concentrations of sulfuric acid studied (0.2, 0.5, 0.86, and 1.7 *N*). This probably arises from the questionable purity of the solutions of these authors,[2] which has also been commented upon previously.[9]

Tafel plots in 0.86 *N* H_2SO_4 (pH 0.37) have been compared with those in 1 *N* CH_3COOH (pH 2.4), and in 2 *N* CH_3COOH + 1 *N* NH_4COOCH_3 (pH 4.4) in Figure 2. These are the results from which various reaction-order derivatives[10-12] have been determined. The derivation of reaction orders from these plots is justified because (a) these are all concentrated solutions[13] with a consequently constant value of ψ potentials;[10,11] (b) the reaction orders have been determined only from potentials equal to or more cathodic than −0.4 V, which is roughly the potential of zero charge for aluminum.[14] At these high cathodic potentials, any complications that otherwise might arise from the specific adsorption of acetate ions are vanishingly small. Absence of specific adsorption of acetate ions is also suggested by the fact that there is no increase in the value of Tafel slope[10] in acetate solutions, even at lower temperatures (see Table I). Hence for reaction-order purposes, the Tafel plots in different sulfuric acid and acetic acid solutions may simply be assumed, to a first approximation, as potential–rate relations obtained in solutions of different pH values (*i.e.*, 0.37, 2.4, and 4.4).

This direct comparison of potential–rate relations in solutions of different chemical composition is further

Table I: Aluminum in 1 *N* CH_3COOH (h.e.r.)

Temp, °C	Temp, °K	*b*, V	i_0, A cm^{-2}	1000(1/*T*), *T* in °K	Rest potential, V
55.5	328.5	0.124	−8.15	3.022	0.430
38.5	311.5	0.118	−8.60	3.214	0.388
30.5	303.5	0.117	−8.82	3.296	0.368
12.5	285.5	0.123	−8.86	3.505	0.312
1.0	274.0	0.125	−9.28	3.650	0.265

justified by the following facts. (a) The species involved in the discharge step in all three solutions must be the same, *i.e.* H_3O^+ and H_3O^+ alone. (b) The Tafel slope in all the three solutions is the same, *i.e.*, $2.3(2RT/F)$ (118 ± 4 mV). (c) Identical transient behavior is observed in the three solutions in the charging curves and in the open-circuit decay profiles.

It may seem rather arbitrary that only one sulfuric acid solution (0.86 *N*) has been chosen for the reaction-order purposes (Figure 2). However, this is the only one which is fairly concentrated with a consequently constant ψ potential[10,11] and at the same time does not

(8) M. Pourbaix, "Atlas D'Equilibres Electrochimiques," Gauthier-Villars and Co., Paris, 1963, p 168.

(9) J. O'M. Bockris in "Electrochemical Constants," National Bureau of Standards Circular 524, U. S. Government Printing Office, Washington, D. C., 1953.

(10) B. E. Conway, "Theory and Principles of Electrode Processes," The Ronald Press Co., New York, N. Y., 1965.

(11) B. E. Conway and M. Salomon, *Electrochim. Acta*, 9, 1599 (1964).

(12) K. J. Vetter, "Electrochemische Kinetik," Springer-Verlag, Berlin, 1961; see also E. Yager, Ed., "Transactions of the Symposium on Electrode Processes," John Wiley and Sons, Inc., New York, N. Y., 1961, p 47.

(13) A. N. Frumkin in "Advances in Electrochemistry and Electrochemical Engineering," Vol. I, P. Delahay, Ed., Interscience Publishers, Inc., New York, N. Y., 1961, p 74.

(14) L. I. Antropov, "Kinetics of Electrode Processes and Null Points of Metals," Council of Scientific and Industrial Research, New Delhi, India, 1960.

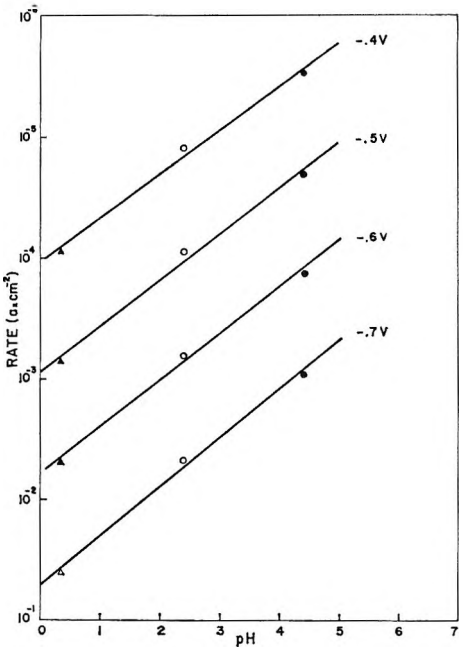

Figure 3. Plot for reaction order, $(\partial \ln i/\partial \ln C_{H_3O^+})_{\eta,\psi}$, for aluminum in solutions of different pH. Data for the four values of η shown in this figure have been obtained from Figure 2; $(\partial \ln i/\partial \ln C_{H_3O^+})_{\eta,\psi} = 0.39$.

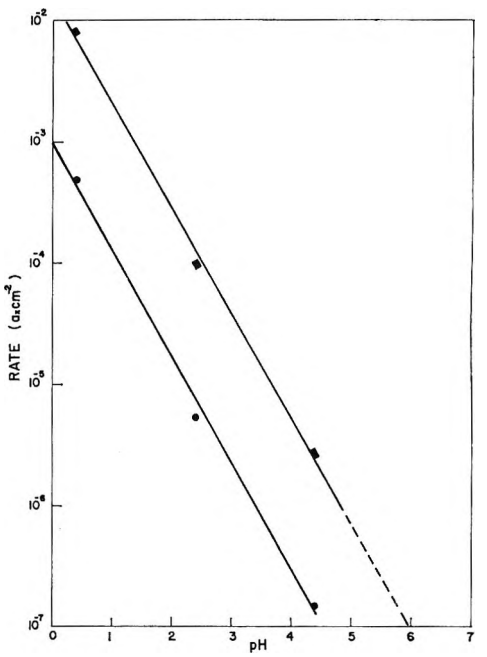

Figure 5. Plot for $(\partial \ln i/\partial \ln C_{H_3O^+})_{\phi,\psi}$ for aluminum in acidic solutions: data calculated from Figure 2 (see text); ●, $\phi = -0.5$ V; ■, $\phi = -0.65$ V. Data obtained from Figure 2; value of $(\partial \ln i/\partial \ln C_{H_3O^+})_{\phi,\psi}$ obtained is 0.87.

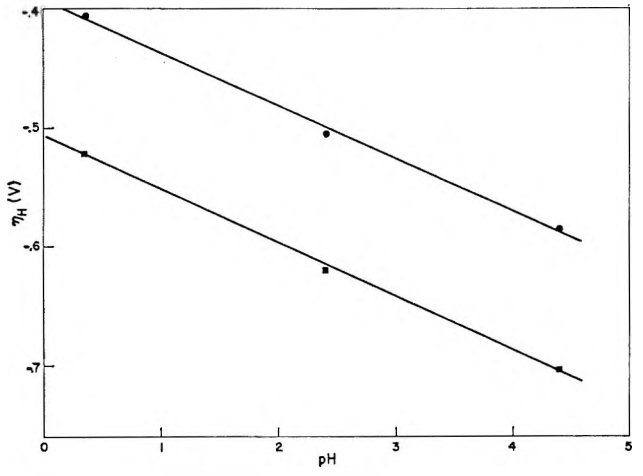

Figure 4. Plot for $(\partial\eta/\partial \log C_{H_3O^+})_{i,\psi}$ for aluminum in acidic solutions: ●, $i = 1 \times 10^{-3}$ A cm^{-2}; ■, $i = 1 \times 10^{-2}$ A cm^{-2}. Data obtained from Figure 2; value of $(\partial\eta/\partial \log C_{H_3O^+})_{i,\psi}$ obtained is 45 mV.

cause as drastic a chemical corrosion reaction as 1.7 *N* sulfuric acid. In any case, a visual examination of the reaction-order plots (Figures 3–5) shows that the values of various derivatives would not change significantly if the Tafel plots obtained in any of the other sulfuric acid solutions (*i.e.*, Figure 1) are used in Figures 2–5, instead of the one obtained in 0.86 *N* sulfuric acid.

It may be mentioned that anomalously high Tafel slopes (>0.13 V) were observed when contamination of the solutions and/or electrode surface was suspected by facts such as vacillating potentials (at constant current), irreproducible rates, very short linear Tafel regions (about one decade), strong susceptibility of the potentials to rate of bubbling in the working compartment and, finally, insensitivity of the electrode potential to low polarizing current densities (*ca.* 1×10^{-5} A cm^{-2}) thereby suggesting impurity reactions. These results have been discarded. Repeatedly, linear Tafel regions over about three decades with a Tafel slope close to 2.3 ($2RT/F$) were obtained, to the exclusion of aforementioned symptoms of contamination, on freshly prepared electrode surfaces in solutions purged of the obvious impurities, *e.g.*, dissolved oxygen. The results were particularly susceptible to impurities diffusing from the anodic compartment, as expected; this situation was remedied by keeping the solution-sealed stopcock between the anode and the cathode compartments *always* closed during the measurements.

B. Reaction Orders. In Figure 3, plots of pH *vs.* rate of h.e.r. at the four indicated values of electrode potential measured against reversible hydrogen electrode in the *same* solution are shown and have been derived from the data presented in Figure 2. The value of the derivative $(\partial \ln i/\partial \ln C_{H_3O^+})_{\eta,\psi}$[10,11] as obtained from these pH–rate relationships is 0.39 for every one of the four electrode potentials shown in Figure 3.

In Figure 4, relationships between pH and overpotential (same as the electrode potential in case of h.e.r.), η, measured against reversible hydrogen electrode in the *same* solution at two shown values of constant current density have been presented. These relations, again, are derived from the data in Figure 2.

The value of the derivative $(\partial\eta/\partial \log C_{H_3O^+})_{i,\psi}$,[10,11] estimated from these plots, for either of the current densities shown, is equal to 45 mV.

An attempt has been made to determine chemically significant reaction orders in Figure 5 by plotting ϕ *vs.* rate for the h.e.r.; ϕ is the value of the electrode potential against *standard* reversible hydrogen electrode. The data used in Figure 5 have been calculated from results in Figure 2 and from a known dependence of potential of standard reversible hydrogen electrode on pH, *i.e.*, 59 mV/pH unit[10,11] at room temperature. The value of this chemically significant reaction order, $(\partial \ln i/\partial \ln C_{H_3O^+})_{\phi,\psi}$, is 0.87.

C. Nonsteady-State (Transient) Studies. A typical transient (in 0.2 *N* H_2SO_4) depicting the electrode potential–time behavior obtained on cessation of initial cathodic polarization[5,6,10,12,15,16] has been shown in Figure 6. *Absence* of any arrests or inflections, which usually are diagnostic of open-circuit desorption of a species (the possible species in this case is adsorbed H), deposited in a previous steady-state polarization[5,6,10,12,15,16] may be noted. In Figure 7, capacity–electrode potential relationship has been presented; this graph is based on the open-circuit potential-decay profiles shown in Figure 6 and steady-state current–potential relationship for 0.2 *N* H_2SO_4 shown in Figure 1. In Figure 7, absence of a characteristic capacity maximum (sharp for the Langmuir case and flat for the Temkin case)[10,17] may be noted. Another point to be emphasized here is the value of the maximum capacity, which is remarkably lower than that estimated for coverage by adsorbed H approaching unity.[17] The magnitude of c observed in Figure 7, however, is greater than the usual values for double layer capacity and probably indicates some pseudo-capacity associated with potential dependence of charge transfer involved in the chemical corrosion reaction at low cathodic potentials. It may be mentioned that the values of capacity, c, associated with potential dependence of any possible coverage obtained from open-circuit potential-decay profiles are closer to the "equilibrium" values and hence more significant than the c values that may be calculated from the charging curves or from profiles depicting the forced discharge behavior of initial steady-state potential.[18]

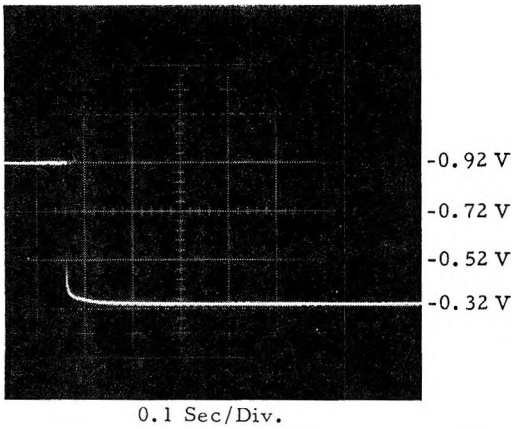

Figure 6. A typical potential–time relationship obtained on open-circuit decay of initial cathodic electrode potential.

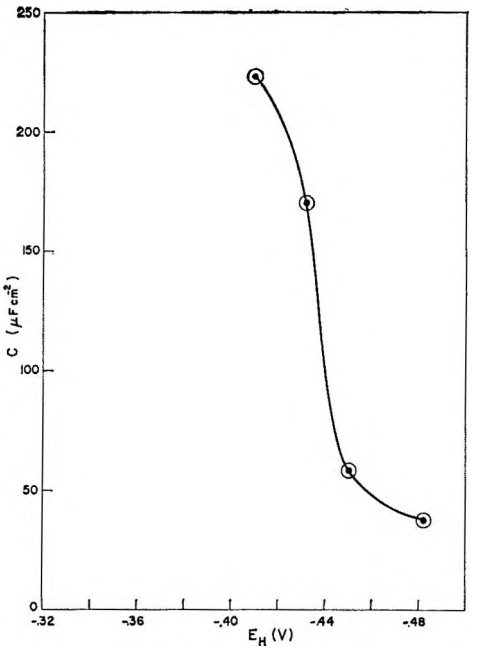

Figure 7. A capacitance–potential profile calculated from experimental data represented in Figures 1 and 6; "rest" potential in this case is *ca.* −320 mV.

A typical cathodic-charging curve (in 0.2 *N* H_2SO_4) has been shown in Figure 8. Any arrests or inflection in the potential–time curve which can be diagnostic of the adsorbed species,[19] are again absent. Absence of inflections in the charging curves has been observed for all values of the cathodic-charging current, *viz.* from 1×10^{-5} to 2×10^{-1} A cm^{-2}. Identical results have been obtained in acetic acid solutions.

D. Apparent Heat of Activation. Tafel relations have been obtained galvanostatically on aluminum in 1 *N* CH_3COOH solutions at 1, 12.5, 30.5, 38.5, and 55.5° and are shown in Figure 9. These relations were obtained from descending temperatures after a steady "corrosion potential" had been achieved at 55.5°. The Tafel slopes, exchange current densities, and "rest" potentials (*i.e.* the mixed corrosion potentials) have been shown along with the corresponding values of temperature, T (in °K) and $1/T$ in Table I.

(15) J. O'M. Bockris in "Modern Aspects of Electrochemistry," Vol. I, J. O'M. Bockris and B. E. Conway, Ed., Butterworth and Co., Ltd., London, 1954, Chapter IV.

(16) J. O'M. Bockris, Graduate Lectures on Electrode Kinetics, University of Pennsylvania, Philadelphia, Pa., 1963–1964.

(17) E. Gileadi and B. E. Conway in "Modern Aspects of Electrochemistry," Vol. III, J. O'M. Bockris and B. E. Conway, Ed., Butterworth and Co., Ltd., London, 1964.

(18) B. E. Conway, E. Gileadi, and H. A. Kozlowska, *J. Electrochem. Soc.*, **112**, 341 (1965).

(19) B. E. Conway, *Trans. Roy. Soc. Can.*, **54-III**, 19 (1960).

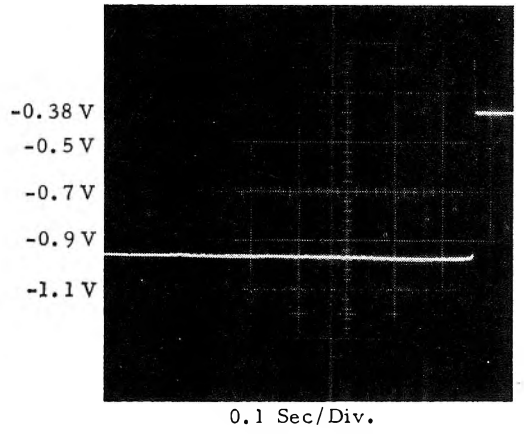

Figure 8. A typical cathodic-charging curve. Charging current density = 1.97×10^{-1} A cm^2.

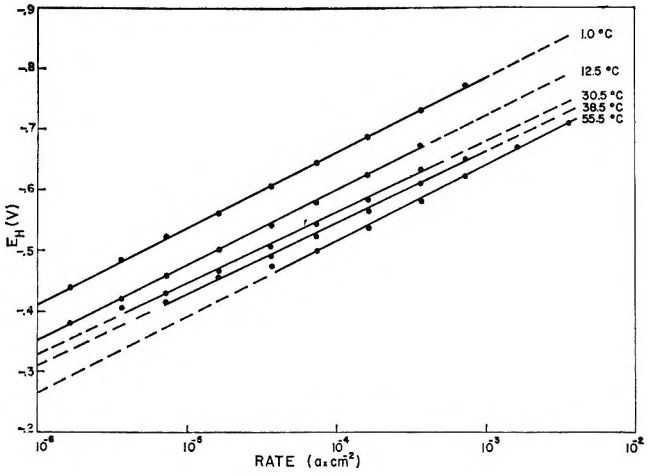

Figure 9. Tafel relationships for h.e.r. on Al in 1 N CH_3COOH at several temperatures; the data obtained from these Tafel lines are shown in Table I and were used for the determination of apparent heat of activation.

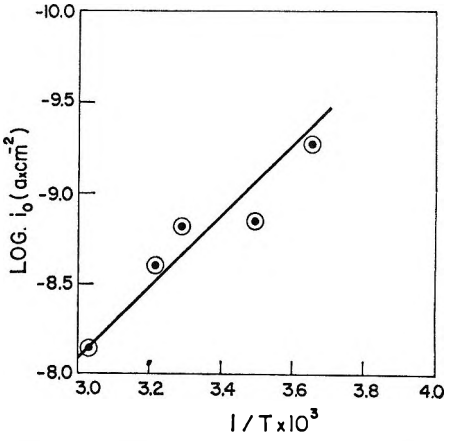

Figure 10. Plot of log i_0 *vs.* $1/T$ for h.e.r. on Al in 1 N CH_3COOH at several temperatures (see Figure 9 and Table I); the value of apparent heat of activation, ΔH^*, obtained from this graph is 9 kcal mol^{-1}.

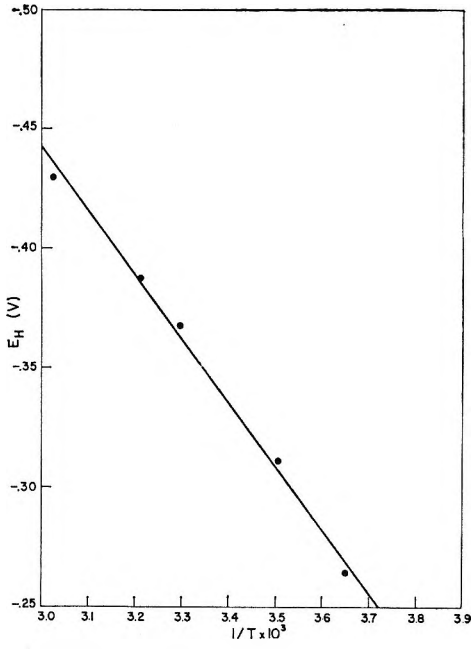

Figure 11. Plot of open-circuit corrosion potential *vs.* $1/T$ on Al in 1 N CH_3COOH (see Table I).

The exchange current densities obtained from Figure 9, at various temperatures have been plotted *vs.* corresponding $1/T$ values in Figure 10 (see also Table I); the slope of this line (Figure 10) gives an apparent heat of activation for the h.e.r. on Al in 1 N CH_3COOH. The value for the apparent heat of activation obtained from Figure 10 is 9 kcal mol^{-1}.

It is assumed that this value of apparent heat of activation, ΔH^*, is also representative of ΔH^* values in all concentrated acidic solutions. Rather large scatter of experimental points in Figure 10 emphasizes the uncertainties involved in accurate determination of exchange current densities on corrodible metals; this also suggests caution against attaching too great a significance to the values of ΔH^*, the apparent heat of activation, on corrodible metals. Similar comments apply to the deduction of any definite mechanistic conclusions from the values of exchange current densities themselves.

An interesting correlation has been observed and is depicted in Figure 11. On plotting the mixed corrosion potential (*i.e.*, the open-circuit rest potential) *vs.* $1/T$ (T in °K) for aluminum in 1 N CH_3COOH, a straight line with a slope equal to 0.269 V is observed. Assuming that this mixed corrosion potential is predominantly determined by the cathodic Tafel line (for chemical evolution of hydrogen) conjugate to the anodic-dissolution Tafel line of the mixed corrosion process and that this Tafel line for the chemical evolution of hydrogen has a slope equal to $2.3(2RT/F)$, a value of 10.1 kcal mol^{-1} may be deduced. This probably represents another way of estimating the apparent heat of activation for the h.e.r. on aluminum in acidic solutions and is comparable to the ΔH^* determined from a plot of log i_0 *vs.* $1/T$ (Figure 10). The exact significance of this

graph (Figure 11), however, seems to be too complex to lend itself to plausible interpretations. In any case, this correlation (Figure 11), though probably interesting in itself, is of no tangible importance to the interpretation of the rest of the results presented in this paper.

IV. Discussion

In case of cathodic hydrogen evolution from acidic solutions, the following consecutive steps have been considered.[3,9-12,15,16,19]

$$H_3O^+ + e_m + M \longrightarrow MH + H_2O \quad (1)$$

followed by

$$H_3O^+ + e_m + MH \longrightarrow M + H_2 \quad (2)$$

or

$$MH + MH \longrightarrow 2M + H_2 \quad (3)$$

In the above scheme, step 1 is always the primary charge-transfer event (initial discharge step) followed either by step 2 (electrochemical desorption or "radical + ion" step) or by step 3 (atomic recombination).

Other steps that have been considered as possible rds and have received little experimental or theoretical support are

$$H_3O^+ + MH \longrightarrow MH_2^+ + H_2O \quad (4)$$

and

$$MH_2^+(H_2O) + e_m \longrightarrow H_2 + M + H_2O \quad (5)$$

Steps 4 and 5 have been convincingly refuted previously[10,11,16,19,20] on the basis of sophisticated theoretical and experimental considerations and will not be considered here. Another step that has recently been suggested, on the basis of evidence from studies under high pressure,[21] as the possible rds in the h.e.r. on mercury is

$$e_{metal} \longrightarrow e_{hydration} \quad (6)$$

This step, if rds, would not predict any isotope effects in general, as well as the observed reaction orders and apparent heats of activation,[22] and is hence also excluded from any further discussion. The observed Tafel slopes and the reaction-order derivatives are uniquely incompatible with step 3 as the possible rds.[10,11,19] The values of Tafel slopes observed in the present investigation indicate that any discussion of the kinetics of h.e.r. under Temkin adsorption conditions[10,17] would be unnecessary in the present case.

The experimentally observed Tafel slope (=0.11 V) would be expected either for step 1 (coverage of the electrode, θ, approaching zero) or for step 2 ($\theta \rightarrow 1$).[10,11,15,16,19] The values of exchange-current densities (Figure 1, Table I) are such as would not lead to a clear-cut distinction to be made between step 1 and 2 as the rds.[23-25] In our opinion, values of exchange-current density between $10^{-7.5}$ and $10^{-9.5}$ A cm^{-2}, which are observed in the present investigation (Figure 1, Table I), are too low for the mechanism involved in the transition metals and too high to be grouped with exchange current densities for the h.e.r. on metals like mercury and lead. Any attempts at deduction of reaction mechanism from a plot of log i_0 *vs.* work function[23-25] hence are of questionable value for the case of aluminum. Similar comments apply to other graphical representations which illustrate the principles of electrocatalysis[23-25] and which have been used to deduce the mechanism of h.e.r. on various metals.[23-25] Such representations[19,23-25] are in some cases even self-contradictory, *e.g.*, Figure 1 and Figure 2 in ref 23 would predict contradictory mechanisms for h.e.r. on Cd and Ga.

It is realized that a major difficulty involved in precise verification of these various electrocatalytic relations[19,23-25] is the lack of accurate experimental data to be used in developing these rather fundamental correlations.

An examination of various reaction-order derivatives[10-12] predicted theoretically for the h.e.r.[10,11] would show that in concentrated acidic solutions it is again difficult to distinguish between 1 and 2 as the possible rds without an *independent* knowledge of the steady-state coverage of the electrode by adsorbed H. The experimentally observed value of the derivative $(\partial \ln i/\partial \ln C_{H_3O^+})_{\eta,\psi}$ is 0.39 (Figure 3) and, very roughly, is comparable to the theoretically predicted value of 0.5[10,11] both for step 1 ($\theta \rightarrow 0$) and step 2 ($\theta \rightarrow 1$). It is interesting to note that the experimental value for the same derivative for mercury in concentrated acidic solutions[11,26] is 0.41, which compares favorably with the present value of 0.39.

A predicted value[10,11] of 59 mV for the derivative $(\partial\eta/\partial \log C_{H_3O^+})_{i,\psi}$ both for step 1 ($\theta \rightarrow 0$) and step 2 ($\theta \rightarrow 1$) in concentrated solutions may be compared with the present value of 45 mV (Figure 4) and a previous value of 56 mV for mercury.[11,26]

For the chemically significant reaction order $(\partial \ln i/\partial \ln C_{H_3O^+})_{\phi,\psi}$, the experimentally indicated value of 0.87 (Figure 5) would be consistent with both step 1 and step 2 as the rds.[10,11] Again, a previous value of 0.83 for $(\partial \ln i/\partial \ln C_{H_3O^+})_{\phi,\psi}$ for mercury in concentrated acidic solutions[10,11,26] may be compared with the present value on aluminum (0.87).

(20) Discussion on the paper, J. Horiuti in "Transactions of the Symposium on Electrode Processes," E. Yeager, Ed., John Wiley and Sons, Inc., New York, N. Y., 1961.

(21) G. J. Hills and D. R. Kinnibrugh, *J. Electrochem. Soc.*, **113**, 1111 (1966).

(22) D. B. Matthews, *ibid.*, **113**, 1117 (1966).

(23) B. E. Conway and J. O'M. Bockris, *J. Chem. Phys.*, **26**, 532 (1957).

(24) H. Kita, Abstract, Electrochemical Society Meeting, Cleveland, Ohio, 1966, No. 153.

(25) J. O'M. Bockris and S. Srinivasan, Proceedings of the 19th Annual Power Sources Conference, 1965.

(26) I. A. Ammar and M. Hassanein, *J. Phys. Chem.*, **62**, 805 (1958).

The value of ΔH^*, the apparent heat of activation (Figure 10), has been obtained by the kinetically preferable method[27] and agrees favorably with the values estimated for mercury by identical procedure.[27] In some previous studies,[28,29] ΔH^* values were calculated from $(\partial\eta/\partial T)_i$ for mercury; this procedure has been shown[27] to yield anomalously high values. Values of ΔH^* close to 9 kcal were interpreted as an evidence against step 1 as the rds in some previous studies.[28,29] However, recently it has been shown theoretically[30] and experimentally[27] that the values of ΔH^* of this magnitude (*i.e.*, 9 kcal mol^{-1}) are quite compatible with step 1 as the rds.[27,30]

From the foregoing discussion, it is quite difficult to distinguish between steps 1 and 2 as the possible rds in the present case. However, the experimental evidence, *i.e.*, Tafel slopes, reaction-order derivatives, and ΔH^* value, follows rather closely the corresponding results for mercury and hence would indicate step 1 as the probable rds. The following further evidence tends to favor this conclusion.

(1) In the profiles showing open-circuit decay of initial cathodic potential (Figure 6), no arrests or inflections are observed.

(2) In the capacity–potential profiles calculated from Figure 6 and Figure 1, no characteristic capacity maximum (either flat or sharp) is observed. Also, the value of the maximum capacity obtained is much lower than that expected for an appreciable electrode coverage.[17]

(3) There are no arrests or inflections observed in the cathodic-charging curves (Figure 8).

(4) If step 2 were the rds, one would expect to observe a Tafel slope of 40 mV[10-12,15,16,19] in the lower current density region [θ, f(V)]; this, of course, is not observed in the present case. However, this argument is not very emphatic, in view of the complications that must arise due to chemical corrosion reaction at lower current densities.

(5) If step 2 were the rds, it would probably exhibit, in some potential region, some characteristics of kinetics under Temkin conditions,[10,11,17,19] which would be indicative of partial coverage of the electrode and would precede the condition of ultimate, complete electrode coverage. This, however, is not observed either in the Tafel slopes or in the reaction-order derivatives.

(6) Evidence from chemisorption studies[31] indicates that aluminum is not a good catalyst (contrast Pt and Pd) for chemisorbing atomic or molecular hydrogen. This would tend to exclude step 2 as the probable rds, since an appreciable steady-state concentration of adsorbed H is required by that mechanism.

(7) On all "soft" metals with melting point below 1000°, approximately, step 1 is believed to be the likely rds. The examples are Hg, Ga, In, Sn, Bi, Tl, Cd, Pb, Zn, Te, and Sb.[24,32] The hydrogen evolution reaction on aluminum, it may be expected, would also proceed with initial discharge as the rds (step 1), since aluminum is one of the soft metals (mp = 660°), even though marginally so. Similar conclusions may be drawn from a consideration of heats of atomization of metals[24] and such conclusions are not without some theoretical justifications.[23,24]

From the foregoing discussion, it may be concluded that step 1 is the likely rds in the h.e.r. on aluminum in acidic solutions; the distinction of step 1 from step 2 as the possible rds, however, is not entirely clear-cut.

The following further approaches might yield some information useful in making distinction between step 1 and 2 as the possible rds in the h.e.r. on aluminum in acidic solutions; (1) determination of hydrogen–deuterium and hydrogen–tritium separation factors,[10,33,34] and (2) attempts aimed at exploring the effect of various crystal faces of aluminum on the rate of h.e.r.[35]

It may be mentioned that certain other diagnostic criteria, *e.g.*, stoichiometric numbers, cannot be determined in cases of corrodible metals like aluminum.[9,10,15,16,36] Any attempts to obtain information on the possible coverage of the electrode (by adsorbed H) and the potential dependence of this coverage (*i.e.*, pseudo-capacitance) from transients involving forced discharge of initial cathodic potential[10,12,15,16] are thwarted by the almost instantaneous growth of the dielectric oxide on reversal of the direction of the current. Similar difficulties, originating in the corrosion reaction of the metal and/or oxide growth, may be anticipated in the potentiodynamic studies.[10,37-40]

In the foregoing discussion, it has been tacitly implied that the Tafel plots, etc., presented in this paper are not vitiated by possible dissolution of aluminum or by oxide films on aluminum, under the experimental conditions that obtained in the present investigation. Here some

(27) B. E. Conway and M. Salomon, *J. Chem. Phys.*, **41**, 3169 (1964).

(28) J. O'M. Bockris and R. Parsons, *Trans. Faraday Soc.*, **45**, 916 (1949).

(29) S. Minc and J. Salskowski, *Bull. Acad. Polon. Sci.*, **8**, 29 (1959).

(30) M. Salomon, C. G. Enke, and B. E. Conway, *J. Chem. Phys.*, **43**, 3989 (1965).

(31) D. O. Hayward and V. M. W. Trapnell, "Chemisorption," Butterworth Inc., Washington, D. C., 1964.

(32) D. B. Matthews, Discussion on Abstract, Electrochemical Society Meeting, Cleveland, Ohio, 1966, No. 153.

(33) J. O'M. Bockris and S. Srinivasan, *Electrochim. Acta*, **9**, 31 (1964).

(34) M. Salomon and B. E. Conway, *J. Phys. Chem.*, **68**, 2009 (1964).

(35) R. Piontelli, G. Poli, and G. Serravalle in "Transactions of the Symposium on Electrode Processes," John Wiley and Sons, Inc., New York, N. Y., 1961, p 67.

(36) A. C. Makrides, *J. Electrochem. Soc.*, **104**, 677 (1957); **109**, 256 (1962).

(37) F. Will and C. A. Knorr, *Z. Elektrochem.*, **64**, 258 (1960).

(38) P. Delahay, "Double Layer and Electrode Kinetics," Interscience Publishers, Inc., New York, N. Y., 1965.

(39) W. Bold and M. Breiter, *Electrochim. Acta*, **5**, 145, 169 (1961); see M. W. Breiter, *Ann. N. Y. Acad. Sci.*, **101**, 709 (1963).

(40) A. K. Vijh and B. E. Conway, *Z. Anal. Chem.*, **224**, 160 (1967).

experimental evidence[8,41-47] and related discussion is presented which tends to support this premise. For the case of metals like Mg, Zn, and Al,[41] the anodic dissolution Tafel lines would be expected to be associated with low activation energies, high exchange current densities, and *low* values of Tafel slopes. From this, it follows that for a given increment of cathodic over-potential, there will be a substantial decrease in the rate of the corrosion reaction; *i.e.*, at potentials even slightly cathodic to the rest potential, the contribution to the total rate of h.e.r. by the hydrogen evolved by chemical corrosion reaction may be neglected.[42] This is corroborated by the lack of pseudo-capacitance at potentials more cathodic than −0.45 V (Figure 7). However, at low cathodic over-potentials, *e.g.*, less cathodic than *ca.* −0.45 V, there may be a significant contribution to the total rate by the chemical corrosion reaction, hence, probably the large spread below −0.4 V in Figure 1. This would not in any way change the mechanistic conclusions arrived at here, since most of the data on which the interpretations are based have been obtained above −0.4 V.

In the course of explorations for a proper sequence for preparation of electrode surface, it was observed that after chemipolishing, an etching period of 10 min in 1 *N* NaOH removes the tenacious surface oxide. Again, surface oxide if not removed by this procedure should result in anomalously high Tafel slopes[5,6,40,43-47] in solutions of unquestionable purity. This results from the kinetic participation of semiconducting surface films, oxides in the present argument. This, of course, is not observed in the present case. Tafel slopes close to $2.3(4RT/F)$ are indeed observed for h.e.r. on aluminum electrodes covered deliberately by oxide[47] in solutions in which the oxide is thermodynamically stable[8] (pH 5.5). Hence, it may be concluded that the present measurements, most likely, are free of significant complications arising either from corrosion reaction or oxide films. It may be mentioned that the value of corrosion potential at room temperature, in the most acidic solutions used in the present investigations (*i.e.*, 1.7 *N* H_2SO_4, pH 0.1), was observed to be −0.39 V. This compares favorably with the corrosion potential that may be estimated for pH ≃0.1 from the data given by Pourbaix[8] on the rate of chemical dissolution of aluminum. From these data,[8] it may be readily calculated that the rate of h.e.r. due to corrosion reaction would be 9.2×10^{-5} A cm^{-2} at pH ≃0.1, which is close to the rate at −0.39 V in Figure 1, *i.e.*, 8×10^{-5} A cm^{-2}.

Finally, it is necessary to emphasize that in Figures 1 and 2, the experimental points obtained at potentials less cathodic than −0.4 V are not very meaningful, as has also been mentioned in the foregoing discussion. These points were obtained *before* the establishment of steady-state rest potentials and, unlike the rest of the results in this paper, are of little theoretical significance in terms of steady-state kinetics. This is the reason why the Tafel lines in Figures 1 and 2 do not seem to terminate in rest potentials in the less-cathodic end and, instead, extend a bit further.

Acknowledgments. Grateful acknowledgment is made to Dr. R. S. Alwitt for numerous critical discussions and suggestions. Our thanks are also due to Professor M. Salomon for helpful comments on reaction-order derivatives and to Professor D. B. Matthews for a personal communication on the reliability of some exchange-current density values available in the literature.

(41) P. L. Joseph, V. Balasubramanian, and B. A. Shenoi, *J. Electrochem. Soc. Jap.*, **35**, 8 (1967); N. P. Fedotere and Un Sak-Li, *Zh. Fiz. Khim.*, **31**, 1295 (1957).

(42) T. P. Hoar in "Modern Aspects of Electrochemistry," Vol. II, J. O'M. Bockris, Ed., Butterworth and Co. Ltd., London, 1959, p 325, Figure 13b.

(43) R. E. Meyer, *J. Electrochem. Soc.*, **107**, 847 (1960).

(44) A. C. Makrides, *ibid.*, **111**, 392, 400 (1964).

(45) A. C. Makrides, "Symposium on Electrode Processes of the Theoretical Division of the Electrochemical Society," Cleveland, Ohio, 1966; see also Discussion on this paper.

(46) A. K. Vijh and B. E. Conway, *Chem. Rev.*, **67**, 623 (1967); *J. Phys. Chem.*, **71**, 3655 (1967).

(47) A. K. Vijh, unpublished data: this paper deals with the mechanism of the hydrogen evolution reaction on oxide-covered electrodes in relation to mechanisms of rectification.

Structure and Properties of Poly-γ-benzyl-L-glutamate Cast from Dimethylformamide

by A. J. McKinnon and A. V. Tobolsky

Frick Chemical Laboratory, Princeton University, Princeton, New Jersey 08540 *(Received August 7, 1967)*

Two different solid-state modifications of poly-γ-benzyl-L-glutamate (PBG) obtained by casting from N,N-dimethylformamide under different conditions are described. One of these (form A) is a poorly ordered material of doubtful structure obtained from the "complex" phase described by previous workers. The other (form B) is a novel well-ordered modification consisting of helices packed on a regular two-dimensional oblique net. This form appears to have a distorted side-chain arrangement. Because of the type of preferred orientation in the cast film, it is suspected that the long-range structure of this material is dictated by the structure of a mesophase occurring in concentrated solution. Volume–temperature and modulus–temperature experiments on both forms are described, and glass-like transition temperatures are recorded. An anisotropic thermal expansion occurs in form B, during which the oblique net gradually changes to a hexagonal net.

Introduction

It has recently been shown[1] that films of poly-γ-benzyl-L-glutamate (PBG) cast from chloroform and several other solvents (*m*-cresol,[2] ethylene dichloride,[2] and dioxane[3]) consist almost entirely of α-helical molecules packed on a rather irregular pseudo-hexagonal net,[3,4] the long-range structure and orientation apparently being dictated by the structure of the anisotropic phase in concentrated solution. Though the structure of these films was interpreted by the present authors[1] in terms of mesomorphic regions (retaining some of the twist of the mesophase) and hexagonal paracrystalline regions, another interpretation could be phrased in terms of a continuous, somewhat disordered phase which would be approximately hexagonal at short range. On the other hand, the experiments to be described on casting films from dimethylformamide (DMF) result in two solid-state modifications which are quite distinct from that described above.

One of these structures is derived from the so-called "complex" phase, described by Luzzati, Cesari, Spach, Masson, and Vincent[5] and found in the system PBG–DMF from about 15 to 70% (wt/wt) PBG. This phase has recently been reinvestigated in detail by Parry and Elliott,[6] who substantially modify the original structural conclusions of Luzzati, *et al.* The other novel modification is a very well-ordered material composed of α helices packed on an accurate two-dimensional net, the primitive mesh of which has unequal sides and displays an anisotropic thermal expansion.

We discuss below the structural details of these materials, calling that derived from the complex phase form A and the new well-ordered phase form B. For comparison, the material from chloroform previously described will be called form C.

Experimental Section

The PBG used (Lot No. G-64, Pilot Chemicals, Watertown, Mass.) had a molecular weight of 380,000, deduced from reduced specific viscosity in dichloracetic acid. X-Ray diagrams were obtained on flat plate or cylindrical cameras using either nickel-filtered Cu K or vanadium pentoxide-filtered Cr K radiations. Samples of the complex phase in DMF and other preparations of PBG in DMF were photographed in cells constructed of Teflon with very thin mica windows to avoid loss of DMF during exposure to the X-ray beam. X-Ray photographs above room temperature were obtained by blowing heated nitrogen over the sample, the temperature at the sample being measured and controlled by a thermocouple pyrometer.

Modulus–temperature curves were obtained using Gehman[7] and Clash–Berg[8] instruments. Specific volume *vs.* temperature plots were determined by a buoyant-weight technique in Dow Corning Corp. silicone oil (viscosity, 2 cSt) and were supplemented by pycnometric determinations at 25°.

Preparation of Forms A and B. To prepare form A, the complex phase described by Luzzati, *et al.*, and Parry and Elliott was prepared by making a concen-

(1) A. J. McKinnon and A. V. Tobolsky, *J. Phys. Chem.*, **70**, 1453 (1966).

(2) A. J. McKinnon, E. T. Samulski, and A. V. Tobolsky, unpublished work.

(3) A. Elliott, R. D. B. Fraser, and T. P. MacRae, *J. Mol. Biol.*, **11**, 821 (1965).

(4) Y. Mitsui, Y. Iitaka, and M. Tsuboi, *ibid.*, **24**, 15 (1967).

(5) V. Luzzati, M. Cesari, G. Spach, F. Masson, and J. M. Vincent, *ibid.*, **3**, 566 (1961).

(6) D. A. D. Parry and A. Elliott, *ibid.*, **25**, 1 (1967).

(7) S. D. Gehman, D. E. Woodford, and C. S. Wilkinson, Jr., *Ind. Eng. Chem.*, **39**, 1108 (1947).

(8) R. F. Clash and R. M. Berg, *ibid.*, **34**, 1218 (1942).

trated solution of about 60% PBG in DMF at 50° and cooling the solution to room temperature. DMF was then removed by slow evaporation at room temperature, the last few per cent of DMF being removed by heating *in vacuo*. The pure solid thus obtained was form A.

Form B was prepared simply by further heating the concentrated solution at 50–60° until the material was quite solid. Removal of all DMF was ensured by heating in an oven at 100° until the final weight of the sample agreed with the original weight of polymer. To obtain uniform films suitable for mechanical tests, the materials were cast in small Teflon-coated dishes. A trace of Ionol antioxidant (2,6-di-*t*-butyl-4-methylphenol) was added to the preparations to prevent yellowing of the DMF.

Results and Discussion

X-Ray Diagrams. Form A. The X-ray diagram of a 60% preparation of the complex phase was similar to that reported by Luzzati, *et al.*, with the addition of a meridional (or near-meridional) reflection of spacing 5.14 Å, in agreement with the value of 5.15 Å quoted by Parry and Elliott. This spacing, in conjunction with the mass per unit length and structure-factor calculations of Luzzati, *et al.*, suggests the presence of coiled coils. However, Parry and Elliott in their more detailed examination of this phase have concluded that coiled coils are not present and that the spacing of 5.15 Å (actually resolvable into meridional and near-meridional components) arises from a quasi-helical arrangement of the benzene rings of the side chains. Luzzati, *et al.*, reported that at higher concentrations (above 70%) the complex phase became disorganized. We find, however, that if DMF is allowed to evaporate slowly at room temperature the X-ray diagram typical of the complex phase persists up to about 90% PBG, though the reflections become more diffuse and the basal lattice contracts. However, when the concentration is increased to 100% (by heating at 80° *in vacuo*), gradual changes occur in the X-ray diagram. The first equatorial disappears, the basal lattice contracts a little, and the meridional decreases in apparent spacing. These changes proceed further with prolonged heating. Spacings observed in a representative 100% PBG sample after heating *in vacuo* at 100° for 24 hr are shown in Table I.

There does not seem to be any simple interpretation of the X-ray diffraction pattern of form A, though it can be noted that the observed equatorials have approximately the right relative ratios for a hexagonal net with 100 not observed. However, there does not appear to be any reason why 100 should be unobservably weak. If the structure is hexagonal, the observed specific volume (0.789 cc/g) implies that there are four chains per cell (calculated specific volume, 0.780 cc/g). It would then appear that the structure in the complex phase with three chains per cell must change at high PBG concentrations to one of four chains per cell, without producing any sudden alterations in the X-ray diagram.

Table I: X-Ray Spacings of 100% PBG Sample, Form A

Spacing, Å	Relative ratio (d_{hkl}/d_{100})[a]	Possible index
14.9	0.578	110
12.8	0.496	200
9.7	0.376	210
8.8	0.341	300
5.05	...	Meridional or near meridional

[a] It is assumed that the first observed reflection is the second-lowest angle reflection (*i.e.*, 110) from a hexagonal net.

Form B. Form B gives a comparatively elaborate X-ray diagram, as shown in Figure 1, which shows photographs with the X-ray beam normal and edge on to the polymer film. It can be seen that the material displays uniplanar orientation, the molecules lying approximately in the film plane, with all possible chain directions in this plane, as in form C. The presence of obvious streaks in the photographs, particularly on the "turn" layer line, which is the only intense nonequatorial region of the molecular transform in the relevant range of diffraction angles, makes it likely that most reflections of small angular width will be equatorial. This consideration, together with the orientation in the edge-on photo, makes it possible to measure the spacings of 17 equatorial reflections, listed in Table II, which extend out to 2.5 Å. These can be indexed on the basis of a rather unusual unit mesh of dimensions: $a = 15.88 \pm 0.03$ Å, $b = 13.00 \pm 0.03$ Å,

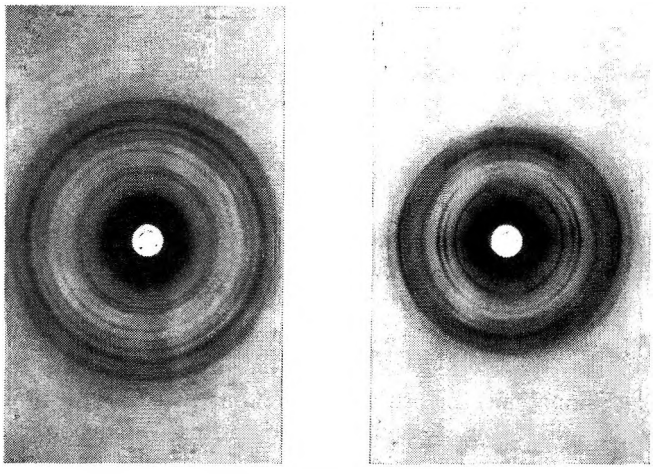

Figure 1. Flat-film X-ray photographs of PBG, form B: (A) X-ray beam normal to PBG film (sample-to-film distance, 9.11 cm); (B) X-ray beam edge-on to PBG film (sample-to-film distance, 7.29 cm). Cu $K\alpha$ radiation, Norelco generator with fine focus tube (40 kV, 18 mA).

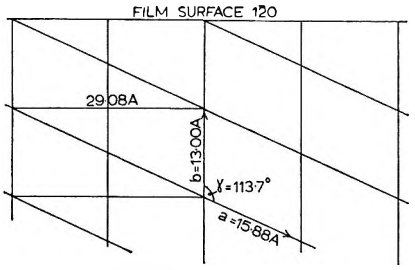

Figure 2. Basal net of PBG, form B, at room temperatures showing the relationship between the primitive and centered orthogonal nets.

and $\gamma = 113.7 \pm 0.5°$. A property of this net is that it is equivalent to a centered orthogonal net of dimensions: $a = 29.08$ Å and $b = 13.00$ Å. Thus the number of $hk0$ reflections occurring appears to be halved. The relationship between the two nets is shown in Figure 2.

The intensities of several reflections in the normal and edge-on positions are shown as I_N and I_E in Table II. From these intensities and from the variation in intensity around the diffraction rings in the edge-on photo, it is possible by consideration of reciprocal lattice diffraction geometry to deduce the preferred orientation of the crystallites with respect to the film surface. Thus it is found that there is a preferred tendency for the $(1\bar{2}0)$ crystal plane (referred to the primitive mesh) to lie in the plane of the film. It can be seen from Figure 2 that it is possible to regard the film in its favored orientation as a succession of compressed layers parallel to the film surface $(1\bar{2}0)$.

Table II: Observed and Calculated Spacings, Intensities, and Indices for Equatorial Reflections from Form B

d_{obsd}, Å	d_{calcd}, Å	I_N	I_E	Index
14.50	14.54	vs	ms	100
11.91	11.90	m	vs	010, $\bar{1}10$
7.79	7.79	m	m	110, $\bar{2}10$
7.27	7.27	m	vw	200
6.51	6.50	vvw	ms	$\bar{1}20$
5.94	5.95	m	ms	020, $\bar{2}20$
5.37	5.32	...	vvw	210, $\bar{3}10$
4.89	4.87	m	m	120, $\bar{3}20$
4.30	4.29	mw	w	$\bar{1}30$, $\bar{2}30$
3.97	3.97	ms	ms	030, $\bar{3}30$
	3.96			310, $\bar{4}10$
3.64	3.63			400
3.47	3.48			130, $\bar{4}30$
3.18	3.18			320, $\bar{5}20$
	3.17			$\bar{3}40$, $\bar{1}40$
3.01	3.01			230, $\bar{5}30$
2.88	2.91			500
2.59	2.60			330, $\bar{6}30$
	2.59			$\bar{2}50$, $\bar{3}50$
	2.59			510, $\bar{6}10$
2.53	2.52			$\bar{1}50$, $\bar{4}50$

It is possible that this type of arrangement is derived from an oriented type of mesophase which occurs in the mobile DMF solution at the temperature of preparation, though no such phase occurs at room temperature.[5]

The significance of the unequal mesh edges is not clear, but presumably implies a distortion of the side chains so that the molecule is no longer cylindrically symmetrical. This distortion may be related to the type of benzene-ring interaction proposed by Parry and Elliott in the complex phase.

There are some further features of the X-ray diagram worthy of mention. Although the structure is α helical (as judged by the residue translation, *ca.* 1.50 Å), the spacing of the intensity maximum on the so-called "turn" layer line streak is consistently above the value of 5.26 Å found for the usual pseudo-hexagonal solid modification of PBG, and is usually from 5.30 to 5.34 Å. The diagram contains several nonequatorial reflections which appear quite sharp, indicating there may be some degree of three-dimensional order. Unfortunately, identification of these reflections has not been possible, since attempts to prepare well-oriented samples by hot or cold drawing result in distortions of the structure toward a hexagonal net, and attempts to produce good orientation by drawing filaments from viscous solution have also proved unsuccessful.

The crystallographic density calculated from the X-ray data, assuming a helix of 18 residues in 5 turns in 27.1 Å[3,4] is 1.280 g/cc. The measured bulk density is 1.269 g/cc. The crystallographic density is thus a little lower than that of the fibers from dioxane studied by Elliott, *et al.*[3]

Specific Volume vs. Temperature. Figure 3 shows specific volume *vs.* temperature curves for both forms A and B from −30 to +50°. It can be seen that both forms display a glass-like transition at 16–17°, behavior which is very similar to that found for form C, which displays a similar transition at 12°.

Table III lists glass-like transition temperatures (T_g), specific volume (V_{sp}) at 25°, and coefficients of expansion (β) above and below the transition temper-

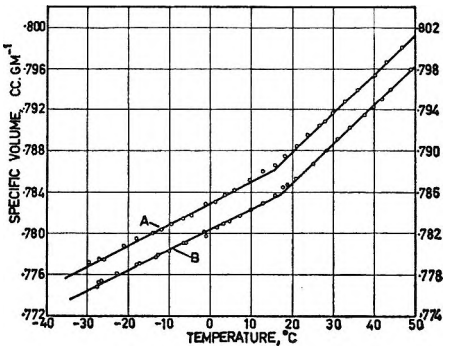

Figure 3. Specific volume *vs.* temperature curves for forms A and B. The left-hand and right-hand ordinates refer to forms A and B, respectively.

ature for all three forms. The coefficients of expansion are subject to considerable variation, possibly due to slightly variable degrees of order in different preparations of the same sample.

Table III: Data from Specific Volume–Temperature Experiments on Forms A, B, and C

	T_g, °C	β ($T > T_g$), °C^{-1}	β ($T < T_g$), °C^{-1}	V_{sp}(25°)
Form A	16	4.5×10^{-4}	2.3×10^{-4}	0.789 ± 0.003
Form B	17	4.3×10^{-4}	1.9×10^{-4}	0.788 ± 0.003
Form C	12	5.1×10^{-4}	2.4×10^{-4}	0.786 ± 0.003

Evidence from nmr experiments suggests that the transition in form C is caused by the onset of side-chain rotation,[9] and it is assumed that the same process is responsible for the similar transition in forms A and B.

Modulus–Temperature Studies. Figure 4 shows plots of $3G$ (G = 10-sec shear modulus) *vs.* temperature for forms A and B. The plot for form C is included for comparison. The curves for both forms A and B should be regarded as schematic only, as in both cases the sample draws and develops a permanent set after deformation in the shear-modulus apparatus, which renders it difficult to reproduce the data. The modulus of form A may vary by a factor of up to 3 at the higher temperatures, depending on the history and extent of deformation of the sample, while with form B the variation is considerably less. The features in which these forms differ from form C are thus represented only in a semiquantitative way in the figure. It can be seen that form A has a much higher modulus at all temperatures between −40 and 140° than either forms B or C, which behave rather similarly. All three forms show a modulus decrease in the vicinity of 15°, in agreement with the volume–temperature experiments. Form A exhibits a large modulus transition at about 135° which is apparently associated with a major structural rearrangement, as the X-ray diagram of a sample after heating to 140° shows only one very diffuse equatorial at about 14.2 Å and a meridional at about 5.15 Å. Form B has a higher modulus than form C in the lower transition region (around 80°) and the modulus curve suggests a second transition may occur around 90°. However, volume–temperature experiments have failed to establish this definitely.

The very different viscoelastic properties of form A suggest that this material must have a structure significantly different from that of forms B and C. It is possible that molecular association caused by the benzene-ring interaction proposed by Parry and Elliott is at least partially responsible for the enhanced modulus of form A.

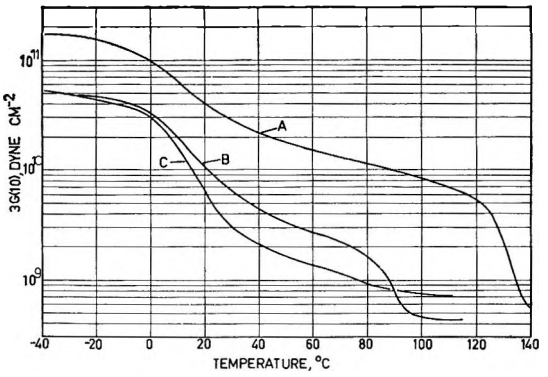

Figure 4. $3G$ *vs.* temperature for forms A, B, and C. (G = 10-sec shear modulus).

Form B. Changes of Structure on Heating. Because of the possibility of a transition at about 90°, an X-ray photograph of form B was taken at 95°. This photograph indicates that the material is exactly hexagonal at 95° and is still well ordered, as judged from the sharpness of the reflections. Photographs at 40 and 60° have shown that there is a continuous change with temperature of the parameters of the unit mesh from those found at room temperature toward those of an exactly hexagonal mesh. Construction of basal reciprocal lattice nets shows that at all times during this progressive change the centered orthogonal property of the net is maintained. The phenomenon thus involves an anisotropic thermal expansion of the lattice on which the molecules are packed, the expansion being greatest (insofar as the preferred orientation is concerned) in a direction perpendicular to the plane of the film. Table IV shows approximate net parameters at room temperature (20°), 40, 60, and 95°. The data shown for the three elevated temperatures are not particularly accurate, due to the difficulty of measuring an accurate sample-to-film distance on the modified camera used for high-temperature photographs. However, the trend in net dimensions is clearly seen. The exact temperature at which the structure becomes hexagonal is not known but appears to be in the vicinity of 90°. The tran-

Table IV: Net Parameters of Heated and Drawn PBG Samples

Temp, °C	a, Å	b, Å	γ, deg
Room temp (20)	15.88	13.00	113.7
40	15.9	13.7	115.7
60	15.7	14.2	117.1
95	15.4	15.4	120.0
Drawn at 20	15.80	13.18	114.8

(9) J. A. E. Kail, J. A. Sauer, and A. E. Woodward, *J. Phys. Chem.*, **66**, 1291 (1962); K. Hikichi, *J. Phys. Soc. Jap.*, **19**, 2169 (1964); S. Sugai, K. Kamashima, S. Makino, and J. Noguchi, *J. Polym. Sci., Part A-2*, **4**, 183 (1966).

sition from an oblique to a hexagonal net on heating is completely reversible on cooling.

Also included in Table IV are net parameters at room temperature of a sample which has been drawn a few per cent at 90°; the basal net changes but preserves its centered orthogonal symmetry during drawing.

Thermal Behavior of PBG–DMF Preparations. During examination of the complex phase, PBG–DMF mixtures were prepared by cooling to room temperature solutions made up at 50°, the concentration of PBG being in the range of 15–35% (wt/wt). These materials, of a semisolid consistency, are presumably composed of mixtures of complex phase and of isotropic solution.[5] They usually show only a very diffuse X-ray photograph, and it appears that a well-ordered complex phase, as studied by Luzzati, *et al.*,[5] occurs only at higher PBG concentrations under the preparative conditions employed. When the material is reheated to 50°, rather than redissolving to form a mobile liquid, a pronounced syneresis occurs, with the formation of a small polymer globule in a larger volume of DMF liquor. The polymer globule can only be redissolved by prolonged heating at a more elevated temperature. However, if almost all the DMF is evaporated from the mixture, the resulting polymer will redissolve quite normally in more added DMF. It appears that in the PBG–DMF mixtures studied there is some kind of intermolecular interaction which effectively resists redispersion of the polymer, but this interaction is destroyed when the polymer becomes almost pure, thus allowing it to redissolve. The suggestion of such an interaction is not at variance with the results of Parry and Elliott on the complex phase.

Acknowledgment. We wish to acknowledge the partial support of a fellowship from the Wool Research Organization of New Zealand.

The Vapor Pressure and Melting Points of Xenon Difluoride and Xenon Tetrafluoride[1,2]

by Felix Schreiner, Geraldine N. McDonald, and Cedric L. Chernick

Argonne National Laboratory, Argonne, Illinois 60439 *(Received August 7, 1967)*

Vapor pressure measurements have been carried out on samples of pure xenon difluoride and xenon tetrafluoride. The preparation and purification of the samples are described as well as the apparatus with which the data for the two reactive fluorine compounds were obtained. For xenon difluoride, the following equation represents the experimental results between 273 and 388°K

$$\log P_{mm} = -\frac{3057.67}{T} - 1.23521 \log T + 13.969736$$

The corresponding vapor pressure equation for xenon tetrafluoride valid between 275 and 390.25°K is

$$\log P_{mm} = -\frac{3226.21}{T} - 0.43434 \log T + 12.301738$$

In addition, the triple-point temperatures of the two compounds have been determined by a thermal arrest method. For xenon difluoride a triple-point temperature of 402.18°K was found, and for xenon tetrafluoride, 390.25°K. The enthalpies of vaporization at 330°K were derived from the vapor pressure equations and the following values were obtained: $\Delta H_{sub} = 55.2 \pm 0.8$ kJ mole^{-1} for XeF_2, and $\Delta H_{sub} = 60.6 \pm 1.0$ kJ mole^{-1} for XeF_4. The standard entropy of xenon tetrafluoride vapor at 298.15°K was calculated from the vapor pressure and heat capacity data and found to be 305.2 J deg^{-1} mole^{-1}. This number is compared with the entropy calculated from molecular data. The entropy of solid xenon difluoride at 330°K was calculated to be 122.8 J deg^{-1} mole^{-1}.

In spite of the fact that the properties of chemical compounds of the rare gas xenon have been studied rather intensively in recent years, the literature contains very few data for the vapor pressures of the two lower xenon fluorides. This is, of course, a consequence of the difficulties encountered in attempts to carry out precise measurements at elevated temperatures with these reactive substances. The available data were obtained around room temperature from direct measurements of the pressure with Monel Bourdon gauges. For xenon difluoride, a pressure of 3.8 mm at 25° was observed by Agron, *et al.*,[3] and for xenon tetrafluoride, Claassen[4] found approximately 3 mm at 20°. The accuracy of these values is approximately ±0.5 mm, based on the reading accuracy of the Bourdon gauges. Both the difluoride and the tetrafluoride have also been the subject of a study of the variation of the vapor pressure with temperature.[5] These measurements were carried out spectroscopically, the chief aim being the evaluation of the slope of the vapor pressure curve in order to estimate the enthalpies of sublimation. In the case of xenon difluoride, the intensity of the characteristic absorption at 1750 Å was followed between −15 and +22°. For the tetrafluoride, similar absorption measurements were made at 1330, 1586, and 2010 Å at temperatures between −3 and +22°. The measured variation of the absorption with temperature was used to calculate the enthalpies of sublimation from the Clausius–Clapeyron equation, and the values 51.5 and 64.0 kJ mole^{-1} were obtained for the difluoride and tetrafluoride, respectively.

The scarcity of the available melting point data for the two xenon fluorides equals that of the vapor pressure data. For xenon difluoride, two values have been reported, 140° by Agron, *et al.*,[3] and more recently 130° by Gróz, *et al.*[6] The only piece of information on record for xenon tetrafluoride is an approximate value of 114° for the melting point, observed by Chernick.[7]

In view of the exiguity of the existing information, the necessity was felt for systematic vapor pressure measurements covering a more extensive range of temperatures and pressures. The results of such studies for pressures up to 1 atm are reported in the present

(1) Based on work performed under the auspices of the U. S. Atomic Energy Commission.

(2) Presented at the 153rd National Meeting of the American Chemical Society, Miami Beach, Fla., April 9–14, 1967.

(3) P. A. Agron, G. M. Begun, H. A. Levy, A. A. Mason, C. F. Jones, and D. F. Smith, *Science*, **139**, 842 (1963).

(4) H. H. Claassen, H. Selig, and J. G. Malm, *J. Am. Chem. Soc.*, **84**, 3593 (1962).

(5) J. Jortner, E. G. Wilson, and S. A. Rice, *ibid.*, **85**, 814 (1963).

(6) P. Gróz, I. Kiss, A. Révész, and T. Sipos, *J. Inorg. Nucl. Chem.*, **28**, 909 (1966).

(7) C. L. Chernick, "Noble Gas Compounds," University of Chicago Press, Chicago, Ill., 1963, p 35.

paper, together with the results of triple-point determinations of the two lower xenon fluorides.

Experimental Procedure

Preparation of Xenon Difluoride. Xenon difluoride was prepared by heating a mixture of 0.79 g-atom of high purity xenon and 0.08 mole of fluorine in a 574-cm^3 nickel reaction can at 300° for 24 hr. According to the equilibrium constants for the homogeneous vapor phase equilibrium of the xenon-fluorine system,[8] the formation of only small amounts of xenon tetrafluoride and negligible amounts of the hexafluoride is expected under these conditions. Purification from XeF_4 and XeF_6 could be achieved by stepwise removal of the vapor above the product. After subliming off a total of 0.2% of the solid, the infrared spectrum obtained showed only bands attributable to difluoride, and the product was judged sufficiently pure for the vapor pressure and melting point determinations.

Preparation of Xenon Tetrafluoride. From an inspection of the vapor phase equilibrium data, it is clear that the tetrafluoride formed in a homogeneous gas reaction will always be accompanied by appreciable quantities of difluoride, or of hexafluoride, or of both. In order to circumvent this difficulty, the sample was prepared in a system where the solid product could condense out as the reaction proceeded. In principle, this method was suggested by Weinstock, *et al.*,[9] and has been adapted here for application at lower temperatures. A 1600-cm^3 nickel reaction can was filled with 0.68 mole of fluorine and 0.30 g-atom of xenon. The upper part of the can was fitted with a sleeve heater surrounded with asbestos tape for thermal insulation. For temperature measurement and control, a chromel–alumel thermocouple was inserted between heater and can. The temperature of the top part of the can was then raised to 400° and kept there for 48 hr in order to let the mixture react. At the same time, the lower part of the can was immersed in a water bath to a depth of about 5 cm. Throughout the reaction time, the temperature of the water bath was kept below 50°. As soon as the pressure of a reaction product exceeds the vapor pressure at the low temperature a condensed phase will be formed in this system. Barring the existence of solid mixtures, only one solid compound can be present at the end of the reaction, and it has to consist of either the pure difluoride or tetrafluoride, depending on the initial proportion of the reactants. In the present case, an atomic ratio F/Xe of 4.5 to 1 was chosen in order to form the tetrafluoride. At the end of the experiment, the reaction can was cooled to 77°K, and the unreacted fluorine was removed. It turned out that about 20% of the initially supplied fluorine had not been consumed. After warming to 195°K it was found that practically all of the xenon had reacted.

An infrared spectrum of the vapor above the product showed traces of difluoride and hexafluoride to be present. By stepwise removal of the vapor, the hexafluoride could be removed from the sample before 1% of the product had been sublimed. The last traces of difluoride, however, disappeared only after about 20% of the sample had been transferred to a second storage can. The tenacity with which the difluoride was retained in the tetrafluoride can be accounted for in two ways: either the evaporation of the difluoride was strongly inhibited by occlusion in tetrafluoride crystals or the difluoride was present as the known 1:1 compound with a much lower partial pressure.[10]

Vapor Pressure Apparatus. The measurements of the vapor pressure were performed on samples ranging in mass from 2 to 3.5 g, contained in the bottom part of a vertically mounted closed-end nickel tube of 300 mm length. The tube was attached to a diaphragm-type pressure transducer which has been described in detail by Sheft.[11] Those parts of the system with which the sample came into contact during the measurements, *viz.*, sample tube, pressure transducer, and connecting valve, were made of nickel or Monel and had been passivated by previous treatment with ClF_3 and XeF_6. The upper part of the apparatus was contained in a heatable box which was kept at a temperature exceeding the highest temperature reached during each series of runs by about 20°. Pressures were determined by operating the diaphragm transducer as a null indicator. A nitrogen pressure equal to the vapor pressure was applied to the reference side of the transducer and measured with a fused quartz Bourdon gauge that had been calibrated against a mercury manometer to give pressures in millimeters of mercury at 0° and standard gravity. The experimental error of the pressure measurement was determined chiefly by the instability of the zero adjustment of the transducer, which produced an uncertainty of ± 0.2 mm.

The lower half of the sample tube was immersed in a bath whose temperature was controlled to several hundredths of a degree. Temperatures were measured with an NBS calibrated platinum resistance thermometer, the resistance of which was determined with a Mueller resistance bridge.

Triple-Point Temperatures. The triple-point temperatures of xenon difluoride and of xenon tetrafluoride were determined by a thermal arrest method on samples of 3.75 and 2.06 g, respectively. The measurements were carried out in nickel tubes of 57 mm length, 9.5 mm o.d., and 0.38 mm wall thickness. The tempera-

(8) B. Weinstock, E. E. Weaver, and C. P. Knop, *Inorg. Chem.*, **5**, 2189 (1966).

(9) B. Weinstock and E. E. Weaver, presented at the 149th National Meeting of the American Chemical Society, Detroit, Mich., April 1965.

(10) J. H. Burns, R. D. Ellison, and H. A. Levy, *J. Phys. Chem.*, **67**, 1569 (1963).

(11) I. Sheft, *Rev. Sci. Instr.*, **37**, 767 (1966).

ture was measured with a copper–constantan thermocouple which had been calibrated against an NBS calibrated platinum resistance thermometer. The thermocouple junction was located near the bottom of the sample tube inside a center thermocouple well of 1.6 mm o.d. Cooling and warming curves were recorded on a strip chart recorder connected to the potentiometer with which the emf of the thermocouple was measured. The samples were placed in a furnace and observations were made at cooling and warming rates of 0.5° min^{-1}. The thermal arrest times were between 15 and 20 min, and the temperature variation during the first half of these periods was at most 0.02° for both samples.

In two independent determinations the triple-point temperature of xenon difluoride was found to be 402.18 ± 0.05°K. Similarly, the triple-point temperature of xenon tetrafluoride was observed to be 390.25 ± 0.05°K. The value for XeF_2 agrees within the experimental error with the temperature reported by Gróz, *et al.*[6] For XeF_4 the new value is 3.1° higher than the one observed by Chernick.[7]

Results and Discussion

Vapor Pressures. The vapor pressure measurements on the two lower fluorides of xenon were carried out over a temperature interval of more than 100° and cover a pressure change of three orders of magnitude. All values were corrected for the pressure head of the column of vapor in the sample tube and the column of nitrogen in the reference line in order to obtain the pressures at the interface of the condensed and vapor phases. This correction amounts to at most 0.14 mm at 1 atm and is proportionately smaller at lower pressures. No correction was applied for dissociation of the compounds in the vapor phase. The maximum error arising from neglecting this correction is 0.6 mm for XeF_4 at the highest temperature. Since the reaction rates are known to be slow, however, the extent to which the equilibrium was established during the time of the vapor pressure measurements is uncertain.

In addition to the vapor pressure data measured with the nickel apparatus described above, two series of earlier measurements had been carried out in a system employing a stainless steel diaphragm transducer. This system did not permit the extension of the measurements beyond 314°K and placed a severe restriction on the measurable pressure range. The data obtained with the stainless steel transducer, however, are in quite good agreement with the more recent measurements and have therefore been used in deriving the vapor pressure equations. It is worth noting that the agreement between the two sets of measurements also attests to the purity of the substances, since the samples originated from different preparations.

For xenon difluoride a total number of 87 data points were available. These were fitted by a least-squares method to yield the equation

$$\log P_{mm} = -\frac{3057.67}{T} - 1.23521 \log T + 13.969736 \quad (1)$$

In the derivation of this equation, empirical weights were applied to take account of the fact that at higher temperatures the pressure deviations increase because of the growing importance of the temperature fluctuations of the bath. Equation 1 represents the experimental data in the temperature range from 273 to 388°K within the limits of the experimental error. Figure 1 shows a plot of the deviations of the observed pressures from the ones calculated from the equation. It is not possible to represent the data by a two-constant equation of the type $\log P_{mm} = -A/T + B$ because the variation of the enthalpy of sublimation over the temperature range of the measurements produces a marked curvature.

The number of data points available for xenon tetra-

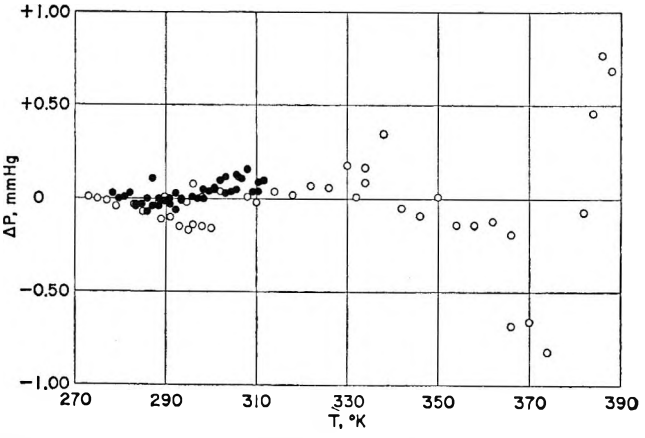

Figure 1. Plot of the deviations of the observed vapor pressures of xenon difluoride from the pressures calculated from eq 1. Filled-in circles refer to data obtained with a stainless steel apparatus.

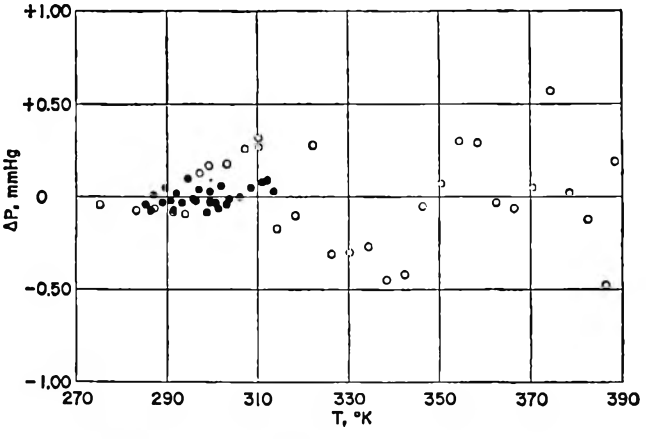

Figure 2. Plot of the deviations of the observed vapor pressures of xenon tetrafluoride from the pressures calculated from eq 2. Filled-in circles refer to data obtained with a stainless steel apparatus.

fluoride was 58. They are represented within the limits of error by the equation

$$\log P_{mm} = -\frac{3226.21}{T} - 0.43434 \log T + 12.301738 \quad (2)$$

This equation is valid for temperatures ranging from 275°K to the triple point for fusion, 390.25°K. Figure 2 shows a plot of the deviations of the observed and calculated pressures.

The scatter of the points on the two deviation plots (Figures 1 and 2) is around several tenths of a millimeter at low pressures where the error of the pressure measurement determines the experimental error, and increases to about 1 mm at the highest temperatures, where the fluctuations of the bath temperature become more important. A single point was measured for liquid xenon tetrafluoride at 390.51°K, and the vapor pressure was found to be 817.97 mm.

A comparison of the vapor pressures of the two compounds shows that throughout the entire temperature range, xenon difluoride is the more volatile substance. At 298.15°K the pressure of the difluoride is 4.55 mm, whereas the tetrafluoride has a vapor pressure of only 2.55 mm.

Enthalpies of Sublimation. The enthalpies of sublimation of XeF_2 and XeF_4 were calculated from the Clausius–Clapeyron equation for a temperature of 330°K, and the following two values were obtained: $\Delta H_{sub} = 55.2 \pm 0.8$ kJ mole^{-1} for XeF_2, and $\Delta H_{sub} = 60.6 \pm 1.0$ kJ mole^{-1} for XeF_4. The limits of error are based on a careful consideration of the maximum uncertainty of the pressures as reflected by the deviations of the measured points from the vapor pressure curve. In deriving the enthalpies of sublimation, the Clausius–Clapeyron equation was considered adequate because of the low vapor pressure values at 330°K (39.05 mm for XeF_2 and 27.01 mm for XeF_4).

In comparing the sublimation enthalpies with the values published previously by Jortner, *et al.*,[5] attention has to be paid to the fact that these latter data refer to an average temperature of 277°K. At this temperature, the enthalpy of sublimation of xenon difluoride derived from eq 1 has the value 55.7 kJ mole^{-1}. Jortner, *et al.*,[5] found 51.5 ± 0.8 kJ mole^{-1} from their spectroscopic studies. The difference between the two numbers exceeds the limits of error considerably.

It has been pointed out by Jortner, *et al.*,[5] that the low volatility of both xenon fluorides implies a high lattice energy of the solid which cannot be accounted for by van der Waals forces alone. Consequently, the bonds in these compounds must have an appreciable polar character. For this reason, Jortner, *et al.*, proposed a model for the bonding in the xenon fluorides which involves a substantial migration of charges to the ligand atoms. It was estimated that the charge carried by a fluorine atom in XeF_2 amounts to 0.5 elementary charge. A similar estimate for XeF_4 resulted in the transfer of 0.42 elementary charge. A calculation of the enthalpy of sublimation based on this model yielded a value of 55.6 kJ mole^{-1} for crystalline xenon difluoride, very close to the value obtained from eq 1.

In the case of xenon tetrafluoride, the enthalpy of sublimation at 277°K was not obtained directly from the slope of eq 2 at that temperature. Since 277°K is rather close to the low end of the range of temperatures for which the vapor pressure equation is valid, it was preferable to correct the more reliable value for ΔH_{sub} at 330°K to the lower temperature. The enthalpy change between 330 and 277°K was calculated from the difference of the heat capacities of gaseous and solid XeF_4. The vapor heat capacity at 298.15°K was obtained from molecular data and has the value 89.8 J deg^{-1} mole^{-1}. The heat capacity of the solid at the same temperature is known from the measurements of Johnston, *et al.*,[12] to be 118.5 J deg^{-1} mole^{-1}. With these numbers the enthalpy change between 330 and 277°K is estimated to be 1.5 kJ mole^{-1}, and one obtains a value of 62.1 ± 1.0 kJ mole^{-1} for the enthalpy of sublimation at 277°K. This is only slightly lower than the value of Jortner, *et al.*[5]

Entropies. The standard entropy of xenon difluoride vapor at 330°K calculated from molecular data is 265.2 ± 0.5 J deg^{-1} mole^{-1}. This number is based on the frequency assignment of Agron, *et al.*,[3] and on the assumption that the Xe–F bond distance is equal to the Xe–F distance in crystalline XeF_2.[13] Since no low-temperature heat capacity data are available, the calculated vapor entropy cannot be compared with a value obtained from calorimetric measurements. However, by adding 24.7 J deg^{-1} mole^{-1} for expansion of the vapor, and subtracting the entropy of sublimation, 167.1 J deg^{-1} mole^{-1}, a value of 122.8 ± 3.0 J deg^{-1} mole^{-1} can be given for the entropy of solid XeF_2 at 330°K.

The comparison of the calculated vapor entropy with the calorimetric value is of particular interest in the case of xenon tetrafluoride because of the unusual planar configuration of the molecule. The pertinent data for such a comparison are listed in Table I. The entropy of solid xenon tetrafluoride at 298.15°K was taken from the heat capacity work of Johnston, *et al.*[12] The entropy of sublimation was obtained from a value of the enthalpy of sublimation adjusted to 298.15°K as described before. No correction for nonideality of the vapor was applied because the vapor pressure of the compound is only 2.55 mm. The calculated entropy value is based on the following set of molecular data. The bond distance of 1.94 Å was taken from the

(12) W. V. Johnston, D. Philipovich, and D. E. Sheehan, "Noble Gas Compounds," University of Chicago Press, Chicago, Ill., 1963, p 139.

(13) H. A. Levy and P. A. Agron, *J. Am. Chem. Soc.*, 85, 241 (1963).

electron diffraction work of Bohn, *et al.*[14] For the frequencies of the seven normal modes of vibration, the assignment of Claassen, *et al.*,[15] was chosen, except for the value of ν_4, which is infrared and Raman inactive and which was taken from a publication of Yeranos,[16] and the value of ν_7, for which the assignment of Weinstock, *et al.*,[8] was adopted. The individual frequencies used in the calculation are: $\nu_1 = 550$ cm^{-1}, $\nu_2 = 291$ cm^{-1}, $\nu_3 = 235$ cm^{-1}, $\nu_4 = 231$ cm^{-1}, $\nu_5 = 519$ cm^{-1}, $\nu_6 = 586$ cm^{-1}, and $\nu_7 = 250$ cm^{-1}. Most of these frequencies are nondegenerate, and only ν_6 and ν_7 are doubly degenerate. The assignment of the lowest frequency, ν_7, might be expected to be as low as 167 cm^{-1} on the basis of force field considerations,[17] but the value chosen here is more consistent with the calorimetric entropy.

Table I: The Standard Entropy of Xenon Tetrafluoride Vapor at 298.15°K (Molecular Weight: 207.29)

Entropy of solid XeF_4	146.4 ± 4.2 J deg^{-1} mole^{-1}
Entropy of sublimation, 61480/298.15	206.2 ± 5.0 J deg^{-1} mole^{-1}
Entropy of compression, $-R$ ln 760/2.55	−47.4 ± 0.7 J deg^{-1} mole^{-1}
Standard entropy of gaseous XeF_4	305.2 ± 10 J deg^{-1} mole^{-1}
Standard entropy of gaseous XeF_4, calculated from molecular data	316.6 ± 1.5 J deg^{-1} mole^{-1}

As can be seen from the table, the calorimetric entropy differs from the calculated one by 11.4 J deg^{-1} mole^{-1}. This difference is barely within the experimental error, but since the limits of error have been assigned rather carefully, the discrepancy appears to be uncomfortably high. In order to obtain complete agreement between the two numbers, for instance, the frequency of ν_7 would have to be increased to 300 cm^{-1}, contrary to all expectation. It seems, therefore, that consideration should be given to the acquisition of more reliable thermodynamic and molecular data of xenon tetrafluoride in order to improve the internal consistency of all available data.

Acknowledgments. The authors wish to express their gratitude to Drs. D. W. Osborne and H. H. Claassen for fruitful discussions and helpful suggestions in the preparation of this paper.

(14) R. K. Bohn, K. Katada, J. V. Martinez, and S. H. Bauer, "Noble Gas Compounds," University of Chicago Press, Chicago, Ill., 1963, p 238.

(15) H. H. Claassen, C. L. Chernick, and J. G. Malm, *J. Am. Chem. Soc.*, **85**, 1927 (1963).

(16) W. A. Yeranos, *Mol. Phys.*, **9**, 449 (1965).

(17) H. H. Claassen, private communication.

Radiolytic Formation and Decomposition of Ozone[1]

by John T. Sears and James W. Sutherland

Brookhaven National Laboratory, Upton, New York 11973 *(Received August 7, 1967)*

The formation of ozone from gaseous oxygen upon irradiation with Co^{60} γ rays was investigated for various dose rates, I, ranging from 7×10^3 to 8×10^6 rads/hr. Yield–dose curves at ambient temperature ($\approx 10°$) and 665 torr were measured until a steady-state ozone concentration was reached. $G(O_3)$ at low doses was found to be independent of I. Ozone concentrations of 2000 ppm at ambient temperatures and 7000 ppm at 195°K were detected. In the gas phase at 77°K, a differential $G(O_3)$ of 10.5 ± 0.5 was found. The concentration at steady state was determined by a separate back reaction(s) which destroyed ozone and by the forward rate of formation of ozone from its precursors. Different dose-rate effects were found under various conditions. The relation, $[O_3]_{ss} \propto I^{0.45\pm0.06}$, was determined for the steady-state yield in all-glass vessels, while $[O_3]_{ss} \propto I^{0.81\pm0.04}$ held when the irradiation vessel was fitted with a fluorocarbon-lubricated stopcock. Both nonradiolytic and radiolytic decomposition of ozone were also investigated.

Introduction

The formation of ozone from oxygen, one of the oldest radiation chemistry systems, was first investigated in 1911 by Lind.[2] Recent workers[3,4] found that ozone was formed more efficiently at low temperatures than at room temperature and that only small concentrations of a few ppm were attained at room temperature. Earlier work[5,6] showed that decomposition of ozone proceeds at an extremely rapid rate under irradiation.

(1) This work was performed under the auspices of the U. S. Atomic Energy Commission.

(2) S. C. Lind, *Amer. Chem. J.*, **47**, 397 (1911).

However, significant gaps in knowledge of the pertinent chemical reactions still remain. An important relatively unexplored area concerns reactions which inhibit formation or actually decompose ozone. The effect of impurities has been difficult to evaluate, even though it has been appreciated that impurities contribute to the difficulty in obtaining reproducible results.

The present study was initiated in order to gain a more comprehensive knowledge of the radiation chemistry of oxygen–ozone gas mixtures. Emphasis was placed on obtaining complete yield–dose curves and final steady-state concentrations under various experimental conditions. Ozone yields were determined at both ambient and low temperatures. Agreement with previous work was reasonable upon consideration of differences in conditions.

Experimental Section

Research grade oxygen from Matheson Co. was used in most of the experiments without further purification. Stated impurity levels in a typical mass spectrometric analysis were as follows: CH_4, 9.6 ppm; Ar, 16 ppm; N_2, 5 ppm; Kr, 8 ppm. Several experiments employed gaseous oxygen obtained from distillation of liquid oxygen or from $KMnO_4$ pyrolysis, and within experimental error no difference in the ozone yield was noted. The effect of additives was investigated. Fluorine (1%, CF_4 and SF_6) was used after passage through a NaF trap. N_2O, NO_2, H_2O, and i-C_5H_{12} were purified by simple vacuum distillation. CF_4 (95% pure), CO(99.5% pure), and H_2 (99.8% pure) were used directly from the gas cylinders as supplied by Matheson Co. After evacuation of the irradiation vessels to $<10^{-4}$ torr, the gases were added to the vessels in order of increasing partial pressure.

One set of experiments utilized all-glass vessels (150 ml) provided with seal-off necks and break-seals (type I). One vessel was evacuated to 10^{-6} torr and baked at 400° for 60 hr prior to irradiation.

Another set of experiments was performed in 300-ml quartz vessels (type II) fitted with stopcocks lubricated with Ascolube-F fluorocarbon grease, which had a vapor pressure of $\approx 10^{-5}$ torr at ambient temperature. Later glass wool was added to these vessels to increase the surface-to-volume ratio. The glass wool was cleaned of reactive organics and contaminants by preirradiation in oxygen to a dose of 7×10^8 rads. The products were then removed by evacuation.

The irradiations were performed in the Brookhaven High Intensity Radiation Development Laboratory (HIRDL) Co^{60} γ-ray facility over a range of dose rates from 7×10^3 to 8×10^6 rads/hr. Total doses varied from 4×10^4 to 2×10^8 rads. The bulk of the experiments were performed at ambient temperature, usually about 10°, except when slight heating from the radiation occurred at dose rates above 10^6 rads/hr. Dose rates were determined by ferrous sulfate dosimetry, corrected by appropriate electron-density ratios.

Ozone was analyzed by ultraviolet spectrophotometry in a gas cell 5 cm long by following the Hartley band absorption at 254 mμ. At this wavelength, the extinction coefficient, ϵ, for ozone is 135 cm^{-1} (STP),[7] and the ϵ's for expected impurities are below 10^{-2} cm^{-1} (STP).[8] Immediately after irradiation a known amount of the irradiated gas mixture was expanded into the analysis cell through glass vacuum lines with stopcocks lubricated with Ascolube-F grease. Calculated concentrations were then expressed in ppm (vol). Increased sensitivity from 5 ppm (the lower limit) to 20 ppm was obtained by condensing oxygen and ozone into the analysis cell at −202°. The incomplete transfer of the gas by this procedure resulted in calculated ozone concentrations 5–10% too low.

Ozone (to 3 vol %) for decomposition experiments was produced by flowing extra-dry grade oxygen (99.6% pure) through a Welsbach ozonator. In nonradiolytic decomposition, the decay was followed spectrophotometrically both in a sealed silica cuvette and an analysis cell fitted with a lubricated stopcock. Radiolytic decomposition was investigated by the following procedure. The gas mixture from the ozonator was transferred into a reaction vessel while a sample was taken for analysis. The mixture was irradiated for the desired period of time and then was analyzed by the expansion technique previously described.

Results

In this paper, the following definitions of G values will be used: $G(X)$ = molecules X formed/E, $G'(X)$ = [d(molecules X)]/dE, and $G_f'(X)$ = d[molecules X formed, excluding back reactions which destroy X]/dE, where E is given in units of 100 eV. Thus at steady state $G'(O_3) = 0$, but $G_f'(O_3)$ has a positive value.

Yield–Dose Curves. The formation of ozone with dose at ambient temperature is illustrated in Figure 1. The $[O_3]$ depended on dose, even far from steady state. $G'(O_3)$ decreased from 4.5 (±0.5) in the dose range 7×10^4–1.5×10^5 rads to ≈3 at 4×10^5 rads and down to ≈2 at 4×10^6 rads and a dose rate of 8.4×10^6 rads/hr (curves A and B). At this dose rate, $G'(O_3)$ continued to decrease with dose until an almost linear yield–dose region was attained: 8×10^6–2.6×10^7 rads (450–1200 ppm), $G'(O_3) = 1.3 \pm 0.2$ (top section, Figure 1). The ozone concentration continued

(3) G. R. A. Johnson and J. M. Warman, *Discussions Faraday Soc.*, **37**, 87 (1964).

(4) J. F. Kircher, J. S. McNulty, J. L. McFarling, and A. Levy, *Radiation Res.*, **13**, 452 (1960).

(5) B. Lewis, *J. Phys. Chem.*, **37**, 533 (1933).

(6) P. C. Capron and R. Cloetens, *Bull. Soc. Chim. Belges*, **44**, 441 (1935).

(7) W. B. De More and O. Raper, *J. Phys. Chem.*, **68**, 412 (1964).

(8) B. A. Thompson, P. Harteck, and R. R. Reeves, Jr., *J. Geophys. Res.*, **68**, 643 (1963).

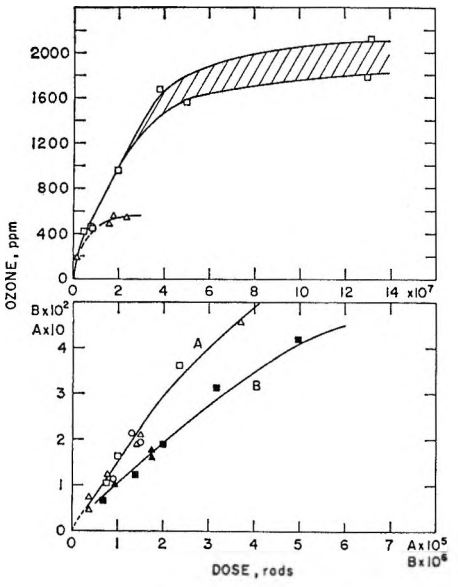

Figure 1. Ozone formation as a function of dose (irradiation in type II vessels: P_{O_2} = 665 torr, temp ≈10°). Dose rate: ■, 8.4 × 10⁵ rads/hr; □, 8.4 × 10⁶ rads/hr; ▲, 8.5 × 10⁵ rads/hr; △, 9.0 × 10⁵ rads/hr; ○, 1.5 × 10⁵ rads/hr.

to increase with dose until a steady state was reached. The steady-state yield, however, was dependent on the dose rate and experimental conditions, although $G'(O_3)$ was independent of dose rate at $[O_3] \ll [O_3]_{ss}$. Results with and without additives are compared in Table I, and no significant effect on the formation of ozone was noted (away from a steady state).

Table I: Ozone Formation: Additive Effects[a]

Additive	P, torr	10⁻⁶I, rads/hr	Dose, rads	[O₃], ppm	[O₃], ppm (no additive)
CO	7.0	8.26	2.06 × 10⁶	192	195
CF_4	3.2	1.06	3.50 × 10⁵	39	44
NO_2	0.45	8.00	2.04 × 10⁶	185	195
H_2	26.5	8.2	8.20 × 10⁵	83.6	88
N_2O	21	6.15	1.30 × 10⁷	681	660

[a] Irradiations in type II vessels: temp ≈10°, P_{O_2} = 665 torr.

Dose-Rate Steady-State Ozone Concentration. A. Effect of Vessel Conditions. The dependence of the concentration at steady state upon dose rate is illustrated in Figure 2 for the two types of vessel. Experiments using type I vessels gave results which yielded the relationship $[O_3]_{ss} \propto I^{0.45\pm0.06}$, while experiments with type II vessels gave results which yielded the expression $[O_3]_{ss} \propto I^{0.81\pm0.04}$. The important difference between the two sets of experiments is that the gas in type II vessels was exposed to Ascolube-F grease.

B. Hydrogen Addition. Upon addition of H_2 to O_2 in type II vessels, a new value of $[O_3]_{ss}$ was obtained. For 4% H_2 addition (26 torr of H_2), the relationship $[O_3]_{ss} \propto O^{0.45\pm0.06}$ was determined (Figure 2). The ozone concentration at steady state was dependent on the amount of hydrogen added (Table II). For I = 3.0 × 10⁵ rads/hr and 9–26 torr of H_2, $[O_3]_{ss} \propto (H_2)^{-0.45\pm0.05}$. Addition of water and isopentane vapors also caused diminution of the final yield with additive.

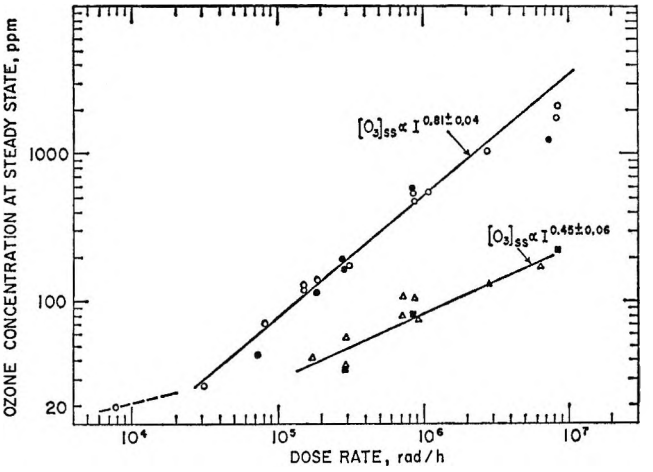

Figure 2. Ozone concentration at steady state as a function of dose rate (P_{O_2} = 665 torr, temp ≈ 10°): ○, type II vessels; △, type I vessels (unconditioned); ▲, type I vessels (60-hr bake at 400°); ■, type II vessels (P_{H_2} = 26 torr); ●, type II vessels (8.0 g of glass wool dispersed throughout the vessel).

Table II: Steady-State Ozone Yields with Hydrogen Impurities[a]

Additive	P, torr	Dose rate, rads/hr	[O₃], ppm	[O₃]ss, ppm (no additive)
H_2O	19	3.0 × 10⁵	40	(190)
i-C_5H_{12}	11.5	7.0 × 10⁶	670	(1800)
H_2	7.5	8.4 × 10⁶	174	(500)
H_2	0	3.0 × 10⁵	190	
H_2	4.3	3.0 × 10⁵	116	
H_2	9.5	3.0 × 10⁵	54	
H_2	14.7	3.0 × 10⁵	44.3	
H_2	26.5	3.0 × 10⁵	35.3	

[a] Irradiations in type II vessels: temp ≈10°, P_{O_2} = 665 torr.

C. Wall Effects. Decomposition of ozone on the walls could possibly influence the final steady-state concentration of ozone.[9] Irradiations were performed in a type II vessel with 8 g of clean glass wool dispersed throughout the flask. No large effects were found upon irradiation to steady state, despite the 100-fold increase in surface area (Figure 2).

(9) F. W. Lampe, E. R. Weiner, and W. H. Johnston, *Int. J. Appl. Radiat. Isotopes*, 15, 363 (1964).

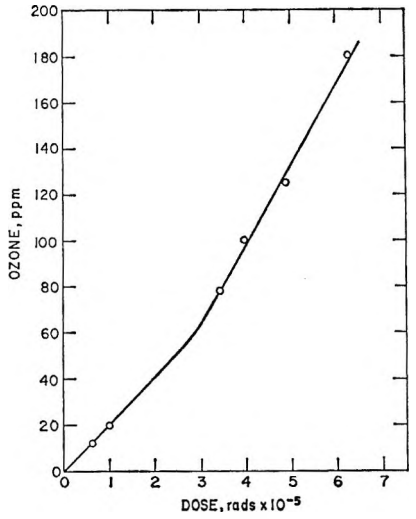

Figure 3. Ozone yield as a function of dose at 77°K (P_{O_2} = 160 torr, I = 1.57 × 10^6 rads/hr).

Temperature Dependence. $G(O_3)$ was temperature dependent; there was also an implied dependence of the steady-state yield on temperature (Table III and Figure 3). At 77°K, some partial inhibiting effect apparently occurred in the gas-phase radiolysis at low doses in our experiments. Upon further irradiation, $G'(O_3)$ increased until a linear yield–dose region was reached at doses >3 × 10^5 rads, with $G'(O_3)$ = 10.5 ± 0.5.

Table III: Low-Temperature Irradiation of Oxygen[a]

I, rads/hr	Dose, rads	$[O_3]$, ppm	$G(O_3)$
9.9 × 10^6	2.5 × 10^6	43.6	5.33
9.9 × 10^6	2.5 × 10^6	46	5.6
6.15 × 10^6	1.54 × 10^6	304	6.0
8.2 × 10^6	3.73 × 10^7	5100	4.1
8.2 × 10^6	5.77 × 10^7	7000	3.65

[a] Irradiations in type II vessels: temp = 195°K, P = 460 torr.

Decomposition Studies. A. Nonradiolytic Experiments. Nonradiolytic decomposition experiments in type II spectrophotometric cells always yielded first-order kinetics over a factor of 20 in $[O_3]$, but a series of five experiments gave a large variance in the individual rate constants, *i.e.*, k = 1, 1.8, 2, 4.4, and 14 × 10^{-6} sec^{-1}.

Different results were obtained with a type I sealed quartz cuvette (but filled through fluorocarbon-greased lines). After a fast initial decomposition with a pseudo-rate constant of the same magnitude as in type II cells, the decomposition slowed very markedly, with a pseudo-first-order constant, k = 1.5 × 10^{-7} sec^{-1} (Figure 4).

B. Radiolytic Experiments. Radiolytic decomposition experiments ($[O_3]$ = 3% down to 3000 ppm) were performed at I = 3.05 × 10^5 rads/hr in a type II vessel. The data were fitted with a first-order rate constant of 5.9 × 10^{-5} sec^{-1}. Radiolytic formation of ozone was negligible at these conditions far from steady state, $[O_3]_{ss}$ = 200 ppm. At 3% O_3, an apparent $G(-O_3)$ of 550 can be calculated, as compared with $G'_f(O_3) \approx 1$–3.

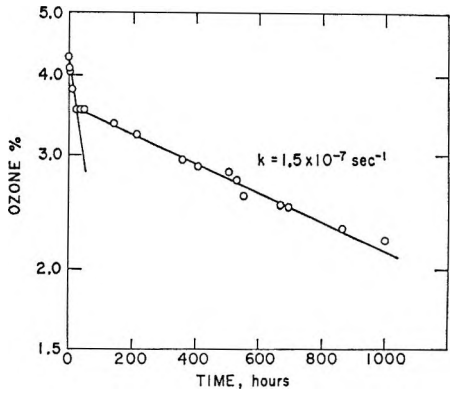

Figure 4. Nonradiolytic decomposition of ozone in a type I vessel (P_{O_2} = 620 torr, temp = 25°). Initial rapid decomposition is the same order of magnitude as nonradiolytic decomposition in a type II vessel.

Experiments at initial concentrations just above steady-state values, in which radiolytic formation of ozone could not be neglected, were also performed. Calculated first-order decomposition rate constants of 2.8 and 3.7 × 10^{-5} sec^{-1} were obtained for I = 2.84 × 10^5 and 6.5 × 10^5 rads/hr at initial concentrations of 560 and 1100 ppm, respectively. First-order constants calculated from steady-state results with type II vessels varied from 2.5 to 4.5 × 10^{-5} sec^{-1}.

Discussion

An important observation in these experiments is that $G'(O_3)$ at low doses was dependent on dose but independent of dose rate; however, the steady-state concentration of ozone was dependent on dose rate (Figures 1 and 2). Indeed, any significant deviation from the general yield–dose curve only occurred at $[O_3]$ approaching the appropriate $[O_3]_{ss}$. Clearly there must be two distinct reaction sequences. One is a mechanism of net ozone formation, *i.e.*, $G_f'(O_3) > 0$; the other is a decomposition mechanism which destroys ozone and leads to a steady-state concentration with $G'(O_3) = 0$. This is borne out by the radiolytic decomposition experiments which approached a steady state from $[O_3] > [O_3]_{ss}$.

Ozone Formation. The competitive reactions of intermediates produced by radiation lead to a dependence of G on dose and temperature. The present results are most consistently evaluated by separation into three major regimes in which different intermediate ozone precursors become deactivated and no longer contribute to ozone production. The precursor groups can then be identified with previously postulated

species.[3] In regime A, $G'(O_3) = 10.5$ at 77°K only after a partial inhibition, while this high G value was not observed at ambient temperature. In regime B, $G'(O_3) = 4.5$ was initially observed at ambient temperature, but decreased with increasing dose (curves A and B, Figure 1). The last linear region of $[O_3]$–dose, $G'(O_3) = 1.3$, is regime C (top, Figure 1).

The precursors C can be correlated with oxygen atoms formed in direct ionization dissociation. Mass spectrometer data[10] indicate that ≈18% of ionic species ($G(e) = 3.1$) are atomic ions formed directly by radiation. Direct dissociation of O_2 into $O + O^+ + e^-$, followed by positive charge transfer to an oxygen molecule, would lead to a partial G value of 1.1. As oxygen atoms always react to form ozone under the present conditions,[11] any significant amount of direct dissociation of O_2 into pairs of neutral atoms would be observed in regime C—the minimum $G_f'(O_3)$ observed. The precursor group A has properties consistent with those of ionic species. Ionic species, which upon neutralization yield two ozone molecules per ion pair, would produce a maximum $G(O_3)$ of 6.2. As calculated from $[G'(O_3)]_{77°} - [G'(O_3)]_{195 \text{ or } 283°} = G(A)$, the partial G value of A is 4.9–6.3 (±1.0), which is consistent with the value expected from ionic precursors. Charge-transfer reactions are generally very fast and have low heats of activation; thus deactivation would occur very easily. Deactivation by fluorocompounds or small concentrations of ozone may account for the nonobservance of A at ambient temperatures in the present results. Precursor group B contributed an initial partial $G(O_3)$ value of 3.2 ± 0.7 at ambient temperature and could well be excited molecular oxygen.[3] The decrease in $G'(O_3)$ possibly could be due to deactivation by ozone itself, as large amounts of additive impurities did not effect ozone formation in this regime (Table I).

A heat of activation, E, of ≈6 kcal/mol for the deactivation reaction(s) of group (B) can be estimated by the fact that with $I = 8 \times 10^6$ rads/hr, $G'(O_3) \approx 4$ at $[O_3] \approx 5000$ ppm at 195°K, while at 283°K, $G'(O_3) \gtrsim 4$ only to $[O_3] \approx 50$ ppm. Kircher, *et al.*,[4] calculated from steady-state and maximum ozone yields an $E \approx 1.8$–2.1 kcal/mol, which, however, is a sum of heats of activation of the pertinent reactions. Apparently most of the important reactions in the radiolysis of oxygen have small heats of activation.

The present result for the maximum G value [$G'(O_3) = 10.5 \pm 0.5$] is in essential agreement with the latest values in the literature: Kircher, *et al.*,[3] gave $G'(O_3) > 9$ at 195°K; Johnson and Warman[4] found $G'(O_3) = 10.3$, corrected for dosimetry,[12] (12.8 uncorrected) at 90 to 195°K.

Decomposition. Under suitable conditions a number of separate, distinct decomposition reaction sequences must occur and limit the steady-state concentrations of ozone.

A. Type I Vessels. The steady-state ozone yields obtained upon irradiation in type I vessels (Figure 2) can most easily be explained by Fueki and Magee's postulation of an ion-chain decomposition,[13,14] which was discussed further by Harteck, *et al.*[15] Other simple decomposition sequences do not fit the experimental facts. The thermal decomposition mechanism of Benson and Axworthy[16] does not predict the observed I dependence of $[O_3]_{ss}$ and the implied rapid radiolytic decomposition. The irradiation experiments with added glass wool show that reactions with vessel walls or impurities from the vessel walls did not occur significantly. As nonradiolytic decomposition in clean glass vessels was exceedingly slow (Figure 4), transient species which are produced by irradiation seem required to yield the observed ozone concentrations. A radical chain initiated by trace impurities could also produce an $I^{1/2}$ dependence; however, the fact that large amounts of additives and hydrogenous materials were required to influence $[O_3]_{ss}$ makes this possibility extremely unlikely.

The experimental $I^{0.45}$ dependence on $[O_3]_{ss}$ implies a radical–radical (or ion–ion) type termination of the decomposition reaction sequence. The following equation holds for the negative-ion chain[14]

$$(O_3)_{ss} = \frac{G'_f(O_3) I^{1/2} k_r^{1/2}}{[G(e)]^{1/2} k_d} \qquad (1)$$

To fit the experimental results, the propagating charge-transfer rate constant, k_d, must be $\approx 10^{-12}$ cm^3 sec^{-1}, for the estimated[13,14] ionic recombination rate constant, k_r, $\approx 10^{-6}$ cm^3 sec^{-1}. This k_d value is slightly lower than negative-ion exchange reaction constants for organics, but it is approximately the estimate of this rate constant by Harteck, *et al.*[15]

B. Type II Vessels. With fluorocarbon lubricant present, greater $[O_3]_{ss}$ were obtained upon irradiation of oxygen (without additives, Figure 2). As the $[O_3]_{ss}$ dependence on dose rate was now almost first order ($I^{0.81}$), the radical chain in type I vessels should not occur significantly. Ozone reaction with lubricant impurities (or radiolytic products) is the simplest consistent proposal for the new decomposition mode. Irradiation could cause increased impurity levels, which

(10) K. J. Laidler and E. K. Gill, *Trans. Faraday Soc.*, **54**, 633 (1958).

(11) F. Kaufman and J. R. Kelso, *Discussions Faraday Soc.*, **37**, 26 (1964).

(12) Johnson and Warman used nitrous oxide dosimetry, $G(N_2) = 12.5$; most literature values are less and $G(N_2) = 10.0$; F. T. Jones and T. J. Sworski, *J. Phys. Chem.*, **70**, 1546 (1966).

(13) K. Fueki and J. L. Magee, *Discussions Faraday Soc.*, **36**, 19 (1963).

(14) K. Fueki and J. L. Magee, *J. Phys. Chem.*, **68**, 2901 (1964).

(15) P. Harteck, S. Dondes, and B. A. Thompson, *Science*, **147**, 393 (1965).

(16) S. W. Benson and A. E. Axworthy, *J. Chem. Phys.*, **26**, 1718 (1957).

would explain the enhancement of the calculated first-order constants of the radiolytic (and steady-state) experiments, as compared to nonradiolytic decomposition. Charge transfer of the electron (in the negative-ion chain) to a fluorocompound with an electron affinity greater than that of ozone [$EA(O_3) = 1.9$ eV][17] would explain why the faster decomposition in type I vessels did not occur. Thus irradiation experiments with fluorine additive in type I vessels yielded results qualitatively similar to experiments with type II vessels.

The early findings of ozone decomposition with α particles[5,6] correlate with a mechanism involving chemical impurities similar to the present work with fluorocompounds, rather than with the mechanism operative in type I vessels (negative-ion chain).

Results with additive hydrogenous materials also illustrate the complex nature impurities can play in this system. The $\approx I^{1/2}$ dependence of $[O_3]_{ss}$ can be explained either by a reversion to the negative-ion chain or by a hydroxyl–perhydroxyl chain similar to that proposed in photolytic decomposition of O_3–H_2O mixtures.[18]

Summary

The data show that there are separate reaction mechanisms which (1) lead to a net forward formation rate of ozone, and (2) destroy ozone and limit its steady-state concentration. The data are consistent with possible reaction schemes involving three previously postulated precursors of ozone. The evidence favors a negative-ion chain decomposition mode in a pure oxygen, glass-encapsulated system. Impurities play a complex role and can radically affect the steady-state yield of ozone.

(17) P. H. Wood and L. A. D'Oranzio, *J. Phys. Chem.*, **69**, 2562 (1965).

(18) W. D. McGrath and R. G. W. Norrish, *Proc. Roy. Soc.* (London), **A254**, 317 (1960).

The Surface of a Carbon with Sorbed Oxygen on Pyrolysis[1a,b]

by Marcellus T. Coltharp and Norman Hackerman

Department of Chemistry, The University of Texas at Austin, Austin, Texas *(Received August 14, 1967)*

Thermal decomposition of Spheron-6 with chemisorbed oxygen was carried out to provide samples of known coverage. Complete pyrolysis gave a total of 2.29 mmoles of oxygen/g of which 60% appeared as CO, 37% as CO_2, and 3% as H_2O. The differential decomposition pattern (amount appearing in a temperature interval *vs.* temperature) for CO indicates 400 to 800° as the main region of appearance with a maximum at 600–700°. For CO_2 this region was at 300 to 700° with a maximum at 500–600°. Decomposition to the major products in the main regions of appearance was complete only after 40 hr or more. The features of the CO_2 decomposition pattern of Spheron-6, *i.e.*, its shape, the range, and the location of the maximum, were different from those of other carbons. The CO decomposition pattern was the same for all carbons checked. Total decomposition products indicated that the fraction of the surface occupied by oxygen-containing groups at maximum coverage was 68% of the BET area. This represents the amount of edge carbons in the surface. The rest is made up of basal crystallite faces. The sequence of functional group decomposition is: simple groups first eliminate water and form more complex groups; groups are then detached from the lattice; and finally, edges are disrupted as groups leave at high temperature. Analysis of both thermodynamic and kinetic data and that of decomposition indicates that no interconversion of products took place. Desorption of oxides from the particle interior was ruled out.

Introduction

To obtain carbon samples of varying known oxygen coverage for a solution adsorption study,[2] we chose to pyrolyze Spheron-6 with a presumed monolayer of oxygen.[3] Preliminary experiments on this extensively characterized carbon black[4] indicated that further examination of the previously reported surface oxide decomposition to CO, CO_2, and H_2O[5,6] was necessary.

The results from this approach make it possible to answer a number of questions about the surface at any

(1) (a) Portions of this paper were presented at the Southeast-Southwest Regional Meeting of the American Chemical Society, Memphis, Tenn., Dec 1965. (b) Based in part on a dissertation submitted by M. T. Coltharp to the Graduate School of The University of Texas at Austin in partial fulfillment of the requirements for the Ph.D. degree, Aug 1966.

(2) M. T. Coltharp and N. Hackerman, to be published.

degree of decomposition. The maximum coverage was evaluated, and the fraction of each of the two major crystallite faces present was determined. Further, the surface functional groups and their decomposition mechanisms were ascertained by combination of the total and differential decomposition data with literature information.[7] Since interconversion of products or desorption from the interior of the particles of the black are alternate mechanisms, the possibility of their interference is examined.

Experimental Section

The apparatus and procedures for decomposition and analysis of the chemisorbed oxygen will be described in detail elsewhere.[8] In brief, a stream of purified helium was passed over a sample of the black which had been predried at 150°. As the pyrolysis proceeded, the exiting H_2O, CO_2, and CO were separated and then measured manometrically (CO was oxidized to CO_2 before collection). The apparatus was calibrated by collection of the products from partial and total combustion of benzoic acid supplied by the Bureau of Standards.

The Spheron-6 (previously characterized[4-6]) was obtained from the Godfrey L. Cabot Corporation. Sample sizes for decomposition were from 5 to 12 g and 55 g for coverage generation.

Results

Thermal Decomposition Patterns. The differential decomposition behavior for the surface oxides of Spheron-6 is given in Figure 1. The amounts in each interval were those produced up to a time where the decomposition reached a very low steady state (normally 0.20×10^{-2} mmole/g hr or less for the last period in an interval). This time was 40 hr or more between 300 and 800° and 20 hr or less outside of this temperature range.[9] The data presented are for one of three runs. There was good agreement except that less CO showed up at and above 600° on one run; 16% less CO appeared in total than on the run shown. (The average total oxygen was 2.17 mmoles/g, and there was +5, −9, and +4% difference from this, respectively.)

Most decomposition occurred between 400 and 700°, with 72% of the tightly bound oxygen coming off in this interval. The rest came off above and below this region. Decomposition was essentially complete at 1000°, below that found by others.[5,6] By comparison, decomposition to hydrogen started at 700° where trace quantities appeared. At 800° the amount of hydrogen evolved became more significant (*e.g.*, 0.326 mmole of H/g after 19 hr). The increase was continuing at 1000–1100°, the highest interval checked. Thus the hydrogen evolution was well separated from that of the oxides.

Figure 1 indicates that CO (60% of the total oxide

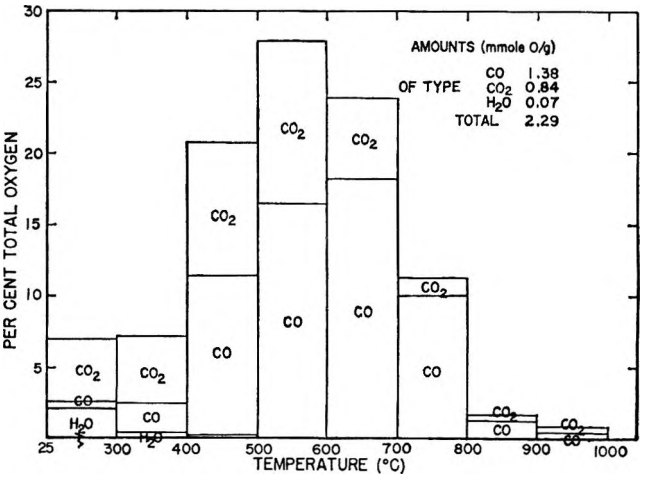

Figure 1. Per cent of total oxygen decomposed from Spheron-6 in 100° intervals.

product) predominated above 400° and had its maximum at 500–700°. CO_2 (37% of the total product) showed up in significant quantities first and exhibited a maximum and last significant interval at 600° just before the CO maximum.

The grouping of the intervals was about the same for each product with two approximately equal central intervals bound by smaller ones of equal size. When the data are plotted on a relative basis for product type (not shown), the similarity between the major products is further accentuated, since for each substance 50% appeared up to the maximum and 95% by the next interval after it. The appearance of the minor product, water (*ca.* 3%), was complete by 400°.

These findings agree well with Smith's generalization[7b] based on a number of carbon types—including blacks, graphites, and charcoals—except that his limit of 700° for water is high for Spheron-6.

Since about a month was needed for a complete differential or stepwise pyrolysis, a faster method for generating coverage involving at least one large interval (200° or more) was used for routine decompositions down to a given coverage. This did not alter the decomposition paths as shown by three runs with

(3) C. G. Gasser and J. J. Kipling in "Proceedings of the 4th Conference on Carbon," Pergamon Press, New York, N. Y., 1960, p 55.

(4) (a) W. R. Smith and D. C. Bean in A. Standen, "Kirk-Othmer Encyclopedia of Chemical Technology," Vol. 4, 2nd ed, John Wiley and Sons, Inc., New York, N. Y., 1964, p 243; (b) R. A. Beebe and D. M. Young, *J. Phys. Chem.*, **58**, 93 (1954), for example; (c) J. Biscoe and B. E. Warren, *J. Appl. Phys.*, **13**, 364 (1942).

(5) R. B. Anderson and P. H. Emmett, *J. Phys. Chem.*, **56**, 753 (1952).

(6) W. D. Schaeffer, W. R. Smith, and M. H. Polley, *Ind. Eng. Chem.*, **45**, 1721 (1953).

(7) (a) V. A. Garten and D. E. Weiss, *Rev. Pure Appl. Chem.*, **7**, 69 (1957); (b) R. N. Smith, *Quart. Rev.* (London), **13**, 287 (1959); (c) H.-P. Boehm, E. Diehl, W. Heck, and R. Sappok, *Angew. Chem., Intern. Ed. Engl.*, **3**, 669 (1954); (d) H.-P. Boehm, *ibid.*, **5**, 533 (1966).

(8) M. T. Coltharp and N. Hackerman, to be published.

(9) Details of the decomposition kinetics will be published elsewhere.

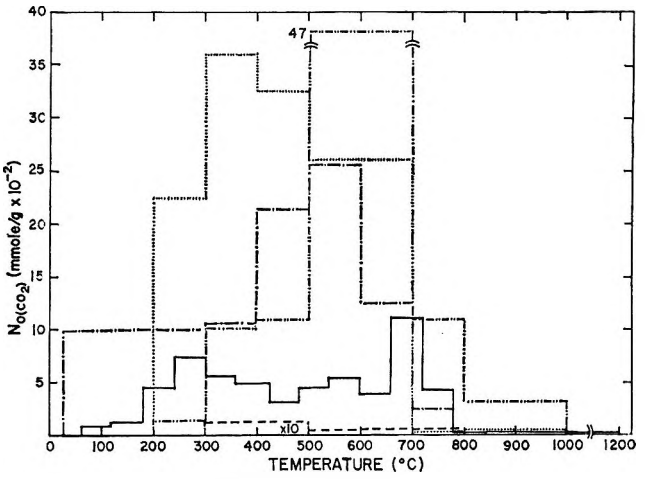

Figure 2. Decomposition to CO_2 (O atom basis): —·—, Spheron-6 (this study); —··—, synthetic pattern; ....., Mogul A[11]; – – – –, Graphon (× 10)[12]; ———, charcoal CWSN-S5[10].

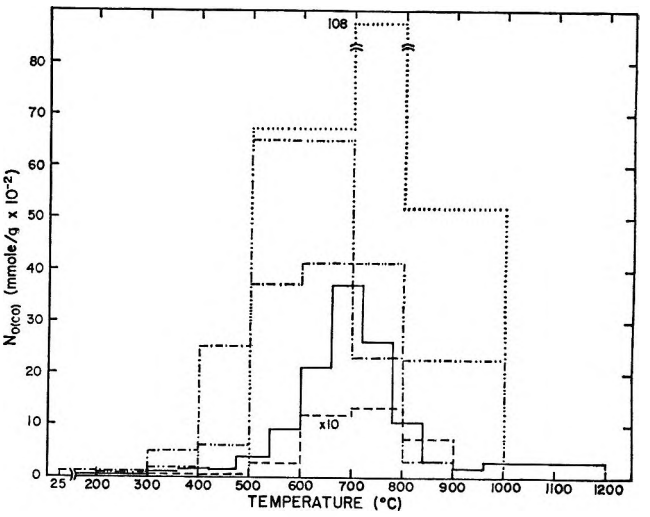

Figure 3. Decomposition to CO: —·—, Spheron -6 (this study); —··—, synthetic pattern; ....., Mogul A[11]; – – – – Graphon (× 10)[12]; ———, CWSN-S5[10].

changes from 25 to 1000° in a single stage which gave oxygen totals within 5% of the runs with 100° stages and $O(CO)/O(CO_2)$ ratios of 1.66 in comparison to 1.69 for the month-long runs.

Comparison of these differential decomposition data with those of Anderson and Emmett[5] and Schaeffer, *et al.*,[6] is complicated by differences in amounts of products,[8] interval sizes, and times needed for completion of decomposition. The first changes the absolute amount in an interval but would not alter the features of the pattern. Use of 200 or 300° intervals with only 1 hr at temperature would, however, affect the features. The larger intervals give a less resolved pattern and the short times move the quantities of a product which would appear at long times in an interval into the next higher interval. (See synthetic patterns below.) The failure to detect products at longer periods in the other studies[5,6] must then be mainly a consequence of using smaller samples (*ca.* 1 g[5,10]) and larger intervals.

Even with these differences, both groups found CO persisted to higher temperatures than did CO_2. Overall findings at variance with this study are: for Anderson and Emmett,[5] CO predominated at all temperatures and water appeared at 600–900°; for Schaeffer, *et al.*,[6] the CO and CO_2 maxima coincided.

Figures 2 and 3 compare the oxide patterns of Spheron-6 with two other blacks, Mogul A[11] and Graphon,[12] and a charcoal,[10] CWSN-S5. Virtually all such data available are given here. Synthetic patterns made by rearranging the data of this study according to reported intervals[11] and times[5] are included here to illustrate the effects of varying these two factors.

Decomposition to CO_2 (Figure 2) appears to be unique to each carbon since there are various pattern shapes and the maxima are spread through all five significant appearance intervals. The failure of the synthetic pattern to closely resemble even the pattern for Mogul A, which has the same amount of oxygen per unit area as Spheron-6 and which is also a channel black, suggests that the individuality is not due to the particular decomposition conditions chosen. However, in the synthetic pattern, the shift of the entire Spheron-6 CO_2 evolution to higher temperatures and the development of the chimney-like maximum does show clearly the distortions introduced by use of large intervals and short collection times. Further, the amount which would have appeared in 1 hr at the synthetic maxima would contain products from three different 100° intervals in the actual pattern: that for long times at 400–500°, all that evolving at 500–600°, and the amount for the first hour at 600–700°. All of this would make the product appearing in the second hour at 500–700° negligible.

In the real case, the Spheron-6 maximum is located between that of Graphon and the second maxima of the charcoal. The first maxima of the charcoal must be from $ZnCO_3$ decomposition rather than surface carbon–oxygen groups since it is at the decomposition temperature of this compound.[13] The carbonate forms from the $ZnCl_2$ in the 7% ash present during conditioning of the charcoal.

The patterns for decomposition to CO differ considerably from those to CO_2. They have more similarities in shape, their maxima are closer (all in the 600–700° interval if the time at temperature compensation is made), and the synthetic pattern better reproduces the

(10) R. B. Anderson and P. H. Emmett, *J. Phys. Chem.*, **51**, 1308 (1947).

(11) B. R. Puri and R. C. Bansal, *Carbon*, **1**, 451 (1964).

(12) N. R. Laine, F. J. Vastola, and P. L. Walker, Jr., *J. Phys. Chem.*, **67**, 2030 (1963).

(13) N. A. Lange, Ed., "Handbook of Chemistry," 8th ed, McGraw-Hill Book Co., Inc., New York, N. Y., 1952, p 310.

Mogul A curve. CO appears at higher temperature than CO_2 on other carbons as well as for Spheron-6. Also on each the CO maximum is above the maxima of the other two products, except for the charcoal where the CO and second CO_2 maxima coincide.

Reoxidation. While being transferred from reactor to storage, treated carbons were partially exposed to dry room air, a condition sufficient for some types of carbon[10,14] to chemisorb oxygen. A check for this was made by exposing each of a carbon series to a flow of dry air at 25° for up to 17 hr and then carrying out decomposition by changing from room temperature to 1000° in a single stage. Series members were chosen to include the main likely site fixation types, *i.e.*, sites that yield CO_2, sites that yield CO, and those left after the large surface area drop at 930°.[15] The surfaces were unreactive. The carbons with partially decomposed oxides were unchanged (their total oxygen was from 2.01 to 2.27 mmoles of O/g—within the range of the unexposed Spheron-6) and the oxygen-free ones gained no more than 1.4% of their original content.

Discussion

Oxide Coverage and Nature of Substrate. The oxide coverage for maximum filling of a uniform continuum substrate is 84% of the BET area,[16] assuming single complexes of the largest radii (O^{2-}).[17] It is 14% for complexes of radii 0.77 Å (the largest covalent radii[18]) where the oxygens on the surface are apportioned as they are in the decomposition products. However, both of these coverages are unacceptable, the first because the ionic carbon–oxygen bond is unlikely as is CO and CO_2 from a one-oxygen complex, and the second because it is too small to be of much influence in physical adsorption in general.

A more reasonable model of the molecular nature of the carbon substrate can be obtained from the following. The crystallites in a black particle consist of parallel sheets of carbon atoms in a hexagonal arrangement. The sheet spacings are larger than in graphite and the layers are oriented randomly about their perpendicular axis.[4a] A crystallite, then, can present only a basal face—one consisting of the carbons in a sheet, or an edge face—one consisting of carbons in edge sheets. The indication from electron optical–combustion studies[19] is that a number of blacks fit a concentric crystallite model. The less organized carbon in the interior, small crystallites and single layers, oxidizes preferentially leaving an outer shell of larger, more perfect crystallites. Here the surface crystallites are oriented with basal faces outward. However, the channel black, *e.g.*, Spheron-6, did not fit this model. It was found to have a "spongy" mode of oxidation and consequently in the study[19] no proposal was made on the crystallite orientation in its surface. It apparently has the same type of crystallites throughout. Graphitized blacks, Graphon being this form of Spheron-6, have virtually all basal faces in their surface.[20] These are homogeneous in physical adsorption,[4b] burn down evenly without developing porosity,[21] and fix little oxygen.[12] Spheron-6, which is heterogeneous to about the same degree with oxygen as without, develops porosity and fixes large quantities of oxygen.

This suggests that the properties of Spheron-6 can be accounted for by a surface with considerable crystallite edges exposed. Further, it seems reasonable that the edge atoms are the complex binding sites since the basal faces should have no free valences. This last is borne out by Hennig's report that only the layer edges of bulk graphite single crystals bind oxygen.[22]

The coverage is 83% for one oxygen complex per edge (8.25 $Å^2$ as for graphite)[23] or 68% if complexes containing two oxygens are included as found in the products. The latter seems most likely of the four possibilities, especially considering the functional groups shown by chemical tests (see below). Estimates of others run from one-third[24] to a virtually complete monolayer[3,25] to a multilayer.[26] In these estimates of others, either the binding site type or functional group information was not considered, or some oxygen was assumed to be inside the particle.

This model also indicates that the total bound oxygen is a measure of the number of edges in the surface, 68% here, the balance being basal faces. The edge count may be low if the surface is not oxygen saturated, if other than closest packing occurs, or if the layer separations are very much wider than for graphite. It

(14) G. G. Fedorov, Y. A. Zarif'yants, and V. F. Kiselev, *Russ. J. Phys. Chem.*, **37**, 1267 (1963).

(15) M. H. Polley, W. D. Schaeffer, and W. R. Smith, *J. Phys. Chem.*, **57**, 469 (1953).

(16) We are indebted to Professor W. H. Wade and Mr. A. C. Falk for this determination. The areas found by the BET nitrogen method were 133 and 115 m^2/g for the untreated and treated (1000–1100°) blacks, respectively. These are higher than those in some reports (for example, reference 6 and references therein), but the value for the parent black is within the limits for this type [M. L. Studebaker, *Rubber Chem. Technol.*, **30**, 1430 (1957)]. The variation is undoubtedly due to fluctuation in the manufacturing process as a representative of the company has pointed out (personal communication).

(17) F. A. Cotton and G. Wilkinson, "Advanced Inorganic Chemistry," Interscience Publishers, Inc., New York, N. Y., 1966, p 45.

(18) P. W. Allen and L. E. Sutton, *Acta Cryst.*, **3**, 46 (1950).

(19) F. A. Heckman and D. F. Harling, *Rubber Chem. Technol.*, **39**, 1 (1966).

(20) (a) D. Graham and W. S. Kay, *J. Colloid Sci.*, **16**, 182 (1961); (b) C. E. Hall, *J. Appl. Phys.*, **19**, 271 (1948).

(21) W. R. Smith and M. H. Polley, *J. Phys. Chem.*, **60**, 689 (1956). See also ref 19 for further evidence on this.

(22) G. R. Hennig in "Proceedings of the 5th Conference on Carbon," Vol. 1, The Macmillan Company, New York, N. Y., 1962, p 143.

(23) This approach was suggested by that which Laine, *et al.*, made on Graphon (ref 12).

(24) J. J. Kipling and P. V. Shooter, *J. Colloid Interface Sci.*, **21**, 238 (1966).

(25) E. H. M. Wright, *J. Chem. Soc.*, 3348 (1965).

(26) R. B. Anderson and P. H. Emmett, *J. Phys. Chem.*, **56**, 756 (1952).

may be high if much of the water lost at 150° is from lactone formation or if much of the CO_2 comes from lactols (see below).

However, the major cause of a low count would be the occupation of edges by hydrogens. Most of the hydrogen is in the interior of the black particles because: (1) it comes from the starting material;[4a] (2) its major appearance region correlates well with the onset of particle reorganization shown by a large area drop and beginnings of atomic rearrangements that end in graphitization;[27] (3) it appears after completion of oxide decomposition, thus suggesting a separate process; (4) inclusion of hydrogen-filled edges together with those occupied by oxygen complexes results in more edges than the surface can accommodate. The highest hydrogen evolution obtained, 1.82 mmoles/g and still incomplete, implies a surface with 68% edges without considering any oxygen complexes present. Finally, the edge count should not be much higher than estimated since a highly ordered surface having only edges is improbable.

Alteration of Surface Groups and Substrate as Pyrolysis Proceeds. At highest coverage it would be expected, *a priori*, that the relatively stable simple groups—carboxylic, carbonyl, phenolic, and ether—are present as well as groups formed by their interaction: anhydride, lactone, and lactol. Direct chemical analyses on Spheron-6[28] confirm all except the ether, anhydride, and lactol for which tests were not made. These may be present, however, since they have been reported on other carbons.[7] Additional groups have been proposed, but it is unnecessary to consider them here.[29] Infrared data support the reagent identification of most of the familiar groups.[30] Other possibly relevant areas—epr,[31] thermal decompositions in liquid (solution)[32] or bulk phases,[33] and physical adsorption of gases[4b]—provide little help at this time.

A likely sequence of paths for decomposition of noninteracting groups is shown in Figure 4. In this model the number of oxygen atoms in the gaseous product equals that in the parent functional group, somewhat as Rivin[28a] or Puri and Bansal[11] have suggested. The water could only be bound by hydrogen bonding to the groups, thus its main appearance below 150°. The hydrogen in all but one of the groups must remain on the surface and appear with that from the interior.

The carboxylic and aldehyde steps should require relatively little energy since only bonds to edges are broken. The prevalence of CO_2 at this stage indicates that most such groups are carboxylic. The remaining steps should occur only when an edge carbon has sufficient energy to break out of the lattice. The fixed location of the CO maximum at high temperature on all the carbons plus the other CO pattern similarities suggests that this decomposition is predominantly from one category of groups. This is much like the

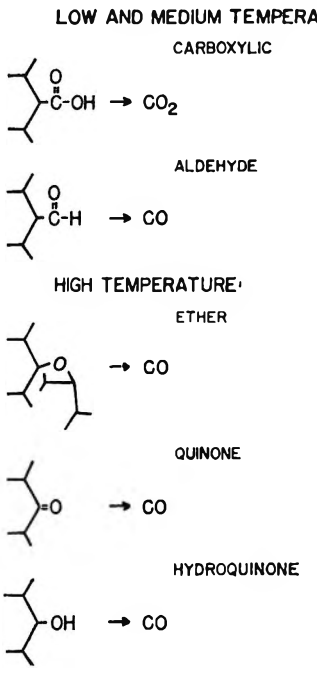

Figure 4. Decomposition of isolated surface groups.

first charcoal maximum for CO_2 (Figure 2) which indicates $ZnCO_3$ decomposition. The quinone–hydroquinone groups together fit this better than the ether since they have been positively identified by different workers and different methods. Further, as over half the product was CO, this is the category at highest concentration on the surface. The alteration of CO_2 pattern characteristics with carbon type, however, cannot be ascribed to isolated group decomposition.

The steps proposed in Figure 5 account for the main deficiencies of the isolated group model. When pos-

(27) N. N. Avgul, in "Surface Chemical Compounds," A. V. Kiselev, Ed., English Translation: AEC-tr-3750, U. S. Atomic Energy Commission, 1959, p 34.

(28) Qualitative and quantitative analyses have been made by: (a) D. Rivin, *Rubber Chem. Technol.*, **36**, 729 (1963). Strictly, however, this analysis was made by combining chemical test data with the totals for decomposition products. (b) W. J. de Bruin and T. van der Plas, *Colloq. Nationaux Centre Natl. Rech. Sci.* (Paris), No. 24, 83 (1963).

(29) (a) Oxidation in the presence of acid (D. Rivin in ref 22, Vol. 2, p 199; see also references in footnote 7) yields groups which bind acids. However, this carbon was not so treated here. (b) B. R. Puri (*ibid.*, Vol. 1, p 165, for example) proposes a CO_2 group unlike those in bulk phase chemistry.

(30) For example: R. N. Smith, D. A. Young, and R. A. Smith, *Trans. Faraday Soc.*, **62**, 2280 (1966).

(31) For example, A. Charlier, P. Taglang, J. B. Donnet, and J. La Haye, *Carbon*, **3**, 231 (1965).

(32) Decarboxylation and decarbonylation take place at 150–200°: C. F. H. Allen, *Chem. Rev.*, **37**, 209 (1945); **62**, 653 (1962).

(33) (a) Decomposition kinetics for crystals in general (P. M. W. Jacobs and F. C. Tompkins in "The Chemistry of the Solid State," W. E. Garner, Ed., Butterworth and Co. Ltd., London, 1955, Chapter 7) indicates there is no specific pattern associated with a given bond type, and the mechanism—nucleation, etc.—is not applicable to this surface. (b) The products from thermal decomposition of a carbon–oxygen polymer of known structure vary with the particular thermal path taken [A. R. Baker and A. F. Hyde, *Trans. Faraday Soc.*, **60**, 1775 (1964)].

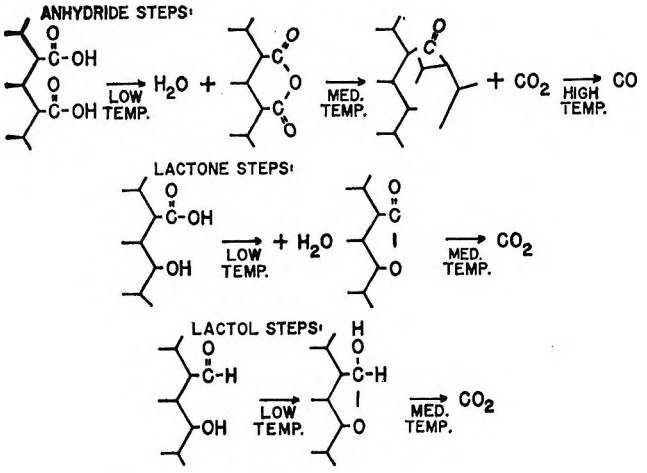

Figure 5. Interacting groups: decomposition paths.

sible, adjacent groups react at low temperatures to form species that detach from the substrate at higher temperatures. At low coverages isolated group decomposition should prevail. Thus, the CO_2 patterns would depend on predominant path, which is controlled by the total oxygen and the number and arrangement of simple groups on carbon. All of the water appearing above 150° and some of it below would be from the anhydride and lactone steps. Additions of these interacting group paths make it possible to account for the bulk of the information. There are, however, the uncertainties mentioned earlier from the two paths where products have different numbers of oxygen atoms from the initial reactions and from the drying temperature which affects the estimate of anhydride and lactone groups.

The state of the edges at the end of a temperature step must be such that heterogeneity[4b] is maintained and, unlike freshly ground graphite[14] or a charcoal,[10] there is no oxygen chemisorption at 25°. For this the unpaired electrons could variously bond with those in an adjacent sheet, form five-membered rings in the same sheet, or pair with a hydrogen left as a functional group decomposes. Some may form stable radicals similar to those found for carbons by epr. In contrast to the other carbons, Spheron-6 cooled slowly after its surface was formed or disrupted and has no ash to fix oxygen or catalyze fixation.[7b,10]

Analysis of Assumptions Involved in the Model. The most important assumption made in associating products and patterns with specific surface groups is that significant interconversion (CO oxidation, CO_2 reduction) does not occur as a product is formed. Interconversion in the surface by diffusing species appears to be ruled out by a report[34] of immobile carbon oxides. The alternative of desorption from the interior of the particle is unlikely since there is sufficient room for the oxygen on the surface, only surface groups would affect gas or solution adsorption, and the oxygen is picked up when the particle cools down after its formation.[4a] Finally, it appears that surface conditions causing alteration of bond length and strain do not change the groups to the point that a continuous distribution of types, as suggested for other surfaces,[35] would be more appropriate.

A detailed analysis of the conversion question is necessary since the previous ones[5,11,28a] are conflicting and cursory. The values of log K_p for the over-all reaction, $CO_2 + C \rightleftarrows 2CO$[36] are -5.72 at 327°, -1.97 at 527°, and 0.28 at 727°. Thus, oxidation is favored at low temperature and reduction at high; this fits the product appearance order. However, the values are small and the sign changes in the region where most decomposition occurs.

As for kinetics, very little of the extensive, related literature[7b,36] seems pertinent because the factors of surface area, difference in carbon types or surface states, and ash catalysis[37] were not considered. Also, the fact that even small amounts of oxygen, present as an impurity in the reactant gases, could yield more product than the reactions was evidently frequently ignored.[38] For the oxidation the only apparent report[38] indicates that at 280–350° it took 11 days for 1.1% of CO_2 to be produced from 1 atm of CO in contact with a nuclear graphite. This eliminates the CO conversion on Spheron-6 since in our experiments pressures were much lower and only 3 days at most were spent at any given temperature. Ergun's study is the most definative on the reduction.[39] His values for the equilibrium constant, ratio of rate constants k_f/k_b, for the reaction $CO_2 + C \rightleftarrows CO + C(CO)$, are only 0.025 at 700° and 0.1 at 800°. Further, it appears that CO retards the reaction of CO_2 with the surface. These results from measurements made at 1 atm are supported by similar work on nuclear graphite where it took 1 day to get 0.70% CO at 800°.[38] Consequently, the kinetic information indicates this conversion was also unlikely under our conditions.

In the decomposition data, the variation of CO_2 patterns with carbon type suggest no interconversion. So does the fixed CO/CO_2 ratio for both the slow decomposition method and the fast decomposition method (the runs where temperature was changed from room to 1000° in about 3 hr), the appearance of only one product, CO_2, from a charcoal previously oxidized,[29b] and

(34) J. B. Marsh and H. E. Farnsworth, *Surface Sci.*, 1, 3 (1964).

(35) P. Y. Hsieh, *J. Catalysis*, 2, 211 (1963).

(36) P. L. Walker, Jr., F. Rusinko, Jr., and L. G. Austin, in *Advan. Catalysis*, 11, 133 (1959). Reference conditions: 18°, 1 atm, and β graphite.

(37) W. K. Lewis, E. R. Gilliland, and H. Hipkin, *Ind. Eng. Chem.*, 45, 1697 (1953), for example.

(38) J. W. Brightwell, *U. S. At. Energy Comm.*, GCM/UK/23, 1 (1961).

(39) S. Ergun, *J. Phys. Chem.*, 60, 480 (1956).

the apparently complete separation of CO and CO_2 evolution on Graphon.[12] The CO similarities support interconversion. All things considered, it appears that interconversion did not obscure the decompositions.

Acknowledgment. We are very grateful to The Robert A. Welch Foundation of Houston, Texas, whose generous support made this research possible. We wish to thank the Cabot Corporation for the Spheron-6. Fellowship support for M. T. C. by the Procter and Gamble Company is gratefully acknowledged.

Spectroscopic Studies of Isotopically Substituted 2-Pyridones

by Robert A. Coburn

Army Materials and Mechanics Research Center, Watertown, Massachusetts 02172

and Gerald O. Dudek

Department of Chemistry, Harvard University, Cambridge, Massachusetts 02138 *(Received August 16, 1967)*

The pmr spectrum of 2(1H)-pyridone-^{15}N provides direct evidence, at low temperatures, of the pyridone form predominating over the hydroxypyridine tautomer by greater than 50:1 in deuteriochloroform solution. The exchange of the enolizable proton appears to be unusually facile under these conditions. Infrared spectra of 2(1H)-pyridone-^{15}N, 2(1H)-pyridone-1-*d*, 2(1H)-pyridone-1-*d*-^{15}N, 2(1H)-pyridone-^{18}O, 2(1H)-pyridone-1-*d*-^{18}O, 1-methyl-2(1H)-pyridone-^{15}N, and 1-methyl-2(1H)-pyridone-^{18}O in solution are reported. Isotopic spectral shifts suggest a revision of previous vibrational assignments and reveal unsuspected anomalous solvent and concentration effects. Implications bearing on molecular structure are discussed.

The infrared absorption spectra of 2-pyridones and secondary amides, in general, have presented a vexatious problem to those who would desire to obtain molecular bonding parameters from such data. Assignments of vibrations are hampered by strong intermolecular interactions as well as extensive coupling of vibrations.[1] A study of the infrared spectra of normal and isotopically substituted benzamides by Kniseley and coworkers[2] gives an indication of the scope of spectral changes which can be produced in amides by changes in state and nitrogen-15 or deuterium substitution. In spite of this, the phase in which such spectra are recorded is often neglected.

Important spectral changes occur with 2-pyridones when proceeding from the solid state[3] (helix) to solutions with nonpolar solvents[4] (dimer) and finally to polar solvents or high dilution in less-polar solvents such as chloroform (hydrogen-bonded monomer). The existence of 2-pyridone in the lactam form is supported by electronic absorption studies,[5] infrared studies,[6] ionization-constant determinations,[7] and pmr data.[8] In view of the classical aromatic properties of 2-pyridones, significant participation of resonance structures such as II and III have been invoked by a number of authors,[6c,7] while others[6d] have argued against a large contribution from them. The data desirous from infrared spectra

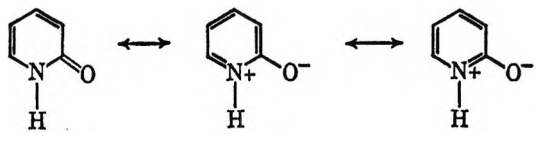

I II III

bearing on this facet of the molecular structure would

(1) L. J. Bellamy, "The Infra-Red Spectra of Complex Molecules," John Wiley and Sons, Inc., New York, N. Y., 1964, pp 203–233.

(2) R. N. Kniseley, V. A. Fassel, E. L. Farquhar, and L. S. Gray, *Spectrochim. Acta*, **18**, 1217 (1962).

(3) B. Penfold, *Acta Cryst.*, **6**, 591 (1953).

(4) (a) M. H. Krackov, C. M. Lee, and H. G. Mautner, *J. Am. Chem. Soc.*, **87**, 892 (1965); (b) G. G. Hammes and H. O. Spivey, *ibid.*, **88**, 1621 (1966).

(5) H. Specker and H. Gawrosch, *Ber.*, **75**, 1338 (1942); V. I. Bliznyukov and V. M. Reznikov, *J. Gen. Chem. USSR*, **25**, 1735 (1955).

(6) (a) P. Sensi and G. G. Gallo, *Ann. Chim.* (Rome), **44**, 232 (1954); (b) A. Albert and E. Spinner, *J. Chem. Soc.*, 1221 (1960); (c) A. R. Katritzky and R. A. Jones, *ibid.*, 2947 (1960); (d) E. Spinner and J. C. B. White, *ibid., Sect. B*, 991 (1966).

(7) A. Albert and J. N. Phillips, *ibid.*, 1294 (1956).

(8) J. A. Elvidge and L. M. Jackman, *ibid.*, 859 (1961).

provide information concerning the natures of the C–O, C–N, and, possibly, N–H bonds. We report here infrared and pmr studies of isotopically substituted 2-pyridones, vibrational assignments which differ from those previously proposed, and implications concerning molecular structure.

Experimental Section

2-Pyridone was obtained from the Aldrich Chemical Co. and was purified by repetitive sublimation and dried over anhydrous phosphorus pentoxide. 2-Pyridone-^{15}N was prepared according to the procedure of Stetten and Schoenheimer[9] from coumalic acid and ammonium chloride containing >95 atom % nitrogen-15 (Bio Rad Laboratories).

2-Pyridone failed to incorporate oxygen-18 when heated to 100° for 24 hr in 90 atom % oxygen-18 enriched water, with or without the presence of an acid catalyst. Therefore, 2-pyridone-^{18}O was prepared from 2-aminopyridine in the following manner. Sodium nitrite (36 mg, 0.514 mmol) in 0.1 ml of 93.7 atom % oxygen-18 enriched water was slowly added to a solution of 2-aminopyridine (47 mg, 0.5 mmol) and fuming sulfuric acid, 30% SO_3 (85 mg) in 0.4 ml of oxygen-18 enriched water which was cooled in an ice bath. The reaction mixture was allowed to stand for $^1/_2$ hr at 0° then for 2 hr at room temperature. After refluxing for 3 hr, the cooled solution was neutralized with 10% sodium bicarbonate solution and the solvent was removed by distillation. Repeated extraction of the residue with chloroform and evaporation of the combined extracts gave crystals of 2-pyridone. Recrystallization from carbon tetrachloride and sublimation provided 23.7 mg (50% yield) of white crystals of 2-pyridone, identical in melting point and mixed melting point with that of an authentic sample. From the ratio of 97 to 95 (m/e) in the mass spectrum of this sample, the oxygen-18 content was found to be 67 atom %.

Deuterated samples of 2-pyridone were obtained by repetitive treatment with a tenfold excess of >99.7 atom % deuterium enriched water followed by sublimation. Greater than 95 % deuteration of the 1-position was estimated from the 3600–2000-cm^{-1} region of the infrared spectrum.

The isotopically substituted N-methyl-2-pyridones were obtained from the correspondingly substituted 2-pyridones by treatment with a freshly distilled ethereal solution containing a fivefold excess of diazomethane. The reaction solution was maintained at 0° for 24 hr. Evaporation of solvent at reduced pressure and drying under vacuum yielded an oil which exhibited properties (tlc, ultraviolet absorption, etc.) identical to those of an authentic sample of N-methyl-2-pyridone.[10] Presumably, any 2-methoxypyridine formed under these conditions[11] is lost during the workup, since it could not be detected in the ultraviolet spectrum or by chromatographic means.

Solvents were carefully dried before each determination, and only fresh solutions were used. In the case of samples prepared for pmr studies, transfers of solids were conducted in a drybox and solvents distilled under nitrogen from their drying agents (anhydrous phosphorus pentoxide, in most cases) directly into sample tubes which were then degassed and sealed.

Infrared spectra were recorded with a Cary-White Model 90 infrared spectrophotometer. The band width was set to 2.5 cm^{-1} or less and spectra recorded in triplicate where applicable. Determinations of frequency generally agreed within 1 cm^{-1}. Solutions were recorded in 0.2-mm sodium chloride, 0.5-mm potassium bromide, 0.02-mm calcium fluoride, and 0.2-mm Irtran compensated cells.

Pmr spectra were recorded with a Varian A-60 spectrometer operating at 60.00 MHz. The chemical shifts were determined by interpolating between side bands of tetramethylsilane (internal) generated by an audiooscillator continuously monitored by a frequency counter. The variable temperature probe was calibrated by measuring the shift between the resonances of methanol. The chemical shifts are accurate to ±0.01 ppm, the spin couplings to ±0.2 Hz, and the temperature to ±1°.

Association studies were conducted using a Mechrolab Model 301A vapor-phase osmometer. Apparent molarities were determined for dry, alcohol-free chloroform solutions of 2-pyridone of known concentrations. Purified benzophenone in the same solvent was used to establish a calibration factor *vs.* concentration curve. Concentrations in the range 0.07–0.005 m were studied.

Results

Table I contains the infrared data for 2-pyridone, 2-pyridone-^{15}N, and 2-pyridone-^{18}O. Also indicated are solvent effects. The 4000–2000-cm^{-1} region has been discussed at length by Bellamy and Rogasch[12] and is not considered here. Deuteration of 2-pyridone was found to produce such extensive changes in the solution spectra that the infrared data for the deuterated normal, nitrogen-15, and oxygen-18 substituted 2-pyridones are listed separately in Table II.

Discussion

No attempt will be made to provide a complete vibrational assignment, although a number of previous assignments are questionable. For instance, the 1477- and 1443-cm^{-1} bands have been assigned to skeletal stretching;[6c] however, the sensitivity of these bands to changes in state, solvent, and isotopic substitution (they disappear entirely upon deuteration) render this

(9) M. R. Stetten and R. Schoenheimer, *J. Biol. Chem.*, **153**, 113 (1944).

(10) E. A. Prill and S. M. McElvain, "Organic Syntheses," Coll. Vol. II, John Wiley and Sons, Inc., New York, N. Y., 1943, p 419.

(11) N. Kornblum and G. P. Coffey, *J. Org. Chem.*, **31**, 3447 (1966).

(12) L. J. Bellamy and P. E. Rogasch, *Proc. Roy. Soc.* (London), **A257**, 98 (1960).

Table I: Infrared Data for Normal, ^{15}N, and ^{18}O 2-Pyridone

2-Pyridone[a] ν, cm^{-1}	ϵ	$\Delta\nu_s$[b]	$\Delta\nu$[c] for ^{15}N	$\Delta\nu$[d] for ^{18}O	$\Delta\nu$[e] for d
1682[f]	340	−9	−7		−15
1658	1200	−2	−5	−7	−10
1620	335	−2, −5[g]	−3	−2	−40[i]
				1604[f]	
1544	140	−2	−2	−6	−5
1477	96	−7 (−14)[h]	−5	...	...
1443	104	−4 (−23)[h]	−2	−4	...
1374	32	..	...	...	...
1251	88	+1	−10	...	...
1228	26	...	−4	...	...
1151	60	...	...	+3	...
1097	12	...	−6	...	...
1007[f]					
991	140	+2	−7	...	−11
922	50	+1	...	...	...
845	30	...	...	...	...
767	290		...		
723	135		−2		−39
611	20		−3		−3
558	170		...		−2
511	135		...		−4
494	160		−4		−4

[a] Data reported for carbon tetrachloride solution and, below 800 cm^{-1}, for carbon disulfide solution. [b] Solvent shift in dry, alcohol-free chloroform. [c] Determined from carbon tetrachloride solution spectra for the first seven peaks, the remaining from carbon disulfide solution spectra. [d] Determined by comparison of chloroform solution spectra. [e] See Table II for details. [f] Shoulder. [g] Broad peak at low concentrations. [h] Solvent shift in aqueous solution. [i] Value is approximate.

Table II: Infrared Data for Normal, ^{15}N, and ^{18}O 2-Pyridone-1-*d*

2-Pyridone-d_1[a] cm^{-1}	ϵ	$\Delta\nu$ for ^{15}N	$\Delta\nu$ for ^{18}O
1667[b]	400	−4	...
1658[b]	570	...	...
1648	1000	−2	...
1586	730	−2	−14
1575[b]		−3	−17
1539	150	−4	...
1310	120	−15	...
1156[b]	30	...	...
1148	110	...	+2
980	150	−7	−2
964[b]	70	...	...
847	75	...	...

[a] Data were determined from carbon tetrachloride solution spectra in all cases. [b] Shoulder.

assignment doubtful, as already noted by Spinner and White.[6d] For the present study, interest is centered on the 2000–1000-cm^{-1} region.

The great difference between the solution spectra of 2-pyridone and 2-pyridone-d_1 is readily apparent. The latter bears a much greater resemblance to that of 2-pyridone in the solid state[6d] or N-methyl-2-pyridone. Undoubtedly, this is due to effects centered about the N–H bond. In the case of 2-pyridone itself, the 1658-cm^{-1} band varies from 1649–1641 cm^{-1} in the solid state[6d] to 1673 cm^{-1} in dilute solution in chloroform.

Table III: Infrared Data for Normal, ^{15}N, and ^{18}O N-Methyl-2-pyridone

N-Methyl-2-pyridone,[a] cm^{-1}	$\Delta\nu$ for ^{15}N	$\Delta\nu$ for ^{18}O
1659 s	−2	−4
1599[b] m	...	...
1583 s	...	−11
1541 m	−2	...
1411 w	−3	...
1384 w	−3	...
1316 m	−14	...
1290 w	...	...
1240 m	...	...
1182 w	...	...
1154	−5	...
1051 m	...	...
876 m	−3	−8
844 m	−2	...

[a] Data were determined from chloroform solution spectra in all cases. [b] Shoulder.

Chloroform as a solvent is particularly interesting, since both dimer and monomer can be observed in the same medium. Vapor-phase osmometric measurements indicate that the per cent dimer varies from *ca.* 90 to 40% over the concentration range whose infrared spectrum can be determined conveniently, *i.e.*, 0.001–0.2 *m*. At low concentrations, the small shoulder at 1673 cm^{-1} becomes equal in intensity to the 1656-cm^{-1} peak (*ca.* 0.003 *m*). At concentrations below 0.001 *m*, the 1673-cm^{-1} peak is the most prominent peak in the spectrum (the 1656-cm^{-1} peak decreases proportionately). In dimethyl sulfoxide, the higher frequency peak at 1668 cm^{-1} is also the most intense.

These results are in accord with the results of Bellamy and Rogasch,[13] who found that the 1659-cm^{-1} band of N-methyl-2-pyridone varies from 1698 cm^{-1} in the vapor state to 1658 cm^{-1} in methylene iodide solution. On this basis, they assigned this band to the carbonyl stretching vibration. Although solvent effects on band frequency and intensity strongly support this contention for both 2-pyridone and its N-methyl derivative, the isotopic results reported here indicate an interesting alternative explanation. (See Table III).

Extensive coupling of carbonyl stretching, carbon–carbon double bond stretching, carbon–nitrogen stretching, and nitrogen–hydrogen in-plane bending modes is

(13) L. J. Bellamy and P. E. Rogasch, *Spectrochim. Acta*, **16**, 30 (1960).

apparent. The results of this intermixing of vibrations can be seen in the first six bands listed in Table I.

As with secondary amides, ν_{CO}, ν_{CN}, and δ_{NH} would be expected to be coupled.[14] It can be noted that when δ_{NH} is removed by deuteration or methylation, the ^{15}N isotopic effect on the high-frequency bands decreases. At the same time, the ^{15}N isotopic shift of 10 cm^{-1} on what must be predominantly ν_{CN}, occurring at 1290 cm^{-1}, increases to 14 and 15 cm^{-1} for the 1316 and 1310-cm^{-1} bands of N-methyl and N-deuterio-2-pyridone, respectively. The latter isotopic shifts compare favorably with a shift of 21 cm^{-1} calculated for an isolated carbon–nitrogen stretching vibation. The conclusion is that upon removal of δ_{NH}, coupling between ν_{CO} and ν_{CN} is considerably reduced. Therefore, in the deuterated or methylated 2-pyridones, bands in the 1400–2000-cm^{-1} region represent largely a mixture of ν_{CO} and ν_{CC}'s.

Oxygen-18 substitution was employed to determine the extent of this coupling and identity of vibrations. A completely isolated carbon–oxygen stretching vibration can be calculated to produce an oxygen-18 isotopic shift of 41 cm^{-1}. Typical observed shifts are: 20–24 cm^{-1} for benzamide,[15] 27 cm^{-1} for benzoic acid in chloroform,[16] and 31 cm^{-1} for 2,4-dimethyl-3-pentanone.[17]

As expected, in 2-pyridone itself both the 1650 and 1620 + 1544-cm^{-1} bands exhibit oxygen-18 sensitivity. In the case of the simplified systems of the N-substituted 2-pyridones, *the lower frequency strong-intensity band exhibits the primary isotopic effect.* This appears to be another instance where the application of the concept of group frequencies would be entirely misleading.[18] The higher frequency band exhibits solvent effects associated with a polar oscillator, while the lower frequency band exhibits the greater sensitivity toward isotopic substitution within that same group. Certainly, one would expect a polar group vibration coupled to a nonpolar group vibration to produce an observable solvent effect. The unexpected result is the extent to which the solvent and isotope effects appear predominantly in one or the other of the two bands.

The unperturbed carbonyl stretching frequency in N-substituted 2-pyridones would lie somewhere between the 1650 and 1580-cm^{-1} bands. Correction for an electronegativity effect from the neighboring nitrogen on the carbonyl frequency would further favor a lower carbon–oxygen bond order and a greater participation of resonance forms II and III than would be implied by a heretofore accepted 1650-cm^{-1} carbonyl stretching frequency. Conversely, similar coupling in the 4-pyridones would lead to an upward revision of the carbonyl stretching frequency, since the lower frequency band has previously been assigned to the carbonyl stretching mode.[13]

Proton Magnetic Resonance Studies

Pmr studies of a number of types of compounds have shown that ^{15}N-substitution can be used to advantage in studying exchange processes in nitrogenous systems.[19] Substitution of the ^{15}N nucleus with its spin of $^1/_2$ and a ^{15}N–H coupling constant of 90 Hz in place of the ^{14}N nucleus with its quadrupole broadening allows the convenient study of exchange processes.[20]

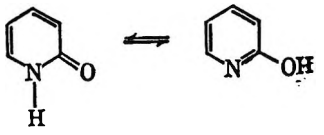

I IV

The lactam form of 2-pyridone (I) has been estimated from ionization-constant studies to predominate by 340:1 over its lactim tautomer (IV) in aqueous solution.[7] Intramolecular proton exchange between nitrogen-15 and oxygen, if slow, would allow the observation of the ^{15}N–H coupled doublet and the O–H singlet of I and IV, respectively. The relative intensities of these signals would provide a measure of the above equilibrium. More likely, the exchange is rapid.[19b] In that case, the magnitude of the observed ^{15}N–H coupling constant would provide an indication of the relative amounts of the two forms involved.[19b]

Results

The enolizable proton of 2-pyridone-^{15}N was found to resonate at δ 13.60 ± 0.01 ppm in carbon tetrachloride, deuteriochloroform, and methylene chloride. In dimethyl sulfoxide, pyridine, and acetone-d_6, the chemical shifts were δ = 11.47, 12.72, and 13.17 ppm, respectively. In all cases, a singlet was observed at room temperature, even though the solvents and samples were rigorously purified and dried. Under similar conditions, the multiplet of the hydroxylic proton of ethanol could easily be resolved.

Cooling, in the case of deuteriochloroform solution, resulted in the broadening of this signal until the coalescence point was reached at −46 ± 2°. The 90-Hz ^{15}N–H coupling constant was observed at −56°. In methylene chloride, the coalescence point was −74 ± 2° and the 90-Hz splitting was achieved at −84°.

(14) T. Miyazawa, T. Shimanouchi, and S. Mizushima, *J. Chem. Phys.*, **29**, 611 (1958).

(15) S. Pinchas, D. Samuel, and M. Weiss-Broday, *J. Chem. Soc.*, 1688 (1961).

(16) S. Pinchas, D. Samuel, and M. Weiss-Broday, *ibid.*, 2382 (1961).

(17) G. J. Karabatsos, *J. Org. Chem.*, **25**, 315 (1960).

(18) Randall, *et al.*, used ^{15}N spectral shifts to indicate the inadvisability of using the group-frequency concept in the case of tertiary amides and their complexes, E. W. Randall, C. M. S. Yoder, and J. J. Zuckerman, *Inorg. Chem.*, **5**, 2240 (1966).

(19) (a) B. Sunners, L. H. Piette, and W. G. Schneider, *Can. J. Chem.*, **38**, 681 (1960); (b) G. O. Dudek and E. P. Dudek, *J. Am. Chem. Soc.*, **85**, 694 (1963); **86**, 4283 (1964); **88**, 2407 (1966); (c) G. O. Dudek and E. P. Dudek, *Chem. Commun.*, 464 (1965).

(20) W. B. Moniz and H. S. Gutowsky, *J. Chem. Phys.*, **38**, 1155 (1963).

Limited solubility or solvent solidification precluded similar observations in other solvents.

As a check against the presence of water or other impurities, four different samples of 2-pyridone-^{15}N were each subjected to a different sequence of recrystallizations from different solvents. The samples were sublimed after each recrystallization and protected from the atmosphere during transfers. Both alcohol-free chloroform and deuteriochloroform were used as solvents and were dried and distilled directly into the sample tubes. The observed coalescence point for the four samples agreed within experimental error (±2°).

Discussion

The unusually low field resonance of the enolizable proton is evidence of the very strong hydrogen bond existing in the dimer of 2-pyridone. In fact, 2-pyridone forms one of the most stable hydrogen-bonded dimers known (excluding zwitterion structures).[4b] This is a consequence of the significant contribution of charge-separated forms II and III to the resonance structure.

The signal for the enolizable proton, appearing as a single peak of varying width depending upon solvent and temperature, can be interpreted in two ways. Either lactim IV predominates by >50:1 over lactam I or the proton in question is exchanging *intermolecularly* very rapidly, thereby being completely decoupled. The convincing ultraviolet spectral evidence[5,21] supporting the lactam structure in a wide variety of solvents argues against the first explanation.

Rapid intermolecular proton exchange could occur within the dimer followed by dissociation and re-association with different monomers, since the latter process has been shown to occur very rapidly.[4b] Another mechanism would be ionization and exchange through anionic or cationic forms. The faster exchange was observed, however, in the less polar solvent where the concentration of monomer would be expected to be smaller and ionic structures less favored. Despite the precautions taken, the catalysis of this exchange by some unknown agent cannot be excluded.

Nevertheless, the possibility of exchange occurring within the dimer is interesting, since Cannon[22] proposed the increased probability of proton transfer across the hydrogen bond in the vibrationally excited state. Bellamy and Rogasch[12] offered infrared spectral indications of this possibility in 2-pyridone. Apparently this type of exchange does not occur in a similar system, 2-hydroxyquinoline, which also has been found to exist in the lactam form, since coupling was detected between the ^{14}N nucleus and a low-field proton.[23]

At very low temperatures, the observed ^{15}N–H coupling of 90 Hz is good evidence that the relative amount of lactim IV is below 2%.[19b]

(21) 3-Hydroxyisoquinoline is an example of a similar system in which ultraviolet studies have revealed the presence of both lactam and lactim forms depending upon the solvent: D. A. Evans, G. F. Smith, and M. A. Wahid, *J. Chem. Soc., Sect B*, 590 (1967).

(22) C. G. Cannon, *Spectrochim. Acta*, **10**, 341 (1958).

(23) P. Hampson and A. Mathias, *Chem. Commun.*, 371 (1967).

Very Low Pressure Pyrolysis. III. *t*-Butyl Hydroperoxide in Fused Silica and Stainless Steel Reactors[1]

by S. W. Benson and G. N. Spokes

Department of Thermochemistry and Chemical Kinetics, Stanford Research Institute, Menlo Park, California 94025
(Received August 22, 1967)

The technique of very low pressure pyrolysis (VLPP) was applied to study the pyrolysis of *t*-BuO_2H in stainless steel and fused silica reactors over the temperature range 300–950°. Evidence was found for both unimolecular and chain-type homogeneous reactions; the chain reaction involves free ·OH radicals. Homogeneous reactions proceed very much faster than heterogeneous reactions in a fused-silica reactor. The products of the unimolecular reaction are acetone and water, together with some other low-mass ($\leq$32 amu) substances (candidates are CH_3OH, CH_2O, CO, and H_2). The chain reaction yields, in addition, isobutylene oxide with H_2O. The acetone-production data lead to a rate constant for *t*-$BuO_2H \rightarrow$ *t*-BuO + OH, in excellent agreement with lower temperature data and thermochemical estimates of a 43 kcal O–O bond. The total range covered is from 500 to 1000°K and 11 powers of 10 in the rate constant. Pyrolysis in a stainless steel reactor produces predominantly *t*-BuOH + O_2. Smaller amounts of isobutylene and some acetone are also formed. This represents a heterogeneous reaction which is much faster than the homogeneous decomposition in silica. While the wall mechanism is uncertain, the high rate points to the existence of a loosely bound, physisorbed precursor which can undergo bond cleavage with a high *A* factor and a relatively low activation energy (*i.e.*, ~10 kcal).

Introduction

Experimental studies of the homogeneous decompositions of hydroperoxides have proven difficult to interpret conclusively. Chain reactions seriously interfere with the kinetics and lead to unsatisfactory Arrhenius plots. Benson[2] applied kinetic and thermochemical reasoning to the extant hydroperoxide decomposition data and concluded that the O–O bond dissociation energies of hydroperoxides should be in the neighborhood of 43 kcal/mole. This value is in disagreement with the values of Bell, *et al.*,[3] who concluded from measurements of the heat of combustion and the pyrolysis of *t*-butyl hydroperoxide that the bond strength should be about 39 kcal/mole.

Further work has subsequently been carried out on the thermal decomposition of *t*-BuOOH by Hiatt and Irwin,[4] who studied the thermolysis in dilute solution. They found that the rate constants obtained were as much as a factor of 8 lower than those of Bell, *et al.*, with activation energies approaching 43 kcal.

We have extended measurements of the decomposition of *t*-butyl hydroperoxide to much higher temperatures, using a very low-pressure pyrolysis (VLPP) technique. From the observed rate constants and application of an appropriate correction to them, we have obtained data which support the high value of O–O bond strength in hydroperoxides.

Wall effects have often been invoked to explain unusual products, and for this reason, we have explored the effects brought about by changing the character of the walls of the reactor. *t*-Butyl hydroperoxide was thus decomposed in a stainless steel (VLPP) reactor. This resulted in a totally different product spectrum.

Experimental Procedure

Experimental procedures followed those outlined in ref 5. High purity (better than 99% by iodometry) gaseous *t*-BuO_2H was passed at the rate of about 5×10^{-9} mole/sec through a (0.5-mm i.d., 1 cm long) capillary to the reactor whose temperature was maintained at various values, up to 1000°, by means of three electrical heaters. Gas pressures in the reactors were very low so that gas–wall collisions predominated over gas–gas reactions. Gaseous products[6] were pumped from the reactor into the mass spectrometer for analysis.

The gas density in the 91-collision fused silica and 108-collision metal reactors was approximately 10^{12} molecules/cm^3, although this changed slightly as decomposition proceeded. Gas density in the 9200-collision reactor was about 100 times this value.

(1) (a) Supported in part by funds from a multisponsored project on hydrocarbon oxidation; (b) Paper II: G. N. Spokes and S. W. Benson, *J. Amer. Chem. Soc.*, **89**, 6030 (1967).

(2) S. W. Benson, *J. Chem. Phys.*, **40**, 1007 (1964).

(3) E. R. Bell, J. H. Raley, F. F. Rust, F. H. Seubold, and W. E. Vaughan, *Discussions Faraday Soc.*, **10**, 242 (1951).

(4) R. Hiatt and K. C. Irwin, submitted for publication in *J. Org. Chem.*

(5) S. W. Benson and G. N. Spokes, *J. Amer. Chem. Soc.*, **89**, 2525 (1967).

(6) No visible change occurred to the reactor's wall condition; that is, there were no carbonaceous deposits and hence no products other than gas.

Table I: Decomposition of *t*-BuO_2H in a 9200-Collision Silica Reactor

Effluent[a]	Cold[b] (~30 ± 10°)	Reactor temp, °C: 300 ± 50	400 ± 50[c]	500 ± 50	600 ± 50	750 ± 50	800 ± 50
t-BuO_2H	96 ± 4	81	26 ± 6	0	0	0	0
Acetone	4 ± 4	13	55 ± 4	96	100	100	100
Isobutylene oxide[d]	0.25	6	19 ± 2	4	0	0	0

[a] Mole per cent of C_3 and C_4 effluent. [b] The apparent presence of acetone at these temperatures is due to errors in the analysis and is representative of the magnitude of the errors to be expected. [c] Data at 400° are averaged from four experiments. [d] Per cent of isobutylene oxide may be systematically higher than quoted amounts, as discussed in text.

The cylindrical stainless steel[7] reactor was 10 cm long and had a 2.5-cm i.d.; the exit aperture was 1 cm in diameter. It was essential to keep the inlet capillary of the metal reactor below 100° to avoid catalyzed decomposition of the gases there. This cooling was accomplished by an air blast on the inlet capillary. Since the inlet end of the reactor was kept down to 100°, even though the rest of the reactor was as hot as 850°, there was a temperature gradient of about 500 deg/cm near the inlet end of the reactor.

Results

The results for each of these three reactors have been reduced in a slightly different way so that data and results for each reactor are treated separately. It has been necessary to cool both the top and the bottom of each reactor with an air blast and this has led to a rather large uncertainty in temperature, owing to the effectiveness of fairly weak drafts in affecting temperatures. About 9 of the 12 chromel–alumel couples for temperature measurement indicated a value within 20° of the central temperature, however.

Decomposition of t-BuO_2H in a 9200-Collision Fused-Silica Reactor. Gas flowing at about 3×10^{15} molecules/sec (5×10^{-9} mole/sec) was pyrolyzed in our 9200-collision fused-silica reactor. Analysis of the results obtained is given in Table I.

The stirred flow reactor equations are used in deriving the apparent first-order reaction rate. The details of treatment of data have been partly described elsewhere.[5] We may note that the average residence time in the reactor is just the reciprocal of k_e and is here typically 0.4 sec. Mass spectral data from this reactor have been analyzed by means of a computer program on the basis of five sets of peaks and intensities derived from mass spectra of (1) residual gases (*e.g.* pump oil), (2) water vapor, (3) cold parent compound, (4) acetone and associated products presumed to be the only species at 750–800°, and (5) an "unknown" substance produced at 400° whose set was derived by subtraction from the observed spectrum of appropriate amounts of sets 1–4. This unknown set resembled strongly that of isobutylene oxide. The only deficiency in this set was that the 43-amu peak was too small by comparison with our standard isobutylene oxide set (not surprising, since only a small error in acetone estimation will lead to this effect). An appropriate correction was made to this set at 43 amu and the resultant set 5 was used in the analysis. We have probably underestimated the per cent isobutylene oxide, since (in the absence of a direct calibration) we have taken the sensitivity of isobutylene oxide at 43 amu to be equal to that of acetone at 43 amu. This would probably lead to underestimation of isobutylene oxide by no more than a factor of 2. The values in Table I are, therefore, a lower limit.

If we regard the acetone produced in the 9200-collision reactor as coming from *t*-BuO, produced by unimolecular split of *t*-BuO_2H, we can use the ratio of acetone to *t*-BuO_2H as an indicator of first-order reaction rate and can construct Table II.

Table II: First-Order Decomposition Rate Constant for *t*-BuO_2H at Very Low Pressure and at Various Temperatures (T) in a 9200-Collision Fused-Silica Reactor

Temp, °K	$\phi(Me_2CO)/\phi(t\text{-}BuO_2H)$	$k_e(=0.087\sqrt{T})$,[a] sec^{-1}	k_{uni}, sec^{-1} [b]
570 ± 50	0.16	2.1	0.34
670 ± 50	2.2	2.25	4.95
770 ± 50	>10	2.4	>24

[a] k_e is the reactor escape rate constant for *t*-BuO_2H (sec^{-1}). [b] k_{uni} is the sought rate constant and is equal to $k_e[\phi(Me_2CO)/\phi(t\text{-}BuO_2H)]$ where $\phi(x)$ is the rate of flow of effluent x.

Decomposition in a 91-Collision Fused-Silica Reactor. Gas flows were about 5×10^{15} molecules/sec. Decomposition was quite clean to give acetone and associated products.[8] The per cent decomposition was followed mass spectrometrically by monitoring two mass peak

(7) The stainless steel type 304 used contains 19–20% chromium, 8–12% nickel, less than 2% Mn, and less than 0.08% P, 0.03% S, and 1.0% Si.

(8) Acetone is formed by decomposition of the *t*-butoxy radical. The $\cdot CH_3$ (from *t*-BuO$\cdot$) and $\cdot$OH from the initial step will react to yield low-mass substances which do not interfere with measurement of acetone flux.

pairs at 41 and 43 and at 57 and 58 amu. From the known sensitivities of the spectrometer to the products and parent substances, we have determined the first-order reaction rate constant of t-BuO_2H. The data are presented in Table III.

Table III: First-Order Decomposition Rate Constant[a] for t-BuO_2H at Various Temperatures (T) in a 91-Collision Fused-Silica Reactor

Temp, °K	300	673	773	873	933	958	973
k_{uni} (43–41)	0	2.7	72	550	1890	1840	2180
k_{uni} (57–58)	0	1.44	96	582	1750	2120	2980
k_{uni} (av)	0	2.07	84	566	1820	1930	2580

[a] k_{uni} (43–41) and k_{uni} (57–58) are rate constants calculated from the intensities of the 41–43 and the 57–58 amu peaks, respectively. k_{uni} (av) is the simple average of these two. For this reactor geometry the escape rate constant k_e for t-BuO_2H was $8.83\sqrt{T}$ sec^{-1}. The acetone to t-BuO_2H ratio can be derived from k_{uni} by dividing by $8.83\sqrt{T}$.

Decomposition in a 108-Collision Stainless Steel Reactor. The results obtained with the metal reactor are summarized graphically in Figure 1. The experiments were carried out with an air-cooled inlet capillary under conditions described above.

The analysis of the mass spectral data from the metal reactor was subject to some error because the stability of the mass spectrometer was insufficiently great to permit a simple analytical procedure to be adopted. Results were analyzed by use of a regression program (which minimizes the squares of the errors) using standard mass spectral sets generated by running cold t-BuO_2H, Me_2CO, H_2O, t-BuOH, and isobutylene gas through the mass spectometer. The results reflect the general pattern of the decomposition, although it is most unlikely that any significant amount of parent was left unchanged at temperatures in excess of 700°. We believe that apart from the parent concentrations at higher temperatures the stated fractions of products are probably correct within a factor of about 2.

In addition to the acetone, t-butyl alcohol, and isobutylene, there were water (detected), oxygen (not detected, owing to air background[9]), and low mass number species such as C_2H_6 (not analyzed for). (Methyl ethyl ketone and isobutylene oxide both have an appreciable 72-amu peak; the complete absence of this peak shows that they were produced in proportions less than 1%.)

Discussion

Pyrolysis in the 91- and 9200-Collision Quartz Reactors. Products of pyrolysis in the 91-collision reactor appear to be only acetone and associated lower mass number substances. The apparent first-order reaction rate constant as determined by measurements of the

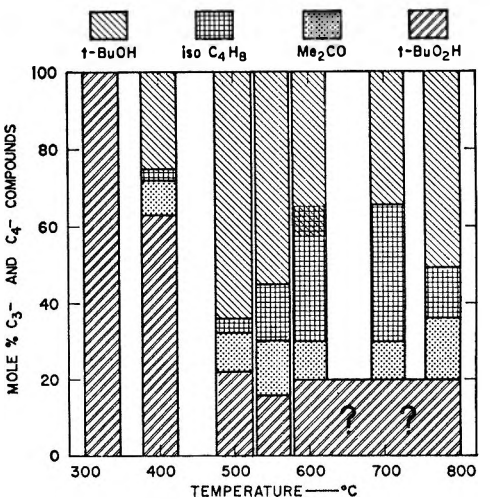

Figure 1. VLPP of t-butyl hydroperoxide in a 108-collision stainless steel reactor.

ratios of the mass peak pairs 43–41 and 57–58 agree satisfactorily, probably within experimental error. These data, together with those obtained from the 9200-collision reactor, are presented in Table IV. Also included in Table IV are high-pressure activation energies derived from these data assuming log A = 15.75 and = 15.0. The derived high-pressure activation energies take into account the fact that our experiments were conducted in the region of pressure falloff. The correction for falloff involves determining E_0 from our observed rate constants and is done by using eq 1 and 2 which have been derived from the Rice, Ramsperger, and Kassel formulation of unimolecular reactions, and whose applicability has been demonstrated elsewhere.[4,10]

$$k_{uni} = \frac{k_w}{2\sqrt{2\pi}}\left[\frac{eE_m}{(s-1)RT}\right]^{s-1}\exp(-E_m/RT) \quad (1)$$

and

$$k_w = A\left[\frac{E_m - E_0}{E_m}\right]^{s-1} \quad (2)$$

where k_{uni} is the observed apparent first-order rate constant; e = 2.7183; E_m is the mean energy required for molecular decomposition in a time $\sim k_w^{-1}$, where k_w is the frequency of wall collisions; and s is the Kassel s, the number of active oscillators in a molecule. Finally, the high-pressure Arrhenius formulation $k_\infty = A\exp(-E_0/RT)$ serves to define A and E_0.

It turns out that while eq 1 has no analytic solution, it is a simple matter to solve for E_m (given the other unknowns) by use of a slide rule with a log scale. E_0

(9) The air leak did not affect the chemistry of the processes being described, since it was from the atmosphere direct into the mass spectrometer and not through the reactor.

(10) S. W. Benson and G. N. Spokes, 11th International Symposium on Combustion, The Combustion Institute, Pittsburgh, Pa., 1967, p. 95

Table IV: Derivation of Effective High-Pressure Activation Energies from Experimental VLPP Data on t-BuO_2H[a]

Temp, °K	570	670	673	773	873	933	958	973
k_{uni}, sec^{-1}	0.34	4.95	2.07	84	566	1820	1930	2580
s	22	23	24	26	29	31.5	32.6	33
E_m, kcal/mole	54	60.5	62.5	64.5	69.6	75.4	78.8	76.2
E_0, kcal/mole								
Log A = 15.75	38.0	41.3	42.7	42.0	42.3	43.4	44.3	42.7
Log A = 15.0	36.5	39.7	41.0	40.3	40.6	41.3	42.5	41.2

[a] Runs at 570 and 670°K were made in the 9200-collision reactor, the others in the 91-collision reactor. k_{uni} is the experimentally observed first-order decomposition rate constant. s is the effective number of molecular oscillators (s is equal to $\frac{1}{2}(C_p - 8)$; C_p was determined from group values which we have generated). E_m is the critical energy in the t-BuO_2H molecule which leads to decomposition in a time roughly equal to the time between wall collisions. E_0 is the activation energy deduced from our experimental data using eq 1 and 2, the only assumptions being (i) the molecules were fully equilibrated to the stated temperature and (ii) the Arrhenius A factor was either $10^{15.75}$ or $10^{15.0}$.

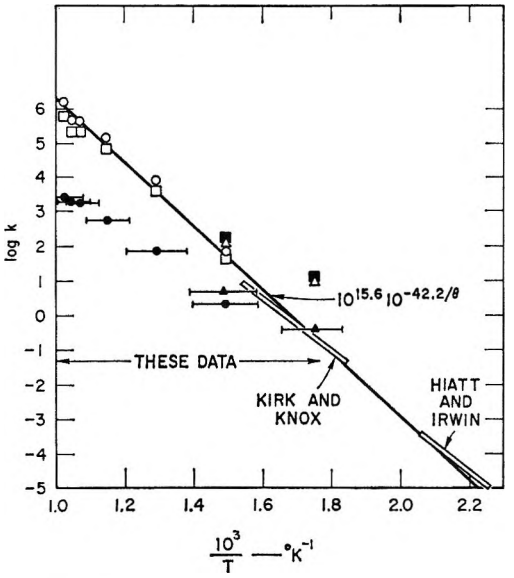

Figure 2. Arrhenius plot of VLPP data for t-butyl hydroperoxide: ⊢●⊣, experimental data points with 91-collision reactor; ⊢▲⊣, experimental data points with 9200-collision reactor; ○, data of 91-collision reactor corrected for falloff assuming log A = 15.75; □, data of 91-collision reactor corrected for falloff assuming log A = 15.0; ■, data of 9200-collision reactor corrected for falloff assuming log A = 15.75; △, data of 9200-collision reactor corrected for falloff assuming log A = 15.0. The data of Kirk and Knox and of Hiatt and Irwin are included for comparison.

is then deduced from relation 2. Figure 2 presents experimental rate constants along with those obtained by using the Arrhenius formulation with the derived values for E_0. Data of Kirk and Knox[11] and Hiatt and Irwin[4] are also given in Figure 2 for comparison. We see that our corrected data fall on a line corresponding to a high-pressure rate constant equal to $10^{15.6\pm0.5}\,10^{-(42.2\pm2)/RT}$ sec^{-1}. These Arrhenius parameters are consistent with data obtained by the different techniques used in work reported in ref 4 and 11. In addition these parameters are consistent with the thermochemistry as deduced by use of group values for heats and entropies of the relevant species involved.[12]

It is, of course, presumed that the reaction proceeds by the simple mechanism

$$(CH_3)_3COOH \longrightarrow (CH_3)_3CO\cdot + \cdot OH$$

$$(CH_3)_3CO\cdot \longrightarrow (CH_3)_2CO + \cdot CH_3$$

$$(CH_3)_2CO \longrightarrow \text{escapes to mass spectrometer}$$

$$\cdot OH \text{ and } \cdot CH_3 \longrightarrow \text{escape to the mass spectrometer and lead to low mass number products, } e.g., C_2H_6,\ H_2O,\ CH_3OH$$

Chain reactions are ruled out in the 91-collision reactor because molecules make on the average only 1 gas–gas collision per 100 wall collisions.

Pyrolysis studies in the 9200-collision quartz reactor were complicated by the appearance of isobutylene oxide as well as acetone. These known products of the chain decomposition can be explained by secondary reactions of HO· and Me·

$$\cdot OH \text{ (or } \cdot CH_3) + (CH_3)_3CO_2H \longrightarrow \cdot CH_2C(CH_3)_2O_2H + H_2O \text{ (or } CH_4)$$

$$\cdot CH_2{-}\overset{O_2H}{\overset{|}{C}}(CH_3)_2 \longrightarrow H_2C{-}\overset{O}{\diagup\diagdown}C(CH_3)_2 + \cdot OH \longrightarrow H_2C{=}C(CH_3)_2 + HO_2\cdot$$

The isobutylene oxide is identified primarily by its contribution to mass peak 72 amu. (All mass peaks

(11) A. D. Kirk and J. H. Knox, *Trans. Faraday Soc.*, **56**, 1296 (1960).

(12) Values used differ slightly from those of Benson (*J. Chem. Phys.*, **40**, 1007 (1964)), inasmuch as we have used +9.3 kcal/mole for ΔH_f^{298} of ·OH and −22 kcal/mole for ΔH_f^{298} of t-BuO. The data of Kirk and Knox may have been affected by reason of the rather short residence time at their highest temperatures. This would lead to an anomalously low reaction rate at these temperatures, owing to the slowness of heat transfer between walls and gas.

corresponding to isobutylene oxide were included in the computer analysis of the data.)

For the chain decomposition reaction to proceed, ·OH free radicals must survive several collisions with the quartz reactor walls. The depletion of parent compound by the competing unimolecular reaction path leads to a continual drop in the rate of chain reaction, in accord with our observations that the amount of the secondary reaction falls to a low value at higher temperatures.

Pyrolysis in the 108-Collision Stainless Steel Reactor. The change in product spectrum and the increased rate of reaction in the stainless steel reactor is quite dramatic.

The mechanism of the decomposition in the 108-collision metal reactor is not certain. There are (as in the case of the 91-collision silica reactor) very few gas–gas collisions and, therefore, we can ignore contributions by gas–phase chain reactions. An adequate mechanism must account for (1) the completely different product spectrum, (2) the production of isobutylene, (3) the production of acetone, and (4) the complex variation of product distribution with temperature. Furthermore, the high probability of reaction per gas–wall collision imposes special constraints on the reaction mechanism. Thus at 450° the decomposition in the stainless steel reactor (Figure 1) leads to about 50% decomposition after 108 collisions for a collision efficiency of approximately 1 in 46. If we interpret such a collision efficiency from the point of view of a bimolecular reaction with a specific wall site and allow a mean roughness factor of 2, then it implies either a steric factor of 1 and 6 kcal of activation energy or else zero activation energy and a steric factor of 10^{-2}. Either of these steric factors is unreasonably large for so large a molecule as t-BuO_2H.

The alternative to a direct bimolecular event is a precursor, physisorbed state, which can competitively dissociate or reevaporate

$$t\text{-BuO}_2\text{H(g)} \underset{-1}{\overset{1}{\rightleftarrows}} t\text{-BuO}_2\text{H(S)}$$

$$\text{O}^{2-}\text{(S)} + t\text{-BuO}_2\text{H(S)} \xrightarrow{2}$$

$$t\text{-BuO}_2^{-}\text{(s)} + \text{HO}^{-}\text{(S)} \text{ (or } t\text{-BuO}^{-} + \text{HO}_2^{-}\text{)}$$

If reaction 2 is irreversible, it can account for the high collision efficiency if its rate is $10^{-2}k_{-1}$. Since k_{-1} and k_2 are essentially unimolecular acts involving simple bond breaking, they can readily have similar A factors. Hence the activation energy of step 2 need only be 6 kcal larger than the heat of reevaporation to account for the data. A reasonable value of ΔH_1 is probably around 15 kcal, so that a value of $E_2 = 21$ kcal would be implied and is not unreasonable.

By way of contrast, we note that the low-temperature metal oxide catalyzed dehydration of t-BuOH appears not to occur to any significant extent over the temperature range of the reaction. This was verified by direct introduction of t-BuOH. This is quite reasonable in terms of our consecutive unimolecular acts since the reaction t-BuOH(g) → i-butene(g) + H_2O(g) is endothermic by 14 kcal, which would represent a minimum activation energy for the system. By contrast, the reaction t-BuO_2H(g) → t-BuOH(g) + $^1/_2O_2$(g) is 19 kcal exothermic. Such analyses can be extended to explain the relative rarity of wall-catalyzed reactions in our VLPP systems at high temperatures.

Mathematical Analysis of Dropping Mercury Electrode. I. Solution of Diffusion Equation for Variable Mercury Flow Rate

by J. L. Duda and J. S. Vrentas

Process Fundamentals Research Laboratory, The Dow Chemical Company, Midland, Michigan 48640
(Received August 18, 1967)

The diffusion current–time relationship describing the diffusion of an electroactive material to an expanding spherical mercury electrode with an arbitrary time-dependent mercury flow rate is derived. The series solution to the diffusion equation utilized in the formulation of the instantaneous current–time relationship is as rigorous a solution for the variable flow-rate case as are the existing equations for the constant flow-rate situation. The developed equation is valid for a nonzero initial drop size and reduces to the Koutecky equation when the flow rate is considered constant and the initial drop radius is set equal to zero.

Introduction

Extensive use has been made of the polarographic method for chemical analysis of solutions since it was devised by Heyrovsky over 40 years ago. Fundamental to this method is the interpretation of current–voltage curves obtained during electrolysis of substances at a dropping mercury electrode. By calibration of a specific polarographic apparatus with a solution of known concentration, quantitative analyses can be obtained without a detailed analysis of the polarographic process. However, there has been a continued interest in employing the basic polarographic technique for applications other than as a chemical analyzer, such as a method of measuring diffusion coefficients. The successful extension of this method requires a mathematical relationship between the instantaneous current and the diffusion coefficient, as well as the growth characteristics of the mercury drop. Such a relationship could, of course, also be used to perform chemical analyses without calibration if the diffusion coefficient is known.

The first significant contribution toward a complete analysis of the polarographic technique was presented by Ilkovic,[1] who analyzed the case of unsteady-state diffusion to an expanding plane electrode. Koutecky[2] improved this analysis by incorporating the spherical geometry of the expanding mercury drop, and alternative formulations have also been presented.[3,4] However, experimental measurements[5–7] of the time dependence of the diffusion current indicate that the available theoretical analyses are not completely adequate, and serious discrepancies between theory and experiment still remain. The conventional model of unsteady-state diffusion to an expanding spherical electrode with an initially uniform concentration field of the electroactive material and a constant mercury flow rate is an idealization of the polarographic process. The following complicating effects should be considered for a rigorous analysis of the dropping mercury electrode.

Depletion Effect. In the derivations of the diffusion-current equation, it is assumed that at the start of the drop life there exists a uniform concentration field of the electroactive material with a concentration equal to the bulk concentration of the solution. However, when a drop dislodges from the capillary, a part of the depleted diffusion layer is left at the orifice because of insufficient mixing, and the succeeding drop starts to grow in a solution which has concentrations less than the bulk concentration. Consequently, every drop after the first drop enters a solution that is partially depleted and the diffusion current is less than that predicted. Experiments have shown[5–7] that the current for the second drop is significantly less than the current realized during the growth of the first drop, and Markowitz and Elving[8] have attempted to include this depletion effect in an analysis of the polarographic process. Their analysis results in a semi-empirical factor which can be used to correlate experimental data if all deviations from the idealized analysis are due to depletion. It is doubtful that an exact mathematical correction for this effect can be developed, since the depletion is a complex function of many factors and its reproducibility is not very good. However, this

(1) D. Ilkovic, *Collect. Czech. Chem. Commun.*, **6**, 498 (1934).

(2) J. Koutecky, *Czech. J. Phys.*, **2**, 50 (1953).

(3) V. G. Levich, "Physicochemical Hydrodynamics," Prentice-Hall, Inc., Englewood Cliffs, N. J., 1962, p 532 ff.

(4) H. Matsuda, *Bull. Chem. Soc. Jap.*, **26**, 342 (1953).

(5) J. M. Los and D. W. Murray, "Advances in Polarography," Vol. II, I. S. Longmuir, Ed., Pergamon Press, London, 1960, pp 408, 425, 437.

(6) W. Hans, W. Henne, and E. Meurer, *Z. Elektrochem.*, **58**, 836 (1954).

(7) M. von Stackelberg and V. Toome, *Collect. Czech. Chem. Commun.*, **25**, 2958 (1960).

(8) J. M. Markowitz and P. J. Elving, *J. Amer. Chem. Soc.*, **81**, 3518 (1959).

effect can be essentially eliminated by changes in experimental conditions. Two modifications have been successfully used to perform experiments which satisfy the idealized initial condition for the concentration distribution. Experiments can be conducted on only the first drop, where the depletion effect is absent, or the capillary can be tilted to promote mixing in the solution between drops, which has been shown to eliminate effectively the depletion.[9]

Variable Mercury Flow Rate. A conventional polarographic apparatus includes a constant-head mercury feed system, and it is assumed in the idealized analyses that the mercury flow rate is constant. This rate, however, increases with drop life because the interfacial tension between the mercury drop and the electrolytic solution causes a significant back pressure, which is a function of the drop radius. It has been shown by von Stackelberg and Toome[7] that the effect of the variation in flow rate can be reduced by using a large mercury pressure head and that, in the absence of depletion effects, the experimental current–time data approach the behavior predicted by the Koutecky equation near the end of drop life. An increased mercury head reduces the effect of the variable back pressure, and an essentially constant flow rate can be realized. The experimental suppression of this effect is not completely satisfactory because the increased pressure head can create other problems, such as convective mixing associated with large flow rates and short drop times. Also, it is of interest to determine how the current approaches the current predicted by the Koutecky equation as the drop grows. An equation predicting the current–time behavior for a variable flow rate would make it possible to use more of the current–time curve (not just the maximum instantaneous current) in determining diffusion coefficients.

Los and Murray[5] attempted to include the effect of the variable flow rate in an analysis of the polarographic process. However, they did not build upon the advances represented by the Koutecky equation, but analyzed an expanding plane electrode using von Stackelberg's approximate method of diffusion layers, taking account of the curvature afterwards. Such an approach is not completely satisfactory, since some of the assumptions are open to question.

Spurious Convection Effects. Any motion of the solution near the polarized electrode other than the radial flow induced by the expanding drop will have a tendency to enhance the rate of migration of the electroactive species. At least three distinct types of convective flows which cause abnormally high currents have been isolated. Tangential motion of the solution past the drop surface can be induced by electrocapillary motion caused by the asymmetry of the electrical field. This flow gives rise to increases in the current which are referred to as maxima of the first kind; they can be effectively suppressed by the addition of surface-active agents which retard tangential motion at the electrode surface. It is assumed that maximum suppressors, such as gelatin, have a negligible effect on the polarographic process. Some experimental justification of this assumption has been given by Scholander.[10] The flow associated with a maximum of the second kind is attributed to turbulence inside the drop due to large mercury flow rates. This complication can be eliminated by maintaining relatively low mercury flow rates. A third type of convective flow is generated by density gradients in the diffusion layer around the drop. If care is taken to maintain a sufficiently short drop time, the diffusion layer will be too thin for the initiation of such convection currents.

Asymmetry of Diffusion Field. In all derivations the dropping mercury electrode is considered to be a free sphere expanding in the solution with its center fixed. However, in practice the drop cannot be spherical in the early stages of growth, and, in addition, it will have a tendency to elongate in the gravitational field. The shielding by the capillary will also tend to disrupt the symmetry of the diffusion field and to prevent part of the surface of the sphere from contacting the surrounding solution. Studies[6,11–14] have revealed that these effects are negligible, except at very early times. In addition, relatively simple modifications, like the use of thin-walled capillaries, can be of value in further minimizing these effects. Since the drop is attached to a fixed capillary, its center will move relative to the diffusion field. Although the influence of this motion on the over-all diffusion process has not been established, it is reasonable to expect this effect to be small.

Initial Drop Size. It is convenient to assume that the drop radius is zero at the start of the polarographic process. This condition is not satisfied in practice, but the error induced is small and is effective only at very early times. It is, nevertheless, possible to remove this restriction by introducing a nonzero initial drop size into the mathematical equations.

The above survey indicates that perhaps the next step in the further sophistication of the analysis of the polarographic process should be the incorporation of the variable flow rate, since it can influence the current for an appreciable part of the drop life, even though simple experimental modifications can reduce its effect somewhat. The other factors can apparently be made completely

(9) J. Heyrovsky and J. Kuta, "Principles of Polarography," Academic Press Inc., New York, N. Y., 1966, p 102.

(10) A. Scholander, "Proceedings of the 1st International Polarographic Congress," Vol. I, Prague, 1951, p 260.

(11) G. S. Smith, *Trans. Faraday Soc.*, **47**, 63 (1951).

(12) W. M. MacNevin and E. W. Balis, *J. Amer. Chem. Soc.*, **65**, 660 (1943).

(13) J. J. MacDonald and F. E. W. Wetmore, *Trans. Faraday Soc.*, **47**, 533 (1951).

(14) J. J. Lingane, *J. Amer. Chem. Soc.*, **75**, 788 (1953).

negligible by proper experimental modifications or can be assumed to be very small at all but the earliest times.

In the first paper of this series, the diffusion current–time relationship is derived for the general case of an arbitrary time-dependent mercury flow rate. The developed equation which includes a nonzero initial drop size reduces to the two-term Koutecky equation when the flow rate is considered to be constant. It should be emphasized that the series solution to the diffusion equation obtained in this paper and utilized in the formulation of a current–time relationship is as rigorous a solution for the case of a variable flow rate as are the solutions of Koutecky[2] and Levich[3] for the case of a constant mercury flow rate. In the second paper the unsteady-state flow in the mercury feed system is analyzed and the time dependence of the flow rate is determined as a function of the system's characteristics. Then, the time dependence of the flow rate is incorporated into the derived diffusion-current equation, and the resulting predictions are compared with available instantaneous current data for first drops. The influences of the individual characteristics of the feed system on the instantaneous current are also determined, and the experimental modifications necessary for the suppression of the variable flow-rate effect are established.

Mathematical Formulation of Problem

Formulation of Equations. Consider the growth of a spherical drop of mercury completely surrounded by a solution of an electroactive agent which diffuses to and is electrolyzed at the surface of the mercury drop. The system is assumed to be isothermal, the center of the drop is taken to be stationary, and velocities in the θ and φ directions in spherical coordinates are considered negligible. The concentration of electroactive agent is assumed sufficiently dilute so that the density of the solution surrounding the mercury drop and the diffusion coefficient of the electroactive agent in this solution can both be considered constant. Furthermore, the initial concentration distribution of electroactive agent in the solution is assumed to be uniform, the initial size of the mercury drop is left unspecified, and the mass transfer from the solution to the drop is considered too small to exert a significant effect on the drop growth. Finally, the rate of the electrode process is assumed to be much faster than the diffusion rate, so that the diffusion process is the determining factor in the transfer of the electroactive agent, and, in addition, the concentration of supporting electrolyte is supposed great enough to render the migration current negligible.

For these conditions, the continuity equation for the mass density, ρ_I, of the electroactive species can be written as

$$\frac{\partial \rho_I}{\partial t} + V\frac{\partial \rho_I}{\partial r} = D\left(\frac{\partial^2 \rho_I}{\partial r^2} + \frac{2}{r}\frac{\partial \rho_I}{\partial r}\right) \tag{1}$$

and the total continuity equation yields the following relationship for the radial velocity in terms of the velocity of the drop surface, V_d, and the drop radius $R(t)$

$$V = \frac{R^2}{r^2}V_d \tag{2}$$

The mass flow rate of mercury, $m(t)$, issuing from the capillary can be related to the drop growth by the equation

$$R^2\frac{dR}{dt} = \beta m \tag{3}$$

where

$$\beta = \frac{1}{4\pi\hat{\rho}} \tag{4}$$

and where $\hat{\rho}$ is the density of the mercury drop. Since

$$V_d = \frac{dR}{dt} \tag{5}$$

it is evident from above that the differential equation and boundary conditions describing the mass density of the electroactive agent can be written as

$$\frac{\partial \rho_I}{\partial t} + \frac{\beta m}{r^2}\frac{\partial \rho_I}{\partial r} = D\left(\frac{\partial^2 \rho_I}{\partial r^2} + \frac{2}{r}\frac{\partial \rho_I}{\partial r}\right) \tag{6}$$

$$\rho_I(r, 0) = \rho_{IO} \tag{7}$$

$$\rho_I(\infty, t) = \rho_{IO} \tag{8}$$

$$\rho_I[R(t), t] = \rho_{IE} \tag{9}$$

The solution of eq 6–9 is facilitated if they are first cast into dimensionless form. Introduction of the dimensionless variables

$$\rho_I^* = \frac{\rho_I - \rho_{IE}}{\rho_{IO} - \rho_{IE}} \tag{10}$$

$$m^* = \frac{m}{m_0} \tag{11}$$

$$R^* = \frac{R}{R_0} \tag{12}$$

$$t^* = \frac{tm_0\beta}{R_0^3} \tag{13}$$

$$\eta = \frac{1}{\sqrt{N_p}}\left(\frac{r}{R} - 1\right) \tag{14}$$

$$N_p = \frac{DR_0}{\beta m_0} \tag{15}$$

into eq 6–9 yields

$$\left(\frac{\partial \rho_I}{\partial t}\right)_\eta - \frac{m(1 + \eta\sqrt{N_p})}{R^3\sqrt{N_p}}\left(\frac{\partial \rho_I}{\partial \eta}\right) + \frac{m}{R^3\sqrt{N_p}(1 + \eta\sqrt{N_p})^2}\left(\frac{\partial \rho_I}{\partial \eta}\right) = \frac{1}{R^2}\left(\frac{\partial^2 \rho_I}{\partial \eta^2} + \frac{2\sqrt{N_p}}{1 + \eta\sqrt{N_p}}\frac{\partial \rho_I}{\partial \eta}\right) \tag{16}$$

$$\rho_I(\eta, 0) = 1 \quad (17)$$

$$\rho_I(\infty, t) = 1 \quad (18)$$

$$\rho_I(0, t) = 0 \quad (19)$$

where the asterisks have been dropped for convenience, since no confusion should arise between dimensionless and dimensional variables in the remainder of the paper. In the above equations R_0 is the radius of the capillary and m_0 is the characteristic mass flow rate of mercury in the capillary; this quantity will be defined explicitly in the second paper.

Formulation of Perturbation Method. Solution of eq 16–19 is a formidable task, even for the case of a constant mercury flow rate. Hence, we shall resort to a series solution, as did Koutecky[2] and, in reality, as did Levich[3] when coping with the simpler case. The approach used here is that of a perturbation series solution, with the first two terms of the series being determined. The possibility exists of calculating higher-order terms, but the computational labor involved is not small. Close examination reveals that the method of Levich is also basically a perturbation method and the results of this investigation necessarily reduce to his results when the mercury flow rate is set equal to a constant.

If the drop times are not exceedingly long, so that essentially all of the concentration boundary layer is confined to a region where the inequality

$$\eta\sqrt{N_p} < 1 \quad (20)$$

is obeyed during the drop life, it is possible to use the following series expansions in obtaining expressions for the coefficients of the diffusion equation

$$\frac{1}{1 + \eta\sqrt{N_p}} = 1 - \eta\sqrt{N_p} + (\eta\sqrt{N_p})^2 - \dots \quad (21)$$

$$\frac{1}{(1 + \eta\sqrt{N_p})^2} = 1 - 2\eta\sqrt{N_p} + 3(\eta\sqrt{N_p})^2 - \dots \quad (22)$$

Substitution of eq 21 and 22 into eq 16 gives

$$\left(\frac{\partial\rho_I}{\partial t}\right)_\eta - \frac{3m\eta}{R^3}\frac{\partial\rho_I}{\partial\eta} + \frac{3m\eta^2\sqrt{N_p}}{R^3}\frac{\partial\rho_I}{\partial\eta} = \frac{1}{R^2}\left(\frac{\partial^2\rho_I}{\partial\eta^2} + 2\sqrt{N_p}\frac{\partial\rho_I}{\partial\eta}\right) + O(N_p) \quad (23)$$

where $O(N_p)$ denotes "order of N_p." A perturbation solution of eq 17–19, and 23 can now be effected by introducing a series expansion in terms of ascending powers of the small paramerer $N_p^{1/2}$

$$\rho_I(\eta, t) = \rho_I^0(\eta, t) + N_p^{1/2}\rho_I^1(\eta, t) + N_p\rho_I^2(\eta, t) + \dots \quad (24)$$

Substitution of eq 24 into eq 17–19 and 23 and introduction of the condition that the coefficients of each power of $N_p^{1/2}$ must separately vanish give the following equations for the zero-order and first-order terms of the perturbation series

$$\frac{\partial\rho_I^0}{\partial t} - \frac{3m\eta}{R^3}\frac{\partial\rho_I^0}{\partial\eta} = \frac{1}{R^2}\frac{\partial^2\rho_I^0}{\partial\eta^2} \quad (25)$$

$$\rho_I^0(\eta, 0) = 1 \quad (26)$$

$$\rho_I^0(\infty, t) = 1 \quad (27)$$

$$\rho_I^0(0, t) = 0 \quad (28)$$

$$\frac{\partial\rho_I^1}{\partial t} - \frac{3m\eta}{R^3}\frac{\partial\rho_I^1}{\partial\eta} + \frac{3m\eta^2}{R^3}\frac{\partial\rho_I^0}{\partial\eta} = \frac{1}{R^2}\frac{\partial^2\rho_I^1}{\partial\eta^2} + \frac{2}{R^2}\frac{\partial\rho_I^0}{\partial\eta} \quad (29)$$

$$\rho_I^1(\eta, 0) = \rho_I^1(\infty, t) = \rho_I^1(0, t) = 0 \quad (30)$$

Differential equations and boundary conditions for higher-order terms of the perturbation series can also be deduced from the above analysis; they are not included here since they are not evaluated in this investigation.

Solution of Equations

Solution of Zero-Order Equations. To effect a solution of eq 25 subject to eq 26–28, it is convenient to introduce the independent variables

$$\zeta = nR^3 \quad (31)$$

$$\tau = \int_0^t R^4\,dt \quad (32)$$

thus converting the pertinent equations to

$$\frac{\partial\rho_I^0}{\partial\tau} = \frac{\partial^2\rho_I^0}{\partial\zeta^2} \quad (33)$$

$$\rho_I^0(\zeta, 0) = 1 \quad (34)$$

$$\rho_I^0(\infty, \tau) = 1 \quad (35)$$

$$\rho_I^0(0, \tau) = 0 \quad (36)$$

In the above manipulations, we have utilized the dimensionless form of eq 3

$$R^2\frac{dR}{dt} = m \quad (37)$$

The solution to eq 33–36 is well known[15] and can be written as

$$\rho_I^0 = \operatorname{erf}\left(\frac{\zeta}{2\sqrt{\tau}}\right) \quad (38)$$

For the case of a constant-mass flow rate of mercury and a zero initial drop size, it follows that

$$m = 1 \quad (39)$$

$$R = 3^{1/3}t^{1/3} \quad (40)$$

(15) H. S. Carslaw and J. C. Jaeger, "Conduction of Heat in Solids," Oxford University Press, London, 1959.

$$\tau = \frac{3^{7/3}t^{7/3}}{7} \tag{41}$$

and eq 38 reduces to

$$\rho_I^0 = \operatorname{erf}\left(\frac{\eta\sqrt{7}}{2t^{1/6}3^{1/6}}\right) \tag{42}$$

which is equivalent to the usual result of polarographic theory.[3]

Solution of First-Order Equations. From eq 31, 32, 37, and 38, it follows that eq 29 and 30 can be written as

$$\frac{\partial\rho_I^1}{\partial\tau} = \frac{\partial^2\rho_I^1}{\partial\zeta^2} + \frac{2e^{-\zeta^2/4\tau}}{R^3\sqrt{\pi\tau}} - \frac{3m\zeta^2e^{-\zeta^2/4\tau}}{R^{10}\sqrt{\pi\tau}} \tag{43}$$

$$\rho_I^1(\zeta, 0) = \rho_I^1(\infty, \tau) = \rho_I^1(0, \tau) = 0 \tag{44}$$

To solve eq 43 subject to eq 44, it is convenient to utilize Duhamel's theorem.[15] Therefore, if $F(\zeta, \lambda, \tau)$ is the solution of

$$\frac{\partial F}{\partial\tau} = \frac{\partial^2F}{\partial\zeta^2} + \frac{2e^{-\zeta^2/4\lambda}}{R^3\sqrt{\pi\lambda}} - \frac{3m\zeta^2e^{-\zeta^2/4\lambda}}{R^{10}\sqrt{\pi\lambda}} \tag{45}$$

$$F(\zeta, 0) = F(\infty, \tau) = F(0, \tau) = 0 \tag{46}$$

then

$$\rho_I^1(\zeta, \tau) = \frac{\partial}{\partial\tau}\int_0^\tau F(\zeta, \lambda, \tau - \lambda)\, d\lambda \tag{47}$$

is the solution to eq 43 and 44.

To obtain a solution to eq 45 and 46, we let

$$F(\zeta, \tau) = \varphi(\zeta, \tau) + \theta(\zeta) \tag{48}$$

and derive the following set of equations

$$\frac{d^2\theta}{d\zeta^2} + Q\zeta^2e^{-\zeta^2/4\lambda} + Pe^{-\zeta^2/4\lambda} = 0 \tag{49}$$

$$\theta(0) = -(2\lambda P + 8\lambda^2Q) \tag{50}$$

$$\theta(\infty) = 0 \tag{51}$$

$$P = \frac{2}{R^3\sqrt{\pi\lambda}} \tag{52}$$

$$Q = -\frac{3m}{R^{10}\sqrt{\pi\lambda}} \tag{53}$$

$$\frac{\partial\varphi}{\partial\tau} = \frac{\partial^2\varphi}{\partial\zeta^2} \tag{54}$$

$$\varphi(\zeta, 0) = (2\lambda P + 8\lambda^2Q)\, e^{-\zeta^2/4\lambda} - \zeta(2\lambda Q + P)(\sqrt{\pi\lambda} - \int_0^\zeta e^{-\zeta^2/4\lambda}\, d\zeta) \tag{55}$$

$$\varphi(\infty, \tau) = 0 \tag{56}$$

$$\varphi(0, \tau) = 2\lambda P + 8\lambda^2Q \tag{57}$$

The derivation of solutions to eq 49–51 and eq 54–57 is straightforward and the details are omitted. Combination of these solutions with eq 47 and 48 gives

$$\rho_I^1(\zeta, \tau) = \int_0^\tau\left[\frac{\lambda^{1/2}P(\lambda)\, e^{-\zeta^2/4\tau}}{\tau^{1/2}}\operatorname{erf}\left(\frac{\zeta}{2}\sqrt{\frac{\lambda}{\tau(\tau-\lambda)}}\right) + \frac{2\lambda^{3/2}(\tau-\lambda)Q(\lambda)\, e^{-\zeta^2/4\tau}}{\tau^{3/2}}\operatorname{erf}\left(\frac{\zeta}{2}\sqrt{\frac{\lambda}{\tau(\tau-\lambda)}}\right) + \frac{\zeta^2\lambda^{5/2}Q(\lambda)\, e^{-\zeta^2/4\tau}}{\tau^{5/2}}\operatorname{erf}\left(\frac{\zeta}{2}\sqrt{\frac{\lambda}{\tau(\tau-\lambda)}}\right) + \frac{2\lambda^2\zeta(\tau-\lambda)^{1/2}Q(\lambda)\, e^{-\zeta^2/4(\tau-\lambda)}}{\tau^2\pi^{1/2}}\right] d\lambda \tag{58}$$

The zero-order and first-order expressions can be combined to give the first two terms of the series solution to eq 16–19. From eq 24, 31, 38, and 58 it is evident that

$$\rho_I(\eta, t) = \operatorname{erf}\left(\frac{\eta R^3}{2\sqrt{\tau}}\right) + \sqrt{N_p}\int_0^\tau\left[\frac{\lambda^{1/2}P(\lambda)\, e^{-\eta^2R^6/4\tau}}{\tau^{1/2}}\operatorname{erf}\left(\frac{\eta R^3}{2}\sqrt{\frac{\lambda}{\tau(\tau-\lambda)}}\right) + \frac{2\lambda^{3/2}(\tau-\lambda)Q(\lambda)\, e^{-\eta^2R^6/4\tau}}{\tau^{3/2}}\operatorname{erf}\left(\frac{\eta R^3}{2}\sqrt{\frac{\lambda}{\tau(\tau-\lambda)}}\right) + \frac{\eta^2R^6\lambda^{5/2}Q(\lambda)\, e^{-\eta^2R^6/4\tau}}{\tau^{5/2}}\operatorname{erf}\left(\frac{\eta R^3}{2}\sqrt{\frac{\lambda}{\tau(\tau-\lambda)}}\right) + \frac{2\lambda^2\eta R^3(\tau-\lambda)^{1/2}Q(\lambda)\, e^{-\eta^2R^6/4(\tau-\lambda)}}{\tau^2\pi^{1/2}}\right] d\lambda \tag{59}$$

For the case of constant m and a mercury drop of zero initial radius, eq 39–41 are applicable and eq 59 reduces to

$$\rho_I(\eta, t) = \operatorname{erf}\left(\frac{\eta\sqrt{7}}{2t^{1/6}3^{1/6}}\right) + \sqrt{N_p}\left[\frac{28(3t)^{1/6}\, e^{-\eta^2a/t^{1/3}}}{11\sqrt{7\pi}} - \frac{56(3t)^{1/7}}{7^{3/7}(11\pi)}\int_{\frac{\eta\sqrt{a}}{t^{1/6}}}^\infty e^{-\mu^2}\left(\frac{3^{1/3}t^{1/3}}{7} - \frac{\eta^2}{4\mu^2}\right)^{1/14} d\mu - \frac{3\eta^27^{1/2}e^{-\eta^2a/t^{1/3}}}{11(3t)^{1/6}\pi^{1/2}}\right] \tag{60}$$

$$a = \frac{7}{4 \times 3^{1/3}} \tag{61}$$

It can be shown that eq 60 is equivalent to the two-term expression derived by Levich[3] for the concentration distribution around an expanding spherical electrode.

It should be noted that eq 59 is a rigorous relationship for the first two terms of the series expansion for the concentration distribution and is as accurate for variable flow-rate calculations as are previously derived two-term expressions for a constant mercury flow rate. We assume here that the remainder of the series contributes an insignificant amount to the series sum under the conditions of usual polarographic experiments. Calculations of the third term for the case of constant m show that its contribution is negligible under ordinary circumstances and, thus, the supposition that the third term is negligible in this case is very probably valid.

Current–Time Equations

The important result from a mathematical analysis of the dropping mercury electrode is of course the current–time equation. The instantaneous current passing through the electrode surface can be shown to be (if only two terms of the series expansion are used)

$$i = \frac{4\pi R(R_0 m_0 D\beta)^{1/2} Fn(\rho_{IO} - \rho_{IE})}{M}\left(\frac{\partial \rho_I{}^0}{\partial \eta}\right)_{\eta=0} + \frac{4\pi R R_0 D F n(\rho_{IO} - \rho_{IE})}{M}\left(\frac{\partial \rho_I{}^1}{\partial \eta}\right)_{\eta=0} \quad (62)$$

where n is the number of electrons consumed by each ion or molecule of the electroactive substance, F is Faraday's constant, and M is the molecular weight of the electroactive substance. In addition, from eq 31, 38, and 58, it follows that for an arbitrary time dependence of the mercury flow rate

$$\left(\frac{\partial \rho_I{}^0}{\partial \eta}\right)_{\eta=0} = \frac{R^3}{\sqrt{\pi\tau}} \quad (63)$$

$$\left(\frac{\partial \rho_I{}^1}{\partial \eta}\right)_{\eta=0} = \frac{2R^3}{\pi\tau}\int_0^\tau \frac{\lambda^{1/2}}{[R(\lambda)]^3 (\tau - \lambda)^{1/2}}\, d\lambda - \frac{12R^3}{\pi\tau^2}\int_0^\tau \frac{m\lambda^{3/2}(\tau - \lambda)^{1/2}}{[R(\lambda)]^{10}}\, d\lambda \quad (64)$$

Equations 62–64 serve to define completely the current–time relationship for a particular system once the radius–time function is known.

For the case of zero electrode surface area at $t = 0$ and constant m, the radius–time relationship is given by eq 40 and eq 63 and 64 reduce to the following forms

$$\left(\frac{\partial \rho_I{}^0}{\partial \eta}\right)_{\eta=0} = \frac{\sqrt{7}}{(3t)^{1/6}\pi^{1/2}} \quad (65)$$

$$\left(\frac{\partial \rho_I{}^1}{\partial \eta}\right)_{\eta=0} = \int_0^\infty \frac{\omega^{16/14}}{\pi(\omega + 1/4)^{18/7}}\, d\omega + \int_0^\infty \frac{\omega^{1/14}}{28\pi(\omega + 1/4)^{18/7}}\, d\omega \quad (66)$$

Introduction of eq 40, 65, and 66 into eq 62 and utilization of dimensional variables give

$$i = 0.732nFD^{1/2}m_0{}^{2/3}t^{1/6}(C_{IO} - C_{IE}) \times \left[1 + 3.96\frac{D^{1/2}t^{1/6}}{m_0{}^{1/3}}\right] \quad (67)$$

where C_I denotes the molar density of the electroactive agent and where the units of length in the equation must be centimeters and the units of mass must be grams. Also, the equation is valid in the strictest sense only at 25°. Equation 67 is in the form of the familiar two-term Koutecky equation. It can be shown that, at long times when the effect of back pressure created by the interfacial-tension phenomenon and the effect of the inertia of the fluid in the capillary tube have faded, eq 62 with eq 63 and 64 approaches the form of eq 67.

For any given drop radius–time function, m can be calculated from eq 37, τ can be derived from eq 32, and the current–time relationship for a particular system can be computed from eq 62–64. In the second paper we derive the form of the drop radius–time relationship by considering the unsteady-state flow behavior in the polarographic feed system. Utilization of this relationship in the equations derived in this paper provides theoretical current–time curves which can be compared with existing experimental data.

Mathematical Analysis of Dropping Mercury Electrode. II. Prediction of Time Dependence of Mercury Flow Rate

by J. L. Duda and J. S. Vrentas

Process Fundamentals Research Laboratory, The Dow Chemical Company, Midland, Michigan 48640
(Received August 18, 1967)

The flow in the conventional polarographic feed system is analyzed and the time dependence of the mercury flow rate is related to the characteristics of the feed system. This relationship is then coupled with the previously derived diffusion-current equation to predict instantaneous current *vs.* time behavior, which is compared with available experimental instantaneous-current data obtained in the absence of depletion effects. This comparison shows that this analysis represents a significant improvement in the description of the polarographic process.

Introduction

In the conventional polarographic experiment, flow to the dropping mercury electrode is maintained by a constant-head feed system. The flow system consists of a reservoir constructed of a relatively large diameter conduit, a length of capillary tubing connected to the reservoir, and the growing mercury drop itself. Due mainly to the back pressure created by the expanding mercury drop, an unsteady-state flow behavior exists in this feed system.

In the following development, this unsteady-state flow is analyzed and the time dependence of the mercury flow rate is related to the characteristics of the feed system. This relationship is then used in conjunction with the diffusion-current equation, which was derived in the first paper,[1] to predict instantaneous current *vs.* time behavior. The predicted current behavior is then compared with available experimental instantaneous-current data obtained on first drops in the absence of depletion effects. This comparison shows that the present analysis represents a significant improvement in the description of the polarographic process. Finally, the effects of the various feed-system characteristics on the flow rate are examined and the experimental modifications which will minimize the effect of the variation of the flow rate are established.

The formulation of a completely rigorous analysis of the mercury-flow behavior is exceedingly difficult because of the complexity of the physical situation. However, it is possible to simplify the problem by introducing reasonable assumptions and thus arrive at a relatively simple and sufficiently accurate description of the polarographic feed system.

Analysis of Polarographic Feed System

A typical polarographic feed apparatus is depicted in Figure 1. The pressure of the atmosphere is denoted by p_a and the inlet pressure to the capillary by p_i. The effect of the hydrostatic head of the solution is considered negligible, so that the pressure in the solution surrounding the mercury drop is assumed to be equal to p_a at an effectively infinite distance from the drop. Also, the height of mercury, h, in the reservoir above the capillary tube is assumed to be independent of time.

Since the flow in the capillary tube is such for the usual polarographic experiment that the $L:R_0$ ratio is large and the Reynolds number small, it can be expected that the end effects at the entrance and exit of the capillary tube will be confined to a very small part of the total length of the capillary and can thus be neglected. In addition, flow interactions between the reservoir and the capillary and between the drop and the capillary are assumed small, and it is possible to proceed by analyzing separately the three parts of the mercury flow system: the reservoir, the capillary, and the drop. The results can then be combined to produce a theoretical relationship for the time dependence of the mercury flow rate.

Flow in Mercury Reservoir. Flow in a mercury reservoir of any shape and with an effective diameter much larger than that of the capillary is such that the pressure and body forces predominate over the viscous and inertia forces. Hence, the equations of motion predict that the pressure at any radial position at the inlet of the capillary is given by the expression[2]

$$p_i = p_a + \hat{\rho}gh \tag{1}$$

This is simply the result that would intuitively be expected, since the mercury in the reservoir is essentially at rest.

Growth of Mercury Drop. As in the first paper, we consider the growth of an isolated sphere in a solution of infinite extent under isothermal conditions. The center of the drop is assumed to be stationary, the flow in the

(1) J. L. Duda and J. S. Vrentas, *J. Phys. Chem.*, **72**, 1187 (1968).

(2) Properties of the mercury phase are denoted by affixing a caret above the symbol for that property.

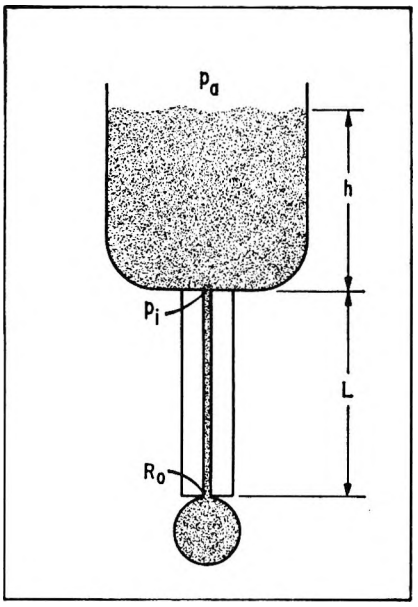

Figure 1. Typical polarographic feed system.

solution phase is taken to be purely radial, and the density and viscosity of the surrounding solution are considered constant. Finally, gravitational effects are neglected, phase volume change due to mass transfer is assumed small, and the surrounding solution is assumed to be a Newtonian fluid. Consequently, the pertinent equation of motion for the solution phase becomes[3]

$$\rho\left(\frac{\partial V}{\partial t} + V\frac{\partial V}{\partial r}\right) = -\frac{\partial p}{\partial r} + \mu\left(\frac{\partial^2 V}{\partial r^2} + \frac{2}{r}\frac{\partial V}{\partial r} - \frac{2V}{r^2}\right) \tag{2}$$

and the continuity equation predicts the following relationship between the radial velocity in the solution, V, and the drop radius, $R(t)$

$$V = \frac{R^2 V_d}{r^2} = \frac{R^2}{r^2}\frac{dR}{dt} \tag{3}$$

Combination of eq 2 and 3 yields

$$\rho\left(\frac{\partial V}{\partial t} + V\frac{\partial V}{\partial r}\right) = -\frac{\partial p}{\partial r} \tag{4}$$

Multiplication of eq 4 by dr, integration from $r = \infty$ to $r = R(t)$, and utilization of eq 3 lead to the following result

$$\frac{d^2R}{dt^2} + \frac{3}{2R}\left(\frac{dR}{dt}\right)^2 = \frac{p(R) - p_a}{R\rho} \tag{5}$$

Here, $p(R)$ denotes the pressure on the solution side of the mercury–solution interface.

Now, it is necessary to relate $p(R)$ to the pressure p_0 on the mercury side of the mercury–solution interface. We can write equations of change for a two-dimensional surface phase between the mercury phase and the solution phase. If it is assumed that the surface density is very small and that there is a negligible effect of the mass-transfer process on the conservation of momentum of the surface phase, then the equations of motion for the surface fluid become[4]

$$(X_\alpha{}^i \tau^{\alpha\beta})_{,\beta} + \hat{T}^{ij}\hat{n}_j + T^{ij}n_j = 0 \tag{6}$$

where

$$X_\alpha{}^i = \frac{\partial X^i}{\partial u^\alpha} \tag{7}$$

and where curvilinear tensor notation has been used.[5] Here, X^i denotes a space coordinate, u^α is a surface coordinate, $\tau^{\alpha\beta}$ is the surface stress tensor, $\hat{T}^{ij}$ and T^{ij} are the space stress tensors at the interface in the mercury and solution phases, respectively, and $\hat{n}_j$ and n_j are the unit normal vectors to the drop surface pointing into the mercury and solution phases, respectively. It is further assumed that the surface phase is inviscid so that the surface stress tensor is given by

$$\tau^{\alpha\beta} = a^{\alpha\beta}\sigma \tag{8}$$

where σ is the interfacial tension and $a^{\alpha\beta}$ is the associated surface metric tensor. The surface-active agent added to suppress tangential motion is considered to be always in adsorption equilibrium, so that σ can be assumed to be a constant during the entire period of drop growth. It, of course, will take some time for adsorption equilibrium to be established, but this time should be a very small fraction of the drop time. In addition, the depression of interfacial tension caused by the surfactant is expected to be relatively small. Both these factors tend to make the assumption of a constant interfacial tension, σ, quite plausible, although it should be pointed out that direct experimental verification is apparently lacking.

If there is no variation of interfacial tension over the surface of the drop, it follows from eq 6 and 8 and well known tensor identities[5] that

$$2\sigma H n^i + \hat{T}^{ij}\hat{n}_j + T^{ij}n_j = 0 \tag{9}$$

where H is the mean curvature of the surface; this is simply

$$H = -\frac{1}{R} \tag{10}$$

for a spherical interface. Evaluation of eq 9 for a spherical interface with purely radial flow in the mercury and solution phases adjacent to the surface phase leads to the relationship

(3) R. B. Bird, W. E. Stewart, and E. N. Lightfoot, "Transport Phenomena," John Wiley and Sons, Inc., New York, N. Y., 1960, p 87.

(4) J. C. Slattery, *Chem. Eng. Sci.*, 19, 379 (1964).

(5) R. Aris, "Vectors, Tensors, and the Basic Equations of Fluid Mechanics," Prentice-Hall, Inc., Englewood Cliffs, N. J., 1962.

$$p(R) = p_0 - \frac{2\sigma}{R} + \frac{4(\hat{\mu} - \mu)}{R}\frac{dR}{dt} \qquad (11)$$

since both the solution and mercury can be considered to be Newtonian fluids. Substitution of eq 11 into eq 5 gives the following expression for the description of drop growth

$$\frac{d^2R}{dt^2} + \frac{3}{2R}\left(\frac{dR}{dt}\right)^2 + \frac{4(\mu - \hat{\mu})}{R^2\rho}\frac{dR}{dt} = \frac{p_0 - p_a}{R\rho} - \frac{2\sigma}{\rho R^2} \qquad (12)$$

An order-of-magnitude analysis of the individual terms in eq 12 shows that the inertia and viscous terms are very much smaller than the surface-force term under usual polarographic conditions. Hence, eq 12 reduces to the simple result

$$p_0 - p_a = \frac{2\sigma}{R} \qquad (13)$$

A rigorous examination of the drop dynamics shows, therefore, that the expanding drop can effectively be described by an equation valid for a static drop. This assumption has appeared often in polarographic literature,[6] but apparently with little justification. Equation 13 describes the pressure on the mercury side of the interface anywhere on an isolated sphere. The perfect symmetry is destroyed somewhat by the presence of the capillary tube, but, to a good degree of approximation, the pressure at the outlet of the capillary can be computed from eq 13 at all but the earliest periods of drop growth.

Flow in Capillary Tube. Since end effects in the capillary tube can be assumed negligible, the problem reduces to describing the laminar flow of a Newtonian fluid of constant density and viscosity in a very long vertical tube with inlet pressure p_i and outlet pressure $p_0(t)$. The axial pressure gradient is simply

$$\frac{\partial p}{\partial z} = -\frac{p_i - p_0(t)}{L} \qquad (14)$$

and the pertinent equation of motion for the axial velocity, U, in the capillary tube reduces to[7]

$$\frac{\partial U}{\partial t} = \frac{p_i - p_0(t)}{\hat{\rho}L} + g + \frac{\hat{\mu}}{\hat{\rho}}\left(\frac{\partial^2 U}{\partial r^2} + \frac{1}{r}\frac{\partial U}{\partial r}\right) \qquad (15)$$

since the radial and azimuthal velocities are identically equal to zero. Symmetry requirements dictate that

$$\frac{\partial U}{\partial r}(0, t) = 0 \qquad (16)$$

and the boundary condition at the tube wall is written as

$$U(R_0, t) = 0 \qquad (17)$$

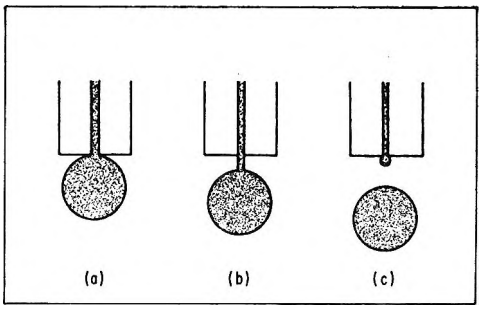

Figure 2. Sequence in separation of mercury electrode from capillary: (a) growing drop attached to capillary; (b) drop begins to fall and thin thread of mercury is formed; (c) unattached drop falls and thread contracts to form new drop.

since there appears to be no slip at this solid boundary, even for the flow of mercury in a glass tube.[8]

Formulation of an initial condition for eq 15 presents some problem. The behavior of the mercury electrode before and after a drop falls is depicted by the drawings in Figure 2, which are based on high-speed motion pictures taken at approximately 1500 frames/sec. The drop hangs by a thin thread which then separates from the drop, snaps back to the capillary orifice, and forms a small drop itself which then begins growing. Consequently, the initial-velocity field in the capillary can best be assumed to be essentially zero everywhere in the capillary at the start of drop growth. Thus the third boundary condition becomes

$$U(r, 0) = 0 \qquad (18)$$

By application of Duhamel's theorem,[9] the solution to eq 15–18 can be shown to be

$$U(r, t) = \frac{8\hat{\mu}}{R_0^2\hat{\rho}}\int_0^t B(\lambda)\sum_{n=1}^{\infty} \times \frac{J_0\left(\frac{\beta_n r}{R_0}\right)\exp\left[-\frac{\beta_n^2(t - \lambda)\,\hat{\mu}}{R_0^2\hat{\rho}}\right]}{\beta_n J_1(\beta_n)}\,d\lambda \qquad (19)$$

where

$$B(\lambda) = \frac{[p_i - p_0(\lambda) + \hat{\rho}gL]\,R_0^2}{4\hat{\mu}L} \qquad (20)$$

and where the β_n are the positive roots of

$$J_0(\beta_n) = 0 \qquad (21)$$

Equation 19 describes the effect of the variable back

(6) I. M. Kolthoff and J. J. Lingane, "Polarography," Vol. I, Interscience Publishers, Inc., New York, N. Y., 1952, p 79.

(7) See ref 3, p 85.

(8) B. D. Coleman, H. Markovitz, and W. Noll, "Viscometric Flows of Non-Newtonian Fluids," Springer-Verlag, New York, N. Y., 1966, p 57.

(9) H. S. Carslaw and J. C. Jaeger, "Conduction of Heat in Solids," Oxford University Press, London, 1959.

pressure and of the inertia of the fluid on the velocity field in the capillary tube.

Derivation of Radius–Time Relationship

In this section the results of the previous section are combined to give an equation for the drop radius as a function of time. This relationship immediately leads to the theoretical time dependence of m, the mercury mass-flow rate, since m and R are directly related by the equation

$$m = 4\pi\hat{\rho}R^2\frac{dR}{dt} \tag{22}$$

The mass-flow rate in the capillary tube is defined by

$$m = \int_0^{R_0} 2\pi r\hat{\rho}U\,dr \tag{23}$$

and it follows from eq 19, 20, and 23 that

$$m = \int_0^t \frac{4\pi R_0^2}{L}\sum_{n=1}^{\infty}\frac{[p_1 - p_0(\lambda) + \hat{\rho}gL]}{\beta_n^2}\times \exp\left[-\frac{\beta_n^2(t-\lambda)\,\hat{\mu}}{R_0^2\hat{\rho}}\right]d\lambda \tag{24}$$

Substitution of eq 1 and 22 into eq 24 and utilization of the dimensionless variables introduced in the first paper[1] yield the following result[10]

$$R^2\frac{dR}{dt} = \int_0^t \frac{16\pi^2\hat{\rho}R_0^5}{m_0^2L}\sum_{n=1}^{\infty}\frac{[p_a - p_0(\lambda) + \hat{\rho}g(L+h)]}{\beta_n^2}\times \exp\left[-\frac{4\pi R_0\hat{\mu}\beta_n^2(t-\lambda)}{m_0}\right]d\lambda \tag{25}$$

If eq 25 is to be integrated, an initial condition for R must be introduced into the development. The assumption made here is that the initial drop radius is equal to the radius of the capillary. This cannot of course be strictly true; the high-speed motion pictures, mentioned previously, show that the initial drop is actually a partial sphere with a radius slightly larger than that of the capillary. However, since the assumption used here is not far from the truth and since the size of the initial drop is not critical except at very early times, the approximation of a sphere of radius R_0 at $t = 0$ should be completely satisfactory. Introduction of eq 13 into eq 25, integration of the resulting equation, and utilization of the initial condition

$$R(0) = 1 \tag{26}$$

lead to the following nonlinear Volterra integral equation of the second kind for the radius of the drop

$$R^3 = 1 + 3t - \frac{3R_0^3\hat{\rho}^2g}{\hat{\mu}^2}\left(1+\frac{h}{L}\right)\sum_{n=1}^{\infty}\times \frac{1-\exp\left[-\frac{4\pi\beta_n^2R_0\hat{\mu}t}{m_0}\right]}{\beta_n^6} - \frac{192\sigma}{R_0\hat{\rho}g(L+h)}\sum_{n=1}^{\infty}\times \frac{1}{\beta_n^4}\int_0^t\frac{1-\exp\left[-\frac{4\pi\beta_n^2R_0\hat{\mu}(t-\lambda)}{m_0}\right]}{R(\lambda)}d\lambda \tag{27}$$

In the derivation of eq 27 we have introduced the following definition for m_0, the characteristic mass-flow rate of mercury in the capillary

$$m_0 = \frac{\pi R_0^4\hat{\rho}^2g(1+h/L)}{8\hat{\mu}} \tag{28}$$

Equation 28 is clearly the Hagen-Poiseuille law,[11,12] valid for flow in the capillary tube with no inertia effect and no interfacial-tension effect. It can be shown that the fluid inertia and interfacial-tension phenomena become vanishingly small as the drop grows, so that m_0 is approached asymptotically in a polarographic capillary at long times.

In the limit of negligible fluid inertia, eq 27 can be shown to reduce to

$$R^3 = 1 + 3t - \frac{6\sigma}{R_0\hat{\rho}g(L+h)}\int_0^t\frac{1}{R(\lambda)}d\lambda \tag{29}$$

Differentiation of eq 29 produces

$$R^2\frac{dR}{dt} = 1 - \frac{2\sigma}{R_0\hat{\rho}g(L+h)\,R} \tag{30}$$

and solution of this differential equation with eq 26 as a boundary condition gives

$$t = \frac{R^3-1}{3} + \frac{N_1(R^2-1)}{2} + N_1^2(R-1) + N_1^3\ln\left[\left(\frac{R-N_1}{1-N_1}\right)\right] \tag{31}$$

where

$$N_1 = \frac{2\sigma}{R_0\hat{\rho}g(L+h)} \tag{32}$$

Equation 31 has been previously derived by Smith[13] and by Los and Murray,[14] who correctly noted that it describes the effect of a variable back pressure on the mercury flow rate. Also, as $\sigma \to 0$, eq 29 reduces to

$$R = (1+3t)^{1/3} \tag{33}$$

and if, in addition, we let

$$R(0) = 0 \tag{34}$$

we recover the familiar radius–time equation of polarographic analysis valid for a constant flow rate and zero initial drop size

(10) Variables are to be considered dimensionless from this point on.

(11) See ref 3, p 46.

(12) See ref 6, p 78.

(13) G. S. Smith, *Trans. Faraday Soc.*, **47**, 63 (1951).

(14) J. M. Los and D. W. Murray, "Advances in Polarography," Vol. II, I. S. Longmuir, Ed., Pergamon Press Ltd., London, 1960, p 429.

$$R = 3^{1/3}t^{1/3} \quad (35)$$

From the above equations it necessarily follows that the flow rate in the capillary tube in the absence of inertia and interfacial-tension phenomena is given by eq 28. Furthermore, it is easy to deduce from the above results that, at long times as the inertia and interfacial-tension effects fade away, the radius–time relationship approaches that given by eq 35.

Equation 27 is the general radius–time relationship, whereas eq 31 is valid for no fluid inertia in the capillary and eq 33 is valid for no inertia or interfacial-tension effects. Equation 35 is the usual polarographic result, applicable for the same conditions as eq 33, but with $R(0) = 0$. Derivation of radius–time data from eq 31, 33, or 35 is, of course, straightforward, but calculation of the time dependence of the radius from eq 27 necessitates a finite-difference solution of the integral equation. Because of the particular form of this integral equation, this can be accomplished very easily. From the calculated R *vs.* t data and from standard application of numerical differentiation and integration techniques, it is possible to compute m, τ, and the instantaneous current from the equations presented in the first paper.[1]

Results and Discussion

In order to determine the influence of the characteristics of the mercury feed system on the polarographic process, the time dependence of the instantaneous current and of the drop radius were computed for several specific cases. The characteristics of the cases considered are summarized in Table I. The effects of the interfacial tension and of the fluid inertia in the capillary tube on the drop-growth behavior for a typical polarographic feed system are shown in Figure 3. Comparison of the general radius–time curve computed from eq 27 with curves calculated from the less general equations indicates the manner in which the interfacial-tension and fluid-inertia phenomena tend to reduce the rate of drop growth. It is evident that the effect of the back pressure created by the interfacial tension is more significant than the inertia effect, which is relatively important only at very small times under usual polarographic conditions.

Several studies of instantaneous current measurements of first drops in the absence of depletion effects have been reported in the literature, among these being the investigations of Hans, Henne, and Meurer,[15] von Stackelberg and Toome,[16] and Los and Murray.[17] However, Los and Murray appear to be the only investigators who included in their presentation the complete details of the feed system which are needed to predict the time variation of the mercury flow rate and, consequently, the instantaneous current *vs.* time behavior. Examination of the data of Los and Murray reveals that the reported flow rate in four of the five cases for which complete details of the mercury feed system are reported is significantly greater than that theoretically possible according to the Hagen–Poiseuille law. This discrepancy may be due to a small error in the measured radius of the capillary, since the flow rate is proportional to the fourth power of the radius. Consequently, eq 27 and the equations presented in the first paper[1] have been used to predict instantaneous current behavior only for the thallium case b experiment of Los and Murray.

For this case, the reported average flow rate is less than that predicted from the Hagen–Poiseuille equation and is only a few per cent different from the average flow rate predicted from theory. In Figure 4, the theoretical predictions of the present analysis for case 5 are compared with the experimental data of Los and Murray and the predictions of the Koutecky equation based on the ideal steady flow rate as computed from the Hagen–Poiseuille law for the capillary used. In this figure the quantity Ω defined by

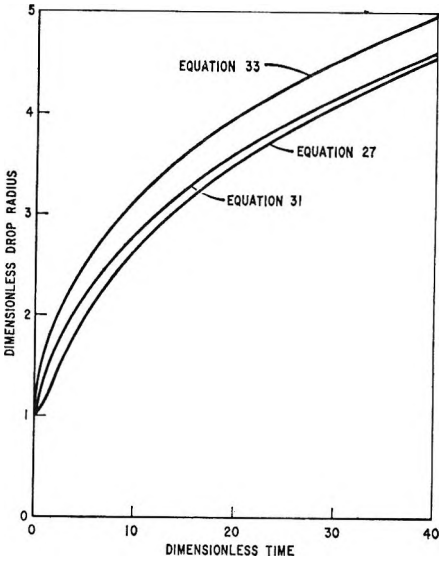

Figure 3. Effects of interfacial tension and fluid inertia on drop growth behavior for case 3: eq 27, both effects included; eq 31, inertia effect omitted; eq 33, both effects omitted.

Table I: Summary of Characteristics of the Cases Considered

Case	h, cm	L, cm	R_0, cm	σ, dynes/cm	$10^5 D$, cm²/sec
1	40	40	0.005	400	...
2	40	10	0.005	400	...
3	10	10	0.005	400	...
4	70	10	0.005	400	...
5	18	12	0.003360	390	1.79
6	18	12	0.003328	390	1.79

(15) W. Hans, W. Henne, and E. Meurer, *Z. Elektrochem.*, **58**, 836 (1954).

(16) M. von Stackelberg and V. Toome, *Collect. Czech. Chem. Commun.*, **25**, 2958 (1960).

(17) J. M. Los and D. W. Murray, "Advances in Polarography," Vol. II, I. S. Longmuir, Ed., Pergamon Press Ltd., London, 1960, p 419.

$$\Omega = \frac{iM}{4\pi(R_0 m_0 D\beta)^{1/3} Fn(\rho_{IO} - \rho_{IE})} \tag{36}$$

is plotted as a function of dimensional time. The data for the experimental curve in Figure 4 were obtained directly from the graph presented by Los and Murray, and the theoretical calculations are based on: the reported capillary characteristics, the value of the diffusion coefficient for the thallium ion as obtained by Wang and Polestra[18] from tracer studies, and the value of interfacial tension estimated by Los and Murray. The deviation between the predicted and experimental curves in Figure 4 ranges from 4 to 6%.

There is definite evidence in the work of Los and Murray of either errors in the measurement of the capillary radius or errors in the flow-rate measurements. Since four flow-rate measurements with the same capillary yielded values which were all substantially greater than the ones predicted from the Hagen–Poiseuille equation for the reported capillary radius, it is reasonable to attribute any anomaly to an error in the measurement of the capillary radius. Figure 5 shows a comparison of the calculated and observed current behavior for case 6 when a capillary radius consistent with the observed flow rate is employed for the thallium

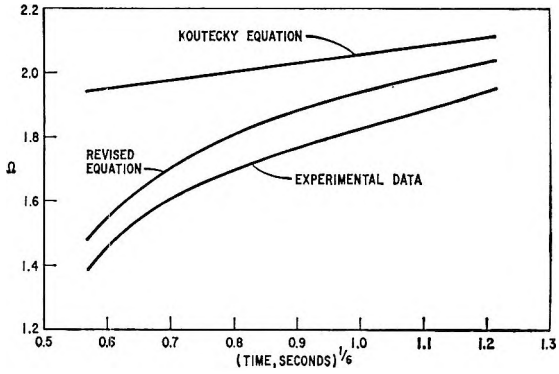

Figure 4. Comparison of predicted instantaneous-current behavior with experimental data of Los and Murray for case 5.

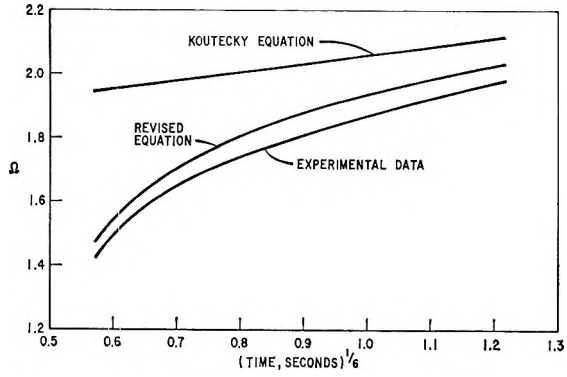

Figure 5. Comparison of predicted instantaneous-current behavior with experimental data of Los and Murray for case 6. Theory based on capillary radius corrected to be in agreement with observed flow rate.

case b experiment. This correction improves the agreement between the predicted and observed curves, the deviations between the predictions of the revised equation developed in this study and the experimental data rangingm for 2 to 4%. Although the available data are too limited for a conclusive test, the above comparisons indicate that incorporation of the variable flow rate, as developed in this analysis, represents a significant improvement in the prediction of instantaneous current behavior, particularly at the earlier periods of drop growth. For the lone case available for consideration, the agreement between experiment and theory can certainly be considered quite good.

In the calculation of the curves for the revised equation in Figures 4 and 5, the following correction for the reduction in effective drop area due to the attachment of the drop to the mercury within the capillary was utilized

$$i_{cor} = i\left[\frac{1}{2}\left(\frac{\sqrt{R^2 - 1}}{R} + 1\right)\right] \tag{37}$$

This correction is completely negligible, except for the earliest times shown in Figures 4 and 5.

It was pointed out in the first paper[1] that the current predicted by the equations of this investigation approaches that predicted by the Koutecky equation (with m_0 used as the flow rate) at long times. Since the Koutecky equation is, of course, easier to utilize than the equations of this work, it is perhaps desirable to examine the best method of manipulating the physical characteristics of the feed system so that the current predicted by the Koutecky equation is essentially indistinguishable from the current predicted by the more general equations for as much of the drop life as possible. This can, of course, be accomplished by designing the polarograph so that the radius–time behavior closely approaches that described by eq 35 for as great a fraction of the drop life as is feasible. The conventional polarographic feed system, as depicted in Figure 1, has three basic parameters, R_0, L, and h, which can be changed independently and relatively easily. A qualitative summary of the influence of each of these parameters on the interfacial-tension effect, the inertia effect, and the drop time is presented in Table II. The nominal drop time is defined in the usual manner by the equation

$$t_D = \frac{16\sigma\hat{\mu}L}{g^2 R_0^3 \hat{\rho}^2 (L + h)} \tag{38}$$

This table shows that changes in the radius of the capillary influence the two effects in an opposite manner, so that one is then faced with searching for an optimum capillary radius which may not subdue either effect satisfactorily. On the other hand, increases in

(18) J. H. Wang and F. M. Polestra, *J. Amer. Chem. Soc.*, **76**, 1584 (1954).

the height of mercury above the capillary will not influence the inertia effect, but will reduce the interfacial-tension effect. Since the inertia effect is usually relatively small, except at the very early stages of drop growth, increasing h could potentially be an effective means of minimizing the effect of a variable flow rate. However, the influence of increasing h is complicated by the fact that the corresponding drop life will be decreased. Figure 6 shows how the drop growth tends to approach the idealized growth realized with a constant flow rate, m_0, as the height above the capillary is increased. Due to the resulting decrease in drop life, an increase in h does not consistently influence the growth behavior in a favorable manner. It should also be noted that the increased flow rate due to an increased value of h will tend to promote spurious convective flows that are associated with current maxima of the second kind.

Table II: Qualitative Summary of the Effect of Increasing Independently Each of the Three Basic Characteristics of the Conventional Polarographic Feed System

Feed system characteristic increased	Change in interfacial-tension effect	Change in inertia effect	Change in drop time
R_0	Decrease	Increase	Decrease
h	Decrease	Unchanged	Decrease
L	Decrease	Unchanged	Increase

Table II indicates that increasing the capillary length, L, will decrease the interfacial tension effect, as well as increase the drop time. Therefore, as Figure 7 shows, increases in the capillary length will consistently promote idealized drop growth. From these considerations it appears that the optimum method for reducing the influence of the variable flow rate obtained with a conventional feed system must include an increase in the length of the capillary, in possible combination with an increase in h.

The equations developed in this investigation can, in principle, be useful in the determination of diffusion coefficients from instantaneous current data. Although they are more difficult to apply than the Koutecky equation, utilization of these equations inherently ensures greater accuracy, since a large portion of the instantaneous current–time curve can be used instead of only the maximum current, as is the case when the Koutecky equation is employed. In addition, analyzing current data with the more complex set of equations makes it easier to detect the spurious convective mixing often present near the end of drop life because of the density gradients in the concentration field. Finally, application of the equations derived in this investigation makes it possible to determine how much error is introduced in the calculated diffusion coefficient

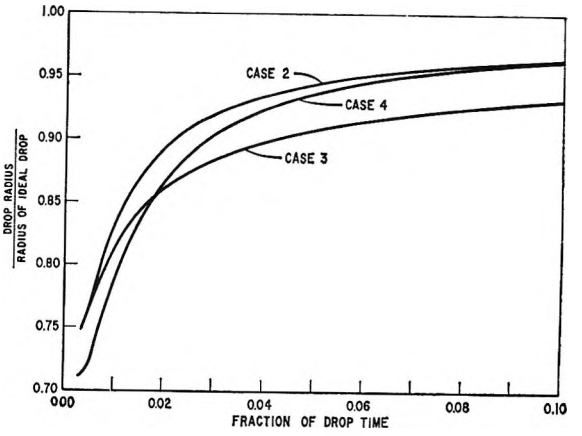

Figure 6. Influence of height above capillary on drop-growth behavior.

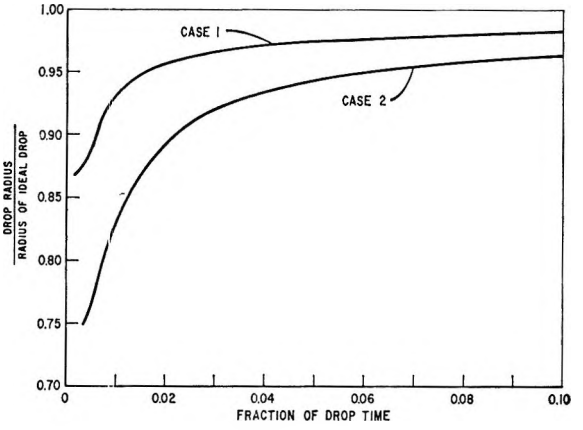

Figure 7. Influence of capillary length on drop-growth behavior.

if the simpler Koutecky equation is used in analyzing the instantaneous-current data. One application of the present analysis for a given polarographic feed system provides an estimate of the error to be expected if the identical polarographic apparatus is used to obtain diffusion coefficients from current data analyzed by the Koutecky equation.

In the conventional method of determining diffusion coefficients, the maximum current is analyzed by the Koutecky equation based on an average flow rate defined as

$$\bar{m} = \frac{\int_0^t m \, dt}{t} \tag{39}$$

This quantity is simply the dimensionless flow rate that the experimentalist measures, and its value asymptotically approaches 1 at long times. Diffusion coefficients obtained in this manner will necessarily be somewhat inaccurate, since the Koutecky equation is being applied for conditions under which it is not valid. The derivation of the Koutecky equation assumes the flow rate to be some constant during the entire drop life,

and it is, of course, not strictly correct to substitute for this value the experimentally measured flow rate, except at long times where the Koutecky equation provides an increasingly better approximation to the current.

However, utilization of the Koutecky equation to analyze instantaneous current–time data substituting the measured or time-average flow rate can sometimes lead to relatively accurate estimates of the diffusion coefficient. The equations developed in this investigation were used to generate an instantaneous current–time curve, which was then analyzed by the usual maximum current procedure based on the Koutecky equation and the measured or time-average flow rate. The errors in the diffusivities calculated by this procedure are depicted as a function of drop time (with a drop detaching device, a wide range of drop times can in principle be obtained) in Figure 8. Even at very small drop times the error is relatively small. Such agreement should be termed as fortuitous, since the Koutecky equation is applied to conditions under which it is not strictly valid. The above calculations were for one specific case and such accuracy should not be expected for all polarographic experiments.

In conclusion, the present analysis can be used either as a basis for determining diffusivities by utilizing a large part of the current *vs.* time curve or as a means of establishing the error in diffusion coefficients calculated from the maximum instantaneous current by the conventional technique using the Koutecky equation.

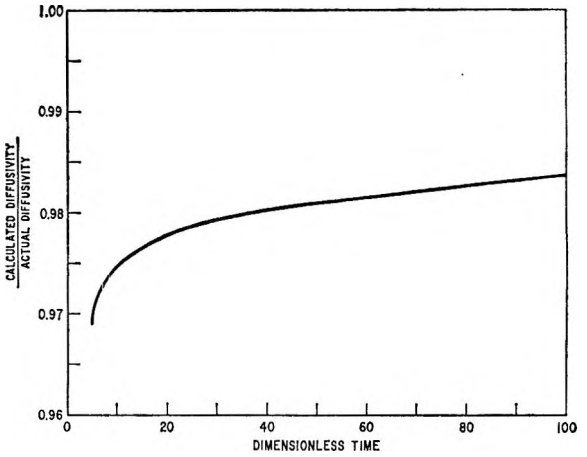

Figure 8. Ratio of diffusivity calculated from Koutecky equation to actual diffusivity value as a function of drop time for conditions of case 5.

Acknowledgment. The authors wish to acknowledge the assistance of R. W. Anderson and G. K. Kimmerly in obtaining photographs of the drop detachment process.

Properties of Organic–Water Mixtures. VII. Self-Diffusion Coefficients of Na^+ in Ethylene Glycol–Water and Glycerol–Water Mixtures at 25°[1]

by Arthur E. Marcinkowsky, Harold O. Phillips, and Kurt A. Kraus

Chemistry Division, Oak Ridge National Laboratory, Oak Ridge, Tennessee 37831 *(Received August 22, 1967)*

Self-diffusion coefficients, $\mathfrak{D}_{Na}$, of Na^+ were measured for water mixtures of ethylene glycol and of glycerol at 25° ($m_{NaCl} = 0.1$) by the radiometric porous-frit method. The diffusion coefficients decrease more rapidly in glycerol than in glycol solutions, qualitatively, as expected from the viscosities of the systems. The diffusion–viscosity product, $\mathfrak{D}\eta/\eta_0$, for the ethylene glycol system is essentially independent of solvent composition. In the glycerol system, however, $\mathfrak{D}\eta/\eta_0$ rises in the organic-rich region. In contrast, $\mathfrak{D}\eta/\eta_0$ for water mixtures of methanol, ethanol, and 1-propanol was earlier found to decrease in the same region. The self-diffusion–composition curves for the ethylene glycol and glycerol systems are similar to the corresponding NaCl limiting equivalent conductance–composition curves.

In a previous paper,[2] it was shown that the radiometric frit method can be used for self-diffusion studies in water–organic–electrolyte systems. The self-diffusion coefficients, $\mathfrak{D}_{Na}$, of Na^+ in water mixtures of methanol (MeOH), ethanol (EtOH), and 1-propanol (PrOH) at a constant salt concentration of $m_{NaCl} = 0.1$ (mol of NaCl/kg of solvent) and at 25° were reported.

The purpose of this paper is to report on the sodium ion self-diffusion coefficient ($\mathfrak{D}_{Na}$) measurements at a constant salt concentration $m_{NaCl} = 0.1$ for the water mixtures of ethylene glycol (EG) and glycerol (G) at 25°. The $\mathfrak{D}_{Na}$ results expressed as a self-diffusion coefficient–viscosity product, $\mathfrak{D}^{\mp} = \mathfrak{D}\eta/\eta_0$, ($\eta$ is the viscosity of the solution, and η_0 is the viscosity of water), for both the EG and G systems are compared with the corresponding limiting equivalent conductance–composition data (Walden products) for NaCl reported by Accascina and coworkers.[3,4]

Experimental Section

1. Method. Self-diffusion coefficients were measured by the radiometric porous-frit method described earlier.[5] Briefly, porous frits are loaded with a solution containing radioactive tracer, and the same solution not containing tracer is pumped past it. The resulting (diffusional) decay of tracer is measured as a function of flow rate; diffusion coefficients are calculated from the decay rates when these are independent of flow rate. All diffusion coefficients reported here were obtained from such a plateau. Porous gold frits with about 50% void volume and approximate dimensions of 1.2 × 0.7 × 0.07 cm, prepared and calibrated as described earlier,[5] were used. The temperature for all calibrations and for the EG–H_2O measurements was maintained at 25 ± 0.1°, and at 25 ± 0.2° for the G–H_2O measurements. Distribution coefficient measurements showed that the gold frits did not adsorb sodium ions significantly from the mixtures.

2. Tracers. Two different radiotracers were used: ^{24}Na($T_{1/2}$ = 15.05 hr) was obtained from the radioisotopes division of ORNL, and ^{22}Na($T_{1/2}$ = 2.58 years) was obtained from the Nuclear Science and Engineering Corp. Examination of the γ-energy spectra showed no detectable impurities in either tracer and no purifications were carried out. The ^{24}Na tracer was always of high specific activity and had stated radiochemical purity greater than 99%. To avoid impurity buildup, use of ^{24}Na tracer was discontinued after approximately 5 half-lives had elapsed.

3. Materials. Reagent grade NaCl was used without further purification. The ethylene glycol and glycerol were purified by vacuum distillation.[6] The EG– and G–H_2O mixtures were prepared on a weight basis. In addition, each solution was separately analyzed for water content by Karl Fischer titration. The titrated water contents agreed within 0.5% of the

(1) (a) Research sponsored by The Office of Saline Water, U. S. Department of the Interior under Union Carbide Corporation's contract with the U. S. Atomic Energy Commission; (b) previous paper in series: R. J. Raridon, W. H. Baldwin, and K. A. Kraus, *J. Phys. Chem.*, in press; (c) presented before the Division of Physical Chemistry, 152nd National Meeting of the American Chemical Society, New York, N. Y., Sept 1966, Abstract 65-V.

(2) A. E. Marcinkowsky, H. O. Phillips, and K. A. Kraus, *J. Phys. Chem.*, **69**, 3968 (1965).

(3) F. Accascina, A. D'Aprano, and M. Goffredi, *Ric. Sci. Rend., Sez. A*, **6**(1), 151 (1964).

(4) F. Accascina, A. D'Aprano, and M. Goffredi, *ibid.*, **4**(4), 443 (1964).

(5) A. E. Marcinkowsky, F. Nelson, and K. A. Kraus, *J. Phys. Chem.*, **69**, 303 (1965).

(6) We thank Dr. W. H. Baldwin and J. Csurny for the ethylene glycol and glycerol purifications.

calculated compositions. We report the solvent compositions in terms of weight per cent and volume per cent. The latter were calculated from the weights, w_1, of water and, w_3, of organic component as: vol % organic = $100/[(w_1\rho_3/w_3\rho_1) + 1]$ where ρ_1 and ρ_3 are the densities of water and organic component, respectively. The densities at 25° used in the calculations are 1.1099[7] and 1.2480[8] for ethylene glycol and glycerol, respectively. The solution viscosities were measured with Cannon–Ubbelohde[9] viscometers.

Results and Discussion

1. Results. The self-diffusion coefficients of the sodium ion in H_2O–EG and H_2O–G at $m_{NaCl} = 0.1$ and the viscosities of the NaCl solutions are given in Tables I and II. The self-diffusion coefficient of Na^+ is highest in the aqueous solution (1.28×10^{-5} cm^2 sec^{-1})[2] and decreases with increasing organic content of the solvent. At comparable solvent compositions, the $\mathfrak{D}_{Na}$ curve decreases more rapidly in the G– system than in the EG– system, qualitatively, as expected from the viscosities of the systems.

Table I: Self-Diffusion Coefficients of Na^+ in NaCl–Ethylene Glycol–Water Mixtures at 25° ($m_{NaCl} = 0.1$)

Wt % EG	Vol % EG	η/η_0	$10^5\mathfrak{D}$, cm^2 sec^{-1}	$10^5\mathfrak{D}\eta/\eta_0$, cm^2 sec^{-1}
0.0	0.0	1.01	12.8	1.29
25.4	23.4	1.89	8.09	1.53
50.0	47.3	3.65	4.38	1.60
74.8	72.7	7.80	2.19	1.71
85.0	83.6	11.26	1.54	1.73
95.0	94.5	16.57	1.07	1.77
100.0	100.0	20.26	0.83	1.69
100.0	100.0	20.26	0.82	1.66[a]

[a] Measurement made with ^{22}Na.

Table II: Self-Diffusion Coefficients of Na^+ in NaCl–Glycerol–Water Mixtures at 25° ($m_{NaCl} = 0.1$)

Wt % G	Vol % G	η/η_0	$10^5\mathfrak{D}$, cm^2 sec^{-1}	$10^5\mathfrak{D}\eta/\eta_0$, cm^2 sec^{-1}
14.7	12.1	1.49	9.71	1.45
25.0	20.9	2.06	7.79	1.61
34.8	29.9	2.87	6.08	1.75
48.9	43.4	5.32	3.39	1.80
50.0	44.2	5.74	3.14	1.80
58.7	53.2	9.06	2.29	2.07
72.7	68.0	25.3	1.03	2.61
75.0	70.4	32.2	0.796	2.56
77.4	73.2	39.6	0.751	2.97
80.0	76.0	53.2	0.558[a]	2.97
82.2	78.6	66.3	0.451	2.99
85.0	81.8	94.6	0.339[a]	3.21
90.0	87.7	194.6	0.168[a]	3.27
95.0	93.8	424.0	0.088[a]	3.73

[a] Measurements made with ^{22}Na.

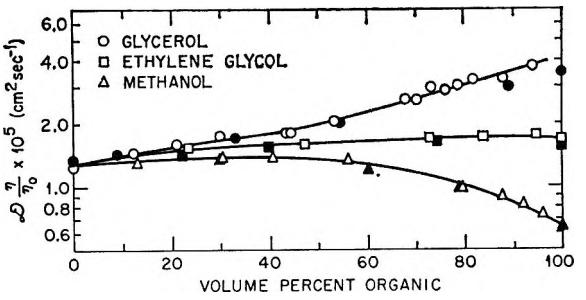

Figure 1. Comparison of self-diffusion coefficient–viscosity products: open symbols, diffusion data ($m_{NaCl} = 0.1$); filled symbols, calculated from limiting conductances.

The viscosities of ethylene glycol and glycerol are 16.84[3] and 945,[4] respectively. A solution 95 wt % G ($m_{NaCl} = 0.1$) with $\eta/\eta_0 = 424$ is the most viscous system that we have studied. Our reproducibility at the higher viscosities is not as great as that at the lower viscosities and uncertainties in the self-diffusion coefficients seem to be of the order of 5%. A correction for tracer decay[5] was applied whenever $(\mathfrak{D}_{uncor} - \mathfrak{D}_{cor})/\mathfrak{D}_{cor}$ was above 0.5%. The maximum correction was 2.1%. For the viscous glycerol–water systems, 75 wt % glycerol and above, the long-lived ^{22}Na tracer was used to avoid this correction.

The self-diffusion coefficient–viscosity products, including the data[2] for the MeOH system, plotted as a function of volume per cent organic, are shown in Figure 1. Up to an organic content of about 40 vol %, the three curves remain similar but not identical. At 40 vol %, the values of $\mathfrak{D}^{\pm}$ are 1.40, 1.55, and 1.75×10^{-5} cm^2 sec^{-1} for the methanol–, ethylene glycol–, and glycerol– systems, respectively. Above 40 vol % organic, $\mathfrak{D}^{\pm}$ for the methanol system decreases, it remains constant for the ethylene glycol system, and increases for the glycerol system. At 95 vol % organic, the values of $\mathfrak{D}^{\pm}$ are 0.76, 1.75, and 3.8×10^{-5} cm^2 sec^{-1}, while the corresponding $\mathfrak{D}_{Na}$ values are 0.93×10^{-5}, 1.03×10^{-6}, and 0.73×10^{-7} cm^2 sec^{-1} for the MeOH–, EG–, and G– systems, respectively. Thus the values of $\mathfrak{D}_{Na}$ for the MeOH and G systems differ by a factor slightly greater than 100, whereas the $\mathfrak{D}^{\pm}$ values, when the solution viscosity is taken into account, differ by a factor of only 5.

If the viscosity is raised to a fractional power k before multiplying by the self-diffusion coefficient (*i.e.*, $\mathfrak{D}(\eta/\eta_0)^k$), the best correlation is found when k is 0.7, the preferred exponent of others.[10] A plot of $\mathfrak{D}(\eta/\eta_0)^{0.7}$ *vs.* volume per cent alcohol describes the

(7) G. O. Curme, Ed., "Glycols," Reinhold Publishing Corp., New York, N. Y., 1952.

(8) C. S. Miner and N. N. Dalton, Ed., "Glycerol," Reinhold Publishing Corp., New York, N. Y., 1953.

(9) We thank Dr. R. J. Raridon and C. G. Westmoreland for the viscosity measurements and Karl Fischer water titrations.

(10) R. A. Robinson and R. H. Stokes, "Electrolyte Solutions," Academic Press Inc., New York, N. Y., 1959.

data for the MeOH–, EtOH–, PrOH–,[2] and the EG– and G– systems to within ±20%.

2. Comparison of Self-Diffusion and Conductance. According to the Onsager limiting theory[11] for 1:1 electrolytes at constant temperature, the diffusion coefficient $\mathfrak{D}_M$ of an ion M depends on the square root of the salt concentration (c) in mol/l., the ionic conductance, λ^0, of both cation and anion, and on the dielectric constant of the solvent medium, ϵ. The relation is given by the equation

$$\mathfrak{D}_M = \frac{RT\lambda_M^0}{|z|F^2}\left[1 - \frac{0.544 \times 10^3}{\epsilon^{3/2}}\zeta\sqrt{c}\right] \quad (1)$$

where

$$\zeta = 1 - \sqrt{(3\lambda^0_K + \lambda^0_M)/4(\lambda^0_K + \lambda^0_M)}$$

λ^0_M is the limiting ionic conductance of the ion M (cm² ohm^{-1} equiv^{-1}); λ^0_K is the limiting ionic conductance of the counterion K; R is the gas constant (J deg^{-1} mol^{-1}); T is absolute temperature; F is the Faraday (international coulombs g-equiv^{-1}). At infinite dilution, eq 1 reduces to the well-known Nernst equation[10]

$$\mathfrak{D}^0_M = \frac{RT\lambda^0_M}{|z|F^2} = 2.663 \times 10^{-7}\frac{\lambda^0_M}{|z|}\ \text{cm}^2\ \text{sec}^{-1} \quad (2)$$

where $\mathfrak{D}^0_M$ is the self-diffusion coefficient of the ion M at infinite dilution and $|z|$ is the absolute value of the charge of the ion.

Using the Nernst and Onsager theories, ionic or self-diffusion coefficients at infinite dilution and at 0.1 m for the water–methanol system were found to correlate well.[2] A similar comparison between diffusion and conductance data for the EG– and G– systems is not possible because the single ion mobilities as a function of solvent composition are lacking. It is, however, possible to compare the values of $\mathfrak{D}_{Na}$ in a semiquantitative manner with the corresponding limiting equivalent conductances, Λ^0_{NaCl}, which are known for both the EG– and G– systems.[3,4]

For comparison, we shall set the transport number, t^0_{Na}, of the sodium ion at infinite dilution, in the various water–organic mixtures, equal to 0.3962, its value in water. This is equivalent to setting $\lambda^0_{Na} = 0.3962 \times \Lambda^0_{NaCl}$ at all solvent compositions.

The filled symbols in Figure 1 for the MeOH–, EG–, and G– systems represent the self-diffusion coefficient–viscosity products, $\mathfrak{D}^0\eta/\eta_0$, calculated in this manner from the limiting conductances. For the EG– and G– systems, the Λ^0_{NaCl} values used are those reported by Accascina and coworkers[3,4] and for the MeOH– system, the data of Shedlovsky reported by Harned and Owen[12] are used. Agreement between the calculated self-diffusion coefficients and the experimental results is surprisingly good. Presumably the expected decrease of the self-diffusion coefficient with concentration is compensated by a similar increase of the sodium ion transport number in the organic–water mixtures.

Acknowledgment. It is a pleasure to thank G. Scatchard, R. M. Fuoss, R. A. Robinson, and F. Nelson for a number of helpful discussions.

(11) L. Onsager, *Ann. N. Y. Acad. Sci.*, **46**, 241 (1945).

(12) H. S. Harned and B. B. Owen, "The Physical Chemistry of Electrolyte Solutions," Reinhold Publishing Corp., New York, N. Y., 1958.

The Binding of Cholate and Glycocholate Anions by Anion-Exchange Resins

by James Blanchard[1] and J. Graham Nairn

Faculty of Pharmacy, University of Toronto, Toronto, Ontario, Canada *(Received August 23, 1967)*

The exchange of cholate ions for chloride ions and glycocholate ions for chloride ions on Dowex 1 resins was investigated. Under the conditions employed, the uptake of cholate and probably glycocholate is due to ion exchange. The extent of ion exchange as determined from the ion-exchange isotherm is greatest when resin beads are used which have a low percentage of cross-linking and a small particle size. A consideration of the separation factor indicates: that the resins possess a high affinity for the bile salt anions, that there is a slightly greater preference for the cholate ions as compared to the glycocholate ions, and that the separation factor is greater with resins of low cross-linking. There is a considerable reduction in exchange sites available to the bile salt anions as the cross-linking is increased from 4 to 8%.

Introduction

Binding of bile salt anions by ion-exchange resins for medicinal purposes has been investigated.[2-4] The therapeutic effectiveness of the resin depends on the selectivity between the bile salt anions and the chloride anion and also the capacity for the organic ion. This research was carried out to determine the capacities of the resins for the anions and the separation factors of the system and, in addition, to investigate some of the properties of the resins and anions responsible for the high affinity of the large organic ions for the ion-exchange resins. The binding of large organic ions by ion exchange has been studied by several investigators.[5,6] The nonion-exchange sorption of ions has also been reported.[7] In the present investigation of chloride–cholate exchange, analysis for both anions was carried out so that nonion-exchange sorption, if any, could be detected. The total concentration of salts was maintained at a definite concentration so that ionic strength of the solution would be constant.

Under the conditions of the experiments (pH $\geq$6.5) the bile acid would be nearly all in the ionized form.[8,9] The concentration of the bile salt in the external solution was kept below 0.01 M, so that association of the anions would not take place.[10]

Experimental Section

Materials. Cholic acid (Mann Research Laboratories) was triply recrystallized from redistilled 95% ethanol. Glycocholic acid (Mann Research Laboratories) was purified by a liquid–liquid extraction procedure, as described by Hofmann,[11] and subsequently recrystallized from 5% ethanol in water. The identities of the bile acids were checked by infrared spectra, melting points, and optical rotations.[12,13] The purity was estimated to be at least 99% by thin-layer chromatography, using the method of Usui and solvent systems numbers 3 and 4.[14-16]

The strongly basic Dowex 1 ion-exchange resins (Dow Chemical Co.) were conditioned, were converted to the chloride form, were washed thoroughly, and were stored in a moist form. Samples of the conditioned resin were then centrifuged at 400g for 30 min using an extraction thimble with a coarse porosity disk.[7] The capacities of the resin samples were then determined using the column technique, by adding excess sodium nitrate solution and analyzing the effluent for chloride. The moisture contents of the centrifuged resins were determined by drying at 105–115° for 12 to 16 hr.

Equilibrium Systems. Samples of wet centrifuged resin (20–80 mg) were added to tared 100-ml round-bottomed flasks. Varying volumetric ratios of known

(1) Taken in part from the thesis of James Blanchard to the School of Graduate Studies of the University of Toronto in partial fulfillment of the requirements for the degree of Master of Science in Pharmacy.

(2) D. M. Tennent, H. Siegel, M. E. Zanetti, G. W. Kuron, W. H. Ott, and F. J. Wolf, *J. Lipid Res.*, 1, 469 (1960).

(3) D. M. Tennent, S. A. Hashim, and T. B. Van Itallie, *Federation Proc., Suppl. 11*, 21, 77 (1962).

(4) C. H. Whiteside, H. B. Fluckiger, and H. P. Sarett, *Proc. Soc. Exp. Biol. Med.*, 121, 153 (1966).

(5) L. V. Dmitryenko and D. K. Hale, *J. Chem. Soc.*, 5570 (1965).

(6) T. R. E. Kressman and J. A. Kitchener, *ibid.*, 1208 (1949).

(7) K. W. Pepper, D. Reichenberg, and D. K. Hale, *ibid.*, 3129 (1952).

(8) B. A. Josephson, *Biochem. Z.*, 263, 428 (1933); *Chem. Abstr.*, 27, 5350 (1933).

(9) P. Ekwall, T. Rosendahl, and N. Lofman, *Acta Chem. Scand.*, 11, 590 (1957).

(10) P. Ekwall, K. Fontell, and A. Sten, *Proc. Intern. Congr. Surface Activity* (London), 1, 357 (1957).

(11) A. F. Hofmann, *Biochem. J.*, 89, 57 (1963).

(12) I. Fischmeister, *Arkiv Kemi*, 16, 151 (1960).

(13) S. J. Levin and C. G. Johnston, *Talanta*, 8, 871 (1961).

(14) T. Usui, *J. Biochem.* (Tokyo), 54, 283 (1963).

(15) G. R. Duncan, *J. Chromatogr.*, 8, 37 (1962).

(16) A. F. Hofmann, *Acta Chem. Scand.*, 17, 173 (1963).

weights of 0.01 *M* sodium bile salt solution (prepared from equivalent amounts of bile acid and sodium hydroxide) and 0.01 *M* NaCl solution were added to give a constant total volume of 70 ml. The flasks were shaken at room temperature (23–25°) for at least twice the time required for the attainment of equilibrium.

Separation and Analyses. After equilibration, the solution was separated from the resin beads by means of a coarse porosity sintered glass filter funnel. The resin in the funnel was then centrifuged, weighed, and dried, as described above. One portion of the equilibrated solution was weighed and analyzed for cholate potentiometrically with approximately 0.04 *N* hydrochloric acid, using a Beckman Research pH meter, a glass–calomel electrode pair, and a microburet. Glycocholate anion concentration was not determined because the potentiometric assay was found to be unsuitable. Another portion of the equilibrated solution was weighed and analyzed for chloride using a method similar to that described by Sendroy.[17] For the determination of low concentrations of chloride (below 4 mequiv/l.) a calibration curve was prepared.

Results and Discussion

All concentrations in this paper were determined on or converted to a molal basis. The amounts of anion in the resin phase were determined from a knowledge of the amounts remaining in solution at equilibrium and the total exchange capacity of the resin. Since the number of equivalents of cholate anion bound and the number of equivalents of chloride anion released by the resin were equal, within the limits of experimental error, it was decided that the binding process was due to ion exchange only. By analogy, the binding of glycocholate was assumed to occur by a similar mechanism. Other workers have been unable to detect any nonion-exchange sorption from solutions of dissociated salts of large organic ions.[6]

The ion-exchange isotherms for some exchanges are shown in Figure 1. In a number of the experiments the curves of the ion-exchange isotherms levelled off at an equivalent ionic fraction less than 1. This indicates an approach to a limiting exchange capacity of the resins for the bile salt anion which is less than the exchange capacity for chloride anion. This limiting exchange capacity was taken to be the value of the ordinate at which the isotherm curve levelled off. These values of maximum uptake for the bile salt anions were then plotted as a function of the degree of cross-linking of the resin and are given in Figure 2.

Either the molalities, m_A, or the equivalent ionic fractions, x_A, can be used to calculate the separation factor defined by

$$\alpha_B^A = \frac{\bar{m}_A m_B}{\bar{m}_B m_A} = \frac{\bar{x}_A x_B}{\bar{x}_B x_A}$$

The equivalent ionic fraction is defined by[18]

$$x_A = \frac{z_A m_A}{z_A m_A + z_B m_B}$$

where z_A is the electrochemical valence of ion A, and m_A is the concentration of species A in moles per unit weight of solvent (molality). The quantities with bars refer to the resin phase, A refers to the bile salt anion, and B refers to the chloride ion. The separation factor does not remain constant but depends on the

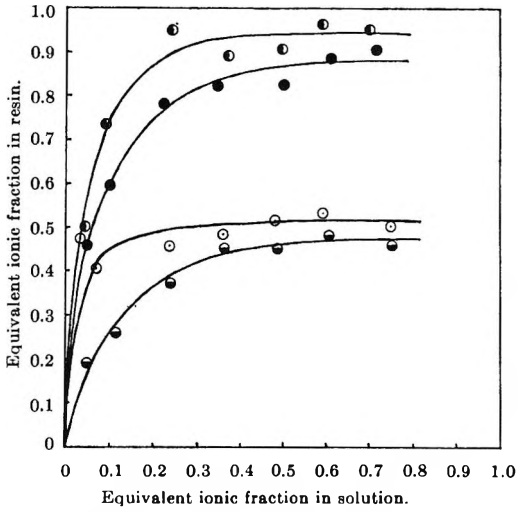

Figure 1. Effect of the degree of cross-linking and type of bile salt on the ion-exchange isotherm: ◐, Dowex 1-X4 (50–100 mesh) with sodium cholate; ⊙, Dowex 1-X8 (50–100 mesh) with sodium cholate; ●, Dowex 1-X4 (50–100 mesh) with sodium glycocholate; ◒, Dowex 1-X8 (50–100 mesh) with sodium glycocholate.

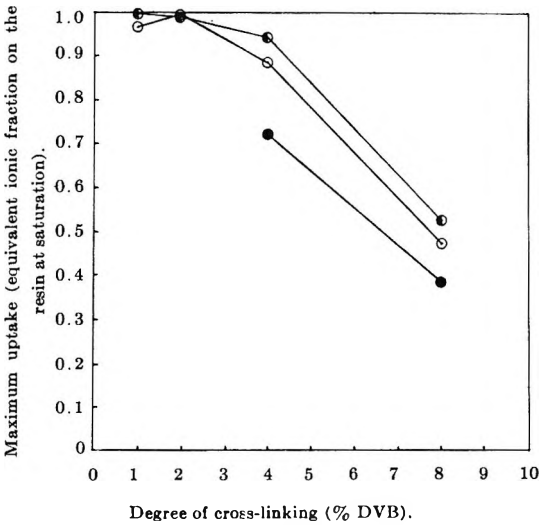

Figure 2. Effect of the degree of cross-linking on the maximum uptake of the resin: ◐, sodium cholate (50–100 mesh resins); ●, sodium cholate (20–50 mesh resins); ⊙, sodium glycocholate (50–100 mesh resins).

(17) J. Sendroy, Jr., *J. Biol. Chem.*, **120**, 335, 405, 419 (1937).

(18) F. Helfferich, "Ion Exchange," McGraw-Hill Book Co., Inc., New York, N. Y., 1962, p 152.

concentration of the solution in the two phases. If both counterions are univalent, then the separation factor and the selectivity coefficient

$$K_B^A = \frac{\bar{m}_A^{|z_B|} m_B^{|z_A|}}{\bar{m}_B^{|z_A|} m_A^{|z_B|}}$$

are the same and their value does not depend on the choice of concentration scale.

The values of the separation factor, α_B^A, were determined from points on the curve of Figure 1 and were then plotted against $\bar{x}_A$, the equivalent ionic fraction of bile salt in the resin phase. It is apparent that the form of these curves (Figure 3) is different from that commonly observed with ion-exchange equilibria involving small univalent ions. The final portion of each curve most likely represents the approach to a limiting exchange for the bile salt anions. It can be seen in Figure 3 that the limiting exchange capacity is reached at lower values of $\bar{x}_A$ for glycocholate than for cholate and also for Dowex 1-X8 than for Dowex 1-X4, respectively. This type of behavior has been discussed by Dmitryenko and Hale[5] and is attributed to the possibility that some regions of the resin are inaccessible to large organic ions and that small ions at these sites cannot be replaced by the large organic ions.

The separation factor can be redefined by assuming that some of the exchange sites are inaccessible to the large organic ions and that the small ions near these sites do not take part in the exchange process. The redefined separation factor is

$$\alpha_B^{A*} = \frac{\bar{m}_A m_B}{\bar{m}_B^* m_A}$$

where $\bar{m}_B^*$ is the concentration of the chloride ions remaining in the resin, which can be replaced by the large organic ions. Therefore

$$\bar{m}_B^* = (\bar{m}_A + \bar{m}_B)R - \bar{m}_A$$

where $\bar{m}_A$ plus $\bar{m}_B$ equals the total concentration of all counterions in the resin, R is the fraction of exchange sites accessible to the large organic ions, and $\bar{m}_A$ is the concentration of the organic ions already on the resin. Therefore

$$\alpha_B^{A*} = \frac{\bar{m}_A m_B}{[(\bar{m}_A + \bar{m}_B)R - \bar{m}_A]m_A}$$

In order to obtain the data from the isotherm graphs (Figure 1), the redefined selectivity coefficients can be expressed in terms of equivalent ionic fractions. The concentration of exchangeable counterions in the resin is now $(\bar{m}_A + \bar{m}_B)R$ and the concentration of the counterions in solution is $m_A + m_B$, the same as before. Thus the redefined separation factor expressed in terms of equivalent ionic fractions is

$$\alpha_B^{A*} = \frac{\bar{x}_A x_B}{(R - \bar{x}_A)x_A}$$

It is possible that the fraction of resin sites entering into mass-action equilibrium with the bile salt anions may not be constant but increases gradually as the concentration of the bile salt anions in the resin increases; thus the value of R was taken to be the horizontal portion of the isotherm curve when the resin contained the greatest amount of the bile salt anion. Concentrations of bile salt anion higher than 0.01 M in the external solution used to obtain higher possible resin loadings were not employed, in order to avoid association of the anions in the external solution. Figure 3 substantiates the postulation that the bile salt anions are unable to replace all of the chloride ions in resins which possess a high percentage of cross-linking.

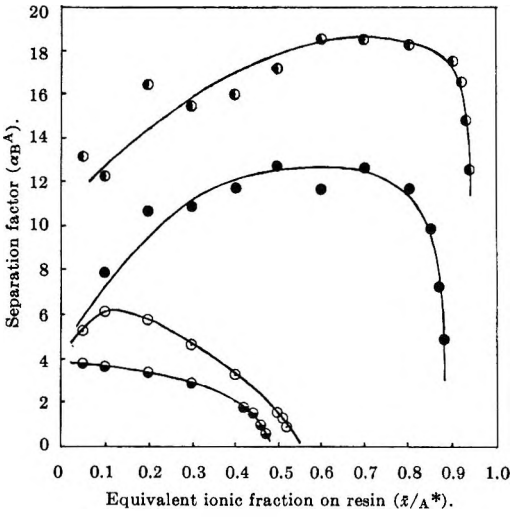

Figure 3. Effect of cross-linking and type of bile salt on the separation factor: ◐, Dowex 1-X4 (50–100 mesh) with sodium cholate; ⊙, Dowex 1-X8 (50–100 mesh) with sodium cholate; ●, Dowex 1-X4 (50–100 mesh) with sodium glycocholate; ◒, Dowex 1-X8 (50–100 mesh) with sodium glycocholate.

When the redefined separation factors, calculated from the isotherm curves, are plotted against the equivalent ionic fraction of accessible sites where exchange has occurred, $\bar{x}_A^* = \bar{x}_A/R$, it can be seen from Figure 4 that with a resin of given cross-linking the value of α_B^{A*} is comparitively low at low values of $\bar{x}_A^*$ but increases rapidly at higher values of $\bar{x}_A^*$. Dmitryenko and Hale[5] have reported similar results for the oxytetracycline–hydrogen ion system. They suggested that the increase in the binding indicated that some form of cooperative process was occurring since the large organic ion was apparently more and more strongly bound as the equivalent ionic fraction of the organic ion in the resin increased. They concluded that aggregate formation occurred in the resin phase

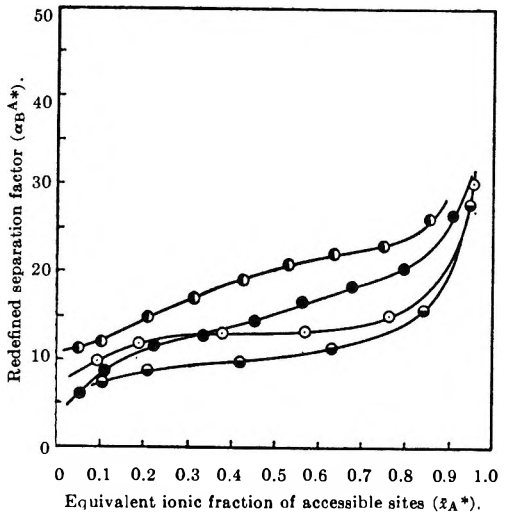

Figure 4. Effect of cross-linking and type of bile salt on the redefined separation factor: ◐, Dowex 1-X4 (50–100 mesh) with sodium cholate; ⊙, Dowex 1-X8 (50–100 mesh) with sodium cholate; ●, Dowex 1-X4 (50–100 mesh) with sodium glycocholate; ◒, Dowex 1-X8 (50–100 mesh) with sodium glycocholate.

and that, in general, an increase in cross-linking or a reduction in exchange capacity leads to an increase in selectivity. Figure 4 shows that as the cross-linking decreased the redefined separation factor increased. Since the two resins compared here had almost identical exchange capacities, this could not be an important factor. A possible explanation is that sodium cholate and sodium glycocholate have a strong tendency to associate in aqueous solution.[10] Thus as the concentration of bile salt anion in the resin phase reaches a critical value, probably different from that reported for aqueous solution, aggregates form, which could enhance the binding. The resin with the lower cross-linking would provide a greater opportunity for aggregates to form and also permit an increase in the size of the aggregate, resulting in an increase in the separation factor.

The fraction of total possible uptake of the bile salt anions by the resins increases with decreasing cross-linkage and is essentially unity for resins with lower cross-linkages as shown in Figure 2. As the percentage of cross-linking is increased the resins have a more rigid matrix, are less liable to swell, and exert a greater sieve action on the large organic anions. Thus it becomes more difficult for the bile salt anions to enter the resin phase due to the inaccessibility of the narrower pores of the resin. A further interpretation of the preference of the ion-exchange resin for the anions can be made, after sieve action has been taken into account, by comparing the redefined separation factors. Figure 4 shows that the redefined separation factors, for both the cholate and glycocholate anions, are dependent upon the degree of cross-linking of the resin. Reichenberg and Wall[19] have postulated that as the cross-linking is increased, the amount of resin material increases and the amount of solute decreases. The resin material can be regarded as having a salting-out effect on the solute. Thus the resin with the lower cross-linking will have more free solvent molecules and hence should show a greater affinity for the solute than a resin of higher cross-linking. It can be seen from Figure 4 that this is the case, and the 4% cross-linked resin exhibits a higher selectivity for the bile salt anions compared to the 8% cross-linked resin.

It was found that there was slightly less uptake of glycocholate anion than of cholate anion (Figures 2 and 4). Gregor[20] has stated that if one counterion is replaced by another counterion which in its solvated state occupies more room, then less "free" water will be in the resin. Thus there will be less water available for dissolution of the solute taken up by the resin. The more solvated ion causes the resin to expand against the elastic forces of the matrix and as a result "free" water is squeezed out. Due to the more hydrophilic nature of the glycine conjugates,[21] it can be assumed that the glycocholate anion should be more strongly solvated and hence less free water would be left in the interior of the resin phase than if cholate anion were taken up by the resin. The resin should, therefore, prefer the less strongly solvated cholate anion as has been found in this study. Gordon, *et al.*,[22] have postulated that a "sorption effect" based primarily on solution of the bile acid in the body of the polymer is operative and that the more hydrophobic the compound, in this case the cholate anion, the more strongly it is retained by the polystyrene matrix. Other effects, such as water structure in the two phases, acid strength, and specific-ion hydration, have been discussed.[23] In this study, however, hydrophilicity and size appear to be the governing factors in the relative uptake of cholate and glycocholate anions.

It was found that resins of smaller particle size bound more cholate than larger particle size resins (Figure 2). The position of equilibrium is normally independent of particle size of the resin, when all exchange groups are accessible to the counterion. However, when pore diameter and molecular size impose limitations on ion exchange, a reduction in particle size can increase the uptake of the counterion.[24] Thus the uptake of bile salt anions by ion-exchange resins is increased when the particle size is reduced, pre-

(19) D. Reichenberg and W. F. Wall, *J. Chem. Soc.*, 3364 (1956).

(20) H. P. Gregor, *J. Amer. Chem. Soc.*, **73**, 642 (1951).

(21) E. H. Ahrens, Jr., and L. C. Craig, *J. Biol. Chem.*, **195**, 763 (1952).

(22) B. A. Gordon, A. Kuksis, and J. M. R. Beveridge, *Can. J. Biochem. Physiol.*, **41**, 77 (1963).

(23) B. Chu, D. C. Whitney, and R. M. Diamond, *J. Inorg. Nucl. Chem.*, **24**, 1405 (1962).

(24) D. A. Hirscher and O. H. Miller, *J. Amer. Pharm. Assoc., NS2*, 105 (1962).

sumably due to the increase in the number of available exchange sites.

Acknowledgment. We are grateful to Dr. G. R. Duncan for assistance with the optical rotation measurements and to the Canadian Foundation for the Advancement of Pharmacy, the National Research Council of Canada, and the University of Toronto for financial support of this research.

Computer Evaluation of Entropy Titration Data. Calorimetric Determination of Log β_i, ΔH_i°, and ΔS_i° Values for the Silver(I)- and Copper(II)–Pyridine Systems[1a]

by Reed M. Izatt[1b,c] Delbert Eatough,[1d] Richard L. Snow, and James J. Christensen[1b,e]

Departments of Chemistry and Chemical Engineering, Brigham Young University, Provo, Utah 84601
(Received August 28, 1967)

Log β_i, ΔH_i°, and ΔS_i° values have been determined in aqueous solution at 25° using a calorimetric titration procedure for the stepwise formation of $AgPy_2^+$ and $CuPy_4^{2+}$ (Py = pyridine) from their constituent ions. The results agree well with previously determined values where available and demonstrate that titration calorimetry can be used to determine log K, ΔH°, and ΔS° values for metal–ligand systems involving simultaneous equilibria. Four iterative methods of data analysis are compared and discussed.

Introduction

The shape of a thermometric titration curve is a function of the equilibrium constants and enthalpy changes for all the reactions involved in the titration. For example, in the simple reaction A + B = AB, where A is titrated with B, the resulting thermometric titration curve will be sufficiently nonlinear to allow calculation of log K, ΔH, and ΔS values, if log K for the reaction is less than approximately 4. This procedure, called the entropy titration method, has been successfully applied to many acid–base systems involving single protonation reactions.[2-5] In general, the equations involved in the calculations cannot be solved exactly for the desired thermodynamic values, and an iterative process must be used to analyze the data. Although iterative calculation methods have been used in the past for the analysis of potentiometric and calorimetric data,[6,7] an extensive study of the problems involved in such calculations as applied to entropy titration data has not been reported nor has complete least-squares fitting of the data been attempted. This study was, therefore, undertaken (1) to compare several different iterative methods for the least-squares analysis of entropy titration data, and (2) to investigate the applicability of the entropy titration procedure to two metal ion–ligand systems involving simultaneous equilibria.

The Ag(I)–pyridine (Py) system was chosen for the first phase of the study because: (1) the equilibrium constants are expected to be independent of ionic strength, μ; (2) competing reactions are negligible; (3) the system is more complex than those previously studied by us in that simultaneous equilibria occur, providing a better test of the various methods of data analysis used; and (4) the system has been previously investigated and the results of this study could be compared with reliable thermodynamic values in the literature. Formation constants for the Ag^+–Py system have been previously determined from solu-

(1) (a) Supported by United States Atomic Energy Commission Contract No. AT(04-3)-299 and National Institutes of Health Grant RG 9430-06; (b) to whom inquiries should be directed; (c) supported (in part) by Public Health Service Research Career Development Award No. 1-K3-GM-35,250-01; (d) National Defense Education Act Predoctoral Fellow, 1964–1967; (e) supported (in part) by Public Health Research Career Development Award No. 1-K3-GM-24,361-01.

(2) J. J. Christensen, R. M. Izatt, L. D. Hansen, and J. A. Partridge, *J. Phys. Chem.*, **70**, 2003 (1966).

(3) R. M. Izatt, J. H. Rytting, L. D. Hansen, and J. J. Christensen, *J. Amer. Chem. Soc.*, **88**, 2641 (1966).

(4) J. J. Christensen, D. P. Wrathall, R. M. Izatt, and D. O. Tolman, *J. Phys. Chem.*, **71**, 3001 (1967).

(5) J. J. Christensen, D. P. Wrathall, and R. M. Izatt, *Anal. Chem.*, **40**, 175 (1968).

(6) L. G. Sillén, *Acta Chem. Scand.*, **16**, 159 (1962).

(7) P. Paoletti, A. Vacca, and D. Arenare, *J. Phys. Chem.*, **70**, 193 (1966).

bility,[8] potentiometric,[9,10] and calorimetric[7,11] data. Corresponding ΔH° values have been determined calorimetrically.[7,11] The Cu(II)–Py system was studied because of its greater complexity, in that Cu^{2+} ion interacts with Py to form four $Cu(Py)_i^{2+}$ (i = 1, 2, 3, 4) complexes. Since all the equilibrium constants for the formation of $CuPy_i^{2+}$ from Cu^{2+} and Py are of the order of magnitude that they can be determined by thermometric titration techniques, this system provides a more extensive test of the numerical least-squares method used in the analysis of the data for the interaction of Py and Ag^+ ion. Equilibrium constants have been reported[9,12-15] for the stepwise formation of $CuPy_4^{2+}$ from Cu^{2+} and Py at μ values ranging from 0.1 to 1.0, but no stepwise ΔH° or ΔS° values or thermodynamic equilibrium constants valid at $\mu = 0$ have been reported. In a recent study, Atkinson and Bauman[12] report an average ΔH value for the interaction of Cu^{2+} with Py.

In this study are reported log β_i, ΔH_i° and ΔS_i° values valid at 25° and $\mu = 0$ for the stepwise formation of $AgPy_2^+$ and $CuPy_4^{2+}$ from their constituent ions. In addition, four methods of data analysis are compared with respect to the Ag^+–Py system and their relative merits are discussed.

Experimental Section

Materials. Reagent grade $AgNO_3$ (Baker Analyzed) and $NaNO_3$ (Baker Analyzed) were dried at 100° for 4 hr and used as primary standards in the preparation of their solutions. Reagent grade Py (Eastman White Label) was purified by distillation under reduced pressure over lithium aluminum hydride and stored under an N_2 atmosphere. A $Cu(ClO_4)_2$ solution with just enough acid to suppress hydrolysis of the Cu^{2+} ion was prepared by dissolving Cu powder (Baker Analyzed) in a known amount of $HClO_4$ (Baker and Adamson). The solution was standardized for Cu^{2+} against EDTA (Baker Analyzed).

Procedure. The calorimetric equipment and operational procedure have been described.[16,17] Thermometric titrations for the Ag^+–Py study were made using both Py and $AgNO_3$ as titrant. The μ values of the runs were varied from 0.005 to 0.02. Heat-of-dilution data[18] were determined as a function of μ for both the Py and $AgNO_3$ titrants by titration of each into H_2O and also into $NaNO_3$ solutions. The heat-of-dilution data were fitted by the method of least squares to a power series in $\sqrt{\mu}$, resulting in values of $(-300 + 45.5\sqrt{\mu})$ and $(507 - 482\sqrt{\mu} + 609\mu)$ cal/mol for the heats of dilution (to final μ values 0.005–0.03) of 0.9886 F Py and 0.9858 F $AgNO_3$ solutions, respectively. Titrations for the Cu(II) study were made in solutions 0.01 and 0.02 F in $Cu(ClO_4)_2$ using Py as titrant. Heat-of-dilution data for the 1.534 F pyridine titrant used in the Cu(II)–Py study were fitted to a power series in $\sqrt{\mu}$ resulting in the values $(1.211 - 9.257\sqrt{\mu}) \times 10^3$ and $(4.724 - 43.95\sqrt{\mu} + 95.15\mu) \times 10^3$ cal/mol for dilution into the 0.01 and 0.02 F $Cu(ClO_4)_2$ solutions, respectively.

Because of the low ionic-strength values employed in the determinations, the ΔH values were taken to be equal to ΔH° values valid at infinite dilution.

Calculations. The numerical calculations for the Ag^+–Py and Cu^{2+}–Py systems are similar. The actual procedure is illustrated with the Ag^+–Py system. The extension to the Cu^{2+}–Py system is straightforward.

The thermodynamic values associated with the reaction of Ag^+ and Py are defined by eq 1 and 2.

$$Ag^+ + Py = AgPy^+ \qquad \beta_1, \Delta H_1^\circ, \Delta S_1^\circ \qquad (1)$$

$$Ag^+ + 2Py = AgPy_2^+ \qquad \beta_2, \Delta H_2^\circ, \Delta S_2^\circ \qquad (2)$$

The heat, Q_t, liberated during the reaction of Ag^+ with Py can be calculated from the expression

$$Q_t = ([AgPy^+]\,\Delta H_1^\circ + [AgPy_2^+]\,\Delta H_2^\circ)\,V_{tt} \qquad (3)$$

where V_{tt} is the volume of solution in the calorimeter at time t_t. Q_t can be expressed as a function of β_1, β_2, ΔH_1°, ΔH_2°, and [Py] by combining eq 3, the expression for Ag^+_{total} (eq 4), and the expressions for β_1 (eq 1) and β_2 (eq 2) to give eq 5.

$$[Ag^+_{total}] = [Ag^+] + [AgPy^+] + [AgPy_2^+] \qquad (4)$$

$$Q_t = [Ag^+_{total}]\,V_{tt}([Py]\beta_1\Delta H_1^\circ + [Py]^2\beta_2\Delta H_2^\circ)/(1 + \beta_1[Py] + \beta_2[Py]^2) \qquad (5)$$

The concentration of pyridine in the solution can also be calculated by combining eq 1 and 2 with the expressions for total Ag^+ (eq 4) and total Py (eq 6) to give eq 7. In eq 6, $[HPy^+]$ has been neglected for simplicity. In the actual calculations, corrections must also be made for the hydrolysis of pyridine.

$$[Py_{total}] = [Py] + [AgPy^+] + 2[AgPy_2^+] \qquad (6)$$

(8) W. C. Vosburgh and S. A. Cogswell, *J. Amer. Chem. Soc.*, **65**, 2412 (1943).

(9) R. J. Bruehlman and F. H. Verhoek, *ibid.*, **70**, 1401 (1948).

(10) R. K. Murmann and F. Basolo, *ibid.*, **77**, 3484(1955).

(11) F. Becker, J. Barthel, N. G. Schmahl, and H. M. Lüschow, *Z. Physik. Chem.* (Frankfurt), **37**, 52 (1963).

(12) G. Atkinson and J. E. Bauman, *Inorg. Chem.*, **2**, 64 (1963). However, the validity of the K values reported in this reference has been questioned (see correspondence from G. Anderegg and reply by G. Atkinson and J. Bauman, *Inorg. Chem.*, **2**, 1082 (1963)).

(13) J. Bjerrum, *Acta Chem. Scand.*, **18**, 843 (1964).

(14) D L. Leussing and R. C. Hansen, *J. Amer. Chem. Soc.*, **79**, 4270 (1957).

(15) K. Kahmann, H. Sigel, and H. Erlenmeyer, *Helv. Chim. Acta*, **47**, 1754 (1964).

(16) J. J. Christensen, R. M. Izatt, and L. D. Hansen, *Rev. Sci. Instrum.*, **36**, 779 (1965).

(17) J. J. Christensen and R. M. Izatt, *J. Phys. Chem.*, **66**, 1030 (1962).

(18) D. Eatough, Ph.D. Dissertation, Brigham Young University, Provo, Utah, 1967.

$$[Py_{total}] = [Py] + \frac{[Ag^+_{total}](\beta_1[Py] + 2\beta_2[Py]^2)}{1 + \beta_1[Py] + \beta_2[Py]^2} \quad (7)$$

In theory, [Py] can be eliminated from eq 5 and 7, and the resulting equation fitted to the experimental data by the method of least squares. However, in practice the resulting nonlinear equations in β_i and $\Delta H_i°$ cannot be directly solved, and some iterative process must be used.

The problem can be simplified mathematically by using a least-squares analysis of eq 8, the error square sum over all data points for the Q_i value calculated from eq 5 and from the corresponding Q_c value

$$U(\beta_i, \Delta H_i°) = \sum_{i=1}^{N} w_i(Q_{ci} - Q_{ti})^2 \quad (8)$$

(experimentally measured heat corrected for H_2O formation, HPy^+ formation, titrant dilution, and calorimeter heat leaks).

This analysis may be carried out in the following manner. Values of β_1 and β_2 are assumed. These β_1 and β_2 values are used to calculate [Py] as a function of titrant added to the calorimeter (eq 7). A least-squares analysis of eq 8 with the weighting terms, w_i, taken as unity is used to calculate the best values of $\Delta H_1°$ and $\Delta H_2°$ for the β_1 and β_2 values chosen. An indication of how well the β_i and $\Delta H_i°$ values describe the thermometric titration curve is obtained by calculation of the error square sum, $U(\beta_i, \Delta H_i°)$ (eq 8). New values of β_1 and β_2 are chosen and the procedure is repeated until the minimum error square sum is obtained. When the process has been completed, the four requirements for least-squares fitting of the data ($\partial U/\partial \Delta H_i° = 0$ and $\partial U/\partial \beta_i = 0$, $i = 1, 2$) have been satisfied. The problem of calculating the β_i and $\Delta H_i°$ values for the interaction of Ag^+ with Py then reduces to finding the minimum value of U, U_{min}. In the past, three different methods have been used to find U_{min}.

(1) *Schematic Map of* $U(\beta_i, \Delta H_i°)$. β_i values may be varied over a large domain and U_{min} found by trial and error. This method has been successfully used in the analysis of data for studies involving a single equilibrium.[4,5] However, for systems involving more than one constant, the computer time required for complete data analysis may be extremely large.

(2) *Pit Mapping.* A functional relationship may be assumed for $U(\beta_i, \Delta H_i°)$ and U_{min} found by direct differentiation. The pit mapping method described by Sillén[6] and used by Paoletti, *et al.*,[7] assumed U to be quadratic and explicitly independent of ΔH, and, therefore, of the form

$$U = C_{00} + 2\sum_{r=1}^{n} C_{0r}\Delta\beta_r + \sum_{r=1}^{n}\sum_{s=1}^{n} C_{rs}\Delta\beta_r\Delta\beta_s \quad (9)$$

where $\Delta\beta_i$ is the deviation of β_i from the initial approximation, $\beta_i°$, and the C_{ij} terms are the coefficients in the expression. For a system of n reactions, $[(n + 1)(n + 2)]/2$ sets of $\Delta\beta_i$ values are required to evaluate the parameters in eq 6. U_{min} can then be evaluated, yielding a new approximation for the β_i values. The cycle is repeated until the calculations are self-consistent.

(3) *Simultaneous Solution of Equations.* Values for β_i and $\Delta H_i°$ can be calculated directly if four equations of the form of eq 5 are solved simultaneously for four t_i values. Corrections are made for activity coefficients and [Py] until the results are self-consistent. It is then assumed that the average of the β_i values calculated from all possible combinations of data points corresponds to those giving U_{min}. There is no way in this method to check this assumption. Entropy titration data for proton dissociation from HSO_4^- and HPO_2^{2-} and several monosaccharides have been analyzed by this method.[2,3]

The major drawback with the iterative methods used in the past is that some assumptions must be made about the functional relationship between $U(\beta_i, \Delta H_i°)$ and its gradient. A substantial improvement in the description of the function $U(\beta_i, \Delta H_i°)$ would result if the actual value of the gradient of $U(\beta_i, \Delta H_i°)$, rather than an approximated value were used in the iterative process. A computer program which incorporates this feature has been developed by Davidon.[19] This program uses a numerical variable metric method of minimization (VMM) to find relative minima for any well behaved function, and can be directly adapted to the problem of least-squares fitting of experimental data. The program uses an iterative gradient method in which calculated values of $\partial U/\partial\beta_i$ and approximated values of $\partial^2 U/\partial\beta_i\partial\beta_j$ for various values of β_i are used to locate those values of β_i for which $\partial U/\partial\beta_i$ is zero and for which the Hessian matrix

$$\left\| \frac{\partial^2 U}{\partial\beta_i\partial\beta_j} \right\|$$

is positive definite.

After a relative minimum has been located, the values of β_i may be randomly varied and a new relative minimum located. Thus, it is possible to calculate a U_{min} value and to explore a given region around this value to determine if it is the only relative minimum in that region.

Each of the above mentioned methods of data analysis ((1), (2), (3), and the VMM method) are used in the calculation of β_i and $\Delta H_i°$ values from the thermometric titration data for the interaction of Ag^+ with Py. Only the VMM method of data analysis was used in the calculation of β_i and $\Delta H_i°$ values for the Cu^{2+}–Py system. Due to the complexity of the function in-

(19) W. C. Davidon, Argonne National Laboratory Report ANL 5990, Rev 2, Argonne, Ill., 1966.

volved, it was found more convenient in the VMM method to approximate the derivatives by assuming

$$\frac{\partial U}{\partial \beta_i} \doteq \frac{\Delta U}{\Delta \beta_i}$$

where $\Delta U = U_2 - U_1$ and $\Delta\beta_i = (1 + k/2)\,\beta_i - (1 - k/2)\,\beta_i = k\beta_i$. Calculations indicated that for the functions involved in these studies, the $\partial U/\partial\beta_i$ values were essentially constant for $k < 10^{-2}$. The value $k = 10^{-3}$ was used in the calculations to minimize the error in the approximation.

Corrections for pyridine hydrolysis were made using the pK value, 5.175,[5,10] and the ΔH° value, −4.90 kcal/mol.[5] The ion product, 1.008×10^{-14}, K_w, and heat of ionization, −13.34 kcal/mol, of water were taken from Harned and Owen[20] and Hale, *et al.*,[21] respectively. A Debye–Hückel expression of the form

$$\log \gamma = \frac{AZ^2\sqrt{\mu}}{1 + Ba^\circ\sqrt{\mu}}$$

where the various terms have their usual significance,[20] was used to convert the thermodynamic K_w value to a concentration quantity. The value $a^\circ = 4$ Å was used in the calculations. Calculations were aided by the use of an IBM 7040 computer.

Table I: Log β_i, ΔH_i°, and ΔS_i° (i = 1, 2) Values Valid at 25° for the Interaction of Ag^+ with Py[a]

i[b]	Log β_i	ΔH_i°, kcal/mol	ΔS_i° cal/mol deg
1	2.04 ± 0.06[c]	−4.6 ± 0.2	−6.2 ± 0.8
	2.05 ± 0.05[d]	−4.6 ± 0.2	−6.0 ± 0.9
	2.05 ± 0.03[e]	−4.5 ± 0.2	−5.8 ± 0.8
	(2.00)[f]	(−4.83)[f]	(−7.0)[f]
	(2.24)[g]	(−4.77)[g]	(−5.7)[g]
	(2.00)[i]		
2	4.09 ± 0.05[c]	−11.25 ± 0.09	−19.0 ± 0.4
	4.10 ± 0.07[d]	−11.24 ± 0 12	−18.9 ± 0.4
	4.11 ± 0.05[e]	−11.21 ± 0.12	−18.8 ± 0.4
	(4.11)[f]	(−11.34)[f]	(−19.2)[f]
	(4.19)[g]	(−11.53)[g]	(−19.5)[g]
	(4.22)[h]		
	(4.11)[i]		

[a] The uncertainties are expressed as standard deviations. [b] The i value refers to the reaction $Ag^+ + i\text{Py} = AgPy_i^+$. [c] This study, $\mu = 0$. Determined by the entropy titration procedure using the VMM method with random steps to analyze the data. [d] This study, $\mu = 0$. Same as c except random steps were not taken. Initial values used were log $\beta_1 = 2.05$ and log $\beta_2 = 4.15$. [e] This study, $\mu = 0$. Determined by the entropy titration procedure using the pit-mapping method to analyze the data. Initial values used were log $\beta_1 = 2.05$ and log $\beta_2 = 4.15$. [f] Reference 7. Determined by conventional calorimetry using the pit-mapping method to analyze the data. Valid at $\mu = 0.5$. [g] Reference 11. Determined by incremental calorimetry using an initial slope method to analyze the data. Valid at $\mu = 0.2$. [h] Reference 9. Determined by potentiometry. Valid at $\mu = 0.6$. [i] Reference 8. Determined by solubility measurements. Valid at $\mu = 0$.

Table II: Log β_i, ΔH_i°, and ΔS_i° Values Valid at 25° for the Interaction of Cu^{2+} with Pyridine[a]

i[b]	Log β_i	ΔH_i°, kcal/mol	ΔS_i° cal/deg mol
1	2.50 ± 0.02[c]	−4.02 ± 0.08	−2.0 ± 0.3
	(2.52)[d]	(3.0)[g]	
	(2.41)[e]		
	(2.59)[f]		
	(2.46)[g]		
2	4.30 ± 0.05[c]	−8.86 ± 0.1	−10.0 ± 0.7
	(4.38)[d]		
	(4.29)[e]		
	(4.33)[f]		
	(4.41)[g]		
3	5.16 ± 0.06[c]	−16.1 ± 0.6	−30.6 ± 2
	(5.69)[c]		
	(5.43)[d]		
	(5.93)[e]		
	(5.68)[f]		
4	6.04 ± 0.1[c]	−21.5 ± 1.5	−41 ± 5
	(6.54)[d]		
	(6.04)[e]		
	(6.54)[f]		
	(6.52)[g]		

[a] The uncertainties are expressed as standard deviations. [b] The i value refers to the reaction $Cu^{2+} + i\text{Py} = CuPy_i^{2+}$. [c] This study, $\mu = 0$. [d] Reference 9. Determined from pH titration data. Valid at $\mu = 0.6$. [e] Reference 13. Determined from potentiometric and spectrophotometric data. Valid at $\mu = 0.5$. [f] Reference 14. Determined from pH titration data. Valid at $\mu = 1.0$. [g] Reference 12. Determined from potentiometric and calorimetric data. Valid at $\mu = 1.0$.

Results

The thermodynamic log β_i, ΔH_i°, and ΔS_i° values determined in this study[22] together with literature values for the interaction of Ag^+ with Py and Cu^{2+} with Py are summarized in Tables I and II, respectively.

Discussion

The log β_i values determined in this study for both the Ag(I)–Py and Cu(II)–Py systems are generally in good agreement with those reported previously, indicating that the entropy titration method can be ap-

(20) H. S. Harned and B. B. Owen, "The Physical Chemistry of Electrolytic Solutions," 3rd ed, Reinhold Publishing Corp., New York, N. Y., 1958.

(21) J. D. Hale, R. M. Izatt, and J. J. Christensen, *J. Phys. Chem.*, 67, 2605 (1963).

(22) Material supplementary to this paper in the form of thermometric titration data has been deposited as Document No. 9718 with the ADI Auxiliary Publications Project, Photoduplication Service, Library of Congress, Washington 25, D. C. 20540. A copy may be secured by citing the Document No. and by remitting $1.25 for photoprints or $1.25 for 35-mm microfilm. Advance payment is required. Make checks or money orders payable to: Chief, Photoduplication Service, Library of Congress.

plied to the determination of the thermodynamic quantities for metal–ligand interaction involving simultaneous equilibria.

Ag^+–Py System. The $\Delta H°$ values reported in Table I are slightly less negative than those reported by earlier workers. This difference is due in part to the difference in the log β_i values used to calculate the $\Delta H_i°$ values. For example, if the values log β_i = 2.00 and log β_2 = 4.11 determined by Paoletti, *et al.*,[7] are used to calculate $\Delta H_i°$ values from the Ag^+–Py thermometric titration data determined in this study,[22] the results ($\Delta H_1°$ = −4.7 ± 0.2 kcal/mol, $\Delta H_2°$ = −11.37 ± 0.09 kcal/mol) are in good agreement with the values obtained by Paoletti, *et al.* ($\Delta H_1°$ = −4.83 kcal/mol, $\Delta H_2°$ = −11.43 kcal/mol). The sensitivity of the $\Delta H_i°$ values to the log β_i values used in the calculations results from the fact that the $\Delta H_i°$ values depend on the concentrations of the species present in the calorimeter at each data point. Since the species distribution is dependent on the per cent error in the β_i and not the log β_i value, a small error in the log β_i value may result in a fairly large error in the calculated $\Delta H_i°$ value. The accuracy of the $\Delta H_i°$ value is improved as the magnitude of the log β_i values increases, since the species distribution becomes less sensitive to errors in the log β_i values.[5]

The shape of a thermometric titration curve will often yield information concerning the nature of the reactions taking place. An example is seen in Figure 1, where a typical thermometric titration curve and corresponding species distribution are given (data for this plot were taken from run 4, ref 22). The S shape of the titration curve shows that $AgPy_2^+$ is formed in a stepwise manner when a solution containing Ag^+ is titrated with Py. This S-shaped titration curve can be explained if two species are formed in the calorimeter and the heat for the stepwise formation of $AgPy_2^+$ from $AgPy^+$ is more exothermic than the heat of formation of $AgPy^+$ from Ag^+.

The standard deviation for $\Delta H_1°$ is large compared to that for $\Delta H_2°$. This is not unexpected, since ($\Delta H_2°$ − $\Delta H_1°$) is more negative than $\Delta H_1°$ and the [$AgPy^+$] in the calorimeter is always small compared to [Ag^+_{total}] making the contribution of $AgPy^+$ to the shape of the thermometric titration curve less than the contribution of the $AgPy_2^+$ species.

The relative merits of the four methods of data analysis can be seen by comparison of the results obtained when each method is used to analyze the data in run 4 of ref 22.

(*1*) *Schematic Map of $U(\beta_i,\Delta H_i°)$.* The dependence of $U(\beta_i, \Delta H_i°)$ on β_1 and β_2 was studied by varying log β_1 values from 1.90 to 2.25 and log β_2 values from 3.95 to 4.30. These results are summarized in Figure 2. Two close-lying minima were found for this run with U_{min}, log β_1, and log β_2 values of 0.0136, 1.92, 4.06, and 0.0130, 1.99, 4.10, respectively. Since the

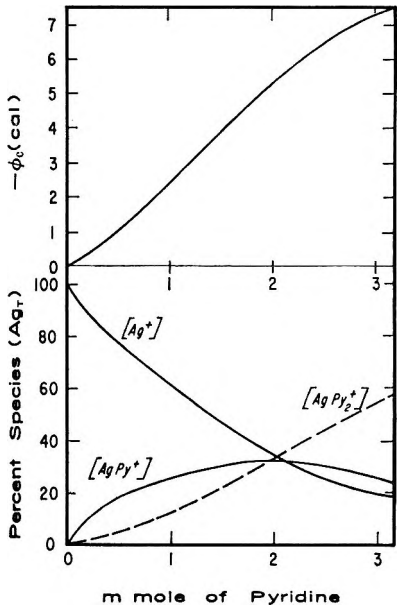

Figure 1.

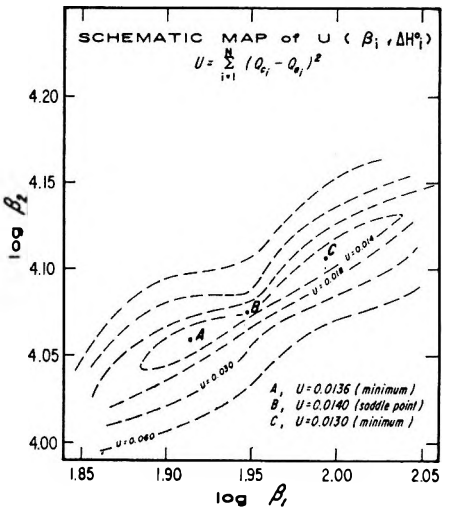

Figure 2.

second U_{min} value lies lower than the first, the β_i values corresponding to this minimum are the "best" values.

(*2*) *Pit Mapping.* In several runs, as many as four minima were found in the region close to U_{min}. The existence of such pits complicates analysis by the pit-mapping method. If the initial guess for the β_i values lies close to either point A or point C in Figure 2, then the corresponding minimum is calculated. If the initial β_i values, however, lie close to point B then, since the pit-mapping method locates extremes only, the value of U at the saddle point B is calculated for U_{min}. For initial guesses of β_i values which do not lie close to A, B, or C, the shape of the pit is much more complicated. If initial β_i values are not close to one of the extremes (within 0.1 log unit), the calculations do not generally zero in on a U_{min} value.

(*3*) *VMM Procedure.* Using this procedure with

Table III: Comparison of Methods and Data Analysis

Method	Advantages	Disadvantages
1. Schematic map of $U(\beta_i, \Delta H_i^\circ)$	The method is thorough and accurate	Computer time required is long (approximately 1 hr/run)
2. Pit mapping	Computer time is short (approximately 1 min/run)	Locates saddle points as well as minima. Area of convergence is smaller than in the VMM method
3. VMM	Only relative minima are located. Area of convergence is much larger than in the pit-mapping method	Requires approximately 25% more computer time than pit mapping
4. Simultaneous solutions of equations	None	Apparently not applicable to systems involving more than one reaction

random steps points A and C were both calculated as relative minima. Point B was not calculated, since the Hessian matrix is not positive definite in this region. The VMM method of data analysis then has three main advantages over the pit-mapping method described by Sillén.[6] (a) Only relative minima are determined as U_{min} values, saddle points are not considered. (b) Extreme values other than the proper U_{min} value may be located and eliminated. (c) For complex functions, the region of convergence to a relative minimum is much larger. The first two disadvantages of the pit-mapping method can be partially eliminated by use of some type of random step program to assist in locating all minima and determining saddle point regions. The third disadvantage, however, is inherent in the assumptions used in the method and cannot be easily overcome. However, the pit-mapping method has the advantage that it is easier to program and uses approximately 25% less computer time.

(4) *Simultaneous Solution of Equations.* All attempts to calculate log β_i and ΔH_i° values using this method were unsuccessful, presumably because of the importance of small errors in the solution of large numbers of independent equations. The advantages and disadvantages of the four methods of data analysis are summarized in Table III.

Cu^{2+}–Py System. The only previously reported ΔH° value for the interaction of Cu^{2+} with Py is the ΔH°_{av} value of −3.0 kcal/mol reported by Atkinson and Bauman.[12] However, this value is valid for the formation of the first species only, and has an uncertainty of ±1.5 kcal/mol.[23] Therefore, within the limit of uncertainty, the value agrees with our value of ΔH_1° = −4.0 kcal/mol. The log β_1 and log β_2 values determined in this study are in good agreement with those values reported previously; however, the log β_3 and log β_4 values are slightly lower. If the values of log β_3 = 5.43 and log β_4 = 6.04, reported by Bjerrum,[13] are used to analyze the thermometric titration data, the resulting enthalpy changes obtained for ΔH_3° and ΔH_4° are −14.7 and −21.5, kcal/mol, respectively. This extreme sensitivity of the ΔH_i° values to the value of the equilibrium constants used in evaluating the data indicates one of the advantages of the determination of log β_i and ΔH_i° values simultaneously. Since the log β_i and ΔH_i° values are determined from the same data, the effects of random errors in the determination are minimized and the resulting log β_i and ΔH_i° values are self-consistent. Of course, the entropy titration technique has the disadvantage that systematic errors are more difficult to detect and eliminate.[24]

The largest deviations among runs in the measured Q_c values occurred in the region where the third and fourth species were forming. When attempts were made to analyze the entire titration curve for all four β_i values, the magnitude of the errors in the region of formation of the $CuPy_3^{2+}$ and $CuPy_4^{2+}$ species was sufficiently larger than the magnitude of the errors in the region of formation of the $CuPy^{2+}$ and $CuPy_2^{2+}$ species that least-squares analysis of the entire curve was insensitive to the β_1 and β_2 values chosen. Therefore, the β_i values were determined by first analyzing the first portions of the curves to obtain the best values of β_1 and β_2 and then by analyzing the entire curve using these β_1 and β_2 values to obtain the best β_3 and β_4 values. This procedure was repeated until the results were self-consistent.

Acknowledgments. The authors wish to express their appreciation to the Argonne National Laboratories, Argonne, Ill., for information on the variable metric minimization program,[25] and to Mr. Glen Enke of the Brigham Young University Computer Research Center for a random number generating subroutine.

(23) Professor J. E. Bauman, Department of Chemistry, University of Missouri, Columbia, Mo., personal communication.

(24) D. P. Wrathall, Ph.D. Dissertation, Brigham Young University, Provo, Utah, 1967.

(25) FORTRAN II copies of the basic metric minimization program are available through the Argonne National Laboratories, Argonne, Ill. Two subroutines must be written to utilize this basic program, an FCN subroutine to calculate $U(\beta_i, \Delta H_i^\circ)$ and $\partial U/\partial \beta_i$ and a RANDM2 subroutine to control the random step routine. A FORTRAN IV copy of the basic metric minimization program with accompanying RANDM2 subroutine is also available through Dr. Reed M. Izatt, Department of Chemistry, or Dr. James J. Christensen, Department of Chemical Engineering, Brigham Young University, Provo, Utah.

Solubilization Behavior of Sodium Dodecylpolyoxyethylene Sulfates in Relation to Their Polyoxyethylene Chain Lengths

by Fumikatsu Tokiwa

Research Laboratories, Kao Soap Co., Wakayama-shi, Japan *(Received September 25, 1967)*

Solubilization behavior of a series of sodium dodecylpolyoxyethylene sulfates (SDPS) with oxyethylene units from 0 to 10 has been studied, in comparison with the behavior of dodecylpolyoxyethylene ethers (DPOE) and sodium alkyl sulfates (SAS), to understand the nature of the polyoxyethylene chain in SDPS. The two surfactants with a polyoxyethylene chain, SDPS aud DPOE, have a much greater solubilizing power than SAS. The absorption spectra of a water-insoluble dye, Yellow OB, in the aqueous solutions of SDPS and DPOE suggest that solubilization occurs in both the hydrocarbon and polyoxyethylene regions of the micelle. With respect to the effect of the chain length of polyoxyethylene part, a different solubilization behavior is observed between SDPS and DPOE, which could be explained by different micellar structures between these two types of surfactants. The nature of the polyoxyethylene part in SDPS is in a sense similar to that of the hydrocarbon part; the solubilizing power increases and the cmc value decreases with increasing oxyethylene content. The numbers of solubilized Yellow OB molecules per micelle at saturation have been calculated by combining the solubilization data with previous data on micellar molecular weights, and they are greater than unity.

Introduction

In a previous paper[1] micellar properties of a series of sodium dodecylpolyoxyethylene sulfates (SDPS), which have an ionic head of $-SO_4^-$ at the end of the molecule of dodecyl polyoxyethylene ethers (DPOE), have been systematically studied from their hydrodynamic data in relation to their polyoxyethylene chain lengths. The micellar properties of SDPS are highly dependent on the chain length of the polyoxyethylene part, as are those of DPOE.[2-4] With respect to the effect of polyoxyethylene chain lengths on the properties of their micelles in solutions, however, some dissimilarities have been found between these two types of surfactants. For instance, different solubilization behaviors are observed between them when the numbers of oxyethylene units in the polyoxyethylene parts are increased.

In general, the solubilization capacity of a nonionic surfactant of polyoxyethylene type for water-insoluble materials is much greater than that of an ionic surfactant having the same hydrocarbon chain length as that of the nonionic surfactant; for example, the solubilizing power of DPOE for a water-insoluble dye, Yellow OB, is about 10 times greater than that of sodium dodecyl sulfate. This fact suggests that the polyoxyethylene part in the molecule plays an important role in solubilization. In the present work, in order to understand the nature of the polyoxyethylene chain of anionic SDPS, the solubilization behavior has been studied in comparison with the behavior of nonionic DPOE and anionic sodium alkyl sulfates (SAS) with changing chain length of the polyoxyethylene or hydrocarbon part. In addition, the hypothesis recently proposed by Schott[5,6] that the limit of solubilization of Orange OT is one dye molecule per micelle has been discussed by combining previous data on micellar molecular weights (mmw)[1,2] with the solubilization data obtained in this work.

Experimental Section

Materials. Sodium dodecylpolyoxyethylene sulfates, $C_{12}H_{25}(OCH_2CH_2)_pOSO_3Na$, were the same samples as those used in a previous work.[1] Dodecyl polyoxyethylene ethers, $C_{12}H_{25}(OCH_2CH_2)_pOH$ with p of 7, 10, 13, 15, and 20 were prepared from dodecyl alcohol of a high purity by addition of ethylene oxide using sodium hydroxide as a catalyst. Polyethylene glycol, a by-product of the reaction, was removed by the solvent extraction method[7] using 1-butanol-saturated water and water-saturated 1-butanol. Paper chromatography showed the purified samples to be free of polyethylene glycol.[8] The value of p for each sample of DPOE was determined from its hydroxyl value. Sodium alkyl sulfates, $C_nH_{2n+1}OSO_3Na$, were prepared from respective alcohols by sulfation with chlorosulfonic acid

(1) F. Tokiwa and K. Ohki, *J. Phys. Chem.*, **71**, 1343 (1967).
(2) F. Tokiwa and T. Isemura, *Bull. Chem. Soc. Jap.*, **35**, 1737 (1962).
(3) F. Tokiwa, *ibid.*, **36**, 222 (1963).
(4) F. Tokiwa, *ibid.*, **37**, 1837 (1964).
(5) H. Schott, *J. Phys. Chem.*, **68**, 3618 (1964).
(6) H. Schott, *ibid.*, **70**, 2966 (1966).
(7) K. Nagase and K. Sakaguchi, *Kogyo Kagaku Zasshi*, **64**, 635 (1961).
(8) K. Hattori and K. Konishi, *ibid.*, **64**, 1195 (1961).

according to the method of Dreger, *et al.*[9] The samples were purified by repeated recrystallization from isopropyl alcohol, followed by extraction with petroleum ether.

Yellow OB (1-*o*-tolyl-azo-2-naphthylamine), the water-insoluble dye used for solubilization experiments, was a particularly good commercial product obtained from Wako Pure Chemicals Co. The sample was purified by repeated recrystallization from a mixed solvent of ethanol–water and was dried under vacuum. Dodecane was of analytical reagent grade. Polyethylene glycol, the molecular weight of which was approximately 400, was obtained from Sanyo Yushi Kogyo Co. Both dodecane and polyethylene glycol were redistilled before use.

Solubilization. Solubilization runs were made in a water bath at 25° for 48 hr to attain equilibrium, the method described in a previous paper being employed.[3] Excess Yellow OB was added either to surfactant solutions of the correct concentration or to solutions which were several times too concentrated, which were later diluted with water or with sodium chloride solution. Agreement between solubilization data obtained from the side of supersaturation and those obtained by starting with the solid dye indicates that both represent equilibrium values. Excess dye was removed by filtration through a glass filter of Shibata Kagaku G-4. Removal of suspended dye was complete because raising the surfactant concentration of filtered samples by adding solid surfactant did not increase the absorbancy. The amounts of the solubilized dye were determined by optical density measurements at a wavelength of 445 mμ.

Absorption Spectra. Spectral measurements were performed with a Shimadzu Model QV-50 spectrophotometer at room temperature (about 25°).

Results and Discussion

Typical results for solubilization in aqueous solutions of SDPS with p from 0 to 10 are shown in Figure 1, in which the amounts of solubilized Yellow OB, S, are plotted against the concentrations of the surfactant, C. The S *vs.* C curves for DPOE and SAS are similar to those for SDPS shown in Figure 1 and are not illustrated here. For all of the surfactants examined, the S *vs.* C curves are linear in the region of relatively low concentrations, although they are slightly curved at higher concentrations. The solubilizing power of each surfactant can, therefore, be obtained from the slope of the linear portion of the curve. In Figure 2, the solubilizing powers of SDPS in water and 0.1 M NaCl solution and of DPOE and SAS in water are plotted against the number of oxyethylene or methylene units. The solubilization of the dye per mole of DPOE is large and almost constant over the range of p examined, while the amounts solubilized by SDPS and SAS are smaller and increase with increasing number of oxyethylene

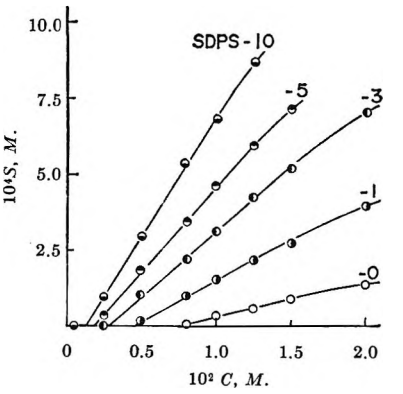

Figure 1. The amount of solubilized Yellow OB, S, plotted against the concentration, C, of SDPS with different numbers of oxyethylene units in water at 25°. The number written after SDPS represents the approximate average number of oxyethylene units per molecule.

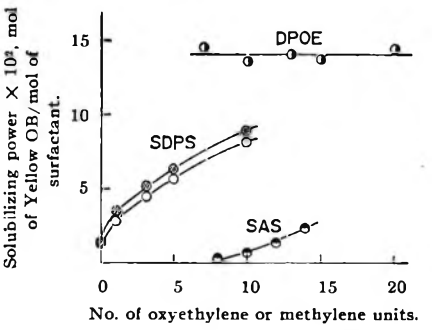

Figure 2. Solubilizing powers of SDPS, DPOE, and SAS for Yellow OB plotted against the number of oxyethylene or methylene units: ○, SDPS in water; ⊘, SDPS in 0.1 M NaCl; ◑, DPOE in water; ⊖, SAS in water.

units or methylene units in the molecule. Both SDPS and DPOE compounds exhibit a greater solubilization than SAS compounds with no polyoxyethylene chain, indicating that the polyoxyethylene portion in the molecule plays an important role in solubilization.

Figure 3 shows the spectra of Yellow OB in dodecane and polyethylene glycol, as well as in the aqueous solutions of SDPS with a p of 5, DPOE with a p of 10, and SAS (sodium dodecyl sulfate). Aside from the shape of the spectra, the wavelength of the maximum absorption of Yellow OB, λ_{max}, in the solution of SAS corresponds closely to the λ_{max} in dodecane, suggesting that the solubilization of Yellow OB occurs mainly in the hydrocarbon region of the SAS micelle. On the other hand, the spectra of Yellow OB in the solutions of SDPS and DPOE are rather similar to the spectrum in polyethylene glycol. This suggests that in the case of SDPS and DPOE the solubilization of the dye also occurs in the polyoxyethylene region of the micelle and, further, that the portion of the dye solubilized in the

(9) E. E. Dreger, G. I. Keim, G. D. Miles, L. Shedlovsky, and J. Ross, *Ind. Eng. Chem.*, **36**, 610 (1944).

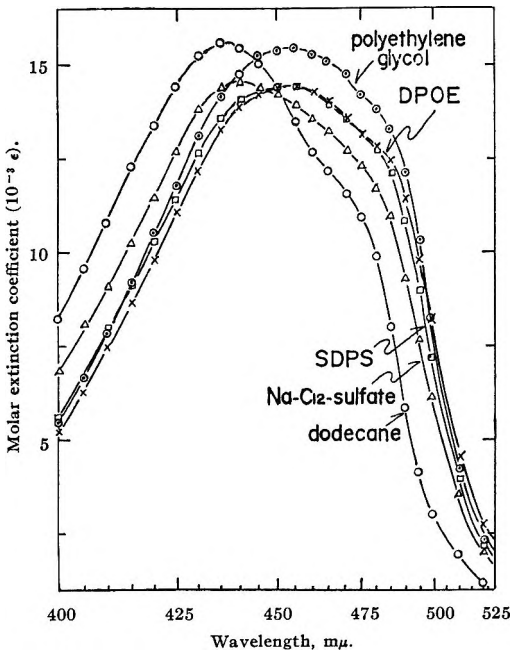

Figure 3. Absorption spectra of Yellow OB in dodecane (—○—) and polyethylene glycol (—⊙—), and in the aqueous solutions of: SDPS with a p of 5 (—□—), DPOE with a p of 10 (—×—), and sodium dodecyl sulfate (—△—).

polyoxyethylene region is larger than that in the hydrocarbon region.

Now, one has to explain the reason why the solubilization by DPOE is almost constant while that by SDPS increases with increasing oxyethylene units. The following explanation seems plausible for this. The polyoxyethylene chains of DPOE in the micelle are not highly extended, as compared with those of SDPS, but the locus of solubilization is the hydrocarbon interior of the micelle and the portion of the polyoxyethylene shell near that hydrocarbon core. Then, after a certain number of oxyethylene units are present, further increase in p will have no further effect on the solubilization process. The much smaller solubilization shown by SDPS micelles of equal p would then be a result of the extension of the polyoxyethylene chains because of the repulsion of their attached charges. This extension would make the oxyethylene units less available for interaction with the polar part of the dye molecule. The extension may be expected to relax somewhat as the number of oxyethylene units is increased. The less extended polyoxyethylene chains of SDPS will favor a greater solubilization and, therefore, in this case the degree of solubilization increases with increasing p. Addition of sodium chloride will cause reduction of the repulsion between charged heads at the surface of the SDPS micelle, which permits compaction of the polyoxyethylene portion of the micelle and makes more oxyethylene units available to the dye, and thus promote solubilization, as seen in Figure 2.

Solubilization is an effect which begins to be noticeable at the critical micelle concentration (cmc). In

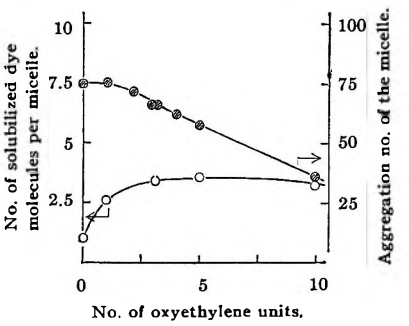

Figure 4. The number of solubilized dye molecules per micelle (○) and the aggregation number of the micelle of SDPS (⌀) in 0.1 M NaCl solution plotted against the number of oxyethylene units. The aggregation numbers were taken from Table I of ref 1.

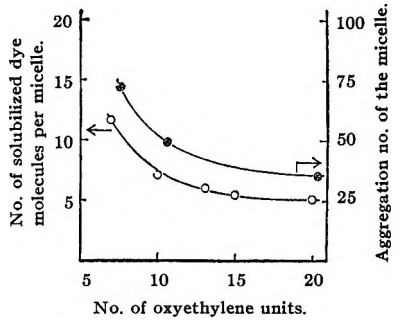

Figure 5. The number of solubilized dye molecules per micelle (○) and the aggregation number of the micelle of DPOE (⌀) in water plotted against the number of oxyethylene units. The aggregation numbers were taken from Table I of ref 2.

Table I: Critical Micelle Concentration Values of SDPS from Solubilization Data at 25°

Samples	Cmc values, 10^{-3} mol/l. In water	In 0.1 M NaCl
SDPS-0	7.8	1.6
SDPS-1	4.6	0.60
SDPS-3	2.8	0.25
SDPS-5	1.9	0.20
SDPS-10	1.3	0.15

Table I are summarized the cmc values of SDPS with different p in water and in 0.1 M NaCl solution at 25° which were taken from sharp breaks in the S *vs.* C curves. The cmc value of SDPS decreases with increasing oxyethylene content. This result is in contrast to the result for DPOE in which the cmc value increases with oxyethylene content.[4,10] Lengthening of the polyoxyethylene chain in the SDPS molecule corresponds in a sense to that of the hydrocarbon chain, although the former effect is not so marked as the latter one. This fact is probably related to the interesting

(10) K. Shinoda, *et al.*, "Colloidal Surfactants," Academic Press Inc., New York, N. Y., 1963, pp 98–112.

solubilization behavior of SDPS, that is, the solubilizing capacity increases with increasing polyoxyethylene chain length.

Combining previous data on the mmw of SDPS[1] and DPOE[2] with their solubilizing capacities for Yellow OB, we obtain the numbers of solubilized dye molecules per micelle, R, by the following relation, under the assumption that the solubilized dye does not change the size of the micelles.[6]

$$R = \frac{\text{mmw}}{m}\frac{S}{C - \text{cmc}} = A\frac{S}{C - \text{cmc}} \qquad (1)$$

where m is the molecular weight of the surfactant, A is the aggregation number of the micelle, and the quantity of $S/(C - \text{cmc})$ is equivalent to the slope of the linear portion of the S *vs.* C curve. In Figures 4 and 5, the values of R for SDPS and DPOE are plotted against the number of oxyethylene units, together with their aggregation numbers. Similar plots for SAS will also be obtained if solubilization data are combined with available mmw values of SAS.[11,12] Recently, Schott[5,6] has postulated that only one dye molecule of Orange OT is solubilized per micelle. If this solubilization limit is general, the R value of about unity would be expected in the present experiment, since Yellow OB is almost equivalent to Orange OT (1-*o*-tolyl-azo-2-naphthol) in molecular weight and chemical structure. The R values obtained from eq 1 are 1.0–3.5 for SDPS with p from 0 to 10, and 1.2–5 for DPOE with p from 7 to 20. These results would suggest that the hypothesis that one dye molecule saturates a micelle is not general but only valid for some limited surfactants.[6]

Acknowledgments. The author expresses his thanks to Professor E. Hutchinson of Stanford University for his helpful discussion, to Dr. P. Becher of Atlas Chemical Industries for his valuable suggestion, and to Dr. H. Kita, the Director of the Research Laboratories, for his encouragement and permission to publish this paper.

(11) H. V. Tarter and A. L. M. Lelong, *J. Phys. Chem.*, **59**, 1185 (1955).

(12) E. Hutchinson and J. C. Melrose, *Z. Phys. Chem.* (Frankfurt), **2**, 363 (1954).

The A_2B_2 Aromatic Proton Nuclear Magnetic Resonance Spectra of *para*-Substituted Anilines, Diphenylamines, and Triphenylamines[1]

by Robert D. Allendoerfer,[2] Griffith Smith,[2] and Robert I. Walter[3]

Department of Chemistry, Haverford College, Haverford, Pennsylvania 19041 *(Received September 5, 1967)*

The aromatic proton nmr spectra of 4-substituted anilines, 4,4′-disubstituted diphenylamines, and 4,4′,4″-trisubstituted triphenylamines with the substituents I, Br, $COCH_3$, SO_3^-, CH_3, and OCH_3 have been analyzed to determine optimum values for the chemical shifts and coupling constants. These parameters display the regularities to be expected with increasing arylation of the amine nitrogen and provide evidence for anisotropic ring field effects exerted on the *ortho* protons by adjacent rings. They also suggest that the electron density measured by the nmr experiment is higher at the protons *meta* to the amino group than at those *ortho* to it, in both di-*p*-anisylamine and tri-*p*-anisylamine. Some problems in the precise analysis of spectra of this type are discussed.

The A_2B_2 proton nmr spectra of a large number of *para*-disubstituted benzene derivatives have been reported, together with the chemical shifts assigned by analysis of these spectra.[4] The effects on the A_2B_2C spectrum of accumulation of phenyl groups on one central atom have been investigated for the diphenylcarbonium and triphenylcarbonium ions,[5] but no systems in which substituents are present in the aromatic rings have been studied. We report here the results of an nmr study of a series of 4-substituted anilines, 4,4′-disubstituted diphenylamines, and 4,4′,4″-trisubstituted triphenylamines in which the same substituents are carried through the series. This work was originally undertaken in order to determine the struc-

(1) This work has been supported in part by Grant GM-10605 from the National Institutes of Health to Haverford College.

(2) Summer research student supported by the National Science Foundation Undergraduate Research Participation Program.

(3) Inquiries should be directed to this author.

(4) Data on these systems have been summarized by G. W. Smith, *J. Mol. Spectry.*, **12**, 146 (1946).

(5) G. A. Olah, *J. Am. Chem. Soc.*, **86**, 932 (1964); D. G. Farnum, *ibid.*, **86**, 934 (1964).

ture of the triiodination product of triphenylamine (for which there is no chemical proof of structure) and to confirm the structures of a number of other substitution products for which chemical determinations of structure are available.[6] In order to assign these structures, it is necessary only to observe that the nmr spectrum of the aromatic protons has a center of symmetry; this characteristic form of the A_2B_2 spectrum requires that two nonidentical substituents be located *para* to one another. We have gone further to carry out analyses of the spectra and assignment of the chemical shifts and coupling constants. These assigned parameters display certain regularities which are also reported here.

Experimental Section

The primary amines studied were obtained from commercial sources and recrystallized or sublimed before use. Sulfanilic acid was converted to its potassium salt by mixing methanol solutions of the acid and of potassium hydroxide; the salt crystallized from the mixture. The preparation of the secondary amines[7] and tertiary amines[6] has already been described. Solutions for the nmr study were made up in deuteriochloroform (with tetramethylsilane as internal reference) or in deuterium oxide in the case of the two amines substituted by sulfonate groups. The concentrations were 1.80 *F* for the primary, 0.90 *F* for the secondary, and 0.60 *F* for the tertiary amines; these values give constant concentrations of ring protons in the samples. No attempt was made to record spectra at a series of concentrations for extrapolation to infinite dilution, and the solutions were not degassed.

The spectra were run on a Varian A-60 spectrometer at ambient temperature.[8] Line frequencies were calibrated with a side-band oscillator which operated on the resonance signal of the tetramethylsilane. We were able to resolve the weak satellites on the four most intense lines of the spectrum of our samples down to separations as small as 0.45 cps. It was impossible to resolve those on the outer intense lines of the spectrum of *p*-toluidine, even though the coupling parameters assigned here are such that the computed *minimum* separation should be 0.50 cps; we assume that this is due to the broadening and splitting of the lines in this spectrum which results from coupling of the aromatic protons with those of the methyl group. A few samples were degassed and sealed, and these oxygen-free samples showed significant improvement in the resolution of the major lines, but not of their satellites or in the observed signal-to-noise ratio. Our data are consistent with the arguments given by Martin and Dailey[9] that the four coupling constants in these compounds must have the same sign; we have not pursued this matter further.

The separations of corresponding lines in the halves of the spectrum were measured to 0.03 cps, averaged over six spectra recorded (half were swept in each direction) for each sample, and divided by 2 to obtain the line positions relative to the spectrum center. We do not consider our data on line intensities sufficiently precise to warrant their use in the analysis of the spectra.

Results

The averaged spectral data were analyzed by procedures which were originally developed for the general A_2B_2 case by Pople, Schneider, and Bernstein.[10] The analysis of the A_2B_2 spectra of *para*-disubstituted benzenes has been reported by Richards and Schaefer (who used some simplifying assumptions),[11] by Rao and Venkateswarlu,[12] and in almost simultaneous papers by Martin and Dailey,[9] by Grant, Hirst, and Gutowsky,[13] and by Cox.[14] Our analysis was carried out with the aid of a program written for the Haverford–Bryn Mawr IBM 1620 computer. This uses Corio's expressions[15] for the complete set of line frequencies and intensities to compute these quantities, together with the errors in the computed frequencies, from the chemical shift difference, coupling constants, and observed line separations from the spectrum midpoint.[16] The program is not iterative; this means that initial values for the chemical shifts and coupling constants must be estimated from the spectrum and from knowledge of the ranges of these values in analogous systems, and the computations must then repeated with systematic variation of the parameters until errors are minimized. The scheme for these variations was based largely upon that used by Martin and Dailey[9] but with the difference that each of our iterations involved complete calcu-

(6) T. N. Baker, W. P. Doherty, W. S. Kelley, W. Newmeyer, J. E. Rogers, R. E. Spalding, and R. I. Walter, *J. Org. Chem.*, **30**, 3714 (1965).

(7) (a) M. M. Chen, A. F. D'Adamo, and R. I. Walter, *ibid.*, **26**, 2721 (1961); (b) preparation of bis(*p*-iodophenyl)amine is described by A. Classen, *Fortschr. Teerfarbenfabrikation*, **4**, 1095 (1896).

(8) We are indebted to Professor Paul von R. Schleyer of Princeton University for making the chemistry department instrument available to us for these measurements. A few spectra were also run at the University of Colorado, where a side-band oscillator was available for the frequency calibrations, and at the Pittsburgh Applications Laboratory of Varian Associates, where an HA-100 instrument was available for checking some features of the spectra.

(9) J. Martin and B. P. Dailey, *J. Chem. Phys.*, **37**, 2594 (1962).

(10) (a) J. A. Pople, W. G. Schneider, and H. J. Bernstein, *Can. J. Chem.*, **35**, 1060 (1957); (b) J. A. Pople, W. G. Schneider, and H. J. Bernstein, "High-resolution Nuclear Magnetic Resonance," McGraw-Hill Book Co., Inc., New York, N. Y., 1959, pp 138–151.

(11) R. E. Richards and T. P. Schaefer, *Trans. Faraday Soc.*, **54**, 1280 (1958).

(12) B. D. Rao and P. Venkateswarlu, *Proc. Indian Acad. Sci.*, **A54**, 1 (1961).

(13) D. M. Grant, R. C. Hirst, and H. S. Gutowsky, *J. Chem. Phys.*, **38**, 470 (1963).

(14) P. F. Cox, *J. Am. Chem. Soc.*, **85**, 380 (1963).

(15) P. L. Corio, *Chem. Rev.*, **60**, 414 (1960).

(16) We are indebted to Professor H. S. Gutowsky for sending some results of his calculations in advance of publication[13] in order to afford a check on our program. We are also happy to acknowledge the substantial contribution of Daniel P. Serwer, a Haverford freshman, to revisions of this program during his tenure of an academic year NSF Undergraduate Research Participation grant.

Table I: Parameters Assigned by Analysis of A_2B_2 Aromatic Proton Nmr Spectra of Aromatic Amines

Compd no.	Structure	Lines in spectrum	Chem shift diff, Δ, ppm	Assigned chem shifts, τ, ppm		Assigned coupling constants, cps				Method of analysis[a]	Spread of minima[b]	Maximum $\Delta(J_{meta})$, cps
						J_{ortho}	J_{para}	J_{meta}	J_{meta}			
1	$IC_6H_4NH_2$	16	0.987	2.615	3.602	8.64	0.31	2.22	2.88	1	1	...
2	$(IC_6H_4)_2NH$	16	0.749	2.489	3.238	8.69	0.30	2.19	2.91	1	2	...
3	$(IC_6H_4)_3N$	16	0.734	2.492	3.225	8.73	0.26	2.17	2.89	1	2	...
4	$BrC_6H_4NH_2$	16	0.724	2.831	3.555	8.68	0.36	2.51	2.84	1	3	...
5	$(BrC_6H_4)_2NH$	16	0.472	2.711	3.183	8.82	0.36	2.52	2.85	1	2	...
6	$(BrC_6H_4)_3N$	14	0.429	2.676	3.104	8.84	0.38	2.63	2.75	2	2	...
7	$CH_3COC_6H_4NH_2$	16	1.176	2.221	3.396	8.64	0.39	2.21	2.47	1	2	...
8	$(CH_3COC_6H_4)_2NH$	12	0.756	2.084	2.840	8.72	0.43	2.28	2.28	2	3	0.15[c]
9	$(CH_3COC_6H_4)_3N$	12	0.755	2.073	2.828	8.72	0.43	2.30	2.30	2	3	0.15[c]
10	$^-O_3SC_6H_4NH_2$	12	0.869	2.241	3.110	8.58	0.30	2.36	2.36	2	5	0.30[c]
11	$(^-O_3SC_6H_4)_3N$	12	0.597	2.505	3.102	8.74	0.36	2.36	2.36	2	4	0.20[c]
12	$CH_3C_6H_4NH_2$	12	0.410	3.093	3.503	8.36	0.49	2.42	2.42	2	1	0.05[c]
13	$(CH_3C_6H_4)_2NH$	11	0.125	2.994	3.119	8.33	0.45	2.47	2.47	3	2	0.45[d]
14	$(CH_3C_6H_4)_3N$	1	0.000	3.035	3.035							
15	$CH_3OC_6H_4NH_2$	15	0.147	3.282	3.428	8.73	0.41	2.98	2.98	3	1	0.42[d]
16	$(CH_3OC_6H_4)_2NH$	12	0.103	3.122	3.225	8.93	0.39	3.00	3.00	3	1	0.50[d]
17	$(CH_3OC_6H_4)_3N$	14	0.194	3.061	3.225	9.00	0.34	2.97	2.97	2	2	0.40[d]

[a] Methods for analysis of the spectra are described in the text. [b] This is a measure of the precision of fit of the spectrum parameters; it is described in the text. [c] The quantity $(J_{meta} - J'_{meta})$ must be less than this value if the separation of satellite lines 9 and 12 from the composite lines is to be less than the 0.4-cps estimated minimum resolution of these lines. [d] The quantity $(J_{meta} - J'_{meta})$ must be less than this value if lines 9 and 10 are to appear as a single peak in the spectrum.

lation of the line positions by diagonalization of the 4×4 matrix for the s_0 functions. We did not interpolate tabulated solutions. An effort was made to follow a rigid procedure through the iterations in order to minimize the personal factors in the choice of parameters. Some difficulties with this procedure are considered in the Discussion section. The results of the fitting of chemical shifts and coupling constants for the systems studied are collected in Table I.

Discussion

For convenience in this discussion, we arbitrarily label the upfield protons in each compound A and the downfield protons B. The difference in chemical shift between the unperturbed (all coupling constants zero) A and B protons is called Δ. Individual lines will be identified by the numbers assigned to them by Pople, Schneider, and Bernstein.[10]

The spectra of those amines substituted by iodine, bromine, or the acetyl group (compounds **1–9** in Table I) all give Δ values which are several times the largest coupling constant. Thus, they approach the A_2X_2 case.[10] For any particular substituent, these compounds show the largest value for Δ in the case of the primary amine; this decreases by 25–40% for the secondary amine and only slightly more for the tertiary amine. These changes are the result of a large downfield shift in the resonance of the A protons and a small downfield shift of that of the B protons, with increasing arylation of the nitrogen. Thus, they are consistent with the expectation that the strong electron-donating capability of the amino group will be decreased by arylation, which permits the unshared electron pair on nitrogen to be delocalized to more than one ring and consequently contribute less to the electron density in any single ring. The two amines substituted by sulfonate groups probably follow the pattern of compounds **1–9**: it appears likely that the apparent upfield shift of the B proton resonance in compound **11**, together with the small change in the position of the A resonance compared with compound **10**, may be due to a shift in the water resonance line which was used as the reference in these measurements.

Compounds **12–17**, which are substituted by methyl or methoxy groups, all have Δ values which are comparable to their largest coupling constants. As a guide in the interpretation of the effects of increased arylation in these compounds, it is helpful to bear in mind the effects of arylation in the series of "normal" compounds **1–9**. The tolyl compounds, **12–14**, show the expected changes in coupling constants from the primary to the secondary amine. (For both compounds, the B lines are split by coupling with the methyl group protons. This splitting is about 0.67 cps in *p*-toluidine and 0.4 cps in di-*p*-tolylamine.) The tertiary amine aromatic proton resonance consists of a single line with a width of about 1 cycle. This is a clean line with less structure at the base than is seen in the aromatic nmr spectrum of toluene. This spectrum is highly solvent dependent: in dimethylformamide solution, the full A_2B_2 spectrum appears, with the chemical shift values 3.097 and 3.287

(in τ units) and *ortho*-, *para*-, and *meta*-coupling constants equal to 8.26, 0.45, and 2.41 cps.

In the anisylamines, compounds **15–17**, the magnitude of Δ decreases slightly from the primary to the secondary amine but *increases* again in the tertiary amine to a value which is even larger than that found for the primary amine. We interpret this as the result of inversion of the normal substituent effects of the amino and methoxyl groups: the amino group is a better electron donor than methoxyl in compound **15**, but the methoxyl group is better than the tertiary amino group in **17**. The situation is less clear for the secondary amine, **16**, but the changes in Δ for this series are more consistent with those in the normal compounds if the chemical shifts are inverted for this compound also. Consequently, we propose that, in both compounds **16** and **17**, the resonance of the *meta* protons is upfield from that of the *ortho* protons, and the electron density measured by the nmr experiment is greater at the protons *meta* to the amino group than at those *ortho* to it.

In view of the proposed correlations of proton chemical shifts with reactivity parameters such as the Hammett σ constant,[17] one could predict from these results that electrophilic substitution reactions of tri-*p*-tolylamine should proceed equally fast at the positions *ortho* and *meta* to the amino group, and in tri-*p*-anisylamine they should be faster at the *meta* positions. (These predictions are of course subject to correction for the greater steric inhibition to attack at the *ortho* positions.) In fact, both of these compounds were found years ago to undergo bromination to tribromo derivatives.[18] We are investigating the structures of these products: it is clear that the reactions proceed cleanly to single products, and it is probable that substitution occurs in the positions *ortho* to the amino group in both compounds.[19] We thus feel somewhat uneasy about pushing too hard analogies between nmr chemical shifts, which reflect electron densities at protons in resting molecules perturbed by a magnetic field, and reactivity parameters, which reflect relative free energy changes in a series of molecules as they approach their transition states for a given reaction.

It has already been pointed out that the electron density contributed by nitrogen to the aromatic rings of these compounds should decrease by the factors $^1/_2$ and $^1/_3$ in a given amine series, as the number of aromatic rings attached to nitrogen is increased from 1 to 2 to 3. This explanation is inadequate, however, to account for the observation that the increment in Δ is much larger when $ArNH_2$ changes to $(Ar)_2NH$ than when $(Ar)_2NH$ changes to $(Ar)_3N$. Two other possibilities arise here, both of which result from rotation of the aromatic rings about the C–N bonds. If the C–N–C bond angles are in the range 109–120° expected for amines,[6] both inspection of models and studies of the analogous diaryl ethers[20] indicate that two rings (and, much less, three) cannot simultaneously be oriented to permit full conjugation with the unshared electron pair on the central oxygen (or nitrogen) because of steric interference between hydrogen atoms in the *ortho* positions of adjacent rings. Furthermore, the protons in this position are subject to anisotropic magnetic fields (usually ascribed to "ring currents") which originate in the adjacent rings. It is difficult to be certain about the direction of these effects because each proton is at the edge of the π region of the adjacent ring where the direction of the anisotropic field changes rapidly. In the flattest possible conformation of the triarylamine system, the *ortho* protons may be just entering that region where this field produces an upfield shift of the resonance. In the more twisted conformations, they are in regions where the anisotropic field is perpendicular to the applied field and has no effect on the resonance or where the resonance is shifted downfield. It is likely that the total effect is a downfield shift. It seems reasonable to expect these effects which arise in the molecular geometry to appear in both the secondary and the tertiary amines, which have roughly the same relative ring conformations. If their magnitude is about as large with two rings as with three, the large downfield shifts in the *ortho* proton resonance of both classes of compounds are accounted for. Protons at the *meta* positions should experience only the general decrease in electron density which results from decreased interaction of the amino group with the rings; they are not subject to direct conjugative effects or to field effects which originate in adjacent rings. Consequently, there is a smaller downfield shift in the resonance due to these protons, with increasing arylation.

A number of considerations in connection with the analysis of these spectra deserve additional comment. In the first place, the positions of the satellites (lines 9, 12 or 10, 11; these possibilities cannot be distinguished) relative to the major peaks cannot be determined experimentally with certainty, since their location on the steep slopes of the latter distorts their shape and probably alters their apparent positions. In the second place, there may be problems in the identification of some lines of the spectrum. These are trivial in those cases where Δ is substantially larger than the coupling constants, but they are more serious when these parameters have approximately the same magnitude. In that case, identification can usually be made by analogy if a series of sample spectra are computed

(17) (a) H. Spiesecke and W. G. Schneider, *J. Chem. Phys.*, **35**, 731 (1961); (b) R. E. Kling and J. B. Strothers, *Can. J. Chem.*, **40**, 1071 (1962); (c) G. Heathcock, *ibid.*, **40**, 1865 (1962).

(18) H. Wieland and E. Wecker, *Ber.*, **43**, 703, 705 (1910).

(19) R. D. Allendoerfer, W. S. Kelley, L. Monack, G. Smith, P. T. Rogge, and R. I. Walter, submitted for publication.

(20) The evidence is reviewed by W. D. Chandler, W. F. Smith, and R. Y. Moir, *Can. J. Chem.*, **42**, 2549 (1964).

with coupling constants of approximately the correct magnitude. A problem of identification of a different sort can arise when a computer program is used which calculates the frequency which corresponds to transition between two particular energy levels and then labels that transition with a particular number. Some of the levels in the array of possible states cross when the parameter Δ is varied at small Δ values. This produces a "jumping" of lines 2 and 8 across the spectrum which was confusing to us until we realized that they were simply interchanging positions, and the noncrossing rule requires that they be relabeled.

A more serious difficulty appears in connection with the selection of input values of Δ and $(J_{ortho} - J_{para})$ for the calculations. These are both given rigorously by the positions of lines 1 and 3 in the spectrum, but both of these lines appear as components of composite lines made up of 1, 2, 10 (or 9) and 3, 4, 11 (or 12). When the component lines are close together, their weighted average is a good approximation to the position of the observed line. When the components are spread out, as they tend to be when Δ and the coupling constants are roughly equal, it is probable that those components which are farther from the line center contribute very little to its position but instead form shoulders within the envelope of the composite line. A detailed line-shape analysis would be required in this case. We have not done this, but we have required self-consistency in the values of Δ and of $(J_{ortho} - J_{para})$. These quantities are computed by our program at each stage of the analysis from the calculated positions of the individual lines 1 and 3.

In practice, we have used three separate procedures for the analysis of the spectra of these compounds. Calculations for compounds **1**–**5** and **7**, where Δ is considerably larger than the coupling constants and 16 lines are resolved and easily identified, were carried out in the manner described above. This is identified as method 1 in the third from last column of Table I. The spectra of compounds **6**, **8**–**12**, and **17** require that Δ be somewhat larger than the coupling constants, but the satellites 1 and 12 are no longer resolved. Consequently, it is easy to identify the major lines, but a question arises as to the number of lines to include in the calculation of the centers of intensity of the composite lines. This is because failure to resolve the satellites implies that the pairs 9 and 10 and 11 and 12 are now close together and well separated from the other (major) components of the composite lines. If all four lines—1, 2, 9, and 10 or 3, 4, 11, and 12—are included in the calculations of the centers of intensity, the computation fails to converge when it is recycled. We finally made the arbitrary decision to include 10 and 11, but not 9 and 12, in the computation of the composite line positions. This use of only half of the satellite intensity seems reasonable, since all of the satellites are rather far from the composite line maxima and, furthermore, computations made on this basis converge. This method of analysis is labeled 2 in Table I.

Finally, for compounds **13**, **15**, and **16**, Δ has the same magnitude as the coupling constants, the pattern typical of the other spectra is lost since the entire spectrum is in process of collapse to a single center line, and the experimental peaks can be identified only by comparison with a series of trial computations. Positions of the composite peaks were computed from three lines, as in method 2. This method of analysis is labeled 3 in Table I. The rate of convergence of computations by method 1 and the precision of fit of the computed spectrum are both better than method 2, and this in turn is better than method 3.

A final major difficulty arises in connection with selection of a suitable criterion for convergence of the computations. This arises because the transition frequencies are determined by a multiparameter system which seems to have a rather shallow minimum for these compounds. As a result, the minimum error found by adjustment of one parameter may still lie above the absolute minimum for the system, and so the apparent minimum may depend upon the sequence of operations by which it is approached. We finally decided upon the following set of conditions which must be met at convergence and selected as a criterion for satisfactory convergence, the number of calculation cycles differing by 0.01 cps in the input constants for the *ortho* and *para* coupling over which these conditions are met. These figures are listed in the next to last column of Table I: (1) minimum total error in the computed positions of all resolved lines; (2) minimum greatest error in the computed position of any single line; (3) minimum error in the computed positions of the centers of intensity; (4) successive cycles self-consistent in the parameters Δ and $J_{ortho} - J_{para}$, within 0.005 cps or better; (5) approximately equal errors in the computed positions of the paired lines 5 and 8, 6 and 7, 9 and 12.

These uncertainties in the computation, and particularly the arbitrary method for calculating the positions of the composite lines, leave us feeling rather ill at ease about the precision of the over-all process. Four of the primary amines which we have investigated, compounds **1**, **4**, **12**, and **15**, were also studied by Martin and Dailey.[9] Our values for the parameter Δ are in all cases within 3% of those reported there, and the coupling constants are within 0.25 cps of their values. This agreement is better than we expected, in view of the great difference in conditions under which the compounds were studied. Martin and Dailey ran their samples on a Varian HR-60 spectrometer in the absence of oxygen in the nonpolar solvent cyclohexane, and their data were extrapolated to infinite dilution. Either there is some cancellation of errors, or the effects of high con-

centrations, polar solvent, and the presence of oxygen are smaller than might have been expected.

Despite this check we feel that substantial errors may exist in the values of the parameters fitted in this way. This expectation apparently is confirmed by recent work carried out by Swalen.[21] His programs, labeled NMREN and NMRIT, for calculation of nmr spectra first determine the energy levels from the observed spectrum and then iterate on these energy levels to self-consistency. This eliminates some of the uncertainties already discussed, since each energy level is involved in several transitions, and errors in the assignment of the frequencies of a few transitions will tend to average out in the computation. We believe that the methods used for the analysis of the spectra reported here are adequate for the type of qualitative conclusions we have reached but that the quantitative correlation of carefully determined experimental values such as that reported by Martin and Dailey[22] justifies analysis by less ambiguous methods such as those developed by Swalen.[21]

Possibly it is worth while to point out the loss of information which results from incomplete resolution of spectra of the type discussed here. When the satellite lines 9 and 12 are not resolved, it is impossible to assign different values to the two *meta*-coupling constants. However, the separation of these satellites from the composite lines is at a minimum when the *meta*-coupling constants are equal, and lines 9, 10 and 11, 12 coincide. As the *meta*-coupling constants diverge, these pairs of lines separate, and one member of each pair moves farther from its neighbor composite line. If the limit of resolution of the satellites is taken at 0.4 cps, an upper limit can be set for the difference between the *meta*-coupling constants: these values are listed in the last column of Table I for compounds **8–12**. In the spectra of compounds **13**, **15–17**, lines 9 and 10 appear as a separate peak; if one assumes that this would be resolved if the separation of peaks 9 and 10 were as great as 0.3 cps, upper limits can again be set on the difference between *meta*-coupling constants. These values also are tabulated in the last column of Table I.

(21) We are indebted to Dr. J. D. Swalen for sending us material in advance of publication and for checking assignments for several of our compounds by independent computation with his programs. The programs are described briefly by J. D. Swalen and C. A. Reilly, *J. Chem. Phys.*, **37**, 21 (1962).

(22) J. S. Martin and B. P. Dailey, *ibid.*, **39**, 1722 (1963).

Varietal Differences in Gelatin, Egg Albumin, and Casein in Relation to Sorption–Desorption Hysteresis with Water

by K. Subba Rao and Bhagwan Das

Chemistry Department, Birla Institute of Technology and Science, Pilani, Rajasthan, India *(Received September 6, 1967)*

By employing the quartz fiber spring technique, a series of sorptions and desorptions of water vapor at 35° have been carried out with different varieties of gelatin, egg albumin, and casein. In the case of egg albumin and casein, studies were made on the activated and denatured samples also. They have all shown certain common characteristics. Either there is no hysteresis loop at all in the first cycle of sorption and desorption, or the hysteresis loop initially exhibited shows a tendency to decrease in size and finally disappears in the subsequent cycles. The tendency to decrease in size varies from sample to sample. In the light of the cavity theory of hysteresis in conjunction with the swelling and shrinkage of gelatins, egg albumins, and caseins with water, the decrease in size of the hysteresis loop and its disappearance are attributed to the gradual collapse of the cavities in successive cycles of sorptions and desorptions. Different varieties of gelatins, egg albumins, and caseins show differences in the tendency of the hysteresis loops to decrease in size and disappear. These varietal differences are probably connected with the hydration capacities. The Difco gelatin has shown a unique and interesting behavior. From the first cycle of sorption and desorption to the twelfth cycle, lasting over a period of 8 months, there is decrease in total sorptive capacity, and the hysteresis loop in the low-pressure region widens. These indicate that the cavity necks have shrunk more than the body, which results in increased entrapping effect. The success of the cavity concept as a general explanation of all cases of hysteresis and associated phenomena is discussed.

Introduction

Earlier investigations on the sorption and desorption of water vapor on different varieties of organo gels, such as rice grain,[1] dhal,[1] gum arabic,[2] ghatti gum,[3] gelatin,[4] casein,[4] egg albumin,[4] and sericin,[5] have revealed certain common characteristics. Either the sorption and desorption curves are coincident, showing no hysteresis effect in the first cycle of sorption and desorption, or the hysteresis effect initially exhibited becomes smaller and disappears in the subsequent cycles. These characteristics are also shown by the leaves of several plants[6] when subjected to successive dehydrations and rehydrations. On the basis of the cavity theory of hysteresis, these observations have been explained by the following: the organocolloid swells on the imbibition of water (the solvating liquid), the cavities collapse, the entrapping effect is lost, and the hysteresis disappears. This generalization is further confirmed by showing in a few cases that with nonsolvating liquids like carbon tetrachloride there is a permanent and reproducible hysteresis loop.[1]

Benson and Richardson[7] have worked with egg albumin, gelatin, and bovine plasma albumin and have reported a reproducible hysteresis loop in three successive cycles in the sorption of water on egg albumin. This result of Benson prompted us to think that varietal differences in the proteins may be responsible for the difference in the behavior in sorption and desorption hysteresis. A systematic study with different grades of gelatin, egg albumin, and casein was undertaken.

Experimental Section

The quartz fiber spring technique[8] described in an earlier paper was employed in the present work. The sorption apparatus was kept at 35° inside an air thermostat of the type built by Vernon.[9] An Edwards high-vacuum pump which produces a pressure of 10^{-2} mm was used. Distilled water was taken in the bulb and made air free by allowing it to evaporate *in vacuo* for 1 hr. Quartz fiber springs used in these experiments had sensitivity ranging from 20 to 40 cm of stretch/g of load. The manometer tube had a bore diameter of 1.2 cm. The mercury used in the manometer was purified by first passing it through a 10% nitric acid column, then distilling in air, and finally distilling *in vacuo*. A cathetometer reading correct to within 10^{-2} mm was employed for measuring the length and stretch of the spring.

(1) K. S. Rao, *J. Phys. Chem.*, **45**, 531 (1941).

(2) K. S. Rao, *Curr. Sci.*, **9**, 19 (1940).

(3) P. H. Elworthy and T. M. George, *J. Pharm. Pharmacol.*, **16**, 258 (1964).

(4) G. N. S. Rao, K. S. Rao, and B. S. Rao, *Proc. Indian Acad. Sci.*, **A25**, 221 (1947).

(5) K. S. Rao, M. B. Rao, A. R. Vasudevamurthy, and B. S. Rao, *Proc. Nat. Inst. Sci. India*, **16**, 1 (1950).

(6) K. S. Rao, M. B. Rao, and B. S. Rao, *ibid.*, **15**, 41 (1949).

(7) S. W. Benson and R. L. Richardson, *J. Amer. Chem. Soc.*, **77**, 2585 (1955).

(8) K. S. Rao, *J. Phys. Chem.*, **45**, 500 (1941).

(9) W. H. J. Vernon, *Trans. Faraday Soc.*, **27**, 241 (1931).

Gelatin. Two different varieties of gelatin—Difco gelatin made by Difco laboratories, Detroit, Mich. and Oxoid gelatin made by Oxo Ltd., London—were used. In the earlier investigation,[4] Merck Gold Label gelatin was used.

Egg Albumin. Egg albumin (Merck's albumin ovi) was used. A sample was activated by heating at 60° *in vacuo* for 6 hr. Another sample was denatured by heating a 10% solution on a boiling water bath for 1 hr. The precipitated albumin was filtered, washed with water, and dried at 40° for 2 hr *in vacuo*. Samples of native, activated, and denatured egg albumins were employed. In the earlier paper,[4] Merck's soluble egg albumin was used.

Casein. Merck's alkali-soluble casein and Oxoid casein hydrolysate were used. A sample of Merck's alkali-soluble casein was activated by heating at 60° for 6 hr. Another sample was denatured by heating in boiling absolute alcohol for 1 hr and drying in an oven at 75° for 1.5 hr. Samples of native, activated, and denatured casein were employed in the studies. In the earlier work,[4] Kahlbaum's casein nach Hammersten was used.

The samples were used in the form of powder. The grain size was between those of 30- and 50-mesh British Standard sieves. A series of sorptions and desorptions of water vapor on the samples was carried out at 35°.

Results

Gelatin. Hysteresis is exhibited by both Difco and Oxoid gelatins. In the case of Difco gelatin, the sorption and desorption studies were continued up to the twelfth cycle. The loops obtained in the first, third, fifth, seventh, ninth, eleventh, and twelfth cycles are shown in Figures 1 and 2. The percentages of water taken at saturation pressure in each of these cycles are 116.4, 119.0, 119.6, 125.3, 113.00, 103.9, and 104.3, respectively. It took about 12 days for completion of each cycle. In each cycle, the gelatin was kept in contact with water vapor at saturation pressure for 2 days, except in cycle 7 in which it was 10 days. The total period required for completing the 12 cycles of sorption and desorption is more than 8 months.

With Oxoid gelatin, the sorption–desorption studies were continued up to the tenth cycle. The loops of the first, fourth, ninth, and tenth cycles are shown in Figure 3. The values at saturation pressure of water are 69.8, 67.8, 69.2, and 68.6%, respectively. The total period required for completing the 10 cycles is 3 months. At the end of each cycle the gelatin was kept in contact with water vapor at saturation pressure for 2 days.

Egg Albumin. The hysteresis loops obtained with native, activated, and denatured egg albumins are shown in Figures 4–6, respectively. With native egg albumin, the amount of water taken at saturation pressure of water in the first, fourth, and fifth cycles are 120.3, 125.4, and 124%, respectively. With activated egg albumin, the amounts of water taken in the second, third, and eighth cycles are 48.1, 46.6, and 46.6%, respectively, and with denatured egg albumin, the amounts of water are 45.8, 46, 47.4, and 48.3%, respectively. The total periods of study with native, activated, and denatured egg albumin were nearly 2, 4, and 4 months, respectively. In all of these cases, the albumin was kept in contact with water vapor at saturation pressure for 2 days.

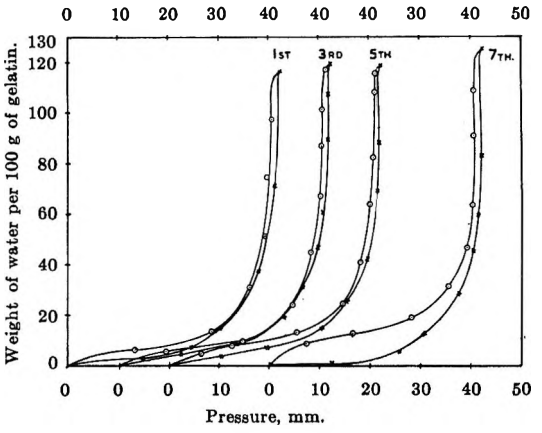

Figure 1. Sorption–desorption hysteresis of water on gelatin (Difco) at the first, third, fifth, and seventh cycles.

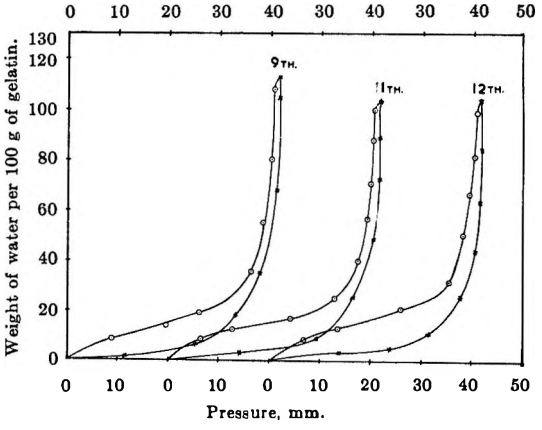

Figure 2. Sorption–desorption hysteresis of water on gelatin (Difco) at the ninth, eleventh, and twelfth cycles.

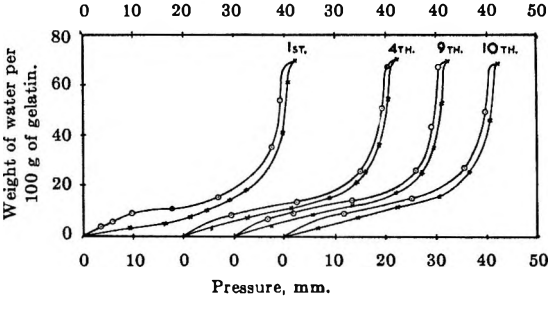

Figure 3. Sorption–desorption hysteresis of water on gelatin (Oxoid) at the first, fourth, ninth, and tenth cycles.

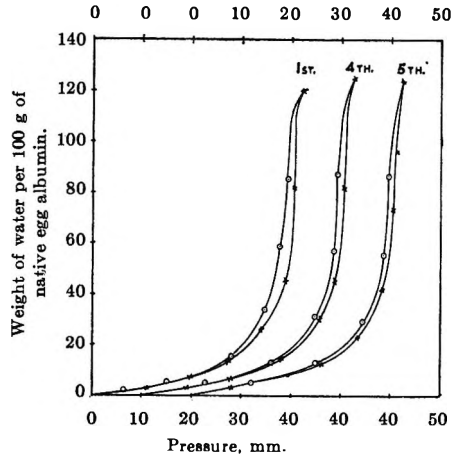

Figure 4. Sorption–desorption hysteresis of water on native egg albumin at the first, fourth, and fifth cycles.

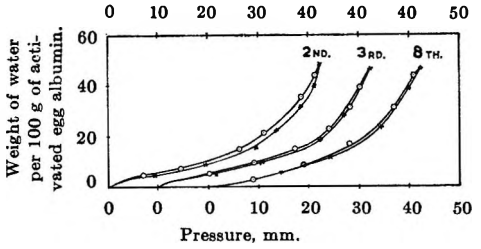

Figure 5. Sorption–desorption hysteresis of water on activated egg albumin at the second, third, and eighth cycles.

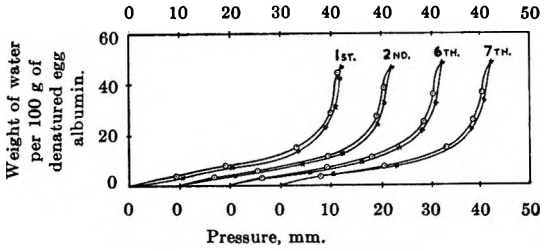

Figure 6. Sorption–desorption hysteresis of water on denatured egg albumin at the first, second, sixth, and seventh cycles.

Casein. With Merck's native casein, Figure 7, sorption–desorption studies have been continued up to the fourth cycle. The amounts of water taken up at saturation pressure in the first, third, and fourth cycles are 40.8, 39.0, and 40.0, respectively. The sorbent was kept in contact with water vapor at saturation pressure for 2, 5, and 5 days in the first, third, and fourth cycles, respectively. The total period for completing the study was 1.5 months.

With Merck's activated casein, Figure 8, sorption–desorption studies were continued up to the fourteenth cycle. The sorption capacities in the first, fourth, fifth, sixth, eighth, and fourteenth cycles are 44.0, 44.0, 47.0, 46.5, 45.6, and 47.0%, respectively. At the end of sorption, the sorbent was kept in contact with water vapor at saturation pressure for 2 days in all cycles except the

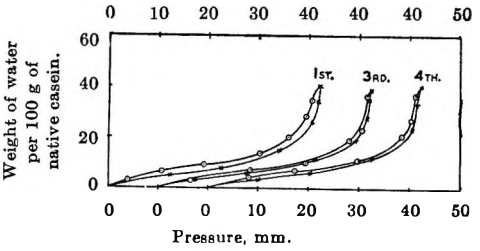

Figure 7. Sorption–desorption hysteresis of water on Merck's native casein at the first, third, and fourth cycles.

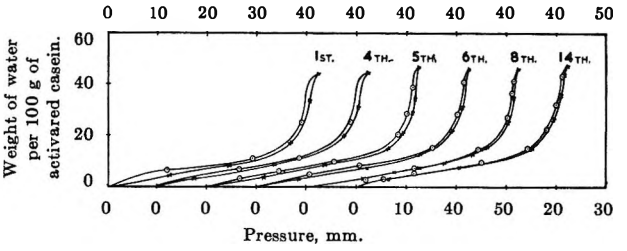

Figure 8. Sorption–desorption hysteresis of water on Merck's activated casein at the first, fourth, fifth, sixth, eighth, and fourteenth cycles.

eighth cycle in which it was kept for 20 days. The total period required to complete this study was 6 months.

In the case of denatured casein, Figure 9, the sorption–desorption studies were continued up to the fifteenth cycle. The sorptive capacities of the casein for water at saturation pressure in the first, second, fifth, sixth, seventh, and fifteenth cycles are 35.7, 41.0, 39.7, 40.3, 35.8, and 29.5%, respectively. The time allowed at saturation was 2 days in all cycles except the sixth and seventh, in which the times were 10 and 20 days, respectively. The study lasted over 6 months.

Sorption–desorption studies were continued up to the sixth cycle in the case of casein hydrolysate, Figure 10. The sorptive capacities in the first, second, fourth, fifth, and sixth cycles are 581.1, 855.1, 857.0, 857.0, and 857.0%, respectively. The sorbent was kept in contact with water vapor at saturation pressure for 14 days in the fourth cycle and 2 days in all others. The total period required for completing the study was 3 months.

Rate Studies. Proteins like other organo gels swell when they sorb water. In all swelling systems, water sorption is a slow process. Incomplete equilibrium during sorption and desorption can cause hysteresis. To eliminate this effect, sufficient time was allowed until equilibrium was attained. Figure 11 shows the time–sorption curves of Difco and Oxoid gelatins. At saturation pressure of water at 35°, Difco gelatin requires about 48 hr for completion of sorption, and Oxoid gelatin requires 24 hr. However, at each intermediate point on the sorption and desorption curves, the time required is about 6 hr, and, actually, about 10 hr was allowed in order to ensure equilibrium.

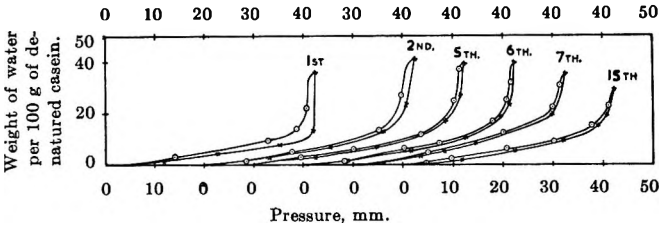

Figure 9. Sorption–desorption of water on Merck's denatured casein at the first, second, fifth, sixth, seventh and fifteenth cycles.

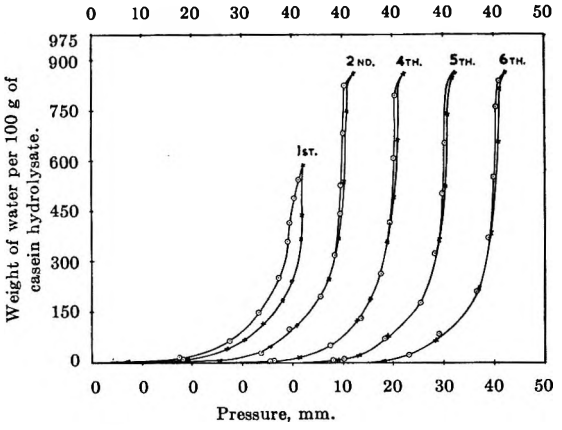

Figure 10. Sorption–desorption hysteresis of water on Oxoid casein hydrolysate at the first, second, fourth, fifth, and sixth cycles.

Time–adsorption curves of egg albumin are shown in Figure 12, and those of casein are shown in Figures 13 and 14.

Discussion

Characteristics of the Hysteresis Loop in Difco Gelatin–Water System. In the sorption of water on Difco gelatin, the hysteresis loops obtained in successive cycles of sorptions and desorptions have shown several interesting characteristics. In the first cycle, the sorption and desorption curves are separated in the low- and high-pressure regions showing hysteresis loops, whereas in the middle, the two are almost coincident. In subsequent cycles there is a tendency for the sorption and desorption curves at the center to separate from each other. In the seventh cycle, the two are completely separated. The hysteresis loop in the low-pressure region has become wider and this further increases slightly up to the twelfth cycle. The amount of water sorbed at saturation pressure has also decreased from the seventh cycle up to the twelfth cycle.

Explanation of the Characteristics in the Light of the Cavity Concept. Difco Gelatin–Water System. Benson[7] does not accept the existence of fine-pore structure in proteins. He explains the hysteresis effect which he has obtained in the sorption of water and other liquids on egg albumin as a case of deformation of the poly-

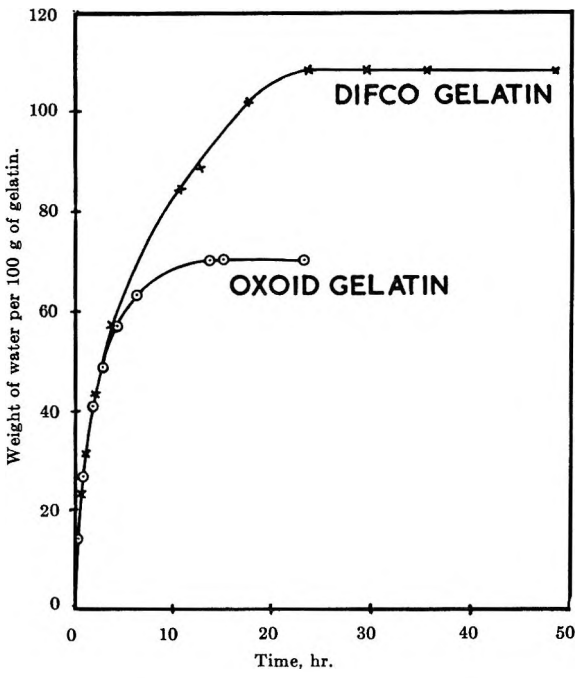

Figure 11. Time–sorption curve of water at saturation pressure at 35° on Difco gelatin and Oxoid gelatin.

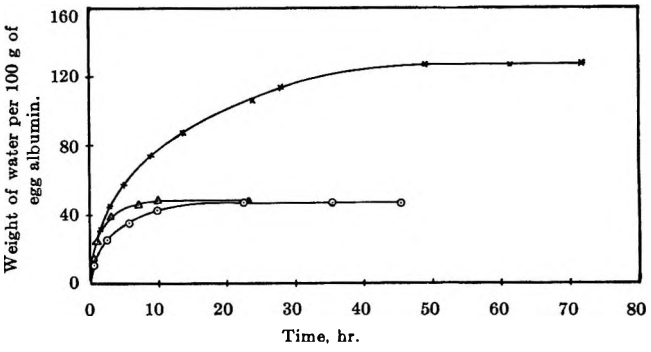

Figure 12. Time–sorption curve of water at saturation pressure at 35° on: native egg albumin, X; activated egg albumin, △; denatured egg albumin, ⊙.

peptide chains within the protein molecule as the polar sorbate settles into suitable positions.

Arnell and McDermot[10] attribute hysteresis to steric effects in swelling systems and this is due to interaction between sorbent and sorbate molecules.

Deformation and steric effect cannot explain a permanent and reproducible hysteresis loop as in the silica gel–water system. It can explain the hysteresis loop which decreases in size and finally disappears, because when the deformation and steric effect cease, the hysteresis effect should cease to exist. The continuous decrease in size of the hysteresis loop and its disappearance in successive sorptions and desorptions have been established by Rao in a large

(10) J. C. Arnell and H. L. McDermot, *Proc. Intern. Congr. Surface Activity, 2nd, London, 1957*, 113 (1957).

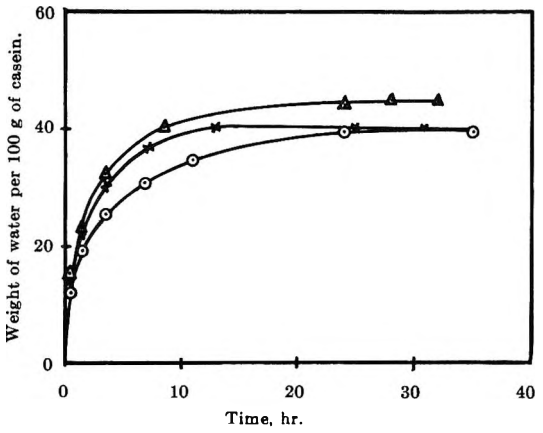

Figure 13. Time–sorption curve of water at saturation pressure at 35° on: native casein, X; activated casein, △; denatured casein, ⊙.

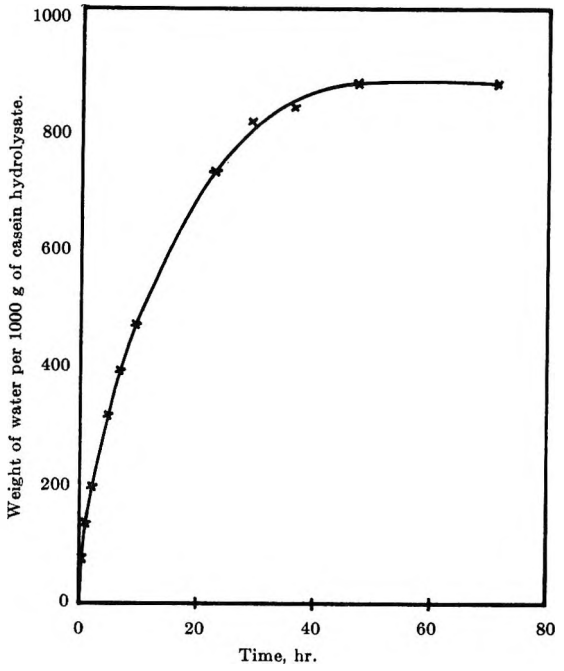

Figure 14. Time–sorption curve of water at saturation pressure at 35° on casein hydrolysate.

number of systems, such as rice, dhal, gum arabic, egg albumin, gelatin, casein, and sericin, which swell with water. With a nonsolvating liquid like carbon tetrachloride, the rice grain has shown a permanent hysteresis loop which has been reproduced up to the ninth cycle of sorption and desorption, and these results cannot be accounted for by the deformation theory and steric effect. The cavity concept alone has been found to explain adequately both the disappearance of the hysteresis effect in the rice–water system[1] and its permanence and reproducibility in the rice–carbon tetrachloride system.[1]

The Cavity Concept. An ideal plane surface adsorption is a rarity. Even nonporous sorbents have cracks and fissures on surface. In such cases, capillary condensation sets in and the entrapping effect of cavity follows. The cavity concept[11,12] has been elaborated in several earlier publications and is found to be a general explanation of the hysteresis effect and all its different aspects—such as drift,[13] scanning,[14] and disappearance.[1]

A cavity is a pore with a constricted neck and it can also have two or more necks. Filling of cavities during sorption is progressive, whereas emptying during the desorption is sudden and abrupt. Every point on the desorption curve denotes the neck radius of the cavity which is emptied. In the Difco gelatin–water system, the tendency for separation of the desorption curve from the sorption curve is noticeable from the first to the fifth cycle, and this has become prominent in the seventh cycle, in which the position of the sorption curve remains practically the same but the desorption curve shifts away from the pressure axis. This indicates that the entrapping effect of the cavities has increased. This is possible if the difference between the cavity radius and neck radius increases.

Swelling and Shrinkage in Relation to Sorption–Desorption Hysteresis. The tendency of the hysteresis loop to decrease in size and finally disappear is found to be a general phenomenon in all nonrigid materials which swell on the imbibition of solvating liquids. Explanation of this interesting phenomenon has been presented earlier in the light of the cavity concept in conjunction with the property of hydration and swelling of the sorbent material in solvating liquid. Dehydrated protein is comparatively rigid in structure. The cavities which are present entrap water and cause hysteresis. At the saturation pressure, protein will be in a swollen condition and the cavity walls become elastic. During desorption, the cavity walls yield, the cavities collapse, the entrapping effect is lost, and thus the hysteresis loop disappears.

Gelatin in contact with water is essentially a changing system. In successive sorptions and desorptions, it is subjected to successive swelling and shrinkage. In these changes, the cavities suffer contraction. The necks are probably more constricted than the cavities, accounting for the increased entrapping effect. Owing to this increased entrapping effect, the gelatin retains at lower vapor pressures more and more of the sorbate in successive sorptions and desorptions. The various changes mentioned above are quite prominent in the seventh cycle, probably because the gelatin was kept in contact with water vapor at saturation pressure for 10 days and gelatin had the facility to swell to a greater extent.

From the seventh to the twelfth cycle, there is a noticeable

(11) J. W. McBain, *J. Amer. Chem. Soc.*, 57, 699 (1935).

(12) S. Brunauer, "The Adsorption of Gases and Vapours," Oxford University Press, London, 1945, p 398.

(13) K. S. Rao, *J. Phys. Chem.*, 45, 522 (1941).

(14) K. S. Rao, *ibid.*, 45, 506, 517 (1941).

reduction, from 125.3 to 104.3%, in the sorptive capacity of gelatin. This indicates that the total cavity volume has decreased owing to shrinkage of the swollen gelatin. The total pore volume including the cavity volume is probably a small fraction of the total sorptive capacity of gelatin. The major portion of water is held by gelatin in association with the protein molecules.

The change which has been noticed in the gelatin–water system is just a particular stage in the continuous process which has taken place over a period of about 8 months. The final stage is the complete collapse of the cavities and the disappearance of the hysteresis effect. If the experiments were continued further, this probably would have been observed. Several cases of the decrease in size of the hysteresis loop and their disappearance after a large number of cycles of sorption and desorption have already been reported. In the sericin–water system,[5] the hysteresis loop has disappeared after eleven cycles. In the hydration and dehydration of grass blades,[6] the hysteresis loop disappeared in the fifteenth cycle.

The behavior of Difco gelatin in the sorption of water is unique and interesting. After the completion of the experiments over a period of 8 months another sample of the same Difco gelatin was studied. The first cycle of sorption and desorption with water was obtained and is shown in Figure 15. This hysteresis loop is identical with the first loop of the first experiment, thereby confirming the reproducibility of the observations. The unique behavior of Difco gelatin cast a doubt on the behavior of the quartz fiber springs. At the end of the sorption–desorption studies, the spring was taken out, its sensitivity was determined, and it was found to be the same.

Oxoid Gelatin–Water System. The hysteresis loops obtained with Oxoid gelatin up to the tenth cycle of sorption and desorption have been shown in Figure 3. There has been a slight decrease in the size of the hysteresis loop in the low vapor pressure region. There is no marked variation in the size and shape of the loop. These results indicate that the tendency of Oxoid gelatin to change is low and cavities tend to decrease in size and collapse slowly.

Merck Gold Label Gelatin. The results of sorption and desorption of water vapor on Merck Gold Label gelatin have been reported in the earlier paper.[4] The system shows no hysteresis effect. The sorption and desorption curves remain coincident in the first two cycles. The experiments were conducted at 30°. In the light of the cavity concept, the cavities that might have been present in the gelatin must have collapsed at the end of the first sorption; consequently there is no hysteresis.

Varietal Differences in Gelatin, Egg Albumin, and Casein in Relation to the Tendency of the Hysteresis Loop to Disappear. If all of the cavities collapse in the very first cycle of sorption and desorption, there will be no hysteresis loop in the first cycle itself and the sorption and desorption curves will be coincident. If, on the other hand, the cavities collapse in stages, the disappearance of the hysteresis loop will not be sudden. The loop decreases gradually in size and finally disappears. Whether the collapse of the cavities is partial or complete is determined by the degree of hydration and swelling. Hydration and swelling are ordinarily slow processes. Sufficient time is necessary for uniformity of swelling. If swelling is nonuniform, internal stresses and strains will be set up in the swelling material, and this affects the ease of collapse of the cavities. The degrees of hydration, swelling, and shrinkage are properties characteristic of each system, and these determine the ease of collapse of cavities and thus the ease of disappearance of the hysteresis loop. Thus, in this general phenomenon of the disappearance of the hysteresis effect, the varietal factor of the sorbent material plays an important role.

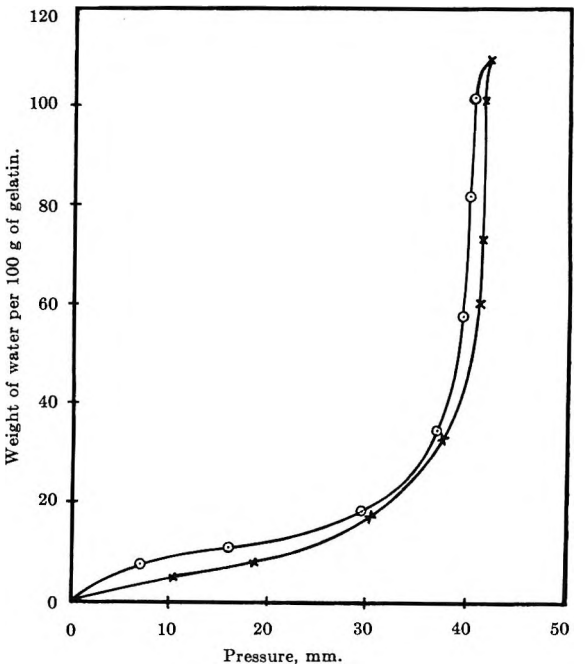

Figure 15. Sorption–desorption hysteresis of water on gelatin (Difco) at the first cycle.

Gelatin. The three different varieties of gelatin have shown marked differences in behavior in the sorption and desorption of water. Merck's Gold Label gelatin has shown no hysteresis effect at all, even in the first cycle. Difco gelatin has shown the hysteresis effect. There is continuous decrease in total sorptive capacity at saturation pressure and enlargement of the hysteresis loop in the low vapor pressure region up to the twelfth cycle of sorption and desorption. Oxoid gelatin has also shown the hysteresis effect. The hysteresis loops persist even up to the tenth cycle of sorption and desorption. The tendency to decrease is low.

Why the three different varieties of gelatin behave differently in the sorption and desorption of water

vapor is a puzzling problem. Any difference in the three varieties could be in the lengths of the polypeptide chains of the protein molecule and the extent of hydration and swelling. The hydration capacities at saturation pressure of water of Difco gelatin, Oxoid gelatin, and Merck Gold Label gelatin are approximately 120, 70, and 50%, respectively. Hydration and dehydration of gelatins cause swelling and shrinkage and these are associated with the development of internal stresses and strains. In Difco gelatin having the highest sorptive capacity, these internal stresses and strains are the highest; consequently the deformation of the cavity wall and the collapse of the cavities are the slowest. In Merck Gold Label gelatin having the lowest sorptive capacity, the stress and strain are least and, therefore, the cavities collapse more easily. The molecular deformation proposed by Benson and the steric effect proposed by Arnell are really involved in these stresses and strains in swelling and shrinking gelatin.

The time of contact of the gelatin with water vapor at saturation pressure is probably an important factor. Though equilibrium is attained in about 10 hr, ordinarily 2 days was allowed. In the seventh cycle in the Difco gelatin–water system, the gelatin was kept in contact with water vapor at saturation pressure for 10 days, and this has resulted in a marked change in the size and shape of the loop.

Egg Albumin. In the sorption and desorption of water vapor on native egg albumin (Merck's albumin ovi), there is a tendency for the decrease in size of the hysteresis loop from the first loop to the fifth. The activated egg albumin also has shown similar tendency from the second to the eighth loop and the tendency is more marked. The denatured egg albumin also has shown the hysteresis loop up to the seventh cycle, and there is a tendency for the decrease in size, though less prominent. Particularly in the low-pressure region, up to a relative vapor pressure of about 0.50, part of the hysteresis loop of the first cycle has disappeared in the seventh cycle.

In the earlier paper,[4] Merck's soluble egg albumin has shown the hysteresis loop in the first cycle of sorption and desorption, and the loop has disappeared in the second and third cycles. The same albumin after denaturation has shown no hysteresis effect at all, even in the first cycle, and the sorption and desorption curves are coincident in the first three cycles. These results, as in the case of gelatin, bring out the relation between the varietal difference in egg albumin and its behavior in sorption–desorption hysteresis. Merck's egg albumin (albumin ovi) has sorption capacity of about 125% water, whereas Merck's soluble egg albumin has sorptive capacity of about 70% water. The variety of egg albumin having high sorptive capacity has shown a lower tendency for the hysteresis loop to decrease in size. On denaturation, the two varieties of albumin have suffered a decrease in their sorptive capacities.

With native egg albumin of Armour and Co., Benson[7] has obtained hysteresis loops in three successive cycles of sorptions and desorptions, and these are practically identical. With bovine plasma albumin and denatured egg albumin employing water, ethyl alcohol, diethyl ether, and ethyl chloride, hysteresis loops have been obtained in the first cycle of sorption and desorption. If the study was continued in the second and subsequent cycles and with those liquids which are solvating, probably the loops would have shown a tendency to decrease in size and finally disappear. In their study of sorption–desorption hysteresis of water on native and denatured egg albumin at different increasing temperatures up to 100°, Altman and Benson[15] have noticed that the hysteresis loop decreases in size as the temperature increases, and at 100°, the decrease in size is prominent.

Casein. Merck's alkali-soluble casein, native, activated, and denatured, and Oxoid casein hydrolysate have all shown a common characterestic in successive sorptions and desorptions of water vapor. They all exhibit the hysteresis effect, and the hysteresis loop decreases in size in successive cycles and tends to disappear. The tendency to disappear is predominent in the case of activated casein, denatured casein, and casein hydrolysate.

Kahlbaum's casein nach Hammersten in the earlier investigation[4] has shown a loop in the first cycle and it has disappeared in the second and third cycles. The above results with the different grades of casein, just as in the case of gelatin and egg albumin, bring out clearly the effect of varietal difference on the tendency of the hysteresis loop to decrease in size and disappear on successive sorptions and desorptions of water vapor.

Success of Cavity Concept as an Explanation of the Sorption–Desorption Hysteresis. Many cases of the gradual decrease in size of the hysteresis loop and its final disappearance on successive sorptions and desorptions are already on record. There is need for a satisfactory explanation of this general phenomenon.

To completely rule out the idea of the existence of pores in proteins and other swelling sorbents is not justifiable, in view of the fact that ideal plane surface sorption is a rarity in nature. If the existence of pores is permitted, the cavity-entrapping effect inevitably follows. The magnitude of this pore volume may be very small compared with the total sorptive capacity of the material which is mostly a case of hydration. This argument is borne out by the fact that, in many of the systems studied, the total sorptive capacity has remained practically the same though the hysteresis loop has disappeared.

Activated rice[1] has taken 25 g of water/100 g of rice,

(15) R. L. Altman and S. W. Benson, *J. Phys. Chem.*, **64**, 851 (1960).

whereas the volume of carbon tetrachloride taken is only 1 $cm^3/100$ g. The volume of carbon tetrachloride taken is a measure of the pore space and this is very small compared with the hydration capacity of rice grains. What portion of the total pore volume the cavities occupy is a difficult problem to tackle. A quantitative formulation of the entrapping effect of the cavity is needed. So far no mathematical formulation of the cavity effect has been made and probably any such attempt would be difficult, because it involves information about the number, shape, size, the neck, and body diameters of the cavities in any particular porous system. Nevertheless, the cavity theory of hysteresis has been successful, so far, in explaining in a qualitative way all cases of hysteresis and the associated phenomena.

Another significant point emerges from the cavity concept. Hysteresis is due to entrapping of liquid. The entrapping effect is determined by the difference between the body radius and neck radius of the cavity. In two cavities of the same body radii, the one having the smaller neck entraps more liquid and, consequently, produces a bigger hysteresis loop. The one having the wider neck produces a smaller hysteresis loop. This is probably the explanation of the difference between the first and twelfth loops in the Difco gelatin–water system. Thus the cavity theory of hysteresis coupled with the swelling and shrinkage of the sorbent in a solvating liquid has been able to explain satisfactorily all of the variations in size and shape of the hysteresis loop observed in successive sorptions and desorptions.

Proteins, gums, and rice grain have no similarity in chemical composition. However, they all behave in the same way with regard to sorption–desorption hysteresis. The properties that are common to them are hydration and swelling.

Acknowledgment. The authors wish to thank Professor V. Lakshminarayanan, Director, for his kind encouragement and the use of his facilities, and the Ministry of Education, Government of India, for financial aid (a research fellowship) to B. D.

The Reduced Equation of State of Argon and Xenon

by Eugene M. Holleran

Chemistry Department, St. John's University, Jamaica, New York 11432 *(Received September 11, 1967)*

The compressibility factors of argon and xenon are compared after reduction of temperature and density by the two characteristic constants of the unit compressibility law. These constants are experimental quantities independent of any molecular model. With values of the constants determined in the region of overlap of the compressibility data, it is found that the reduced equation of state obeys the principle of corresponding states better than with the critical constants or with the parameters of the Lennard-Jones or the Kihara intermolecular potentials. Excess energies and entropies also show a good correspondence.

In a study of the correspondence of the reduced properties of argon and xenon, Levelt[1] employed both the critical constants and the parameters of the Lennard-Jones potential to reduce the temperature and density. Both of these sets of reducing constants resulted in considerable deviations from corresponding-states behavior. Levelt noted, however, that use of any set of reducing constants having xenon:argon ratios of the temperature factors of about 1.931 and of the density factors of about 0.633 would bring the compressibility isotherms of these gases into fairly close correspondence at the minima and in the high-density range, with an over-all agreement of about 1% in the region of overlap of the data available.

After determining the parameters of the Kihara potential for argon and xenon, Danon and Rossi[2] noted that their ratios approached the optimum and could, therefore, be expected to provide a closer adherence to the principle of corresponding states. Recently, Crivelli and Danon[3] carried out this comparison. They found a very significant decrease in the differences between the compressibilities tabulated for the two gases at equal reduced temperatures and densities, compared to those found by Levelt. The greatest remaining differences, up to 0.0165, appear in the region of lowest temperatures and highest densities.

(1) J. M. H. Levelt, *Physica*, **26**, 361 (1960).
(2) F. Danon and J. C. Rossi, *J. Phys. Chem.*, **70**, 942 (1966).
(3) I. Crivelli and F. Danon, *ibid.*, **71**, 2650 (1967).

The purpose of the present paper is to report the correspondence found upon reduction by a new set of natural experimental constants.

Determination of the Reducing Constants

A linear relation has recently been discovered[4] between the temperatures and densities at which the compressibility factor, $Z = P/dRT$, equals unity. Thus, for $Z = 1$

$$(T = T_B(1 - (d/d_0)) \quad (1)$$

in which T_B, the Boyle temperature, and d_0 are constants characteristic of each substance. These constants may be used to define a natural set of reduced variables

$$\theta = T/T_B$$
$$\delta = d/d_0 \quad (2)$$
$$\pi = P/d_0RT_B$$

in terms of which eq 1 becomes, for $Z = 1$

$$\theta + \delta = 1 \quad (3)$$

We now wish to determine whether the thermodynamic states of argon and xenon characterized by equal values of θ and δ are corresponding states having the same values for Z, π, and other reduced properties. In order to carry out the proposed comparison, it is necessary first to determine values of T_B and d_0 by fitting eq 1 to the experimental compressibility data for the gases. Unfortunately, the exact values of these constants are extremely sensitive to uncertainties in the data. An independent method of determination would be helpful. However, since eq 1 probably cannot survive the liquid–solid transition, low-temperature crystal densities cannot be expected to provide more than an approximation to d_0. The Boyle temperature can be found independently as the temperature at which the second virial coefficient $B(T)$ is zero, but this procedure also requires highly accurate compressibility data, and the resulting values of T_B are subject to about the same uncertainties (often 1 or 2%) as those found from eq 1.

In the absence of the "true" values of the constants, two different sets will be used. Set I represents the values found in ref 4 by fitting eq 1 to the compressibility data of Michels, Levelt, and DeGraaff[5] for argon and Michels, Wassenaar, and Louwerse[6] for xenon. These values of T_B in degrees Kelvin are 408.3 for argon and 793.2 for xenon, and the values of d_0 in amagat units are 1047 for argon and 659.9 for xenon. Set II represents the constants found in the region where the data for the two gases overlap. Six of the experimental compressibility isotherms of argon and eight of the isotherms for xenon provide data in an overlapping region of θ and δ. The temperatures of these isotherms are listed in Tables I and II. Their density dependences are given in ref 5 and 6 as polynomials in powers of d up to six, seven, or eight. These polynomials were solved numerically for $Z = 1$, and the resulting values of d are also listed in Tables I and II. These T and d points for the unit compressibility factor were then fitted to eq 1 by minimizing the sum of squares of $(\theta + \delta - 1)$. The resulting least-squares values of T_B are 410.4 for argon and 792.3 for xenon, and the values of d_0 are 1043 for argon and 660.6 for xenon. The ratios of these two T_B values and the two d_0 values agree with Levelt's "ideal" ratios. They should, therefore, provide a generally good correspondence of compressibility factors.

Table I: The Unit Compressibility Law for Argon in the Overlap Region

Temp, °C	d, amagats	θ	δ	$10^4(\theta + \delta - 1)$
−120	653.6[a]	0.3733	0.6265	−2
−110	628.4	0.3976	0.6023	−1
−100	603.2	0.4220	0.5782	+2
−85	565.2	0.4585	0.5417	+2
−70	527.0	0.4951	0.5051	+2
−50	475.6	0.5438	0.4559	−3

[a] This value is an extrapolation beyond the maximum experimental density of 640 amagats.

Table II: The Unit Compressibility Law for Xenon in the Overlap Region

Temp, °C	d, amagats	θ	δ	$10^4(\theta + \delta - 1)$
25	411.9	0.3764	0.6235	−1
30	407.7	0.3827	0.6172	−1
40	399.4	0.3953	0.6046	−1
50	391.2	0.4079	0.5922	+1
75	370.4	0.4395	0.5607	+2
100	349.5	0.4711	0.5290	+1
125	328.6	0.5026	0.4974	0
150	307.6	0.5342	0.4656	−2

Table III: The Correspondence of Compressibility Factors for Constants of Set I

θ	δ = 0.1	0.2	0.3	0.4	0.5	0.6
0.38	0.6724	0.4524	0.3288	0.2877	0.3961	0.8450
	−18	−61	−100	−137	−150	+7
0.45	0.7716	0.6247	0.5577	0.5877	0.7891	1.3152
	−15	−39	−74	−98	−75	+77
0.52	0.8382	0.7451	0.7270	0.8118	1.0724	1.6401
	−11	−29	−51	−51	−31	+128

(4) E. M. Holleran, *J. Chem. Phys.*, in press.

(5) A. Michels, J. M. Levelt, and W. DeGraaff, *Physica*, **24**, 659 (1958).

(6) A. Michels, T. Wassenaar, and P. Louwerse, *ibid.*, **20**, 99 (1954).

Table IV: The Compressibility Factor of Xenon and the Difference $10^4[Z(\mathrm{Ar}) - Z(\mathrm{Xe})]$ as Functions of θ and δ for the Constants of Set II

θ	δ = 0.05	0.10	0.15	0.20	0.25	0.30	0.35	0.40	0.45	0.50	0.55	0.60
0.38	0.8227	0.6712	0.5473	0.4505	0.3782	0.3268	0.2946	0.2852	0.3115	0.3940	0.5609	0.8456
	27	40	36	23	12	0	−8	−21	−40	−50	−47	−16
0.40	0.8401	0.7044	0.5937	0.5074	0.4432	0.3994	0.3765	0.3798	0.4214	0.5205	0.7028	0.9998
	26	38	37	29	16	4	−9	−21	−36	−42	−38	−12
0.42	0.8553	0.7333	0.6343	0.5575	0.5017	0.4663	0.4529	0.4677	0.5225	0.6353	0.8304	1.1370
	24	35	36	30	18	4	−10	−19	−33	−35	−26	−1
0.44	0.8691	0.7592	0.6706	0.6028	0.5549	0.5274	0.5230	0.5483	0.6149	0.7399	0.9460	1.2610
	18	27	29	24	17	8	−3	−13	−27	−32	−27	−10
0.46	0.8811	0.7818	0.7026	0.6431	0.6030	0.5834	0.5875	0.6223	0.6992	0.8344	1.0496	1.3708
	18	29	31	28	19	10	−1	−11	−22	−21	−12	+9
0.48	0.8919	0.8023	0.7316	0.6798	0.6470	0.6348	0.6468	0.6903	0.7764	0.9207	1.1439	1.4705
	16	25	29	26	20	12	3	−7	−17	−17	−10	+7
0.50	0.9018	0.8207	0.7579	0.7133	0.6873	0.6820	0.7014	0.7528	0.8473	0.9997	1.2298	1.5609
	13	25	28	26	21	14	5	−3	−13	−14	−6	+13
0.52	0.9106	0.8375	0.7820	0.7440	0.7245	0.7257	0.7520	0.8107	0.9126	1.0721	1.3081	1.6427
	12	23	24	23	19	14	5	−3	−12	−15	−9	+15

Table V: Differences between Direct and Interpolated Compressibilities on the −110° Isotherm of Argon

	δ = 0.05	0.10	0.15	0.20	0.25	0.30	0.35	0.40	0.45	0.50	0.55	0.60
$10^4\Delta Z$	−4	−8	−11	−12	−4	6	18	18	12	3	−2	−11

The last columns in Tables I and II show that these experimental isotherms obey the unit compressibility law, eq 1 or 3, to within 3 parts/10,000. Even these small discrepancies, being apparently systematic, render the constants somewhat uncertain. As it happens, the deviations for the two gases are similar in magnitude and direction, and any adjustments that may later be required would, therefore, probably tend to preserve their ratios. Set II thus seems to provide the best available constants for the present purpose.

The Reduced Equation of State

Table III for set I and Table IV in greater detail for set II list the values of Z for xenon and the difference $10^4[Z(\mathrm{Xe}) - Z(\mathrm{Ar})]$ at uniformly spaced values of θ and δ in the region of overlap.

The range of overlap of the data is fairly extensive. The θ range (0.38–0.52) is only moderate, but it is in the difficult low-temperature region just above the critical temperature. The δ range (0–0.6) is large, and, significantly, the Z range (0.29–1.64) is also large. The unit-compressibility line cuts diagonally across the overlap region at high densities.

The compressibility values for Tables III and IV were found as follows. The 14 isotherm polynomials were solved for Z at values of d corresponding to the tabulated values of δ and adjusted slightly for the deviations of the polynomials from experiment according to tables provided in ref 5 and 6. At each δ, the Z values were then interpolated between temperatures to the tabulated θ values, assuming that at constant density Z is nearly linear in $1/\theta$.

An attempt was made to verify the reliability of this temperature interpolation by interpolating for the values of Z on the −110° isotherm from those on the isotherms at −100 and −120°. The interval of θ here is 0.049, as great as any needed in the interpolations for Table IV. The results are shown in Table V. Any inadequacy of the interpolation appears to be obscured by an undulation of the differences. This apparent waviness of one isotherm compared to nearby isotherms of the same substance is probably not real but may be due to the polynomial representation. Interpolation errors are evidently not as large as the waviness.

The agreement of the compressibility factors in Table III for the constants of set I is fairly good, being roughly comparable to that found by Crivelli and Danon for the Kihara parameters. The agreement shown in Table IV for the overlap constants of set II is still better. The maximum difference of 0.0050 and the average absolute difference of 0.0020 are 30 and 40% of those found for the Kihara parameters. The wavy behavior appearing in Table V for the comparison of different isotherms of the same substance also appears to provide the main variation in the compressibility differences of the two gases in Table IV. Any real differences that may exist are apparently obscured here also. For this reason and also because of the uncertainty in the constants, the tabulated dif-

Table VI: Correspondence of Negative Reduced Excess Energies for Set I

θ	δ = 0.1	0.2	0.3	0.4	0.5
0.38	0.2695	0.5082	0.7081	0.8841	1.0671
	0	−38	−63	−63	−91
0.45	0.2430	0.4603	0.6562	0.8431	1.0320
	9	5	−25	−51	−85
0.52	0.2267	0.4343	0.6277	0.8155	1.0034
	4	−3	−16	−37	−60

Table VII: Correspondence of Negative Reduced Excess Energies for Set II

θ	δ = 0.1	0.2	0.3	0.4	0.5
0.38	0.2703	0.5097	0.7101	0.8861	1.0696
	49	42	37	45	37
0.45	0.2436	0.4615	0.6579	0.8450	1.0344
	43	56	60	50	40
0.52	0.2273	0.4354	0.6292	0.8175	1.0056
	35	53	41	63	61

Table VIII: Correspondence of Negative Excess Entropies for Set I

θ	δ = 0.1	0.2	0.3	0.4	0.5
0.38	0.713	1.364	1.914	2.438	3.096
	8	−10	−20	−10	−16
0.45	0.584	1.130	1.660	2.238	2.925
	8	4	−2	−6	−15
0.52	0.514	1.021	1.539	2.121	2.803
	4	4	−1	−3	−9

Table IX: Correspondence of Negative Excess Entropies for Set II

θ	δ = 0.1	0.2	0.3	0.4	0.5
0.38	0.715	1.368	1.918	2.443	3.101
	18	9	2	11	10
0.45	0.585	1.132	1.663	2.242	2.929
	15	16	13	13	10
0.52	0.515	1.021	1.541	2.125	2.808
	9	11	11	14	16

ferences cannot be considered physically significant. If sufficient refinement in the data and their representation can be achieved, perhaps physically significant differences in the reduced equations of state can be observed.

Energy and Entropy

Levelt also compared, for the Lennard-Jones parameters, the reduced excess energies and entropies as derived from the compressibility data by Michels, Levelt, and Wolkers[7] for argon and Michels, Wassenaar, Wolkers, and Dawson[8] for xenon. The correspondence of these properties was not good. The differences increased with density, reaching about 4% for the excess energy and 11% for the excess entropy at the high-density end of the overlap region.

Reduction by T_B and d_0 provides a much better correspondence of these properties, as shown in Tables VI, VII, VIII, and IX. The entries in these tables were found by direct interpolation in the tables of ref 7 and 8. The energy values are reduced by RT_B; it is not necessary to reduce the entropy. The agreement at high densities is particularly good, averaging 0.5% at δ = 0.5. The deviations (Xe − Ar) for set I constants are smaller on the average, but those for set II exhibit smaller maxima and a rough constancy which may possibly be significant.

(7) A. Michels, J. M. Levelt, and G. J. Wolkers, *Physica*, **24**, 769 (1958).

(8) A. Michels, T. Wassenaar, G. J. Wolkers, and J. Dawson, *ibid.*, **22**, 17 (1956).

Vapor Pressures of the Isotopic Waters and Ices

by W. Alexander Van Hook

Chemistry Department, University of Tennessee, Knoxville, Tennessee 37916 *(Received September 15, 1967)*

A detailed application of the theory of isotope effects in condensed systems is made to the various D, T, O^{17}, and O^{18} vapor pressure isotope effects (VPIE) for liquid and solid water between 230 and 400°K. Force fields for the liquid and solid are developed which quantitatively correlate the VPIE's for the 18 different isotopic isomers of water over this temperature range. The general precision of the agreement between calculated and observed results (where available) is excellent. Some limitations on the calculation are pointed out. Finally, nonideality in H_2O, HDO, and D_2O solutions is discussed.

Introduction

The vapor pressure isotope effects (VPIE) displayed by the isotopic waters and ices are a matter of considerable interest from both a theoretical and a practical point of view. In the present paper our interest lies in making a straightforward application of the theory of isotope effects in condensed systems[1] to water. The results should prove to be of somewhat broader application, however, in view of the considerable geochemical interest in the natural isotopic fractionation processes of water[2] as well as because of the interest in isotopic separation by distillation techniques.[3] The general interest in this problem then and the success of our cell model calculations of the H–D vapor pressure isotope effects for several hydrocarbon systems[4] led us to apply the model to the very complicated condensed phases of water.

Most of the data on the VPIE's of the isotopic waters and ices which are available in the literature are plotted as the points in Figure 1. The lines are calculated and discussed below. The isotope effects are normal for all species below about 450°K. At or around that temperature they undergo a crossover and become inverse. Our own calculations are limited to temperatures below 130° ($P_{H_2O} \sim 3$ atm) because at higher temperatures the corrections for gas imperfection, etc., become large. Around 130° the VPIE is only about 2% for DOD; this increases an order of magnitude to 20% at the melting point and in ice all the way to 40% at −35°. The magnitude of the low-temperature effects and the temperature coefficients of the effects are truly large. This is, of course, a consequence of the hydrogen bonding in the condensed phases.

The data in Figure 1 include (for the ices) that of Jones[5] on T_2O, of Kiss, Jakly, and Illy[6] and Matsuo, Kuniyoshi, and Miyake[7] on D_2O, and of Merlivat and Nief[8] on HDO, and (for the waters) that of Jones[5] on T_2O and D_2O, of Popov and Tazetdinov[9] on T_2O, of Combs, Googin, and Smith[10] on D_2O and of Smith and Fitch,[11] Avinur and Nir,[12] and Zel'vinski, Shalygin, Tatrainskii, and Nikolaev[13] on HOT, of Merlivat, Botter, and Nief[14] on HDO, of Kiss, Jakly, and Illy,[6] and Whalley[15] (smoothed from earlier workers) on D_2O, of Dostrovsky and Raviv[16] on H_2O^{18}, and of Szapiro and Steckel[17] on H_2O^{18} and H_2O^{17}.

The Model

The theory of the vapor pressure isotope effect has been formulated by Bigeleisen.[1] The result may be expressed in general terms as

$$\ln \frac{P'}{P} = \ln \left(\frac{s}{s'} f_c\right) - \ln \left(\frac{s}{s'} f_g\right) + \frac{1}{RT}(P'V' - PV) + \{(B_0P + {}^1/_2C_0P^2) - (B_0P + {}^1/_2C_0P^2)'\} - G(\sigma, \sigma') \quad (1)$$

In this equation P'/P is the VPIE (the prime by con-

(1) J. Bigeleisen, *J. Chem. Phys.*, **34**, 1485 (1961).

(2) See for example: E. Roth, *J. Chim. Phys.*, **60**, 339 (1963); R. Weston, *Geochim. Cosmochim. Acta*, **8**, 281 (1955).

(3) See for example: T. F. Johns in "Separation of Isotopes," H. London, Ed., George Newnes, Ltd., London, 1961, pp 41–94; R. Casini, *Proc. Intern. Symp. Isotope Separation, Amsterdam, 1957*, 368 (1958).

(4) (a) W. A. Van Hook, *J. Chem. Phys.*, **44**, 234 (1966); **46**, 1907 (1966); *J. Phys. Chem.*, **71**, 3271 (1967); (b) M. J. Stern, W. A. Van Hook, and M. Wolfsberg, *J. Chem. Phys.*, **39**, 3179 (1963).

(5) W. M. Jones, LADC 5905 (1964).

(6) I. Kiss, G. Jakly, and H. Illy, *Acta Chim. Acad. Sci. Hung.*, **47**, 379 (1966).

(7) S. Matsuo, H. Kuniyoshi, and Y. Miyake, *Science*, **145**, 1454 (1964).

(8) L. Merlivat and G. Neif, *Tellus*, **19**, 122 (1967).

(9) M. M. Popov and F. I. Tazetdinov, *At. Energ.* (U.S.S.R.), **8**, 420 (1960).

(10) R. L. Combs, J. M. Googin, and H. A. Smith, *J. Phys. Chem.*, **58**, 1000 (1954).

(11) H. A. Smith and K. R. Fitch, *ibid.*, **67**, 920 (1963).

(12) P. Avinur and A. Nir, *Nature*, **188**, 652 (1960).

(13) Y. A. Zel'venski, V. A. Shalygin, V. S. Tatarinskii, and D. A. Nikolaev, *At. Energ.* (U.S.S.R.), **18**, 56 (1965).

(14) L. Merlivat, R. Botter, and G. Neif, *J. Chim. Phys.*, **60**, 56 (1963).

(15) E. Whalley, "Proceedings of the Joint Conference on the Thermodynamic and Transport Properties of Fluids, 1957," Institute of Mechanical Engineering, London, 1958, pp 15–26.

(16) I. Dostrovsky and A. Raviv, *Proc. Intern. Symp. Isotope Separation, Amsterdam, 1957*, 336 (1958).

(17) S. Szapiro and F. Steckel, *Trans. Faraday Soc.*, **63**, 883 (1967).

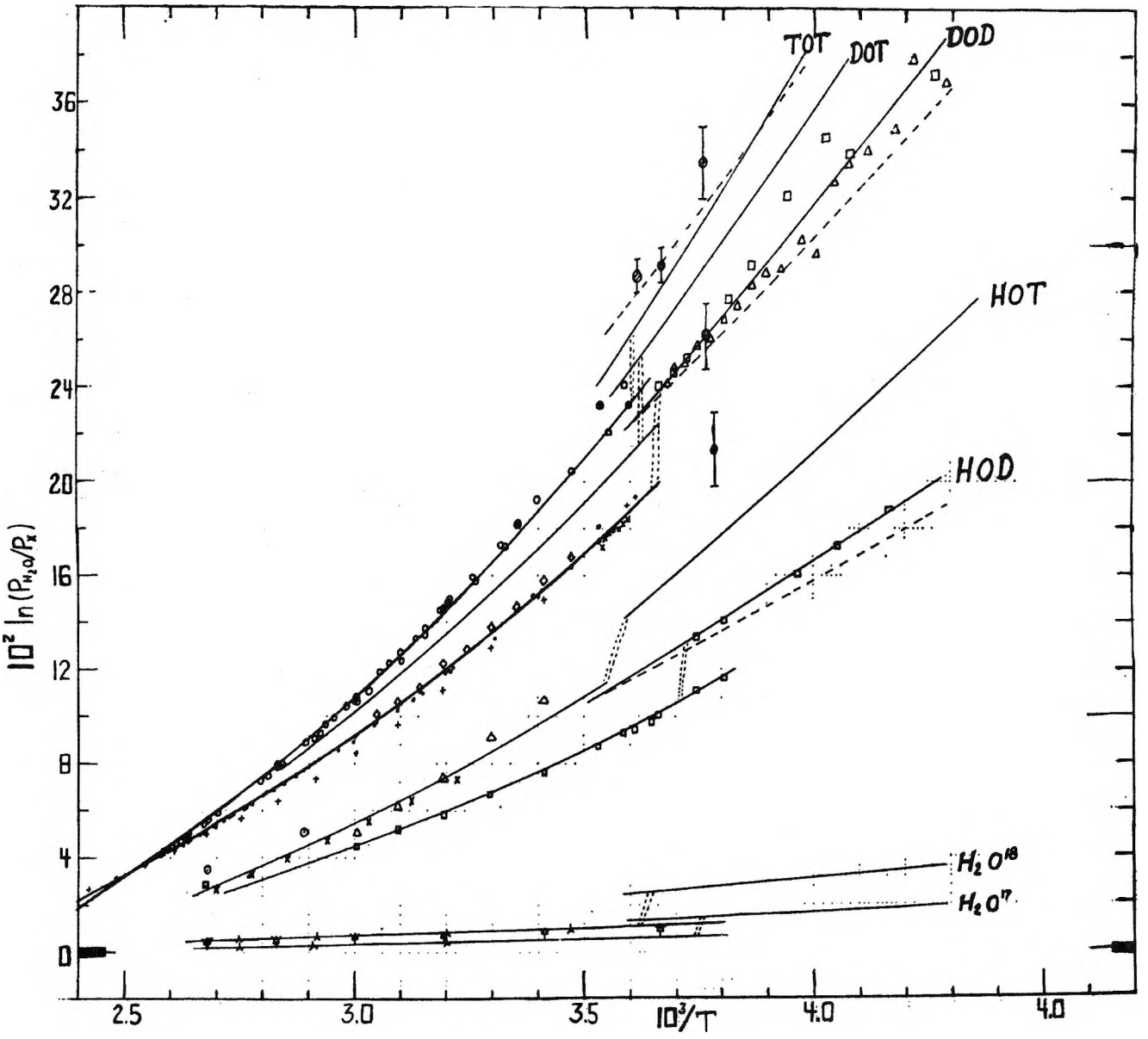

Figure 1. Vapor pressure isotope effects of isotopic waters and ices. On the left, waters; on the right, ices. The lines are calculated: waters, see Tables I and VI (column I); ices: solid, see Tables I and V; dotted, see text. The points are experimental: Ices: TOT, ⧗, Jones;[5] DOD, △, Kiss, Jakly, and Illy;[6] □, Matsuo, Kuniyoshi, and Miyake;[7] HOD, □, Merlivat and Nief.[8] Waters: TOT, ○, Jones;[5] ●, Papov and Tazetdinov;[9] DOD, ●, Jones;[5] ◇, Combs, Googin, and Smith;[10] X, Kiss, Jakly, and Illy;[6] ●, Whalley;[15] HOT, △, Smith and Fitch;[11] ○, Avinur and Nir;[12] X, Zel'vinski, Shalygin, Tatarinskii, and Nikolaev;[13] HOD, □, Merlivat, Botter, and Nief;[14] H_2O^{18}, ✡, Dostrovsky and Raviv;[16] ⅄, Szapiro and Steckel;[17] H_2O^{17}, ⅄, Szapiro and Steckel.[17]

vention refers to the lighter isotope), and $(s/s')f_c$ and $(s/s')f_g$ are the reduced partition functions for the condensed and gaseous phases introduced by Bigeleisen and Mayer.[18] The last three terms correct for the isotope effect on molar volume of the condensed phase, for the effect of gas imperfection, and for nonclassical rotation in the gas phase. This last term may be neglected at the high temperatures ($T \geqslant 230°K$) of our calculation. We shall see that the other two terms are also negligibly small over the temperature range of the calculation. They are needed in the general formulation because the vapor pressures of the two (separated) isomers are being compared at the same temperature but at different pressures and molar volumes.

The correction for the molar volume isotope effect is easily evaluated, at least for D_2O, from the data cited in the review by Whalley.[15] The correction is completely negligible ($<1 \times 10^{-4}$ in $\ln(P'/P)$) for all temperatures below 500°K. We shall make the plausible assumption that this is true for the other isotopic isomers as well and drop it from consideration.

The correction for gas imperfection can be made from

(18) J. Bigeleisen and M. G. Mayer, *J. Chem. Phys.*, **15**, 261 (1947).

the second virial coefficients given by Hirschfelder, Curtiss, and Bird.[19] If we assume the contribution from the third and higher coefficients is negligible and further that $B = B'$, we find at 100° a correction of 7×10^{-4} in the natural logarithm of the VPIE, and at 150° we find 8×10^{-4}. Such corrections are small. In fact, they are within the precision of the data and as such are neglected. (The corrections at lower temperatures are much smaller.) In addition, the correction remains small even at higher temperatures owing to the fact that the isotope effect $(P'-P)$ as well as the virial coefficient, B, both fall off rapidly with temperature. If, however, there is an isotope effect on B, depending on its magnitude, it begins to modify the calculations significantly at temperatures above 100°. For example, one finds for $B_{D_2O}/B_{H_2O} = 1.1$ the correction is -7×10^{-4} at 100°, -28×10^{-4} at 150°, and -77×10^{-4} at 200°. If $B_{D_2O}/B_{H_2O} = 0.9$, the correction is 21×10^{-4} at 100°, 75×10^{-4} at 150°, and 146×10^{-4} at 200°. Although these are unreasonably generous upper and lower limits for the virial coefficient isotope effect, it is still clear that gas imperfection corrections become alarmingly large at elevated temperatures even for more reasonable estimates of B/B'. For this reason we have restricted our calculations to temperatures below approximately 150° where the gas imperfection correction should be small enough to neglect. We again assume that this procedure is valid for the other isotopic isomers.

Returning to eq 1 we are now left with only the first two terms which give reduced partition function ratios. We shall approximate these ratios using harmonic oscillator partition functions, obtaining

$$\frac{P'}{P} = \prod_{\substack{3N-6 \\ \text{internal} \\ \text{frequencies}}} \left[\frac{(u/u')_c}{(u/u')_g}\right]\left[\frac{\exp(u'-u)_c/2}{\exp(u'-u)_g/2}\right] \times \left[\frac{(1-\exp(-u')_c)/(1-\exp(-u)_c)}{(1-\exp(-u')_g)/(1-\exp(-u)_g)}\right] \times \prod_{\substack{6 \\ \text{external} \\ \text{condensed} \\ \text{frequencies}}} \frac{u}{u'}\left[\exp\left(\frac{u'-u}{2}\right)\right]\left[\frac{1-\exp(-u')}{1-\exp(-u)}\right] \quad (2)$$

Here the prime denotes the lighter isotope, $u = h\nu/kT$, and c and g refer to the condensed and gas phases, respectively.

Equation 2 succinctly describes the model which has been selected. It consists of a one-state condensed phase in which each n-atom molecule executes $3n$ vibrations in the force field determined by the presence of its neighbors ($3n - 6$ internal, 3 hindered librations, and 3 hindered translations). In other words, we are describing the condensed phase in terms of the properties of the average condensed-phase molecule. The potential surface for the motions of this average molecule is approximated with a set of effective harmonic force constants which are assumed to be isotopically invariant. This should be a reasonable approximation in view of the fact that our particular interest lies in the calculation of ratios of partition functions in order to determine isotope effects. Accordingly we might expect many of the difficulties connected with small anharmonicities, etc., to cancel when we take ratios to determine the VPIE.

Model calculations on the thermodynamic properties of water have been frequent. A voluminous literature on this topic exists, and it is not our purpose to review and comment in any detail on the approaches which are current. Very briefly, however, calculations may be divided into two general categories: "mixture" models and "continuum" models.[20] (Only a few of the more recent references will be cited.) Continuum models[21-24] describe the liquid as an essentially complete hydrogen-bonded network with a distribution of energies and geometries. Most calculations have been made using mixture models.[25-30] These describe liquid water as an equilibrium mixture of molecular species with different numbers of hydrogen bonds. Alternatively one could say that some of liquid molecules are clustered into icelike structures; others remain gaslike. Frank and Wen[31] assumed lifetimes of as short as 10^{-10} sec for these structures and called them "flickering clusters." A good deal of the discussion subsequent to their paper has been couched in terms of the concepts which they introduced. In particular, the nature of the solvent role in electrolyte solutions has often been phrased in terms of the "ordering" or "disordering" influence of the various ions on the structure of the clusters and hence of the water. The ratio of the two types of structure is taken as a function of the temperature. None of the model calculations to date have been successful in predicting the vapor pressure isotope effect quantitatively.

In the brief review above it has not been our intent to enter the controversy that is current between advocates of the mixture and the continuum models.

(19) J. O. Hirschfelder, C. F. Curtiss, and R. B. Bird, "Molecular Theory of Gases and Liquids," John Wiley and Sons, Inc., New York, N. Y., 1954, p 214.

(20) M. Falk and T. A. Ford, *Can. J. Chem.*, **44**, 1699 (1966).

(21) J. A. Lennard-Jones and J. A. Pople, *Proc. Roy. Soc.* (London), **A205**, 155 (1951).

(22) J. A. Pople, *ibid.*, **A205**, 163 (1951).

(23) D. N. Glew, *J. Phys. Chem.*, **66**, 605 (1962).

(24) J. A. Barker, *Ann. Rev. Phys. Chem.*, **14**, 229 (1963).

(25) M. Orentlicher and P. O. Vogelhut, *J. Chem. Phys.*, **45**, 4719 (1966).

(26) G. Nemethy and H. A. Scheraga, *ibid.*, **36**, 3382, 3401 (1962); **41**, 680 (1964).

(27) K. Bujis and G. R. Choppin, *ibid.*, **39**, 2035 (1963).

(28) V. Vand and W. A. Senior, *ibid.*, **43**, 1869, 1873, 1878 (1965).

(29) C. M. Davis and T. A. Litovitz, *ibid.*, **42**, 2563 (1965).

(30) M. S. Jhon, J. Grosh, T. Ree, and H. Eyring, *ibid.*, **44**, 1465 (1966).

(31) H. S. Frank and W. Y. Wen, *Discussions Faraday Soc.*, **24**, 133 (1957).

It is no concern of the present formulation whether the effective frequencies which are employed are better considered as averages over some continuous distribution which itself exhibits some kind of temperature dependency or alternatively whether the averages are over mixtures of two or more states where the relative contributions are weighted as a function of the temperature. In this regard it should be pointed out that the calculation is not sophisticated enough to reproduce some of the fine points of the thermodynamic properties. For example, this model, like any one-state model, does not contain enough parameters to predict the maximum in the density–temperature curve. Also note that it is a cell model so that communal entropy effects are not properly handled. On the other hand, recall that in the calculation of the VPIE, one is essentially interested in a ratio of ratios of partition functions, *i.e.*, $(Q_D^{gas}/Q_H^{gas})/(Q_D^{liq}/Q_H^{liq})$, and a great many complicating factors cancel when the ratios are taken. Furthermore, in spite of the prevalence of two- (or more-) state calculations there is little or no agreement on the coordination of the average water molecule. For example, Falk and Ford[20] cite 23 different estimates of the "percentage of broken hydrogen bonds" in water, most at 0°. These vary from 70% down to 0.1% with 6 between 50 and 70%, 6 between 30 and 50%, 8 between 10 and 30%, and 3 less than 10%, the estimates varying with the particular experimental basis of the approach. Such considerations lead us to the conclusion that at least for VPIE calculations the simpler one-state model is to be preferred, particularly because it keeps the number of parameters smaller.

In the numerical calculations we have employed eq 2 exclusively. Force fields for the gas, liquid, and solid phases were selected which were consistent with spectroscopic data (see below), the frequencies for all 18 isotopic isomers were calculated, and the isotope effects were determined. Proper attention was paid to the coupling between the internal and external modes in the condensed phase.[4b,32]

Under certain conditions it can be shown that eq 2 reduces to the form

$$\ln \frac{P'}{P} = \frac{A}{T^2} - \frac{B}{T} \tag{3}$$

Here the A term is a first-order quantum correction appropriate to the low-lying (usually lattice) modes and B is a difference of differences of zero-point energy terms

$$A = \frac{1}{24}\left(\frac{h}{k}\right)^2 \left\{\sum_{\nu_A} (\nu'_{Ac}{}^2 - \nu_{Ac}{}^2)\right\}; \quad u_A \ll 2\pi \tag{4}$$

$$B = \frac{h}{2k}\left\{\sum_{\nu_B} [(\nu'_{Bg} - \nu'_{Bc}) - (\nu_{Bg} - \nu_{Bc})]\right\}; \quad u_B > 2\pi \tag{5}$$

For the case of the condensed phases of water, approximation 3 is not very useful because a number of the lattice frequencies lie high enough so that they do not fall nicely into either the A or the B set.

Calculations

The force fields which were employed for the final calculations are shown in Table I. That for the gas phase is the harmonic field of Papousek and Pliva.[33] The fields for the other phases have been adjusted from the gas field to fit the frequency shifts observed on the phase change to ice by Bertie and Whalley[34] and to liquid water at 40° by Walrafen.[35] In the adjustment the observed frequency shifts on condensation were directly transferred to the (harmonic) calculation as the single most important spectroscopic criterion governing the adjustment of the force field. This rough and ready approximation was employed because we had no way to assess properly anharmonic corrections in the condensed phases. (While on this topic it is appropriate to point out that just as the frequencies which enter isotope effect calculations of the precision we report here must be calculated in a consistent fashion so must the anharmonic corrections in cases when these are included. Since such corrections cannot be assessed in the condensed phase, it is meaningless to apply the well-known corrections for anharmonicity in the gas phase. This would amount to correcting one side but not the other of the equilibrium. It is interesting to note, even in the gas phase where the corrections are well known, that employing our computational approach in the harmonic approximation leads to better agreement with equilibrium constant

Table I: Force Fields[a]

	Gas	Liquid (40°)	Solid
OH stretch	8.4543	7.7470	6.6435
HOH bend	0.6994	0.7448	0.7520
Stretch–stretch	−0.1002	−0.2705	−0.3577
Stretch–bend	0.2272	0.2371	0.2371
Stretch–libration		−0.0234	−0.0480
Bend–libration		0.0072	0.0086
Translations		0.2789	0.8020
Libration 1		0.0896	0.1625
Libration 2		0.1705	0.4858
Libration 3		0.2575	0.6249

[a] Units are mdyn/Å for stretches and mdyn Å/radian² for bends.

(32) In the *FG* calculations the H_2O basis was employed exclusively for the condensed phase.[4b]

(33) D. Papousek and J. Pliva, *Collect. Czech. Chem. Commun.*, **29**, 1973 (1964).

(34) J. E. Bertie and E. Whalley, *J. Chem. Phys.*, **40**, 1637 (1964).

(35) G. E. Walrafen, *ibid.*, **36**, 1036 (1962).

Table II: Frequencies of Ices[a]

H_2O				D_2O				HDO			
G[c]	S(−100°)[b]	(G − S)obsd	(G − S)calcd	G	S	(G − S)obsd	(G − S)calcd	G	S	(G − S)obsd	(G − S)calcd
					2545						
					2485 ± 10						
3755.8	3380 − 30	375.8	375.9	2788.1	2425 ± 5	363 ± 5	368.3	3707.5	3277 ± 4	430 ± 4	431.6
	3220 ± 5								2445		
									2421 ± 4		
3656.7	3150 − 10	506.7	506.5	2671.5	2395 − 60	277	274.8	2726.7	2395	332	331.0
	2266 ± 20				2332 ± 5						
					2240						
1594.6	1650 ± 30	−55.4	−55.4	1178.3	1210 ± 10	−31.7 ± 10	−43.1	1402.2			
	900						596.8				775.0
	840		843.6		675		557.7				632.9
	770		772.9		640		501.2		515		529.7
	660		666.7								
	555				425						
			275.0				260.6				267.6
	250–300		275.0				260.2				267.0
			275.0				258.4				266.5

[a] Observed frequencies are from Bertie and Whalley[34] for ice except those below 500 cm^{-1} from Ockman;[40] those for gas are from Benedict, *et al.*[39] [b] S = solid (ice). [c] G = gas.

data.[36,37] The reasons for this apparent anomaly have been discussed by Wolfsberg.[38] These observations reinforce our opinion that the standard harmonic approach employed in the present paper is a reasonable one.)

Table II lists the frequencies of ice I for H_2O, D_2O, and HDO reported by Bertie and Whalley[34] together with the observed gas-phase frequencies[39] and the observed and calculated frequency shifts on phase change. The observed frequencies below 500 cm^{-1} are from Ockman,[40] who listed frequencies at 212, 232, 252, 272, and 294 cm^{-1} as components of a rather broad band which we have taken as 275 cm^{-1}. The adjustments of the force constants from the gas to the condensed phase were made by considering only the observed shifts for H_2O. The shifts calculated for the other isomers then serve as test of the force field. The agreement between the calculated and observed shifts appears satisfactory in view of the limited accuracy of both the observations and the calculations. In the fitting process the measured internal and hindered translational shifts were matched. The ratio of librational frequencies one to the other also was fixed from the observations, and finally the librational force constants were adjusted so that the VPIE for D_2O agreed with experiment at 273°K. The fact that this adjustment changed the librational frequencies by only a few wave numbers from the observed ones is worthy of note. In another calculation we employed a force field selected from an alternative assignment to that shown in Table II. This was made by assuming that the 3756-cm^{-1} frequency of gaseous H_2O shifted to 3220 cm^{-1} in ice, *i.e.*, some 536 cm^{-1} instead of the 376 cm^{-1} shown in the table. This latter field was completely unreasonable from the point of view of the VPIE data because it simply did not fit the temperature dependency of the isotope effect nor did it give agreement with the values of any one of the possible sets of observed lattice librational frequencies.

In Table III we show the frequencies reported by Walrafen[35,41,42] for liquid H_2O and D_2O together with the observed gas frequencies[39] and the observed and calculated frequency shifts on phase change. The assignments are due to Walrafen.[35] The agreement is again satisfactory for the internal modes although the calculated phase frequency shift for the 2788-cm^{-1} gaseous frequency of D_2O appears low.

(36) L. Friedman and V. J. Shriner, *J. Chem. Phys.*, **44**, 4639 (1966).

(37) J. W. Pyper, R. S. Newbury, and G. W. Barton, Jr., *ibid.*, **46**, 2253 (1967).

(38) M. Wolfsberg, Abstracts of Papers, 153rd National Meeting of the American Chemical Society, Miami Beach, Fla., 1967, No. 49.

(39) W. S. Benedict, N. Gailar, and E. K. Plyler, *J. Chem. Phys.*, **24**, 1138 (1956).

(40) N. Ockman, *Advan. Phys.*, **7**, 199 (1958).

(41) G. E. Walrafen, *J. Chem. Phys.*, **44**, 1546 (1966).

(42) G. E. Walrafen, *ibid.*, **47**, 114 (1967).

Table III: Frequencies of Waters[a]

H_2O				D_2O			
G[b]	L(40°)[c]	$(G - L)_{obsd}$	$(G - L)_{calcd}$	G	L(40°)	$(G - L)_{obsd}$	$(G - L)_{calcd}$
3755.8	3630	125.8	125.8	2788.1	2662	126.1	92
3656.7	3450	206.7	206.6	2671.5	2515	156.5	150.4
1594.6	1645	−50.4	−50.6	1178.3	1225	−46.7	−38.0
	780		500.0		500		371.7
	450		496.5		350		358.0
			495.4				353.6
			162.2				153.7
	150–175		162.2		150–175		153.5
			162.2				153.0

[a] Observed frequencies are from Walrafen[35,42] for liquid and from Benedict, Gailar, and Plyler[39] for gas. [b] G = gas. [c] L = liquid.

Walrafen[35,42] has been quite careful to point out the importance of the 780-cm^{-1} band which he assigns to a fundamental libration together with another band around 450 cm^{-1}. The third (unobserved) libration then must lie at a much lower frequency because otherwise the net librational contribution to the partition functions would be too high to permit agreement with the VPIE. In our calculations we have preferred to use three approximately degenerate librations around 500 cm^{-1} rather than to select one very low librational frequency. The librational frequencies were adjusted, as in the ice case, to reproduce the VPIE for DOD at the temperature of the fit (40°). The assignment of the three librations at ~500, 500, 500 cm^{-1} instead of 780, 450, ? cm^{-1} is really immaterial from the point of view of the calculated isotope effects which after all are our point of focus. This is because the isotopic ratios of the three moments of inertia, $I_i(H_2O)/I_i(ABO)$ ($i = x$, y, or z; A and B = H, D, or T), are all equal within about 10%. Therefore within the accuracy of the calculation it does not make any difference to the VPIE as to how the librations are assigned with respect to the motions about the various axes or as to how the librational frequencies are distributed in the total rotational contribution. This is because the isotope effect due that contribution is effectively insensitive to the assignment or to the distribution. What does make a difference is the size of the total rotational contribution which is fixed from the internal and (small) hindered translational contribution and the fit to the DOD effect at 40°. It is interesting to note that our selection of three degenerate librations around 500 cm^{-1} is in reasonable agreement with the 480-cm^{-1} libration reported from neutron scattering by Larsson, Holmryd, and Otnes[43] although it is somewhat lower than the 667 cm^{-1} employed by Swain and Bader[44] in their calculations. A similar argument has been given by Blue.[45]

We conclude that the agreement between the observed frequencies and those calculated from the force fields of Table I is quite satisfactory for both the condensed liquid and solid phases; that is, it is well within the limitations of the model and the experimental precision.

One of the most interesting features of the condensed-phase force fields shown in Table I is that they contain terms which couple the internal motions with the external librations. (These coupling terms are in addition to the ones in the G matrix which couple internal and external motions for certain selected isotopic isomers.[4b]) That these terms are necessary can be seen as follows. First consider the data in Table IV. It shows the ratio of the changes which appear in the calculated HOD and TOT isotope effects for unit change in the DOD effect. The force constants are grouped into those which describe internal modes, external modes, and the coupling constants. Now consider in addition the important experimental fact that the law of the geometric mean is very nearly obeyed by the H_2O–HOD–D_2O data. Also any simple force field (without external internal coupling) predicts DOD/

Table IV: The Effect of Varying Force Constants on Ratios of Vapor Pressure Isotope Effects

F	$[d(VPIE)_x/dF]/[d(VPIE)_y/dF]$ x = HOD, y = DOD	x = TOT, y = DOD
OH stretch	0.5	1.4
HOH bend	0.5	1.4
Stretch–stretch[a]	...	...
Stretch–bend	0.6	1.3
Translations	0.5	1.5
Rotation 1	0.5	1.4
Rotation 2	0.5	1.4
Rotation 3	0.5	1.4
Stretch–rotations	1.0	1.5
Bend–rotations	14.0	1.5

[a] $d(VPIE)/dF$ for this mode is 0.

(43) K. E. Larsson, S. Holmryd, and K. Otnes, *Inelastic Scattering Neutrons Solids Liquids, Proc. Symp., 2nd, Chalk River, Ontario, Canada, 1962*, 1, 329 (1963).

(44) C. G. Swain and R. F. W. Bader, *Tetrahedron*, 10, 182 (1960).

(45) R. W. Blue, *J. Chem. Phys.*, 22, 280 (1954).

HOD < 2 as a natural consequence of the contribution of the external modes. (For example, the liquid field of Table I gives 1.9; the solid field gives 1.8.) It is easy to show that for any force field one can by varying the relative internal and external contributions fit both the D_2O and T_2O effects at any temperature, but then in the absence of cross terms between externals and internals HDO (and HTO) are calculated too high. It is clear from Table IV that no adjustment of the force constants can be made to preserve the D_2O and T_2O fits and at the same time lower the HDO because the TOT effect is a simple multiplicative factor of the HOD effect which is identical for all force constants. This is no longer the case if coupling constants are introduced. One sees in the last line of the table that there is an important term which couples the internal bending mode with the external rotations, shifting the frequency of both appreciably for the unsymmetrical but not for the symmetrical isomers. The final step in the determination of the fields of Table I then consisted of the introduction of the bend–libration constant. (A small stretch–libration constant was also introduced as a convenience in order to hold the frequencies of the unsubstituted compounds constant. Its use was not unequivocally dictated by the data.)

We note that the presence of force constants which couple the internal bend and the external rotations has been suspected on spectroscopic evidence.[34] The force fields then have been selected by a number of criteria. First, reasonable agreement between the observed and calculated frequency shifts on phase change has been demanded. With this established, the value of the DOD VPIE at one temperature has been employed to fix the precise value of the rotational contribution and finally the value of the HOD/HOH effect at that temperature was used to determine the force constant coupling the internal bend with the external librations. The data on the remaining isotopic isomers and at other temperatures should serve as a test of the approach.

Results, Temperature Dependency of the Liquid Field

Let us first consider the calculations for the solid field shown in Table I. Frequencies for all 18 of the isotopic isomers of water were calculated with this field employing nine-dimensional G matrices with proper account of external–internal coupling. The isotope effects were then calculated using eq 2 at 12 temperatures between 230 and 275°K. These results were then empirically fit by the method of least squares to equations of the type

$$\ln \frac{P'}{P} = \frac{A}{T^2} + \frac{B}{T} + C \qquad (6)$$

Generally speaking, the experiments are good to ±0.001, or so, in ln (P'/P). The calculations were carried out to ±0.00001, and the least-square fits always agreed with them to better than ±0.00002 in ln (P'/P). For purposes of comparison with experiment then, the least-square lines are exact representations of the calculations. They are given for all 18 isomers in Table V.

Table V: Calculated Vapor Pressure Isotope Effects for Isotopic Ices in the Temperature Range 0 to −40°. Values of A, B, C Given for the Fit to

$$\ln \frac{P_{H_2O}}{P_x} = \frac{A}{T^2} + \frac{B}{T} + C$$

x	A	B	C
D_2O^{16}	21,577.6	69.3358	−0.305394
T_2O^{16}	33,453.7	62.4058	−0.395542
HDO^{16}	11,484.5	35.3315	−0.159290
HTO^{16}	18,464.5	31.0436	−0.207520
DTO^{16}	27,722.4	66.5930	−0.351698
H_2O^{17}	933.651	1.0953	−0.002805
H_2O^{18}	1,740.59	2.2965	−0.005793
D_2O^{17}	22,420.6	70.3787	−0.308791
T_2O^{17}	34,316.8	62.7057	−0.397903
HDO^{17}	12,362.4	36.5554	−0.162766
HTO^{17}	19,352.5	31.9501	−0.210616
DTO^{17}	28,574.4	67.2863	−0.354632
D_2O^{18}	23,206.1	71.0812	−0.311421
T_2O^{18}	35,062.5	63.1985	−0.400488
HDO^{18}	13,218.3	37.0780	−0.164751
HTO^{18}	20,154.1	32.7122	−0.213328
DTO^{18}	29,345.9	67.8547	−0.357205

The calculated results are plotted for seven of the isomers in Figure 1 as the solid lines. The agreement is quite good. In particular the very precise data for HOD of Merlivat and Nief[8] are fitted quantitatively. The less precise experimental temperature dependency of the DOD data is also nicely fitted. (Remember the field is specified by appealing to the data at one temperature only. For the ices this was at 273°K.) Finally the line calculated for the T_2O VPIE appears a little below the best line through the first three experimental points. (See below.) The data here are not as precise as those for the other isomers because of considerable experimental difficulty in making the measurements.[5] It would appear that the two lowest temperature experimental points for TOT are in error.

We turn now to the liquid-phase calculations. Proceeding as in the case of the solid, one finds excellent agreement at 40°, the temperature where the field has been evaluated, but as the temperature is raised or lowered, the experimental and calculated effects part. For example, at 0° the calculated effect (units of ln (P_H/P_D)) for D_2O is 0.179 and the observed is 0.199, while at 100° the calculated is 0.054 and the observed is 0.051. The agreement for the other isotopic isomers is proportionate. The differences are reasonably small

Table VI: Calculated Vapor Pressure Isotope Effects for Isotopic Waters in the Temperature Range 0-130°. Values of A, B, C Given for the Fit to

$$\ln \frac{P_{H_2O}}{P_x} = \frac{A}{T^2} + \frac{B}{T} + C$$

	A		B		C	
x	I[a]	II[b]	I	II	I	II
D_2O^{16}	49,314.9	36,713.5	−164.266	−85.5889	0.140049	0.017703
T_2O^{16}	68,702.3	50,838.3	−244.687	−126.772	0.224388	0.030516
HDO^{16}	26,398.8	19,645.4	−89.6065	−48.5026	0.075802	0.013615
HTO^{16}	37,813.2	27,965.1	−136.751	−74.0753	0.124096	0.024637
DTO^{16}	59,313.4	44,016.2	−204.941	−106.377	0.182686	0.024378
H_2O^{17}	1,057.8	745.9	−2.2400	−1.2853	0.000668	0.000806
H_2O^{18}	1,991.1	1,422.3	−4.1887	−2.5028	0.001197	0.001624
D_2O^{17}	50,338.2	37,434.2	−166.780	−86.9715	0.141349	0.018480
T_2O^{17}	69,673.3	51,549.7	−247.236	−128.291	0.225912	0.031398
HDO^{17}	27,458.3	20,385.5	−92.0736	−49.8658	0.076889	0.014442
HTO^{17}	38,848.4	28,712.9	−139.232	−75.5551	0.125273	0.025554
DTO^{17}	60,314.1	44,731.8	−207.488	−107.823	0.184111	0.025199
D_2O^{18}	51,251.8	38,080.8	−169.027	−88.2302	0.142509	0.019214
T_2O^{18}	70,552.4	52,175.5	−249.589	−129.595	0.227388	0.032110
HDO^{18}	28,384.7	21,051.5	−94.1726	−51.1089	0.077717	0.015198
HTO^{18}	39,792.0	29,385.3	−141.572	−76.9185	0.126515	0.026446
DTO^{18}	61,222.2	45,378.7	−209.853	−109.156	0.185518	0.025978

[a] Calculation I, see text. [b] Calculation II, see text.

and the behavior is not unexpected. It is well known that water frequencies shift with temperature[20] (or alternatively that the weighted average of temperature-independent components of absorption bands shifts with temperature as the intensity of the components varies[42]). In either case it is clear that our effective force constants must be temperature dependent and we have accounted for this temperature dependency by introducing Falk and Ford's[20] observed spectral frequency shifts as (calculation I)

$$\frac{df_{st}}{dT} = 2.8 \times 10^{-3} \frac{\text{mdyn}}{\text{Å deg}} \text{ or } \frac{d\nu_{OH}}{dT} = 0.696 \frac{\text{cm}^{-1}}{\text{deg}}$$

$$\frac{df_{bend}}{dT} = -0.052 \times 10^{-3} \frac{\text{mdyn Å}}{\text{radian}^2 \text{ deg}} \text{ or}$$

$$\frac{d\nu_{HOH}}{dT} = -0.061 \frac{\text{cm}^{-1}}{\text{deg}}$$

Changes must also be made in the external force constants in order to reproduce the temperature dependency of the DOD data. We have elected to make the best one-parameter fit and have taken the change in external constants as

$$y = -0.0041T + 1.2839$$

where y is the fractional change in the external force constants. These temperature shifts are of reasonable magnitude. In another calculation (II) we arbitrarily placed all of the temperature dependency in the external frequencies according to

$$y = (10.29/T) - 0.03287$$

This latter calculation was made in analogy to the method employed in calculations on liquid hydrocarbon VPIE's.[4] It is to be recognized in either procedure I or II that the correction which is being made to the temperature-independent calculation is only a small fraction of the total effect.

The isotope effects were calculated for all 17 ratios at eight temperatures between 273 and 400°K for both calculations I and II. The results could be distinguished only with great difficulty on the scale of Figure 1 (calculation I is plotted). They were fitted to equations of type (6) by least-squares. The derived parameters are given in Table VI. (It is felt that calculation I is to be preferred because it includes the experimentally observed temperature dependence of the internal modes.)

Discussion

The results presented above are in remarkably good agreement with available data although, as we shall see, a closer look reveals some minor discrepancies.

Let us first look at the liquid data. The agreement of the calculations with the observed TOT, DOD, HOT, and HOD ratios is all very good. In particular, consistency between all four ratios is preserved over the whole temperature range of the available data. This holds true all the way down to the freezing point and in the case of HOD, the only one where data are available, into the supercooled liquid at −10°. We note that for DOD the older data quoted by Whalley[15] are appreciably lower over a considerable portion of the temperature than the more recent results.[5,10] In view

Table VII: Calculated and Observed[17] Oxygen Separation Factors

Temp, °C	Ln ($P_{H_2O^{16}}/P_{H_2O^{17}}$)		Ln ($P_{H_2O^{16}}/P_{H_2O^{18}}$)		Ln ($P_{D_2O^{16}}/P_{D_2O^{18}}$)	
	Calcd	Obsd	Calcd	Obsd	Calcd	Obsd
20	0.0053	...	0.0101	0.0094	0.0088	0.0078
40	0.0043	0.0046	0.0081	0.0081	0.0070	0.0067
90	0.0025	0.0030	0.0048	0.0054	0.0040	0.0045

of the consistency of this recent data with other modern results on other isotopes it is felt that it is to be preferred in this temperature range (20–90°).

The comparison with the data for the O^{18} and O^{17} ratios cannot profitably be made on the scale of Figure 1. Therefore, in Table VII the present calculations are compared with the data of Szapiro and Steckel[17] at three temperatures. The agreement is remarkably good in view of the fact that the hindered translational frequencies (these are the ones which determine the major part of the O^{17} and O^{18} effects) were assigned from spectroscopic considerations alone. In particular both experiment and theory agree that the law of the mean is not obeyed in this system of isotopes: $([\alpha(H_2O^{17}) - 1]/[\alpha(H_2O^{18}) - 1])_{obsd} = 0.564 \pm 0.014$; $([\alpha(H_2O^{17}) - 1]/[\alpha(H_2O^{18}) - 1])_{calcd} = 0.53$; neither ratio is a function of temperature. There is also agreement that the O^{16}–O^{18} fractionation factor is significantly lowered upon deuteration: $([\alpha(D_2O^{18}) - 1]/[\alpha(H_2O^{18}) - 1])_{obsd} = 0.825 \pm 0.022$; $([\alpha(D_2O^{18}) - 1]/[\alpha(H_2O^{18}) - 1])_{calcd} = 0.86$.

It is reasonable to conclude that the excellent consistency which has been demonstrated between the calculated and the available data on seven of the isotopic isomers of liquid water between 273 and 400°K indicates that the calculated VPIE's for the ten other isotopic isomers which have not yet been measured are also substantially correct over this temperature range.

We turn now to the data on the ices. The excellent agreement with the data for HOD and DOD ices has already been pointed out. The TOT calculation is low although this is not unequivocal on the basis of the vapor pressure data alone. However, the consistency of the ice calculation with the liquid calculation can be tested quite nicely by comparing calculated and observed triple points. The calculated triple points can easily be found by combining analytical fits of water vapor pressure data with the equations of Table VI and of ice vapor pressure data with Table V and then solving the resulting equations simultaneously to obtain the triple points. This is a very sensitive test of the calculations because dP/dT is almost equal for both phases around the triple point (for H_2O, $dP/dT = 0.330$ mm/deg; for ice, 0.375).[46] It is the isotope effect on this difference, $\Delta(dP/dT) = 0.045$ mm/deg, that is directly related to the isotope effects on the triple point. Therefore, we see that a small error in the calculation of the isotopic vapor pressures between phases is reflected in a much larger error in the calculation of the triple point.

The results of the calculation of the triple points were: TOT, 3.15°; DOT, 3.63°; DOD, 3.85°; HOT, 2.38°; HOD, 2.32°; H_2O^{18}, 1.41°; H_2O^{17}, 0.75°. The agreement with the measured triple point for D_2O, 3.82°,[15] is excellent, but there is a large difference between the calculated triple point and that observed for T_2O (4.49 ± 0.02°)[47] and estimated for H_2O^{18} (0.05 ± 0.01°)[48] from fractionation data. These are the only isomers for which data are available. The low result for T_2O led us to examine another force field for ice. In the new calculation we determined the amount by which the OH stretching force constant must be raised (while compensating for this elevation by lowering the external force constants so as to keep the triple point of DOD approximately constant) to give agreement with the TOT triple point. (The force constants for this field were in the order of Table I: 7.301, 0.749, −0.300, 0.237, −0.023, 0.007, 0.490, 0.131, 0.300, 0.414.) The VPIE's predicted by the field are shown as the dotted lines in Figure 1. The calculated triple points were: TOT, 4.46°; DOT, 4.19°; DOD, 3.86°; HOT, 2.67°; HOD, 2.15°; H_2O^{17}, 0.29°; H_2O^{18}, 0.54°. It seems clear, however, that, in spite of the improved triple-point agreement, this field is a very poor one. For example, the predicted phase-frequency shifts are 226, 323, and −53 cm^{-1} for H_2O while the observed ones are (Table II) 376, 507, and −55 cm^{-1}. Therefore the field is in grave error from spectroscopic standards. In fact, it most nearly resembles the water field in Table I. Also the predicted slopes for the VPIE for DOD and HOD are no longer in agreement with experiment, another severe criticism of the field. The calculation is a valuable one, however, because it informs us that the calculated triple points are not particularly sensitive to the choice of the force field within the framework of the model which we are employing. It therefore appears that the model and force field which are employed here and which give reasonable agreement with the VPIE and with the spectroscopic data

(46) "Handbook of Chemistry and Physics," 35th ed, Chemical Rubber Publishing Co., Cleveland, Ohio, 1953, p 4201.

(47) W. M. Jones, *J. Am. Chem. Soc.*, **74**, 6065 (1952).

(48) W. Kuhn and M. Thürkauf, *Helv. Chim. Acta*, **41**, 938 (1958).

are not able to reproduce the observed triple points for all isomers. One rather obvious shortcoming in the model calculations which might help to account for this discrepancy is the failure to make corrections for anharmonicity.[49]

With regard to the ice calculations, we conclude the DOD and HOD effects are in good agreement with experiment, but the effects calculated for the tritium-containing species are a little low. In spite of the difficulty with the T_2O triple point, we feel that the good agreement between calculation and experiment for the deuterium-containing species implies that the calculated triple point for HOD is reasonable. (It is interesting in both sets of calculated triple points to note that the law of the mean is not obeyed.) Finally the VPIE's calculated for the heavy-oxygen ices appear to be high. This is a direct consequence of the large shift in the hindered translational lattice frequency ($162 \rightarrow 275$ cm^{-1}) which was assigned to this phase change on spectroscopic grounds. In summation, it thus appears that the VPIE's calculated for the ices do not form as self-consistent a set as did the calculations for liquid water. This is in spite of the fact that the only precise data on the VPIE which are available (DOD and HOD) are apparently fitted quantitatively by the calculation. Reasons for the discrepancy with the other isotopic isomers could lie in anharmonic corrections.

Ideality of H_2O–HDO–D_2O Solutions[50]

It is interesting to compare the calculated freezing points of H_2O–D_2O solutions with the precise measurements of LaMer and Baker.[51] With accurate values for the vapor pressures of the three components in both phases available (Tables V and VI, ref 46), the freezing points can be calculated as the temperature at which

$$\gamma^l_{H_2O}X^l_{H_2O}P^{ol}_{H_2O} + \gamma^l_{HDO}X^l_{HDO}P^{ol}_{HDO} + \gamma^l_{D_2O}X^l_{D_2O}P^{ol}_{D_2O} = \gamma^s_{H_2O}X^s_{H_2O}P^{os}_{H_2O} + \gamma^s_{HDO}X^s_{HDO}P^{os}_{HDO} + \gamma^s_{D_2O}X^s_{D_2O}P^{os}_{D_2O} \quad (7)$$

where the γ's are activity coefficients and the X's mole fractions. We have made the assumption of ideality in both phases, *i.e.*, all γ^j_i's = 1, and have calculated the freezing temperatures as a function of deuterium analysis. The mole fractions were calculated from the now well-known equilibrium constant[36] corrected for condensation to the liquid or solid, respectively. Equilibrium fractionation was assumed on freezing. It was also assumed that only an infinitesimal quantity of ice formed so that the liquid analysis did not change (note that the data[51] were also thus corrected). The P's were found by combining the data in Tables V and VI with fits to water and ice (extrapolated) vapor pressures over the temperature range of interest (0–3.8°). The calculations were normalized to give $t_f(H_2O) = 0.000°$ and $t_f(D_2O) = 3.802°$ which was the extrapolated value reported by LaMer and Baker.[51] In this fashion a smooth curve was derived which could be compared with the experimental one;[51] $(\Delta t)_{exptl} = 4.213N_D - 0.411N_D^2$. ($N_D$ is the atom fraction of H + D which is D.) The maximum deviation from this best-fit experimental relation was −0.012° found at the intermediate concentrations (0.5915 and 0.4158 atom fraction D). This is to be compared with a standard deviation of the eight experimental points from the smoothed line of ±0.004°. It is therefore clear that the deviation of the experimental curve from that predicted assuming ideal solid and liquid solutions is quite small. Thus, if we fix $\gamma^s_i = 1$ and $\gamma^l_{H_2O} = 1$ and $\ln \gamma^l_{HDO} = {}^1/_2 \ln \gamma^l_{D_2O}$, we find at 59 atom % D that setting $\gamma^l_{D_2O} = 0.99974$ brings the calculated and the smoothed experimental curves into agreement. The implication is that the difference in nonideality of the solid and liquid solutions of H_2O, HDO, and D_2O is almost insignificantly small. (We repeated the calculation choosing $K_{eq} = 3.80$ instead of the best value, $K_{eq} = 3.75$, in order to ensure that there was not a hypersensitive dependence on K_{eq}. No significant difference was found.) It is unfortunate that the experiment really only measures the difference in nonideality between liquid and solid solution. It would of course be possible to have values of γ^l and γ^s different from 1 such that an exact cancellation still occurred in eq 7. This is probably unlikely and the results above therefore imply that isotopic solutions of the deuterated waters are very nearly ideal. A number of authors[6,11] have measured the vapor pressure of isotopic solutions of H_2O, D_2O, and HOD but the data which are available are simply not precise enough to determine deviations from ideality. In fact, these measurements have even been interpreted as substantiating the law of the mean for H_2O–HDO–D_2O. The recent French data[8,14] as well as the present calculations clearly indicate that this is only an approximate relation.

Conclusions, Summary

In the present paper it has been demonstrated that the vapor pressure isotope effects of the substituted waters and ices can be understood quantitatively within the framework of the theory of isotope effects in condensed systems. A force field has been developed which correlates quantitatively the VPIE's for the 18 different isomers in both phases over a temperature

(49) Another possibility which was considered was that dimer, trimer, or tetramer units needed to be considered in the calculation. Some preliminary calculations on dimers and trimers were made but abandoned because the many more adjustable parameters could simply not be specified in any satisfactory fashion. Properly speaking, the unit cell should be the basis of the calculation, but for ice this is simply too complicated.

(50) The calculations in this section were performed in collaboration with Mary L. Foster, NSF Undergraduate Summer Research Participant, University of Tennessee, 1967.

(51) V. K. LaMer and W. N. Baker, *J. Am. Chem. Soc.*, **56**, 2641 (1934).

range extending from 230 to 400°K. The calculated results offer the best available set of correlated effects in this system. Some limitations on the calculation were pointed out, particularly for the predicted triple points, and directions for improvement of the calculation are indicated. Finally nonideality in the HOH–HOD–DOD system was discussed.

Acknowledgment. Appreciation is expressed to the donors of The Petroleum Research Fund administered by the American Chemical Society for support of this research. Thanks are also due J. H. Schachtschneider and M. Wolfsberg for the use of their computer programs and the University of Tennessee Computing Center for the use of its facilities.

An Electron Paramagnetic Resonance Study of the Bonding in Copper Complexes

by Virginia Chapin Swett and Emily Pitcher Dudek

Chemistry Department, Wellesley College, Wellesley, Massachusetts 02181 *(Received September 18, 1967)*

The epr spectra of 20% toluene–80% chloroform solutions of some Cu(II) complexes of β-keto enolates and Schiff bases were recorded at 300 and 77°K. The in-plane bonding parameters calculated from the spectral data denoted covalency in both the σ and π bonding. The $g_{\|}$ values indicated that the covalency increases in the order: β-keto amides < β-keto enolates < *trans*-bidentate Schiff bases < *cis*-tetradentate Schiff bases.

Electron paramagnetic resonance (epr) has proven to be an effective probe for assessing the covalency of the coordinate bonding in copper(II) complexes. Compared with studies for single crystals,[1-5] epr investigations of polycrystalline samples or "glasses" are almost as informative.[6-11] A theoretical treatment for the paramagnetic resonance absorption of copper(II) compounds in glasses has been presented by Kivelson and Nieman.[6] Following their approach as modified by Gersmann and Swalen,[8] we have obtained the metal–ligand bonding parameters, α and β_1, for 21 copper complexes. The complexes under investigation are of β-keto enolates and Schiff bases, two types of copper compounds of considerable interest to chemists.[12,13] From measurements of the covalency of the σ bonding, gauged by α, and the in-plane π bonding, estimated by β_1, we have endeavored to establish general differences in the coordinate bonding of these copper(II) complexes. The current controversies over the correct orientation and symmetry and the assignment of the electronic absorption spectra[14] of β-keto enolate complexes plus the difficulties in analyzing the epr spectra for $g_{\perp}$ and $a_{\perp}$ values due to "extra absorptions"[8] have deterred us from examining the nature of the out-of-plane bonding.

Experimental Section

Compounds. All of the copper(II) complexes, except the three described below, were prepared according to published procedures.[15-18] The compounds were recrystallized at least twice and the purity was checked by

(1) H. S. Jarrett, *J. Chem. Phys.*, **28**, 1260 (1957).

(2) A. H. Maki and B. R. McGarvey, *ibid.*, **29**, 31, 35 (1958).

(3) J. F. Gibson, D. J. E. Ingram, and D. Schonland, *Discussions Faraday Soc.*, **26**, 72 (1958).

(4) H. P. Fritz, B. Golla, and H. J. Keller, *Z. Naturforsch.*, **21b**, 97 (1966).

(5) F. A. Cotton and J. J. Wise, *Inorg. Chem.*, **6**, 915 (1967).

(6) D. Kivelson and R. Neiman, *J. Chem. Phys.*, **35**, 149 (1961).

(7) R. Nieman and D. Kivelson, *ibid.*, **35**, 156 (1961).

(8) H. R. Gersmann and J. D. Swalen, *ibid.*, **36**, 3221 (1962).

(9) A. K. Wiersema and J. J. Windle, *J. Phys. Chem.*, **68**, 2316 (1964).

(10) R. Wilson and D. Kivelson, *J. Chem. Phys.*, **44**, 4445 (1966).

(11) H. A. Kuska, M. T. Rogers, and R. E. Drullinger, *J. Phys. Chem.*, **71**, 109 (1967).

(12) J. P. Fackler, Jr., *Progr. Inorg. Chem.*, **7**, 361 (1966).

(13) R. H. Holm, G. W. Everett, Jr., and A. Chakravorty, *ibid.*, **7**, 83 (1966).

(14) F. A. Cotton and J. J. Wise, *Inorg. Chem.*, **6**, 917 (1967), and references cited therein.

(15) P. Pfieffer and H. Glaser, *J. Prakt. Chem.*, **153**, 265 (1939); P. Pfieffer and H. Krebs, *ibid.*, **155**, 77 (1940).

(16) H. Smith, *J. Chem. Soc.*, 803 (1953).

(17) H. F. Holtzclaw, Jr , J. P. Collman, and R. M. Alire, *J. Am. Chem. Soc.*, **80**, 1100 (1958).

(18) R. L. Belford and W. A. Yeranos, *Mol. Phys.*, **6**, 121 (1963), and references cited therein.

melting point measurements. The mass spectrum of each complex gave the correct molecular ion.

Bis(2-acetiminodimedonato)copper(II). The complex was prepared according to the general procedure established by Holm and Everett for synthesizing metal complexes of Schiff bases.[19] Bis(tetraethylammonium) tetrabromocuprate(II) (2.75 mmol) and potassium *t*-butoxide (5.5 mmol) were dissolved in *t*-butyl alcohol which had been distilled previously from calcium hydride. 2-Acetiminodimedone (dimedone = 5,5-dimethylcyclohexane-1,3-dione) (5.5 mmol) was added to the solution, and the mixture was stirred at room temperature until a distinct color change was observed. The alcohol was then removed by rotary evaporation. The remaining solid was dissolved in benzene, and the solution was filtered in order to remove inorganic impurities. On addition of *n*-heptane, a purple solid precipitated. The material was recrystallized from benzene, mp 202–203°, yield 75%. *Anal.* Calcd for $(C_{10}H_{14}O_2N)_2Cu$: C, 56.65; H, 6.65; N, 6.61. Found: C, 56.81; H, 6.85; N, 6.74.

Bis(N-phenyl-2-acetiminodimedonato)copper(II). The procedure used to prepare the 2-acetiminodimedone complex of copper was followed. A brown-green, crystalline product was isolated, mp 226°, yield 75%. *Anal.* Calcd for $(C_{16}H_{18}O_2N)_2Cu$: C, 66.70; H, 6.30; N, 4.86. Found: C, 67.07; H, 6.30; N, 5.12.

Bis(2-acetyldimedone)ethylenediiminocopper(II). Bis-(2-acetyldimedone)ethylenediamine (5 mmol) and sodium methoxide (10 mmol) were dissolved in methanol. Copper(II) acetate (7 mmol) was added, and the mixture was stirred for 1 hr at 50°. The solvent was removed by rotary evaporation. The remaining solid was washed with water, dried *in vacuo* over phosphorus pentoxide, and recrystallized from benzene–hexane to produce purple fibers, mp 257–259°, yield 80%. *Anal.* Calcd for $C_{22}H_{30}O_4N_2Cu$: C, 58.71; H, 6.72; N, 6.23. Found: C, 59.31; H, 7.12; N, 6.27.

Electron Paramagnetic Resonance Spectra. Spectra were recorded with a Varian V-4502 epr spectrometer employing 100-kHz modulation and detection and operating at about 9.5 GHz. The klystron frequency was measured with a transfer oscillator and frequency counter. The magnetic field was measured by a proton gauss meter monitored by the same frequency counter. Dilute solutions of dried chloroform–toluene (80:20 by volume) were used since the solvent mixture yielded a good glass[8] and satisfied solubility requirements. Dried chloroform did not produce a good glass. Reagent grade chloroform with about 0.75% ethanol provided a satisfactory glass but this solvent mixture was not used owing to the uncertainty in the per cent alcohol and to the added complication of coordination of the alcohol to the copper. The solutions were studied at 300 and 77°K. All spectra were run in triplicate and the measurements were averaged. The precision of the data is ±3% and the values of the bonding parameters are accurate to 5%.

Visible and Near-Ultraviolet Spectra. A Beckman DB spectrometer was used to record the spectra. The solutions studied were chloroform–toluene (80:20 by volume). All data were obtained at room temperature.

Spectral Analysis. Assuming D_{2h} symmetry for the *trans*-bidentate planar copper(II) complexes, the expressions for the in-plane antibonding wave functions are[8]

$$\psi_{B_{1g}} = \alpha d_{xy} - {}^1/_2\alpha'[-\sigma^{(1)}{}_{xy} + \sigma^{(2)}{}_{xy} + \sigma^{(3)}{}_{xy} - \sigma^{(4)}{}_{xy}]$$

$$\psi_{A_g} = \beta_1 d_{x^2-y^2} - {}^1/_2(1 - \beta_1{}^2)^{1/2} \times [-p^{(1)}{}_{xy} - p^{(2)}{}_{xy} + p^{(3)}{}_{xy} + p^{(4)}{}_{xy}]$$

For the tetradentate Schiff base chelates of C_{2v} symmetry, the comparable functions are

$$\psi_{B_2} = \alpha d_{xy} - {}^1/_2\alpha'[-\sigma^{(1)}{}_{xy} + \sigma^{(2)}{}_{xy} + \sigma^{(3)}{}_{xy} - \sigma^{(4)}{}_{xy}]$$

$$\psi_{A_1} = \beta_1 d_{x^2-y^2} - {}^1/_2(1 - \beta_1{}^2)^{1/2} \times [-p^{(1)}{}_{xy} - p^{(2)}{}_{xy} + p^{(3)}{}_{xy} + p^{(4)}{}_{xy}]$$

The ligand orbitals involved in the in-plane σ bonding are viewed as sp^2-hybrid orbitals.[2] Overlap is included for the function describing the in-plane σ bonding, $\alpha^2 + \alpha'^2 - 2\alpha\alpha'S = 1$, where S, the overlap integral, has been given the values 0.076 for the β-keto enolate complexes and 0.084 for the Schiff base chelates.[6]

Values of g_0 and $g_{||}$ were obtained from the spectra recorded at 300 and 77°K, respectively. The $g_\perp$ values were then calculated from the equation[9,11] $g_0 = {}^2/_3g_\perp + {}^1/_3g_{||}$. Errors in the $g_\perp$ values introduced by this approximation will not affect, within the estimated experimental error of 5%, the accuracy of the in-plane bonding parameter. From the measured value of $a_{||}$ and using the approximate formula established by Kivelson and Neiman,[6] $\alpha^2 = -(A_{||}/P) + (g_{||} - 2) + {}^3/_7(g_\perp - 2) + 0.04$, with $P \approx 0.036$ cm^{-1}, the α values were calculated. The values of β_1 were calculated from the equation[6,8] $g_{||} - 2.0023 = -8\rho[\alpha\beta_1 - \alpha'\beta_1 S - (\alpha'(1 - \beta^2)^{1/2}T(n)/2)]$ where $\rho = \lambda_0\alpha\beta_1/(E_{x^2-y^2} - E_{xy})$ and where $T(n)$ was set equal to 0.220 for the β-keto enolate chelates and 0.276 for the Schiff base complexes. The spin–orbit coupling constant for the free Cu(II) ion, λ_0, had the value -828 cm^{-1}.

Values of α'^2 were also calculated from the nitrogen hyperfine splitting exhibited by three complexes. The α'^2 parameter is related to the interaction energy, W_L, by the equation

$$W_L = (4\pi/9)\gamma_L\beta_0\beta_N\alpha'^2|\rho_N(0)|^2S_ZI_{ZL}$$

where γ_L is the magnetic moment of the ligand atom L, β_0 is the Bohr magneton, β_N is the nuclear magneton,

(19) G. W. Everett, Jr., and R. H. Holm, *J. Am. Chem. Soc.*, **87**, 2117 (1965).

Table I: Magnetic Parameters

No.	Compound	g_0	$g_\parallel$	$-A_\parallel \times 10^4$, cm^{-1}	$E_{xy} \rightarrow E_{x^2-y^2}$ transitions, cm^{-1}	α	α^2	β_1	β_1^2
			β-Keto Enolates						
I	Bis(acetylacetonato)copper(II)	2.123	2.253	194	15,800	0.92	0.85	0.85	0.72
II	Bis(2-acetylcyclohexanonato)copper(II)	2.115	2.246	193	15,900	0.91	0.83	0.85	0.72
III	Bis(2-acetyldimedonato)copper(II)	2.122	2.289	174	16,100	0.91	0.83	0.94	0.88
IV	Bis(salicylaldehydato)copper(II)	2.127	2.256	178	15,400	0.90	0.81	0.88	0.77
V	Bis(*o*-hydroxyacetophenonato)copper(II)	2.104	2.255	178	15,700	0.90	0.81	0.88	0.77
VI	Bis(2-hydroxy-1-naphthaldehydato)-copper(II)	2.122	2.250	189	15,800	0.91	0.83	0.86	0.74
VII	Bis(2-acetyl-1-naphtholato)copper(II)	2.125	2.250	189	15,600	0.91	0.83	0.85	0.72
			β-Keto Amides						
VIII	Bis(acetoacetanilidato)copper(II)	2.142	2.262	190	16,000	0.94	0.88	0.88	0.77
IX	Bis(N-phenyl-2-carbamoyldimedonato)-copper(II)	2.143	2.304	197	16,700	0.95	0.90	0.93	0.86
			Bidentate Schiff Bases						
X	Bis(4-amino-3-penten-2-ono)copper(II)	2.105	2.200	174	17,900	0.86	0.74	0.87	0.76
XI	Bis(2-acetiminodimedonato)copper(II)	2.112	2.199	175	18,500	0.86	0.74	0.88	0.77
XII	Bis(N-methylsalicylaldiminato)copper(II)	2.111	2.222	182	16,700	0.89	0.79	0.86	0.74
XIII	Bis(N-methyl-2-acetimino-1-naphtholato)-copper(II)	2.119	2.221	183	15,600	0.89	0.79	0.82	0.67
XIV	Bis(4-anilino-3-penten-2-ono)copper(II)	2.110	2.234	165	16,700	0.85	0.72	0.92	0.85
XV	Bis(N-phenyl-2-acetiminodimedonato)-copper(II)	2.107	2.209	182	18,500	0.88	0.77	0.89	0.79
XVI	Bis(N-phenylsalicylaldiminato)copper(II)	2.112	2.234	168	16,100	0.88	0.77	0.87	0.76
XVII	Bis(N-phenyl-1-formimino-2-naph-tholato)copper(II)	2.113	2.215	180	15,800	0.88	0.77	0.82	0.67
			Tetradentate Schiff Bases						
XVIII	N,N′-Bis(acetylacetone)ethylenediimino-copper(II)	2.111	2.175	214	18,800	0.91	0.83	0.79	0.62
XIX	N,N′-Bis(2-acetiminodimedone)ethylene-diiminocopper(II)	2.105	2.184	214	18,900	0.91	0.83	0.80	0.64
XX	N,N′-Bis(salicylaldehyde)ethylenedi-iminocopper(II)	2.110	2.190	208	18,000	0.91	0.83	0.80	0.64
XXI	N,N′-Bis(*o*-hydroxyacetophenone)-ethylenediiminocopper(II)	2.096	2.188	213	18,400	0.91	0.83	0.80	0.64
I (chloroform)[a]		...	2.283	176	...	...	...	...	...
I (chloroform)[b]		...	2.288	173	...	...	...	...	...
I (chlofororm)[c]		...	2.285	175	16,800	0.89	0.79	0.98	0.96
I (crystal)[d]		...	2.27	160	...	0.90	0.81	0.92	0.85
I (crystal)[e]		...	2.26	160	15,000	0.87	0.76	0.94	0.88
XVIII (crystal)[f]		...	2.18	207	18,000	0.90	0.81	0.83	0.69
XVIII (powder)[f]		...	2.18	203	18,000	0.90	0.81	0.83	0.69
XX (polycrystalline)[g]		...	2.186	192	...	...	...	...	...

[a] This investigation. [b] See ref 10. [c] See ref 11. [d] A. H. Maki and B. R. McGarvey, *J. Chem. Phys.*, **29**, 31 (1958). [e] See ref 6. [f] See ref 4. [g] G. M. Larin, G. V. Panova, and E. G. Rukhadze, *Zh. Strukt. Khim.*, **6**, 699 (1965).

$|\rho_N(0)|^2$ is the value of the ligand 2s function at the ligand nucleus, having a value of 33.4×10^{24} cm^{-3},[2] S_Z is the Z component of the spin angular momentum of the electron, and T_Z is the Z component of the spin angular momentum operator for the nucleus.

Results and Discussion

For the bidentate chelates investigated here the distinct absorption maximum occurring at the longest wavelength in the visible spectrum has been assigned to the transition, $E_{xy} \rightarrow E_{x^2-y^2}$. The values so obtained for this transition lie between 15,400 and 18,500 cm^{-1}. Our value of 16,100 cm^{-1} for bis(acetylacetonato)-copper(II) agrees well with the 16,800-cm^{-1} value estimated by Cotton and Wise,[12] and the frequency of 16,700 cm^{-1} which we assigned to bis(N-methylsalicylaldiminato)copper(II) is close to the 17,000-cm^{-1} band observed by Ferguson[20] in the polarized spectrum

of the compound and assigned to the $E_{xy} \rightarrow E_{x^2-y^2}$ transition by Cotton and Wise.[14] We have attributed the absorption maximum exhibited by each tetradentate chelate at about 18,000 cm^{-1} to the $E_{xy} \rightarrow E_{x^2-y^2}$ transition in accord with Belford and Yeranos' analysis of the solution spectrum of bis(acetylacetone)ethylenediiminocopper(II).[18] Thus the error in our values for the $E_{xy} \rightarrow E_{x^2-y^2}$ transition presented in Table I appears to be no more than 10% leading to an error of only 3% in β_1.[6]

Of the 21 compounds listed in Table I, epr studies for three—I, XVIII, and XX—have been previously reported. The published results are cited at the end of the table. The agreement between our data and those of other investigators is satisfactory with respect to $g_{||}$ values. In this study of 80:20 solutions of dried chloroform–toluene, the $a_{||}$ values are noticeably larger than those reported in the literature for chloroform solutions and for crystalline or powdered samples. The discrepancy is attributed to the differences in media. We obtain a value of $a_{||} = 176 \times 10^{-4}$ cm^{-1} for bis(acetylacetonato)copper(II) in chloroform containing 0.75% alcohol but a value of $a_{||} = 194 \times 10^{-4}$ cm^{-1} for the same copper chelate in 80:20 dried chloroform–toluene. In a comparison of the values of α and β_1 where a variety of media are used, the effect of solvent upon $a_{||}$ should be noted. Large values of $a_{||}$ generally lead to relatively small α and large β_1 values.

The bonding parameter α is a measure of the covalency of the in-plane σ bonding. A value of $\alpha^2 = 1$ indicates complete ionic character while $\alpha^2 = 0.5$ denotes essentially 100% covalent bonding assuming negligibly small values of the overlap integral. The complexes studied here display considerably covalent in-plane σ bonding. The greatest amount of covalent character in the σ bonding is exhibited by the bidentate Schiff base chelates ($\alpha^2 = 0.72$–0.79) while the complexes of the β-keto enolates and tetradentate Schiff bases are equally less covalent ($\alpha^2 = 0.81$–0.85). The β-keto amide complexes possess the greatest ionic character in the σ bonding. The electronegativity of the nitrogen in the amide group may be responsible for the ionicity.

The β_1 parameter is the gauge for covalency in the in-plane π bonding. A value of $\beta_1^2 = 1.00$ indicates no covalent character while $\beta_1^2 = 0.50$ corresponds to total covalent character. The β_1^2 values arrived at in this study show some covalency in the in-plane π bonding of all of the complexes, it being particularly pronounced in the tetradentate Schiff base chelates (the chelates with the largest $a_{||}$ values and high-energy $E_{xy} \rightarrow E_{x^2-y^2}$ transitions). Of the β-keto enolates, the covalent character of the in-plane π bonding is least for the dimedone derivatives, possibly owing to the presence of a second carbonyl group. Admittedly, the complexes of N-substituted 2-acetiminodimedones do not have particularly large β_1^2 values for bidentate Schiff base chelates. The bidentate Schiff bases exhibiting the most covalent in-plane π bonding are the naphthaldehyde derivatives. The corresponding β-keto enolates of the naphthaldehyde chelates also possess appreciably covalent in-plane π bonding.

Kivelson and Neiman[6] suggested that $g_{||}$ serves as a single parameter measuring the total covalency of the in-plane coordinate σ and π bonding; the lower the $g_{||}$ value, the more covalent the coordinate bonding. According to the $g_{||}$ criterion, this epr study of copper(II) chelates indicates that the covalent character of the in-plane copper–ligand bonding generally increases in the order: β-keto amides < β-keto enolates < bidentate Schiff bases < tetradentate Schiff bases.

In the spectra which we recorded at 300°K, nitrogen hyperfine splitting was noted only for the three N-substituted 2-acetiminodimedone (2-acetimino-5,5-dimethylcyclohexane-1,3-dione) chelates. The values of the splittings are 11.7, 11.5, and 13.4 $\times 10^{-4}$ cm^{-1} for compounds XI, XV, and XIX, respectively. At

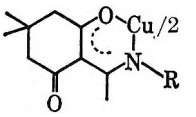

XI, R = H
XV, R = C_6H_5
XIX, R = $-CH_2$

300°K the samples of the other bidentate Schiff bases gave broader resonances than did the β-keto enolates and β-keto amides, but the five-line multiplet due to coupling with two equivalent nitrogen nuclei ($I = 1$) was not resolved. Gersmann and Swalen[8] reported that no nitrogen hyperfine splitting was observed for bis(salicylaldiminato)copper(II), and Larin, *et al.*,[21] found none for bis(salicylaldehyde)ethylenediiminocopper(II).

The nitrogen hyperfine splittings lead to α^2 values of 0.81, 0.81, and 0.79 for complexes XI, XV, and XIX, respectively. The covalency of the in-plane σ bonding measured by the nitrogen splitting is less than that calculated from the copper hyperfine splittings (see Table I), as has also been reported by others.[6,9] Furthermore, the α^2 values obtained from the nitrogen hyperfine splittings indicate a higher covalency in the tetradentate Schiff base chelate, XIX, than in the bidentate Schiff bases, XI and XV, in accord with the $g_{||}$ values but at variance with the α^2 values calculated from the copper hyperfine splittings. Other examples of such discrepancies have been cited.[22]

(20) J. Ferguson, *J. Chem. Phys.*, **35**, 1612 (1961).

(21) G. M. Larin, G. V. Panova, and E. G. Rukhadze, *Zh. Strukt. Khim.*, **6**, 699 (1965).

(22) H. A. Kuska and M. T. Rogers, *J. Chem. Phys.*, **43**, 1744 (1965).

Acknowledgment. We thank Dr. Gerald O. Dudek for helpful suggestions. We are indebted to Harvard University for the use of its equipment. This work was supported in part by the National Science Foundation Undergraduate Research Program (Grant No. GE-6220).

Mechanism of Gaseous Siloxane Reaction with Silica. I

by William Hertl

Corning Glass Works, Research Laboratories, Corning, New York 14830 *(Received September 20, 1967)*

The reaction between gaseous methyltrimethoxysilane and the surface silanol groups on silica was studied in the temperature range 90–220°, infrared spectroscopy being used to measure the changes with time in the surface silanol concentration. Physical adsorption was measured concurrently with the chemical reaction. The reaction follows third-order kinetics with respect to the number of surface sites. The reactions taking place are: (a) $(RO)_3SiR + HOSi\lessdot = R(RO)_2Si(OSi\lessdot) + ROH$, (b) $(RO)_3SiR + HOSi\lessdot + HOSi\lessdot = R(RO)Si(OSi\lessdot)_2 + 2ROH$, and (c) $ROH + HOSi\lessdot = ROSi\lessdot + HOH$, where R is CH_3. About 40% of the siloxane molecules react monofunctionally and 60% react difunctionally. There is also some hydrogen bonding between unreacted siloxane groups on the surface and the surface silanol groups, and there is a considerable reaction of the product alcohol with the surface hydroxyl groups. The rate-determining step is the reaction of a physically adsorbed siloxane molecule to form a $\gtrdot SiOSi\lessdot$ bond on the surface. The rate of reaction can be expressed as rate $= A \exp(-30600/RT)[OH]^3[\theta]^3$, where A is a constant for a given sample of silica, which depends on the previous heat treatment, [OH] is the number of nonhydrogen-bonded surface hydroxyl groups, and $[\theta]$ is the fraction of these groups covered by physically adsorbed siloxane. The fraction θ is a function of the ambient gas pressure and decreases with increasing temperature.

Introduction

It is becoming increasingly important to bond various organic molecules to glass surfaces in the forms of films and coatings. Generally a coupling agent is used to create a strong bond between the glass surface and the organic film, and siloxanes are often used. It has been reported that a siloxane in solution reacts with the surface silanol groups on silica as follows:[1] $R_3SiOR + HOSi\lessdot = R_3SiOSi\lessdot + ROH$ or $R_3SiOR + HOSi\lessdot + HOSi\lessdot = R_3SiOSi\lessdot + ROSi\lessdot$, depending upon the solvent used. In the present study infrared spectroscopy has been used to measure the changes with time of the surface silanol group concentration when a gaseous trifunctional siloxane reacts with the silica surface. Physical adsorption was measured concurrently with the chemical reaction. A kinetic analysis of the data is made in order to elucidate the reaction mechanism.

Experimental Section

Materials. Methyl trimethoxysilane (Z-6070, Dow Corning Corp., Midland, Mich.) was used as is, except for degassing in the vacuum rack. The vapor pressure at room temperature is about 30 torr.

The silica (Cab-O-Sil, M-5, Cabot Corp., Boston, Mass.) was pressed into disks[2] by placing a 50-mg sample, sandwiched between tissue paper, in a 1-in. die. The silica and tissue paper in the die were moistened with acetone and pressed at 5000 psi for 1 min and at 24,000 psi for 5 min. The pressed silica sandwiched between the tissue paper was removed from the die and placed in a furnace at 500° for several hours to burn off the paper. The BET surface area of the pressed silica disk was 152 m^2/g.

Procedure. The reaction of the gaseous siloxane with the silica disk was carried out in a 1-in. i.d. (3-in. long) cylindrical brass furnace wound with a spiral of nichrome wire. The silica disk was mounted upright against a machined lip at the midpoint of the furnace and was maintained in place with a glass cylinder pushed against the disk. Cylindrical brass end caps with Irtran-2 windows were fitted into the ends of the furnace and made vacuum tight with silicone-rubber gaskets. The furnace was connected to a conventional glass vacuum rack *via* a fitting in one of the end caps. A vacuum of at least 10^{-5} torr was attained. The furnace temperature was measured and controlled with a Leeds & Northrup recorder–controller connected

(1) J. G. Koelling and K. E. Kolb, *Chem. Commun.*, 1, 6 (1965).

(2) M. L. Hair, "Infrared Spectroscopy in Surface Chemistry," Marcel Dekker, Inc., New York, N. Y., 1967, p 69.

to a thermocouple mounted in a cavity in the furnace wall.

To carry out a reaction, the furnace, with the silica disk in place, was evacuated as the furnace was raised to the operating temperature. Several initial spectra of the disk were taken. The siloxane was admitted to the vacuum rack from a trap containing the reagent, and the tap to the furnace was opened. After the reaction proceeded for a given time, the furnace was evacuated and a spectrum of the silica disk was taken. The procedure was repeated at intervals of several per cent reaction until the desired amount of reaction had taken place, generally about 75%. Spectra were also taken of the disk with the gas present in the furnace.

Spectra were taken on a Perkin-Elmer Model 421 grating infrared spectrophotometer. A 22% open-space screen was used in the reference beam to compensate for energy losses through the windows and silica sample. For gas-phase spectra without the silica disk in the furnace, a 40% open-space screen was used. High-resolution settings (spectral slit width ≈ 1.6 cm^{-1}) were used on the spectrophotometer; on the sharp peaks a scanning speed of about 10 cm^{-1}/min was used.

Results

Reaction Products. To determine the gaseous reaction products, an excess of pressed silica was placed on the floor of the furnace so that the infrared beam passed only through the gas phase. The siloxane was admitted to the furnace and allowed to react for at least 24 hr. A spectrum of the gas phase was taken initially and at the end of the reaction. The gaseous siloxane was completely consumed and the spectrum of gaseous methyl alcohol was observed. The partial pressure of the product methyl alcohol was determined by comparing the intensities of the observed bands against those observed when methyl alcohol was admitted to the furnace at various pressures. The results of two experiments are given in Table I. The important point to note is that for each siloxane molecule which reacts with the silica, less than one molecule of the product methyl alcohol appears in the gas phase. Part but not all of the methyl alcohol is bonded to the silica surface. Thus the over-all reactions taking place are: $RSi(OR)_3 + HOSi\lessdot = RSi(OR)_2OSi\lessdot + ROH$ and $ROH + HOSi\lessdot = ROSi\lessdot + HOH$, where $R = CH_3$. The reaction as written involves only one OR group; more than one OR group in each siloxane molecule can react with the surface. This will be discussed.

Spectra. Spectra of the silica were taken in the range 2700–4000 cm^{-1}. Some typical spectra taken during the course of the reaction are shown in Figure 1. For clarity only the initial, final, and one intermediate spectrum are shown. During any typical run the spectra were taken at intervals of a few per cent reaction.

Table I

Initial pressure of siloxane, torr	Methyl alcohol found, torr	Ratio
18	11	0.61
25	16	0.64

In Figure 1 the sharp peak at 3745 cm^{-1} is due to nonhydrogen-bonded surface silanol groups, and the rounded peak at 3675 cm^{-1} is due to the hydrogen-bonded silanol groups.[3] As the reaction proceeds (Figure 1, curves 2 and 3), the intensity of the band due to nonhydrogen-bonded silanol groups decreases, and a broad peak appears at 3350 cm^{-1}. This is due to the presence of strongly hydrogen-bonded silanol groups. The rounded peak at 3675 cm^{-1} does not appear to change during the course of the reaction.

The bands between 2800 and 3000 cm^{-1} (Figure 1, curves 2 and 3) are the various symmetric and asymmetric CH stretching frequencies associated with the siloxane which is bonded to the silica surface.

For the spectra of the silica taken with the gas present (both at room and reaction temperature), only the bands above 3000 cm^{-1} were recorded, since the gaseous siloxane absorbs strongly in the 2800–3000-cm^{-1} region.

The change in the extinction (*i.e.*, log (I_0/I)) of the sharp band at 3745 cm^{-1} was used to follow the course of the reaction quantitatively. The value of I_0 used was the transmission in the region 3750–3800 cm^{-1}.

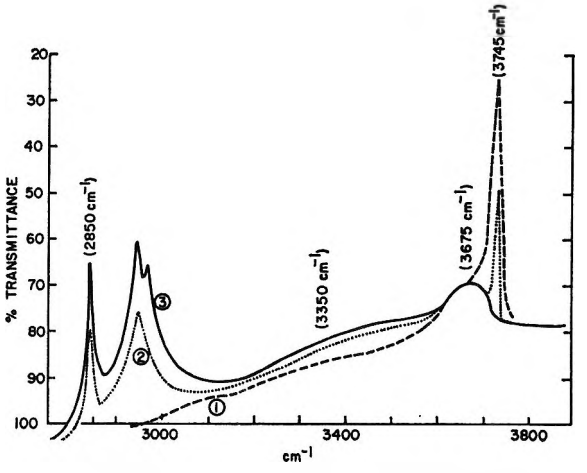

Figure 1. Typical spectra of silica taken during the course of reaction at 158°: (1) initial spectrum, (2) spectrum part way through reaction, (3) spectrum at end of complete reaction.

(3) See ref 2, p 80 ff.

Figure 1 (curve 3) shows that the background transmission (I_0) at 3745 cm^{-1}, when no nonhydrogen-bonded hydroxyl groups remain, is the same as in the region 3750–3800 cm^{-1}. The value I is the transmission at the point of maximum absorbance of this band.

In order to obtain a good initial value of the extinction, several spectra were taken at reaction temperature *in vacuo*. This initial extinction is defined as 1.000. The subsequent extinctions measured during the course of the reaction were compared to the initial extinction, in order to obtain the fraction of nonhydrogen-bonded hydroxyl groups remaining. These values plotted *vs.* the time of the reading give the reaction curve. Comparing all readings in a given run to the initial value obviates any slight differences between different runs in the amount of silica in the beam.

The buildup of the band at 2850 cm^{-1}, due to a CH vibration, was also used several times, concurrently with the decrease in the band intensity at 3745 cm^{-1}, in order to obtain the reaction curve. To use the band at 2850 cm^{-1} it was necessary to let the reaction go to completion in order to obtain a reference value of the extinction with which to compare the extinctions measured during the course of the reaction. Good agreement was found when using either of these two bands for following the reaction course.

Physical Adsorption. The degree of physical adsorption on the silica was measured at room temperature by admitting the siloxane or methyl alcohol at various pressures to the cell and measuring the decrease in the intensity of the band at 3745 cm^{-1}. Several of the spectra are shown in Figure 2. The band at 3745 cm^{-1} decreases in intensity with increasing gas pressure, and a broad band appears at 3350 cm^{-1}. This latter band is attributed to a strongly hydrogen-bonded hydroxyl group. At room temperature most of the physically adsorbed material can be removed by pumping.

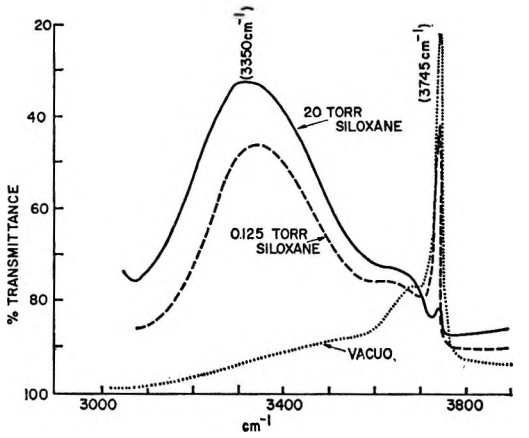

Figure 2. Spectrum of silica showing the effect of physically adsorbed siloxane at room temperature.

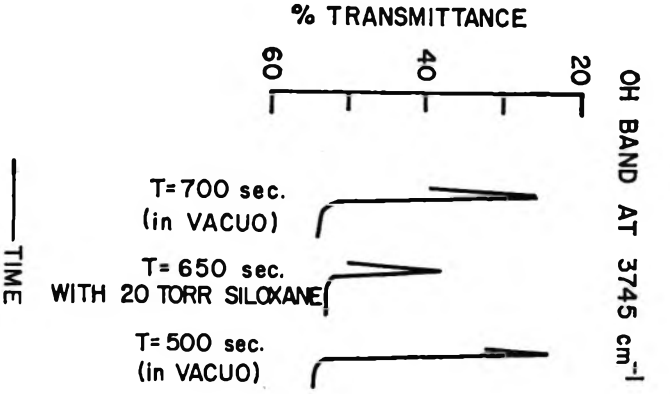

Figure 3. Typical spectra of silica taken during the course of reaction at 120°, illustrating spectra used for determining the fraction of freely vibrating hydroxyl groups covered by physically adsorbed siloxane.

The ratio of the intensity of the band at 3745 cm^{-1} in the presence of the added gas to the intensity in the absence of added gas gives the fraction of the surface sites not covered by physically adsorbed molecules ($1 - \theta$). The fraction of the surface sites covered by physically adsorbed molecules, θ, is defined here as the fraction of originally nonhydrogen-bonded hydroxyl groups which are perturbed when the silica is exposed to the added gas.

The degree of coverage (θ) by physical adsorption at reaction temperatures was also measured by taking spectra of the silica with the gas present in the furnace, while the reaction was going on. Figure 3 shows some spectra of the band at 3745 cm^{-1} taken during the course of a run at 120°. To determine θ, the extinction value was interpolated between t = 500 and 700 sec in order to estimate the extinction at t = 650 sec, the time at which the extinction was measured with the gas present. The ratio of the extinction with the gas present to the interpolated value gives the fraction of surface sites not covered by physically adsorbed siloxane, *i.e.*, $1 - \theta$. Since only a few per cent reaction takes place in this time interval, there is virtually no error introduced by the interpolation. This measurement was made at various stages during a reaction and good agreement was found throughout the reaction for the fraction of available surface sites not covered by physically adsorbed molecules (estimated error was usually within ±2.5%, *cf.* Figure 4).

When the siloxane chemically bonds to the surface, a low, broad band appears at 3350 cm^{-1} (*cf.* Figure 1). This band arises owing to an interaction between an unreacted CH_3O group and a surface hydroxyl group. To estimate the fraction of hydroxyl groups tied up in this manner, a silica sample was allowed to react to completion and was cooled to room temperature. A spectrum was then taken. From the room-temperature physical-adsorption measurements, the intensity of the band at 3350 cm^{-1} is known as a function of the

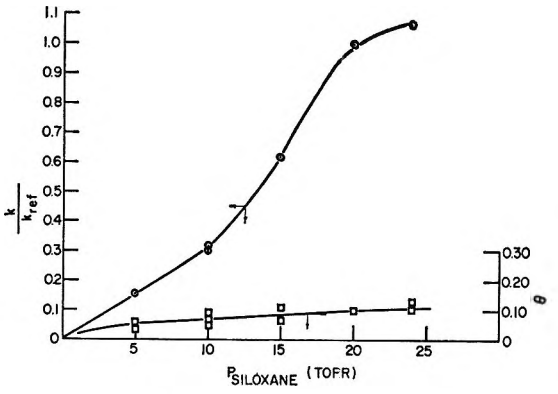

Figure 4. k/k_{ref} for various ambient siloxane pressures at 200°, -⊙-. k/k_{ref} is the ratio of the third-order rate constant for a given disk at the given pressure to the third-order rate constant measured under standardized conditions on the same disk. k_{ref} was measured using 20 torr of siloxane. Fraction of available freely vibrating OH groups covered by physically adsorbed siloxane (θ) at 200° for various ambient siloxane pressures, -□-.

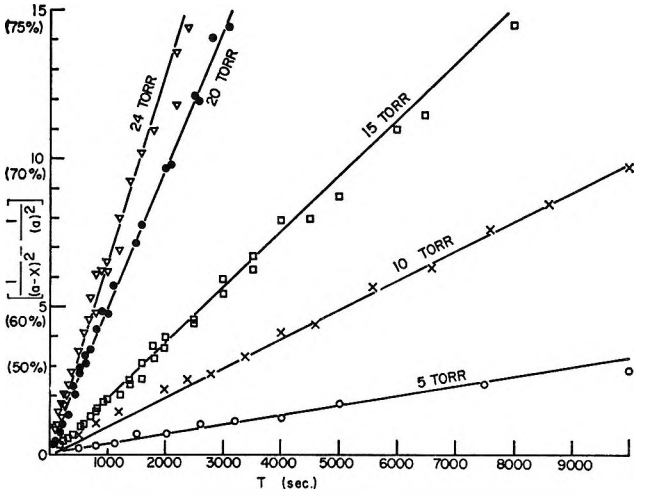

Figure 5. Third-order kinetic plot, as defined in text (eq 1), for various ambient siloxane pressures at 154°: ○, 5 torr; ×, 10 torr; □, 15 torr; ●, 20 torr; ▽, 24 torr.

degree of surface coverage. Comparison of the intensity of the band at 3350 cm^{-1} at the end of a reaction with the intensity observed when the siloxane is physically adsorbed allows one to determine the fraction of originally nonhydrogen-bonded hydroxyl groups which are tied up *via* hydrogen bonding. It is estimated that 10–15% of the hydroxyl groups are thus tied up.

Analysis of the Kinetic Measurements. In all the kinetic runs, the system was evacuated between readings. Readings were taken at intervals of several per cent reaction and then fresh gas was added. Thus the gas-phase composition is essentially constant throughout any given run.

The data were analyzed using the integrated form of a formal third-order kinetic rate equation, which is

$$\frac{1}{(a-x)^2} - \frac{1}{a^2} = 2k_{p,T}t \qquad (1)$$

where a is the initial concentration of reactant, in this case the nonhydrogen-bonded hydroxyl groups; x is the fraction of nonhydrogen-bonded hydroxyl groups which have reacted at time t; and $k_{p,T}$ is the third-order rate constant for any given pressure and temperature. Since all values of the extinction are compared to the initial extinction, a is defined as equal to 1.000.

The data from some reactions carried out with various siloxane pressures are plotted in Figure 5 as the left-hand side of eq 1 *vs.* t. The slopes of these plots give the values of k. The third-order kinetic plots are linear to greater than 80% reaction.

The chemical bonds, once formed, are thermally stable in the temperature range used here, so that any back reaction can be neglected. Heating a reacted silica disk *in vacuo* for 5.5 hr at 300° resulted in no significant change in the CH band intensities. Also, during the course of several of the runs, water vapor at a pressure of 5 torr was admitted to the furnace, both with and without the siloxane vapor present. No discontinuities were noted in the kinetic plots, nor when water vapor was added alone were there any changes, after evacuation, in the intensities of the bands due to the CH and OH vibrations. The effect of the product water may thus be neglected under the conditions in which these experiments are carried out.

After carrying out a number of runs, all of which followed the formal third-order kinetics, it was found that the reactivity of the silica surface varied from sample to sample. A rough correlation was found between the reactivity of the silica and the temperature at which it was heated prior to use, the reactivity being higher with higher heating temperatures. To avoid this difficulty the sample was first allowed to react under standard conditions (generally 200° with 20 torr of siloxane) for about 20–30% reaction. The desired reaction conditions were then used and the remaining part of the reaction carried out. The third-order kinetic plot was made and the slope of the latter part of the plot was compared to the slope of the initial part of the plot. In the case of the temperature series, the standarized reaction was carried out at 200°, the temperature was changed, and the remainder of the reaction was carried out. For this series a new zero point was defined after the temperature was changed. This was necessary, since the bands broaden somewhat with increasing temperature.

Figure 4 shows the variation in the rate constant, k, with varying pressures of siloxane, determined at 200°. The degree of coverage by physical adsorption (θ) is also shown on this plot.

Discussion

The course of the reaction between siloxane and the silica surface, out to at least 80% completion, follows

formal third-order kinetics, and the gas phase is held constant during any given run. Hence, each time that a siloxane molecule chemically reacts with the surface, three surface sites, on the average, are removed from the reaction system. The hydroxyl groups can be permanently removed from the reaction system in three ways: (i) by reaction of a R_3SiOCH_3 group with a surface hydroxyl group to form $R_3SiOSi\lessdot$ (one or more methoxy groups in each siloxane molecule can react in this way with the surface), (ii) by reaction of the product CH_3OH with a surface hydroxyl group to form $CH_3OSi\lessdot$, and (iii) by hydrogen bonding between an unreacted methoxy group of a siloxane molecule which has reacted with the surface and a surface hydroxyl group.

From Table I it is seen that for every 1.00 molecule of gaseous siloxane that reacts with the surface only 0.64 molecule of CH_3OH is detected in the gas phase. Therefore, for every methoxy group of the siloxane molecule that reacts with the surface, 0.36 molecule of the alcohol produced must react with the surface. Similarly, when 2 methoxy groups per siloxane molecule react, 1.36 molecules of the CH_3OH must remain bonded to the surface. Also, at the end of a reaction, 15% of the total of originally nonhydrogen-bonded hydroxyl groups are tied up *via* hydrogen bonding.

If we consider a group of three freely vibrating hydroxyl groups, then 0.45 hydroxyl group is hydrogen bonded, and, if x is the fraction of siloxane molecules which react monofunctionally and $1-x$ is the fraction of siloxane molecules which react difunctionally, the following mass balance can be set up

$$\underset{b}{1(x)} + \underset{c}{2(1-x)} + \underset{d}{(0.36)x} + \underset{e}{(1.36)(1-x)} + \underset{f}{0.45} = \underset{g}{3.00}$$

where b is the number of hydroxyl groups reacted when the siloxane molecule reacts monofunctionally, c is the number of hydroxyl groups reacted when the siloxane molecule reacts difunctionally, d is the number of hydroxyl groups that react with the CH_3OH which is produced *via* (a), e is the number of hydroxyl groups that react with the CH_3OH produced *via* (b), f is the number of hydroxyl groups removed *via* hydrogen bonding, and g is the total number of hydroxyl groups which are consumed when one siloxane molecule reacts with the surface. Solving the equation gives a value of $x = 0.40$. Thus about 40% of the siloxane molecules react monofunctionally and about 60% react difunctionally. On steric grounds, it is not considered likely that any significant number of siloxane molecules react trifunctionally.

The surface reaction studied here can be compared with any heterogeneous process in which a series of

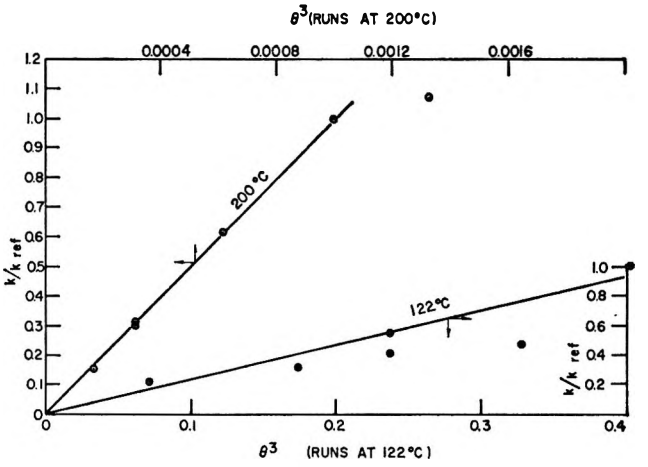

Figure 6. k/k_{ref} *vs.* θ^3 for runs at 200 and 122°. k/k_{ref} and θ are defined in Figure 4.

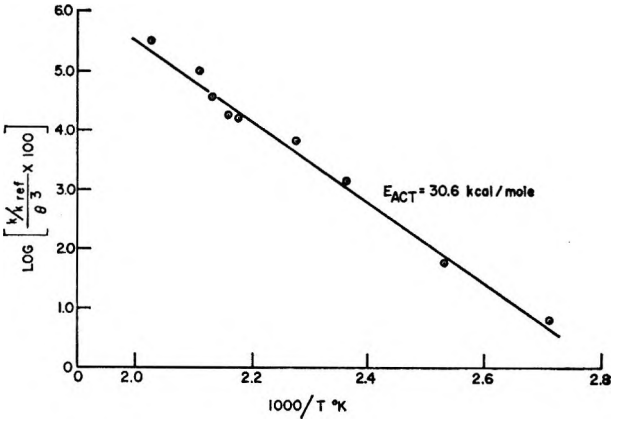

Figure 7. Plot of log $[(k/k_{ref})/\theta^3]$ *vs.* $1/T$. k/k_{ref} is the ratio of the third-order rate constant for a given disk at the given temperature to the third-order rate constant measured under standardized conditions on the same disk. k_{ref} was measured at 200° using 20 torr of siloxane. θ is the fraction of available freely vibrating OH groups covered at various temperatures by physically adsorbed siloxane for 20-torr of ambient siloxane pressure.

consecutive steps takes place. In physical adsorption, the rate at which molecules adsorb on a surface is proportional to $1-\theta$, where θ is the fraction of surface which is covered with physically adsorbed molecules. The rate at which a molecule will desorb is proportional to θ when one surface site is occupied and to θ^2 when two surface sites are occupied.[4] In heterogeneous catalytic reactions, a molecule is first physically adsorbed as above and this is followed by chemisorption with the surface, reaction between chemically adsorbed molecules, and final desorption of the products into the gas phase. In the process studied here, the initial physical adsorption is followed either by desorption of the siloxane or by chemical reaction of the physically adsorbed molecule with freely vibrating surface hydroxyl groups. The surface sites are permanently re-

(4) K. J. Laidler in "Catalysis," Vol. 1, Reinhold Publishing Corp., New York, N. Y., p 176 ff.

moved from the system when chemisorption takes place.

In comparing the consecutive steps observed in the physical adsorption and heterogeneous catalytic processes, it can be seen that if three surface sites were to be occupied by the physically adsorbed siloxane molecule, the rate at which the chemical reaction takes place should be directly proportional to θ^3. In Figure 6, the third-order rate constants measured at 200 and 122° are plotted against θ^3 and this relationship is demonstrated. Similarly, the rate constants measured at various temperatures, divided by θ^3 measured at each temperature, are given on the Arrhenius plot in Figure 7. This plot is also linear and gives an experimental activation energy of 30.6 kcal/mol.

The fact that three sites are occupied in the physical-adsorption process should not be confused with the third-order chemical reaction; these can be independent processes, so far as the number of surface sites occupied per molecule is concerned. It is implicitly assumed that the fraction of originally freely vibrating hydroxyl groups which are perturbed in the presence of added siloxane (θ) is equal to the fraction of surface sites which are covered by physically adsorbed siloxane molecules. The fraction θ is, of course, a function of the ambient gas pressure.

That the rate of buildup of the CH bands gave the same result as the rate of decrease in the band at 3745 cm^{-1} shows that the extinction coefficient of the freely vibrating hydroxyl group does not change during the course of the reaction. This is evidence that the hydroxyl groups have the same reactivity throughout the course of the reaction.

The rate at which the siloxane molecules physically adsorb on the surface is much faster than the rate of the chemical reaction on the surface; hence the rate-determining step is the chemical reaction of a physically adsorbed siloxane molecule to form an $\geqslant SiOSi \leqslant$ bond on the silica surface. The rate of reaction can be expressed

$$\text{rate} = A \exp(-30600/RT)[OH]^3[\theta]^3$$

where [OH] is the number of nonhydrogen-bonded surface hydroxyl groups, θ is the fraction of hydroxyl groups available for reaction which are covered by physically adsorbed siloxane molecules, and A is a constant which depends on the previous heat treatment of the silica.

Acknowledgment. I wish to thank Miss E. R. Herritt for assistance in the experimental work and Dr. M. L. Hair for some helpful discussions.

Current Dependence of Water Transport in Cation-Exchange Membranes

by N. Lakshminarayanaiah and V. Subrahmanyan

Department of Pharmacology, School of Medicine, University of Pennsylvania, Philadelphia, Pennsylvania 19104
(Received September 20, 1967)

Transfer of water following application of an electric field to a cation-exchange membrane in contact with 0.01 N solution of an electrolyte has been measured at 25° using different current densities. Two cation-exchange membranes of different water content and the alkali metal chloride solutions have been used. $\bar{l}_w$, the number of moles of water transported for the passage of 1 faraday of electricity in high water content membranes was high at low current density and low at high current densities for all the alkali metal ions. Similar behavior was noted for the other membrane of low water content for Li^+, Na^+, and K^+ ions, whereas in the case of Rb^+ and Cs^+ ions, $\bar{l}_w$ was not significantly affected by current density. Values of $\bar{l}_w$, however, for the low water content membrane were lower than corresponding values obtained with the high water content membrane. All of these results have been discussed from the standpoint of an existing theory of electroosmosis due to Spiegler.

Introduction

Electromigration of ions through an ion-exchange membrane bisecting an aqueous solution of an electrolyte results in a net transfer of water. This transport composed of two components—water of ion hydration and water transferred electroconvectively—is called, in a phenomenological way, electroosmosis, which in recent literature[1] is indicated by $\bar{l}_w$ (water-transference number), the number of moles of water transferred for the passage of 1 faraday of electric current.

(1) N. Lakshminarayanaiah, *Chem. Rev.*, 65, 525 (1965).

The $\bar{l}_w$ values for different ions using various ion-selective membranes have been determined by a number of investigators employing a variety of techniques and cell designs.[2-31] The results of these studies establish conclusively the dependence of $\bar{l}_w$ on (a) the external electrolyte concentration ($\bar{l}_w$ decreasing with increasing concentration) and (b) the water content of the membrane ($\bar{l}_w$ decreasing with decreasing water content). However, the studies of the dependence of $\bar{l}_w$ on the intensity of current are not definitive. Mackay and Meares[13] in 1959 reported the complete independence of $\bar{l}_w$ of current strength, employing NaCl solutions in the concentration range 0.01–1.0 N. Carr, *et al.*,[18] obtained the same current independence of $\bar{l}_w$ with 0.02 N KCl solution. Similar observations have been made by others[19,22] using higher concentrations and moderate current densities. On the contrary, Lakshminarayanaiah[1,6,30,32] for the first time in 1956 showed, using 0.01 N solutions, that $\bar{l}_w$ depended on the current density displaying two main characteristics: (1) at high current density $\bar{l}_w$ approached a limiting value and (2) at low currents it rose to a large value. Subrahmanyan and Lakshminarayanaiah[14,15,30] showed later that these relationships changed as the concentration of the external electrolyte was increased to 0.1 N and above, when $\bar{l}_w$ became independent of current density. In a recent paper[31] George and Courant have confirmed the current dependence of $\bar{l}_w$, noted by Lakshminarayanaiah, employing leached membranes in 0.01 N NaCl solution. In order to probe these findings further, we reinvestigated this problem using two strong-acid cation-selective membranes of widely differing water content in a solution environment (0.01 N) in which the membranes were little invaded by the co-ion.

Experimental Section

The cation-exchange membranes used in the study were cross-linked phenolsulfonic acid (PSA) and commercially available AMF C-103. PSA membranes were prepared following the procedure already described[24] and the AMF membrane [poly(ethylene–styrene) graft copolymer containing sulfonic acid groups] was supplied by the American Machine and Foundry Co.

Conversion of the membrane to the various ionic forms was carried out by repeated equilibration with approximately 1.0 N solution of the appropriate metal chloride followed by thorough rinsing with deionized water to remove the sorbed electrolyte. Finally the membranes were equilibrated with the appropriate 0.01 N solution. In the case of the rubidium and cesium chlorides, the conversion into the ionic form and equilibration were carried out with 0.01 N solutions.

The water content of the membranes existing in different ionic forms was determined by the method already described.[33] The capacity was determined by equilibrating a known weight of the membrane in the appropriate ionic form with 0.1 N HCl solution (10 ml). The excess acid after repeated washing of the membrane was titrated against standard alkali.

Water-Transfer Measurement. The apparatus shown in Figure 1 was used. The two half-cells between which the membrane, M, was clamped were 500 ml in capacity. The industrial glass pipings holding the membrane–

(2) K. S. Spiegler, *J. Electrochem. Soc.*, **100**, 312C (1953).

(3) W. R. Walters, D. W. Weiser, and L. J. Marek, *Ind. Eng. Chem.*, **47**, 61 (1955).

(4) Y. Oda and T. Yawataya, *Bull. Chem. Soc. Jap.*, **28**, 263 (1955); **29**, 673 (1956); **30**, 213 (1957).

(5) A. G. Winger, R. Ferguson, and R. Kunin, *J. Phys. Chem.*, **60**, 556 (1956).

(6) N. Lakshminarayanaiah, Thesis, London University, 1956; *Proc. Indian Acad. Sci.*, **A55**, 200 (1962).

(7) A. Despić and G. J. Hills, *Discussions Faraday Soc.*, **21**, 150 (1956).

(8) J. W. Lorimer, E. I. Boterenbrood, and J. J. Hermans, *ibid.*, **21**, 141 (1956).

(9) R. J. Stewart and W. F. Graydon, *J. Phys. Chem.*, **61**, 164 (1957).

(10) N. W. Rosenberg, J. H. B. George, and W. D. Potter, *J. Electrochem. Soc.*, **104**, 111 (1957).

(11) J. G. McKelvey, Jr., K. S. Spiegler, and M. R. J. Wyllie, *ibid.*, **104**, 387 (1957).

(12) G. Schulz, *Z. Anorg. Allgem. Chem.*, **301**, 97 (1959).

(13) D. Mackay and P. Meares, *Trans. Faraday Soc.*, **55**, 1221 (1959).

(14) V. Subrahmanyan and N. Lakshminarayanaiah, *Curr. Sci.*, **29**, 307 (1960); *Bull. Chem. Soc. Jap.*, **34**, 587 (1961).

(15) V. Subrahmanyan, Thesis, Madras University, Madras, India, 1961.

(16) G. J. Hills, P. W. M. Jacobs, and N. Lakshminarayanaiah, *Proc. Roy. Soc.* (London), **A262**, 257 (1961).

(17) D. K. Hale and D. J. McCauley, *Trans. Faraday Soc.*, **57**, 135 (1961).

(18) C. W. Carr, R. McClintock, and K. Sollner, *J. Electrochem. Soc.*, **109**, 251 (1962).

(19) A. S. Tombalakian, H. J. Barton, and W. F. Graydon, *J. Phys. Chem.*, **66**, 1006 (1962).

(20) F. Runge, F. Wolf, and R. Bachmann, *Dechema Monograph.*, **47**, 465 (1962).

(21) M. Block and K. S. Spiegler, *J. Electrochem. Soc.*, **110**, 577 (1963).

(22) T. R. E. Kressman, P. A. Stanbridge, and F. L. Tye, *Trans. Faraday Soc.*, **59**, 2129 (1963).

(23) T. R. E. Kressman, P. A. Stanbridge, F. L. Tye, and A. G. Wilson, *Trans. Faraday Soc.*, **59**, 2133 (1963).

(24) N. Lakshminarayanaiah and V. Subrahmanyan, *J. Polymer Sci.*, **A2**, 4191 (1964).

(25) N. Krishnaswamy and V. K. Indusekhar, *Indian J. Technol.*, **2**, 169 (1964); **3**, 358 (1965).

(26) N. Lakshminarayanaiah, *J. Phys. Chem.*, **70**, 1588 (1966).

(27) N. Lakshminarayanaiah and K. R. Brennen, *Electrochim. Acta*, **11**, 949 (1966).

(28) G. B. Willis and E. N. Lightfoot, *Ind. Eng. Chem., Fundam.*, **5**, 114 (1966).

(29) A. S. Tombalakian and W. F. Graydon, *J. Phys. Chem.*, **70**, 3711 (1966).

(30) N. Lakshminarayanaiah, *Desalination*, **3**, 97 (1967).

(31) J. H. B. George and R. A. Courant, *J. Phys. Chem.*, **71**, 246 (1967).

(32) N. Lakshminarayanaiah, *Curr. Sci.*, **28**, 321 (1959).

(33) N. Lakshminarayanaiah, *Biophys. J.*, **7**, 511 (1967).

Table I: Capacity and Water Content of Membranes in Different Ionic Forms

	PSA membrane					AMF C-103 membrane				
	Li^+	Na^+	K^+	Rb^+	Cs^+	Li^+	Na^+	K^+	Rb^+	Cs^+
Water content, g of H_2O/g of wet membrane	0.61	0.59	0.59	0.55	0.51	0.21	0.18	0.15	0.14	0.13
Capacity, mequiv/g of wet membrane	0.61	0.70	0.52	0.53	0.49	0.57	0.57	0.51	0.52	0.43
$\bar{m}_+$, equiv/1000 g of H_2O	1.00	1.19	0.88	0.96	0.96	2.71	3.17	3.40	3.71	3.31
$\bar{m}_w$, mol of H_2O/g-equiv ion	55.6	46.7	63.1	57.9	57.9	20.5	17.5	16.3	15.0	16.8

rubber gasket (G) assembly were 1.9 cm in diameter. The membrane area was adjusted by interposing on either side of the membrane two Lucite sheets, L, containing holes of the required diameter in the center. The smaller membrane area exposed to the solution, with which most of the experiments reported here were performed, was 0.317 cm^2, and the largest area was 2.86 cm^2.

The two half-cells provided with stout Ag–AgCl electrodes were filled with the same solution which was degassed prior to use by evacuation and vigorous stirring under low pressure. They were equipped with detachable glass assembly containing stopcocks, S, and a horizontal precision bore capillary, C. T's were pieces of rubber tubing, with the help of which connection between the two half-cells was established at the top. Using a syringe containing the solution and to which a narrow polyethylene tubing was attached, the cell was filled completely by manipulating the stopcocks, S, in such a way that a tiny air bubble was trapped in the middle of the capillary. With the stopcocks open and the membrane–gasket assembly covered with Plasticine clay, the whole assembly was immersed in a water thermostat maintained at 25 ± 0.01°.

Efficient magnetic stirring of the solutions was employed. Two robust rotating magnets kept just below the two half-cells and outside the thermostat stirred the bulk solutions with the help of Teflon-covered magnetic bars, BT, while two tiny bars, ST, stirred the solution near the membrane–solution interfaces. This was made possible by holding small but powerful magnets, enclosed in water-tight frameworks, just above the surface of the glass piping. When the apparatus attained temperature equilibrium, the stopcocks, S, were closed and the position of the air bubble, B, was noted on a cathetometer placed in a horizontal position. A constant dc current from a constant-current stimulator (Electronics for Life Sciences, Rockville, Md.) was passed through the cell and a calibrated milliammeter in series for a known period of time. Enough quantity of current to displace the air bubble by about 1 cm was passed. The corresponding concentration change was about 1% in the case of PSA membranes and about 5% in the case of AMF membranes. In the next experiment the direction of current was reversed.

Results

The capacity and water content of membranes in different ionic forms are given in Table I. The average deviation of these values was better than ±2%. $\bar{m}_+$, which expressed the membrane capacity in equivalents of counterion associated with 1000 g of interstitial water present in the membrane, and $\bar{m}_w$, the number of moles of water associated with 1 equiv of the mobile counterion, are also shown in Table I.

The movement of air bubble B (Figure 1) in a water-transport experiment was continuously followed on the cathetometer with time. This enabled detection of any sudden changes in volume likely to arise following occurrence of events such as the evolution of gas at the electrodes due to electrode polarization or membrane movement or bulging which can vitiate observed volume changes by making them too low or too high. Kressman, *et al.*,[22] have called attention to this irksome factor whose nonrecognition has tarnished the validity of some of the published $\bar{l}_w$ values. However, this membrane movement can be easily controlled by using suitable techniques described by Lakshminarayanaiah and Brennen.[27] In this study, membrane movement or oscillation was controlled either by using a very small area (0.317 cm^2) of the membrane or by using stainless steel mesh supports when 2.86-cm^2 area of membrane was used.

Examination of the rate of movement of the air bubble indicated that in the first few minutes of the experiment, the rate was always less than the steady-state value. The initial values were, therefore, omitted. Only the constant steady-state values were used to derive $\bar{l}_w$ values. The average deviation of these values was ±1%. The $\bar{l}_w$ values were corrected for the electrode reactions in the manner described elsewhere.[6,27,30]

A number of exploratory experiments were carried out to sort out the effect of the area of the membrane on $\bar{l}_w$ and to see if the phenomenon of the effect of current density on $\bar{l}_w$ was observable in the different techniques used to control membrane movement during electrolysis. These experiments were carried out with PSA membranes and 0.01 *N* NaCl solution. The values of $\bar{l}_w$ obtained with different techniques (membrane area = 2.86 cm^2) and shown in Figure 2 are not comparable, as

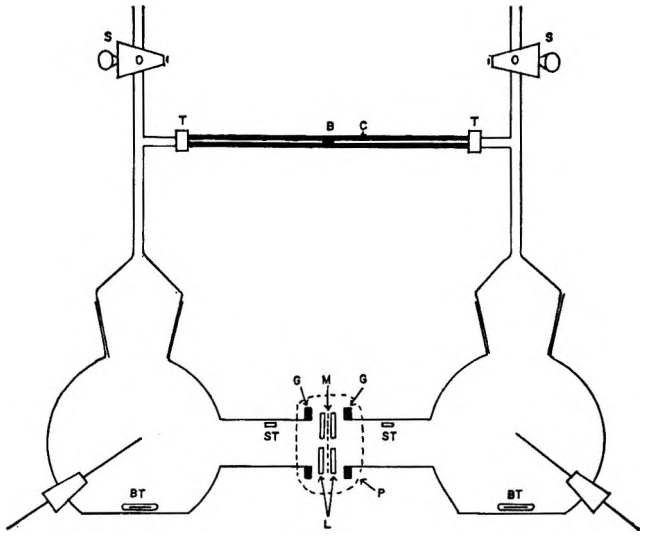

Figure 1. All-glass water-transport cell. The membrane, M, is held between Lucite sheets, L. G are rubber gaskets. Big Teflon magnetic bars, BT, stirred the bulk solutions. The small bars, ST, stirred the solution near membrane–solution interfaces. Plasticine clay, P, covered the membrane–gasket assembly. B is the tiny air bubble in the precision-bore capillary, C, held in pieces of rubber tubing, T, attached to glass tubing containing stopcocks, S, of the two half-cells.

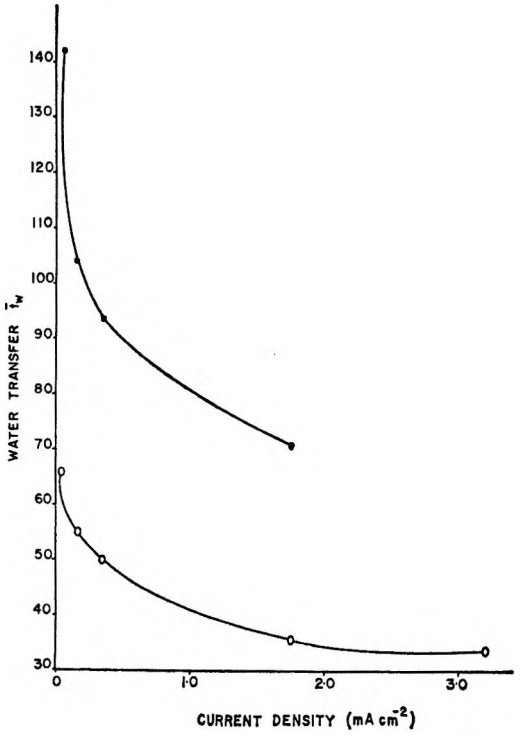

Figure 2. Water transfer, l_w, in Na form of PSA membrane as a function of current density: curve ● obtained with membrane of high water content supported by stainless steel mesh; curve O obtained with membrane of moderate water content and membrane movement controlled by application of pressure. Membrane area = 2.86 cm².

membranes of different water content were used. Results shown in Figure 3 depicting the independence of $\bar{l}_w$ on membrane area were derived for the same

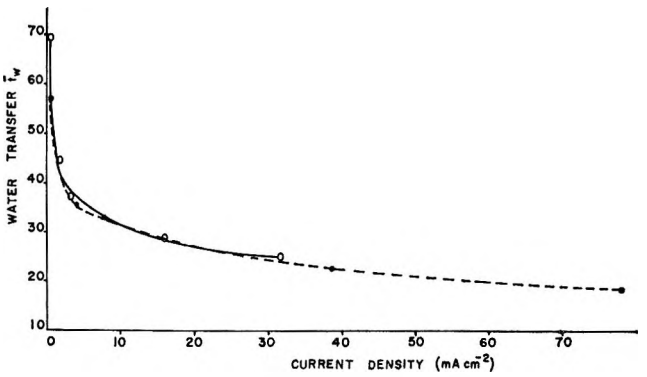

Figure 3. Water transport, l_w, in Na form of PSA membrane as a function of current density: curve ● obtained using membrane area = 0.13 cm²; curve O obtained using membrane area = 0.32 cm².

membrane or membranes belonging to the same batch. The effect of current density on $\bar{l}_w$ is quite obvious.

The $\bar{l}_w$ values given in Table II were obtained from experiments carried out with PSA and AMF membranes whose characteristics are presented in Table I.

Table II: Transference Number of Water, l_w, across Cation-Exchange Membranes in Contact with 0.01 *N* Solutions of Alkali Metal Chlorides as a Function of Current Density at 25°

Current density, mA/cm²	Li^+	Na^+	K^+	Rb^+	Cs^+
		PSA Membrane			
0.32	72.6	62.1	55.5	45.5	46.9
1.58	42.6	39.3	34.2	33.4	30.8
3.15	36.9	32.9	27.7	26.2	25.8
15.75	27.6	24.7	20.3	19.5	19.6
		AMF Membrane			
0.32	12.1	9.6	7.1	4.9	4.8
1.58	10.3	7.0	4.7	4.9	4.9
3.15	10.3	7.0	4.5	4.5	4.9
15.75	10.1	6.9	4.2	4.6	5.0

Discussion

The results obtained with PSA membranes confirm our earlier findings[1,6,14,15,30,32] about the current dependence of $\bar{l}_w$ in 0.01 *N* solutions. The data realized with AMF membranes, the water contents of which are comparatively low, support both the dependence of $\bar{l}_w$ on current density and also its independence of current density. The two parameters that control the pattern of behavior of $\bar{l}_w$ as a function of current density are membrane water content (or pore size) and the size of the migrating ion.

The equivalent radius of the pores of these membranes in H form has been determined by Lakshminarayanaiah[33] to be 33 and 8 Å for PSA and AMF membranes, respectively. The size of the hydrated ion of

the alkali metal series may be considered very small compared to the pore radius of the PSA membrane. However, in AMF membranes ion and pore sizes become comparable. In this membrane it is noticed that the $\bar{l}_w$ values (Table II) at low currents (0.32 mA/cm²) are higher, although the rise is small in the case of Li^-, Na^+, and K^+ ions and becomes independent of current density in the case of Rb^+ and Cs^+ ions.

The variation of $\bar{l}_w$ values with current density may be attributed to some of the conditions existing both at the membrane–solution interface and within the membrane. The interfacial phenomena involved, *viz.*, concentration polarization leading to membrane polarization, have been considered in detail by Lakshminarayanaiah.[1,6,30] These polarization effects may, however, be eliminated by efficient stirring of solutions and using low currents, the conditions under which the $\bar{l}_w$ values of Table II have been measured. Even the interruption technique described by Lakshminarayanaiah[6,30] was employed with PSA membranes in NaCl solution and the values obtained are in agreement with the values given in Table II. Consequently, the causes for the variation of $\bar{l}_w$ with current density were sought elsewhere within the membrane.

In the case of an ion-exchange membrane in which interactions (frictional or otherwise) between membrane–water and membrane–counterion are absent, one may assume water to move in the capillaries of the membrane (each capillary of radius r cm) at the same linear velocity, U cm/sec, as the counterion when an electric potential of E V acts across the thickness, X cm, of the membrane. If V is the volume (ml) of liquid flowing through the membrane per second, then the volume of liquid transferred for the passage of 1 faraday of current (F) is given by

$$\text{ml}/F = VF/I \tag{1}$$

where I is the current in amperes passing through the membrane. Therefore

$$\bar{l}_w = VF/18I \tag{2}$$

but

$$I = (E/X)n\pi r^2\bar{k} \tag{3}$$

n is the number of capillaries and $\bar{k}$ is the specific conductance of the pore liquid and

$$V = n\pi r^2 U \tag{4}$$

Substituting eq 3 and 4 into eq 2

$$\bar{l}_w = \frac{UF}{18(E/X)\,\bar{k}} \tag{5}$$

However, $UF/(E/X)$ is $\bar{\lambda}$ (equivalent conductance of pore liquid).

Therefore

$$\bar{l}_w = \frac{\bar{\lambda}}{18\bar{k}} = \frac{1000}{18}(1/\bar{C}) \approx \frac{55.6}{\bar{m}_+} \tag{6}$$

According to eq 6, $\bar{l}_w$ values measured should be the same as $\bar{m}_w$ values given in Table I. However, $\bar{l}_w$ values, in the case of PSA membranes, are higher than $\bar{m}_w$ at 0.32 mA/cm² and at higher currents lower than $\bar{m}_w$, in the case of Li^+ and Na^+ ions. All other ions with the two membranes give values for $\bar{l}_w$ lower than $\bar{m}_w$ but always increasing with decreasing current density, excepting Rb^+ and Cs^+ ions (AMF membrane) which show little dependence on current density.

This gross divergence of $\bar{l}_w$ values from the values predicted by eq 6 is due to omissions of interactions between the different components—membrane matrix, counterion, and water—of the membrane system. Spiegler[34] has considered these factors in great detail and, by applying the principles of irreversible thermodynamics to transport processes in ion-exchange membranes, has shown that the ratio of fluxes of free water (J_3) and mobile counterion (J_1) is given by

$$J_3/J_1 = C_3/[C_1 + C_3(X_{34}/X_{13})] \tag{7}$$

where C_3 and C_1 are concentrations of water and counterion in the membrane and X_{34} and X_{13} are friction coefficients between water–membrane matrix and counterion–water. When X_{34} is almost zero and X_{13} is large, *i.e.*, no interactions between membrane components, $J_3/J_1 = C_3/C_1$ which means $\bar{l}_w = 55.6/\bar{m}_+ = \bar{m}_w$; *i.e.*, eq 6 and 7 are identical. Both ion and water move at the same linear velocity.

When X_{34} is large and X_{13} is small, which is akin to moving the counterion through its surroundings without removing much free water with it, $\bar{l}_w$ will be small.

In order to explain the observed results (Table II and Figures 2 and 3) in terms of eq 7, it becomes nec-

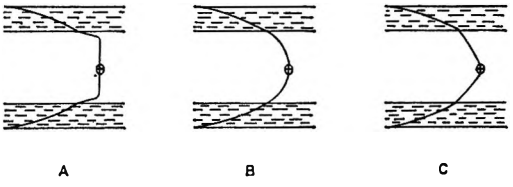

Figure 4. Water-flow profiles when the slipping plane is located in the compact Stern layer at: A, low current density; B, moderate current density; C, high current density.

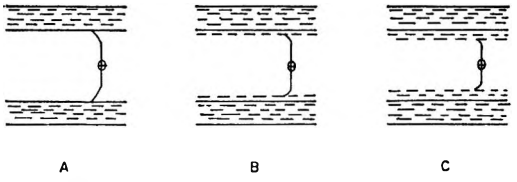

Figure 5. Water-flow profiles when the slipping plane is located in the diffuse Gouy layer at: A, low current density; B, moderate current density; C, high current density.

(34) K. S. Spiegler, *Trans. Faraday Soc.*, **54**, 1408 (1958).

essary to postulate that X_{34} and X_{13} are affected differently at different current densities. This is probably what is happening in PSA and AMF membranes. When pore size and ion size become comparable, as it seems they are in AMF membrane containing Cs^+ ions, X_{34} and X_{13} are affected to the same extent at different applied forces, *i.e.*, different current density, to produce the same quantity of water flow.

It is interesting to indicate that the changes in X_{34} and X_{13} following passage of different currents may cause shifting of the slipping plane between the fixed and the moving liquid to different regions in the electric double layer. If the slip plane is situated in the compact Stern layer,[35] the water-flow profiles at different current densities may be as shown in Figure 4. As 0.01 N electrolyte solutions are used with the membrane, there is little free salt present in the membrane phase. Consequently, the double layer will be broader than what it would be if the pore solution were concentrated by the presence of free salt.[36] The slip plane, therefore, is likely to be situated in the diffuse Guoy layer and at different current densities it may shift to different regions of the diffuse layer. Since a purely laminar flow is postulated[37] for the electroosmotic flow of liquid, the flow profiles indicated in Figure 5 probably prevail in these systems. All these possibilities, however, cannot explain the transport of 72.6 and 62.1 mol of water in the case of Li^+ and Na^+ ions (PSA membrane) at 0.32 mA/cm^2. These values exceed the interstitial water associated with 1 g-equiv ion by 17 and 15 mol, respectively. This may be caused by one of two factors. (1) All the ions may not be taking part in transport in which case molality $\bar{m}_+$ (Table I) is not the effective value; (2) transfer may be taking place through uncharged or slightly charged pores. In this case the molality of the counterion in the pore will be very small.

Factor 1 implies the existence of different types of ions which are mobilized at different current densities. At low currents, ions in the diffuse part of the double layer may carry the major part of the current. The other counterions existing closest to the fixed charges may take part in the transport at high currents. This points to an apparent breakdown of Ohm's law. It is shown, however, by Lakshminarayanaiah[32] that the system obeys Ohm's law giving the same resistance value at all currents. So it is concluded in accordance with discussions given elsewhere[1,6,30] that $\bar{l}_w$ values produced in excess of $\bar{m}_w$ are due probably to factor 2.

Acknowledgments. This work was supported by Grant No. 14-01-0001-1164 from the Office of Saline Water, U. S. Department of the Interior.

(35) J. Th. G. Overbeek in "Colloid Science," Vol. 1, H. R. Kruyt, Ed., Elsevier Publishing Co., New York, N. Y., 1952, p 132.

(36) S. Glasstone, "Text Book of Physical Chemistry," 2nd ed, Van Nostrand Co., Inc., New York, N. Y., 1946, p 1227.

(37) Reference 35, p 197.

Metachromasy of a Thiacarbocyanine Dye in Aqueous Solution: The Formation of Dimers and Trimers

by J. F. Padday

Research Laboratories, Kodak Limited, Wealdstone, Harrow, Middlesex, England *(Received September 20, 1967)*

Two hypotheses are current to explain the metachromasy of solutions of some dyes induced by such factors as dye concentration, addition of salt, and temperature. One explanation invokes the association of two or more dye ions to form an aggregate, the other the association of a dye ion with its counterion. Metachromasy of aqueous solutions of 3,3′-dimethyl-9-ethylthiacarbocyanine bromide has been studied by analyses of spectra coupled with estimates of counterion activities derived from emf measurements. It was concluded that ion pairing did not take place and that the spectral data were best interpreted as involving the formation of dimers and trimers of dye ions. Thermodynamic properties of the aggregates have been estimated from the temperature coefficients of the association constants and are consistent with strong dispersion force interaction between dye ions.

Introduction

The metachromatic behavior of cyanine and other dyes in solution has been the subject of a number of recent papers.[1-13] Spectral perturbations have been interpreted by some authors[2-7,12] on the basis of dye ions forming aggregates, principally dimers, following the early work of Sheppard and of Sheppard and Geddes[14] and supported by earlier workers.[15-18] Hillson and McKay[8-10] have interpreted the same spectral perturbations on the basis of a dye ion interacting with its counterion, following a hypothesis of Feichtmäyr and Schlag.[13] Electrochemical measurements of the counterion activity by the present author[19] have shown that for solutions of some dyes the ion–counterion interaction (ion pairing) was untenable.

Hillson and McKay[11] have withdrawn their original hypothesis of dye ion–counterion interaction in respect of one type of perturbation in water, the D state of the dye, but their interpretation of the further perturbation, the H state of the dye, remains in terms of ion–counterion interaction. Lamm and Neville[1] have further shown that analysis of the components of their spectra, although accurate, could not discriminate between dimer formation and ion association.

This study endeavors to determine the metachromatic states of the dye 3,3′-dimethyl-9-ethylthiacarbocyanine bromide in aqueous solution. The thiacarbocyanine dye was chosen for its stability to oxidation and because it showed well-defined D and H bands. The work also considers the special role of water structure[20] which involves, according to Diamond,[21] a special type of ion pairing of large organic cations induced by a phenomenon referred to as hydrophobic bonding.[22]

Experimental Section

Materials. 3,3′-Dimethyl-9-ethylthiacarbocyanine bromide was prepared and purified in these laboratories. The dye was recrystallized three times from water to give violet crystals which corresponded to the formula $C_{21}H_{21}BrN_2S_2 \cdot 2H_2O$. *Anal.* Calcd: C, 52.4; H, 5.20; Br, 16.6; N, 5.83; S, 13.3. Found: C, 51.9; H, 5.1; Br, 16.85; N, 5.87; S, 13.2. On warming under reduced pressure, water was given off and the crystals changed to a metallic greenish yellow color. These latter crystals corresponded to $C_{21}H_{21}BrN_2S_2$ but were unstable, as they picked up water from the atmosphere. The dye salt dihydrate was used to make up all solu-

(1) M. E. Lamm and D. M. Neville, *J. Phys. Chem.*, **69**, 3872 (1965).
(2) K. K. Rohatgi and G. S. Swigal, *ibid.*, **70**, 1695 (1966).
(3) G. S. Levinson, W. T. Simpson, and W. Curtis, *J. Amer. Chem. Soc.*, **79**, 4314 (1957).
(4) K. L. Arvan and N. E. Zaitseva, *Opt. Spectrosc.* (U.S.S.R.), **11**, 38 (1961).
(5) K. Bergman and C. T. Okonski, *J. Phys. Chem.*, **67**, 2169 (1963).
(6) G. R. Hughes and W. H. Melhuish, *Trans. Faraday Soc.*, **60**, 386 (1964).
(7) G. R. Haugen and E. R. Hardwick, *J. Phys. Chem.*, **67**, 725 (1963).
(8) R. B. McKay, *Trans. Faraday Soc.*, **61**, 1787 (1965).
(9) P. J. Hillson and R. B. McKay, *ibid.*, **61**, 1800 (1965).
(10) R. B. McKay and P. J. Hillson, *ibid.*, **62**, 1439 (1966).
(11) R. B. McKay and P. J. Hillson, *ibid.*, **63**, 777 (1967).
(12) W. West and S. Pearce, *J. Phys. Chem.*, **69**, 1894 (1965).
(13) F. Feichtmäyr and J. Schlag, *Ber. Bunsenges. Phys. Chem.*, **68**, 95 (1964).
(14) S. E. Sheppard, *Proc. Roy. Soc.*, **A82**, 256 (1909); S. E. Sheppard and A. L. Geddes, *J. Amer. Chem. Soc.*, **66**, 2003 (1944).
(15) G. Scheibe, *Kolloid-Z.*, **82**, 1 (1938); *Angew. Chem.*, **50**, 212 (1937).
(16) E. Rabinowitch and L. Epstein, *J. Amer. Chem. Soc.*, **63**, 69 (1941).
(17) L. Michaelis and S. Granick, *ibid.*, **63**, 1636 (1941).
(18) V. Zanker, *Z. Physik. Chem.* (Leipzig), **199**, 225 (1952).
(19) J. F. Padday, *J. Phys. Chem.*, **71**, 3488 (1967).
(20) M. J. Blandamer, M. C. R. Symons, and G. S. P. Verma, *Chem. Commun.*, 629 (1965).
(21) R. M. Diamond, *J. Phys. Chem.*, **67**, 2513 (1963).
(22) G. Nemethy and H. A. Scheraga, *J. Chem. Phys.*, **36**, 3382 (1962).

tions. Water was distilled in an all-glass still and checked for organic impurities by surface-tension measurement.

Method. The spectra of the dye solutions were measured on a Perkin-Elmer 137 uv recording spectrophotometer, the wavelength scale of which was calibrated with a holmium oxide filter. Matched cells were used where possible, but for concentrated dye solutions special cells were made by cementing together two pieces of optically flat glass separated by wire (0.005-in. diameter). The temperature of the solution in the cell was controlled by using a heating block attachment.

The activities of bromide ions in solution were derived from emf measurements of a reversible cell composed of a saturated calomel half-cell linked to a solution of the dye salt *via* a salt bridge and a reversible silver bromide electrode, as previously described.[19]

Results and Discussion

The measured optical densities of aqueous solutions of the dye 3,3′-dimethyl-9-ethylthiacarbocyanine bromide were converted into molecular extinction coefficients and are plotted as a function of wavelength in Figure 1. The main absorption peak in dilute solution (M band) occurred at λ 538 mμ, but at concentrations of dye in excess of 3.0×10^{-5} *M* a band (D band) at λ 502 mμ predominated. Above 1.0×10^{-3} *M* a new band appeared at λ 466 mμ (H band) which predominated in the region of saturation, 2.0×10^{-3} *M*. Other absorptions at λ 350, 445, and 650 mμ were observed but were not analyzed in the case of λ 445 and 650 mμ because the absorption was too small. The band at λ 350 mμ was only partially registered; hence it too was not analyzed. Designation of absorption bands follows that of West and Pearce.[12]

There is complete agreement that the state of the dye giving rise to the M band (M state) is that of the single dye cation. Electromotive force measurements[19] confirm that the counterion is fully dissociated from the dye existing in this state. Other states giving rise to the D and H bands (D and H states) are regarded as perturbed. Nonisosbestic behavior of the data of Figure 1 arises because there are at least three components and because some dye became adsorbed at the surface of the cells and produced errors which were relatively serious with dilute solutions but were of diminishing importance at higher concentrations. However, by altering the temperature of a cell to change the relative amounts of M and D states of the dye, a well-defined isosbestic point is obtained in dilute solution, as seen in Figure 2. At this concentration the amount of H state is insignificant and the losses from adsorption are constant. A similar but not so well defined isosbestic point is found at high concentrations, *ca.* 3×10^{-4} *M*, between the D and H bands, where

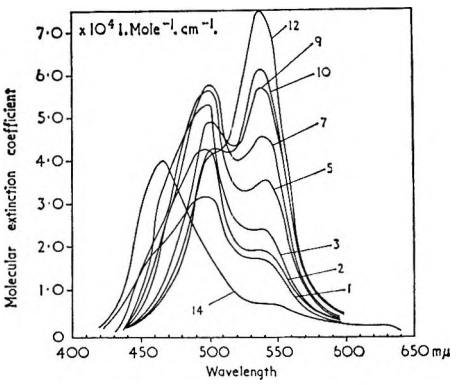

Figure 1. Molecular extinction coefficients of aqueous solutions of dye as a function of wavelength (at 20.0°). Molar concentrations: 1, 1.0×10^{-3}; 2, 7.0×10^{-4}; 3, 5.0×10^{-4}; 5, 1.5×10^{-4}; 7, 7.0×10^{-5}; 9, 3.0×10^{-5}; 10, 1.5×10^{-5}; 12, 7.0×10^{-6}; 14, saturated.

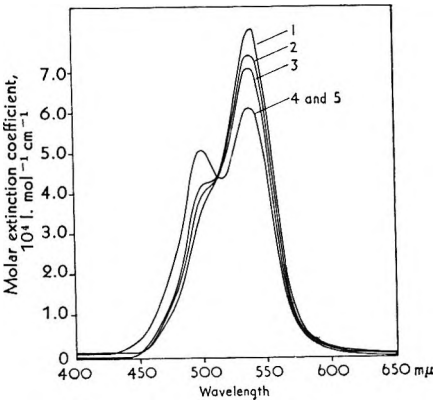

Figure 2. Molecular extinction coefficient of 10^{-5} *M* dye varying with temperature: 1, 60°; 2, 50°; 3, 40°; 4, 30°; 5, 20°.

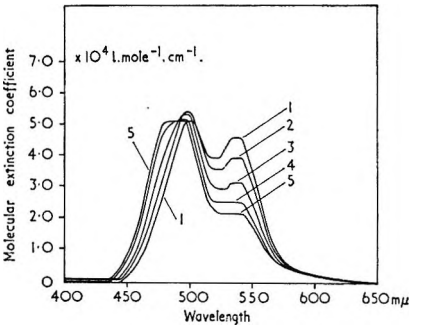

Figure 3. Molecular extinction coefficient of 3×10^{-4} *M* dye varying with temperature: 1, 60°; 2, 50°; 3, 40°; 4, 30°; 5, 20°.

now the amount of dye in the M state is of diminishing importance. This isosbestic point is seen in Figure 3.

The data of Figures 1–3 show the main features of the experimental results. The spectral absorption of 15 solutions of different concentrations in the range 5×10^{-6}–2×10^{-3} *M* have been measured at the temperatures 20, 30, 40, 50, and 60°. Only a representative portion of the original data is shown.

The spectral curves were resolved to give the amounts of dye in each state by the following steps. Let the amounts of dye in the M, D, and H states be C_M, C_D and C_H, respectively, and let the residue adsorbed to the side of the cell and otherwise lost be C_R. The amounts of dye in the M and D states together were obtained from the equation

$$C_M + C_D = \frac{\epsilon_{513}}{0.46 \times 10^4} \Sigma C_T \qquad (1)$$

where ϵ_{513} is the molecular extinction coefficient at λ 513 mμ and ΣC_T is the total dye concentration. The factor 0.46×10^4 is the maximum value of the extinction coefficient at this wavelength. Below the concentration 5×10^{-6} M, the difference $\Sigma C_T - C_M - C_D$ is the amount of dye adsorbed or otherwise lost, because at this concentration no H state is present. However, above 10^{-4} M, $\Sigma C_T - C_M - C_D$ is now principally a measure of C_H; this is because the amount of dye lost, C_R, is now insignificant. The method used for resolving C_M and C_D from the molecular extinction coefficient curves was that described by West and Pearce.[12] In this method the molecular extinction coefficient of the monomer (*i.e.*, at λ 538 mμ) is required and the value used was 1.05×10^4 l. mol^{-1} cm^{-1}, the value in methanol obtained under conditions where adsorption on the cell did not occur. The overlap of spectral absorption by the D state at the wavelength of the M band and by the M state at the wavelength of the D band was taken into account in the successive approximation method of West and Pearce's analysis.

The concentrations C_M, C_D, and C_H obtained in this way are plotted as a function of total dye in Figure 4. This figure shows the concentration regions in which each of the states M, D, and H predominates. The values of C_M were then plotted on a logarithmic scale as a function of log C_D, as in Figure 5. Below $C_D = 4 \times 10^{-4}$ M ($\Sigma C_T = 10^{-3}$ M), the plots were linear functions with a common gradient of 1.82 ± 0.05. Deviations from linearity above this concentration were probably due to the H band absorbing at the wavelength of the isosbestic point between the M and D states.

The slope of 1.82 is regarded as being sufficiently near 2.0 for the D state of the dye to be interpreted, through the law of mass action, as dimerization of the monomer according to

$$2M^+ \rightleftharpoons D^{2+} \qquad (2)$$

where M^+ refers to a single dye ion and D^{2+} refers to a dimer. The alternative reaction

$$M^+ + Br' \rightleftharpoons MBr \qquad (3)$$

though less likely, is not ruled out by these data.

A similar plot of log C_M as a function of log C_H at the same five temperatures is shown in Figure 6. Again it is found that the functions at each temperature

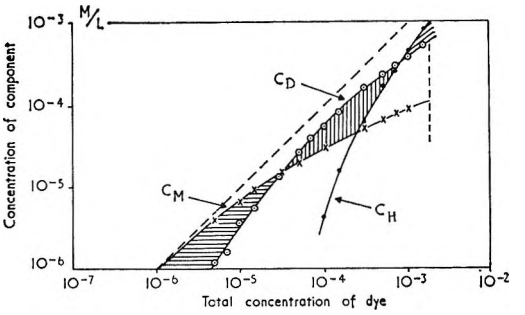

Figure 4. Log C_M, log C_D, and log C_H as functions of log concentration of total dye at 20°.

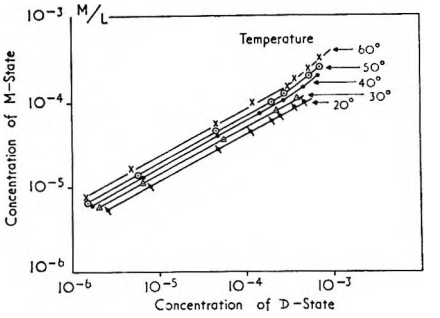

Figure 5. Log C_M as a function of log C_D at the temperatures 20, 30, 40, 50, and 60°.

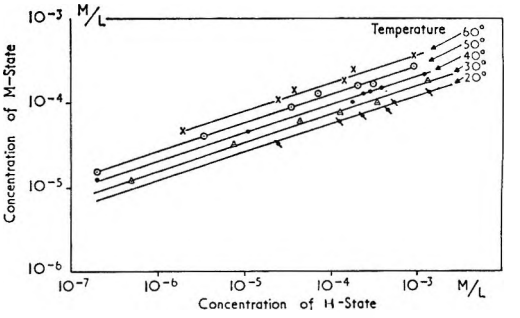

Figure 6. Log C_M as a function of log C_H at the temperatures 20, 30, 40, 50, and 60°.

are linear with a common gradient of 3.0 ± 0.06, but with a larger scatter than that found in Figure 5. By the law of mass action the likely reactions are

$$3M^+ \rightleftharpoons T^{3+} \qquad (4)$$

and

$$2M^+ + Br' \rightleftharpoons DBr^+ \qquad (5)$$

where T^{3+} indicates the formation of a trimer.

The ambiguity of interpretation from spectral data alone was overcome by measuring the bromide ion activity of solutions of higher concentrations of dye, on the basis that any dye–counterion interaction would lower the mean ionic activity coefficient of the dye and of the bromide ions. Accordingly, the emf's of the reversible cells with aqueous dye salt as electrolyte were

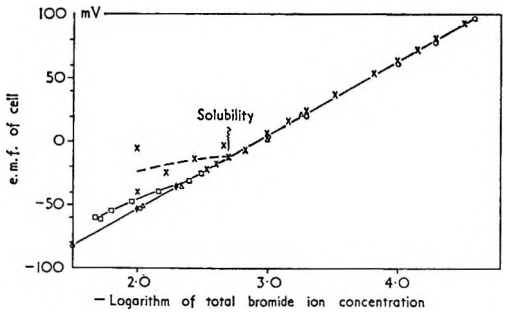

Figure 7. Reversible emf of the Ag–AgBr electrode with dye solution as electrolyte as a function of the logarithm of the total bromide concentration: O, KBr only; ×, dye salt only; Δ, 10^{-4} M dye salt and KBr; □, 10^{-3} M dye salt and KBr.

measured at the different concentrations. All emf data are plotted in Figure 7 as a function of the logarithm of the total amount of bromide added. At higher concentrations the measured emf was corrected by a very small amount, ΔE, given by the Debye–Hückel law where

$$\Delta E = -59.1\left\{\frac{0.5056\sqrt{C}}{1 + 1.444\sqrt{C}}\right\} \text{ mV} \qquad (6)$$

The emf data show clearly that the activity of the bromide ion in these solutions does not vary significantly from the concentration in any part of the concentration range of dye up to saturation at 2×10^{-3} M. Above this concentration the emf deviated markedly and steady measurements were impossible to obtain. The solubility of dye was measured directly by two methods (extraction with 1-butanol or with chloroform in the presence of salt) to give values of 1.94×10^{-3} and 1.80×10^{-3} M. These values agree with the concentration at which the emf first deviates from ideality. By measuring the emf of solutions of the dye salt well below the solubility limit of the dye, but with added KBr, the bromide ions were found to behave ideally. These data, in agreement with emf measurements on solutions of five other dyes,[19] are taken as substantial evidence that dye–counterion interaction did not take place when the dye was in true solution and showed marked metachromasy. Metachromasy involving the formation of either the D or H states of the dye cannot be explained by the ion-pairing reactions of eq 3 and 5, but metachromasy is entirely consistent with the formation of dimers for the D state, as already suggested, and of trimers for the H state according to eq 2 and 4, respectively.

To maintain consistency with experimental results the association constants of the dimers and trimers are defined by

$$k_1 = \frac{[C_D]}{[C_M]^{1.82}} \qquad (7)$$

and

$$k_2 = \frac{[C_H]}{[C_M]^{3.0}} \qquad (8)$$

The plots of log k_1 and of log k_2 as a function of $1/T$°K were both linear and were represented by

$$\log k_1 = \left[\frac{1.258 \times 10^3}{T(°K)} - 0.42\right] \pm 0.04 \qquad (9)$$

$$\log k_2 = \left[\frac{3.25 \times 10^3}{T(°K)} - 2.33\right] \pm 0.02 \qquad (10)$$

The free energy of dimer formation did not vary greatly with temperature: −5.20 kcal/mol at 20° and −5.12 kcal/mol at 60°.

The entropy of dimer formation was found to be −1.9 eu and was constant between 20 and 60°; the heat of formation was in consequence 5.76 kcal/mol.

The free energy of trimer formation dropped more rapidly with temperature than that of the dimer, that is, from a value of −11.7 kcal/mol at 20° to −11.2 kcal/mol at 60°. The entropy of trimer formation was again constant with a value of −10.6 eu, giving a constant heat of formation of 14.8 kcal/mol.

The formation of either a dimer or a trimer of this large dye ion is relatively insensitive to temperature, but the main effect of increasing temperature and hence thermal energy is to break up the aggregates of dye. This thermal effect is similar to the breaking up of micelles of a surfactant by increasing the temperature. The forces holding the aggregates together are very likely van der Waals forces and these hold the aggregate against thermal agitation and mutual electrostatic repulsion forces that would tend to separate individual dye ions.

van der Waals forces operate in three separate and distinct ways, each of which may be seen by reference to Figure 8. In this figure it is seen that dimerization involves the replacement of a volume of water, A, adjacent to the dye ion A^+ with another dye ion B^+, the displaced water, A, being removed to the vacated site formerly occupied by the dye ion B^+. This operation involves energy gained by (1) the total attraction of two dye ions adjacent to one another (*i.e.*, A^+ and B^+) and (2) the total attraction of the equivalent volumes of water adjacent to one another (*i.e.*, A and B) and energy lost in separating each dye ion from its adjacent volume of water that is to be replaced.

The strength of these forces will depend on the atomic structure of the dye, on its polarity and ability to bond with water, and on the configuration or geometry of the dimer. Although no direct evidence is available for the geometric arrangement of the two ions of a dimer, Wheatley[23] has shown that in the crystalline state, the dye 3,3′-diethylthiacarbocyanine bromide forms pairs. He has also shown that the atoms of each dye ion are arranged in a plane, with the chromophore

(23) P. J. Wheatley, *J. Chem. Soc.*, 3245 (1959); 4096 (1959).

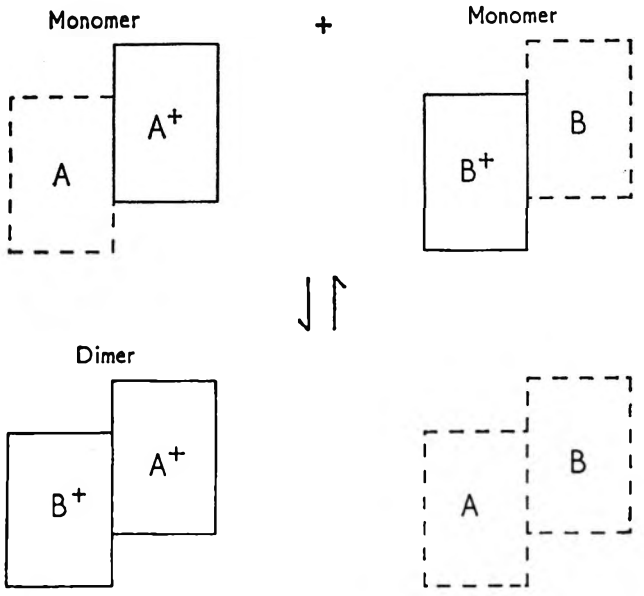

Figure 8. The exchange of places of a single dye ion with an equal volume of solvent adjacent to another single dye ion to form a dimer: ⊟, dye ion; □, equivalent volume of H_2O.

lying along the longest side. The single dye ions possess the shape of a rectangular prism of approximately $4 \times 8 \times 16$ Å, so that the pair of dye ions of Wheatley's crystal arrange themselves with their two largest faces adjacent to each other. As this arrangement is that to be expected from strong van der Waals forces, it will be assumed that the dimer is arranged similarly, with the positively charged chromophores of each dye lying *trans* to each other.

With this assumed geometric arrangement, it is now possible to make an estimate of the energies involved in forming the dimer. The area of surface affected (*i.e.*, one side of each of two dye ions and one side of each of two equivalent volumes of water) is 128 Å^2 (8×16 Å). The work of cohesion, W_c, of water at 20° is taken as 144 erg/cm^2 ($W_c = 2\gamma$); hence the work involved per mole of monomer is 13.3 kcal/mol. The work of cohesion between two dye ions is more difficult to obtain because in isolation two dye ions cannot possibly possess the same cohesion as in the bulk state. It is assumed here that the work of cohesion is 60 ergs/cm^2, this being a reasonable value obtained from the surface tension of similar compounds. This value produces an estimate of 5.5 kcal/mol as the work of attraction between two dye ions and it is based on the assumption that the dimer is held together mainly by dispersion forces.

The interaction between dye ion and water will be principally a dispersion interaction; if other polar forces were involved, the dye would be very much more soluble. The mean interaction energy must, therefore, lie between the value of water and that of dye. The value of the dispersion force contribution to the work of cohesion acting between two water molecules is 40 ergs/cm^2, as given by Fowkes,[24] and the value for the dye–dye interaction we have already taken as 60 ergs/cm^2. As the true value of the interfacial attraction must lie between these values, it seems reasonable to take 50 ergs/cm^2 as a crude estimate. This value gives a value of 4.6 kcal/mol for the dispersion interaction between dye and water, but to form one molecule of dimer two interfaces of dye–water have to be destroyed, as seen in Figure 8. The total energy of attraction is thus the sum of water–water attraction plus dye–dye attraction less twice the dye–water attraction: 13.3 kcal/mol + 5.5 kcal/mol − 9.2 kcal/mol = 9.6 kcal/mol.

This value must of course be greater than the effective attraction, because the electrostatic repulsion between two positive charges must be taken into account. The model chosen possesses an interchromophoric distance of 7 Å between two dye ions of the dimer, and this, with a dielectric constant for water of 78, gives an electrostatic repulsion of 0.6 kcal/mol. The dielectric constant would, however, be somewhat, if not considerably, lower as there is little room between the dye ions for many water molecules. If, for instance, the effective dielectric constant were 10, then the repulsion would be 4.7 kcal/mol.

These estimates then give a final value for the effective attraction between 4.9 and 9.0 kcal/mol of dimer or 2.5–4.5 kcal/mol of monomer. Although the experimental value lies close to the upper limit, the method of calculation cannot possibly show more than the relative magnitudes of the separate terms giving rise to the effective attraction energy.

There is little point in performing the same calculation for the trimer, as the order of magnitude of forces is likely to be about the same but with increased errors, since there is no way of knowing how its three dye ions are geometrically arranged.

Any agreement between the calculated and the measured energy of dimerization must be fortuitous, because the calculations have assumed that the surface tension of the dye can be used to calculate both the dye–dye and dye–water interactions and this would only be true for the bulk state and not for isolated dye ions. However, the estimates do give an idea of the maximum values of these energies. The interesting feature is that these maximum values are much lower than that of the water–water interaction; therefore, the main force giving rise to dimerization appears to be mutual attraction between water molecules rejecting the surface dye–water. Diamond[21] invokes a similar hypothesis to describe the deviations from the Debye–Hückel limiting law of large tetraalkylammonium ions in aqueous solution, but with the important difference that he supposed that the layer of water around

(24) F. M. Fowkes, *J. Phys. Chem.*, **67**, 2538 (1963).

the large organic ion possessed a structure different from that of bulk water. Although such an oriented layer may exist around the large organic ions and around the dye ions of this investigation, an unstructured water layer around the dye ions is quite sufficient to account for the aggregation of this dye in aqueous solution.

Some cyanine dyes form large aggregates, typified by strong absorption in the J-band region, that is, an intense narrow band at a wavelength longer than the M band.[25,26] Such aggregates and consequent J-band formation were found with the present dye in the concentration range of these experiments but in an amount too small to be of any significance to mass action effects. They have been reported for this dye when adsorbed on the surface of silver bromide.[26]

Aggregates larger than the dimer of dye in solution and yet showing the H-band type of absorption have been reported.[27-29]

A study of a thiacarbocyanine dye by Emerson, *et al.*,[27] revealed absorption peaks due to the dimer, trimer, and tetramer and possibly higher polymers. These aggregates were found to be substantially unaffected by the counterion. The study of the aggregation of thionine by Haugen and Hardwick[28] suggests the formation of higher polymers but with a substantial uptake of counterions.

The dye of these experiments follows closely the behavior of Emerson's system, but higher polymers, although probably present in small amounts, are prevented from forming in quantity by the solubility limit of the dye. Both thionine chloride of Haugen and Hardwick's study and the thiocarbocyanine dye of Emerson's study possess solubilities an order of magnitude greater than the dye of this study. It is thus very likely that higher aggregates are more readily detected at the high concentrations used in their experiments than at the solubility limit of the dye here.

Large aggregates of the H-band type may well account for perceptible absorption at λ 350 and 445 mμ, while absorption at 650 mμ must be derived from a J-band-type aggregate.

The counterion activity measurements in the region of the solubility limit suggest, though not conclusively, that higher aggregates, if present, do not take up counterions appreciably. Hence the model of Emerson, *et al.*, of highly charged aggregates seems more tenable than that of Haugen and Hardwick, who suggest that a thionine aggregate of N dye ions takes up $N - 1$ counterions.

(25) E. E. Jelley, *Nature*, **138**, 1009 (1936); **139**, 631 (1957).

(26) C. E. K. Mees, "The Theory of the Photographic Process," The Macmillan Co., New York, N. Y., 1954, p 459 ff.

(27) E. S. Emerson, M. A. Conlin, A. E. Rosenoff, K. S. Norland, H. Rodroquey, D. Chin, and G. R. Bird, *J. Phys. Chem.*, **71**, 2396 (1967).

(28) G. R. Haugen and E. R. Hardwick, *ibid.*, **67**, 725 (1963); **69**, 2988 (1965).

(29) R. Weingarten, *Melliand Textilber.*, **48**, 301 (1967).

Studies of Concentrated Polymer Solutions by the Fluorescence Polarization Method. II. Polyacrylamide in Water

by T. Yanagida, A. Teramoto, and H. Fujita

Department of Polymer Science, College of Science, Osaka University, Toyonaka, Japan *(Received September 20, 1967)*

The rotational friction coefficient, ζ_r, of a fluorescent residue attached to the terminal segment of polyacrylamide (PAA) was determined in aqueous solutions of PAA samples of different molecular weights, M. The variation of ζ_r at fixed temperature T with the polymer concentration was virtually independent of M over the range investigated. Steady-flow viscosities, η, of these solutions were measured over wide ranges of T and concentration. The apparent activation energy for viscous flow, E_a, calculated from these data depended significantly on M, especially in the region of relatively low concentration. A theory to account for this effect was developed, starting with the general expression $\eta = KM\phi_p\zeta G(M/M_c)$, where K is a constant characteristic of a given system, ϕ_p is the volume fraction of polymer, ζ is the average friction coefficient of polymer segments in solution, M_c is the average molecular weight between points of chain entanglement, and G is a function which expresses the contribution of chain entanglements to η. We assumed that ζ may be substituted by ζ_r derived from fluorescence measurements and that M_c varies with ϕ_p and T according to the equation $M_c = M_c^0(\phi_p)^{-\beta} \exp(-E_e/RT)$. Here E_e may be taken to indicate the energy for the formation of a chain entanglement in the undiluted polymer. It was found that the values of G calculated from our data formed a single composite curve when plotted against M/M_c, with M_c being evaluated from the above expression with $\beta = 1.63$ and $E_e = 2.2$ kcal/mol. On a log–log graph, this curve was represented approximately by two intersecting lines of slopes 0 and 2.8; this latter value is slightly higher than the usually suggested one, 2.5. It was found that the M dependence of E_a was attributable to the nature of this composite curve for G and the nonzero value of E_e obtained.

Introduction

The fluorescence polarization method, when applied to polymer solutions, allows one to estimate the free volume, f_e, of the local medium around a particular polymer segment to which a fluorescent residue is conjugated. In part I,[1] this method was applied to aqueous solutions of relatively low molecular weight samples of polyethylene oxide, and it was shown that the values of f_e around the terminal segment of this polymer agreed with those of the average free volume, f, of the entire solution calculated from the temperature dependence of its bulk viscosity. The assumptions made in these determinations were as follows. The bulk viscosity, η, was written in the form

$$\eta = F \exp(1/f) \tag{1}$$

with f being taken to be a linear function of temperature T

$$f = f_0 + \alpha_f(T - T_0) \tag{2}$$

and F, f_0, and α_f being assumed to be independent of temperature. Here T_0 is a reference temperature to be chosen suitably. Next, f_e was related to the rotational friction coefficient, ζ_r, of the fluorescent residue attached to the polymer chain by the equation

$$\zeta_r = A_r \exp(1/f_e) \tag{3}$$

with A_r being assumed not only to be independent of the temperature but also of the polymer concentration. Finally, it was assumed that ζ_r can be evaluated from the degree of polarization of fluorescence, p, by means of the relation

$$(1/p) - (1/3) = [(1/p_0) - (1/3)][1 + (6RT\tau/\zeta_r)] \tag{4}$$

where p_0 is the limiting value of p at zero of the absolute temperature T, R is the gas constant, and τ is the excited lifetime of the fluorescent residue. Actually, we set

$$f_e = f/B_r \tag{5}$$

and examined how the factor B_r changed with the temperature, the polymer concentration, and the molecular weight of the polymer. The result was that B_r was virtually independent of these variables over fairly wide ranges studied.

The present paper is intended to report a similar study made with aqueous solutions of polyacrylamide. Here again, for the measurement of p and hence for the calculation of ζ_r, a fluorescent dye was conjugated to the terminal segment of the polymer chain and a very small amount of the labeled polymer was dispersed in solutions of an unlabeled polymer of the same species. The important difference from Part I is that the polymer samples used in this work had much higher molecular weights.

(1) H. Tanaka, T. Yanagida, A. Teramoto, and H. Fujita, *J. Phys. Chem.*, 71, 2416 (1967).

Experimental Section

Materials. Seven samples of polyacrylamide (PAA) were prepared by radical polymerization in aqueous solutions of methanol at 80–90°, using hydrogen peroxide as initiator. Each of them was separated into three or four fractions by fractional precipitation, and the major middle fractions were chosen for the present study. Their codes are indicated in Table I.

Table I: Molecular Weights of Polyacrylamide Samples Used

Sample code	$[\eta]$, dl/g[a]	$10^{-4}\bar{M}_v$	$10^{-4}\bar{M}_w$
PAA-1	0.164	1.22	1.22
PAA-2	0.192	1.68	
PAA-5	0.363	4.0	
PAA-10	0.610	7.6	
PAA-21	1.14	16.2	
PAA-45	2.3	38	
PAA-70	4.0	87	
PAA-C1	0.096	0.56	0.55
PAA-C16	0.838	11.9	

[a] In water at 25°.

Two fluorescent conjugates of PAA, in which fluorescein was bound by a covalent bond at the terminal segment of the polymer chain, were prepared by the method of Nishijima, *et al.*,[2] and each of them was separated into several fractions. Two appropriate fractions, designated below as PAA-C1 and PAA-C16, were selected for use in the fluorescence measurements.

The weight-average molecular weights, $\bar{M}_w$, of two of these fractions were determined by the sedimentation equilibrium method[3] with water at 25° as solvent. The Rayleigh interference optical system was used for the measurements. The necessary value for the partial specific volume of PAA in water at 25° was determined with a pycnometer having a capacity of about 24 ml, and a value of 3.707 ml/g was obtained. This result is significantly lower than the value (0.769 ml/g) reported by Scholtan.[4] The reason for this discrepancy is not clear to us. With our new value, we recalculated Scholtan's molecular weight data, which had been deduced from the measurements of sedimentation and diffusion coefficients using the Svedberg relation. Then Scholtan's data for the limiting viscosity number in water at 25° were plotted against these corrected molecular weights on a log–log graph paper, and a smooth line fitting the plotted points was drawn. Molecular weights (viscosity average) of other samples were estimated using this line and are listed in Table I under the heading $\bar{M}_v$.

Test Solutions. Solutions to be used for viscosity measurements were prepared by mixing weighed amounts of water and a given PAA fraction in a stoppered flask, and those for fluorescence measurements were obtained by adding a small amount of either PAA-C1 or PAA-C16 to them. The concentration of the fluorescein residue in each solution was kept as low as 10^{-5} mol/l. or less. A dependence of the degree of polarization of fluorescence on the pH of the solution, similar in nature to that observed previously with polyethylene oxide,[1] was also found here. In order to avoid the complexity due to this effect, we adjusted the pH value of each solution to 6.5–8 by addition of $NaHCO_3$.

Viscosity Measurement. The following three types of viscometer[5,6] were used, depending on the magnitude of η of a given solution: capillary viscometers of the Ubbelohde type for η up to 1 P, pipet-type viscometers or uniform-bore viscometers for η ranging from 10^{-2} to 10^3 P, falling-ball viscometers for η between 1 and 10^6 P. These were calibrated at 20° with either an NBS liquid oil (Lot No. 32) or distilled water being used as a reference liquid.[6] Measurements were made in the range from 0 to 60° for all samples but PAA-45, for which the range was from 5 to 90°. The concentration range studied depended on the molecular weight of the chosen sample. When necessary, the measured viscosities were corrected for the shear rate effect in the manner described previously.[5]

The density of the solution, ρ, as a function of the weight fraction of the polymer component, w_p, was determined at a number of temperatures, with fractions PAA-2 and PAA-21 being chosen as samples. For example, the data at 25° were represented accurately by the relation

$$\rho = 0.9971 + 0.30w_p$$

for $0.02 < w_p < 0.5$.

Fluorescence Measurement. The apparatus and method used were similar to those described in Part I. Use was made of cylindrical cells having a capacity of about 30 ml for solutions of low viscosity and a square cell of dimensions $1.5 \times 1.5 \times 4.0$ cm^3 for solutions of high viscosity. Air bubbles, when trapped in the solutions, were removed under reduced pressure. Each solution was excited by vertically polarized light of the wavelength of 436 mμ, and the degree of polarization of fluorescence was calculated according to the usual definition. The temperature range of measurement was from 5 to 50°. Effects of polymer concentration were most extensively studied with PAA-5 in the range of w_p from 0 to 0.5. The measurements over a similar

(2) Y. Nishijima, A. Teramoto, M. Yamamoto, and S. Hiratsuka, *J. Polym. Sci., Part A-2*, 5, 23 (1967).

(3) H. Fujita, "Mathematical Theory of Sedimentation Analysis," Academic Press Inc., New York, N. Y., 1962, Chapter V.

(4) W. Scholtan, *Makromol. Chem.*, 14, 196 (1954).

(5) R. Okada, A. Teramoto, and H. Fujita, *J. Phys. Chem.*, 67, 1228 (1963).

(6) A. Teramoto, S. Kusamizu, H. Tanaka, Y. Murakami, and H. Fujita, *Makromol. Chem.*, 90, 78 (1966).

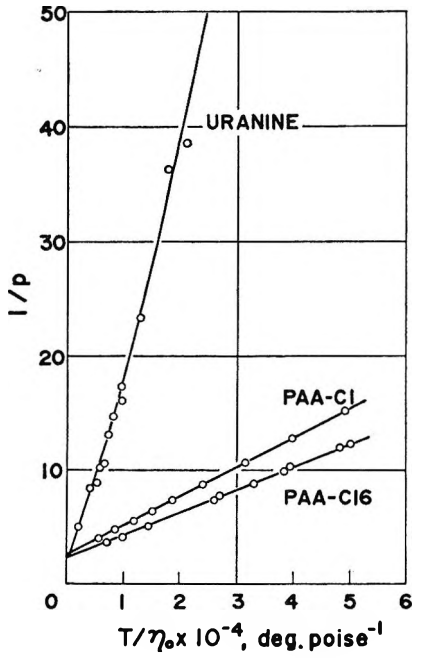

Figure 1. Plots of $1/p$ (p is the degree of polarization of fluorescence) *vs.* T/η_0 for uranine and fluorescein conjugates of polyacrylamide in aqueous media.

range of w_p were also made with solutions of PAA-5 in which uranine was freely dispersed as a fluorescent indicator.

Results

Fluorescence Data. At infinite dilution of the solution, it may be expected that the rotational friction coefficient, ζ_r, of a fluorescent molecule or a polymer segment to which a fluorescent residue is conjugated changes in proportion to the viscosity of the solvent medium, η_0. Hence, according to eq 4, a straight line should be obtained if one plots values of $1/p$ measured in the absence of polymer solute against T/η_0.[2] Figure 1 shows that this prediction is well borne out by the data with our PAA conjugates and uranine in water, although the line with uranine exhibits a slight upward curvature. It is seen that the three lines indicated converge to nearly identical points on the ordinate axis, thus yielding essentially the same values for p_0. This result is consistent with the prediction that p_0 should be a photochemical constant characteristic of fluorescein.

Once the value of p_0 is obtained in this way, we can calculate ζ_r at nonzero polymer concentrations by substituting the corresponding measured values of p into eq 4, provided that the value of τ for the conjugate is known in advance. In the present calculations, a value of 4.8×10^{-9} sec was assumed for τ in all cases examined.[2,7,8] Figure 2 shows log ζ_r so obtained for PAA-C1 in aqueous solutions of PAA-5 as a function of temperature. Similar results were obtained with PAA-C16 and uranine in aqueous solutions of the same PAA. From these as well as similar data obtained in

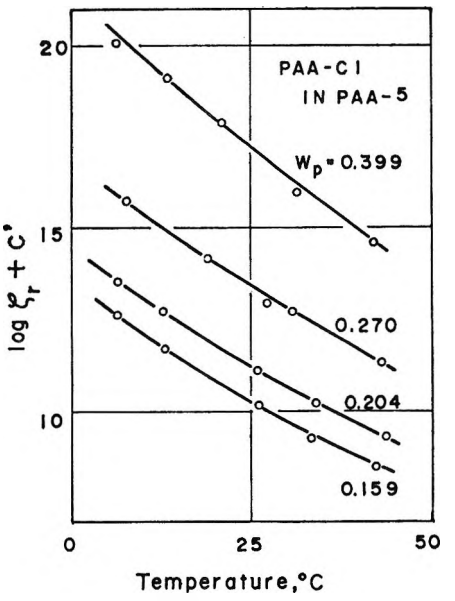

Figure 2. Temperature dependence of ζ_r (in erg sec/mol) for PAA-C1 at various weight fractions, w_p, of PAA-5 in water.

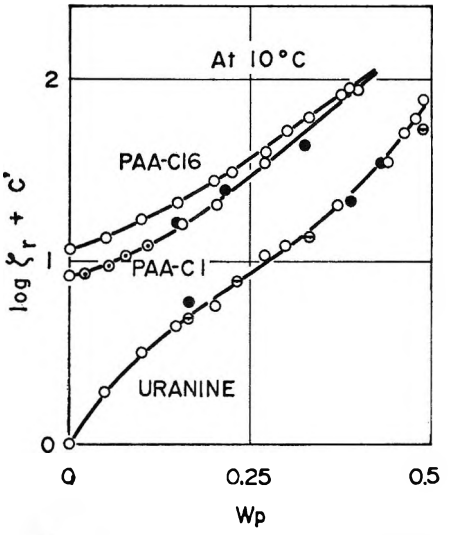

Figure 3. Concentration dependences of ζ_r for PAA-C1, PAA-C16, and uranine in aqueous solutions of PAA samples of different molecular weights at 10°: ●, in PAA-2; ○, in PAA-5; ⊖, in PAA-10; ⊙, in PAA-70.

solutions of other PAA samples, the values of ln ζ_r at 10° were directly taken or interpolated and plotted against the weight fraction of PAA in Figure 3. It is seen from the plots for uranine and PAA-C1 that for a given fluorescent conjugate the relation between ζ_r and w_p is hardly affected by the molecular weight of the polymer present in the solution. Though not checked experi-

(7) A. Teramoto, S. Hiratsuka, and Y. Nishijima, *J. Polym. Sci., Part A-2*, 5, 37 (1967).

(8) R. F. Steiner and A. J. McAlister, *J. Polym. Sci.*, 24, 105 (1957).

mentally, this same conclusion could have been obtained with PAA-C16. Features of this family of curves is essentially similar to those on this same system reported by Teramoto, *et al.*,[7] and also on the polyethylene oxide–water system studied previously.[1] Of special notice is the fact that the curve for PAA-C16 lies a little above that for PAA-C1. This difference may be accounted for by the idea as proposed in part I. It has been suggested that a relatively low molecular weight conjugate should be used to evaluate the net effect of the surrounding medium on the mobility of a polymer segment.[1,7] Following this suggestion, we here regard the curve for PAA-C1 as representing the net effect of PAA concentration on the friction coefficient of the segment to which the fluorescein residue is conjugated.

Viscosity Data. Zero-shear viscosities of PAA-5 and PAA-10 in water at various fixed values of w_p are shown as a function of temperature in Figure 4. The results obtained with other PAA samples were similar to this graph. Figure 5 indicates log η at 40° for the six PAA samples studied as a function of w_p. From this family of curves the values of log η at fixed w_p are plotted against log $\bar{M}_v$ in Figure 6. The slopes of the curves at high molecular weights are about 4.0, which is a little higher than the generally suggested value of 3.4.[9–11] However, it is difficult to say whether this small deviation is real or not. Obviously, a more detailed study is needed in order to elucidate this point.

The data for each sample were plotted in the form of ln η against $1/T$, and the slope of the resulting line was determined graphically at 40° to evaluate the apparent

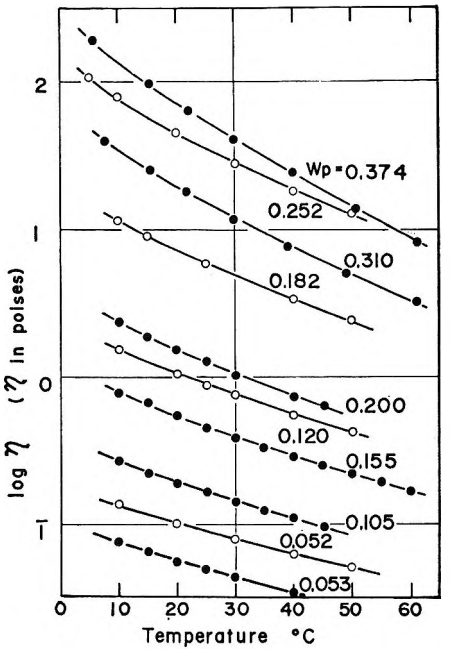

Figure 4. Plots of log η *vs.* temperature for aqueous solutions of PAA-5 and PAA-10 as functions of the weight fraction of the polymer, w_p: ○, PAA-10; ●, PAA-5.

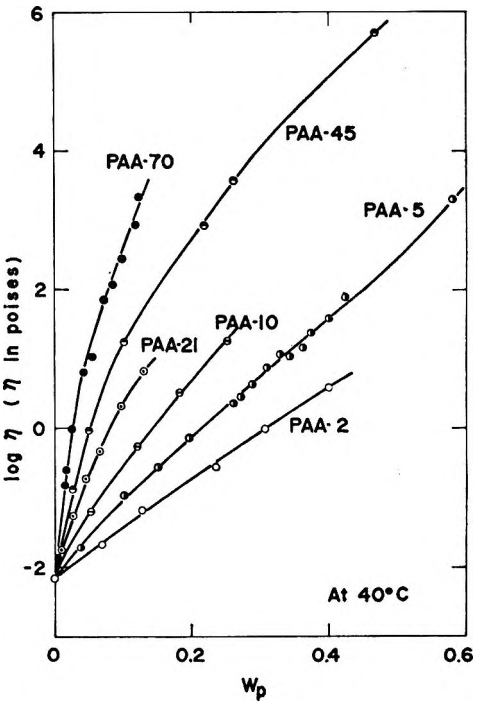

Figure 5. Concentration dependence of η for PAA fractions of different molecular weights in water at 40°.

activation energy for viscous flow, E_a, defined by the relation

$$E_a = R\mathrm{d} \ln \eta/\mathrm{d}(1/T)$$

The values of E_a so obtained for PAA-45, PAA-5, and PAA-2 are plotted against w_p in Figure 7. Although the accuracy of the plotted points may not be high, it is evident that when compared at a fixed w_p the value of E_a depends significantly on the molecular weight of the sample. A similar dependence of E_a on molecular weight has been reported for other polymer–diluent systems, *e.g.*, for poly(methyl methacrylate) in diethyl phthalate by Bueche.[12] The molecular weights of the samples used in this study were not low enough to exhibit end effects. It is, therefore, least likely that the observed dependence of E_a on molecular weight stemmed from the molecular weight dependence of the glass transition temperature of the polymer.

Discussion

Free-Volume Treatment. As in many other systems so far studied,[5,6,13] viscosity data from the present measurements on aqueous solutions of PAA were also fitted accurately by eq 1, with f being a linear function

(9) T. G Fox, S. Gratch, and S. Loshaek, "Rheology," Vol. I, F. R. Eirich, Ed., Academic Press Inc., New York, N. Y., 1956, Chapter 12.

(10) T. G Fox and V. R. Allen, *J. Chem. Phys.*, **41**, 344 (1964).

(11) G. C. Berry and T. G Fox, *Fortschr. Hochpolym. Forsch.*, in press.

(12) F. Bueche, C. J. Coven, and B. J. Kinzig, *J. Chem. Phys.*, **39**, 128 (1963).

(13) A. Teramoto and H. Fujita, *Makromol. Chem.*, **85**, 261 (1965).

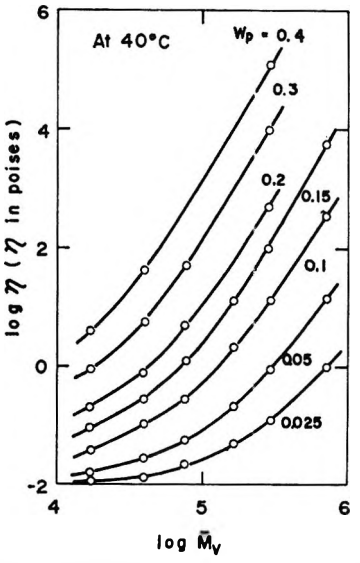

Figure 6. Molecular weight dependence of η for PAA in water at 40° as a function of the weight fraction of polymer, w_p.

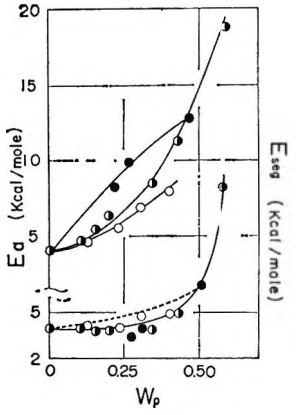

Figure 7. Upper part: apparent activation energy, E_a, associated with viscous flow of PAA in water at 40° as a function of the weight fraction of the polymer, w_p. Lower part: apparent activation energy, E_{seg}, associated with segmental motion of PAA in water at 40° as a function of w_p. Points calculated from E_a using the procedure explained in the text: ○, PAA-2; ◑, PAA-5; ●, PAA-45. Dashed line directly evaluated from the data for ζ_r given in Figure 2.

of T. In Figure 8 are shown the resulting values of f at $T = 40°$ as a function of w_p. One can observe that the plots for samples of different molecular weights do not collect to a single line. If, as generally conceived, f in eq 1 were the average fractional free volume of a polymer–diluent system, its form as a function of concentration should become independent of the chain length of the polymer, unless the sample is short enough to exhibit an end effect. For the relatively high molecular weight samples treated in this work, no significant end effect is conceivable. Therefore, we cannot help concluding that the values of f presented in Figure 8 are a combined effect of the average free volume of a polymer segment and something else which depends both on the temperature and the molecular weight of the polymer.

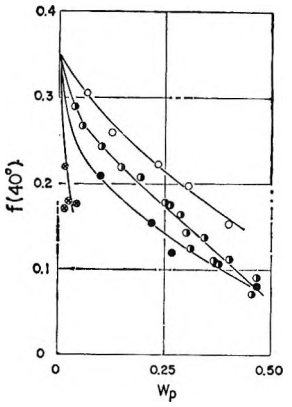

Figure 8. Values of f in aqueous solutions of various PAA fractions at 40° as a function of the weight fraction of the polymer, w_p: ○, PAA-2; ◐, PAA-5; ●, PAA-45; ⊗, PAA-70.

It is evident that this latter is responsible for the molecular weight dependence of E_a, as displayed in Figure 7.

The fact that the value of ζ_r at infinite dilution of the solution, designated here by ζ_r^0, varies in proportion to the viscosity of pure solvent, η_0, implies that f_e in eq 3 coincides with f at this limit. Therefore, it follows from eq 3 that f_e can be calculated using the expression

$$f_e^{-1} = (f^0)^{-1} + \ln (\zeta_r/\zeta_r^0)$$

where f^0 is the value of f obtained by fitting eq 1 and 2 to the temperature dependence data of η_0.

Figure 9 shows the values of f_e at 40° calculated from the fluorescence data for PAA-C1 using the above-mentioned method. It can be seen that, unlike f plotted in Figure 8, f_e in solutions of PAA samples of different M virtually follow a single curve when plotted against w_p. The factor B_r defined by eq 5 was evaluated from this curve and the curves for f shown in Figure 8. Though not displayed here, the result was that B_r decreased significantly upon increase of w_p, and, more important, this trend was more appreciable in solutions of a higher molecular weight sample. As has been noted in the Introduction, B_r was essentially independent of w_p and M in the system polyethylene oxide–water studied in part I.

Unless the molecular chain is short enough to exhibit end effects, the mobility of a polymer segment in solution and hence its free volume may be expected to be independent of chain length. The data shown in Figure 9 indicate that the quantity f_e associated with ζ_r has the character just consistent with this usual concept of the free volume of a polymer segment. Based on this fact, we wish to assume here that ζ_r as a function of w_p and T may be taken to represent the concentration and temperature dependence of the average friction coefficient, ζ, of all polymer segments in solution. This is equivalent to assuming the proportionality between

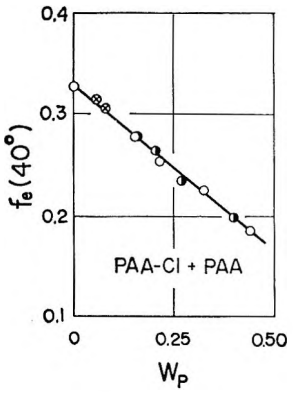

Figure 9. Values of f_e for PAA-Cl in aqueous solutions of various PAA fractions at 40° as a function of w_p; the same symbols as in Figure 8.

ζ and ζ_r. Our data for ζ_r have been determined with a fluorescent residue attached to the end of a polymer chain. On the other hand, the major contribution to ζ comes from the segments which belong to the central part of dissolved polymer chains. Therefore, it must be recognized that, as far as the present case is concerned, there is an additional uncertainty in assuming the direct proportionality between ζ and ζ_r.

Interpretation of Viscosity Data. The viscosity of a polymer solution, η, is generally expressed by the equation

$$\eta = K\phi_p MG\zeta \tag{6}$$

unless the solution is so dilute that the contribution of the solvent viscosity to the total viscosity may not be neglected. In eq 6, K is a constant characteristic of the given polymer–diluent system, ϕ_p is the volume fraction of the polymer component, M is the molecular weight of the polymer, ζ is the average friction coefficient of a polymer segment, and G is the factor which expresses the effect that, in concentrated solutions of a polymer, the molecular chains entangle each other so that the motion of each chain as a whole, either rotational or translational, may be hampered by other chains entangling with it.

It is reasonable to assume that G depends on the average number of other chains which entangle with any given chain. This number is given by M/M_c, where M_c is the average molecular weight of chains between points of entanglement. The friction coefficient, ζ, is essentially a function of temperature and polymer concentration, unless the molecular weight, M, is too low. Thus eq 6 can be written explicitly as

$$\eta = K\phi_p MG(M/M_c)\zeta(T,\phi_p) \tag{7}$$

where the volume fraction, rather than the weight fraction, has been used to indicate the dependence of ζ on concentration. Fox and Allen[10] (see also Berry and Fox[11] have assigned for $G(M/M_c)$ a specific form such that

$$G(M/M_c) = (M/M_c)^{2.5} \quad (M_c < M)$$
$$= 1 \quad (M_c > M) \tag{8}$$

in accordance with the theory of Bueche.[14] They also have taken M_c to vary with ϕ_p following the relation

$$M_c = M_c^0/\phi_p \tag{9}$$

and assumed that M_c^0, the value of M_c for the undiluted system, does not depend on temperature. Under these assumptions, it turns out that η depends on temperature only through the friction coefficient, ζ, and, therefore, the form of this dependence becomes independent of M at any fixed concentration. This is equivalent to saying that the apparent activation energy, E_a, at a specified temperature and concentration becomes identical irrespective of the value of M. It has been shown above (see Figure 7) that this feature was not exhibited by the PAA–water system studied. Accordingly, for the interpretation of the viscosity behavior of this system, the treatment of Fox and Allen[10] is no longer applicable but must be modified so that an additional temperature dependence may arise from the G factor. This can be done only by allowing M_c to vary with temperature.

In the present treatment, we shall not specify the form of G but shall assume the following form for M_c

$$M_c = M_c^0(\phi_p)^{-\beta}\exp(-E_e/RT) \tag{10}$$

where M_c^0, β, and E_e are taken to be independent of M, ϕ_p, and T. E_e may be regarded as the energy for the formation of a chain entanglement in the undiluted state of a given polymer. When $\beta = 1$ and $E_e = 0$, eq 10 reduces to eq 9, that has been assumed by Fox and Allen.[10]

If G depends only on M/M_c and if eq 10 is valid, it follows that, for a suitable set of values of β and E_e, data for G at different M, ϕ_p, and T can be collected on a single curve when plotted against $M(\phi_p)^\beta\exp(E_e/RT)$. In order to check this possibility, we calculated values of G at 10 and 40° from our viscosity data, substituting the measured values of ζ_r (obtained with the lower molecular weight conjugate PAA-C1) for ζ, and found that they yielded a nearly satisfactory composite curve when we assigned about 2.2 kcal/mol for E_e and about 1.6 for β. Figure 10 shows such a composite curve for the case where $E_e = 2.2$ kcal/mol and $\beta = 1.63$. The data for ϕ_p below 0.05 are not included in this graph, since they may contain an appreciable contribution from solvent viscosity (note that eq 7 applies only under the condition in which such a contribution is negligible).

The value of E_e obtained is not unreasonable, considering that a weak attractive force may be responsible

(14) F. Bueche, *J. Chem. Phys.*, 20, 1959 (1952); "Physical Properties of Polymers," Interscience Publishers, Inc., New York, N. Y., 1962.

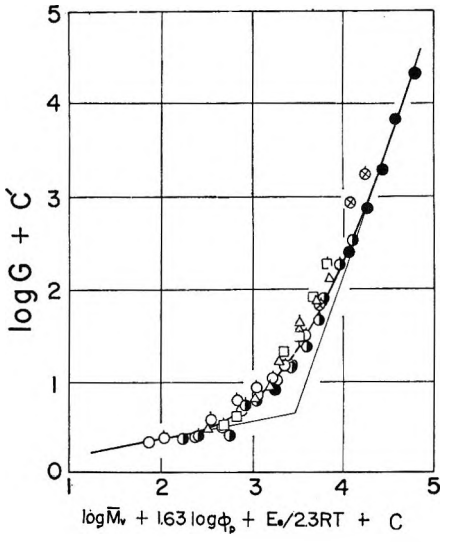

Figure 10. Reduction of G values at various M_v, ϕ_p, and T to a single composite curve. C and C' are numerical constants; actually, C equals $-E_e/2.303\ R[313(°K)]$ with E_e = 2.2 kcal/mol. In the graph, the data for a given M and different ϕ_p are indicated by an identical mark: PAA-2, ○ (40°), ◌ (10°); PAA-5, ◑ (40°), ◔ (10°); PAA-10, △ (40°), ◬ (10°); PAA-21, □ (40°), ⬚ (10°); PAA-45, ● (40°), ◉ (10°); PAA-70, ⊗ (40°), ⊗ (10°).

for the formation of a chain entanglement. The value obtained for β is appreciably greater than unity, implying that in the system PAA–water the average distance between entangling points increases much faster with the increase of the solvent content than would be expected from eq 9. However, it is a little hazardous to accept this implication literally, since we have substituted ζ_r for ζ. If ζ has a stronger concentration dependence than ζ_r, the correct β should be closer to unity than the value obtained above.

The composite curve for log G shown in Figure 10 does not follow eq 8, nor does it display a definite break. However, it can be approximated reasonably well by two intersecting lines of different slopes. The line above the break has a slope of 2.8, instead of 2.5 indicated in eq 8. Thus it follows from eq 7 that the viscosity at a fixed concentration of PAA increases linearly with $M^{3.8}$ above a certain value of M. This same fact has already been remarked in Figure 6.

Molecular Weight Dependence of E_a. Substituting eq 7 into the defining equation for E_a, the apparent activation energy for viscous flow, yields

$$E_a = \alpha E_e + E_{seg} \tag{11}$$

where

$$\alpha = \mathrm{d}\ln G(x)/\mathrm{d}\ln x \tag{12}$$

with

$$x = M(\phi_p)^{\beta}\exp(E_e/RT) \tag{13}$$

and E_{seg} is the contribution from ζ, *i.e.*, the activation energy for segmental motion. The first term on the right-hand side of eq 11 stems from the dependence of M_c on temperature, but it is not the energy for chain entanglement itself. As illustrated in Figure 10, the curve for ln $G(x)$ *vs.* ln x may not be linear. Hence, in general, α varies with x, *i.e.*, with M, ϕ_p, and T. On the other hand, E_{seg} is essentially independent of M. Thus the molecular weight dependence of E_a as observed in Figure 7 can be attributed to the fact that the term αE_e is not only nonzero but changes with M through the factor α.

For PAA-2, PAA-5, and PAA-45, we have calculated αE_e at 40° as a function of w_p, using the curve for log $G(x)$ *vs.* log x depicted in Figure 10, and we have subtracted the resulting values from the corresponding values of E_a to find E_{seg}. The results are plotted in the bottom half of Figure 7. It is seen that the plotted points for different molecular weights nearly collect to a single curve, which comes quite close to the values (dashed line) estimated directly from the experimental data for ζ_r shown in Figure 2. It should be noted that this coincidence is no more than a check on the internal consistency of the analysis of viscosity data presented above.

The major assumption in the above development was to replace ζ by ζ_r determined from fluorescence measurements. This may be open to criticism. When E_e = 0, the G factor does not depend on T, and the temperature dependence of η is determined solely by that of ζ. In this case, the G factor may be evaluated by removing the temperature-dependent factor from measured values of η, using, for example, the method described by Fox and Allen[10] or by Berry and Fox.[11] This method is equivalent to assuming eq 1 and 2 and determining the parameters f_0 and α_f as functions of concentration from the temperature dependence data of η at various fixed w_p. The values of F (see eq 1) calculated from η with f so obtained may be taken to be proportional to $M\phi_p G(M/M_c)$, and so G can be evaluated as a function of M, T, and ϕ_p. There must be many polymer–diluent systems in which M_c depends appreciably on T, so that E_e may not be negligibly small. For such a system we now have no definitive way to separate ζ and G from experimentally determined η, and the introduction of a suitable assumption into either ζ or G becomes inevitable in order to proceed further. The substitution of ζ_r for ζ, which has been proposed in the present discussion, may be viewed from such a standpoint.

Acknowledgment. This study was supported in part by a grant-in-aid from the Ministry of Education. The help of Mr. Y. Hayashi of this laboratory in some of the fluorescence measurements is gratefully acknowledged.

Enthalpy and Entropy Increments above 298°K and a Σ-Plot Treatment of Vaporization Data for Niobium Pentachloride[1]

by F. J. Keneshea, D. Cubicciotti, G. Withers, and H. Eding

Stanford Research Institute, Menlo Park, California 94025 *(Received September 22, 1967)*

The saturation enthalpy increments above 298°K for the condensed phases of niobium pentachloride were measured in a drop calorimeter up to the critical point. The equation obtained for solid niobium pentachloride is $(H^\circ_T - H^\circ_{298})$(s)(298–478.9°K) = $[-10.53 + (3.535 \times 10^{-2}T)] \pm 0.07$ kcal/mol of $NbCl_5$. The equation for the liquid up to 600°K is $(H^\circ_T - H^\circ_{298})$(l)(478.9–600°K) = $[-12.12 + (5.726 \times 10^{-2}T) - (7.340 \times 10^{-9}T^3)] \pm 0.22$ kcal/mol of $NbCl_5$. Above 600°K and to the critical point (804°K), saturation enthalpy increments for the liquid are given in tabular form. Tables of entropy increments above 298°K to the critical point are also given for the condensed phases. These results were applied to literature vaporization data in a Σ-plot treatment. The values of the heat and entropy of sublimation obtained from this treatment are ΔH°_{298}(subl) = 22.41 ± 0.06 kcal/mol and ΔS°_{298}(subl) = 45.40 ± 0.11 eu.

Introduction

Niobium pentachloride gaseous molecules have been shown by electron diffraction to have a trigonal-bipyramidal structure.[2] Vibrational frequencies have been assigned to the gas molecules based on spectroscopic measurements made on the solid and on organic solutions containing the compound.[3,4] Thermodynamic functions for $NbCl_5$ gas have been calculated from these data.[3,5] For the condensed phases of niobium pentachloride, the enthalpy of formation has been measured[6,7] but other thermodynamic data have only been estimated.[6,8] In order to gain some needed information on the thermodynamics of the condensed phases of niobium pentachloride, we have measured the enthalpy increments above room temperature, using drop calorimetry. These results are reported below, along with derived values of the entropy increments. From the gaseous absolute entropy and the entropy of sublimation, a value for the absolute entropy of the solid at 298°K can be calculated. We obtained the entropy of sublimation at 298°K by making a Σ-plot treatment[9] of the many vapor pressure studies which have been reported in the literature,[10–15] using our enthalpy increment data in this treatment. The results of this Σ-plot treatment are also reported below and the resultant value of S°_{298}(s) is discussed.

Experimental Work

A. Method. Samples of $NbCl_5$ sealed in quartz ampoules were heated to the critical point and dropped into a calorimeter at room temperature to measure the heat evolved. Details of the calorimeter are described in earlier reports.[16,17]

B. Preparation of Samples. Commercially obtained $NbCl_5$ was stated to be 99.95% free of metal impurities. The powdered form used, however, contained over 2000 ppm of oxygen, probably present as the oxychloride and arising from hydrolysis of the pentachloride. The material used was freed of oxygen by sublimation in a stream of He saturated with $SOCl_2$. The use of $SOCl_2$ to convert the oxychloride to chloride has been discussed by Schafer and Kahlenberg[18] and the technique has been used by Pray[19] to convert other hydrated chlorides to the anhydrous salt. The reaction that takes place may be written as

$$NbOCl_3 + SOCl_2 = NbCl_5 + SO_2 \qquad (1)$$

(1) This work was supported by the Space Nuclear Propulsion Office, a joint agency of the U. S. National Aeronautics and Space Administration and U. S. Atomic Energy Commission, under USAEC Contract AT(04-3)-115.

(2) H. A. Skinner and L. E. Sutton, *Trans. Faraday Soc.*, **36**, 668 (1940).

(3) J. Gaunt and J. B. Ainscough, *Spectrochim. Acta*, **10**, 52 (1957).

(4) G. L. Carlson, *ibid.*, **19**, 1291 (1963).

(5) G. Nagarajan, *Bull. Soc. Chim. Belges*, 71, 324 (1962).

(6) H. Schafer and F. Kahlenberg, *Z. Anorg. Allgem. Chem.*, **305**, 291 (1960).

(7) C. A. Shchukarev, M. Oranskaya, and T. Shemyakina, *Russ. J. Inorg. Chem.*, **5**, 1036 (1960).

(8) V. M. Amosov, *Izv. Vysshikh Uchebn. Zavedenii, Tsvetn. Met.*, **6**, 104 (1963).

(9) D. Cubicciotti, *J. Phys. Chem.*, **70**, 2410 (1966).

(10) J. W. Johnson, W. Silva, and D. Cubicciotti, to be submitted for publication.

(11) W. 't Hart and G. Meyer, *Rec. Trav. Chim.*, **83**, 1233 (1964).

(12) K. M. Alexander and F. Fairbrother, *J. Chem. Soc.*, S223 (1949).

(13) J. B. Ainscough, R. J. W. Holt, and F. W. Trowse, *ibid.*, 1034 (1957).

(14) M. A. Opykhtina and N. A. Fleisher, *Zh. Obshch. Khim.*, **7**, 2016 (1937).

(15) D. N. Tarasenkov and A. V. Komandin, *ibid.*, **10**, 1319 (1940).

(16) H. Eding and D. Cubicciotti, *J. Chem. Eng. Data*, **9**, 524 (1964).

(17) D. Cubicciotti and H. Eding, *ibid.*, **10**, 343 (1965).

(18) H. Schafer and F. Kahlenberg, *Z. Anorg. Allgem. Chem.*, **305**, 327 (1960).

(19) A. R. Pray, *Inorg. Syn.*, **5**, 153 (1957).

In our procedure, dry He was bubbled through liquid $SOCl_2$ at room temperature and the saturated gas was passed over impure $NbCl_5$, heated to 200°. The gas stream from the $NbCl_5$ flask then passed through a 10-cm length of glass tubing (10–15 mm o.d.) heated to about 400°. The purified $NbCl_5$ was condensed directly into the quartz heat-content ampoules attached to the exit. After the ampoules were filled to the desired level, the system was flushed for at least 1 hr with He, occasionally heating the $NbCl_5$ to its melting point to remove any sulfur-containing gases trapped in the material. Finally the system was evacuated for at least 1 hr and the ampoules sealed off. The mass of the sample was determined by weighing the sealed and empty ampoule. The ampoule internal volume was determined by displacement of water by the sealed capsule and by the quartz alone. Data for the samples used are shown in Table I. After the calorimeter measurements were made, sample 2 was analyzed for Nb by weighing as Nb_2O_5. We found 34.31% Nb, compared to 34.39% calculated for $NbCl_5$.

Table I: Data for Heat-Content Samples

Sample	Weight of $NbCl_5$, g	Weight of quartz, g	Internal volume of capsule, cc
1	9.2194	5.8255	6.9605
2	1.4163	6.3656	1.9278
3	1.4333	5.6327	1.7827
4	3.5230	3.7830	3.2913

The melting temperature of the purified $NbCl_5$, determined by visual observation on four different samples sealed in evacuated capsules, was 205.7 ± 0.5°. (This is actually the triple point, but the difference between it and the melting point is negligible.) By contrast the impure material before treatment with $SOCl_2$ had a melting point of 204.7°. Values in the literature, reviewed for example by Schafer and Kahlenberg[6] and by Meyer, *et al.*,[20] range from 202 to 215°. Our value of 205.7 ± 0.5° is close to the value of 206.8 ± 0.3° obtained by Meyer, *et al.*, by extrapolating the liquidus curve of the $NbCl_5$–$NbOCl_3$ system to 100% $NbCl_5$.

The critical point of $NbCl_5$ was determined on sample 2 by heating it in a furnace provided with a viewing port and measuring the temperature for disappearance of the meniscus between the gas and liquid phases. We found a value of 531 ± 3° compared to 534° obtained by Nisel'son, *et al.*[21]

C. Results of Heat Measurements. A substantial fraction of the heat liberated during each drop was due to the heat content of the quartz; corrections were made using the equation given by Cubicciotti, *et al.*[22]

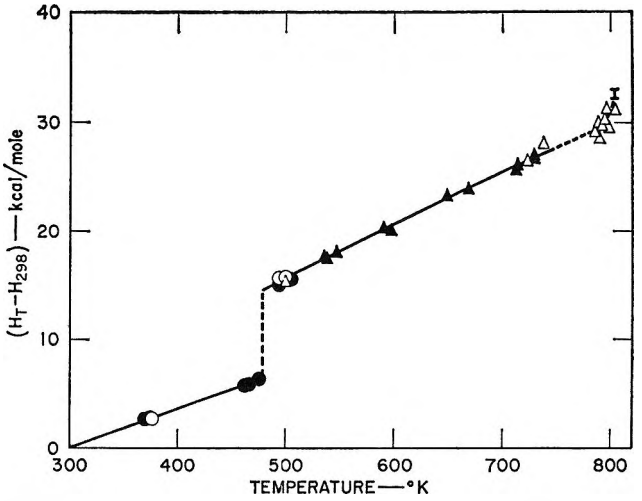

Figure 1. Enthalpy increments above 298°K for $NbCl_5$ solid and liquid; samples: ●, 1; ○, 2; △, 3; ▲, 4. Critical point shown by I.

A small part of the heat given up by the sample resulted from condensation of the vapor in the ampoule. This heat was calculated for each drop from the liquid and vapor densities,[10,21] the volumes of the ampoules, and the enthalpy of vaporization. The vaporization enthalpy was calculated from the Clausius–Clapeyron equation

$$\frac{dP}{dT} = \frac{\Delta H}{T\Delta V} \qquad (2)$$

with dP/dT taken from the vapor pressure equation of Hart and Meyer[11] and ΔV (gas volume minus liquid volume) determined from the vapor and liquid densities.[10,21] It was assumed that all of the vapor condensed at the drop temperature. The more exact calculation using the integrated heat of condensation and also the correction for the heat capacity of the vapor was considered unnecessary, since the vapor correction used was for the most part less than 0.7% of the total heat.

The data obtained from the drop-calorimeter experiments are shown as points in Figure 1.[23] The enthalpy increments above room temperature were fitted by the method of least squares to polynomial equations in T, T^2, and T^3. The linear equation obtained for solid $NbCl_5$ is

$$(H_T - H_{298})(s)(298\text{–}478.9°K) = [-10.53 + (3.535 \times 10^{-2}T)] \pm 0.07 \text{ kcal/mol of } NbCl_5 \qquad (3)$$

where the error shown is the standard deviation of the

(20) G. Meyer, J. F. Oosterom, and W. J. Van Oeversen, *Rec. Trav. Chim.*, **80**, 502 (1961).

(21) L. A. Nisel'son, A. I. Pustil'nik, and T. D. Sokolova, *Russ. J. Inorg. Chem.*, **9**, 574 (1964).

(22) D. Cubicciotti, H. Eding, F. J. Keneshea, and J. W. Johnson, *J. Phys. Chem.*, **70**, 2389 (1966).

points from the regression line. The liquid data from the melting point of 478.9°K to 750°K were best fitted by an equation in T and T^3.

$$(H_T - H_{298})(l)(478.9\text{–}750°K) = [-12.12 + (5.726 \times 10^{-2}T) - (7.340 \times 10^{-9}T^3)] \pm 0.22 \text{ kcal/mol of } NbCl_5 \quad (4)$$

The solid lines in Figure 1 were derived from eq 3 and 4. The dashed line extending from the solid line to the critical point was drawn so as to pass through as many data points as possible. The enthalpy increment at the critical temperature was estimated by the same method as described for $BiCl_3$.[22] It has been pointed out before[22,24] that the drop-calorimeter measurements give the saturation heat capacity, C_σ, and this is related to the saturation enthalpy and to the heat capacity at constant pressure, C_P, by the equations

$$\left(\frac{\partial H}{\partial T}\right)_\sigma = C_\sigma + V\left(\frac{\partial P}{\partial T}\right)_\sigma \quad (5)$$

$$= C_P + V\left[1 - \frac{T}{V}\left(\frac{\partial V}{\partial T}\right)_P\right]\left(\frac{\partial P}{\partial T}\right)_\sigma \quad (6)$$

At temperatures where the vapor pressure is less than a few atmospheres, the last term is neligible so that drop-calorimeter measurements give constant pressures as well as saturation-enthalpy increments. At higher pressures the differences become significant, although small. Since we have no information on the coefficient of expansion of the liquid, we can only evaluate saturation quantities above the temperature where the vapor pressure is a few atmospheres. We have taken 600°K, where the pressure is 4.5 atm,[11] as the dividing point for treatment of the data in the following sections.

Discussion

A. Enthalpy and Entropy Increments to 600°K. The enthalpy increments calculated for the condensed phases from eq 3 and 4 up to 600°K may be taken as standard increments (*i.e.*, referring to the substance in its standard state—under a constant pressure of 1 atm), since the differences from the saturation values are negligible in these measurements. Values of these standard enthalpy increments are listed for selected temperatures in Table II. The derivative with respect to temperature of eq 3 and 4 up to 600°K thus gives the constant-pressure heat capacity, C_P, and by integrating $C_P d \ln T$, values of the standard-state entropy increments have been calculated and are also listed in Table II. There are apparently no other experimental data with which to compare our results.

The heat capacity of the solid, C_P, from eq 3 has the constant value of 35.35 cal/deg mol. Schafer and Kahlenberg[6] give an estimated C_P (based on C_P for $ZrCl_4$ and $HfCl_4$) of $38 - (3 \times 10^5 T^{-2})$, which gives values in fair agreement with our results. Amosov's estimate[8] of $C_P = 26.71 + (35.2 \times 10^{-3}T)$, based on Neumann and Kopp's rule, gives a value 20% higher than our C_P at the melting point.

Table II: Thermodynamic Functions for $NbCl_5$ in Standard-State Condensed Phases up to 600°K[a]

Temp, °K	$H°_T - H°_{298}$, cal/mol	$S°_T - S°_{298}$, eu
300	75	0.25
350	1,843	5.67
400	3,610	10.40
450	5,378	14.57
478.9(s)	6,399	16.77
478.9(l)	14,493	33.67
500	15,589	35.91
550	18,149	40.77
600	20,648	45.15

[a] Calculated from eq 3 and 4.

Extrapolation of the solid and liquid enthalpy curves to the melting point gives a heat of fusion of 8.09 ± 0.23 kcal/mol. From the heats of sublimation and vaporization of $NbCl_5$, Alexander and Fairbrother[12] obtained a heat of fusion of 7.7 kcal/mol, while Meyer, *et al.*,[20] obtained 8.30 kcal/mol.

The entropy of fusion (16.9 eu/mol of $NbCl_5$) is quite large compared to those of the usual molecular solids (*e.g.:* WCl_5, 9.4; $TiCl_4$, 9.5; $ZrCl_4$, 12.7; $AlBr_3$, 7.3). The unusually large value for aluminum trichloride (18.1 eu) is attributed to a change in character on melting from an ionic solid to a molecular liquid. The large value for niobium pentachloride may be due to a dissociation of the dimer molecules Nb_2Cl_{10}, which are known to exist in the solid,[25] to monomers in the liquid.

The liquid heat capacity from the melting point (478.9°K) to 600°K may be expressed as

$$C_P = 57.36 - (22.02 \times 10^{-6}T^2) \text{ cal/deg mol} \quad (7)$$

and gives a value of $C_P = 56.8$ cal/deg mol at the

(23) One reviewer of this paper has commented that in drop calorimetry, in general, there is the inherent possibility for the error that when the sample is quenched, structural defects can be frozen into the sample and the energy associated with them is not released to the calorimeter. Such an error may be involved in the present measurements. However, if the defect energy were appreciable, one would expect to find abnormal scatter of replicate observations made on different samples. No such scatter was observed and the data for 500°K especially bear out the concordance of results. Another pertinent factor is that because these samples were contained in quartz-glass capsules, their rate of cooling was not very rapid. A rough calculation of the half-time for cooling, based on their geometry and the thermal conductivity of quartz, combined with a logarithmic decay of the sample temperature, was about 50 sec. This value is in accord with the observed fact that it took about 0.5 hr for the heat from the samples to be delivered to the calorimeter. Therefore, because of the slow quenching rate and the concordance of replicate determinations, we think that any defect energy stored in the quenched sample was negligible.

(24) D. Cubicciotti, H. Eding, and J. W. Johnson, *J. Phys. Chem.*, 70, 2989 (1966).

(25) Z. Zalkin and D. E. Sands, *Acta Crystallogr.*, 11, 615 (1958).

melting point. We estimated a value of 42–48 cal/deg mol, using a C_P value of 7–8 cal/deg g-atom, typical of many inorganic liquids.[26] The high experimental value compared to the estimated value may be connected with the dissociation of the dimer, which may persist in the liquid above the melting point. It is interesting to note that there is a slight curvature in the plot of liquid density *vs.* temperature just above the melting point,[10,21] which may also be due to dimer dissociation.

B. Enthalpy and Entropy Increments above 600°K. At some temperature above 600°K, C_P and C_σ differ by the quantity $T(\partial V/\partial T)_P$, and since this quantity is not known for the liquid we can only evaluate saturation thermodynamic quantities above 600°K.

The saturation enthalpy increments above 298°K were calculated from 600 to 804°K (the critical point) in 20° increments by numerical integration of eq 5. Values of C_σ up to 750°K were obtained from eq 4, and above 750°K, C_σ was obtained from the slope of the line through the data (dashed line in Figure 1). The values of $V(\partial P/\partial T)_\sigma$ were calculated from liquid density[10,21] and vapor pressure[11] data. The resulting values of the enthalpy increments for selected temperatures are shown in Table III. The entropy increments for the liquid were calculated by integrating the expression $C_\sigma d \ln T$, and the resulting data are also given in Table III. The value of $(S_T - S°_{298})_\sigma$ at the critical point was estimated by extrapolation of the curves for the liquid and vapor entropy increments *vs.* temperature.

Table III: Thermodynamic Functions for Liquid $NbCl_5$ under Saturation Conditions to the Critical Point

Temp, °K	$H_T - H°_{298}$, cal/mol	$S_T - S°_{298}$, eu
600	20,648	45.15
620	21,638	46.76
640	22,621	48.31
660	23,598	49.80
680	24,568	51.23
700	25,531	52.61
720	26,488	53.93
740	27,439	55.20
760	28,385	56.43
780	29,326	57.61
804	32,800	60.7

C. Σ-Plot Treatment of Vapor Pressure Data. If a value for the absolute entropy of solid $NbCl_5$ at 298°K were available, then the absolute entropies and free energy functions of the condensed phases at higher temperatures could be calculated from the data in Tables II and III. This quantity has not been measured, so it is necessary to estimate it. One way to

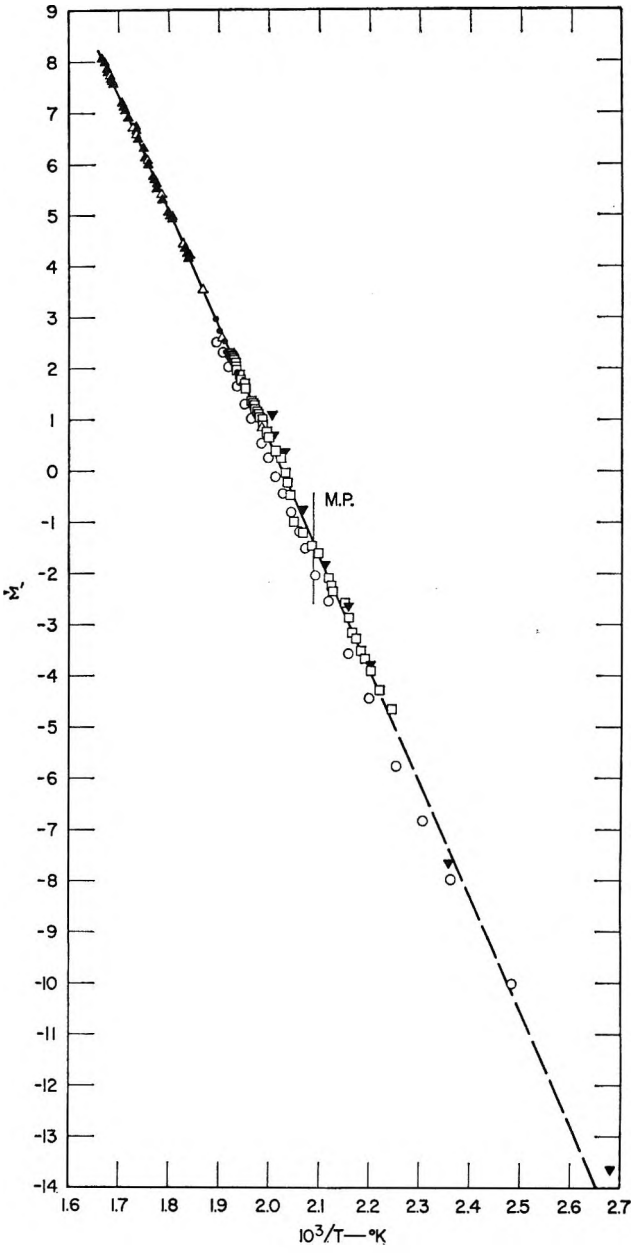

Figure 2. Σ plot for $NbCl_5$ vaporization data: ●, Ainscough, Holt, and Trowse;[13] ▲, Hart and Meyer;[11] ○, Alexander and Fairbrother;[12] ▼, Opykhtina and Fleisher;[14] □, Tarasenkov and Komandin;[15] △, Johnson, Silva, and Cubicciotti.[10]

estimate $S_{298}(s)$ is from the entropy of sublimation at 298°K and the absolute entropy of the gas

$$S_{298}(s) = S_{298}(g) - \Delta S_{298}(subl) \quad (8)$$

The entropy of $NbCl_5$ gas has been calculated from molecular constant data by Gaunt and Ainscough[3] and Nagarajan.[5] The entropy of sublimation at 298°K can be determined from vapor pressure data using the Σ-plot method of Cubicciotti.[9] In addition to determining $\Delta H_{298}(subl)$ and $\Delta S_{298}(subl)$, this method

(26) O. Kubaschewski and E. Evans, "Metallurgical Thermochemistry," Pergamon Press, Inc., New York, N. Y., 1958, p 186.

also affords an intercomparison of all vapor pressure data over the solid and the liquid. In this procedure the quantity Σ' is defined by the equation

$$-\Sigma' = R \ln p(\text{atm}) + \Delta\text{fef incr} \quad (9)$$

in which

$$\Delta\text{fef incr} = \text{fef}_T(\text{g}) - \text{fef}_{298}(\text{g}) - \text{fef}_T(\text{cond}) + \text{fef}_{298}(\text{cond}) \quad (10)$$

and fef is the usual free energy function, $(G^\circ_T - H^\circ_{298})/T$. Values for the fef increment for the condensed phases were calculated from the enthalpy and entropy increments in Table II by the methods described in ref 9. Values for the fef increment for the gas were calculated from Nagarajan's data.[5] A large-scale plot of the Δfef increment was used to find values of the Δfef increment corresponding to each pressure measurement.

Only vapor pressure data were used which extended to a temperature of 600°K, above which deviations from ideality may become too large. For the Σ plot the vapor pressure data from the following references were included, with temperature range and method of measurement indicated in parentheses: Ainscough, Holt, and Trowse[13] (516–530°K, boiling point); Hart and Meyer[11] (544–600°K, static); Alexander and Fairbrother[12] (403–528°K, static); Opykhtina and Fleisher[14] (373–503°K, transpiration); Tarasenkov and Komandin[15] (446–506°K, static, and 504–520°K, boiling point); Johnson, Silva, and Cubicciotti[10] (504–594°K, boiling point). The Σ' values are shown as a function of $1/T$ in Figure 2. With the exception of the points of Alexander and Fairbrother and Opykhtina and Fleisher, all of the data fall quite close to a straight line. The line drawn through the points was evaluated by least squares, using all of the data except those of Alexander and Fairbrother and Opykhtina and Fleisher. The former workers reported a triple point for $NbCl_5$ of 209.5 ± 0.5° which is 4° higher than our value of 205.7° for pure $NbCl_5$ and 5° higher than the value for impure $NbCl_5$, and their vapor pressure temperatures are also fairly consistently 4–5° higher than the least-squares line in Figure 2. The values of the heat and entropy of sublimation obtained from the least-squares treatment are $\Delta H^\circ_{298}(\text{subl}) = 22.41 \pm 0.06$ kcal/mol and $\Delta S^\circ_{298}(\text{subl}) = 45.40 \pm 0.11$ eu.

The value of $S^\circ_{298}(\text{g})$ was calculated by Nagarajan[5] to be 90.9 eu, which was based on the frequency assignments of Gaunt and Ainscough.[3] Using the frequency values listed by Krynauw, Pistorius, and Pistorius,[27] which were based on Carlson's data,[4] we calculated a value of 91.9 eu for $S^\circ_{298}(\text{g})$. Combining this latter number with the above value for $\Delta S^\circ_{298}(\text{s})$, the value of $S^\circ_{298}(\text{s})$ is calculated by eq 8 to be 46.5 eu. (However see note added in proof.)

The compound $NbCl_5$ has a heat capacity very near the Dulong and Petit value of 3 cal/deg g-atom at 298°K, and thus the method of Latimer[28] can be used to estimate $S^\circ_{298}(\text{s})$. For this calculation we used the Nb entropy value of 12.2 eu given by Latimer and estimated the Cl entropy contribution to be 7.5 eu/g-atom, based on the entropy estimated[29] for WCl_5. Such a calculation gives an estimate of $S^\circ_{298}(\text{s}) = 50$ eu for $NbCl_5$. Schafer and Kahlenberg[6] give an estimate (based on values for $ZrCl_4$, $HfCl_4$, UCl_5, and UCl_6) of 54 ± 2 eu, while Amosov[8] gives an estimate of 58.6 eu. If the value of 46.5 that we derived from the molecular constants of the gas is correct, the reason that it is lower than these estimates should be explored. On the other hand, the absolute entropy of the gas may be too low because the vibrational frequencies have not been properly assigned. Therefore, a calorimetric value for the absolute entropy of the solid would be very valuable.

The estimate for $S^\circ_{298}(\text{s})$ made by Latimer's rules may be too high, since the estimates for other solids are sometimes too high; *e.g.*, the Latimer estimates for $ZrCl_4$ and ZrF_4 are 4 and 7 eu too high, respectively. Also, since niobium pentachloride is a dimeric molecule in the solid, it may have a lower entropy than the average (which Latimer's values presumably represent). That is, it would probably have a smaller contribution from rotational or "rocking" modes because the molecule is so large.

It is also possible that the absolute entropy calculated for the gas from its molecular constants may be too small because the vibrational frequencies may not all have been observed. The vibrational frequencies used in calculating the entropy of the gas were obtained by Raman and infrared spectroscopy on the solid and on liquid solutions of niobium pentachloride dissolved in carbon disulfide or carbon tetrachloride.[3,4] It was assumed by both Gaunt and Ainscough[3] and by Carlson[4] that the frequencies should be assigned on the basis of D_{3h} symmetry because the $NbCl_5$ gas molecule has been shown by electron diffraction to have a trigonal-bipyramidal structure.[2] However, the solid has been shown by X-ray analysis to consist of Nb_2Cl_{10} dimers, in the form of distorted double octahedra sharing a common edge.[26] There is evidence that carbon tetrachloride solutions of niobium pentachloride also contain Nb_2Cl_{10} dimers.[30,31] Thus the vibrational frequencies seem to have been determined on systems

(27) G. N. Krynauw, C. W. F. T. Pistorius, and M. C. Pistorius, *Z. Phys. Chem.* (Frankfurt), **43**, 213 (1964).

(28) W. M. Latimer, "Oxidation Potentials," 2nd ed, Prentice-Hall Inc., Englewood Cliffs, N. J., 1952, Appendix III.

(29) "JANAF Thermochemical Tables," The Dow Chemical Co., Midland, Mich., Dec 31, 1966.

(30) R. F. W. Bader and A. D. Westland, *Can. J. Chem.*, **39**, 2306 (1961).

(31) D. L. Kepert and R. S. Nyholm, *J. Chem. Soc.*, 2871 (1965).

containing the dimer but have been assigned to the monomer. The existence of the dimer was known to Carlson[4] but he preferred to interpret the spectroscopic data on the basis of a weak association in the chlorine bridge-type bonding between the Nb atoms, in which the molecule retains an approximate D_{3h} structure. Krynauw, *et al.*,[27] have used Carlson's frequencies in a vibrational analysis to derive a set of force constants which they considered satisfactory. However, since the frequencies were not measured for the gas and because of the difficulty of these measurements, some low-lying frequencies may have been missed.

Since there is still some uncertainty about the value for $S°_{298}(s)$, we have not calculated the absolute entropies or free energy functions at temperatures above 298°K from the data in Tables II and III.[32]

(32) NOTE ADDED IN PROOF. After this report was submitted, Werder, *et al.* (R. D. Werder, R. A. Frey, and Hs. H. Gunthard, *J. Chem. Phys.*, **47**, 4159 (1967)), published the results of spectroscopic studies of niobium pentachloride in the solid state, in organic solvents, and in low-temperature matrices. Frequency assignments for both the monomer and dimer were made. Their frequency assignments are somewhat different from those of Gaunt, *et al.*,[3] and Krynauw, *et al.*,[27] and lead to a value of $S°_{298}(gas)$ for the monomer of 95.82 eu instead of the value we calculated above (91.9 eu) The assignments made by Werder, *et al.*, are clearly to be preferred since they were able to distinguish between monomer and dimer spectra by means of the matrix isolation technique. Using $S°_{298}(gas) = 95.82$ and $\Delta S°_{298}(subl) = 45.40$, we calculate $S°_{298}(solid) = 50.42$ eu (instead of 46.5), which is in agreement with the Latimer estimate. We think this value is sufficiently well substantiated that reliable values of free energy functions can be calculated from it and the data in Tables II and III.

Diffuse Transition and Melting in Fluorite and Anti-Fluorite Type of Compounds: Heat Content of Potassium Sulfide from 298 to 1260°K[1]

by A. S. Dworkin and M. A. Bredig

Chemistry Division, Oak Ridge National Laboratory, Oak Ridge, Tennessee *(Received September 25, 1967)*

The heat content and entropy of K_2S from 298 to 1260°K have been measured by means of a copper block drop calorimeter. K_2S was found to have the low entropy of fusion of 3.16 eu mole^{-1}, similar to those in CaF_2 and $SrCl_2$ with which it is anti-isotypic. As in these latter crystals, this is connected with the occurrence of a diffuse transition, with a heat capacity maximum of 45 cal deg^{-1} mole^{-1} at about 780° but extending from about 550° to the melting point at 948°, and involving an entropy change of 4 eu mole^{-1}. It is suggested that the occurrence of a diffuse transition is a general characteristic of the substances AB_2 of fluorite and anti-fluorite types of crystal structure. It is attributable to the gradual distribution of the B ions, with rising temperature, over both the octahedrally and tetrahedrally coordinated lattice positions. This leads to the high rate of diffusion and electrical mobility of the B ions. Heat content data found in the literature for such fluorite type crystals as UO_2, ThO_2, and Na_2O indicate that diffuse transitions also occur in these compounds although more information is needed in these cases.

Introduction

Through our observations on the anomalous heat content of solid strontium dichloride[2] which is isotypic in structure with calcium difluoride, we have become interested quite generally in the thermal and structural behavior of the substances possessing either the fluorite (MX_2) or the anti-fluorite (M_2Y) type of structure. The former group (MX_2) includes certain halides of divalent metals and oxides of tetravalent metals, such as CaF_2 and $SrCl_2$, and ZrO_2, ThO_2, and UO_2, while the group M_2Y consists mainly of the oxides and other chalcogenides of the alkali metals.[3] The present calorimetric study of potassium sulfide was further motivated, as was the earlier one of strontium chloride, by the need for knowledge of the entropy of fusion in attempts to extract from the fusion equilibria some information about the nature of the solution of the metal in the molten compound.[4]

Experimental Section

The copper block drop calorimeter used for the present heat content measurements and the experimental procedure were the same as described in detail

(1) Research sponsored by the U. S. Atomic Energy Commission under contract with the Union Carbide Corp.

(2) (a) A. S. Dworkin and M. A. Bredig, *J. Phys. Chem.*, **67**, 697 (1963); (b) A. S. Dworkin and M. A. Bredig, *J. Chem. Eng. Data*, **8**, 416 (1963).

(3) *Cf., e.g.*, R. W. G. Wykoff, "Crystal Structures," Vol. 1, Interscience Publishers, Inc., New York, N. Y., 1963, p 239 ff.

(4) A. S. Dworkin and M. A. Bredig, *J. Phys. Chem.*, **71**, 764 (1967).

previously.[5] The preparation of the K_2S and its analysis (better than 99% K_2S) have also been described elsewhere.[4] The defined calorie is equal to 4.184 absolute joules, and the molecular weight of K_2S is 110.27.

Results and Discussion

The measured heat contents of K_2S are given in Table I. The "run number" indicates the order in which the measurements were made. The following equations were obtained by the method of least squares for $H_T - H_{298.15}$ (cal mole^{-1}).

$$H_T - H_{298.15} = -5230 + 16.78T + 2.370 \times 10^{-3}T^2 (\pm 0.5\%) \quad (298\text{–}820°K)$$

$$H_T - H_{298.15} = -18{,}370 + 34.02T (\pm 0.05\%) \quad (1100\text{–}1221°K)$$

$$\Delta H_{fusion} = 3860 \pm 40 \text{ cal mole}^{-1} \quad (1221°K)$$

$$H_T - H_{298.15} = -2440 + 24.13T (\pm 0.05\%) \quad (1221\text{–}1260°K)$$

Figure 1 illustrates the occurrence of a diffuse transition beginning at about 820°K and continuing to the melting point at 1221°K after showing a sharp specific heat

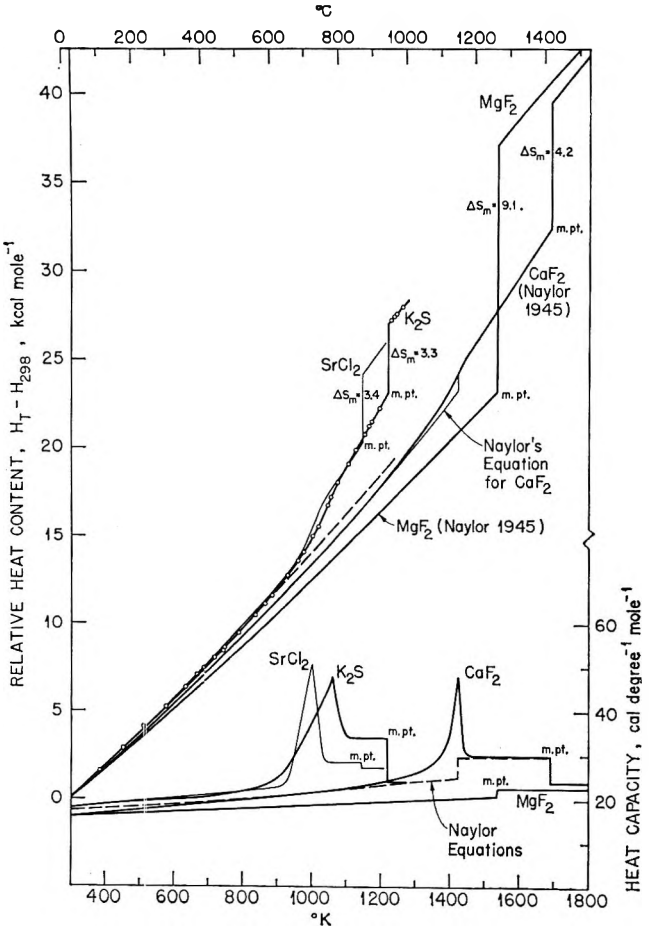

Figure 1. Heat content and molar heat capacity of K_2S compared with $SrCl_2$, CaF_2, and MgF_2.

Table I: Measured Heat Contents of K_2S

Run no.	T, °K	$H_T - H_{298.15}$, kcal mole^{-1}
	Solid	
23	384.4	1.55
18	452.5	2.84
19	516.3	4.03
20	575.9	5.22
21	634.8	6.39
24	667.8	7.08
22	686.6	7.44
25	717.4	8.03
9	741.6	8.44
29	745.7	8.61
10	789.3	9.46
11	835.8	10.47
26	864.4	11.13
12	882.5	11.59
13	929.5	12.73
27	959.6	13.56
14	975.9	14.07
30	1000.7	15.00
15	1016.9	15.59
16	1045.2	16.81
28	1054.6	17.24
17	1073.9	18.09
4	1103.8	19.19
5	1126.3	19.93
6	1150.2	20.76
31	1163.7	21.22
7	1172.6	21.50
8	1194.9	22.29
32	1208.3	22.91[a]
	Liquid	
3	1228.7	27.20
33	1237.5	27.43
2	1243.7	27.56
1	1260.4	27.97

[a] Premelting.

maximum at about 1050°K. The smoothed heat content values in the temperature range 820–1100°K which appear in Table II were obtained from the curve since no equation was used for the temperature range of transition. The entropy values in Table II were calculated from the heat content data by the method suggested by Kelley.[6] The premelting effect evident in $H_T - H_{298}$ at 1208.3°K is small because the suspected impurities (K_2O, K) are likely to be soluble in solid K_2S.[4]

The diffuse transition as well as the low heat of fusion (3.86 kcal mole^{-1} at 1221°K corresponding to an entropy of 3.16 eu mole^{-1}) is analogous to that in $SrCl_2$[2b] and CaF_2[7] to which K_2S is structurally antiisotypic. The specific heat maximum of about 45 cal

(5) A. S. Dworkin and M. A. Bredig, *J. Phys. Chem.*, **64**, 269 (1960).
(6) K. K. Kelley, U. S. Bureau of Mines Bulletin 584, U. S. Government Printing Office, Washington, D. C., 1960, p 8.
(7) B. F. Naylor, *J. Am. Chem. Soc.*, **67**, 150 (1945).

Table II: Smoothed Values of Heat Content and Entropy for K_2S

T, °K	$H_T - H_{298.15}$, kcal mole^{-1}	$S_T - S_{298.15}$, cal deg^{-1} mole^{-1}
400	1.86	5.37
500	3.75	9.54
600	5.69	13.08
700	7.67	16.13
800	9.71	18.85
850	10.80	20.17
900	11.97	21.51
950	13.27	22.92
1000	14.92	24.61
1050	17.02	26.65
1100	19.05	28.55
1150	20.76	30.07
1200	22.45	31.50
1221 (S)	23.16	32.09
1221 (L)	27.02	35.25
1250	27.72	35.82

deg^{-1} mole^{-1} at about 1050°K corresponds to those found earlier in CaF_2 and $SrCl_2$ at 1423 and 993°K (Figure 1). The transition is believed to reflect the gradual disordering of the potassium cation sublattice analogous to the disordering of the anion sublattice observed by X-ray diffraction in $SrCl_2$[8] and also assumed in CaF_2.[9] In all these cases, the B ions which are the anions in the fluorite type and the cations in the anti-fluorite type of compounds AB_2 become distributed increasingly with increasing temperature over two sets of positions between the A ions, the latter being arranged on a face-centered cubic lattice. In the first set of positions numbering eight per unit cell, the B ions (eight per unit cell) are tetrahedrally surrounded by four A ions. This is the set occupied by the B ions at low temperature. In the other set of positions of which there are also eight per unit cell, half of them, however, occupied permanently by the A ions, the B ions are octahedrally surrounded by six A ions. At the melting point the eight B ions of the unit cell may be assumed to be randomly distributed and freely moving over the total of 12 positions of both these sets of B ion positions.

The high heat capacity (C_p = 34 cal deg^{-1} mole^{-1}) in the temperature region 1100–1221°K, which compares with the almost equally high values of 28.5 for $SrCl_2$ and 30 for CaF_2 below their melting points, indicates that the transition, *i.e.*, the particular process of disordering, continues all the way up to the melting point. For comparison, the heat content of MgF_2 which has the tetragonal rutile rather than the cubic fluorite type of structure is included in Figure 1 as an example for "normal" behavior ($C_{p(solid)} \approx 21$ cal deg^{-1} mole^{-1}). In this case, all the disordering occurs on melting (ΔS_m = 9.1 eu mole^{-1}).

To estimate the entropy involved in the K_2S transition, the least-squares curve for the heat content below the transition was extrapolated to the melting point. The difference between the entropy calculated from the measured curve and that from the extrapolated curve is about 4 eu mole^{-1}. This value is a good estimate of the entropy of transition and accounts for the unusually low value for the entropy of fusion. The entropy of transition for $SrCl_2$ calculated in the above manner is 2.3 eu mole^{-1}. Our earlier value[2b] of 1.65 eu mole^{-1} was a rough estimate obtained by treating the transition *as if* it were first order and extrapolating the heat contents to the temperature of maximum heat capacity.

It is interesting to note that thermal analysis (both cooling and heating) runs on K_2S failed to detect the diffuse transition even though the apparatus was found by us to be capable of detecting isothermal transition heats of less than a few hundred calories per mole. Thermal analysis runs for $SrCl_2$ and CaF_2 gave the same results as with K_2S, *i.e.*, no transition halt. Thermal analysis, then, may be used in conjunction with heat content measurements to aid in distinguishing between a first-order transition and a diffuse transition with a sharp heat capacity maximum. This test is pertinent to the case of $SrCl_2$ where a first-order transition (ΔH_{tr} = 650 cal/mole) has been claimed.[10] For CaF_2, an isothermal heat of transition of 1140 cal/mole is reported[7,11] although the original paper[7] clearly states that "The heat content curve shows no discernible discontinuity," and the heat of transition was obtained by treating the transition *as if* it were first order. No change in over-all symmetry from the low-temperature face-centered cubic structure to a "cubic" one as has been suggested[10] is indicated for the fluorite and anti-fluorite type of substances AB_2. The transition is wholly attributable to the disordering of the B ions, with the A ions retaining the face-centered-cubic arrangement. The process is very likely to occur in dioxides of this structure type also, *e. g.* in UO_2 or ThO_2, and has been discussed by Möbius[9] in connection with ionic (O^{2-}) conduction in ZrO_2 in terms of the geometry of the lattice and the relative ease of escape of the two kinds of ions through their first shells of coordination of oppositely charged neighbors.

The heat contents of UO_2 and ThO_2 have been reported[12] but only in the solid up to temperatures well below the melting points. The heat content and heat capacity curves shown in Figure 2 indicate the beginning of what may be the diffuse transitions in these two compounds. The heat capacity increases after

(8) U. Croatto and M. Bruno, *Gazz. Chim. Ital.*, **76**, 246 (1946).

(9) H. H. Möbius, *Z. Chem.*, **2**, 100 (1962).

(10) G. J. Janz, F. J. Kelly, and J. F. Perano, *Trans. Faraday Soc.*, **59**, 2718 (1963).

(11) See ref 6, p 39.

(12) T. G. Godfrey, J. A. Wooley, and J. M. Leitnaker, ORNL-TM-1596, 1966.

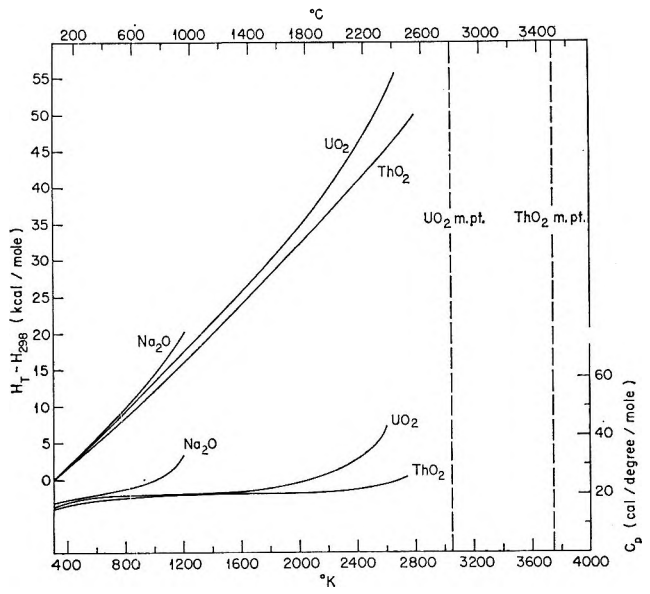

Figure 2. Heat content and molar heat capacity of Na_2O, UO_2, and ThO_2.

remaining constant over a rather large temperature range. The increase is much more rapid for UO_2 as the measurements extend much closer to the melting point than do those for ThO_2. In neither case, however, has the temperature of maximum heat capacity been reached and further measurements will be necessary to demonstrate whether or not these transitions are similar to those shown in Figure 1.

Of the anti-fluorite type compounds not already discussed, there are some heat content data in the literature for solid Na_2S,[13] Na_2O,[14] and Li_2O.[15] Unfortunately, the presence of a rather large impurity (4.2%, either wt or mole?) in the Na_2S caused an obvious premelting effect obscuring the indications of a diffuse transition beginning at about 1000°K, about 450° below the melting point.

The heat content and heat capacity curves for Na_2O shown in Figure 2 were derived directly from the measurements of Grimley and Margrave[14] rather than from their equations. The equations give a much poorer fit (*e.g.*, −13% in the heat content at 1100°K) than the data seem to justify and obscure the fact that C_p turns up sharply at about 800°K after having remained essentially constant for more than 300°. By analogy with the isomorphous K_2S, disordering of the Na^+ ions is likely to be responsible for the rapid rise in C_p. However, their measurements were terminated due to destruction of their gold capsule at higher temperatures. Further measurements at higher temperatures, possibly in a platinum capsule, are needed to determine whether or not a sharp maximum in C_p occurs before the melting point of about 1400°K[16] is reached. Such a maximum, at 1240°K, is possibly indicated by differential thermal analysis reported recently by Bouaziz, *et al.*[16] It seems likely that the high-temperature form of Na_2O has the disordered face-centered cubic anti-fluorite type of structure, but it is not certain whether the reported transition is of the first order,[16] with a considerable pretransition region, or whether the dta maximum corresponds only to a high maximum in C_p in a diffuse transition occurring in a relatively narrow temperature range.

For Li_2O, there is no indication of an upturn in C_p at temperatures below 1000°K. We believe that the transition would be observed at higher temperatures, *i.e.*, closer to the melting point (variously reported as 1700°K[17a] and 1840°K[17b]). The different behavior of Li_2O at temperatures below 1000°K is likely to be connected with the much higher lattice energy due to the small size of the Li^+ ion. The high melting point of Li_2O is above that of Na_2O while the melting points of the lithium halides lie considerably (and "abnormally") below not only those of the corresponding sodium but even those of the potassium halides. The ("normal") behavior of the oxide must be due mainly to the absence of anion–anion contact between a lower number of mutually repulsive anions around the small Li^+: $4O^{2-}$ in the oxides as compared with $6X^-$ in the halides (X = F, Cl, Br, I).

The upper temperature limit of about 1000° of our present calorimeter precludes further heat content measurements for most fluorite and anti-fluorite type compounds with the exception of K_2O. We have obtained a melting point for K_2O contained in silver of at least 750° (and probably somewhat higher). However, silver was attacked slightly either by the K_2O or by an impurity in the K_2O (*e.g.*, K or K_2O_2) limiting its use as a container for heat content measurements, and a platinum container proved to withstand K_2O even less than did the silver.

Möbius, Witzmann, and Hartung[18] have reported electrical conductivity (κ) and self-diffusion measurements for Na_2S and found the Na^+ to be the mobile ion as expected. A diffuse transition similar to that in K_2S is very likely also to occur in Na_2S. Therefore, the conclusion (reached by extrapolation of the conductivity values below 800°) that at the melting point of 1169° κ_{solid} would be as high as 63 mho cm^{-1} (~1400 mho cm^2 $equiv^{-1}$), far above any ionic conductivity even in the molten state, was unwarranted. To extrapolate κ into the region above the transition using the very high temperature dependence of conduction cor-

(13) M. N. May, *Tappi*, **35**, 511 (1952).

(14) R. T. Grimley and J. L. Margrave, *J. Phys. Chem.*, **64**, 1763 (1960).

(15) C. H. Shomate and A. J. Cohen, *J. Am. Chem. Soc.*, **77**, 285 (1955).

(16) R. Bouaziz, G. Papin, and A. Rollet, *Compt. Rend.*, **C262**, 1051 (1966).

(17) (a) L. Brewer and J. Margrave, *J. Phys. Chem.*, **59**, 421 (1955); (b) A. E. Van Arkel, E. A. Flood, and N. F. H. Bright, *Can. J. Chem.*, **31**, 1009 (1953).

(18) H. H. Möbius, H. Witzmann, and R. Hartung, *Z. Physik. Chem.*, **227**, 40 (1964).

responding to an activation energy of 38 kcal/mole valid below the transition temperature is not justified. The activation energy for conduction in the disordered high-temperature structure is likely to be very much lower than in the essentially ordered one below the transition temperature for Na_2S which may be estimated to be approximately 1000° (*cf.*, *e.g.*, the very small temperature dependence of the conductivity[19] in the disordered high-temperature form of solid AgI above 145°).

However, in the transition regions of these substances, a rapid increase in conductivity must occur similar in extent to, but more gradual than, the (isothermal) one in AgI. Its start seems to have been observed in $SrCl_2$ near 700°, corresponding to the unusually high activation energy of 70 kcal/mole.[20] This rapid rise is, however, not expected to lead to as impossibly high a κ value, at the melting point, as that cited above for Na_2S. One of the highest ionic conductivities of a solid measured, beside that of AgI, $\kappa = 2.5$ ohm^{-1} cm^{-1}, seems to be that recently obtained for cubic Li_2SO_4 near its melting point, $\kappa = 2.6$, corresponding to an equivalent conductance of 68 ohm^{-1} cm^2 equiv^{-1}.[21] With the arrangement of the SO_4^{2-} ions on a face-centered cubic lattice,[22] this is in essence another case of anti-fluorite type of crystal AB_2 with disordered and mobile B ions (Li). However, this structure forms here not in a diffuse but in a *first*-order transition from the *monoclinic* low-temperature phase at 575° with an entropy change ΔS_{tr} of approximately 8 cal/deg mole. Together with the very low entropy of fusion, 2.7, the high value of ΔS_{tr} is taken to reflect the disordering and mobilizing of the lithium ions in the cubic structure. In addition, the relatively high heat capacity of this phase, 52 cal/deg mole, as compared with 46 for the liquid, further suggests that the disordering process is not completed at, but continues above, the transition temperature as it does in K_2S.

(19) "Landolt-Börnstein Tabellen," Vol. II, 6th ed, 1959, p 237.

(20) E. Barsis and A. Taylor, *J. Chem. Phys.*, **45**, 1154 (1966). Older literature is cited there.

(21) A. Kvist and A. Lundén, *Z. Naturforsch.*, **20a**, 235 (1965).

(22) T. Forland and J. Krogh-Moe, *Acta Chem. Scand.*, **11**, 565 (1957).

Electronic and Electron Spin Resonance Spectra of the Perfluoro-2,1,3-benzoselenadiazole Anion Radical[1]

by J. Fajer, B. H. J. Bielski,

Departments of Nuclear Engineering and Chemistry, Brookhaven National Laboratory, Upton, New York 11973

and R. H. Felton

Department of Chemistry, Brandeis University, Waltham, Massachusetts 02154 *(Received September 25, 1967)*

The electronic absorption and electron spin resonance (esr) spectra of the perfluoro-2,1,3-benzoselenadiazole radical anion are presented. Results of a semiempirical self-consistent field–molecular orbital (SCF–MO) study of the molecule and the isologs, 2,1,3-benzoselenadiazole and 2,1,3-benzothiadiazole, are assessed by comparison of calculated and experimental esr and electronic spectra of the radicals. Similar comparisons were made of the neutral species. It is concluded that a p-orbital model satisfactorily describes the pertinent experimental data.

Introduction

Examples of nitrogen or oxygen aromatic heterocyclic radical anions are well known; less familiar are anions in which the heteroatom is sulfur or selenium. The increasing interest[2-4] shown in the electronic properties of 2,1,3-benzoselenadiazole (I), 2,1,3-benzothiadiazole (II), and their derivative anions prompts us to report on similar properties of the perfluoro-2,1,3-benzoselenadiazole (III) anion.

One source of interest in these molecules is the possible interaction of empty d orbitals with the π-electron

(1) This work was performed under the auspices of the U. S. Atomic Energy Commission.

(2) E. T. Strom and G. A. Russell, *J. Amer. Chem. Soc.*, **87**, 3326 (1965).

(3) N. M. Atherton, J. N. Ockwell, and R. Deitz, *J. Chem. Soc.*, **A**, 771 (1967).

(4) J. Fajer, *J. Phys. Chem.*, **69**, 1773 (1965).

system. Previous studies[2,3,5] of I, II, and the radical anions were carried out within the framework of the Hückel molecular-orbital theory, and, therefore, the conclusion that d orbitals were not needed was necessarily qualitative. We have applied a more sophisticated treatment of electronic structure, *viz.*, self-consistent field–molecular-orbital theory, to these molecules. Rather than make arbitrary and untested assumptions as to the nature of the d–p interactions, we employed a basis set which included only the 3p orbital of sulfur and the 4p orbital of selenium. Parameters relating to these orbitals are well characterized and may be chosen *a priori* from atomic spectral data or theoretical investigations of related molecules. In addition, an extensive configuration interaction treatment was performed for both closed- and open-shell molecules to ascertain if the customary neglect of doubly excited states was justified.

With reasonable choices for parameters we not only find good agreement between calculated and experimental electronic spectra, but also note that the SCF-MO treatment predicts spin-density distributions generally in accord with those observed.

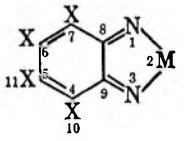

I, M = Se; X = H
II, M = S; X = H
III, M = Se; X = F

Experimental Section

Samples of III were prepared by the reaction of selenous acid with tetrafluoro-*o*-phenylenediamine[6] and were sublimed twice. *Anal.* Calcd for $C_6F_4N_2Se$: C, 28.26; N, 11.07; F, 30.01 Found: C, 28.26; N, 10.99; F, 29.80 (Galbraith Laboratories, Knoxville, Tenn.). The infrared spectrum was consistent with that reported[7] for I (with allowances for the CF instead of CH absorptions). The anion was prepared at room temperature by sodium or potassium reduction of III dissolved in tetrahydrofuran. Optical absorption measurements and extinction coefficients were obtained as previously described.[4] Electron spin resonance spectra were measured on a Varian V4500 spectrometer equipped with a 9-in. magnet and 100-kc field modulation.

Experimental Results

Compound III reacts with sodium in tetrahydrofuran to yield reddish solutions. Representative absorption spectra, at various stages of reduction, are displayed in Figure 1. The successive spectra develop through well defined isosbestic points as the reaction proceeds, suggesting formation of a single new species. Oxidation of the product by exposure to dry air regenerates 80–85% of the original spectrum. The esr spectrum

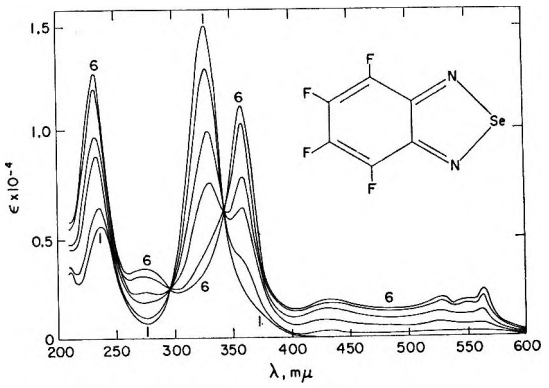

Figure 1. Sodium reduction of III in tetrahydrofuran: 1, absorption spectrum of starting material; 6, final product. (ϵ is in liters per mole centimeter.)

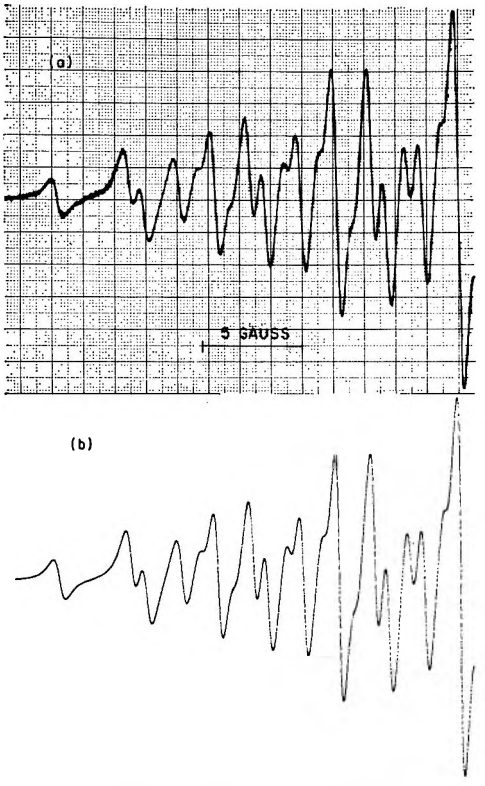

Figure 2. (a) Electron spin resonance spectrum of $III\cdot^-$ in tetrahydrofuran; (b) computer-simulated spectrum.

of the radical obtained by potassium reduction is shown in Figure 2a. Analysis of the observed 39-line spectrum yields the following isotropic hyperfine splitting constants: a_F = 3.56 and 4.34 G for the two sets of two equivalent fluorine atoms, and a_N = 6.08 G for the two equivalent nitrogen atoms. A computer-simulated spectrum employing the above values is shown in Figure 2b. The line-shape function for

(5) N. K. Ray and P. T. Narasimhan, *Theoret. Chim. Acta*, **5**, 401 (1966).

(6) We are indebted to M. W. Buxton of Imperial Smelting Corp. for a sample of the diamine.

(7) V. A. Pazdyshev, Z. V. Todres-Selektor, and L. S. Efros, *J. Gen. Chem. USSR*, **30**, 2533 (1960).

individual hyperfine lines was Lorentzian with a half-width of 0.62 G. We were unable to detect splitting due to either the potassium gegenion or the Se^{77} (7% natural abundance). These extra transitions may contribute to the rather broad line widths.

Similar reduction of I in tetrahydrofuran yielded esr spectra essentially equivalent to those obtained earlier.[2]

SCF-MO Calculations

A. Method. The SCF-MO's for closed-shell molecules were obtained by the method of Pariser and Parr,[8] and Pople (PPP).[9] For the open-shelled doublets, the method of Adams and Lykos[10] was employed. This latter treatment is an extension of the PPP approximations to Roothaan's SCF theory of open shells.[11] Our computational scheme apparently differs from recent calculations[12] of aromatic anions, in that excitation energies here are related to one-electron energies of the SCF-MO's *via* Roothaan's open-shell Fock operator.

$$F = H + 2J_T - K_T + 2(M_T - K_o) \qquad (1)$$

In eq 1, H is the one-electron operator; J_T and K_T are the total Coulomb and exchange operators, respectively; K_o is the exchange operator for the half-filled shell; and M_T is an exchange coupling operator. As a result, excitation energies (relative to the ground-state energy) differ slightly from those derived by Longuet-Higgins and Pople.[13] Table I gives these energies for

Table I: Excitation Energies of Singly Excited Radical States[a]

State	Energy
$^2\chi_1$	$\epsilon_m - \epsilon_k + {}^1/_2J_{mm} + {}^3/_2K_{km} - J_{km}$
$^2\chi_2$	$\epsilon_n - \epsilon_m + {}^1/_2J_{mm} + {}^3/_2K_{mn} - J_{mn}$
$^2\chi_3$	$\epsilon_n - \epsilon_k + K_{mn} + K_{mk} + 2K_{kn} - J_{kn}$
$^2\chi_4$	$\epsilon_n - \epsilon_k + 2K_{mn} + 2K_{mk} - J_{kn}$

[a] $\epsilon_l \equiv F_{ll}$; $J_{ll'}$ and $K_{ll'}$ are Coulomb and exchange integrals for MO's l and l'.

the following excited states.

$$^2\chi_1 = |\phi_1\bar{\phi}_1 \ldots \phi_k\phi_m\bar{\phi}_m|$$

$$^2\chi_2 = |\phi_1\bar{\phi}_1 \ldots \phi_k\bar{\phi}_k\phi_n|$$

$$^2\chi_3 = 2^{-1/2}\{|\phi_1\bar{\phi}_1 \ldots \phi_k\phi_m\bar{\phi}_n| - |\phi_1\bar{\phi}_1 \ldots \bar{\phi}_k\phi_m\phi_n|\}$$

$$^2\chi_4 = 6^{-1/2}\{2|\phi_1\bar{\phi}_1 \ldots \phi_k\bar{\phi}_m\phi_n| - |\phi_1\bar{\phi}_1 \ldots \phi_k\phi_m\bar{\phi}_n| - |\phi_1\bar{\phi}_1 \ldots \bar{\phi}_k\phi_m\phi_n|\} \qquad (2)$$

where the ground state is

$$^2\chi_0 = |\phi_1\bar{\phi}_1 \ldots \phi_k\bar{\phi}_k\phi_m| \qquad (3)$$

In referring to individual orbitals, the indices 1, 2, ..., k relate to filled orbitals (in the ground state), m is the unique half-filled shell, and n,o, ... are virtual orbitals. The Slater-determinant notation is familiar.

Excited states of the type $^2\chi_4$ were allowed to interact with the ground state, and configurational-interaction matrix elements among the excited states were reduced by utilizing the diagonality of F in the SCF-MO basis. In addition, we corrected spin densities after configuration interaction in a nonperturbative manner, thereby involving all excited states of appropriate symmetry. This differs from the customary procedure[12] of using only configurations $^2\chi_4$. As a check, the total spin density was computed. In all instances the total was 1.0000.

Furthermore, the computer program developed has the additional flexibility of allowing the incorporation of doubly excited states in both closed- and open-shell computations. For closed-shell electronic spectra, one has the option of including the five distinguishable[14] types of double excitations with configuration interaction not only between them and the ground or singly excited states, but also among the doubly excited states themselves. For the open-shell molecules the (presumably) four lowest doubly excited states could be included for configuration-interaction calculations. In this case no interaction among doubly excited states was considered. This neglect is inconsistent; nevertheless, for the molecules considered here, doubly excited states had little effect upon the predicted electronic spectra. The four types of configurations were generated from the excitations: 2k → 2n, m → n, and k → n, and two doublets arising from k → n and m → o.

B. Parameters. The same set of parameters was used for both neutral and radical forms of a given molecule. Table II lists the needed parameters. There for the μth atom of core charge, Z_μ, I_μ is the valence-state ionization potential of a pπ electron, and γ_μ is the monocentric electron repulsion integral. For selenium, parameters were obtained from the paper of Hinze and Jaffé.[15] Fluorine values were obtained from different sources.[16] Other one-center integrals are conventional choices with the exception of $I_c = -9.6$ eV. This value is a member of the parameter set,[17]

(8) R. Pariser and R. G. Parr, *J. Chem. Phys.*, **21**, 466 (1953).
(9) J. A. Pople, *Trans. Faraday Soc.*, **50**, 901 (1954).
(10) O. W. Adams and P. G. Lykos, *J. Chem. Phys.*, **34**, 1444 (1961).
(11) C. C. J. Roothaan, *Rev. Mod. Phys.*, **32**, 179 (1960).
(12) A. Hinchliffe, *Theoret. Chim. Acta*, **5**, 208 (1966); A. Hinchliffe, R. Stainbank, and M. Ali, *ibid.*, **5**, 95 (1966).
(13) H. C. Longuet-Higgins and J. Pople, *Proc. Phys. Soc.*, **68A**, 591 (1955).
(14) J. Murrell and K. L. McEwen, *J. Chem. Phys.*, **25**, 1143 (1956); H. Ito and Y. l'Haya, *Theoret. Chim. Acta*, **2**, 247 (1964).
(15) J. Hinze and H. H. Jaffé, *J. Phys. Chem.*, **67**, 1501 (1963).
(16) L. Oleari, L. Di Sipio, and G. De Michelis, *Mol. Phys.*, **10**, 97 (1966).
(17) K. Nishimoto, *Theoret. Chim. Acta*, **7**, 207 (1967).

Table II: Semiempirical Parameters (eV)

Atom	I	γ	Z	β
C	−9.6[a]	9.4915[b]	1	$\beta_{CF} = -1.75$
N	−14.12[b]	12.12[b]	1	$\beta_{SeN} = -1.10$
Se	−23.85[c]	11.15[c]	2	$\beta_{SN} = -1.68$
S	−22.88[d]	9.90[e]	2	
F	−35.36[e]	16.70[e]	2	

[a] Reference 17. [b] C. Weiss, H. Kobayashi, and M. Gouterman, *J. Mol. Spectrosc.*, **16**, 415 (1965). [c] Reference 15. [d] M. Bielefeld and D. D. Fitts, *J. Amer. Chem. Soc.*, **88**, 4804 (1966). [e] Reference 16.

used here, that included variable core resonance integrals $\beta_{\mu\nu}$ and bicentric repulsion integrals $\gamma_{\mu\nu}$.

Bicentric repulsion integrals were calculated according to the recently proposed scheme[17] which treats vertical correlation in an approximate manner by assigning electrons alternately above and below the molecular plane. Different formulas are then used for upper–upper and upper–lower interactions. For the electrons "associated" with selenium or sulfur, we simply averaged the results of the two formulas.

Core resonance integrals β_{CN} and β_{CC} were calculated by the variable β method.[17] The only parameters which then had to be judiciously guessed were β_{SeN}, β_{SN}, and β_{CF}. The integrals β_{SeN} and β_{SN} were calculated from an overlap approximation

$$\beta = \beta_0 S(r)$$

where $S(r)$ is the overlap of $2p\pi$ orbitals centered on carbons a distance r apart, and $-2.48 \text{ eV} < \beta_0 < -2.39$ eV. (We arbitrarily chose the $2p\pi$–$2p\pi$ overlap integral here since there are at present insufficient data to allow the determination of a β_0 appropriate to NS or NSe interactions.) The value of β_{CF} was allowed to vary between −1.75 and −2.5 eV.

The crystal structures of I and II are known.[18] The geometry of III was approximated by using the atomic positions of I and a CF bond distance of 1.30 Å.

Results and Discussion

Hydrogen hyperfine splittings were computed using two relations suggested by Hinchliffe,[12] *i.e.*

$$a_H = -27\rho_\mu \quad \text{(A)}$$

$$a_H = -27\rho_\mu - 12.8\epsilon_\mu\rho_\mu \quad \text{(B)}$$

where ρ_μ is the carbon spin density and $\epsilon_\mu = 1 - P_\mu$ is the excess charge at carbon atom μ having a charge density P_μ. A similar McConnell relation for a_N was employed[12]

$$a_N = -21\rho_N$$

Determination of a_F is quite approximate. The difficulty resides in the (probably) erroneous assumption that

$$a_F = Q_F\rho_C \quad (4)$$

holds rather than the theoretically expected form

$$a_F = Q_{FF}\rho_F + Q_{FC}\rho_C \quad (5)$$

Equation 5 reflects the splitting contributions from $2p\pi$ spin on fluorine. Since little is known[19] with regard to parameters in eq 5, we use, instead, eq 4 with $Q_F = 50 \pm 10$ G.[19,20]

The computed hyperfine splitting constants are displayed in Table III. Included there are spin densities before and after configuration interaction (CI). The latter spin densities were used in the McConnell relations, and charge densities did not include the minor effects of CI. The assignment of the hydrogen hyperfine splitting constants agrees with previous results.[2,3] The assignment of a_F values is quite reasonable, in view of the observation[19] that substitution of weakly electron-withdrawing groups in radicals already containing strongly electron-attracting groups does not greatly perturb the spin density; however, this assignment is not to be regarded as definitive because of the aforementioned difficulties in relating coupling constants and spin densities.

Table III: Spin-Density Distributions and Coupling Constants (G)

Molecule	Position	Spin density: No CI	Spin density: CI	a (calcd)	a (exptl)
I	1	0.203	0.270	5.67	5.79[a]
	4	0.115	0.119	(A) 3.21	
				(B) 3.01	2.48
	5	0.091	0.061	(A) 1.65	
				(B) 1.61	1.65
II	1	0.242	0.295	6.19	5.18[a]
	4	0.092	0.104	(A) 2.81	
				(B) 2.67	2.59
	5	0.066	0.049	(A) 1.32	
				(B) 1.28	1.59
III[b]	1	0.208	0.252	5.29	6.08
	4	0.103	0.116	5.8 ± 0.6	4.34
	5	0.085	0.065	3.25 ± 0.3	3.56
III[c]	1	0.208	0.291	6.11	6.08
	4	0.103	0.103	5.15 ± 0.5	4.34
	5	0.085	0.061	3.05 ± 0.3	3.56

[a] Reference 3. [b] Number of excited states, 13. [c] Number of excited states, 67.

(18) V. Luzzati, *Acta Cryst.*, **4**, 193 (1951).

(19) M. Kaplan, J. R. Bolton, and G. Fraenkel, *J. Chem. Phys.*, **42**, 955 (1965).

(20) A. Carrington, A. Hudson, and H. C. Longuet-Higgins, *Mol. Phys.*, **9**, 377 (1965).

Table IV: Bond Orders

Molecule	Bond	Neutral species: Interatomic distance, Å SCF-MO	Neutral species: Interatomic distance, Å Exptl[a]	Neutral species: Bond order SCF-MO	Neutral species: Bond order HMO[b]	Radical (SCF-MO): Interatomic distance, Å	Radical (SCF-MO): Bond order
I	1–2	...	1.83	0.1868	...	...	0.0981
	3–9	1.296	1.30	0.8596	...	1.329	0.6848
	4–9	1.431	1.42	0.3135		1.431	0.4760
	4–5	1.356	1.30	0.8961		1.384	0.7399
	5–6	1.458	1.42	0.3526		1.420	0.5399
	8–9	1.467	1.46	0.2773		1.451	0.3697
II	1–2	...	1.60	0.2982	0.579	...	0.1960
	3–9	1.305	1.34	0.8131	0.548	1.336	0.6396
	4–9	1.457	1.46	0.3321	0.566	1.430	0.4830
	4–5	1.357	1.29	0.8886	0.723	1.381	0.7529
	5–6	1.451	1.46	0.3682	0.603	1.421	0.5331
	8–9	1.457	1.41	0.3321	0.528	1.436	0.4484

[a] Reference 18. [b] Hückel calculations of ref 5.

Table V: Charge Densities

Molecule	Atom 1	2	4	5	9	10	11
I	1.269	1.931	1.025	0.950	0.790		
$I\cdot^-$	1.505	1.969	1.137	1.051	0.818		
II	1.265	1.834	1.020	0.962	0.836		
II (HMO)[a]	1.272	1.437	1.010	1.005	0.994		
$II\cdot^-$	1.499	1.913	1.107	1.066	0.872		
III	1.277	1.933	1.040	0.788	0.960	1.985	1.984
$III\cdot^-$	1.520	1.971	1.138	1.062	0.833	1.979	1.978

[a] Reference 5.

Large nitrogen and C(5) spin-density alterations are caused by CI. Increasing the number of excited states generally improves the agreement with experiment. We find that spin densities calculated from neutral molecule MO's are quite bad.

Bond distances of I, II, and their anions are compared with experimental interatomic distances in Table IV. The bond order–bond distance relations used were[21]

$$r^{CC} = 1.517 - 0.18P_{\mu\nu}$$

$$r^{CN} = 1.451 - 1.18P_{\mu\nu}$$

with $P_{\mu\nu}$ the total mobile bond order between atoms μ and ν. Formation of the radical tends to remove the strongly alternating character of the neutral molecule while decreasing the bond order between the heteroatoms. This latter point may be the reason why we have not been able to form stable dinegative ions. The charge densities listed in Table V show that nitrogen atoms possess considerable excess charge in both neutral and radical forms, indicating that a variable self-consistent electronegativity feature[22] might be useful in future studies of these or related molecules. The observation that selenium or sulfur atoms carry a slight positive charge while the fluorine atoms are essentially neutral increases our confidence in the one electron parameters of these atoms. Indeed, the ground-state properties are parameter insensitive.

Included in Tables IV and V for comparison are results of an HMO treatment[5] of benzothiadiazole. One observes from the bond orders that the simple theory imparts more aromatic character to the molecule than the experimental bond distances warrant. Also, the charge density on the sulfur atom is low, particularly in view of the higher charge densities (1.628 or 1.844) obtained with different Hückel parameters.[2]

Tables VI and VII contain the computed transition energies and oscillator strengths for neutral and radical species, respectively. The first column gives results obtained when only a few (12–27) singly excited states are used; the third column shows the effect of inclusion of many (60–70) configurations, both singly and doubly excited. Columns two and four give the principal configurations ($\geq 10\%$) constituting the excited state. It is clear that the number of excited states exerts a

(21) K. Nishimoto and L. S. Forster, *Theoret. Chim. Acta*, **4**, 155 (1966).

(22) R. D. Brown and M. L. Heffernan, *Trans. Faraday Soc.*, **54**, 757 (1958).

Table VI: Electronic Spectra of Neutral Molecules

Molecule	Singly excited configurations: Energy[a]	Singly excited configurations: Wave function	Singly and doubly excited configurations: Energy	Singly and doubly excited configurations: Wave function	Expt
I	29.04 (0.327, y)	(5 → 6), 90%	27.32 (0.281, y)	(5 → 6), 81%	30.0 (0.22)[b]
	44.49 (0.483, x)	(4 → 6), 96%	39.00 (0.123, x)	(4 → 6), 53%; (4^2 → 6^2), 22%; (5 → 8), 13%	42.2 (0.16)
	49.35 (0.073, y)	(3 → 6), 90%	44.17 (0.200, x)	(4^2 → 6^2), 28%; (4 → 6), 25%; (3, 5 → 6^2), 12%	
	53.41 (0.029, y)	(5 → 7), 85%	44.42 (0.060, y)	(3 → 6), 47%; (5 → 7), 22%	
	55.67 (0.908, x)	(5 → 8), 91%	49.20 (0.023, y)	(5 → 7), 39%; (3 → 6), 34%	
			53.92 (0.009, x)	(2 → 6), 36%; (1 → 6), 16%; (3, 5 → 6^2), 14%	
			57.06 (0.960, x)	(5 → 8), 45%; (2 → 6), 32%	
II	29.79 (0.275, y)	(5 → 6), 83%	29.04 (0.227, y)	(5 → 6), 75%; (4 → 8), 10%	32.3 (0.22)[b]
	43.34 (0.523, x)	(4 → 6), 93%	39.45 (0.181, x)	(4 → 6), 67%; (5 → 8), 13%; (4^2 → 6^2), 10%	44.8 (0.3)
	49.84 (0.064, y)	(3 → 6), 89%	45.09 (0.040, y)	(3 → 6), 32%; (5 → 7), 26%; (4, 5 → 6^2), 10%	
	52.18 (0.002, y)	(5 → 7), 73%; (4 → 8), 12%	46.94 (0.111, x)	(4^2 → 6^2), 34%; (5^2 → 6, 7), 15%; (3, 5 → 6^2), 12%; (2 → 6), 10%	
	55.38 (1.064, x)	(5 → 8), 84%	50.06 (0.066, y)	(3 → 6), 45%; (5 → 7), 27%; (5 → 6), 10%	
			56.36 (0.002, x)	(2 → 6), 38%; (4^2 → 6^2), 16%; (4 → 7), 12%	
			57.42 (0.994, x)	(5 → 8), 53%; (4 → 6), 16%	
III	27.08 (0.294, y)	(9 → 10), 87%	27.82 (0.240, y)	(9 → 10), 88%	30.5 (0.21)
	43.68 (0.553, x)	(8 → 10), 94%	39.21 (0.094, x)	(8 → 10), 47%; (9^2 → 10^2), 26%; (9 → 12), 14%	41.7 (0.16)
	48.17 (0.121, y)	(7 → 10), 90%	45.28 (0.159, y)	(7 → 10), 53%; (9 → 11), 19%; (8, 9 → 10^2), 12%	
	51.08 (0.011, y)	(9 → 11), 81%	47.15 (0.362, x)	(8 → 10), 40%; (6 → 10), 22%; (9^2 → 10^2), 22%	
	54.30 (0.125, x)	(6 → 10), 49%; (9 → 12), 41%	49.88 (0.000, y)	(9 → 11), 52%; (7 → 10), 26%	
	55.44 (0.903, x)	(9 → 12), 50%; (6 → 10), 45%	55.09 (0.606, x)	(6 → 10), 53%; (9 → 12), 28%	

[a] Energies in kilokaisers = 1000 cm^{-1}; values in parentheses are first oscillator strength, then polarization where x is long axis. [b] Solution spectra in tetrahydrofuran.

Table VII: Electronic Spectra of Radicals

Molecule	Singly excited configurations: Energy[a]	Singly excited configurations: Wave function[b]	Singly and doubly excited configurations: Energy	Singly and doubly excited configurations: Wave function	Exptl
I	14.93 (0.005, y)	(5 → 6), 62%; (6 → 8), 27%	12.54 (0.005, y)	(5 → 6), 64%; (6 → 8), 21%	18, 22 (0.03)[c]
	21.67 (0.085, x)	(6 → 7), 81%; (4 → 6), 10%	20.47 (0.071, x)	(6 → 7), 79%; (4 → 6), 10%	
	28.62 (0.246, y)	(6 → 8), 53%; (5 → 6), 25%	24.22 (0.176, y)	(6 → 8), 49%; (5 → 6), 16%; (3 → 6), 10%	27.5 (0.11)
	31.38 (0.051, y)	(3 → 6), 52%; (5 → 7)$_4$, 17%; (6 → 9), 11%	29.00 (0.065, y)	(3 → 6), 52%; (6 → 8), 13%	33.0 (0.07)
	37.89 (0.582, x)	(4 → 6), 74%	33.11 (0.455, x)	(4 → 6), 62%	40.7 (0.4)
	47.66 (0.005, y)	(5 → 7)$_3$, 36%; (6 → 9), 26%; (3 → 6), 13%	41.04 (0.005, y)	(4 → 8)$_3$, 29%; (3 → 7)$_3$, 17%; (5 → 7)$_3$, 14%	45.5 (0.06)
II	15.98 (0.002, y)	(5 → 6), 54%; (6 → 8), 34%	14.43 (0.004, y)	(5 → 6), 56%; (6 → 8), 27%	16 (0.02)[c]
	20.63 (0.083, x)	(6 → 7), 81%; (4 → 6), 10%	20.07 (0.078, x)	(6 → 7), 81%; (4 → 6), 10%	23.5 (0.04)
	28.35 (0.223, y)	(6 → 8), 48%; (5 → 6), 29%	24.80 (0.154, y)	(6 → 8), 44%; (5 → 6), 17%; (3 → 6), 10%	29.4 (0.1)
	32.36 (0.044, y)	(3 → 6), 49%; (5 → 7)$_4$, 17%; (6 → 9), 13%	30.64 (0.079, y)	(3 → 6), 46%; (4 → 9)$_4$, 14%; (6 → 8), 12%	40.3 (shoulder)
	37.01 (0.609, x)	(4 → 6), 79%	34.16 (0.470, x)	(4 → 6), 64%	43.0 (0.3)
	46.60 (0.012, y)	(5 → 7)$_3$, 41%; (3 → 7)$_3$, 16%; (4 → 8)$_3$, 13%; (6 → 9), 10%	42.13 (0.084, x)	(2 → 6), 27%; (3 → 8)$_4$, 19%; (4 → 6), 14%; (5 → 8)$_4$, 12%	
III	15.34 (0.008, y)	(9 → 10), 67%; (10 → 12), 22%	13.08 (0.007, y)	(9 → 10), 64%; (10 → 12), 20%	17.5, 23.0 (0.04)
	22.82 (0.076, x)	(10 → 11), 81%; (8 → 10), 12%	21.28 (0.071, x)	(10 → 11), 80%; (8 → 10), 11%	
	27.38 (0.221, y)	(10 → 12), 60%; (9 → 10), 14%	24.69 (0.147, y)	(10 → 12), 42%; (7 → 10), 16%; (9 → 10), 12%; (9 → 11)$_4$, 12%	27.8 (0.13)
	33.12 (0.081, y)	(7 → 10), 68%; (9 → 11)$_4$, 13%	29.98 (0.115, y)	(7 → 10), 46%; (10 → 12), 20%; (9 → 11)$_4$, 11%	36.0 (0.06)
	35.47 (0.541, x)	(8 → 10), 62%; (10 → 11), 11%; (9 → 12)$_4$, 10%	33.45 (0.424, x)	(8 → 10), 56%; (9 → 12)$_4$, 12%	42.5 (0.30)
	44.56 (0.042, x)	(6 → 10), 36%; (7 → 12)$_4$, 16%; (5 → 10), 14%; (8 → 10), 13%; (9 → 12)$_4$, 10%	42.38 (0.107, x)	(6 → 10), 28%; (5 → 10), 16%; (7 → 12)$_4$, 16%; (8 → 10), 14%; (8 → 11)$_4$, 10%	

[a] Energies in kilokaisers, 1000 cm^{-1}; values in parentheses are first oscillator strength, then polarization where x is long axis. [b] Subscript on configuration denotes $^2\chi_3$ or $^2\chi_4$. See eq 2. [c] Reference 4.

moderate influence upon the energies, and in the case of neutral molecules, doubly excited states are needed to decrease the intensity of the lowest x-polarized (long axis) band relative to that of the first y-polarized band.

The predicted radical spectra of the selenium compounds possess the general features of the observed spectra, particularly with regard to the intensity distribution. Transition energies are somewhat low, with the discrepancy increasing as more excited states are added to the CI basis.

A striking effect was noticed when γ_S was set at 11.90 eV.[23] Then the one-electron energy ϵ_4 increased by about 1 eV, causing an inversion in the ordering of the fourth and fifth states of $II\cdot^-$ and, simultaneously, an impressive decrease in the energy of the strongly allowed x-polarized transition. The other states were only mildly altered. This inversion occurred for $\gamma_S > 11.0$ eV and was not present in the neutral molecule. The reason for the change in ϵ_4 could be traced back to the large alteration in the nitrogen atom coefficient for this MO. Apparently, the set of linear equations constituting the open-shell Fock Hamiltonian is not well poised with respect to this eigenvector; other MO's did not display substantial variations.

The essential point of the calculation is not the accuracy which we deem acceptable, but rather the sensitivity of the computation to: (a) parameters, and (b) amount of CI. With regard to point a, the effect of increasing γ_S has been noted; in addition, a dramatic change occurred when I_C was set equal to the Pariser–Parr value of -11.22 eV. Then neutral electronic spectra were clearly incorrect, since two strong absorptions appeared at about 30,000 cm^{-1}, instead of the observed single absorption. This feature was present irrespective of mild variations in other parameters. Conversely, fixing I_C and varying β_{CF}, β_{SeN}, or β_{SN} had little effect. Point b indicates an unsatisfactory feature of the present theory, *i.e.*, the neglect of highly energetic configurations is not theoretically or computationally justified. This is particularly so when one is dealing with molecules of low symmetry. Our experience leads us to agree with the conclusion of Evleth[24] that the conventional parameters should be readjusted to account for extensive CI. It is doubtful whether such features as inclusion of non-nearest neighbor β's, penetration integrals, or self-consistent electronegativity will alter the above remark.

If it is possible to obtain a rationalization of pertinent experimental results using only a p-orbital basis, what is the role of sulfur and selenium d orbitals? The two d orbitals which are symmetric and antisymmetric with respect to reflection in the vertical plane will mix with π orbitals. It is possible that higher excited states at *ca.* 45,000 cm^{-1} will be shifted some 4000–8000 cm^{-1}.[25] However, there is no unique manner of estimating the additional atomic integrals needed. For this reason we do not believe that, at present, the SCF–MO theory is capable of unambiguously demonstrating d-orbital participation. One needs a completely nonempirical theory. This remark is exemplified by considering the anomalously low energies of the strongly allowed x-polarized transitions of $II\cdot^-$ and $III\cdot^-$ (at energies 37,010 and 35,470 cm^{-1}, respectively). The orbitals involved are just those whose one-electron energies are sensitive to γ_S or γ_{Se}. Clearly no conclusion regarding d-orbital participation is justified until one is certain that values of γ_S, γ_{Se}, γ_{SN}, and γ_{SeN} are correctly chosen. With this one exception (which is not the case for $I\cdot^-$) a p-orbital model is satisfactory.

Acknowledgments. We are indebted to Dr. D. C. Borg for the use of his esr simulation program, EPRSYN, and to Mrs. V. H. Wilson for her aid with the experiments.

(23) M. Bielefeld and D. D. Fitts, *J. Amer. Chem. Soc.*, **88**, 4804 (1966).

(24) E. M. Evleth, *J. Chem. Phys.*, **46**, 4151 (1967).

(25) Shifts of this order were found by Bielefeld and Fitts[23] when d orbitals were included in the basis set of thiophene.

A Floating Spherical Gaussian Orbital Model of Molecular Structure. III. First-Row Atom Hydrides

by Arthur A. Frost

Department of Chemistry, Northwestern University, Evanston, Illinois *(Received September 25, 1967)*

The FSGO model is applied to the first-row hydrides and several isoelectronic ionic species as follows: BeH_2, LiH_2^-, BH_2^+, BH_3, BeH_3^-, CH_3^+, CH_4, BH_4^-, NH_4^+, H_4O^{2+}, NH_3, CH_3^-, H_3O^+, H_2O, NH_2^-, H_2F^+, HF, OH^-. The trends in the bond lengths and electronegativities are correctly predicted. Furthermore, the bond lengths are predicted quantitatively within an accuracy of 6%. Bond angles in NH_3 and H_2O are low by about 17%, calculated angle in NH_3 being 87.6° compared with the experimental value of 106.6°, while for H_2O the values are 88.4° compared with 104.5°.

Introduction

The floating spherical Gaussian orbital model (FSGO) as presently used applies to singlet ground states of molecules having localizable orbitals. Each localized orbital is represented by a spherical Gaussian function

$$\varphi_i(r) = \left(\frac{2}{\pi\rho_i^2}\right)^{3/4} \exp[-(r/\rho_i)^2]$$

with variable "orbital-radius" ρ_i and with variable position of its center. The total electronic wave function is a single Slater determinant of closed shells. The separate orbitals are nonorthogonal with overlap-matrix S. The inverse overlap matrix, $T = S^{-1}$, is involved in the energy formula

$$E = \sum_{j,k}(j|k)\ T_{jk} + \sum_{k,l,p,q}(kl|pq)\,[2T_{kl}T_{pq} - T_{kq}T_{lp}]$$

By minimizing the total energy with respect to all parameters, the orbital radii and positions and the nuclear coordinates, the electronic and geometrical structure is predicted. Paper I[1] of this series details the calculations and discusses the result for the LiH molecule at length. Paper II[2] presents results of one- and two-orbital systems, including among others the He and Be atoms and the molecules and molecule ions H_2, He_2^{2+}, HeH^+, H_3^+, H_4^{2+}, HeH^-, and BeH^+, and the He_2 interaction.

The present paper contains results of calculations on systems of more general chemical interest, including compounds of the first-row elements from Li to F. Possible compounds of interest are the homonuclear diatoms Li_2–F_2 and the diatomic hydrides LiH, BeH, BH, CH, NH, OH, and HF. The first series raises complications because of the rapidly increasing number of electron pairs and orbitals as one proceeds toward F_2 with its 18 electrons. Also there is the particular difficulty with B_2 and O_2, which have ground-state triplets. The present calculations which involve only a single closed-shell Slater determinant would presumably provide approximations to the lowest singlet states of such molecules.

The diatomic hydrides BeH, BH, CH, NH, and OH can be calculated on this model, but are chemically unstable with respect to the higher valence species BeH_2, BH_3, CH_4, NH_3, and H_2O. It is this latter series including also HF and the previously discussed[1] LiH that will be described now. The increasing number of hydrogen atoms as CH_4 is approached adds little to the computation time, as this depends primarily on the number of electrons which in the molecules from CH_4 to HF is constant at ten.

Computational Procedure and Results

Preliminary results on this series of molecules have previously been reported.[3] LiH with its four electrons and two orbitals has been discussed in papers I and II.

BeH_2 was assumed to be linear and symmetrical. Of the three localized orbitals for the six electrons, one is an inner shell centered on the Be nucleus while the other two are bonding orbitals located on the molecular axis and equidistant from the Be. The energy was minimized with respect to variations in all the possible parameters consistent with the symmetry, namely four: the orbital radius of the inner shell, the orbital radius for each bonding orbital both considered equal, the position of a bonding orbital, and the bond distance Be–H. Results for the BeH_2 isoelectronic series are in Table I. Figure 1 shows the orbitals and nuclear positions schematically.

BH_3 with four orbitals was assumed to be planar with trigonal symmetry, therefore D_{3h}. There were four

(1) Paper I: A. A. Frost, *J. Chem. Phys.*, **47**, 3707 (1967).

(2) Paper II: A. A. Frost, *ibid.*, **47**, 3714 (1967).

(3) A. A. Frost, B. H. Prentice, III, and R. A. Rouse, *J. Amer. Chem. Soc.*, **89**, 3064 (1967). Also presented in part at the Symposium on Computers in Chemistry, San Diego, Calif., June 1967, and at the 154th National Meeting of the American Chemical Society, Chicago, Ill., Sept 1967.

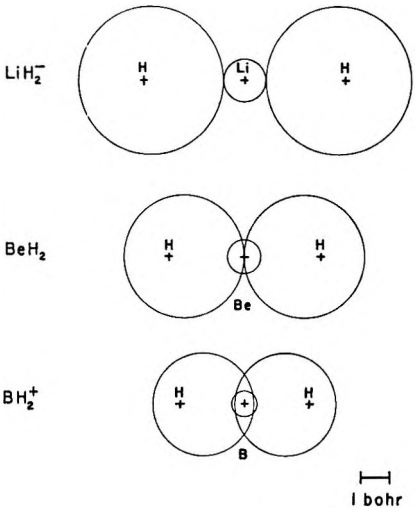

Figure 1. Schematic diagram of localized orbitals in the BeH_2 sequence. Each spherical Gaussian orbital is represented by a circle drawn with its radius equal to the orbital radius ρ.

Table I: FSGO Model Calculations for BeH_2 Isoelectronic Series[a]

Molecule	$-E$, hartrees	Orbital radii,[b] Bohrs	Bond orbital distance from center, Bohrs	Bond length, Bohrs
LiH_2^-	7.026	0.707	3.287	3.514[c]
		2.524		
BeH_2	13,214	0.510	2.107	2.669
		2.108		
BH_2^+	21.563	0.398	1.438	2.292
		1.794		

[a] Atomic units. [b] First value for inner shell, second for bonding orbital. [c] A calculation by H. Preuss and G. Diercksen, *Intern. J. Quantum Chem.*, **1**, 631 (1967), with their SCF–MO–LC(LCGO) method yields 3.5 ± 0.2 au.

parameters varied as in the case of BeH_2, namely: the orbital radius of the inner shell, the orbital radius of the bonding orbitals, the distance of the bonding orbitals from the B nucleus, and the B–H bond distance. Table II presents the calculated results for BH_3 and the isoelectronic CH_3^+ and BeH_3^-.

CH_4 with five orbitals was assumed to be tetrahedral. Again there were just four parameters defined in a similar manner to those used for BeH_2 and BH_3. The isoelectronic ions BH_4^-, NH_4^+, and H_4O^{2+} were calculated in the same manner by merely changing the charge on the central nucleus. Table III shows the results.

The NH_3 molecule and its isoelectronically related ions CH_3^- and H_3O^+ constitute a much more involved calculation because of the lowered symmetry. Assuming C_{3v} symmetry, let the heavy nucleus be at the origin of a set of Cartesian coordinates with the z axis

Table II: FSGO Model Calculations for BH_3 and Related Ions[a]

Molecule	$-E$, hartrees	Orbital radii, Bohrs	Bond orbital distance from center, Bohrs	Bond length, Bohrs
BeH_3^-	13.655	0.511	2.462	2.878
		2.199		
BH_3	22.297	0.399	1.672	2.353
		1.851		
CH_3^+	33.300	0.327	1.150	2.062[b]
		1.590		

[a] Atomic units. [b] Compare this with the value 2.05 au calculated by the SCF–MO–LC(LCGO) method: G. von Bünau, G. Diercksen, and H. Preuss, *Intern. J. Quantum Chem.*, **1**, 645 (1967).

Table III: FSGO Model Calculations for CH_4 and Its Isoelectronic Ions[a]

Molecule	$-E$, hartrees	Orbital radius, Bohrs	Bond orbital distance from center, Bohrs	Bond length, Bohrs
BH_4^-	22.692	0.400	1.905	2.493
		1.970		
CH_4	33.992	0.328	1.256	2.107
		1.694		
NH_4^+	47.893	0.278	0.795	1.876
		1.469		
H_4O^{2+}	64.527	0.240	0.473	1.756
		1.276		

[a] Atomic units.

being the threefold axis. Let one H nucleus and the corresponding NH bonding orbital be at arbitrary positions in the yz plane and the other nuclei and bonding orbitals at equivalent positions out of the plane. The inner shell and lone-pair orbitals are assumed to be on the z axis with variable z coordinates. All together there are then three parameters for orbital radii, four parameters for orbital positions, and two parameters for nuclear positions, making a total of nine parameters in the variation problem. Results are shown in Table IV.

The H_2O molecule and related ionic species are assumed to have C_{2v} symmetry with the z axis as the C_2 axis of the molecule and the three nuclei in the yz plane. The heavy nucleus is at the origin. Variable parameters would then include the y and z coordinates of one H nucleus, the y and z coordinates of a bonding orbital, the z coordinate of the inner shell orbital, the x and z coordinates of a lone-pair orbital assumed to be in the xz plane, and the orbital radii of each of the three different kinds of orbitals. When the compu-

Table IV: FSGO Model Calculations for NH_3 and Related Ions[a,b]

	CH_3^-	NH_3	H_3O^+
Negative total energy	33.315	47.568	64.647
Orbital radii			
Inner shell	0.327	0.277	0.240
Bonding	1.899	1.554	1.297
Lone pair	2.032	1.627	1.332
Orbital positions			
Inner-shell z coordinate	0.0008	0.0007	0.0006
Lone-pair z coordinate	−0.068	0.160	0.157
Bonding in yz plane			
y coordinate	1.079	0.611	0.368
z coordinate	0.824	0.515	0.329
H nuclei positions			
H in yz plane			
y coordinate	1.823	1.527	1.390
z coordinate	1.374	1.147	0.979
AH bond length	2.283	1.910	1.700
HAH bond angle	87.5°	87.6°	90.2°

[a] Axis of molecule is z; heavy atom at origin; one H atom and bonding orbital in yz plane. [b] Atomic units: energy in hartrees, distances in Bohrs.

Table V: FSGO Model Calculations for H_2O and Related Ions[a,b]

	NH_2^-	H_2O	H_2F^+
Negative total energy	46.791	64.288	84.874
Orbital radii			
Inner shell	0.277	0.240	0.212
Bonding	1.618	1.308	1.097
Lone pair	1.660	1.331	1.104
Orbital positions			
Inner shell			
z coordinate	0.0006	0.0005	0.0004
Lone pairs			
x coordinate	(±0.100)	(±0.100)	(±0.100)
z coordinate	−0.0039	0.022	0.020
Bonding			
y coordinate	±0.656	±0.369	±0.207
z coordinate	0.726	0.426	0.249
H nuclei positions			
y coordinate	±1.345	±1.161	±1.103
z coordinate	1.431	1.195	1.061
AH bond length	1.964	1.666	1.531
HAH bond angle	86.4°	88.4°	92.2°

[a] Axis of molecule is z; heavy atom is at origin with molecule in yz plane. [b] Atomic units: energy in hartrees, distances in Bohrs; values in parentheses held constant.

tation is allowed to proceed toward a minimum in the total energy by the variation of all ten parameters, the calculation soon breaks down owing to the tendency of the two lone-pair orbitals to coalesce. As these orbitals approach each other their overlap integral tends toward unity, causing the overlap matrix to become nearly singular. The inverse overlap matrix needed in the energy calculation[1] then "blows up" causing too great a loss in significant figures in the energy. To get around this difficulty, the x coordinates of the lone-pair orbitals were held constant at values such as ±0.4, ±0.2, and ±0.1, while the nine other parameters were varied. In this manner it was found that the energy and the geometrical parameters approached limiting values rapidly enough so that with $x = \pm 0.1$ sufficient accuracy was attained. At this pair of values such that the centers of the lone-pair orbitals were separated by 0.2, the calculation proceeded satisfactorily, even though the overlap integral between these orbitals was approximately 0.99.

The actual limiting case of the coalescence of the two like orbitals was handled by replacing the two orbitals by their sum and difference. In the limit the sum is an s orbital and the difference a p orbital. Details are given in the Appendix. Such a linear transformation of basis orbitals in a closed-shell Slater determinantal wave function causes no change in the many-electron wave function, but does make possible a more accurate calculation of the energy since the s and p orbitals are orthogonal. The energy for a fixed set of parameters was calculated by the POLYATOM program[4] confirming the results obtained with spherical lone-pair orbitals at a small finite separation. Results for these molecular species are shown in Table V.

The final member of the hydride series is HF. This molecule and the isoelectronic species OH^- were calculated assuming the inner shell and bonding orbitals were on the internuclear z axis and that the three lone-pair orbitals were located about this axis with C_{3v} symmetry. The complete minimization problem, while preserving this orbital symmetry, would involve the variation of eight parameters. There are three different orbital radii, three different z coordinates for orbital positions, one off-axis y coordinate for a lone-pair orbital arbitrarily restricted to the yz plane, and the z coordinate of the H nucleus or bond length taking the O or F nucleus at the origin. Again there was a tendency for the lone-pair orbitals to coalesce on the molecular axis. It was necessary to go through a limiting procedure where the off-axis distance of the three lone-pair orbitals was held constant at successively smaller values, all other parameters being varied in each case to minimize the energy. The calculation was still valid with the orbitals off the axis by 0.2 Bohr where the overlap integrals were 0.95. At this distance the limiting structure appeared to be obtained with sufficient accuracy. Results are in Table VI.

The computations were carried out on a CDC3400 computer. In a typical calculation the first variation involved 10% changes in the starting values of the parameters. The step size was diminished successively

(4) J. G. Czismadia, M. C. Harrison, J. W. Moskowitz, and B. T. Sutcliffe, *Theor. Chim. Acta*, 6, 191 (1966). The POLYATOM program was obtained from the Quantum Chemistry Program Exchange, Indiana University, Bloomington, Ind.

to the order of 0.001% with the energy becoming constant to eight significant figures. The most time-consuming calculation was that of H_2O, where a single energy calculation for fixed parameters required about 0.2 sec and the total energy minimization involving several hundred such energy calculations took about 2 min. This time requirement is, of course, far less than would be used in a typical SCF–MO calculation, even with a minimal basis set.

Table VI: FSGO Model Calculations for HF and OH [a,b]

	OH^-	HF
Negative total energy	63.488	84.571
Orbital radii		
Inner shell	0.241	0.212
Bonding	1.350	1.111
Lone pair	1.362	1.107
Orbital positions		
Inner shell		
z coordinate	0.0004	0.0003
Lone pairs		
y coordinate	(0.200)	(0.200)
z coordinate	0.0067	0.018
Bonding		
z coordinate	0.678	0.345
Bond length	1.679	1.482

[a] Axis of molecule is z; heavy atom at origin; H in $+z$ direction. [b] Atomic units: energy in hartrees, distances in Bohrs; values in parentheses held constant.

Discussion of Results

The calculated molecular structures are all qualitative, as one would expect. The bond lengths decrease regularly as the atomic number of the first-row atom increases. This is obviously a shrinkage effect due to the increased electrostatic attraction of the bonding electrons. There is even a semiquantitative agreement between calculated and observed bond lengths, as shown in Table VII, with an average error of 6% for the five molecules where experimental data are available. Also shown in the table are the relative positions of the bond orbitals with respect to the A and H nuclei. As the central atom A varies from Li to F, the bond orbital shifts from a position near the H nucleus to a position near A. This effect obviously relates to the increasing electronegativity of A. NH_3 and H_2O are special cases, in that the bond orbitals are not centered on the internuclear lines but rather slightly displaced toward the molecular axis forming what might be considered as bonds bent inward. Figure 2 shows in schematic fashion the situation for H_2O.

H_2O and NH_3 are properly predicted to be nonlinear and pyramidal, respectively. However, the HOH and HNH bond angles, which were calculated to be 88.4 and 87.6°, are rather low compared to the experimental values of 104.5 and 106.6°, having an average error of 17%. A large error in bond angles as compared with bond lengths might be expected on account of the smaller force constant for the bending distortion, as compared with that for a stretching distortion. That the bond angle of NH_3 is too small can be related to the extremely high inversion barrier[3] predicted by this simple model.

It may be observed in Tables IV–VI that the z coordinates of the lone-pair orbitals in NH_3, H_2O, and HF are positive. This would appear to be quite contrary to expectations, in view of the general result of more conventional LCAO theory according to which the lone pairs would occupy orbitals aimed generally in the opposite direction. However, the present orbitals are nonorthogonal, a situation which seriously complicates

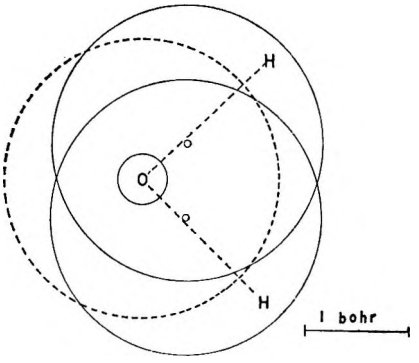

Figure 2. Schematic diagram of the localized orbitals and the predicted geometric structure of H_2O. The center of each bonding orbital is slightly displaced from its internuclear axis. The lone-pair orbitals are indicated by the dashed circle and are displaced above and below the plane of the nuclei.

Table VII: FSGO Model. Summary of Results for Neutral Hydrides

Molecule	Bond length, Å: Calcd[a]	Bond length, Å: Obsd[b]	Percentage distance of bond orbitals toward H nuclei
LiH	1.712	1.595	89.3
BeH_2	1.412		78.9
BH_3	1.245		71.2
CH_4	1.115	1.093	59.7
NH_3	1.011	1.012	44.9[c]; 40.1[d]
H_2O	0.881	0.957	35.7[c]; 31.7[d]
HF	0.784	0.917	23.3

[a] A few of the values quoted here differ slightly from the corresponding values presented in ref 3, owing to improved accuracy of calculation. [b] Observed values from L. E. Sutton, Ed., "Interatomic Distances," Special Publication No. 18, The Chemical Society, London, 1965. [c] Along axis. [d] Perpendicular to axis.

the interpretation. If the basis floating orbitals were orthogonalized by a suitable linear transformation (with no effect on the total many-electron antisymmetric wave function) a more familiar picture might be obtained. Unfortunately, there is no unique way to carry out the orthogonalization.

The energies of the various molecular species as calculated with this model may be compared with Hartree–Fock–Roothaan SCF–LCAO–MO energies, inasmuch as in each type of calculation the energy is minimized for the wave function expressed as a single Slater determinant.

Naturally, the present model has a comparatively crude wave function, so it is expected that the calculated energy will be well above the Hartree–Fock limit. A comparison of available results[3] shows that the present model provides almost universally about 85% of the Hartree–Fock energy. The 15% loss is primarily due to the lack of suitable cusps for the inner-shell wave functions. This error in total energy would not necessarily mean a drastic error in the shape of the energy hypersurface, but might be primarily just a displacement upward in energy in which case geometrical predictions by the present model could conceivably still be reasonably good. Bond distances and bond angles as predicted by SCF–LCAO–MO theory[5] appear to be somewhat better however.

Acknowledgments. The National Science Foundation supported this research. Mr. Robert A. Rouse provided assistance.

Appendix

Coalescence of Two Orbitals. Consider two normalized spherical Gaussian orbitals, φ_1 and φ_2, with equal radii, ρ, and centered on the z axis at $\pm R/2$, respectively. These are nonorthogonal and have an overlap integral, S, approaching unity as R approaches zero. A convenient pair of orthogonalized orbitals is the sum and difference. When normalized, these are

$$\psi_1 = \frac{1}{\sqrt{2 + 2S}}(\varphi_1 + \varphi_2)$$

$$\psi_2 = \frac{1}{\sqrt{2 - 2S}}(\varphi_1 - \varphi_2)$$

In the limit $\psi_1 = \varphi_1 = \varphi_2$ and is just a Gaussian s orbital. ψ_2 becomes a Gaussian p_z orbital as follows

$$\psi_2 = \frac{1}{\sqrt{2 - 2S}}\left(\frac{2}{\pi\rho^2}\right)^{3/4}\left\{\exp\left[-\left(\frac{r - \frac{R}{2}}{\rho}\right)^2\right] - \exp\left[-\left(\frac{r + \frac{R}{2}}{\rho}\right)^2\right]\right\}$$

$$= \frac{1}{\sqrt{2 - 2S}}\left(\frac{2}{\pi\rho^2}\right)^{3/4}\exp[-(r/\rho)^2] \times \exp[-(R/2\rho)^2]\left\{\exp\left[+\frac{zR}{\rho^2}\right] - \exp\left[\frac{zR}{\rho^2}\right]\right\}$$

When the bracketed quantity is expanded it becomes $+2zR/\rho^2$ plus terms higher order in R. By expanding

$$S = \exp[-\tfrac{1}{2}(R/\rho)^2]$$

$$S = 1 - \tfrac{1}{2}\left(\frac{R}{\rho}\right)^2 + \cdots$$

the expression for S, the normalizing factor $1/\sqrt{2 - 2S}$, becomes

$$\frac{1}{\sqrt{2 - 2S}} \simeq \frac{1}{\sqrt{2\left(\frac{1}{2}\frac{R}{\rho}\right)^2 + \cdots}}$$

$$\simeq \frac{\rho}{R} + \cdots$$

Therefore, the limit of ψ_2 as R approaches zero is

$$\psi_2(R = 0) = \frac{2}{\rho}\left(\frac{2}{\pi\rho^2}\right)^{3/4} z \exp[-(r/\rho)^2]$$

which is a normalized p_z Gaussian orbital centered at the origin.

Coalescence of Three Orbitals in Equilateral Triangular Array. Consider three normalized spherical Gaussian orbitals with equal radii and positioned at the corners of an equilateral triangle: φ_1 centered at $(x, y) = (0, R)$; φ_2 centered at $(+\sqrt{3}R/2, -R/2)$; φ_3 centered at $(-\sqrt{3}R/2, -R/2)$. These may be replaced by the orthogonal linear combinations

$$\psi_1 = \frac{1}{\sqrt{3 + 6S}}(\varphi_1 + \varphi_2 + \varphi_3)$$

$$\psi_2 = \frac{1}{\sqrt{2 - 2S}}(\varphi_2 - \varphi_3)$$

$$\psi_3 = \frac{1}{\sqrt{6 - 6S}}(2\varphi_1 - \varphi_2 - \varphi_3)$$

where S is the overlap integral for any pair of φ orbitals. In going to the limit ($R = 0$)

$$\psi_1 = \varphi_1 = \varphi_2 = \varphi_3$$

and is just an s orbital. ψ_2 and ψ_3 both have nodal surfaces and in the limit become p_x and p_y Gaussian orbitals, respectively.

(5) See, for example, M. Krauss, *J. Res. Nat. Bur. Stand.*, **68A**, 635 (1964), and S. D. Peyerimhoff, R. J. Buenker, and L. C. Allen, *J. Chem. Phys.*, **45**, 734 (1966).

Thermodynamics of the λ Transition in Sodium Nitrate

by William Klement, Jr.

Department of Engineering, University of California, Los Angeles, California 90024 *(Received September 28, 1967)*

Critically evaluated thermodynamic data for the λ transition in crystalline $NaNO_3$ are interrelated by means of the Garland relations. The transition appears to be essentially one dimensional, in the sense that the most salient anomalies in the crystalline properties occur parallel to the *c* axis. Corresponding anomalies, *ca.* 0.3% as large, are predicted in the properties perpendicular to the *c* axis, but appropriate experiments are lacking.

Apparent success[1,2] for the high–low quartz inversion suggests that the thermodynamic relations[2] of Garland may be applied to λ transitions in other anisotropic crystals. This paper, correlating the data for $NaNO_3$, follows upon the recent report[3] for the trajectory of the λ line at high pressures, in which difficulties with the thermodynamic description were encountered.

The Garland relations[2] are

$$\frac{1}{l_i}\left(\frac{\partial l_i}{\partial T}\right)_i = \left(\frac{\partial T_\lambda}{\partial p}\right)_i \left(\frac{c_p}{TV}\right) - g_i' \qquad (1)$$

$$s^T{}_{ij} = \left(\frac{\partial T_\lambda}{\partial p}\right)_j \frac{1}{l_i}\left(\frac{\partial l_i}{\partial T}\right)_p - \left(\frac{\partial T_\lambda}{\partial p}\right)_i g_j' - (T - T_\lambda) g_i''\delta_{ij} - h^{ij} \qquad (2)$$

and, since

$$s^S{}_{ij} = s^T{}_{ij} - \frac{1}{l_i}\left(\frac{\partial l_i}{\partial T}\right)_p \frac{1}{l_j}\left(\frac{\partial l_j}{\partial T}\right)_p \left(\frac{c_p}{TV}\right)^{-1}$$

$$s^S{}_{ij} = -(T - T_\lambda) g_i''\delta_{ij} - h^{ij} - g_i' g_j' \left(\frac{c_p}{TV}\right)^{-1} \qquad (3)$$

where $1/l_i(\partial l_i/\partial T)_p$ is the linear coefficient of thermal expansion along axis i; $(\partial T_\lambda/\partial p)_i$ is the rate of change of the λ temperature, T_λ, with stress in direction i; $s^T{}_{ij}$ and $s^S{}_{ij}$ are the isothermal and adiabatic elastic compliance moduli, respectively, etc.; g_i' and h^{ij} are regarded as constants, with g_i'' vanishing identically. Summations over the indices of $(\partial T\lambda/\partial p)_i$, $1/l_i(\partial l_i/\partial T)_p$, and $s^T{}_{ij}$ and $s^S{}_{ij}$ yield, respectively, $(dT/dp)_\lambda$ (the rate of change of the λ temperature with pressure), the volume coefficient of thermal expansion, and the isothermal and adiabatic compressibilities.

Presumably, eq 1–3 are exact as $T \to T_\lambda$, but it is not known over what temperatures ranges about T_λ they constitute useful approximations; inevitably, the thermodynamic data are less accurate in the regions of rapid variation near T_λ. The following is an attempt to evaluate the measurements of volume, specific heat, thermal expansions, and elastic compliance moduli as a function of temperature at zero pressure so as to obtain a preferred set of data for discussion in the framework of the Garland relations.

There is substantial agreement for the volume *vs.* temperature among the results of Kracek[4] (volumetric dilatometry), Ravich and Egorov[5] (linear dilatometry), and Kantola and Vilhonen[6] (X-ray diffraction). Near $T_\lambda \approx 275°$, $V \approx 39.6$ cm^3 fw^{-1}.

The smoothed c_p data[7] of Mustajoki appear acceptable, except in the range $|T - T_\lambda| \lesssim 5°$ where these values may be low. Miekk-oja[7] and Sokolov and Schmidt[8] approximately corroborate Mustajoki's data,[7] for which an excess entropy for the transition of 5.27 J deg^{-1} fw^{-1} was suggested.[7]

The volumetric thermal-expansion data[5] of Ravich and Egorov are preferred to those[4] of Kracek and, below 260°, approximately corroborate the volumetric expansions calculated from the linear expansion data[9] of Austin and Pierce. The Austin–Pierce thermal expansion coefficients[9] parallel to the *c* axis, the *a* axis, and perpendicular to the {10.1} face ($\equiv 1/l'(\partial l'/\partial T)_p$) may be scrutinized by realizing that eq 1 becomes

$$\frac{1}{l_i}\left(\frac{\partial l_i}{\partial T}\right)_p = \left(\frac{\partial T_\lambda}{\partial p}\right)_i \left(\frac{\partial T_\lambda}{\partial p}\right)_j^{-1} \frac{1}{l_j}\left(\frac{\partial l_j}{\partial T}\right)_p + \left[\left(\frac{\partial T_\lambda}{\partial p}\right)_i \left(\frac{\partial T_\lambda}{\partial p}\right)_j^{-1} g_j' - g_i'\right] \qquad (4)$$

None of the thermal expansions is particularly reliable near T_λ, where plastic deformation and hystereses were

(1) W. Klement and L. H. Cohen, *J. Geophys. Res.*, in press.

(2) C. W. Garland, *J. Chem. Phys.*, **41**, 1005 (1964).

(3) E. Rapoport, *J. Phys. Chem. Solids*, **27**, 1349 (1966).

(4) F. C. Kracek, *J. Amer. Chem. Soc.*, **53**, 2609 (1931).

(5) G. B. Ravich and B. N. Egorov, *Russ. J. Inorg. Chem.*, **5**, 1257 (1960).

(6) M. Kantola and E. Vilhonen, *Ann. Acad. Sci. Fenn.*, **AVI**, 54 (1960).

(7) A. Mustajoki, *ibid.*, **AVI**, 5 (1957).

(8) V. A. Sokolov and N. E. Shmidt, *Izv. Sektora Fiz.-Khim. Anal. Inst. Obshch. Neorg. Khim. Akad. Nauk SSSR*, **26**, 123 (1955); quoted by ref 5.

(9) J. B. Austin and R. H. H. Pierce, *J. Amer. Chem. Soc.*, **55**, 661 (1933).

encountered, but $1/l_z(\partial l_z/\partial T)_p$ is the most nearly reliable since it contributes the bulk of the volumetric thermal expansion, which is corroborated[5,6] up to 260°. Also, Austin and Pierce averaged out some of the hysteresis for $1/l_z(\partial l_z/\partial T)_p$ by obtaining measurements on cooling, whereas this could not be done for $1/l_x(\partial l_x/\partial T)_p$ and $1/l'(\partial l'/\partial T)_p$. Plots of the thermal expansion coefficients against one another yield the linear relations: $1/l_z(\partial l_x/\partial T)_p = -2.7 \times 10^{-3}[1/l_z(\partial l_z/\partial T)_p] + 11.0$ Mdeg^{-1} over 175–250°, $1/l_x(\partial l_x/\partial T)_p = -3.7 \times 10^{-3}[1/l'(\partial l'/\partial T)_p] + 10.9$ Mdeg^{-1} over 175–225°, and $[1/l'(\partial l'/\partial T)_p] = 0.70[1/l_z(\partial l_z/\partial T)_p] - 0.035$ kdeg^{-1} over 175–225°. In view of the uncertainties in the data, it can be assumed that the $1/l_i(\partial l_i/\partial T)_p$ are indeed linearly related into the vicinity of T_λ (as for quartz[1,2]) and that, from eq 4, $(\partial T_\lambda/\partial p)_x(\partial T_\lambda/\partial p)_z \approx -2.7 \times 10^{-3}$ and $g_x' + 2.7 \times 10^{-3} g_z' \approx -11.0$ Mdeg^{-1}.

Kornfel'd and Chubinov[10] reported the adiabatic compliance moduli s^S_{11}, s^S_{33}, s^S_{44}, and s^S_{12} from 20 to 300°; since absorption and dispersion were negligible at 0.12 and 0.17 kHz, it is assumed that the relaxation time is very small and that there are no misleading effects such as encountered in sound-velocity measurements in other λ transitions.[11,12] It is probable that the values for the smoothed compliance moduli[10] at T_λ (=275.5°) are not reliable, except perhaps as lower bounds, because of the possibility of temperature gradients in such long specimens of poor thermal conductivity. Also, the s^S_{12} moduli are probably the least accurate throughout, because they result as the small differences between large (measured) quantities. A cusp is found only for s^S_{33} *vs.* temperature; the discontinuities in slope shown[10] at T_λ for the plots of s^S_{11}, s^S_{12}, and s^S_{44} *vs.* temperature appear to be due almost entirely to the density data,[4] the sound velocities varying smoothly through the transition.

The plot of $1/l_z(\partial l_z/\partial T)_p$ *vs.* (c_p/TV) in Figure 1 yields, according to eq 1, upper bounds of ~8.6 deg kbar^{-1} for $(\partial T_\lambda/\partial p)_z$ and ~0.45 kdeg^{-1} for g_z'. The lack of reliable data close to T_λ (and none above T_λ) infers some uncertainty into these and the following estimates. From the above deductions *via* eq 4 or by plotting $1/l_x(\partial l_x/\partial T)_p$ *vs.* (c_p/TV), $(\partial T_\lambda/\partial p)_x \sim -0.02$ deg kbar^{-1} and $g_x' \sim -0.013$ kdeg^{-1}.

The plot of s^S_{33} *vs.* $(c_p/TV)^{-1}$ in Figure 2 yields, according to eq 3, upper bounds of ~0.45 kdeg^{-1} for $|g_z'|$ and ~7.9 Mbar^{-1} for $-h^{33}$. The value of 7.0 Mbar^{-1} given[10] for s^S_{33} at T_λ might be considered as a lower bound for $-h^{33}$.

For s^T_{33} calculated from the preferred data and plotted *vs.* $1/l_z(\partial l_z/\partial T)_p$ in Figure 3, there results the upper bounds of ~8.6 deg kbar^{-1} for $(\partial T_\lambda/\partial p)_z$ and ~4.0 Mbar^{-1} for $-(\partial T_\lambda/\partial p)_z g_z' - h^{33}$.

Rearrangement of eq 3 suggests[2] that $s^S_{11} - s^S_{12}$ is approximately constant near T_λ and the smoothed data[10] indeed indicate this with $h^{12} - h^{11} \approx 4.5$ Mbar^{-1}. Equation 3 [and 2] and the estimates for g_x' and g_z'

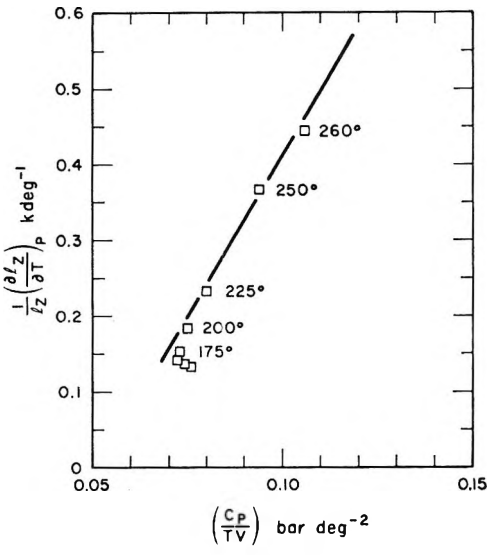

Figure 1. Plot of eq 1 for various temperatures below T_λ; suggested asymptote is shown.

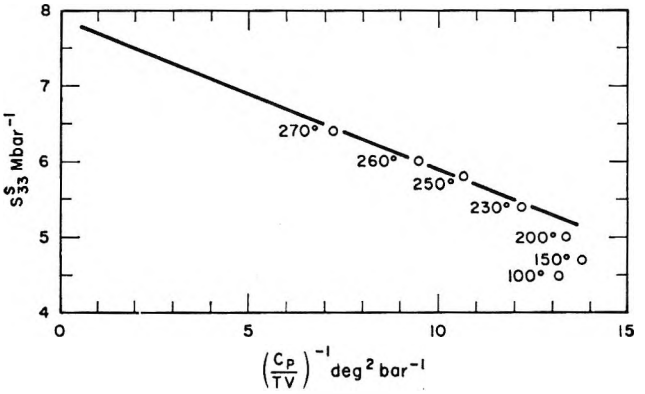

Figure 2. Plot of eq 3, including suggested asymptote.

dictate the variation of s^S_{11} and s^S_{12} near T_λ, but these predictions are not borne out by the existing data.[10] The available measurements[10] are probably not a critical test of the present theory and, besides, it is entirely possible that the temperature range is very limited for the validity of eq 3 in the plots of s^S_{11} and s^S_{12} *vs.* temperature. Another sensitive test of the theory is by the variation near T_λ of s^S_{13}, for which no measurements exist to compare with the present predictions of a slight decrease.

Some limited comparisons of the ranges of validity of the various relations can be made between $NaNO_3$ and quartz,[1] the only other anisotropic crystal so far studied in detail in this way. Equation 4 appears to hold over the longest temperature range for both quartz and $NaNO_3$. Equations 1 and 2 hold over a more limited range for quartz than for $NaNO_3$. Equation 3 appears to hold over the greatest range for s^S_{33} of $NaNO_3$, with

(10) M. I. Kornfel'd and A. A. Chubinov, *Soviet Phys. JETP*, **6**, 26 (1958).

(11) C. W. Garland, *Phys. Rev.*, **A135**, 1696 (1964).

(12) W. Klement, *J. Chem. Phys.*, **45**, 1421 (1966).

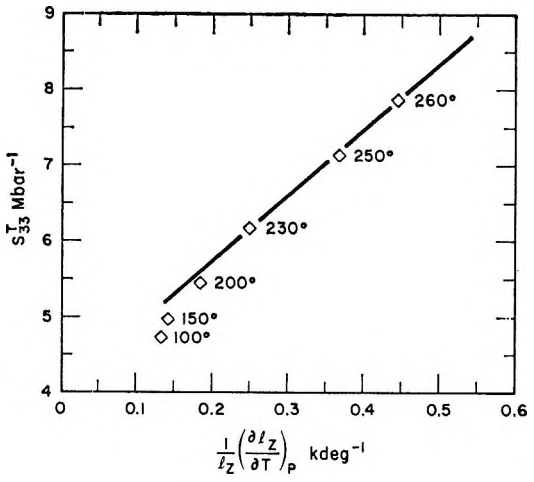

Figure 3. Plot of eq 2, including suggested asymptote.

lesser ranges of validity for the s^S_{ij} of quartz and, presumably, the other s^S_{ij} of $NaNO_3$. Also, in striking analogy[1] with quartz, the Poisson ratio $-s^S_{12}\,(s^S_{11})^{-1}$ becomes *negative* upon approaching the transition in $NaNO_3$ (near 230°[10]).

Application of the Garland relations to the quartz data was much expedited[1] by the existence of a reliable value[13] (26 ± 1 deg kbar^{-1}) for $(dT/dp)_\lambda$. For $NaNO_3$, the present estimated upper bound of ~8.6 deg kbar^{-1} can only be compared with Rapoport's suggestion[3] of 6.1 ± 0.2 deg kbar^{-1}. Some of the uncertainties in Rapoport's experiments[3] are: extrapolation to zero pressure of data only obtained above 5 kbar; inability to determine T_λ at zero pressure and concomitant uncertainty about the temperature scale (*e.g.*, the melting point seems to be uncertain within 4°); inability to observe distinct differential thermal analysis signals on heating and thus to identify and correct for the hystereses which might be expected[5] under such relatively rapid rates of cooling; and uncertainties in the hydrostaticity of the pressure distribution, especially for solid–solid transitions at relatively low temperatures.

Rapoport[3] made a Pippard plot (essentially a summation of eq 1) using Mustajoki's smoothed c_p data[7] and $1/V(\partial V/\partial T)_p$ deduced from Kracek's measurements[4] (also with a slight shift in temperature scales); $(dT/dp)_\lambda$ was estimated as 11.7 deg kbar^{-1}, primarily on data from 250–280°. This estimate is clearly unsatisfactory since the data[4, 7] used are least reliable close to T_λ where, somehow, they must be smoothed and the temperature hysteresis averaged out. Rapoport[3] also attempted to use an "integrated Clausius–Clapeyron equation," dissecting out an entropy and a volume in excess of the "normal" and treating the transition as first order; this approach[3] suggested ~8.8 deg kbar^{-1} for $(dT/dp)_\lambda$. Again, and in analogy with quartz,[1] this approach is precarious because of the uncertainty in identifying the "normal" variation of entropy and, especially, volume with temperature. Another attempt[14] at the thermodynamics, by Dzialoshinskii and Lifshitz, postulates discontinuities at T_λ which are not convincingly established.

Thus Garland's relations seem to provide the best framework so far for correlating the thermodynamic data for the λ transition in sodium nitrate. It is clear that the transition is essentially one dimensional in that the pronounced anomalies are associated with the crystalline properties parallel to the *c* axis. However, the present theory suggests that there are also anomalies associated with the crystalline properties in the other directions; the magnitude of anomalies perpendicular to the *c* axis compared with those parallel is estimated as $\sim(\partial T_\lambda/\partial p)_x\,(\partial T_\lambda/\partial p)_z^{-1} \sim g_x'(g_z')^{-1} \sim 0.3\%$. There is now no decisive evidence for or against this consequence of the present theory.

(13) L. H. Cohen and W. Klement, *J. Geophys. Res.*, **72**, 4245 (1967).

(14) I. E. Dzialoshinskii and E. M. Lifshitz, *Soviet Phys. JETP*, **6**, 233 (1958).

Studies of Chloroform as Hydrogen Donor to Some Organophosphorus Compounds and Long-Chain Tertiary Alkylamines[1]

by Sanji Nishimura, Charles H. Ke, and Norman C. Li

Department of Chemistry, Duquesne University, Pittsburgh, Pennsylvania *(Received September 28, 1967)*

Proton magnetic resonance studies of hydrogen bonding between chloroform as hydrogen donor and tri-*n*-butyl phosphate, tri-*n*-octylphosphine oxide, tri-*n*-butylamine, tri-*n*-hexylamine, and tri-*n*-octylamine as hydrogen acceptors in cyclohexane have been carried out. Of the two organophosphorus compounds studied, tri-*n*-octylphosphine oxide has the greater hydrogen acceptor strength. The three long-chain tertiary alkylamines are much poorer hydrogen acceptors than the phosphorus compounds toward chloroform, in spite of the greater proton affinity of the amines. Due to hydrogen bonding of chloroform to organophosphorus compounds and long-chain tertiary alkylamines, extraction of solutes by these compounds as extractants is appreciably depressed in chloroform medium.

Introduction

Evidence on hydrogen bonding between chloroform and organophosphorus compounds or long-chain tertiary alkylamines has come from the solvent effects in various solvent-extraction studies involving organophosphorus compounds[2-4] and long-chain tertiary alkylamines[5,6] as extractants. However, no quantitative thermodynamic data are available in the literature. This paper presents proton magnetic resonance (pmr) studies of chloroform as hydrogen donor to tri-*n*-butyl phosphate (TBP), tri-*n*-octylphosphine oxide (TOPO), tri-*n*-butylamine (TBA), tri-*n*-hexylamine (THA), and tri-*n*-octylamine (TOA) in cyclohexane as inert solvent. These hydrogen acceptors were chosen because of their wide-spread use in the extraction of metal ions from aqueous to organic phase.

Experimental Section

Materials. TBP was purified in the manner previously described.[7] TOPO, an Eastman Organic chemical, was used without further purification. TBA, THA, and TOA were purified by vacuum purification. The fractions collected have boiling points: 71–73° (3 mm), 139–141° (3 mm), and 213–215° (3 mm), respectively, for TBA, THA, and TOA. Chloroform was purified by shaking with concentrated sulfuric acid and then water until the washing was neutral. It was dried over anhydrous sodium sulfate, distilled, and the fraction boiling at 60° was collected. Cyclohexane was Fisher Spectroanalyzed reagent liquid.

Nuclear Magnetic Resonance Measurements. The preparation of samples and method of pmr measurements, using an A-60 nmr spectrometer, were identical with those described by Pukanic, *et al.*[7] Chemical shifts of the CH signal in chloroform were measured with respect to cyclohexane and are quoted as cps. The signals are all downfield from cyclohexane and the reported chemical shifts are accurate to ±0.2 cps. During the running of the spectra, the temperature remained constant to within ±1°. The molarity of the solutions, at temperatures other than room temperature, was calculated from the change in density with temperature of cyclohexane, TBP, the tertiary alkylamines, and of solutions containing TOPO.

Calculation of Equilibrium Constants. By keeping the concentration of the hydrogen donor AH constant at a low concentration in an inert solvent and varying the concentration of an electron donor, D, keeping the latter in large excess over the complexed AH, Mathur, *et al.*,[8] calculated the equilibrium constant for hydrogen bond formation of a 1:1 complex using the equation

$$\frac{1}{\nu - \nu_M} = \frac{1}{K(\nu_c - \nu_M)}\frac{1}{(D)} + \frac{1}{(\nu_c - \nu_M)} \qquad (1)$$

where ν_M and ν_c are the characteristic pmr frequencies of the free (monomeric) and complexed AH, respectively, and K is the equilibrium constant for the formation of AH···D from monomeric AH and D. From eq 1, a plot of $1/(\nu - \nu_M)$ *vs.* $1/(D)$ yields a straight line, from which the values of $(\nu_c - \nu_M)$ and K can be determined separately.

In our experiments chloroform was kept constant at 0.05 M in cyclohexane, while the concentrations of the

(1) This investigation was supported by the U. S. Atomic Energy Commission through Contract No. AT(30-1)-1922. Paper No. NYO-1922-42.

(2) T. J. Conocchioli, M. I. Tocher, and R. M. Diamond, *J. Phys. Chem.*, **69**, 1106 (1965).

(3) N. C. Li, S. M. Wang, and W. R. Walker, *J. Inorg. Nucl. Chem.*, **27**, 2263 (1965).

(4) T. V. Healy, *ibid.*, **19**, 314, 328 (1961).

(5) Y. Marcus, *Chem. Rev.*, **63**, 139 (1963).

(6) W. Müller and R. M. Diamond, *J. Phys. Chem.*, **70**, 3469 (1966).

(7) G. Pukanic, N. C. Li, W. S. Brey, Jr., and G. B. Savitsky, *ibid.*, **70**, 2899 (1966).

(8) R. Mathur, E. D. Becker, R. B. Bradley, and N. C. Li, *ibid.*, **67**, 2190 (1963).

Table I: Proton Magnetic Resonance Frequency of Proton in Chloroform (0.05 *M* in Cyclohexane) as a Function of Concentrations of Phosphorus Compounds and Alkylamines

(a) $CHCl_3$–TBP

42°		35°		21°		10°	
C_{TBP}	Cps	C_{TBP}	Cps	C_{TBP}	Cps	C_{TBP}	Cps
0	338.8	0	338.8	0	338.8	0	338.8
0.491	388.5	0.496	392.3	0.503	398.1	0.508	403.0
0.687	395.1	0.694	397.9	0.703	403.1	0.711	407.3
0.982	400.8	0.992	403.2	1.004	408.0	1.016	410.9
1.179	403.3	1.190	406.1	1.205	410.4	1.219	412.3
1.278	404.2	1.289	406.8	1.306	410.8	1.321	413.0
1.475	406.0	1.488	408.3	1.508	411.9	1.524	414.1

(b) $CHCl_3$–TOPO

45°		35°		21°		10°	
C_{TOPO}	Cps	C_{TOPO}	Cps	C_{TOPO}	Cps	C_{TOPO}	Cps
0.295	422.6	0.298	428.1	0.303	437.0	0.306	443.9
0.393	430.0	0.397	434.3	0.404	441.8	0.408	447.6
0.492	434.5	0.496	438.7	0.506	445.6	0.511	449.9
0.590	438.1	0.596	441.8	0.604	447.8	0.612	451.8
0.689	440.7	0.695	444.0	0.708	449.4	0.715	453.0

(c) $CHCl_3$–TBA

36.5°		22°		10°		2°	
C_{TBA}	Cps	C_{TBA}	Cps	C_{TBA}	Cps	C_{TBA}	Cps
0	338.8	0	338.8	0	338.8	0	338.8
0.488	347.9	0.497	350.5	0.503	353.1	0.508	356.7
0.739	351.8	0.752	355.7	0.761	359.8	0.769	363.2
1.021	356.4	1.037	361.2	1.051	365.7	1.060	370.0
1.466	361.5	1.490	367.0	1.510	373.7	1.522	377.5
1.983	367.3	2.013	372.9	2.038	379.6	2.057	384.5

(d) $CHCl_3$–THA

36.5°		22°		10°		2°	
C_{THA}	Cps	C_{THA}	Cps	C_{THA}	Cps	C_{THA}	Cps
0.485	344.7	0.493	346.8	0.499	349.4	0.504	351.5
0.730	347.2	0.742	350.2	0.752	353.3	0.758	357.0
0.994	350.2	1.009	353.6	1.023	358.0	1.031	362.2
1.482	355.6	1.506	359.6	1.523	364.8	1.534	370.3
2.002	360.0	2.030	365.4	2.052	370.2	2.067	376.3

electron donors were varied and kept in large excess. In the absence of D, the pmr frequency of chloroform was found to be constant at 338.8 cps up to 0.15 *M* in cyclohexane over the temperature range 10–45°. This frequency therefore is taken to be ν_M. Equation 1 was used to obtain $(\nu_o - \nu_M)$ and K.

Results

Table I lists the pmr results for chloroform bonding to two phosphorus compounds and two alkylamines in cyclohexane. An example of plots of eq 1 at different temperatures is given in Figure 1 for the system $CHCl_3$–TOA. Values of K, ΔH, ΔS, and $(\nu_c - \nu_M)$ are tabulated in Table II.

Discussion

The values of K for the system $CHCl_3$–TOPO are larger than for the system $CHCl_3$–TBP. This order is in line with the results of Diamond and co-workers that the equilibrium constants for water hydrogen-bonding to TOPO[2] and TBP[9] are 0.56 and 0.15 l./mole, respectively. Comparison of the enthalpy changes for the system $CHCl_3$–TOPO and $CHCl_3$–TBP also leads to the conclusion that TOPO is a stronger electron donor than TBP toward chloroform.

It must be mentioned that for $CHCl_3$–TOPO system at 10°, where K = 20.2, 86% of the chloroform is complexed at the lowest TOPO concentration and 93% at the highest. The equilibrium constant is thus derived from a very small change in frequency (9 cps) as compared to the total change, $\nu_c - \nu_M$, of 122 cps. This constitutes a weakness of the method in determining large equilibrium constants.

The enthalpy and entropy changes for chloroform hydrogen-bonding to TBA, THA, and TOA are almost

(9) D. C. Whitney and R. M. Diamond, *J. Phys. Chem.*, **67**, 209 (1963).

Table II: Summary of Results for Chloroform Hydrogen Bonding

System	Temp, °C	K, l./mole	$-\Delta H$, kcal/mole	$-\Delta S$, eu	$(\nu_c - \nu_M)$, cps
$CHCl_3$–TBP	42	3.2	4.3	11.3	82
	35	3.8			
	21	5.2			
	10	7.0			
$CHCl_3$–TOPO	45	7.5	5.0	11.8	122
	35	9.3			
	21	13.9			
	10	20.2			
$CHCl_3$–TBA	36.5	0.22	3.6	14.8	96
	22	0.28			
	10	0.36			
	2	0.45			
$CHCl_3$–THA	36.5	0.13	3.6	15.6	100
	22	0.17			
	10	0.23			
	2	0.29			
$CHCl_3$–TOA	33	0.13	3.4	15.3	114
	22	0.15			
	10	0.20			
	2	0.24			

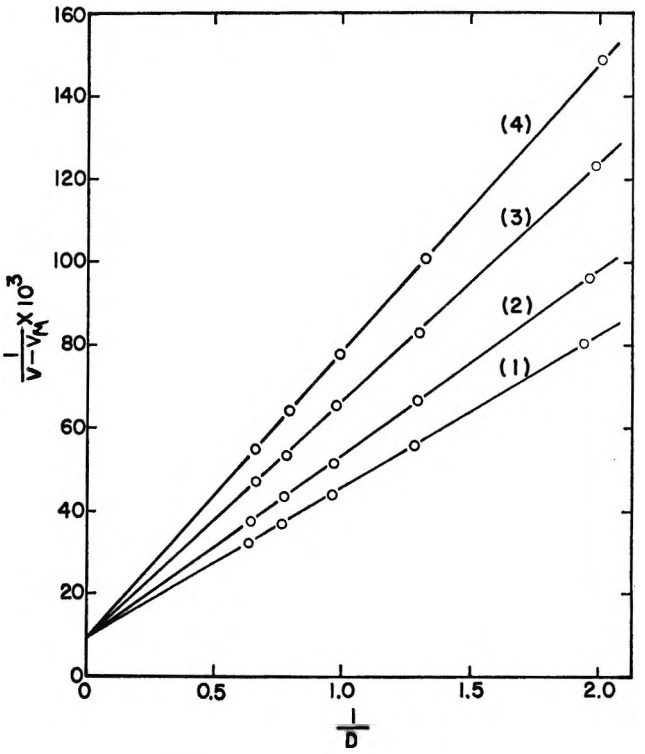

Figure 1. CHCl–TOA system in cyclohexane. Plots of $1/(\nu - \nu_M)$ *vs.* 1/(TOA) at the following temperatures: (1) 2°; (2) 10°; (3) 22°; (4) 33°.

the same. However, the K values decrease in the order TBA > THA, TOA. It has been reported by Grinstead[10] on the basis of the apparent pK_a values that the order of base strength in tertiary alkylamines correlates fairly well with the extent of steric hindrance about the nitrogen atom, but the chain length or molecular size is not of great consequence. Grinstead concluded that the basicities of THA and TOA are the same. Our pmr results are in agreement with this.

In a proton magnetic resonance study of chloroform hydrogen-bonding to triethylamine (TEA), Creswell and Allred[11] reported K = 0.51 l./mole at 25°, while Whetsel and Lady[12,13] reported K = 1.10 l./mole at 25° for chloroform bonding to cyclohexylamine (CHA) obtained by an infrared method. The equilibrium constants thus decrease in the order CHA > TEA > TBA > THA, TOA. It may be considered from the large difference of equilibrium constants between CHA and the tertiary alkylamines that the alkyl groups of tertiary alkylamines apparently offer considerable steric hindrance to the approach of a chloroform molecule.

The proton affinity of the alkylamines is reported to be greater than the organophosphorus compounds.[6] One may expect the alkylamines to have larger equilibrium constants and enthalpy changes of hydrogen-bond formation than the organophosphorus compounds. However, the opposite is true, as shown in Table II, so that the higher proton affinity of the alkylamines cannot be generalized to include better coordination with chloroform. On the other hand, the higher hydrogen-acceptor strength of the phosphorus compounds over the alkylamines toward chloroform is reflected in the greater extracting power of the organophosphorus compounds.[6,9] Thus, a dilute solution of trilaurylamine in the usual diluents extracts a negligible amount of water, whereas a dilute solution of TOPO extracts a considerable amount of water.[6] The higher ΔH values for the organophosphorus compounds over the alkylamines as shown in Table II probably reflects steric hindrance by the alkyl groups of tertiary alkylamines to the approach of a chloroform molecule, whereas in organophosphorus compounds no steric effect is present since the hydrogen-acceptor site is the phosphoryl oxygen. The differences in the term $T\Delta S$ are, however, about equal to the differences in ΔH, and indicate that the difference in the nature of CH···N and CH···O bonds is as much responsible as are the steric effects for the large difference in K values between the organophosphorus compounds and the alkylamines.

The results of this investigation can well be used to

(10) R. R. Grinstead in D. Dyrssen, J. C. Liljenzin, and J. Rydberg, Ed., "Solvent-Extraction Chemistry," North-Holland Publishing Co., Amsterdam, 1967, p 426.

(11) C. J. Creswell and A. L. Allred, *J. Phys. Chem.*, 66, 1469 (1962).

(12) K. B. Whetsel and J. H. Lady, *ibid.*, 68, 1010 (1964).

(13) K. B. Whetsel and J. H. Lady, *ibid.*, 69, 1596 (1965).

interpret the frequently observed solvent effects in solvent-extraction studies. Due to hydrogen-bonding of chloroform to organophosphorus compounds and long-chain tertiary alkylamines, extraction of solutes by these compounds as extractants is appreciably depressed in chloroform medium, and this has been observed.[14,15]

(14) T. Sato, *J. Inorg. Nucl. Chem.*, **29**, 555 (1967).
(15) T. Sekine and D. Dyrssen, *ibid.*, **26**, 1727 (1964).

The Kinetics of the Rearrangement of 2′,4′-Dinitro-2-aminodiphenyl Ether in Methyl Alcohol–Carbon Tetrachloride Solutions

by Frances Wright Balfour and Thomas F. Fagley

Richardson Chemistry Laboratory, Tulane University, New Orleans, Louisiana 70118 *(Received October 2, 1967)*

The kinetics of the rearrangement of 2′,4′-dinitro-2-aminodiphenyl ether to the diphenylamine in methyl alcohol–carbon tetrachloride solutions over a wide composition range at 25 and 35° has been investigated. Corrections of the activation parameters for the cosolvent effect reveal that the enhanced rate with increase in methyl alcohol is probably due to the trimer of the methanol.

I. Introduction

Studies of the isomerization of the *o*-aminodiphenyl ethers were undertaken by Roberts and De Worms[1] and Roberts, De Worms, and Clark,[2] who reported that such reactions are irreversible and, at the temperatures used in the kinetic studies reported here, produce only the diphenylamine as a product. This observation has been confirmed by a comparison of the melting point of the diphenylamine produced by the standard method[3] with that of the product of the rearrangement of the ether. Both products melted at 198–199°.

Roberts, De Worms, and Clark[2] observed that hydroxylic solvents aid the rearrangement of the ether to the amine. We have followed the kinetics of this rearrangement in methyl alcohol–carbon tetrachloride solutions as part of a program of study of the "cosolvent effect" in solution kinetics. Since the methanol does not react with the ether chemically but does play a role in the activation process, such a mechanism should be a severe test of a model of the cosolvent effect.[4]

II. Experimental Section

Materials. Baker Analyzed reagent grade methanol was purified further to remove water by treatment with magnesium.[5] Distillation from the methoxide was carried out using a Todd still. The pure methanol (n^{25}D 1.3265, lit. n^{25}D 1.3264) was stored under dry nitrogen in a tightly capped brown bottle, placed within a desiccator, for periods no longer than 2 weeks.

Baker Analyzed reagent grade carbon tetrachloride was purified by the method of Scatchard,[6] distilled, and similarly stored under dry nitrogen. The product had a refractive index n^{25}D 1.4573 (lit., 1.4573). The 2′,4′-dinitro-2-aminodiphenyl ether was prepared by adding to 0.05 mol of sodium ethoxide in 50 ml of dry ethanol, 0.05 mol (5.5 g) of K & K Chemical Laboratories *o*-amino phenol, with shaking. Then 10 g of 2,4-dinitrochlorobenzene (K & K Chemicals reagent grade) was ground to a fine powder in a mortar and added in small portions to the first solution with shaking after each addition until the dinitrochlorobenzene went into solution. The mixture was immediately placed in an ice bath and within a few minutes crystallization of the ether began. After 3 hr, the brown crystals were collected on a Büchner funnel and washed with small portions of ethanol until they turned yellow. The washed precipitate was extracted with warm benzene and filtered. This extraction was repeated on an average of five times. Ether recrystallized from these extrac-

(1) K. C. Roberts and C. G. De Worms, *J. Chem. Soc.*, 727 (1934).
(2) K. C. Roberts, C. G. De Worms, and M. B. Clark, *ibid.*, 196 (1934).
(3) *Chem. Ber.*, **53**, 2265 (1920).
(4) T. F. Fagley, G. A. Von Bodungen, J. J. Rathmell, and J. D. Hutchison, *J. Phys. Chem.*, **71**, 1374 (1967).
(5) J. F. Fieser, "Experiments in Organic Chemistry," D. C. Heath and Company, Boston, Mass., 1955.
(6) G. Scatchard, S. E. Wood, and J. M. Mochel, *J. Amer. Chem. Soc.*, **61**, 3206 (1939).

tions was subsequently recrystallized four more times before use in kinetic meaurements. The pure compound melted at 123° (lit. 123°).[2] Inadequate washing of the crystals, impurities in the benzene, or failure to crystallize the ether early in its preparation proved to decrease substantially ether yield; in some cases, ether recovery was impossible.

The 2′,4′-dinitro-2-hydroxydiphenylamine was prepared by the standard method[3] and also by the rearrangement of the ether in methanol. The products of both these preparations melted at 189–199°.[3]

Apparatus. A constant temperature bath, A. H. Thomas infrared research Model 9926-D, fitted with a water-levelling device, maintained a constant temperature within 0.001°. Round-bottomed flasks of 125-ml capacity, fitted with Teflon stopcocks, were used as reaction flasks. They were so designed to permit attachment to a source of dry nitrogen and to permit sampling by a no. 18 needle, 6 in. long, which was fitted to a dried, nitrogen-filled syringe. The flasks were held in a rocking rack which allowed constant stirring of the reaction mixture. A Beckman DU spectrophotometer with a power supply was used for all absorption measurements. An A. H. Thomas calibrated thermometer was used to measure the bath temperature. A General Electric clock with a second hand which had been calibrated against National Bureau of Standards time was used to time all runs.

Procedure. Into a weighed 100-ml volumetric flask, filled with dry nitrogen and capped with a standard medical serum cap under which was a polyethylene liner, methanol was added from a dry hypodermic syringe in the amount needed to produce the desired mole fraction. The flask was reweighed and carbon tetrachloride added to the mark and the flask again weighed. After buoyancy corrections, mole fractions could be calculated. The solid ether was added to the solution in the following manner: within a drybox, the serum cap on the solution flask was removed, leaving the polyethylene liner in place, and a small hole was punctured in the liner and a weighed amount (between 0.0035 and 0.0045 g) of the ether quickly added through the hole with the aid of a small funnel and a brush. The serum cap was immediately replaced and the flask shaken. The flask was then placed in a dry bag under dry nitrogen, and transfer of the solution to the reaction bulb (which had been previously filled with dry nitrogen) was made by means of a syringe. All dry nitrogen was obtained by passing the gas successively through concentrated sulfuric acid, phosphorus pentoxide, and a scrubber consisting of a cylinder filled with glass wool. Sampling was accomplished with a 5-ml hypodermic syringe fitted with a 6-in. no. 18 needle. This syringe was flushed with dry nitrogen prior to use. The needle was then inserted into the open stopcock of the reaction vessel under a positive pressure of dry nitrogen, the solution was withdrawn and was placed in a cuvette. A maximum time of 1 min elapsed between the sampling and the reading in the spectrophotometer; the reaction time was taken as the time of the reading. Rates were made by following the appearance of product.

Absorbancy measurements were made at 410 mμ where the product has maximum absorption and the reactant (ether) minimal absorption at the concentrations used (1.5×10^{-4} *M*) in the kinetic runs.

The molarity of the methanol was calculated from the weight fractions and the densities of the mixtures at 25 and 35° calculated from Scatchard's formula.[7]

Rate Constants. Initial rate studies at 25.07° showed that the rate was doubled when the methanol concentration was increased from 0.0991 to 0.1982 *M*, the ether concentration being fixed at 6.2×10^{-4} *M*. Pseudo-first-order rate constants were calculated from least-squares fitting of log $(A_\infty - A)$, time data, after plots of log $(A_\infty - A)$ *vs.* time were shown to be linear. Any data which showed significant scatter of points were rejected and another kinetic run was made. *A* is the absorbancy of the product, the diphenylamine. At least two to three runs at each of the nine mole fractions of methanol at 25 and 35° were made. In order to be certain, in the instances of the extremely slow reactions, that the true infinity absorbancy reading had been obtained, preliminary rate constants were estimated from a limited number of readings by the Guggenheim method and from these *k*'s an infinity time was estimated. The true infinity reading was then taken a considerable time later than that estimated. The concentration of the ether was varied from 1×10^{-4} to 2×10^{-4} *M* and rates followed over usually 2–4 half-lives; in some instances, rates were followed for 5 half-lives. In this range of concentrations of ether, the rates were cleanly first order in ether. Plots of log $(A_\infty - A_t)$ *vs.* time were

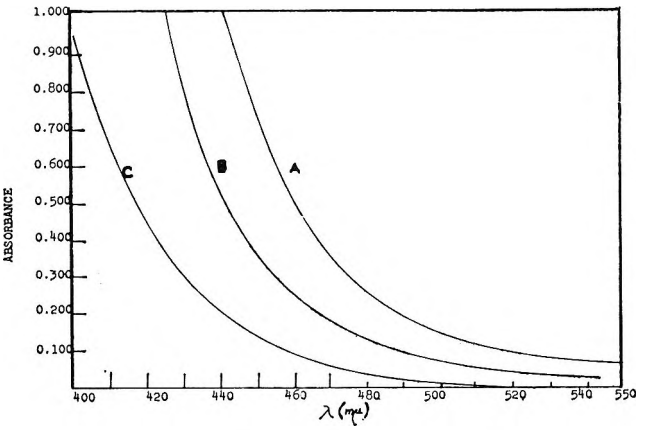

Figure 1. Spectra of 2′,4′-dinitro-2-aminodiphenyl ether in methanol–carbon tetrachloride solution: (A) 0.01807 *M* MeOH, 0.01807 *M* ether; (B) 0.02711 *M* MeOH, 0.00904 *M* ether; (C) 0.03253 *M* MeOH, 0.003614 *M* ether.

(7) G. Scatchard, S. E. Wood, and J. M. Mochel, *J. Amer. Chem. Soc.*, **68**, 1960 (1946).

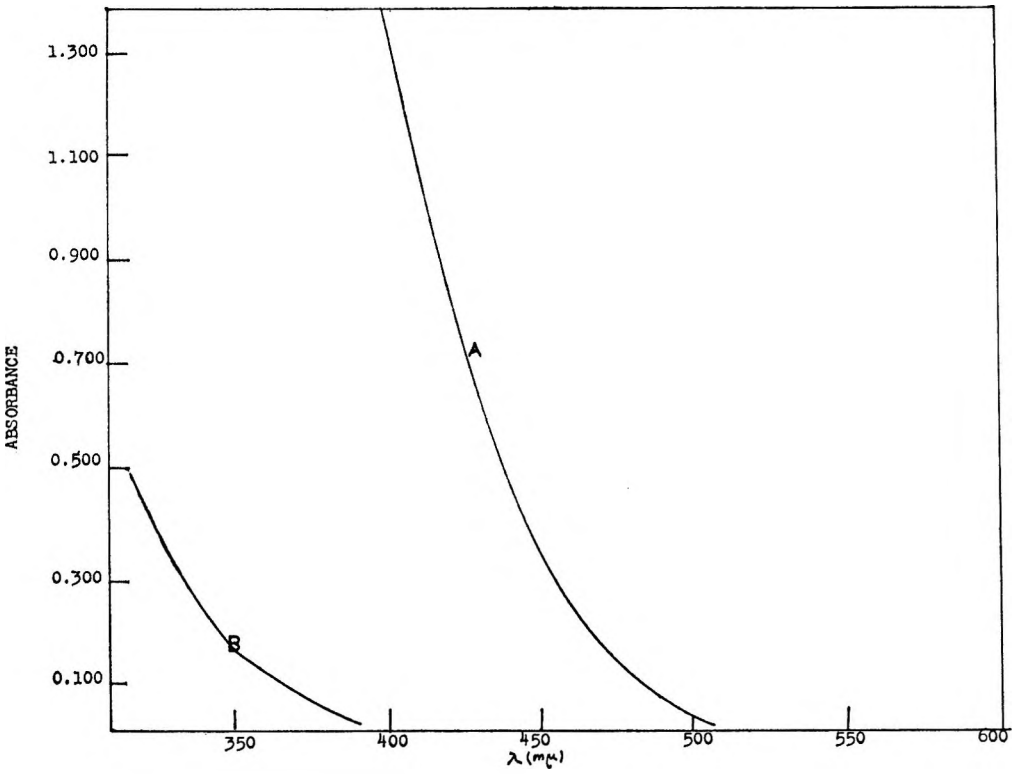

Figure 2. Spectra of ether and diphenylamine in dilute methanol solutions: (A) 0.00015 *M* diphenylamine, 0.0014 *M* MeOH; (B) 0.00015 *M* ether, 0.0014 *M* MeOH.

linear; those of the reciprocal of $(A_\infty - A_t)$ *vs.* time definitely were not linear.

Spectra and Continuous-Variations Study. When the enthalpies and entropies of activation were calculated from the second-order rate constants (first order each in ether and in alcohol), the cosolvent corrections, to be discussed later, suggested that three molecules of methanol were involved. We then attempted to make a continuous-variations study. Preliminary studies had shown a general increase in absorptivity of the ether with methanol concentration. Several difficulties were encountered that make such a study of limited accuracy, but, within these experimental limitations, the results strongly suggest that a complex of 1 ether–3 methanols does form. The difficulties were: (1) low solubility of the ether in pure carbon tetrachloride (*ca.* 0.018 *M*); (2) at this concentration an autocatalytic isomerization of the ether to the diphenylamine was observed—a phenomenon not observed at the low concentrations (10^{-4} *M*) used in the kinetic studies; (3) the necessity of making rapid measurements and at the same time eliminating contamination of the solutions by moisture; and (4) the ether at these concentrations does not obey Beer's law, so that a different reference solution had to be made for each ether–methanol–carbon tetrachloride solution, containing ether in pure carbon tetrachloride at the same concentration as in the ternary system. The differences in absorption of ternary and binary solutions were plotted, as shown in Figure 1 at three

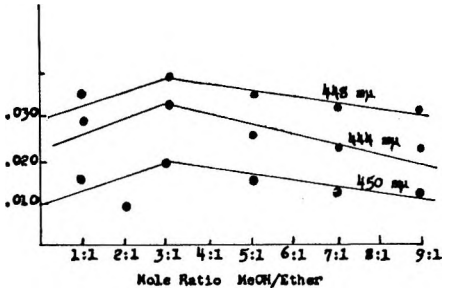

Figure 3. Continuous-variation study of the ether–methanol complex.

wavelengths. That these differences are not due to a general solvent shift in the absorption spectra was demonstrated by separate studies of the spectra (Figure 2), in a concentration range where Beer's law is obeyed. (See also Figure 3.)

III. Discussion

From the first-order rate constant at 25 and 35° and the molarities of the alcohol at each temperature, the enthalpies and entropies of activation were calculated by use of the Eyring equation. The corrections for variations in these parameters, as well as in the rate constants, with a binary solvent composition were made in the manner described in previous work.[4] As seen from Tables I and II the assumption that the active molecular species is the trimer of methanol accounts for the ob-

Table I: Activation Parameters for Rearrangement of 2′,4′-Dinitro-2-aminodiphenyl Ether Corrected for Co Solvent Effect

Mole fraction MeOH	$\Delta H^{\ddagger}_{app}$, kcal (±0.15)	$\bar{L}_{MeOH}$, kcal	ΔH^{*}, kcal	$-\Delta S^{\ddagger}_{app}$, eu (±0.50)	$-\bar{S}^{e}_{MeOH}$, eu	$-\Delta S^{*}$, eu
0.0994	14.43	0.251	14.94	39.1	3.18	45.5
0.2011	14.81	0.092	14.99	40.0	2.31	44.6
0.2999	15.06	0.035	15.13	40.7	1.70	44.1
0.3952	15.09	0.028	15.14	41.8	1.21	44.2
0.4999	15.00	−0.021	14.96	43.3	0.95	45.2
0.5994	15.26	−0.038	15.18	43.3	0.69	44.6
0.7002	15.12	−0.035	15.05	44.8	0.44	45.6
0.8001	15.23	−0.022	15.19	45.0	0.22	45.4
0.8991	15.17	−0.007	15.16	45.9	0.06	46.0
		Mean	15.08 ± 0.09			Mean 45.0 ± 0.6

Table II: Comparison of Observed and Predicted Changes in ln k_4 at 35°

Mole fraction MeOH	$(\Delta \ln k_4)_{obsd}$	$(2\Delta\bar{L}/RT) - (2\Delta\bar{S}^{e}/R)$
0.0994	...	...
0.2011	−1.11	−1.38
0.2999	−1.80	−2.19
0.3952	−2.52	−2.52
0.4999	−3.06	−3.10
0.5994	−3.52	−3.44
0.7002	−3.98	−3.67
0.8001	−4.26	−3.87
0.8991	−4.66	−3.97

served variations. One definition of a catalyst, in homogeneous reacting systems, is: a molecular species, the concentration of which appears in the rate equation to a higher power than in the stoichiometric equation. Methanol in the system described here satisfies such a definition. That the species kinetically involved is not the monomer is shown by the fact that the fraction of methanol in carbon tetrachloride solution existing as monomer decreases with total alcohol concentration.[8] First-order participation of the methanol in the rate expression is not inconsistent with the 3:1 complex surmised from the continuous-variations study, for the variations study was made in solutions dilute in both ether and methanol (0.01 *M* and less), while the initial rate study was made at 0.1 and 0.2 *M* methanol, necessitated by the extremely slow reaction at low alcohol concentrations. Self-association constants for methyl and ethyl alcohols in "inert" solvents are known to be large (of the order of 1 or 10). Thus in the initial rate study, doubling the stoichiometric concentration of alcohol has the effect of nearly doubling the trimer concentration, giving an apparent order of unity. The assumption that the trimer is the catalytic species is necessary, furthermore, to explain the change in the specific reaction-rate constant with the composition of the binary solvent. Finally, a Fisher–Hirschfelder–Taylor molecular model of the ether supports the use of the trimer. The simultaneous rotation of the phenyl groups about the ethereal oxygen bonds and rotation of the amino group reveal one most favorable position in which the nitrogen and the carbon in the dinitrophenyl group are in closest contact; in this position, the amino hydrogens are in the least favorable position for transfer to the oxygen. However, a trimer of the methanol

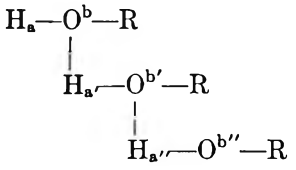

can easily span the ethereal oxygen and the amino hydrogen through hydrogen bridges. The trimer's hydrogen, H_a, bonds to the ether oxygen and the amino hydrogen bonds to the trimer's oxygen, $O^{b''}$. The transfer of hydrogen to ether oxygen, to form the hydroxy diphenylamine, is then facilitated *via* the trimer, leaving the trimer unchanged at the end of the activation process.

The partial molar enthalpies and entropies of methanol were calculated from the data of Moelwyn-Hughes and Missen[9] by both analytical differentiation and graphical differentiation, using, in the latter, the method suggested by Goates and Sullivan.[10]

Corrections to the activation parameters were made with these thermodynamic data, assuming that all changes in these kinetic parameters are reflections of the variations in the properties of the methanol.[4] The mechanism for the rearrangement is

(8) I. Prigogine and R. Defay, "Chemical Thermodynamics," Longmans Green and Co., New York, N. Y., 1954, Chapter XXVI.

(9) E. A. Moelwyn-Hughes and R. W. Missen, *J. Phys. Chem.*, **61**, 518 (1957).

(10) J. R. Goates and R. J. Sullivan, *ibid.*, **62**, 188 (1958).

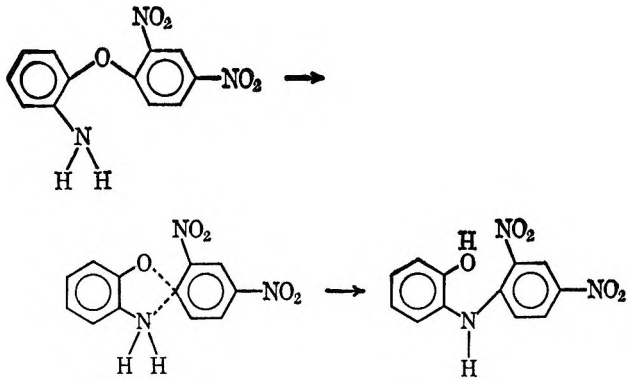

The specific role of methanol in the reaction can be represented by

$$E + T \underset{}{\overset{\text{fast}}{\rightleftharpoons}} C \xrightarrow{\text{slow}} DPA \qquad (1)$$

$$\frac{d(PDA)}{dt} = k(C) = kK(E)(T) = k_0(E) \qquad (2)$$

where DPA is diphenylamine, E is ether, T is trimer of MeOH, and C is the complex between ether and trimeric methanol; k_0 is the pseudo-first-order observed rate constant; K is the equilibrium constant for the trimer–ether complex.

$$k_0/(\text{MeOH})^3 = kK'' = k_4 \qquad (3)$$

Differentiation of eq 3 with respect to temperature, according to the Eyring equation, will give an apparent enthalpy of activation, which must be corrected for changes in the partial molar enthalpy of the methanol with concentration; similar corrections must be made for the entropies

$$\Delta H^{\ddagger} = (\bar{H}^{\ddagger} - \bar{H}_E) - 2\bar{H}_{MeOH} \qquad (4)$$

$$\Delta(\Delta H^{\ddagger}) = -2\Delta\bar{H}_{MeOH} \qquad (5)$$

and

$$\Delta(\Delta S^{\ddagger}) = -2\Delta\bar{S}_{MeOH} \qquad (6)$$

These calculations give corrected enthalpy and entropy of activation for the isomerization, which represent parameters for the rearrangement in pure methyl alcohol; that is, the standard state for the methanol is pure liquid methanol.

These thermodynamic corrections, interestingly, involve $2\bar{H}$ and $2\bar{S}^e$, that is, two partial molar enthalpies and two partial molar excess entropies (not the total partial molar entropies). In the activation process only the hydrogen bridges at the ends of the trimer are reorganized, the central methyl alcohol unit is essentially undisturbed; similarly, only the excess partial molar entropies (which are reflections of the restrictions on vibration and rotation of the monomer units imposed by the hydrogen bridges) are involved.

The corrected activation parameters and the correlation of changes in ln k_4 with those predicted from the thermodynamic properties of methanol are given in Table II. k_4 is the pseudo-first-order rate constant divided by the cube of the stoichiometric methanol concentration.

$$\Delta \ln k_4 = 2/RT(\Delta\bar{H}_{MeOH}) - 2/R(\Delta\bar{S}^e)$$

Table III: Rate Constants for the Isomerization at 25 and 35°

Mole fraction MeOH (±0.0001)	25.07° Molarity MeOH	25.07° 10^5k_2, M^{-1} min^{-1}	35.08° Molarity MeOH	35.08° 10^5k_2, M^{-1} min^{-1}
0.0996	1.088	3.260 ± 0.019[a]	1.072	7.428 ± 0.014[a]
0.2011	2.345	4.926 ± 0.009	2.315	11.46 ± 0.02
0.3000	3.743	6.187 ± 0.014	3.694	14.59 ± 0.03
0.3945	5.274	6.61 ± 0.013		
0.3952			5.218	15.61 ± 0.05
0.4987	7.228	6.579 ± 0.029		
0.4999			7.168	15.47 ± 0.08
0.6002	9.501	7.066 ± 0.014		
0.5994			9.360	16.85 ± 0.01
0.6993	12.14	7.370 ± 0.034		
0.7002			12.019	17.44 ± 0.02
0.8000	15.40	8.807 ± 0.060	15.22	20.97 ± 0.04
0.8991	19.39	9.425 ± 0.006	19.15	22.37 ± 0.30

[a] Standard deviation.

Table IV: Analysis of a Typical Kinetic Run[a,b]

Time, min	A	$A_\infty - A$	$y_i = \log(A_\infty - A)$	$-t_iy_i$	t_i^2
0	0.165	0.693	−0.15927	0	0
10	0.187	0.671	−0.17328	1.7328	100
20	0.207	0.651	−0.18642	3.7284	400
30	0.226	0.632	−0.19928	5.9784	900
40	0.245	0.613	−0.21254	8.5016	1,600
52	0.271	0.587	−0.23136	12.0307	2,704
80	0.318	0.540	−0.26761	21.4088	6,400
90	0.341	0.517	−0.28651	25.7859	8,100
105	0.356	0.502	−0.29930	31.4265	11,025
121	0.380	0.478	−0.32057	38.7890	14,641
125	0.386	0.472	−0.32606	40.7575	15,625
140	0.402	0.456	−0.34104	47.7456	19,600
150	0.422	0.436	−0.36051	54.0765	22,500
160	0.437	0.421	−0.37572	60.1152	25,600
171	0.450	0.408	−0.38934	66.5771	29,241
185	0.462	0.396	−0.40230	74.4255	34,225
190	0.475	0.383	−0.41680	79.1920	36,100
200	0.487	0.371	−0.43063	86.1260	40,000
220	0.510	0.348	−0.45842	100.8524	48,400
230	0.520	0.338	−0.47108	108.3484	52,900
240	0.535	0.323	−0.49080	117.7920	57,600
251	0.545	0.313	−0.50446	126.6195	63,001
281	0.580	0.278	−0.55596	156.2248	78,961
320	0.600	0.258	−0.58838	188.2816	102,400
351	0.630	0.228	−0.64207	225.3666	123,201
379	0.644	0.214	−0.66959	253.7746	143,641
389	0.665	0.193	−0.71444	277.9172	151,321
4530			−10.47374	2213.5746	1,090,186

[a] $m = [n\Sigma t_iy_i - (\Sigma t_i\Sigma y_i)]/[n\Sigma t_i^2 - (\Sigma t_i)^2(\Sigma y_i)^2]$, m = 1.3820 × 10^{-3} min^{-1}, k = 3.183 × 10^{-3} min^{-1}. [b] Temp, 35°; mole fraction of methanol, 0.7998.

In calculating the change in ln k_4, differences in partial molar quantities are used; these, in turn, are calculated from differences (through graphical or analytical differentiation) between measured quantities, such as heats of mixing. The errors in the partial molar quantities, therefore, may vary from 10 to 20%. The agreement between observed and calculated changes in ln k_4, then, is quite good.

It is noted that Hudson and Loveday[11] have previously observed specific solvation between alcohol and the transition state in nucleophilic substitutions involving alcohols and acid chlorides. The rates were found to be approximately proportional to the concentration of the self-associated alcohol. More recently, Fletcher and Heller[12] reported evidence for specific catalysis by the tetramer of octanol.

(For data on the rate constants for the isomerization at 25 and 35° and an analysis of a typical kinetic run, see Tables III and IV, respectively.)

(11) R. F. Hudson and G. W. Loveday, *J. Chem. Soc. Sect. B*, 766 (1966).

(12) A. N. Fletcher and C. A. Heller, *J. Phys. Chem.*, **71**, 3742 (1967).

Adsorption and Oxidation of Carbon Monoxide on Platinized Platinum Electrodes

by M. W. Breiter

General Electric Research and Development Center, Schenectady, New York 12301 *(Received October 2, 1967)*

Carbon monoxide is adsorbed at open circuit on platinized platinum as two types that are oxidized in different potential regions in acid and alkaline electrolytes. The different mechanisms of the anodic oxidation of the two types of CO_{ad} are discussed. The saturation coverage of H atoms decreases in a linear fashion with the CO_{ad} coverage. The isotherms of hydrogen adsorption degenerate to Temkin-type isotherms with increasing coverage of CO_{ad}. The CO_{ad} coverage is equal to 1 between 0.1 and 0.4 V under potentiostatic or galvanostatic conditions in acid solutions stirred with carbon monoxide. The beginning of the rapid decrease of CO_{ad} with potential depends upon the experimental conditions. The oxidation of dissolved carbon monoxide under steady-state conditions appears to involve the one type of CO_{ad} as intermediate between 0.2 and 0.4 V and the other type above 0.4 V. Adsorption of the one type is the rate-determining step between 0.2 and 0.4 V. Diffusion of CO and adsorption of the other type are rate determining above 0.4 V.

Introduction

In recent years the adsorption of carbon monoxide has been studied[1-6] extensively on smooth platinum electrodes in acid electrolytes. Carbon monoxide was allowed to interact with the platinum surface at potentials between 0.2 and 0.4 V. Voltammetric[1-4] and galvanostatic[5,6] techniques were used to determine the adsorbed amount from the charge required for its anodic oxidation to CO_2. It was reported in two of the publications that the charge ${}_sQ_{CO}$ corresponding to saturation coverage with CO_{ad} is smaller than twice the charge ${}_sQ_H$ of a monolayer of H atoms on the same electrode ($2{}_sQ_H/{}_sQ_{CO} = 1.8$ in ref 2, and 1.08 in ref 6). Gilman[2] attributed this ratio to the presence of two forms of CO_{ad} in analogy to the interpretation[7] of infrared data of carbon monoxide adsorption on platinum in the gas phase. One molecule of the bridged or linear form occupies two or one platinum atoms, respectively. Warner and Schuldiner[5] found that $2{}_sQ_H/{}_sQ_{CO} = 0.94$. Physical adsorption of carbon monoxide on top of a chemisorbed monolayer was suggested[5] as a reason that more than a monolayer was present. Codeposition of hydrogen atoms on a surface having the saturation coverage of CO_{ad} led to the conclusion[2] that carbon monoxide is only adsorbed on about 80% of the Pt atoms. In contrast, a percentage of 98% was given in ref 6. The investigations[8,9] of carbon monoxide

(1) S. Gilman, *Phys. Chem.*, **66**, 2657 (1962).

(2) S. Gilman, *ibid.*, **67**, 78 (1963).

(3) S. Gilman, *ibid.*, **67**, 1898 (1963).

(4) S. Gilman, *ibid.*, **68**, 70 (1964).

(5) T. B. Warner and S. Schuldiner, *J. Electrochem. Soc.*, **111**, 992 (1964).

(6) S. B. Brummer and J. I. Ford, *J. Phys. Chem.*, **69**, 1355 (1965).

(7) R. P. Eischens and W. Pliskin, *Advan. Catal.*, **10**, 18 (1958).

(8) A. B. Fasman, G. L. Padyukova, and D. V. Sokolskii, *Dokl. Akad. Nauk SSSR*, **150**, 856 (1963).

adsorption on platinized platinum are not detailed enough for the quantitative establishment of similar relations. Sokolskii and coworkers concluded[8,9] that physical adsorption occurs at about 10° in 0.5 *M* H_2SO_4. Conversion to CO_2 and H_2 was postulated for temperatures between 20 and 30°. Initial conversion and subsequent chemisorption were suggested between 50 and 70°. Binder, Köhling, and Sandstede[10] concluded from measurements on Raney platinum electrodes in phosphoric acid and sulfuric acid solutions that chemical conversion is the first step in the anodic oxidation of carbon monoxide at temperatures between 90 and 150°.

It is the purpose of this article to report on quantitative studies of carbon monoxide adsorption at open circuit on platinized platinum in acid electrolytes and in 1 *M* KOH at 25 ± 1°. The charge Q_{CO} for the oxidation of CO_{ad} was measured simultaneously with the charge Q_H corresponding to a monolayer of H atoms on the Pt atoms remaining free of CO_{ad}. The mechanisms of the oxidation of adsorbed (CO_{ad}) and dissolved (CO) carbon monoxide in acid solutions will be discussed.

Experimental Section

The experiments were made in a Pyrex vessel of standard design. The electrolytic solutions were prepared from reagent grade chemicals and double-distilled water. The apparent surface of the platinized Pt electrode was 50 cm². The electrode has been aged by frequent use so that the gradual decrease[11] of ${}_sQ_H$ due to a sintering effect was smaller than 5% during the course of the investigation. The electrode potential, *U*, was measured *vs.* a hydrogen electrode in the same electrolyte as the test electrode.

The measurements of every set of runs were always started by a cathodic-charging curve with −50 mA from *U* = 1.3 V, which had been established by previous anodic charging. The cathodic-charging curve served to reduce the oxygen layer and to form the hydrogen layer[12] up to 0.06 V in electrolytic solutions flushed extensively with purified helium. When *U* = 0.06 V was reached, the current was reversed to 50 mA and an anodic-charging curve was recorded up to 1.1 V. The charge ${}_sQ_H$ for the hydrogen arrest and the absence of an arrest in the double-layer region[12] were used as a test for the absence of oxidizable species absorbed on the surface or dissolved in the electrolyte. Since the cathodic charging is slow compared to the time constant, about 0.67 sec, for the transition from instationary to steady-state diffusion, the equilibrium gradient of molecular hydrogen in the diffusion layer is practically present at any moment at potentials in the hydrogen region. The maximum contribution of H_2 diffusing back to the surface from the solution during the anodic charging is of the order of 7×10^{-3} mC/cm². This value is considerably smaller than ${}_sQ_H$. The recent treatment of hydrogen diffusion by BenDaniel and Will[13] is not applicable here because of different boundary conditions and the use of platinized platinum in the present work.

After the electrode had been brought back from 1.1 to 0.1 V with −50 mA, it was left at open circuit in the studies of adsorption as a function of time. The stirring with helium was replaced by stirring with a mixture of 80% Ar and 20% CO at about 2 cm³/sec. The gas mixture was Matheson CP grade. Interaction between carbon monoxide and the platinum surface was allowed for various times. The electrode potential decreased[9] with time during the initial part of the stirring with CO. Then helium stirring was started and maintained for 1000 sec to remove the dissolved CO from the solution. It was verified by analysis of the CO content of the helium gas by gas chromatography that 1000 sec were sufficient to reduce the bulk concentration of CO to at least one hundredth of its initial value. Since a limiting diffusion current of about 10 mA was measured at large anodic potentials during the stirring with 80% Ar and 20% CO, the contribution to the arrest of the oxidation of CO_{ad} or to the decrease of the length of the hydrogen arrest from the diffusion of traces of CO to the surface is not larger than 0.1 mA. The latter value is very small in comparison to the anodic charging rate of 50 mA. A second anodic charging curve was measured from 0.06 V with 50 mA. When the potential reached 1.3 V, the current was interrupted. The electrolyte was removed[14] from the vessel by gas pressure and subsequently replaced by fresh one saturated with He.

The electrode potential was brought to about 0.5 V after the initial charging curve in the determinations of the carbon monoxide coverage as a function of *U* under potentiostatic conditions. Then the desired potential was applied by the Wenking 6ITRS potentiostat. Stirring with CO (Matheson CP grade) was started at 2 cm³/sec and maintained for 500 sec. A longer period of stirring did not lead to larger coverages with CO_{ad}. Then the stirring was replaced by intensive He stirring. Simultaneously, the electrode was disconnected from the potentiostat. The potential decays to values between 0.2 and 0.3 V. The potential was adjusted galvanostatically to 0.06 V after 1000 sec of He stirring before taking the final *U*–*t* curve with 50 mA. The rest of the procedure is the same as for the studies of adsorption at open circuit. These measurements on

(9) G. L. Padyukova, A. B. Fasman, and D. V. Sokolskii, *Elektrokhimiya*, **2**, 885 (1966).

(10) H. Binder, A. Köhling, and G. Sandstede, *Advan. Energy Conversion*, **6**, 135 (1966).

(11) J. Giner, *Electrochim. Acta*, **8**, 857 (1963).

(12) A. Slygin and A. Frumkin, *Acta Physicochim. URSS*, **3**, 791 (1935).

(13) D. J. BenDaniel and F. G. Will, *J. Electrochem. Soc.*, **114**, 909 (1967).

(14) M. W. Breiter, *Electrochim. Acta*, **12**, 1213 (1967).

platinized platinum allow a comparison with the studies of carbon monoxide adsorption on smooth platinum at potentials between 0.2 and 0.4 V.

Current and coverage with CO_{ad} under steady-state conditions of galvanostatic measurements were obtained as follows. The solution was stirred for 500 sec with CO at 0.5 cm³/sec at open circuit. Then the potential was determined 20 min after every adjustment of the current. The CO stirring was maintained. A cathodic charging curve was recorded by switching from the positive current to −200 mA. Afterwards the anodic current was increased to its next value. The relative decrease $1 - ({}_sQ_H'/{}_sQ_H)$ of the hydrogen branch is a direct measure of the coverage with CO_{ad}, as demonstrated later on. Here ${}_sQ_H'$ designates the charge of a monolayer of H atoms in the presence of CO_{ad}.

Experimental Results

The charging curves in Figure 1 were taken in 0.5 *M* H_2SO_4 with 50 mA. Curve a is typical for the curve in the absence of CO_{ad}. It displays the three characteristic regions:[12] hydrogen region, double-layer region, and initial part of the oxygen region. The adsorption of carbon monoxide occurs at 25° on platinized platinum,[14] as on smooth platinum.[1-6] This is demonstrated in Figure 1 by the decrease of the length of the hydrogen branch and the appearance of additional arrests at potentials in the double-layer region. The arrests between 0.55 and 0.65 V of curves b and c are due to the reaction

$$CO_{ad} + H_2O = CO_2 + 2H^+ + 2e^- \qquad (1)$$

in acid solutions. This was confirmed[14] recently by determining simultaneously the charge Q_{CO} from the charging curve and the amount of evolved CO_2 by gas chromatography. The length of the arrest increases with the time of adsorption (curve b, 100 sec; c, 500 sec; d, 2000 sec). As noticed[14] previously, a second short arrest appears at less anodic potentials, when the coverage is close to the saturation coverage. The length of the two arrests did not become larger with adsorption times greater than 2000 sec. Saturation coverage is practically achieved in 2000 sec under the given conditions. Adsorbed carbon monoxide that is oxidized in the upper arrest will be designated as type 1. The adsorbed species that are oxidized in the short arrest will be called type 2.

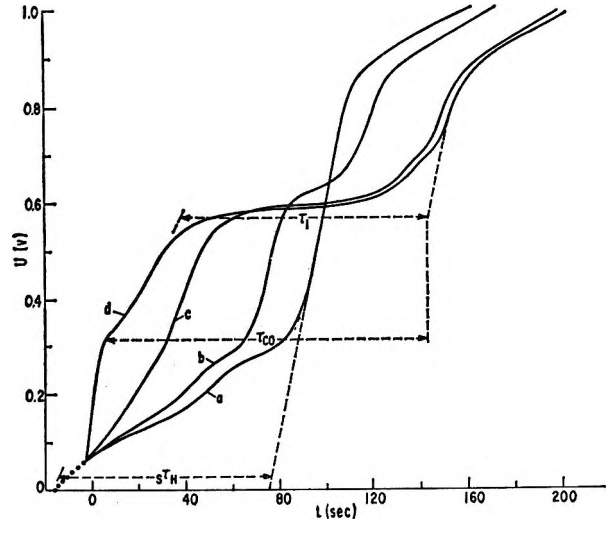

Figure 1. Charging curves with 50 mA in 0.5 *M* H_2SO_4 on platinized platinum (50 cm² apparent surface) after different times, t_{ad}, of carbon monoxide adsorption at open circuit: curve a, t_{ad} = 0; curve b, t_{ad} = 100 sec; curve c, t_{ad} = 500 sec; curve d, t_{ad} = 2000 sec.

The determination of different transition times is illustrated for curves a and d under consideration of the charging of the double layer. Curve a was extrapolated to $U = 0$ (dotted line). The product $I_s\tau_H$ represents the charge ${}_sQ_H$ corresponding to a monolayer of H atoms in the absence of CO_{ad}. The transition time τ_{CO} is required for the oxidation of all the adsorbed molecules. The U–t curves are practically parallel at $U \geq 0.8$ V. This demonstrates that the oxidation of CO_{ad} is completed before the formation of the oxygen layer starts. A correction for the later process does not have to be applied on platinized platinum, in contrast to smooth platinum. The approximate determination of τ_1 of the upper arrest is shown in curve c. The same correction as for the double-layer charging in the absence of CO_{ad} was used. This introduces only a slight error in τ_1, since a large portion of the upper arrest is in a narrow potential range. The error due to the correction for double-layer charging is also small for τ_{CO}, because the surface is largely covered when the second arrest appears and because the double-layer capacity of platinum is considerably smaller[5,6] in the presence of CO_{ad} than in the absence.

The adsorption of carbon monoxide at open circuit was studied with equal adsorption times of 2000 sec in 0.5 *M* H_2SO_4, 0.1 *M* Na_2SO_4 + 0.05 *M* H_2SO_4, and 0.1 *M* Na_2SO_4 + 0.005 *M* H_2SO_4. The U–t curves in 0.5 *M* H_2SO_4 and 0.1 *M* Na_2SO_4 + 0.05 *M* H_2SO_4 coincide nearly in the hydrogen region if CO_{ad} is absent (see Figure 2). The curve in 0.1 *M* Na_2SO_4 + 0.005 *M* H_2SO_4 is located between 10 to 20 mV above the curves in the other two solutions. The measurements of the reaction

$$H_{ad} = H^+ + e^- \qquad (2)$$

are nearly independent of pH, as to be expected, since a hydrogen electrode in the same electrolyte as the test electrode served as reference electrode. A large difference was found for the pH dependence of the processes occurring in the upper and lower arrest. The U–t curves are shifted by 40 to 50 mV against each other at a given time between 10 and 30 sec in the region of the lower arrest. In contrast, they coincide nearly in the upper arrest.

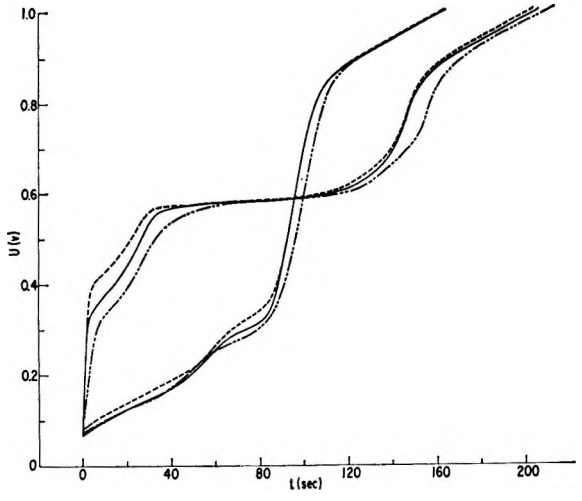

Figure 2. Charging curves with 50 mA in the absence (lower curves) and presence (upper curves) of CO_{ad}: ———, 0.5 M H_2SO_4; ———, 0.1 M Na_2SO_4 + 0.05 M H_2SO_4; - - - -, 0.1 M Na_2SO_4 + 0.005 M H_2SO_4.

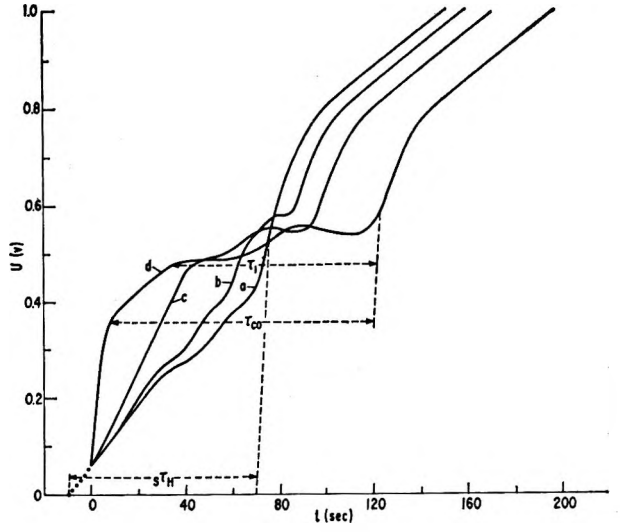

Figure 3. Charging curves after different adsorption times at open circuit in 1 M KOH: a, t_a = 0 sec; b, t_a = 100 sec; c, t_{ad} = 500 sec; d, t_{ad} = 2000 sec.

A series of U–t curves, b, c, and d, measured after adsorption times of 100, 500, and 2000 sec in 1 M KOH is shown in Figure 3. The adsorption of carbon monoxide decreases the length of the hydrogen branch and causes the appearance of arrests at potentials in the double-layer region. Curves b and c demonstrate that the formation of type 1 carbon monoxide, that is subsequently oxidized at anodic potentials between 0.47 and 0.55 V, occurs first. Carbon monoxide that interacts with the surface after about 750 sec is oxidized at less anodic potentials, between 0.36 and 0.47 V (type 2). Limiting lengths corresponding to saturation coverage with CO_{ad} are reached at 2000 sec. In contrast to acid solutions, the determination of the transition times is complicated in alkaline electrolytes by the overlapping of different electrode reactions. The slope of the U–t curve between 0.4 and 0.6 V cannot be used for the double-layer correction because the oxygen layer begins to form[12] there. An approximate determination of $s\tau_H$ is illustrated for curve a in Figure 3. A similar procedure was adopted to obtain τ_{CO} and τ_1 for saturation coverage. A further evaluation of the curves in Figure 3 was not attempted because of the large uncertainty in the transition times.

Charging curves that were measured with 50 mA after adsorption of carbon monoxide for 500 sec at different potentials in 0.5 M H_2SO_4 are replotted in Figure 4. Curve a in Figure 4 appears similar to curve d in Figure 1. The arrest corresponding to the oxidation of type 2 species becomes shorter and appears at more positive potentials with increasing adsorption potential between 0.1 and 0.3 V. Simultaneously, an overshoot develops in this region. The width of the overshoot after adsorption at 0.4, 0.5, and 0.6 V is nearly equal to the length of the arrest of the oxidation of the type 2 species. The overshoot was also observed

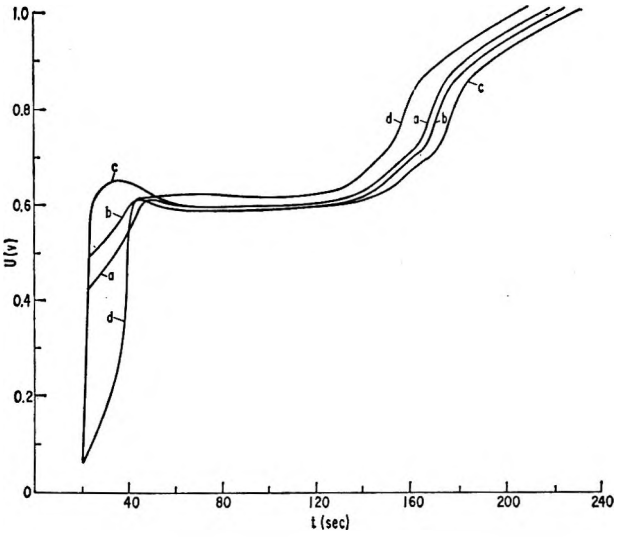

Figure 4. Charging curves with 50 mA after adsorption times of 500 sec at different potentials in 0.5 M H_2SO_4: a, U = 0.1 V; b, U = 0.3 V; c, U = 0.5 V; d, U = 0.7 V.

in studies[5,6] carried out under similar conditions on smooth platinum. Curve d indicates that the CO_{ad} coverage decreases with U above 0.6 V.

The ratio Q_{CO}/sQ_{CO} and the current after 500 sec of CO stirring are shown as a function of U in Figure 5. A limiting current of 50 mA was measured at 0.8 and 0.9 V at the stirring rate of 2 cm³/sec. The above technique for the determination of Q_{CO} is not reliable when $Q_{CO}/sQ_{CO} < 0.8$. Readsorption of CO on the bare surface cannot be eliminated completely, since the removal of dissolved CO from the electrolyte by vigorous stirring is not instantaneous. The value of Q_{CO}/sQ_{CO} at 0.7 V is probably too large. Current and coverage Q_{CO}/sQ_{CO} under galvanostatic conditions are plotted as a function of U in Figure 6. The coverage is

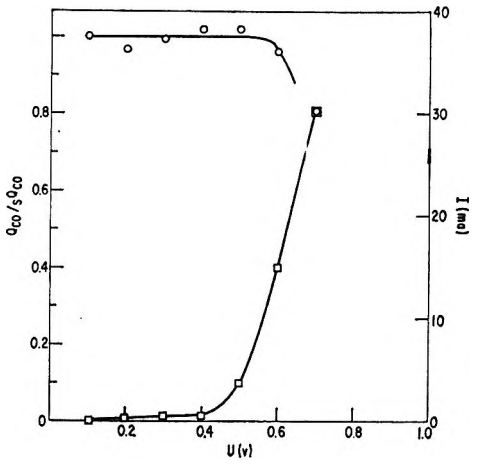

Figure 5. Current (□) and coverage (○) with CO_{ad} as functions of potential under potentiostatic conditions.

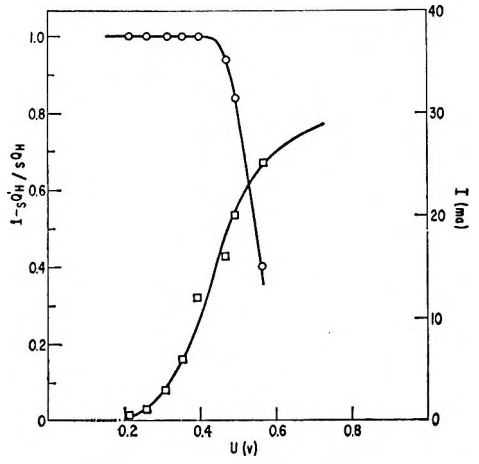

Figure 6. Current (□) and coverage (○) with CO_{ad} as functions of potential for steady-state measurements under galvanostatic conditions.

equal to 1 between 0.2 and 0.4 V, in agreement with the results obtained under potentiostatic conditions. A rapid decrease of coverage with potential is observed between 0.5 and 0.6 V. Although the general shape of the I–U curve is reproducible, the potential at a given current may vary by as much as 0.1 V at $I > 10$ mA in different runs. The drift of potential with time to more positive values is about 10 mV/hr at $I \leq 10$ mA. It becomes larger at $I > 10$ mA. A steady-state potential could not be achieved at 30 mA anymore. A current of about 30 mA (0.6 mA/cm² of apparent surface) represents the limiting diffusion current of dissolved CO as a computation with the numerical values for the diffusion coefficient and the solubility of CO in ref 1 and a diffusion-layer thickness of 0.08 cm at the small stirring intensity of 0.5 cm³/sec demonstrates.

Discussion

Adsorption at Open Circuit. The platinum surface is covered with H atoms to about 90% at 0.1 V when the adsorption of carbon monoxide starts at open circuit. The potential decreases[9,14] with time, passes through a broad minimum, and becomes more positive afterwards at a slow rate. It was already suggested[14] that stirring with CO leads to the production of molecular hydrogen under the given conditions

$$H_{ad} + H_{ad} + CO = H_2 + CO_{ad} \qquad (3)$$

Type 1 material is formed predominantly during the initial potential decrease, which is due to an increase in hydrogen pressure, P_{H_2}. The pressure remains nearly constant in the region of the broad minimum. The potential becomes more positive after the minimum, when the hydrogen pressure decreases because of the continued stirring with 80% Ar and 20% CO. The hydrogen coverage of the platinum atoms on which carbon monoxide has not yet been adsorbed is nearly 1 at $U = 0.05$ V. The reaction

$$CO + H_2O = CO_2 + H_2 \qquad (4)$$

is considered a side reaction at 25°, in agreement with the gas analysis[9] that only about 3% of CO is converted to CO_2 and H_2 at $U = 0$ and $U = 0.5$ V in 0.5 M H_2SO_4 at 20 and 30°.

While the slope of the U–t curve b is practically the same as that of curve a between 0.35 and 0.5 V, the respective slope of curve c is smaller. The effect could be detected with certainty at ${}_sQ_{CO}/{}_sQ_{CO} \geqq 0.6$. It is attributed to the oxidation of type 2 species. The net reaction for the oxidation of type 2 species was established by interrupting the charging curve when the upper arrest had been reached. The amount of Q_{CO_2} of evolved CO_2 was determined[14] together with the charge Q_2 consumed in the lower arrest. The ratios Q_1/Q_{CO_2} and Q_2/Q_{CO_2} agreed with each other within the error limits (20%) of the technique.[13] The net reaction is represented in both cases by eq 1.

Ratios of characteristic charges are put together in Table I for saturation coverage of the surface with CO_{ad}. Since ${}_sQ_H$ is representative for the number of exposed Pt atoms, the ratio $2{}_sQ_H/{}_sQ_{CO}$ corresponds to the number of Pt atoms per adsorbed molecule in acid solutions. The average value of $2{}_sQ_H/{}_sQ_{CO}$ is 1.37 in these solutions. It lies between the two values reported for smooth platinum in ref 2 and in ref 6. The

Table I: Ratios of Characteristic Charges on Platinized Platinum

	$2{}_sQ_H/{}_sQ_{CO}$	${}_sQ_1/{}_sQ_{CO}$
0.05 M H_2SO_4	1.44 ± 0.14	0.82 ± 0.08
0.5 M H_2SO_4	1.27 ± 0.13	0.76 ± 0.08
0.1 M Na_2SO_4 + 0.05 M H_2SO_4	1.37 ± 0.14	0.78 ± 0.08
0.1 M Na_2SO_4 + 0.005 M H_2SO_4	1.40 ± 0.14	0.80 ± 0.08
1 M KOH	1.16 ± 0.12	0.77 ± 0.08

average value of 0.79 for ${}_sQ_I/{}_sQ_{CO}$ in acid solution demonstrates that about 21% of the adsorbed molecules are of type 2. The latter value on platinized platinum is nearly the same as the value of 0.25 found for the ratio of the volumes of weakly and strongly adsorbed CO_{ad} on platinum powder in the gas phase[15] at room temperature. In this case, the amount of weakly bonded CO_{ad} desorbs by pumping alone. The value of $2{}_sQ_H/{}_sQ_{CO}$ is somewhat smaller in 1 *M* KOH than the corresponding values in the acid solutions. The ratio ${}_sQ_I/{}_sQ_{CO}$ is about the same.

Recently the adsorption of carbon monoxide was studied[16] on different samples of platinum–silica catalysts in the gas phase. The ratio of exposed Pt atoms to adsorbed molecules varied from about 1 to 2 with increasing platinum content. It was suggested that the coverage of Pt with CO_{ad} depends upon the crystallite size. Linear bonding occurs predominantly on small, highly dispersed crystallites. Bridge bonding is favored when the uninterrupted area of platinum has attained a reasonable size. A distinction between weakly and strongly bonded CO_{ad} was not made.

It is demonstrated in Figure 7 of the subsequent section that the parameter $1 - ({}_sQ_H'/{}_sQ_H)$ is equal to $Q_{CO}/{}_sQ_{CO}$. The same number $2{}_sQ_H/{}_sQ_{CO}$ of Pt atoms is covered on the average by one molecule of both types of CO_{ad} for this reason. The result that the average number of exposed Pt atoms per adsorbed molecule is larger than 1 may imply the presence of linearly and bridged bonded CO_{ad}. A quantitative determination of the amount of these two forms is difficult because of the influence of the crystallite size[16] and because of the restriction that "packing" rules[17] apply to the linearly bonded CO_{ad}, but not to the bridged CO_{ad} on crystallites. of sufficient size.

The values of $2{}_sQ_H/{}_sQ_{CO}$ and ${}_sQ_I/{}_sQ_{CO}$ obtained in 1 *M* KOH indicate that the oxidation of CO_{ad} is a two-electron process, as in acid solutions. The following scheme is suggested for alkaline electrolytes.

$$CO_{ad} + OH^- = COOH_{ad} + e^- \quad (5)$$

$$COOH_{ad} + 3OH^- = CO_3^{2-} + 2H_2O + e^- \quad (6)$$

Carbon dioxide was not detected in the He stirring gas by gas chromatography after the oxidation of CO_{ad} in agreement with eq 5 and 6.

Effect of Adsorbed Carbon Monoxide on the Hydrogen Coverage in Acid Electrolytes. The parameter $1 - ({}_sQ_H'/{}_sQ_H)$ was determined as a function of $Q_{CO}/{}_sQ_{CO}$ from the measurements in 0.5 *M* H_2SO_4. The adsorbed amount of H atoms becomes very small when Q_{CO} approaches ${}_sQ_{CO}$, as evidenced by the curves d in Figure 1 and 3 and the curves in Figure 2 and 4. The results are plotted in Figure 8. A straight line may be drawn through the experimental points, as for smooth platinum.[6] Thus the parameter $1 - ({}_sQ_H'/{}_sQ_H)$ is a direct measure of the coverage of platinized platinum with CO_{ad}.

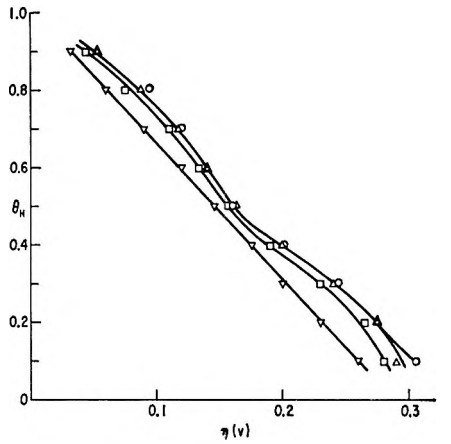

Figure 7. Isotherms for hydrogen adsorption in the presence of CO_{ad}: ○, $Q_{CO}/{}_sQ_{CO} = 0$; □, $Q_{CO}/{}_sQ_{CO} = 0.41$; △, $Q_{CO}/{}_sQ_{CO} = 0.25$; ▽, $Q_{CO}/{}_sQ_{CO} = 0.52$.

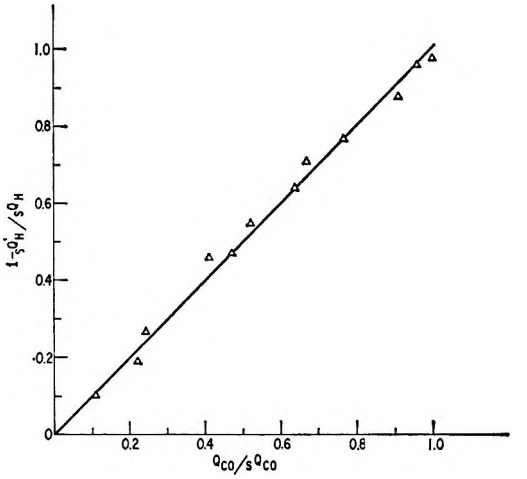

Figure 8. Parameter, $1 - ({}_sQ_H/{}_sQ_H)$, as a function of $Q_{CO}/{}_sQ_{CO}$.

The hydrogen coverage, $\theta_H = Q_H'/{}_sQ_H'$, was obtained as a function of hydrogen overvoltage, η, in the presence of CO_{ad} from the hydrogen branch of anodic-charging curves taken with 50 mA in 0.5 *M* H_2SO_4. The procedure was outlined[18] previously. The θ_H–η curves in Figure 7 coincide for $\theta_H > 0.2$, as long as $Q_{CO}/{}_sQ_{CO} < 0.25$. A decrease of hydrogen coverage is already detectable for $\theta < 0.2$ at small coverage with CO_{ad}. The θ_H–η curves are shifted to the left with increasing $Q_{CO}/{}_sQ_{CO}$ (>0.25). The free energy of hydrogen adsorption becomes less negative, as in the case[19] of simultaneous adsorption of H atoms and specifically adsorbable anions. A distinction between

(15) D. W. McKee, personal communication. See D. W. McKee, *J. Catal.*, **8**, 240 (1967).

(16) T. A. Dorling and R. L. Moss, *ibid.*, **7**, 378 (1967).

(17) D. Brennan and F. H. Hayes, *Phil. Trans. Roy. Soc.* (London), **B258**, 347 (1965).

(18) M. W. Breiter, *Trans. Faraday Soc.*, **60**, 1445 (1964).

(19) M. W. Breiter, *Ann. N. Y. Acad. Sci.*, **101**, 709 (1963).

weakly and strongly bonded hydrogen may still be made at $Q_{CO}/_sQ_{CO} = 0.41$. The distinction is not feasible at $Q_{CO}/_sQ_{CO} = 0.52$ any more. The θ–η curve degenerates to a straight line (Temkin isotherm). An interaction between CO_{ad} and H_{ad} is likely, as in the gas phase.[20] A similar behavior was reported[21] recently for hydrogen adsorption in the presence of adsorbed carbonaceous species formed previously by anodic polarization in 0.5 *M* H_2SO_4 and 0.5 *M* CH_3OH.

Coverage with CO_{ad} under Potentiostatic Conditions in Acid Solutions. The *U*–*t* curves a, b, and c in Figure 4 demonstrate that the amount of type 2 species depends strongly upon potential. If the adsorption occurs at $U < 0.1$ V, the available 21% of sites are covered by that form. The coverage $Q_2/_sQ_2$ of the type 2 species decreases from 0.78 at 0.1 V to 0.65 at 0.2 V and to 0.32 at 0.3 V. Simultaneously, the respective sites become covered again, probably by type 1 species. The decrease of the amount of type 2 species between 0.1 and 0.4 V is attributed to a kinetic effect, which will be discussed in more detail in the section concerning the oxidation mechanism of dissolved CO. The overshoot in curve c suggests that the hindrance of the oxidation of type 1 species is initially larger when the surface coverage with type 1 species is between 0.8 and 1. There are very few free sites for the formation of other adsorbed species like OH_{ad}.

Since the adsorption of carbon monoxide has been studied[2,5,6] at $U \geq 0.2$ V on smooth platinum and since relatively large current densities were employed[5,6] during the subsequent oxidation of CO_{ad}, the formation of type 2 species was not observed there. However, the existence of sites on which type 2 species may be formed is demonstrated by the overshoot of the *U*–*t* curves[5,6] on smooth platinum and by the desorption of CO_{ad} at 0.4 V after the stopping of the CO stirring. The ratio of the charge of the desorbed amount to the total charge in the presence of stirring is 0.22, according to the data in Figure 4 of ref 1. It was also noted[6] that the initial 16% of the charge required for the oxidation of CO_{ad} which had been adsorbed at 0.3 V possessed properties different from the residual 84%.

The total coverage, as defined by $Q_{CO}/_sQ_{CO}$, is practically 1 between 0.1 and 0.5 V (see Figure 5). This is in agreement with the results on smooth platinum.[1,2,6] The coverage decreases with *U* above 0.6 V. Measurements made under equivalent conditions have not been reported for smooth platinum. The observation of a sudden depletion of coverage at about 0.91 V during the anodic sweep of periodic voltammetric measurements with 40 mV/sec is considered characteristic for the voltammetric technique. In general, the decrease of the coverage of type 1 species with potential started in the present studies when the current became larger than about 15 mA (compare Figure 6).

Oxidation of Adsorbed Carbon Monoxide. The different pH dependence for the oxidation of type 1 and type 2 species in Figure 2 is evidence for different oxidation mechanisms. The shift of the *U*–*t* curves to more positive potentials with increasing pH in the lower arrest corresponds roughly to the respective change of the potential of the hydrogen reference electrode. A reaction mechanism in which the electrode potential is not determined by an equilibrium between H_{ad} and H^+ or between OH_{ad} and H_2O is consistent with these results. In contrast, the pH dependence during the oxidation of type 1 species requires[22] the assumption of such an equilibrium.

Charging curves were taken with currents between 10 and 200 mA after adsorption at open circuit in 0.5 *M* H_2SO_4 to obtain more information on the mechanisms. The potentials at $Q_2/_sQ_2 = 0.17$, 0.33, 0.50, 0.67, and 0.83 were determined as a function of *I* in the lower arrest. Since the slope of the *U*–*t* curves is small in the upper arrest, the same determination was only carried out for $Q_1/_sQ_1 = 0.5$. The results are presented in a semilogarithmic plot in Figure 9. Although the data obtained in the lower arrest scatter, parallel straight lines may be drawn through the points at the same coverage. The slope of these Tafel lines is 100 mV/decade of current, in contrast to a slope of 70 mV for type 1 species.

Plots of *U vs.* $Q_2/_2Q_S$ at constant *I* were constructed with the aid of the Tafel lines in Figure 9. Parallel lines were obtained. The potential decreases approximately in a linear fashion with $Q_2/_sQ_2$ between $Q_2/_sQ_2 = 0.17$ and 0.83. Thus the current may be expressed

$$I = k_2 \exp\left(\beta_2 Q_2/_sQ_2 + \frac{\alpha_2 n_2 UF}{RT}\right) \qquad (7)$$

The parameters in eq 7 have the following values: $k_2 = 1.3 \times 10^{-4}$ mA $\beta_2 = 6.1$, $\alpha_2 n_2 = 0.58$. Equation 7 with an $\alpha_2 n_2$ value smaller than 1 is consistent with the interpretation that the reaction

$$CO_{ad} + H_2O = COOH_{ad} + H^+ + e^- \qquad (8)$$

is rate determining. The subsequent steps in the oxidation of type 1 species are less hindered and cannot be elucidated by the present method. The dependence of the rate upon coverage is of the Temkin type.[23] A similar mechanism involving OH^- instead of H_2O is proposed for the oxidation of type 2 species in 1 *M* KOH.

Two mechanisms have been suggested[4,5] recently for the oxidation of type 1 species. Gilman[4] postulated the "reactant-pair" mechanism, in which an adsorbed

(20) H. Heyne and F. C. Tompkins, *Trans. Faraday Soc.*, **63**, 1274 (1967).

(21) B. I. Podlovchenko and V. F. Stenin, *Elektrokhimeya*, **3**, 649 (1967).

(22) A. N. Frumkin and B. I. Podlovchenko, *Dokl. Akad. Nauk SSSR*, **150**, 349 (1963).

(23) M. Temkin, *Zh. Fiz. Khim.*, **15**, 296 (1941).

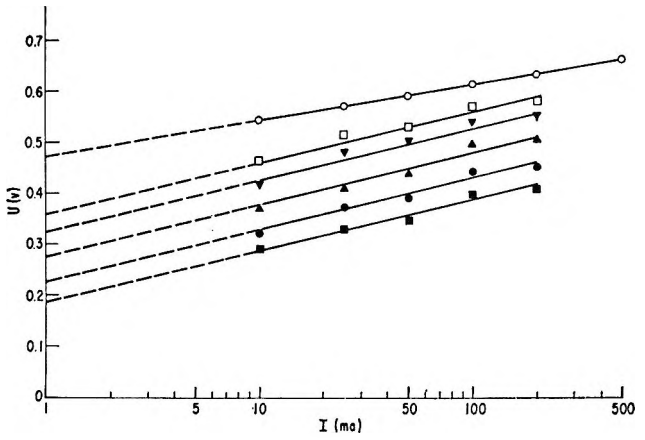

Figure 9. Current–potential relation for the oxidation of type 2 and type 1 species at different coverage: ○, $Q_1/{}_sQ_1 = 0.5$; ●, $Q_2/{}_sQ_2 = 0.66$; □, $Q_2/{}_sQ_2 = 0.17$; ■, $Q_2/{}_sQ_2 = 0.83$; ▲, $Q_2/{}_sQ_2 = 0.50$; ▼, $Q_2/{}_sQ_2 = 0.17$.

carbon monoxide molecule reacts with a water molecule adsorbed at an adjacent site. The transfer of the first electron from the adsorbed complex is supposed rate determining. Warner and Schuldiner[5] proposed a reaction between CO_{ad} and adsorbed oxygen O_{ad}. The formation of O_{ad} from water molecules is assumed rate determining.

Neither the reactant-pair mechanism[4] nor the water-discharge mechanism are consistent with the pH dependence found here for the oxidation of type 1 species. The pH dependence may be explained as suggested by Frumkin and Podlovchenko[22] in their discussion of the mechanism of ethanol oxidation. A chemical reaction between adsorbed carbonaceous species and adsorbed OH radicals is supposed rate determining on a heterogeneous surface of the Temkin type[23]

$$I = kf(Q_1/{}_sQ_1) \exp\left(\frac{\beta\mu_{OH}}{RT}\right) \qquad (9)$$

Here $f(Q_1/{}_sQ_1)$ describes the dependence of the rate upon CO_{ad} and μ_{OH} is the chemical potential of the adsorbed OH radicals

$$\mu_{OH} = FU + \text{constant} \qquad (10)$$

The correctness of the latter interpretation depends in a critical way upon the validity of the exponential dependence of I upon μ_{OH} in eq 9. Since this dependence cannot be verified in an independent way, owing to the small coverage with OH_{ad}, the preceding mechanism for the oxidation of type 1 species in acid electrolytes is considered tentative.

The U–t curves c and d in Figure 3 consist of two parts in the potential region of the oxidation of type 1 material in 1 M KOH. The appearance of two arrests was also reported for the oxidation of adsorbed carbonaceous species that had been formed previously by anodic oxidation of methanol,[24] formic acid,[25] or formaldehyde[25] on platinized platinum in alkaline electrolytes. It was suggested[24,25] that two forms of chemisorbed substance are present on the surface and that the second form results from the interaction between OH^- ions with carbonaceous species, which are solely formed in acid solutions. It was noted in the present study that the length of the two parts in the upper potential region is about the same, independent of Q_1 (see Figure 3). Therefore, it is proposed that the first arrest is due to reaction 5. The further oxidation of $COOH_{ad}$ to CO_3^{2-} occurs during the second arrest. A separation of the two one-electron steps may be observable in alkaline solutions, since three OH^- ions are required in the second step. In contrast, a hydrogen atom has only to be split up from $COOH_{ad}$ in acid solutions, making the second step a rapid process. The two arrests during the oxidation of adsorbed carbonaceous species[24,25] are also of about equal lengths in 0.1 M KOH and 1 M KOH (see Figure 7b in ref 24 and Figure 8 in ref 25). A two-electron process that is similar to the mechanism of the oxidation of CO_{ad} is considered likely in agreement with results[13] on the oxidation of these carbonaceous species in acid solutions.

Oxidation of Dissolved Carbon Monoxide under Steady-State Conditions in Acid Solutions. The current–potential data in Figure 6 represent steady-state values in the usual sense. The current was increased every 20 min. The change of potential after 20 min is small at $I < 10$ mA, although it is not zero. In contrast, the I–U curve in Figure 5 was obtained by starting the CO stirring at a given potential, which was maintained potentiostatically, and by measuring the current when the change of current with time had become small after 500 sec. The two techniques do not yield the same I–U curve. The potentiostatic I–U curve is shifted by about 0.2 V toward positive potentials with respect to the galvanostatic curve. Different interpretations of this effect are conceivable. (a) A truly steady state has not been achieved during the galvanostatic measurements. (b) The current distribution differs under potentiostatic and galvanostatic conditions. The local potential of some centers may be larger than the measured potential under galvanostatic conditions. It is considered likely that both effects contribute simultaneously. The poor reproducibility of the data in Figure 6 is probably due to factor a. An evaluation of the galvanostatic I–U curve on the basis of a Tafel plot was not attempted for the above reasons. The data in Figures 5 and 6 indicate, independent of the experimental conditions, that the decrease of $Q_{CO}/{}_sQ_{CO}$ with U starts when the current becomes larger than 10 mA. The Tafel plots for type 2 species in Figure 9 show oxidation rates which are larger or comparable to the oxidation rates of dissolved CO under

(24) O. A. Petry, B. I. Podlovchenko, A. N. Frumkin, and H. Lal, *J. Electroanal. Chem.*, 10, 253 (1965).

(25) B. I. Podlovchenko, O. A. Petry, A. N. Frumkin, and H. Lal, *ibid.*, 11, 12 (1966).

potentiostatic or galvanostatic conditions, respectively, at $U \leq 4$ V. It is suggested that the oxidation of dissolved CO involves the type 2 species as intermediates at $U < 0.4$ V. This interpretation is substantiated by the shape of the potentiostatic I–U curve, which consists of an initial part with small oxidation rates between 0.1 and 0.4 V and of a second part with larger rates above 0.5 V. The decrease of Q_2 between 0.1 and 0.4 V implies that the rate of adsorption of type 2 species is insufficient to maintain full coverage with increasing oxidation rates. Adsorption of type 2 species is the rate-determining step at $U \leq 0.4$ V.

The type 1 species are considered the intermediates during the oxidation of dissolved carbon monoxide at $I > 10$ mA. The oxidation rates of type 1 species in Figure 9 are comparable to the rates of the oxidation of CO in Figure 5 and 6. The coverage $Q_1/{}_sQ_1$ decreases with potential at currents which are approaching the limit imposed by mass transport. Insufficient supply which leads to a smaller adsorption rate is the reason for the decrease of $Q_1/{}_sQ_1$. Partial mass-transport control was also concluded for the CO oxidation on smooth platinum free of CO_{ad}. In contrast to the voltammetric measurements on smooth platinum,[1,26] the decrease of $Q_1/{}_sQ_1$ with U occurs here in a potential region in which the coverage with OH_{ad} and O_{ad} is small.

(26) P. Stonehart, *Electrochim. Acta*, 12, 1186 (1967).

The Brønsted α and Isotope Effects for Vinyl Ether Hydrolysis[1a]

by Maurice M. Kreevoy and Robert Eliason[1b]

Department of Chemistry, University of Minnesota, Minneapolis, Minnesota 55455 *(Received October 2, 1967)*

Like other reactions in which proton transfer is rate determining, ethyl vinyl ether hydrolysis is shown to obey the Brønsted catalysis law with a variety of carboxylic acids, but acids of other structure give rates substantially varying from those predicted by the carboxylic acid correlation. The value of α for carboxylic acids is 0.66. The over-all solvent isotope effect, k_H/k_D, is 3.2 ± 0.1. The competitive isotope effect, $\varkappa_H/\varkappa_D$, is 7.0 ± 0.1. If proton transfer is directly from M_3O^+ to the substrate, these lead to a primary isotope effect, $(k_H/k_D)_I$, of 4.8 and a secondary solvent isotope effect, $(k_H/k_D)_{II}$, of 0.66. From the latter an isotopic α, α_i, of 0.56 is obtained. Competitive tritium isotope effects have been measured and the Swain–Schaad relations are obeyed. The reaction coordinate seems to be largely proton translation.

A number of papers have recently appeared establishing that vinyl ether hydrolysis is general-acid catalyzed,[2,3] shows a solvent isotope effect, k_H/k_D, around 3 when catalyzed by mineral acid in water,[2-6] and shows a substantially larger isotope effect when catalyzed by molecular formic acid.[4] It has also been shown that the proton, once covalently affixed to the substrate, does not revert to the solvent.[3] These observations convincingly show that vinyl ether hydrolysis proceeds through the mechanism given in eq 1 and 2. The mechanism is given for the specific case of ethyl vinyl ether hydrolysis, with which this paper is concerned.

$$CH_2{=}CHOC_2H_5 + H^+ \xrightarrow{RD} CH_3CH{\cdots}OC_2H_5^+ \quad (1)$$

$$CH_3CH{\cdots}OC_2H_5^+ + H_2O \xrightarrow[\text{fast steps}]{\text{series of}} CH_3CH{=}O + C_2H_5OH \quad (2)$$

The present paper provides a Brønsted α for a series of carboxylic acids and separates k_H/k_D into primary and secondary solvent isotope effects. From the latter, an isotopic α is obtained in general agreement with the Brønsted α. A test of the Swain–Schaad relation is also described.[7] Some details of transition-state structure can be surmised.

(1) (a) Supported, in part, by the National Science Foundation through Grant No. GP-5088; (b) Hercules Corp. Summer Fellow, 1965; Du Pont Co. Summer Fellow, 1966; Ethyl Corp. Fellow, 1966–1967.

(2) P. Salomaa, A. Kankaaperä, and M. Lajunen, *Acta Chem. Scand.*, 20, 1790 (1966).

(3) A. J. Kresge and Y. Chiang, *J. Chem. Soc., Sect. B*, 53 (1967).

(4) A. J. Kresge and Y. Chiang, *ibid., Sect. B*, 58 (1967).

(5) (a) D. M. Jones and N. F. Wood, *ibid.*, 5400 (1964); (b) A. Ledwith and H. J. Woods, *ibid., Sect. B*, 753 (1966).

(6) M. S. Shostakovskii, A. S. Atavin, B. V. Prokopev, B. A. Trofimov, V. I. Lavrov, and N. M. Driglazov, *Dokl. Akad. Nauk SSSR*, 163, 1412 (1965).

(7) C. G. Swain, E. C. Stivers, J. F. Reuwer, Jr., and L. J. Schaad, *J. Amer. Chem. Soc.*, 80, 5885 (1958).

Experimental Section

Ethyl vinyl ether was purchased from Aldrich Chemical Co. and purified by distillation. Aqueous inorganic acids and bases were made up and standarized in the usual ways,[8] as were formic acid solutions. Chloroacetic and cyanoacetic acids were purified by distillation under vacuum. Chloroacetic acid hydrolyzes slowly to glycolic acid and HCl in its aqueous solutions.[9] In our buffer solutions this hydrolysis was found, by periodic titration over a 2-month period, to consume ~2% of the acid per week. All the work described in this paper was done with solutions no more than 2 days old, whose pH had been verified with a pH meter.

Kinetic measurements were made by conventional spectroscopic techniques and pseudo-first-order rate constants, k_1, could be replicated with discrepancies of no more than 5%.

p-Nitrophenylhydrazone Collection. A mixture of 5 ml of ethyl vinyl ether with a solution of 1 g of *p*-nitrophenylhydrazine in 100 ml of 0.1 *N* hydrochloric acid was stirred vigorously for about 1 min, after which a yellow precipitate appeared. The precipitate was collected and the solvent recovered by distillation so that its H:D ratio could be determined. The precipitate was purified by three recrystallizations from a methanol–water mixture and sublimed; mp 125.9–126.2° (lit.[10] 128.5°). This sufficed to bring it nearly to analytical purity. *Anal.* Calcd for $C_8H_9N_3O_2$: C, 53.62; H, 5.06; N, 23.45. Found: C, 52.93; H, 5.00; N, 23.71. It was probably contaminated with a few per cent of the hydrazine, which would not influence the mass ratios in the region of the parent peak.

The RH:RD ratio was determined mass spectroscopically.[11-13] The principal cause of imprecision and inaccuracy in these determinations was chemical decomposition at the temperatures required to volatilize the hydrazone. This was shown by a systematic variation in the ratio with time of residence in the heated inlet system. Results were extrapolated to zero time, but it can be seen that they are less precise by an order of magnitude than those previously reported for gases, using the same mass spectroscopic techniques.[12, 13]

4-Phenylsemicarbazone Collection. Technique A. A mixture of 4 ml of ethyl vinyl ether and 50 ml of 0.1 *M* tritiated aqueous acid was stirred at 25° until the water-insoluble ether was consumed. The acetaldehyde was then driven over, by heating, into an untritiated neutral solution containing 0.5 g of 4-phenylsemicarbazide. The derivative precipitated after about 15 min and was purified by two crystallizations from methanol–water or ethanol–water mixtures. The melting point of the 4-phenylsemicarbazone of acetaldehyde, so prepared, lay between 131.8 and 133.8° (lit.[14] 151–152°), but it is analytically pure. It is apparently polymorphic. *Anal.* Calcd for $C_9H_{11}H_3O$: C, 61.00; H, 6.26; N, 23.72. Found: C, 61.26; H, 5.99; N, 23.66.

Technique B. This was the same as technique A, except that the acetaldehyde was carried over into the derivatizing solution by a nitrogen stream at room temperature, instead of by heating. With either technique a small amount of isotope exchange occurs after the acetaldehyde is formed. Tritium contents of derivatives prepared by both techniques were corrected for the tritium content of derivatives prepared from identical reaction mixtures, except that untritiated acetaldehyde was used in the place of ethyl vinyl ether. For both techniques these corrections amounted to about 10–15% of the radioactivity of the derivative, but the corrections were much more reproducible by technique B.

In all cases the tritium content of the derivatized acetaldehyde and that of the water were determined by liquid scintillation counting, using either Nuclear-Chicago, Model 724, or Beckman liquid scintillation systems. The chemical composition of all the counting solutions was the same; they contained 10.00 ml of the dioxane-based scintillation solution described by Friedman and Leete,[15] 1.00 ml of water, and 1.00 ml of methanol containing 10.0 mg of the phenylsemicarbazone of acetaldehyde.

In using these heterogeneous reaction mixtures it was assumed that the reaction takes place in the homogeneous aqueous phase, and the dissolved vinyl ethyl ether is continuously replenished from the organic phase. This assumption is supported by the typical results obtained in two experiments, using technique B, where the ethyl vinyl ether was added in small increments over a period of several hours, so that its solubility was never exceeded. The values of κ_K/κ_T obtained were 15.5 and 16.7. This can be compared with a mean value of 15.8 and an average deviation from the mean of 0.7.

Results

All of the following results were obtained at 25.0° in aqueous solution. The best value of k_H, defined as $k_1/(H^+)$ and determined from 22 measurements of k_1

(8) I. M. Kolthoff and E. B. Sandell, "Textbook of Quantitative Inorganic Analysis," The Macmillan Co., New York, N. Y., 1952.

(9) A. J. Kresge, personal communication.

(10) E. Hyde, *Chem. Ber.*, **32**, 1813 (1899).

(11) M. M. Kreevoy and R. A. Kretchmer, *J. Amer. Chem. Soc.*, **86**, 2435 (1964).

(12) M. M. Kreevoy, P. J. Steinwand, and W. V. Kayser, *ibid.*, **86**, 5013 (1964).

(13) M. M. Kreevoy, P. J. Steinwand, and W. V. Kayser, *ibid.*, **88**, 124 (1966).

(14) P. P. T. Sah and T. S. Ma, *J. Chinese Chem. Soc.*, **2**, 32 (1934).

(15) A. R. Friedman and E. Leete, *J. Amer. Chem. Soc.*, **85**, 2141 (1963).

Table I: Dissociation Constants and Catalytic Coefficients

Acid	K_{HA}, M	K'_{HA},[d] M	k_{HA},[e] M^{-1} sec^{-1}
HCOOH	1.77×10^{-4} [a]	3.29×10^{-4}	$(5.92 \pm 0.10) \times 10^{-3}$
$ClCH_2COOH$	1.36×10^{-3} [a]	2.41×10^{-3}	$(3.36 \pm 0.05) \times 10^{-2}$
$NCCH_2COOH$	3.40×10^{-3} [a]	6.03×10^{-3}	$(3.89 \pm 0.14) \times 10^{-2}$
H_3PO_4	7.16×10^{-3} [b]	1.57×10^{-2}	$(4.03 \pm 0.08) \times 10^{-1}$
H^+	55.5 [c]	55.5	1.71 ± 0.01

[a] G. Kortum, W. Vogel, and K. Andrussow, "Dissociation Constants of Organic Acids in Aqueous Solution," Butterworth and Co., Ltd., London, 1961. [b] P. Salomaa, L. L. Schaleger, and F. A. Long, *J. Amer. Chem. Soc.*, **86**, 1 (1964). [c] Assuming 55.5 for the activity of water in dilute, aqueous solutions. [d] Obtained as indicated in ref 20. [e] The cited uncertainties are 50% confidence limits (probable errors).

in HCl and $HClO_4$, was 1.71 ± 0.01 M^{-1} sec^{-1}. It was determined by the least-squares criterion, with k_1 forced to be zero when (H^+) is zero.[16]

The best value of k_D was 0.57 ± 0.01 M^{-1} sec^{-1}. After the kinetic measurements were made, each reaction mixture was analyzed for H in the D_2O, using the near infrared.[17] Atom percentages of H were between 1 and 2, averaging 1.1%. The small correction to 100% D was then made using the equations of Kresge[18] and an α_i of 0.6 (defined and obtained below). The resulting value of k_D was 0.53 M^{-1} sec^{-1}. This gives the value of k_H/k_D as 3.2, with a probable error of 0.1.

At higher total electrolyte concentrations k_H showed a tendency toward higher values. With 1.9×10^{-3} M $HClO_4$ and $NaClO_4$ between 0.05 and 1.60 M, k_H is accurately governed by eq 3,[19] with C, 0.31, and k_H^0, 2.00 M^{-1} sec^{-1}. Since k_H^0 is significantly above the

$$\log k_H = \log k_H^0 + C\mu \qquad (3)$$

value of k_H obtained experimentally in dilute solution, the ionic-strength dependence of k_H must be somewhat steeper with $\mu < 0.05$ M.

General-acid catalytic coefficients, k_{HA}, were obtained for a number of molecular acids. These were obtained from the slopes of plots of $[k_1 - k_H(H^+)]$ against (HA) in buffered solutions of constant ionic strength (0.2 M, maintained by appropriate additions of $NaClO_4$) and nearly constant (H^+). The method has been described in more detail previously.[20] As before a least-squares criterion of fit was used to evaluate the slopes, k_{HA}, but in each case the line was forced through the origin. Table I lists the catalytic coefficients, their 50% confidence limits, the apparent dissociation constants, K'_{HA} (in 0.2 M electrolyte), and the thermodynamic dissociation constants, K_{HA}. For comparison k_H is also listed.

In a series of experiments in H_2O containing small concentrations of T, the product, acetaldehyde, was trapped as its 4-phenylsemicarbazone,[14] and its level of labeling was compared with that of the solvent. The quantity κ_H/κ_T is defined by $(RH/RT)_{prod}(T/H)_{solv}$.[11-13] Two experimental techniques were used to isolate the product, described as techniques A and B in the Experimental Section. Fifteen experiments by technique A gave a mean value of 17.1, with an average deviation from the mean of 1.6 and a probable error of the mean of 0.4. Six experiments by technique B gave a mean value of 15.8, with an average deviation from the mean of 0.7 and a probable error of the mean of 0.3. The best value of κ_H/κ_T was taken as 16.4, and it is probably uncertain by about 0.2.

Five determinations of RM/RT were made by technique B in water containing 97–98 atom % D. (The symbol, M, is used to indicate hydrogen without specifying the isotope.) Each of these was used to evaluate κ_D/κ_T by means of eq 4. Experiments described below were used to evaluate κ_H/κ_D. For this purpose only an approximation is required in any event, as $(\kappa_H/\kappa_D)(H/D)$ is only about 0.15. The

$$\frac{(RM/RT)(T/D)}{(\kappa_H\kappa_D)(H/D) + 1} = \frac{\kappa_D}{\kappa_T} \qquad (4)$$

average value of κ_D/κ_T was 2.42, with an average deviation from the mean of 0.08 and a probable error of 0.03.

In eight experiments in H_2O–D_2O mixtures the product was trapped as the *p*-nitrophenylhydrazone and its deuterium content was determined mass spectroscopically.[11-13] The hydrogen:deuterium ratio of the solvent was determined by the near-infrared technique.[17] The average value of κ_H/κ_D obtained from these was 6.8, with an average deviation from the mean of 0.8 and probable error of the mean of 0.3.

Discussion

The present value of k_H at 25°, 1.71 M^{-1} sec^{-1}, is in

(16) C. A. Bennett and N. L. Franklin, "Statistical Analyses in Chemistry and the Chemical Industry," John Wiley and Sons, Inc., New York, N. Y., 1954, pp 231–233.

(17) T. S. Straub, M.S. Thesis, University of Minnesota, Minneapolis, Minn., 1966, pp 48–54.

(18) A. J. Kresge, *Pure Appl. Chem.*, **8**, 243 (1964).

(19) A. A. Frost and R. G. Pearson, "Kinetics and Mechanism," John Wiley and Sons, Inc., New York, N. Y., 1961, p 152.

(20) M. M. Kreevoy, T. S. Straub, W. V. Kayser, and John L. Melquist, *J. Amer. Chem. Soc.*, **89**, 1201 (1967).

entirely reasonable agreement with the value 1.89 M^{-1} sec^{-1} of Salomaa, *et al.*,[2] and the value 1.81 M^{-1} sec^{-1} which can be inferred from the results of Kresge and Chiang[3] at 26.7°.

The present value of k_H/k_D, 3.2, is a little larger than either that of Kresge and Chiang for the same compound, 2.95, or that of Salomaa, *et al.*,[2] for chloroethyl vinyl ether, 2.46. It is similar to the value, ~3.4, found by Shostakovskii, *et al.*,[6] for 2-hydroxyethyl vinyl ether. However, none of the previous groups report analysis for H in their "completely deuteriated" reaction mixtures. Moreover, even using the nominal H content, 0.5%, and the equations of Kresge,[18] we extrapolate the measured ratio of Kresge and Chiang to 3.02. They obtained the value, 2.95, by a linear extrapolation.

The present values of k_{HA} for carboxylic acids and the value, 1.5×10^{-4} M^{-1} sec^{-1}, which can be ascribed to acetic acid at 25°[3] obey the Brønsted catalysis law,[21] with deviations not much larger than their experimental uncertainties. They give an α of 0.66 ± 0.04 by the method of least squares.[22] As in previous work[20] k_H is much too small (by a factor of ~15) to fit the correlation line and $k_{H_3PO_4}$ is too large by a similar factor.

The value of α is in rather poor quantitative agreement with the value 0.51 obtained by Salomaa, *et al.*,[2] for methyl isopropenyl ether. Partly, the difference arises from the choice of acids. Salomaa's study included only four acids, of widely varying structure, including H^+. A line drawn between k_H and any other point on the Brønsted plot would be of much lower slope than the line defined by carboxylic acids.

Simple theory and its more obvious elaborations would lead one to expect that k_H/k_T should be equal to the product $(k_H/k_D)(k_D/k_T)$. The success of this relationship, within the combined statistical uncertainties, lends confidence in the individual values.

The "low temperature" Swain–Schaad relation is shown in eq 5 and 6.[7] (They are not independent.) The value of k_H/k_D predicted by eq 7 and k_H/k_T is 6.96, with a probable error of 0.10. The predicted

$$k_H/k_D = (k_H/k_T)^{0.693} \quad (5)$$

$$k_D/k_T = (k_H/k_T)^{0.307} \quad (6)$$

value of k_D/k_T is 2.36 ± 0.03. These are in good accord with the experimental values, 6.8 ± 0.3 and 2.42 ± 0.08. The low-temperature Swain–Schaad relation has recently been shown to be very useful in analyzing aromatic hydrogen exchange results.[23] The present experimental support for the relation, in a reaction of closely related type, strengthens this analysis (particularly in view of the recent production of evidence[24] that the Swain–Schaad relation is *not* obeyed in base-catalyzed abstraction of M from variously substituted acetophenones).

Because of the relative unreliability of the direct experimental value of k_H/k_D the "best" value is probably that derived from k_H/k_T by means of eq 5, 6.96 ± 0.10. Assuming that the proton is transferred directly from the M_3O^+ unit of the aquated proton to the substrate, the primary kinetic isotope effect, $(k_H/k_D)_I$, can be obtained by multiplying k_H/k_D by l.[12,13] The latter is the constant required to convert $(D/H)_{solv}$ into $(D/H)_{M_3O}$ and is assumed, in this paper, to have the value 0.69.[25-28] The value of $(k_H/k_D)_I$ so obtained is 4.8. From the relation $k_H/k_D = (k_H/k_D)_I \cdot (k_H/k_D)_{II}$, the secondary solvent isotope effect, $(k_H/k_D)_{II}$, then takes the value 0.66. An isotopic α, α_i, can readily be obtained from $(k_H/k_D)_{II}$ and l by means of eq 7[13,18,20] and has the value 0.56. The significance of α_i is the same as that of α, except that the acid "strength" is varied by varying the isotopic composition of the *untransferred* part of the aquated proton, instead of varying R in RCOOH. The numerical similarity of the two α's supports the model used for the transition state. The value of α_i is experimentally indistinguishable from the value 0.6 suggested by Kresge and Chiang to fit rates of ethyl vinyl ether hydration in H_2O–D_2O mixtures or the value 0.52 suggested by Salomaa, *et al.*,[2] to fit similar results on chloroethyl vinyl ether hydration but obtained by an entirely independent technique.

$$\alpha_i = \frac{\log (k_H/k_D)_{II}}{2 \log l} \quad (7)$$

In conclusion then, the present paper supports and refines the mechanistic conclusions previously reached.[2-4] The results require that proton transfer is rate determining and suggest that it is a little more than half complete in the transition state. The magnitude of k_H/k_D requires that the largest component of the reaction coordinate is proton translation.[29] Most of the parameters of this reaction are very similar to those of allylmercuric iodide cleavage,[13] but k_H/k_D is significantly smaller. This difference suggests the inclusion of slightly more heavy-atom motion in the present reaction coordinate than in that for allylmercuric iodide cleavage.

(21) J. N. Brønsted, *Chem. Rev.*, 5, 231 (1928).

(22) Reference 16, pp 36–43, 231.

(23) A. J. Kresge and Y. Chiang, *J. Amer. Chem. Soc.*, 89, 4411 (1967).

(24) J. R. Jones and J. A. Rowlinson, personal communication.

(25) A. J. Kresge and A. L. Allred, *J. Amer. Chem. Soc.*, 85, 1541 (1963).

(26) V. Gold, *Proc. Chem. Soc.*, 141 (1963).

(27) H. H. Huang, R. R. Robinson, and F. A. Long, *J. Amer. Chem. Soc.*, 88, 1866 (1966).

(28) Previously [12,13] a value of 0.7 has been assumed.

(29) L. Melander, "Isotope Effects on Reaction Rates," The Ronald Press Co., New York, N. Y., 1960, p 20.

Electron Spin Resonance Line Width of the Hexaaquochromic Ion as a Criterion of Outer-Sphere Coordination Interactions

by K. M. Sancier

Stanford Research Institute, Menlo Park, California 94025 *(Received October 2, 1967)*

The esr line width Δh of the hexaaquochromic ion, Cr(III), in aqueous solutions was studied as a function of the concentration of various diamagnetic electrolytes: Na_2SO_4, $(NH_4)_2SO_4$, $Ca(NO_3)_2$, $Mg(NO_3)_2$, $Mg(ClO_4)_2$, $NaNO_3$, $NaClO_4$, NH_4ClO_4, HNO_3, and $HClO_4$. The Cr(III) concentration was 0.04 *M* for all solutions and magnetic dipolar broadening was negligible. Variations of Δh were observed in the range of 115–310 G. In general, as the concentration of the salts was increased, Δh initially decreased and then increased; measurements were made approaching the solubility limits of the salts. At a given ionic strength the order (decreasing) of line-width broadening is $SO_4^{2-} > HSO_4^- > NO_3^- > ClO_4^-$ for anions, $Na^+ > NH_4^+ > H^+$ for univalent cations, and $Mg^{2+} > Ca^{2+}$ for divalent cations. The line-width effects are ascribed to ionic interactions of Cr(III) with second coordinated anions and third coordinated cations. For the case of concentrated nitric acid, the possible role of HNO_3 molecules is discussed. The mechanisms of spin relaxation by the diamagnetic ions are discussed chiefly in terms of two models: restricted tumbling of the microcrystalline complex (TMC) and electric field anisotropy (EFA) of the Cr(III) symmetry. Anions of greater charge density lead to greater line broadening by both models. Cations of greater charge density lead to line broadening by the TMC model and to line narrowing by the EFA model.

Introduction

The description of ionic interactions in concentrated solutions of strong electrolytes has long been a challenging problem. Little is known about the interaction between diamagnetic ions in solution and about the dependence of these interactions on parameters such as the charge density of the ions, the local dielectric constant, and the distortion of the hydration sphere about the ions as well as of the ions themselves. Such knowledge is important in physical and electrochemistry and to an understanding of the biological functions of ions, for example, their function at membranes and in cell fluids. Limited information on electrolytic solutions has been obtained from measurements of average properties such as ionic mobility, electrical conductivity, and dielectric behavior. Recently, investigations of the magnetic and vibrational properties of ions in solution have provided some valuable information on a molecular level. The present paper is concerned with a study of a paramagnetic ion whose esr line width indicates interactions among ions in solution.

In an earlier study[1] we reported that esr line width measurements provided evidence of several outer-sphere coordination effects between the hexaaquochromic ion, $Cr(H_2O)_6^{3+}$, which is referred to as Cr(III), and diamagnetic ions and molecules. The line broadening was tentatively ascribed to ion pairing between Cr(III) and diamagnetic anions in the second coordination sphere and between these anions and diamagnetic cations in the third coordination sphere. The amount of line broadening was qualitatively related to the charge density of the diamagnetic ions. Line broadening was also noted in concentrated nitric acid solutions, but not in perchloric acid. The present study is an extension of the earlier work, and the emphasis is on the probable mechanisms of spin relaxation resulting from the interactions of diamagnetic ions.

Experimental Section

The technique and procedures used in this study have been reported earlier.[1] Briefly, the solutions were measured in a 0.5-mm i.d. quartz capillary. The esr measurements were made at room temperature by a Varian V-4502 X-band spectrometer with a multipurpose cavity and 100-kc field modulation. The esr line width, Δh, is the separation between the maximum and minimum points on the derivative of the absorption curve. The experimental error of Δh is estimated to be less than $\pm 5\%$. Chemicals (Baker) were of reagent grade.

Results

The line-width dependence of the Cr(III) resonance on the molar concentrations of various salts and acids is summarized in Table I. All solutions contained 0.04 *M* Cr(III) provided by an aliquot of a concentrated chromic perchlorate solutions. Esr line broadening caused by interactions between Cr(III) ions, *i.e.*, self-broadening, was observed only at concentrations exceeding about 0.6 *M* chromic perchlorate or nitrate and 0.06 *M* chromic sulfate. The line width decreased slightly when the Cr(III) concentration was increased in concentrated salt solutions. For example, the line

(1) K. M. Sancier and J. S. Mills, *J. Phys. Chem.*, 67, 1438 (1963).

Table I: Line-Width Dependence of Cr(III) on Concentration of Electrolytes[a]

Acids[b]				Salts (+1, −1)			Salts (+2, −1)				Salts (+1, −2)			
	$M = \mu$	α	Δh		$M = \mu$	Δh		M	μ	Δh		M	μ	Δh
$HClO_4$	0.001	1.0	150	NH_4ClO_4	2.66	154	$Ca(ClO_4)_2$	1.18	3.53	144	$(NH_4)_2SO_4$	0.241	0.72	226
	0.01	1.0	145		3.32	141		1.47	4.41	138	pH 3.4	0.301	0.92	238
	0.1	1.0	140		4.15	144		1.82	5.46	142		0.376	1.12	238
	0.32	1.0	140					2.28	6.84	145		0.471	1.41	244
	1.0	1.0	130	$NaClO_4$	2.05	146		2.86	8.58	149		0.589	1.77	245
	3.2	1.0	115		2.56	150		3.58	10.7	166		0.735	2.21	252
	10	~0.9	115		3.20	149		4.48	13.4	198		0.918	2.75	264
					4.00	150						1.15	3.44	277
HNO_3	0.001	1.0	155		5.01	164	$Mg(ClO_4)_2$	1.23	3.69	146		1.43	4.29	300
	0.1	1.0	155		6.28	173		1.54	4.62	153		1.79	5.37	295
	0.32	1.0	155		7.83	190		1.93	5.76	160				
	1.0	1.0	140		9.79	230		2.4	7.2	165	Na_2SO_4	0.001	1.0	149
	3.2	0.93	140					3.0	9.0	171	pH 0	0.011	1.0	145
	4.5	0.85	145	$NaNO_3$	0.70	155						0.034	1.1	146
	6.8	0.72	165		1.71	163	$Ca(NO_3)_2$	0.685	2.06	151		0.103	1.3	146
	10	0.55	160		2.14	165		0.856	2.57	146		0.31	1.9	162
	11.8	0.39	165		2.67	152		1.07	3.21	152		0.93	3.8	203
	15.9	0.09	195		3.34	173		1.37	4.02	154		2.8	9.4	305
	21.4	0.05	310		4.16	172		1.67	5.01	165				
					5.21	177		2.09	6.27	166				
					6.52	192		2.61	7.83	171				
					8.14	227		3.26	9.78	199				
								4.06	12.2	226				
								5.09	15.3	264				

[a] In all solutions $[Cr^{3+}] = 0.04\ M$; pH 2, except for the acids and the sulfates. Abbreviations: M = molarity; μ = ionic strength; α = degree of dissociation. [b] Values of α are from ref 3–5 and Δh is from ref 1.

width decreased about 4% for an increase from 0.02 to 0.08 *M* Cr(III) in 1.7 *M* $(NH_4)_2SO_4$ at pH 3.4 and about 6% for an increase from 0.02 to 0.5 *M* Cr(III) in 4.9 *M* $NaNO_3$ at pH 2. Over a period of 6 days at room temperature these two solutions showed no significant changes in line width.

Perchlorate salts were dissolved in 0.01 *M* $HClO_4$, nitrate salts in 0.01 *M* HNO_3, $(NH_4)_2SO_4$ in 0.004 *M* HNO_3, and Na_2SO_4 in 1 *M* HNO_3. These acid concentrations were selected because they fall within the acidity range 0.001–1 *M*, for which the spin density of Cr(III) is constant (see Figure 1 of ref 1). Most solutions were adjusted to 0.01 *M* acidity. The 0.004 *M* acidity was chosen so that hydrolysis would favor the SO_4^{2-} ion, and at this acidity about 95% of the sulfate is present as this ion. The 1 *M* acidity was chosen to provide near-maximum concentration of HSO_4^- with minimum concentrations of H_2SO_4 and SO_4^{2-}, and about 75% of the sulfate is present as HSO_4^-. Measurements were made on the salts up to near their maximum solubility.

The relationships between Δh and the ionic strength, μ, of various salt solutions are shown in Figure 1. The values of μ were calculated from the expression $^1/_2\Sigma_i \nu_i M_i$, where ν is the charge of the ith ion and M is its molarity. Ionic strength, rather than concentration, was chosen to represent the salt data because in this way both the charge and concentration of ions were considered and also the curves for the various electrolytes were better separated. However, little physical significance is attached to μ at the high electrolyte concentrations. The acid data are also plotted in Figure 1 for comparison with the salt data. However, the abscissa for the acids is plotted in terms of total acid concentration and not in terms of μ; *i.e.*, association effects are not considered. The line-width data for the acids have been taken from ref 1. The degree of dissociation, α, of nitric acid below 13 *M* HNO_3 was obtained from the smooth curve in Figure 2 of McKay[2] and at higher concentrations from the data of Masuda and Kanda.[3] The value of α for $HClO_4$ is essentially unity up to about 10 *M* where its value has been reported to be in the range of 0.85–0.95;[3-5] an average value appears in Table I.

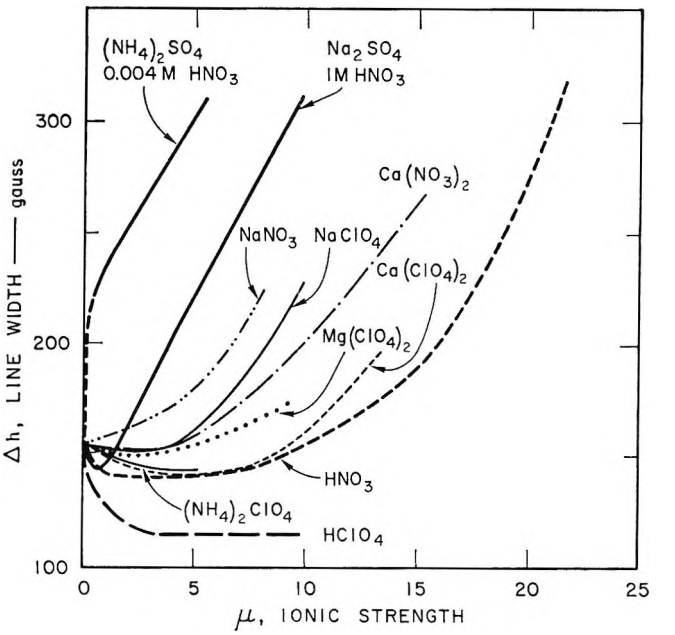

Figure 1. The dependence of esr line width, Δh, of Cr(III) on the ionic strength, μ, of salts and acids. [Cr(III)] = 0.04 *M*; salts dissolved in water at pH 2, except $(NH_4)_2SO_4$ at pH 3.4 and Na_2SO_4 at pH 0; for acids the degree of dissociation was not considered in calculating μ.

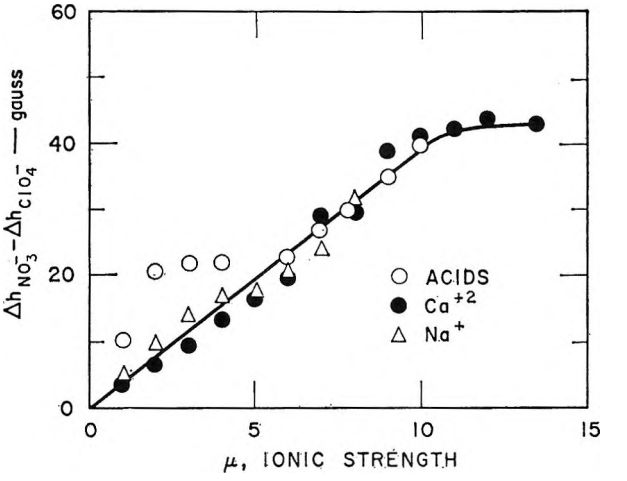

Figure 2. The difference in line widths, $\Delta h_{NO_3^-} - \Delta h_{ClO_4^-}$, for acids and for salts of Na^+ and Ca^{2+}. Data taken from Figure 1.

Discussion

(*1*) *Line-Width Effects of Diamagnetic Ions.* The results in Figure 1 show that the esr line width of Cr(III) is dependent on the type and concentration of the added electrolyte. The line-width broadening processes will be discussed first, and the line-width narrowing, which occurs upon initial addition of most electrolytes, will be considered later.

It is possible to a limited extent to distinguish the line-width broadening effects of anions from those of cations by comparing the data with given values of μ and with common counterions. In this way it can be shown that markedly different broadening effects are produced among the anions and among the cations.

Anions. In general, greater line-width broadening is observed for nitrate ions than for perchlorate ions. This effect is clearly evident in the case of the two acid solutions at concentrations for which both are dis-

(2) H. A. C. McKay, *Trans. Faraday Soc.*, **52**, 1568 (1956).

(3) Y. Masuda and T. Kanda, *J. Phys. Soc. Japan*, **9**, 82 (1954).

(4) G. C. Hood, O. Redlick, and C. A. Reilly, *J. Chem. Phys.*, **22**, 2067 (1954).

(5) K. Heinzinger and R. E. Weston, Jr., *ibid.*, **42**, 272 (1965).

sociated. The greater line-broadening effects produced by nitrate than by perchlorate ions are also demonstrated in Figure 2 in which the differences in the line widths, $\Delta h_{NO_3^-} - \Delta h_{ClO_4^-}$, for nitrate and perchlorate salt solutions of given cations are plotted against μ. The data, taken from the smoothed curves in Figure 1, seem to fall on one curve; however, the coincidence of the data may be fortuitous because the anion concentrations are quite different for the sodium and calcium salt solutions at a given μ and because nitric acid is only partly dissociated in its concentrated solutions. The broadening effect which occurs in concentrated nitric acid solutions will be discussed later.

The line-width broadening produced by solutions containing sulfate is much greater than the broadening produced by solutions containing either perchlorate or nitrate. In the sulfate solutions it is assumed that the magnitude of the broadening is determined by the degree of hydrolysis of the sulfate. Accordingly, greater broadening is produced by SO_4^{2-}, the dominant anion in the $(NH_4)_2SO_4$ solutions, than by HSO_4^-, the dominant anion in the Na_2SO_4 solutions. The difference in the Δh values of these two sulfate solutions at a given μ cannot simply be attributed to the difference between the effects of NH_4^+ and Na^+ ions, since a reverse effect is observed for the perchlorate solutions of these cations.

The qualitative order of the broadening effect of anions, obtained by comparison of the data with common cations at given values of μ, gives an order (decreasing) of the line-width-broadening effect of $SO_4^{2-} > HSO_4^- > NO_3^- > ClO_4^-$. The SO_4^{2-} ion has been included with the univalent anions in this comparison because its broadening effect is much greater than that of the other ions.

Cations. The relative line-width broadening effects also depend on the type of cation. For example, comparison of the results of the perchlorates in Figure 1 shows that the order (decreasing) of the effect on Δh is $Na^+ > NH_4^+ > H^+$ for univalent cations and $Ca^{2+} > Mg^{2+}$ for divalent cations. The univalent and divalent cations cannot be compared easily because their effects are not clearly separated.

In general, the broadening effect appears to be more the result of increased concentrations of the cation than of the anion. This becomes most evident from a comparison of the salt and acid curves for a given anion. While the line width depends on the type of anion, as in the case of ClO_4^- and NO_3^-, the line width appears to be essentially independent of anion concentration over a limited range for perchloric acid at $\mu > 1$. This behavior suggests that in this limited range ionic association of Cr(III) with anions is complete.

(2) Spin-Relaxation Mechanisms Involving Diamagnetic Ions. Before discussing the probable spin-relaxation mechanisms, we shall discuss those mechanisms and effects which do not apply. In the present study the time-dependent processes causing spin relaxation of Cr(III) cannot arise from substitution of the water of the inner-sphere complex by anions because this complex is very stable with respect to exchange of water, even at high ionic strength.[6,7] Therefore, the active relaxation mechanisms must be related to the interaction of Cr(III) with ions or molecules in the outer spheres of coordination.

We have ruled out line broadening resulting from magnetic dipole interactions because the chromic ion concentration was kept below the limit at which such interactions occur. Magnetic interactions are reported[8-10] to occur when two paramagnetic cations associate with SO_4^{2-} ions. However, in the present case such ionic association of Cr(III) ions is not appreciable, and if it occurs, it may account for the slight line-width decrease in the concentrated salt solutions of $(NH_4)_2SO_4$ and $NaNO_3$.

The observed line-broadening effects cannot be related to changes in the macroviscosity of the electrolyte solutions because the two effects have entirely different concentration dependences. For example, solutions of perchloric and nitric acids at about room temperature exhibit maxima in viscosity at 4.5 and 9.5 m by factors about 6 and 2 larger than for water, respectively; the pure acids have viscosities about the same as water.[11] Salt solutions generally show smaller increases in viscosity, but the orders of the viscosity and line-width data do not correlate.

Furthermore, the broadening effects cannot be attributed entirely to changes in the dielectric constant of water, ϵ, although such changes would be expected to occur and to affect interionic attractive forces. The ϵ of water is decreased by addition of salts, and for one salt (NaCl) ϵ decreased to a limiting value at high concentrations.[12] However, a comparison of the effects of added electrolytes on the line width and on the expected changes of ϵ shows that ϵ is not a dominant factor. For example, the molar depressions of ϵ for Na_2SO_4 and HCl are about equal[12] while the line-width effects for Na_2SO_4 and the acid (particularly $HClO_4$) solutions are strongly opposed. The absence of a dominant ϵ effect on esr line broadening can be accounted for by considerations of macro and local dielectric constants of water. The macro value is decreased because ions orient the hydrated water molecules so that the molecules cannot respond to an exter-

(6) J. P. Hunt and H. Taube, *J. Chem. Phys.*, **18**, 757 (1950).

(7) J. P. Hunt and R. A. Plane, *J. Am. Chem. Soc.*, **76**, 5960 (1954).

(8) R. G. Pearson and T. Buch, *J. Chem. Phys.*, **36**, 1277 (1962).

(9) S. Fujiwara and H. Hayashi, *ibid.*, **43**, 23 (1965).

(10) S. Fujiwara, S. Katsumata, and T. Seki, *J. Phys. Chem.*, **71**, 115 (1967).

(11) "International Critical Tables," Vol. 5, McGraw-Hill Book Co., Inc., New York, N. Y., 1933, p 12.

(12) J. B. Hasted, D. M. Ritson, and C. H. Collie, *J. Chem. Phys.*, **16**, 1 (1948).

nal electric field. However, the local value of the dielectric constant of these bound water molecules may be high in the sense that these water molecules are oriented in the most favorable way to minimize the interionic attractive force between ions of opposite charge.

The above considerations lead to the conclusion that the spin-relaxation mechanisms are related primarily to ionic association between ions of opposite charge. Anions will tend to ion pair with Cr(III) and to occupy the second coordination sphere of Cr(III); diamagnetic cations will tend to ion pair with these anions and to occupy a position, distant from the Cr^{3+} cation, in the third coordination sphere where they are partially shielded by the anion from the positive field of Cr^{3+}.

In general, the attractive force between ions of opposite charge is given by $(\nu_+\nu_-)/\epsilon(r_- + r_+)^2$, where ν is the ionic charge, r is the ionic radius, and ϵ is the dielectric constant of the medium. If ion pairing occurs only between Cr(III) and an anion, the attractive force will increase as ν_- increases, r_- decreases, and ϵ decreases. Similar but more complicated considerations apply to the association of a cation with a second coordinated anion. This simplified electrostatic model has neglected the distribution and polarizability of ionic charge of an anion and the distortion of the hydration sphere because of ion pairing.

The mechanisms of spin relaxation of Cr(III), which depend on ionic association, can be discussed in terms of two models: restricted tumbling of the microcrystalline complex (TMC) and electric field anisotropy of the complex (EFA).

The microcrystalline model of an ion in solution was developed by McConnell,[13] who showed that paramagnetic, relaxation phenomena could be related in part to a correlation time, $\tau_c = 4\pi\eta\alpha_0^3/3kt$, describing the Brownian tumbling motion of the microcrystal in the liquid state; η is the local viscosity and α_0 is the effective radius of the microcrystalline complex. Lower values of τ_c correspond to restricted tumbling of the complex and less efficient averaging of the anisotropy of the complex.

Electric field anisotropy about Cr^{3+} can result when diamagnetic anions ion pair with Cr(III) and distort the symmetry of the water molecules of the inner sphere of Cr(III). McGarvey[14] applied McConnell's model to chromic ion complexes and concluded that the observed esr line broadening could be accounted for by considerations of the values of D and τ_c associated with the microcrystal in solution. In particular, distortion of the hydration sphere of Cr^{3+} can modify the D term of the spin Hamiltonian, $\mathcal{H} = g\beta SH + D[S_z^2 - (1/3)\cdot S(S+1)]$, while the g value is normally isotropic. If the distortion is increased by strong ion pairing, favored by the proximity of ions in concentrated solutions, the fine-splitting D term and the esr line width will be increased.

The treatments of McConnell and McGarvey are concerned primarily with inner-sphere effects of the complex. However, outer-sphere effects may be expressed by the α_0 and η terms upon which τ_c depends and by the D term described above. For the consideration of outer-sphere effects observed in this study, it may be necessary to postulate several τ_c, each with characteristic radius and viscosity terms. For example, we may expect separate τ_c's for Cr(III) in infinitely dilute solution, for the Cr(III) complex with a second coordinated anion, and for the complex including a third coordinated cation.

The two spin-relaxation mechanisms will now be discussed, and, insofar as possible, the effects of anions and cations will be separated. As a guide to this discussion, the predicted effect of increased charge density of ions on the line width is summarized according to the relaxation model in Table III. In the following discussion we assume that spin relaxation arises from direct ionic interactions and that by comparison we can ignore relatively weaker interactions such as salt effects on solvent structure.

For anions, both relaxation mechanisms are expected to lead to esr line-width broadening as the attractive force between Cr(III) and a second coordinated anion becomes larger. A larger attractive force between these ions, *i.e.*, larger charge density on the anion, implies according to the TMC model a larger effective radius and greater restricted tumbling of the microcrystalline complex; according to the EFA model, it implies a greater distortion of the spatial arrangement of the inner coordinated water molecules, especially localized in the vicinity of closest approach of the ions. The experimental observations concerning anions are consistent with the above principles. The order of observed effect on line width (*i.e.*, $SO_4^{2-} > HSO_4^- > NO_3^- > ClO_4^-$) is qualitatively the same as that of the charge density which can be estimated from the ionic radii of the anions[15,16] in Table II. Since no information is available on the radius of HSO_4^-, it is assumed that its radius is about that of SO_4^{2-}. However, the conclusions concerning the sole effect of HSO_4^- in the Na_2SO_4 solution must take into account the possible influence of SO_4^{2-} and H_2SO_4 species and of the higher acid concentration in the Na_2SO_4 than in the $(NH_4)_2SO_4$ solutions.

For diamagnetic cations, which interact with the anion of the Cr(III) anion complex, the sign of the line-width change depends on whether the TMC or EFA relaxation mechanism applies. According to the TMC model, cationic association with the Cr(III) anion complex may cause line-width changes of either sign,

(13) H. M. McConnell, *J. Chem. Phys.*, **25**, 709 (1956).
(14) B. R. McGarvey, *J. Phys. Chem.*, **61**, 1232 (1957).
(15) E. R. Nightingale, Jr., *ibid.*, **63**, 1381 (1959).
(16) J. Padova, *J. Chem. Phys.*, **40**, 691 (1964).

Table II: Ionic Radii[a] (Å)

Ion	Crystal	Stokes	Hydration	Solvation
Na^+	0.95	1.84	3.58	2.28
NH_4^+	1.48	1.25	3.31	1.59
Mg^{2+}	0.65	3.47	4.28	3.09
Ca^{2+}	0.99	3.10	4.12	3.10
ClO_4^-	2.92	1.35	3.38	
NO_3^-	2.64	1.29	3.35	2.23
SO_4^{2-}	2.90	2.30	3.79	3.64

[a] The crystal, stokes, and hydration radii are taken from ref 15; the solvation radii are taken from ref 16.

and in both cases a greater change will be produced by cations of greater charge density. Line broadening will result when cationic association increases the effective radius of the whole microcrystalline complex. Line narrowing will result when cationic association decreases the effective charge on the second coordinated anion so that the correlation time for the interaction between this anion and Cr(III) is decreased. The line-width-broadening mechanism according to the TMC model must be active because it appears to be the only available mechanism to account for line broadening by diamagnetic cations. Accordingly, the line-narrowing mechanism by the TMC model is probably not active and hence has not been included in Table III, since cations are not likely to produce two effects of opposite sign by the same model. Therefore, on the basis that the TMC line-broadening mechanism applies, the order of the effect of cations on Δh should be the same as their charge densities. This order of charge densities is satisfied only by the crystal radii; the other types of radii in Table II follow a different order. For example, the decreasing order of the effect on Δh of $Na^+ > NH_4^+$ and $Mg^{2+} > Ca^{2+}$ corresponds to a decreasing order of charge densities (ν/r) based on crystal radii, *e.g.*, $^{+1}/_{0.95} > {}^{+1}/_{1.48}$, and $^{+2}/_{0.65} > {}^{+2}/_{0.99}$, respectively. This result suggests that, at least for the cation, the approach to the anion is not limited strongly by the waters of hydration of the cation. In this connection, vibrational spectral studies of concentrated zinc[17] and calcium[18] nitrate solutions have provided evidence of the existence of ion-contact pairs, *i.e.*, pairs with no intervening waters of hydration. These studies have also provided evidence of a distortion of the symmetry of the nitrate ion by association with the solvent and the cation.

According to the EFA model, cationic association will tend to decrease the effective charge of the second coordinated anion, which in turn decreases the attractive force between the anion and Cr(III) and decreases the distortion of the Cr(III) complex due the anion. As the charge densities of cations increase, the line width tends to decrease. Such a mechanism may account for the observed reduction of line width as the concentration of most salts is initially increased. This line-width-narrowing effect is greatest for the acids, which suggests that the narrowing depends on the H^+. The high mobility of this ion may in fact provide an effective mechanism for reducing the anisotropy of Cr(III), *e.g.*, by increasing the tumbling. In this connection the lower line widths of some Cr^{3+} complexes, *i.e.*, 33 G for $Cr(NH_3)_6^{3+}$, are attributed partly to greater tumbling.[14] However, the effect of H^+ cannot account for the narrowing observed for the salt solutions whose acidity was maintained at about 0.01 *M*. For these solutions the narrowing effect of cations by the EFA model is most useful, but at higher concentrations broadening dominates because of the interactions of cations by the TMC model.

Table III: Relaxation Model and the Predicted Effect of Increased Charge Density of Ions on Δh

Relaxation model	Δh	
	Anion	Cation
EFA	Broadening	Broadening
TMC	Broadening	Narrowing

Line-width narrowing has been attributed to exchange interactions in solutions between Cu^{2+} ions which associate with a common diamagnetic anion.[9,10] The narrowing increases as $[Cu^{2+}]$ is increased, and the greater narrowing reported for SO_4^{2-} than for NO_3^- is in accordance with expectations on the basis of the charge densities of these anions. However, a significant exchange-narrowing mechanism for Cr(III) is unlikely for two reasons: (1) dipolar broadening is observed as the concentration of Cr(III) is increased, except a slight narrowing is observed in concentrated salt solutions, and (2) the order (decreasing) of the effect on Δh by exchange narrowing may be expected to be $ClO_4^- > NO_3^- > SO_4^{2-}$ on the basis of the charge densities of these anions, whereas the opposite order is observed.

The tentative conclusions concerning the relaxation mechanisms of diamagnetic ions are summarized as follows. The magnitude of the line broadening produced by second coordinated diamagnetic anions is related to their charge densities, and the relaxation mechanism may be described by either the TMC or the EFA model. Additional line broadening is produced in concentrated solutions by diamagnetic cations, and the relaxation mechanism is probably described by the TMC model. The results suggest that the effective charge density of the cation is determined by its crystal radius. The line-width narrowing observed upon initial addition of electrolytes to solution appears to be caused by diamagnetic cations which decrease the effective charge density of the second coordinated

(17) R. E. Hester and R. A. Plane, *J. Chem. Phys.*, **45**, 4588 (1966).
(18) D. E. Irish and G. E. Walrafen, *ibid.*, **46**, 378 (1967).

anions and affect the relaxation mechanism by the EFA model.

(3) *Concentrated Acid Solutions.* The line-width broadening observed for concentrated nitric acid solutions is discussed separately because of the possible influence of undissociated HNO_3 molecules as well as of NO_3^- ions. Broadening appears when the degree of dissociation, α, of nitric acid drops to about 0.85, and the broadening continues as α becomes smaller. In contrast, no broadening is observed in the most concentrated perchloric acid solutions up to the highest concentrations for which α is about 0.9. The difference in behavior of these acid solutions appears to be related to the greater association of nitric acid.

One possible explanation for the line broadening is that in concentrated nitric acid solutions the dielectric constant decreases sufficiently to increase the interionic attractive force between Cr(III) and the NO_3^- in solution. The spin-relaxation mechanism would then be the same as for second coordinated anions, *i.e.*, by either the EFA or the TMC model. Although information on the dielectric constant of nitric acid solutions is not available, its behavior is expected to be similar to that of HCl for which the value of ϵ decreases with increasing concentration.[12] Another possibility is that more elaborate outer-sphere complexes result such as

$$NO_3^- \cdots Cr(III) \cdots HNO_3 \qquad (a)$$

or

$$Cr(III) \cdots NO_3^- - - HNO_3 \qquad (b)$$

where the double dashed line indicates a second coordination interaction, and the single dashed line an interaction between second and third spheres of coordination. Second coordination of HNO_3 molecules, as in type a, may possibly occur through hydrogen bonding to the ligand water molecules of Cr(III). A complex of type b may be stabilized either by proton transfer between HNO_3 and NO_3^-, as suggested earlier,[1] or by resonance (delocalization) of the electron of the nitrate ion over the $\cdots NO_3^- - - HNO_3$ part of the complex. It is suggested that one of these complexes may account for the observed broadening. The other complex, or one combining the features of (a) and (b), may lead to a very much broader esr line because of greater restriction of tumbling of the complex, thus accounting for the apparent loss of spin density of Cr(III) in the very concentrated nitric acid solutions.[1]

(4) *Related Findings of Other Investigators.* Other investigators have reported data which show that diamagnetic salts affect the esr line width of paramagnetic ions in solution; however, the discussions of the results deal almost exclusively with modification of magnetic interaction between the paramagnetic ions.

Pearson and Buch[8] have shown that the addition of a diamagnetic salt, KCl, affected in a predictable way the interactions between paramagnetic anions (self-broadening) and, in another case, the interaction between a paramagnetic anion and a paramagnetic cation. Mention has already been made of the exchange interaction between paramagnetic Cu^{2+} ions produced by their interaction with a common anion.[9,10] Hayes[19] has also noted that the esr line width, in this case for Mn^{2+}, is affected by various salts, and for SO_4^{2-} solutions he ascribed the effects to inner- and outer-sphere complexing. His data show that the order (decreasing) of the effect on Δh for anions is $SO_4^{2-} > Cl^- > ClO_4^-$. The results of Pearson and Buch and of Hayes can be explained qualitatively by the arguments developed in the present paper concerning the charge density of anions.

In other esr studies of the line width of Mn^{2+} a slight broadening effect by diamagnetic salts was attributed to the ClO_4^- ion.[20] In another study of Mn^{2+}, inner-sphere complexes with Cl^- and SO_4^{2-} were found to dominate the line-width effects, but some outer-sphere effects were also noted.[21]

Esr measurements have been employed to study ionic association between a free-radical anion and alkali metal cations in nonaqueous solutions.[22] The observed hyperfine splitting indicates interactions of the unpaired electron of the radical with the nucleus of the cation, and the line-width broadening of certain lines indicates more than one type of ion pair.

Although the discussion in this paper has been confined to esr results, nmr has also provided information on ion–solvent and ion–ion interactions. Proton resonance shifts of water produced by diamagnetic ions have been discussed in terms of the polarization of water molecules and the breakdown of the hydrogen-bond structure.[23] These shifts have also been discussed in terms of the local variations in the mobility of water molecules.[24] The resonance shifts of ions in aqueous solutions of various salts have been studied,[25] and the results of the resonance shifts of fluoride ion by alkali metal ions and the shifts of the cesium ion by halide ions generally follow the expected charge-density sequence expected for these ions.

Acknowledgments. It is a pleasure to acknowledge Drs. Shizuo Fujiwara and Takeo Yamamoto of the University of Tokyo for many valuable discussions. This research was supported in part by The National Science Foundation under Grant GF-234.

(19) R. G. Hayes, Lawrence Radiation Laboratory Report UCRL-9873, University of California, Berkeley, Calif., Sept 29, 1961.

(20) C. C. Hinckley and L. O. Morgan, *J. Chem. Phys.*, **44**, 898 (1966).

(21) R. G. Hayes and R. J. Meyers, *ibid.*, **40**, 877 (1964).

(22) T. E. Gough and M. C. R. Symons, *Trans. Faraday Soc.*, **62**, 269 (1966).

(23) S. H. Shoolery and B. J. Adler, *J. Chem. Phys.*, **23**, 805 (1955).

(24) S. Broersma, *ibid.*, **24**, 659 (1956).

(25) A. Carrington, F. Dravnicks, and M. C. R. Symons, *Mol. Phys.*, **3**, 174 (1960).

The Study of the Hindered Rotation of Methyl Groups Using Nuclear Magnetic Resonance

by Joseph H. Noggle

Department of Chemistry, University of Wisconsin, Madison, Wisconsin 53706 *(Received October 9, 1967)*

The nuclear magnetic relaxation of ^{13}C and ^{2}D in an anisotropically rotating methyl group is considered and formulas are derived for the T_1 of a ^{13}C nucleus in $^{13}CH_3$ and $^{13}CD_3$ and for the T_1 of a ^{2}D nucleus in CD_3. The conditions for validity of these formulas and their application to the study of methyl group motion in solids and glasses are discussed. It is suggested that the study of ^{13}C and ^{2}D relaxation in $^{13}CD_3$ is the best method for obtaining information relating to such motions. Such a method could be used for separating effects due to the hindered internal rotation of methyl groups and the main chain motion in macromolecules. The effects of cross-correlation are considered and found to be negligible.

A. Introduction

Nuclear magnetic resonance (nmr) has been often used to study the motion of molecules or parts of molecules in solids or polymers.[1,2] This work has been recently reviewed by ref 2. One of the more interesting areas has been the study of hindered internal rotation of methyl groups attached to polymers.[3] The data thus obtained are difficult to interpret quantitatively because of the complicated interactions of the methyl protons both with themselves and with protons on other parts of the molecule. The study of ^{13}C nmr in such cases has much to recommend it. The principal relaxation mechanism of the ^{13}C nucleus will probably be due to dipole–dipole interactions with the directly attached protons. Under some conditions (described herein) this relaxation will be exponential and a formula is derived for the T_1 thus obtained. Another simple case which can be studied is the relaxation of ^{2}D in a CD_3 group. This is even simpler than C^{13} and formulas for the deuterium T_1 are presented. The T_1 of ^{13}C in $^{13}CD_3$ is also given.

B. The Equation of Motion

Before calculating T_1's it behooves one to make certain that the equation of motion is a simple exponential. The relaxation of spin I due to dipole–dipole coupling with spin S is given by ref 4 and will not in general be exponential. The solution of these simultaneous differential equations for $\langle I_z \rangle$ and $\langle S_z \rangle$ under the conditions that $\langle S_z(t = 0) \rangle = S_0$ will be exponential provided the spin S has an additional mechanism of relaxation so that it relaxes much more efficiently than I. Under the condition that

$$\left| \frac{1}{T_1^{SS}} - \frac{1}{T_1^{II}} \right| \gg \frac{1}{T_1^{IS}}$$

and $T_1^{SS} \ll T_1^{II}$ the equation of motion for $\langle I_z \rangle$ will be

$$\frac{d\langle I_z \rangle}{dt} = -\frac{1}{T_1^{II}}[\langle I_z \rangle - I_0] \qquad (1)$$

and a T_1 is defined. This requires that the spin S have mechanisms of relaxation other than I–S dipole–dipole and that spin I have no such mechanisms. If I relaxes only by dipole–dipole coupling with S, then we have $T_1^{IS} = 2T_1^{II}$ (extreme narrowing) so the condition for eq 1 to hold becomes $(2/3)T_1^{II} \gg T_1^{SS}$, where T_1^{SS} includes effects of relaxation other than I–S dipole–dipole coupling.

Under what conditions might eq 1 be valid? The relaxation of the proton nuclei in a methyl-^{13}C group due to interactions within the methyl group will be about as efficient as the relaxation of the ^{13}C nucleus. However, because of their exposed position, the protons can interact with spins on adjacent parts of the same molecule, or other molecules, with the solvent, or even with dissolved molecular oxygen. These interactions may make the proton relaxation more efficient than the ^{13}C relaxation as required. The condition is even more likely to hold in $^{13}CD_3$. The D nuclei will relax by quadrupole relaxation which will be very efficient. On the other hand, the ^{13}C nucleus will have very long T_1's owing to the weak dipole–dipole interactions with deuterium. In this case, however, one must be concerned that ^{13}C will have some other relaxation mechanism which may contribute significantly to the relaxation (see section E).

In the case of CD_3 each deuterium will relax independently by quadrupole relaxation. The requirement[5] for such relaxation to be exponential outside the extreme narrowing region, that the nuclear spin I be equal to 1, is satisfied for deuterium.

(1) H. S. Gutowsky and G. E. Pake, *J. Chem. Phys.*, **18**, 162 (1950).
(2) E. R. Andrew and P. S. Allen, *J. Chim. Phys.*, **63**, 85 (1966).
(3) W. P. Slichter, *Rubber Chem. Technol.*, **34**, 1574 (1961).
(4) A. Abragam, "Principles of Nuclear Magnetism," Oxford University Press, London, 1961, p 295.
(5) See ref 4, p 314.

C. Calculation of T_1 for ^{13}C in $^{13}CH_3$ (and $^{13}CD_3$)

Denoting the ^{13}C spin by I and the spins of the three protons by $S(1)$, $S(2)$, and $S(3)$, the interactions resulting in ^{13}C relaxation can be written as

$$\mathcal{H}'(t) = \sum_{i=1}^{3}\mathcal{H}'_i(t) \tag{2}$$

where $\mathcal{H}'_i(t)$ represents the dipole–dipole interaction between I and $S(i)$. $\mathcal{H}'_i$ is usually written in terms of the spin and lattice variables as[6]

$$\mathcal{H}'_i(t) = \sum_q A^{(q)}(i)F_i^{(q)}(t) \tag{3}$$

where the A's represent the spin variables and the F's represent the lattice variables. This notation is not convenient for, while the F's resemble the spherical harmonics of order 2, they do not transform as such. We therefore define

$$\tilde{F}_i^{(q)} = a_q F_i^{(q)} \text{ and } \tilde{A}^{(q)}(i) = a_q^{-1}A^{(q)}(i)$$

where

$$a_0 = {}^1/_2,\ a_{\pm 1} = \mp\sqrt{{}^3/_2},\ a_{\pm 2} = \sqrt{{}^3/_8}$$

we now have that $\tilde{F}_i^m(t) = \sqrt{4\pi/5}(1/r_i^3)Y_{2m}(\theta_i\phi_i)$. θ_i and ϕ_i give the orientation of the vector between I and $S(i)$ with respect to the laboratory fixed coordinate system and are time dependent. The distance r_i is independent of time.

The correlation function for nuclear relaxation

$$G(\tau) = \langle\mathcal{H}'(t)\mathcal{H}'(t+\tau)^*\rangle_{av} \tag{4}$$

will involve correlation functions of the type

$$\tilde{G}_{ij}^{qq'}(\tau) = \langle\tilde{F}_i^{(q)}(t)\tilde{F}_j^{(q')}(t+\tau)^*\rangle_{av} \tag{5}$$

The vectors $r'(t)$ and r in the laboratory system can be written with respect to the rigid frame of the methyl group and the F's will transform using the Wigner D matrices.[7] Thus the transformation of $r'(t)$ in the laboratory coordinate system to r in the principal axis system of the methyl group will be

$$\tilde{F}_i^{(q)}(r'_i) = \sum_p \tilde{F}_i^{(p)}(r_i)D_{pq}^{(2)}(\Omega) \tag{6}$$

where $\Omega = \Omega(t)$ is the orientation of the principal axis system with respect to the laboratory coordinate system. The correlation function is now

$$\tilde{G}_{ij}^{qq'} = \sum_{pp'}\tilde{F}_i^{(p)}(r_i)\tilde{F}_j^{(p')}(r_j)^*\langle D_{pq}^{(2)}(\Omega_0)D_{p'q'}^{(2)}(\Omega)^*\rangle_{av} \tag{7}$$

Favro[8] has discussed the evaluation of such correlation functions in terms of a rotational diffusion tensor. In the present case we define $R_\parallel$, the diffusion constant for rotation parallel to the threefold axis of the methyl group, and $R_\perp$ for diffusion about an axis perpendicular to the threefold axis. The required average then gives

$$\tilde{G}_{ij}^{qq'} = (1/5)\delta_{qq'}\sum_p \tilde{F}_j^{(p)}(r_i)\tilde{F}_j^{(p)}(r_j)^*e^{-\tau/\tau_p} \tag{8}$$

where

$$\tau_p^{-1} = R_\perp(6 - p^2) + R_\parallel p^2 \tag{9}$$

with $p = 0, \pm 1, \pm 2$.

The required over-all correlation function is now

$$G(\tau) = \sum_{ij}\sum_q \tilde{A}^{(q)}(i)\tilde{A}^{(q)}(j)\tilde{G}_{ij}(\tau) \tag{10}$$

where $\tilde{G}_{ij}$ is independent of q.

In the principal axis system of the methyl group θ and r are equal for all protons; only ϕ_i is different. It is therefore convenient to write

$$\tilde{F}_i^{(q)}(r_i,\theta_i,\phi_i) = f_q(\theta,r)e^{iq\phi_i} \tag{11}$$

where

$$f_0 = {}^1/_2\frac{3\cos^2\theta - 1}{r^3},\quad f_{\pm 1} = \sqrt{{}^3/_2}\frac{\sin\theta\cos\theta}{r^3},$$

$$f_{\pm 2} = \sqrt{{}^3/_8}\frac{\sin^2\theta}{r^3} \tag{12}$$

The correlation function $\tilde{G}_{ij}$ will depend only on the difference between ϕ_i and ϕ_j. There will thus be only two cases: when $i = j$ we get the autocorrelation function

$$\tilde{G}_a = (1/5)\sum_{m=-2}^{+2} f_m{}^2e^{-\tau/\tau_m} \tag{13}$$

and the cross-correlation function (when $i \neq j$)

$$\tilde{G}_x = (1/5)[f_0{}^2e^{-\tau/\tau_0} - f_1{}^2e^{-\tau/\tau_1} - f_2{}^2e^{-\tau/\tau_2}] \tag{14}$$

We can, as usual, define spectral densities as the Fourier transform of the correlation functions by

$$\tilde{J}_a(\omega) = \int_{-\infty}^{\infty}\tilde{G}_a(\tau)e^{i\omega\tau}\,d\tau = (2/5)\sum_m \frac{f_m{}^2\tau_m}{1 + \omega^2\tau_m{}^2}$$

with a similar relation between $\tilde{J}_x$ and $\tilde{G}_x$.

The total relaxation will be due to $J(\omega)$ defined as the Fourier transform of $G(\tau)$ (eq 10)

$$J(\omega) = \sum_q\sum_i|\tilde{A}^{(q)}(i)|^2\tilde{J}_a(\omega) + \sum_q\sum_{i\neq j}\tilde{A}^{(q)}(i)\tilde{A}^{(q)}(j)^*\tilde{J}_x(\omega) \tag{15}$$

To get eq 15 into a more familiar form we define a new set of operators $\tilde{A}^{(q)}(T) = \sum_i\tilde{A}^{(q)}(i)$. These will be similar to the A operators except the spin operators $S(i)$ will be replaced by the total spin operators, $S(T) = \sum_i S(i)$. For example

$$A^{(2)}(T) \propto I_-(S_-(1) + S_-(2) + S_-(3)) = I_-S_-(T)$$

and similarly for the others.[9] Equation 15 can now be written

(6) See ref 4, p 289.

(7) M. E. Rose, "Elementary Theory of Angular Momentum," John Wiley and Sons, Inc., New York, N. Y., 1957.

(8) L. D. Favro, *Phys. Rev.*, **119**, 53 (1960).

(9) See ref 4, p 289 ff.

$$J(\omega) = \sum_q \sum_i |A^{(q)}(i)|^2(\tilde{J}_a - \tilde{J}_x) + \sum_q A^{(q)}(\mathrm{T})A^{(q)}(\mathrm{T})^*\tilde{J}_x \quad (16)$$

Each of the two terms in eq 16 can now be evaluated in a manner completely analogous to that described by Abragam.[9] Evaluating the necessary double commutators in the high-temperature approximation ($\hbar\gamma H_0 \ll kT$, where H_0 is the magnetic field strength), one gets for T_1

$$1/T_1 = \sum_q C_q \sum_i \langle S(i)^2\rangle[\tilde{J}_a - \tilde{J}_x] + \sum_q C_q\langle S(\mathrm{T})^2\rangle\tilde{J}_x = \sum_q C_q \sum_i \langle S(i)\rangle^2 J_a(\omega_q) + \sum_q C_q J_x(\omega_q)[\langle S(\mathrm{T})^2\rangle - \sum_i \langle S(i)^2\rangle] \quad (17)$$

where $C_0 = (1/3)\gamma_I^2\gamma_S^2\hbar^2$, $C_{\pm 1} = (1/2)\gamma_I^2\gamma_S^2\hbar^2$, $C_{\pm 2} = \gamma_I^2\gamma_S^2\hbar^2$, $\omega_0 = \omega_I - \omega_S$, $\omega_1 = \omega_I$, and $\omega_2 = \omega_I + \omega_S$.

In the high-temperature approximation where the Boltzmann factor can be represented by a linear expression, *i.e.*, when $e^{-\Delta E/kT} \simeq 1 - (\Delta E/kT)$, it can be shown that $\langle S(\mathrm{T})^2\rangle = \sum_i \langle S(i)^2\rangle$ where $S(\mathrm{T}) = \sum_i S(i)$.

This cancellation of the cross-correlation terms in situations of high symmetry agrees with the results obtained by Hubbard[10] for the relaxation of three and four identical spins under more restrictive conditions, namely, isotropic reorientation ($R_{||} = R_\perp$) and extreme narrowing ($\omega^2\tau_c^2 \ll 1$). A closer comparison of these results with Hubbard's cannot be made readily since his calculation was for identical spins; assuming I and S are identical in the present case would violate the restrictions of section B.

Finally the T_1 of a ^{13}C due to dipole–dipole interactions with the protons in $^{13}CH_3$ is given by

$$1/T_1 = (9/10)\frac{\gamma_H^2\gamma_C^2\hbar^2}{r_{CH}^6}[(1/3)j(\omega_C - \omega_H) + j(\omega_C) + 2j(\omega_C + \omega_H)] \quad (18)$$

where

$$j(\omega) = (1/4)\frac{(3\cos^2\theta - 1)^2\tau_0}{1 + \omega^2\tau_0^2} + \frac{(3\sin^2\theta\cos^2\theta)\tau_1}{1 + \omega^2\tau_1^2} + (3/4)\frac{(\sin^4\theta)\tau_2}{1 + \omega^2\tau_2^2} \quad (19)$$

and

$$\tau_0^{-1} = 6R_\perp,\ \tau_1^{-1} = 5R_\perp + R_{||},\ \tau_2^{-1} = 2R_\perp + 4R_{||} \quad (20)$$

and θ is the angle between the CH bond and the threefold axis.

The result for ^{13}C relaxation in $^{13}CD_3$ is obtained by replacing γ_H and ω_H with γ_D and ω_D and changing the numerical factor in front of eq 18 from $^9/_{10}$ to $^{12}/_5$.

D. Quadrupole Relaxation of D in CD_3

The formula for the T_1 of a spin 1 assuming isotropic reorientation $R_{||} = R_\perp = 1/6\tau_C$ is given by eq 138 of ref 5. Shimizu[11] has given a formula for T_1 assuming extreme narrowing (but not isotopic rotation). These results are easily generalized to give

$$1/T_1 = (3/40)\left(\frac{e^2qQ}{\hbar}\right)^2[j(\omega_D) + 4j(2\omega_D)] \quad (21)$$

where $j(\omega)$ is given by eq 19 and 20. Note that eq 21 is valid only for spin 1 nuclei.

E. Discussion

Dipole–dipole relaxation due to hindered rotation of methyl groups is described by three correlation times which involve, in turn, two rotational diffusion constants, $R_{||}$ and $R_\perp$, for reorientation about an axis parallel or perpendicular to the methyl group principal axis. Studies of T_1 as a function of temperature should be able to separate these contributions. If this motion has an Arrhenius-type temperature dependence, the activation energy will be related to the barrier to internal rotation.

It would appear that the best method for studying the hindered rotation of methyl groups in solids or polymers is to measure the T_1's of ^{13}C and ^2D in $^{13}CD_3$. The formula for the T_1 of ^{13}C will not be invalidated, in this case, by considerations discussed in section B. It is possible, however, that ^{13}C may have a competing relaxation mechanism. The most probable competitor would be relaxation due to the anisotropy of the chemical shift tensor; for this reason the ^{13}C measurements should be done at, at least, two widely separated frequencies.

In general $\tilde{J}_x$ due to the correlation of the concerted motion of spin rigidly attached will not be much smaller than $\tilde{J}_a$, the latter being the only part usually considered. In fact, in the limit of extreme narrowing and when $R_{||} = R_\perp$, the relation is $\tilde{J}_x = \tilde{J}_a P_2(\cos\beta)$ where P_2 is the Legendre polynomial and β is the angle between the symmetrically spaced internuclear vectors. These effects, however, cancel in the cases considered in this paper. The results of this paper, which do not require extreme narrowing or isotropic reorientation ($R_{||} = R_\perp$), suggest that the conclusions of ref 10 may be more general than implied therein. The assumptions made about the axial symmetry of the spins are, however, quite necessary. The method used in this paper could be used for calculation of cross-correlation effects in situations of lower symmetry.

Aside from the approximations discussed in section B, the principal assumption limiting the accuracy of eq 18, 19, and 21 are (a) the assumption that the rotational motion of the methyl group obeys a diffusion equation[8]

(10) P. S. Hubbard, *Phys. Rev.*, **109**, 1153 (1958); **128**, 650 (1962).
(11) H. Shimizu, *J. Chem. Phys.*, **40**, 754 (1964).

and (b) the high-temperature approximation. At the magnetic fields used in nmr, assumption b should be valid down to a few degrees Kelvin.

Acknowledgments. The author wishes to acknowledge the support of the Petroleum Research Fund under Grant PRF 684-G2 and of the Graduate Research Committee of the University of Wisconsin. He also wishes to acknowledge the helpful discussions with Mr. Stephen P. Chen on the subject of macromolecules.

Phase Diagrams of the Bismuth Trihalides at High Pressure[1]

by A. J. Darnell and W. A. McCollum

Atomics International Division of North American Aviation, Inc., Canoga Park, California 91304
(Received October 10, 1967)

The phase diagrams of BiF_3, $BiCl_3$, $BiBr_3$, and BiI_3 were determined at pressures up to 36 kbars by differential thermal analysis, resistance, and dilatometric techniques. The phase diagrams for BiF_3 and $BiCl_3$ are relatively simple; no new polymorphs were detected between room temperature and the melting point. A new solid phase (γ) of $BiBr_3$ stable at high pressure was found. The triple point for $BiBr_3$ ($\alpha \rightleftarrows \beta \rightleftarrows \gamma$) is 300° and 12.5 kbars. Both a new high-temperature (β) and a high-pressure (γ) form of BiI_3 are reported. The triple point for BiI_3 ($\alpha \rightleftarrows \beta \rightleftarrows \gamma$) is 510° and 25.5 kbars, and for BiI_3 ($\beta \rightleftarrows \gamma \rightleftarrows$ l) it is 800° and 25 kbars. The transition volumes for the phase changes ($\alpha \rightarrow \gamma$), ($\beta \rightarrow \gamma$), and ($\alpha \rightarrow \beta$) around the triple point are −5.3, −5.7, and 0.1 cm³/mole, respectively. The melting temperatures of these salts as a function of pressure are fitted to the Simon equation, $P - P_0 = A[(T/T_0)^c - 1]$. The respective values for P_0 (bars), A (bars), T_0 (°K), and c for these salts are: BiF_3, 0, 130,000, 1030, 1.01; $BiCl_3$, 0, 8660, 507, 2.70; $BiBr_3$ (β), 0, 14,400, 492, 1.85; BiI_3 (β), 0, 17,700, 681, 1.95; BiI_3 (γ), 25,000, 16,800, 1073, 2.38.

Introduction

The bismuth halides $BiCl_3$, $BiBr_3$, and BiI_3 have been well characterized at atmospheric pressure or under their own vapor pressure.[2-6] This group of compounds offers a good example for study of transport properties of molten salts such as electrical conductivity and viscosity at constant volume for comparison with the existing data at constant atmospheric pressure. However, in order to maintain constant volume of the liquid state over a wide range of temperatures, it is necessary to maintain very high external pressure upon the salt. This paper gives the equilibrium melting curve of these salts as a function of pressure at pressures up to 36 kbars. The pressure–temperature dependence of the polymorphic transitions in the compounds $BiBr_3$ and BiI_3 is also reported.

Experimental Section

Materials. BiF_3. Bismuth trifluoride was prepared from reagent grade Bi_2O_3 and analytical reagent grade aqueous hydrofluoric acid.[6c] The BiF_3 precipitate was washed and then vacuum dried at 100° for 24 hr. Its melting point was 755 ± 5°. The X-ray powder pattern agrees with the pattern for BiF_3 given by Swanson, *et al.*[6c]

$BiCl_3$. Analytical reagent grade bismuth trichloride was treated by bubbling HCl gas through the molten salt; this was followed by triple distillation under an atmosphere of pure argon.[7] The salt thus prepared had a melting point of 233.6°, in good agreement with the literature value.

$BiBr_3$ and BiI_3. Bismuth tribromide and bismuth triiodide were synthesized by direct combination of the elements at high temperatures in a sealed evacuated

(1) (a) This work was supported by the Research Division of the U. S. Atomic Energy Commission. (b) Presented before the Division of Physical Chemistry, 154th National Meeting of the American Chemical Society, Chicago, Ill., Sept 11–15, 1967.

(2) (a) M. Blander, "Molten Salt Chemistry," Interscience Publishers, Inc., New York, N. Y., 1964; (b) B. R. Sundheim, "Fused Salts," McGraw-Hill Book Co., Inc., New York, N. Y., 1964.

(3) L. F. Grantham and S. J. Yosim, *J. Phys. Chem.*, **67**, 2506 (1963).

(4) (a) F. J. Keneshea and D. Cubicciotti, *ibid.*, **62**, 843 (1958); (b) J. W. Johnson and D. Cubicciotti, *ibid.*, **68**, 2235 (1964).

(5) J. D. Kellner, *ibid.*, **71**, 3254 (1967).

(6) (a) G. M. Wolten and S. W. Mayer, *Acta Cryst.*, **11**, 739 (1958); (b) H. E. Swanson, N. T. Gilfrich, and M. I. Cook, "Standard X-Ray Diffraction Powder Patterns," National Bureau of Standards Circular 539, Vol. 6, U. S. Government Printing Office, Washington, D. C., 1956, p 20; (c) H. E. Swanson, M. C. Morris, R. P. Stinchfield, and E. H. Evans, "Standard X-Ray Diffraction Powder Patterns," National Bureau of Standards Monograph 25, Vol. I, U. S. Government Printing Office, Washington, D. C., 1962, p 7.

(7) S. J. Yosim, A. J. Darnell, W. G. Gehman, and S. W. Mayer, *J. Phys. Chem.*, **63**, 230 (1959).

Vycor system.[8] Each of the salts was triply sublimed under reduced pressure after removal of the excess halogen. The melting points of the tribromide and triiodide were 218.5 ± 0.5 and 407.5 ± 1.0°, respectively, in good agreement with reported values.[8] The X-ray powder pattern of this BiI_3 checks with the powder pattern for BiI_3 given by Swanson,[6b] *et al.*

Experimental Methods and Procedure. The phase studies upon the bismuth trihalides at elevated pressures were carried out in a piston–cylinder high-pressure chamber similar to the apparatus of Coes,[9] Hall,[10] and Kennedy, *et al.*[11] A high-pressure chamber cell utilizing an internal graphite or metal strip heater similar to the design used by Kennedy and Newton[12] was used to carry out the high-temperature phase transition studies. A high-pressure, high-temperature cell of this design can attain pressures from a lower limit of approximately 2 kbars to an upper limit of approximately 55 kbars at temperatures from ambient to 1500°. Several experimental techniques were used to detect the phase transitions as no single technique was suitable for detection of the variety of phase transitions found in these salts. These techniques include (a) differential thermal analysis (dta), (b) electrical resistance measurements, (c) differential joule heating method, and (d) the volume discontinuity method.[13] A description of these methods follows.

(a) A differential thermal analysis cell and technique similar to those used by Kennedy and Newton[12] and by Pistorius[14] were used to determine the high-pressure melting points of the four halides. Nickel or boron nitride dta cells were used for BiF_3. Platinum cells were used for $BiCl_3$, and gold cells were used for $BiBr_3$ and BiI_3. The dta method was found to have adequate sensitivity for the detection of the melting and freezing points of these salts. However, the solid–solid phase transitions in $BiBr_3$ and BiI_3 are difficult to detect by dta, because of a small heat of transformation and/or a slow transformation rate.

(b) Electrical resistance measurements were also used to detect phase changes in these salts. Both isobaric and isothermal measurements of the alternating current resistance as a function of temperature and pressure, respectively, were carried out at a frequency of 1000 Hz using a General Radio Type 1650-A resistance bridge. A phase change was signaled by a discontinuity or a change in slope of the resistance as a function either of temperature or of pressure.

(c) The differential joule heating method utilizes a change in resistance of the sample associated with a phase change to alter the heating or cooling rate. This is accomplished by placing the salt sample in a parallel resistance path with the graphite or nickel furnace heating element. The heat generated by the alternating current passing through the sample contributes to the heat generated by the furnace heating element and thus a relatively small change in the resistance of the sample affects the heating rate. Experimentally this is done by placing a solid cylindrical sample directly inside a tubular furnace heating element. The advantage of this method is its simplicity and high sensitivity. The techniques and equipment used for this method are the same as for ordinary thermal analysis, but with a much greater sensitivity to phase transitions than ordinary thermal analysis and much simpler experimentally than the dta method.

(d) The volume discontinuity method has been used by Bridgman[13] and by Kennedy and LaMori[11] to detect solid–solid phase transitions. This method works well on transitions which have a large transition volume and a large dT/dP term such as the $\alpha \rightleftarrows \gamma$ and $\beta \rightleftarrows \gamma$ transitions in BiI_3. This volumetric method is complementary to the thermal method which is more satisfactory for detection of transitions with a large ΔH and a small dT/dP term. The principal reason, however, for use of the volume discontinuity method here is the additional thermodynamic information gained from measurement of the ΔV of the phase transition.

Temperature measurements were made with chromel–alumel thermocouple junctions located within the pressure chamber in direct contact with the sample ampoule. The effect of pressure on the thermoelectric potential of chromel–alumel junctions is relatively small (*i.e.*, <1%) at pressures below 50 kbars and temperatures below 1000°.[15] Therefore, the emf–temperature tables for atmospheric pressure have been used to obtain the temperatures reported here.

Results

BiF_3. The melting curve of BiF_3 as a function of pressure from 2 to 15 kbars is shown in Figure 1. Melting points at higher pressures were not made because of the extreme corrosiveness of the molten BiF_3 at the correspondingly higher temperatures. The results shown in Figure 1 are from the first or second melting point determination on a given sample by the differential joule heating method in a nickel cell and by the dta method in a nickel or a boron nitride container. In general, melting points were not reproducible after

(8) S. J. Yosim, L. D. Ransom, R. A. Sallach, and L. E. Topol *J. Phys. Chem.*, **66**, 28 (1962).

(9) L. Coes, *J. Amer. Ceram. Soc.*, **38**, 298 (1955).

(10) H. T. Hall, *Rev. Sci. Instr.*, **29**, 267 (1958).

(11) G. C. Kennedy and P. N. LaMori in "Progress in Very High Pressure Research," F. P. Bundy, W. R. Hibbard, and H. M. Strong, Ed., John Wiley and Sons, Inc., New York, N. Y., 1961, p 304.

(12) G. C. Kennedy and R. C. Newton in "Solids under Pressure," W. Paul and D. M. Warschauer, Ed., McGraw-Hill Book Co., Inc., New York, N. Y., 1963.

(13) P. W. Bridgman, "The Physics of High Pressures," G. Bell and Sons, London, 1958.

(14) C. W. F. T. Pistorius, *J. Phys. Chem. Solids*, **26**, 1543 (1965).

(15) F. P. Bundy in "Progress in Very High Pressure Research," F. P. Bundy, W. R. Hibbard, and H. M. Strong, Ed., John Wiley and Sons, Inc., New York, N. Y., 1961, p 256.

Table I: Thermodynamic Properties of Fusion of the Bismuth Trihalides

Salt	$(dT/dP)_{P=0}$, deg/kbar	ΔS_f, eu	ΔV_f, cm³/mole (calcd)	V_l at mp, cm³/mole	V_s at mp $(V_l - \Delta V_f)$, cm³/mole	V_l/V_s
BiF_3	7.6	...	...	...	...	...
$BiCl_3$	15.5	11.2[23]	7.3	80.0[27]	72.7	1.11
$BiBr_3$ (β)	16.6	10.55[24] / 10.1[25]	7.2	95.2[28]	88.0	1.08
BiI_3 (β)	17.5	13.7[26]	10.1	126[29]	116	1.09
BiI_3 (γ)	25.0	...	...	...	...	...

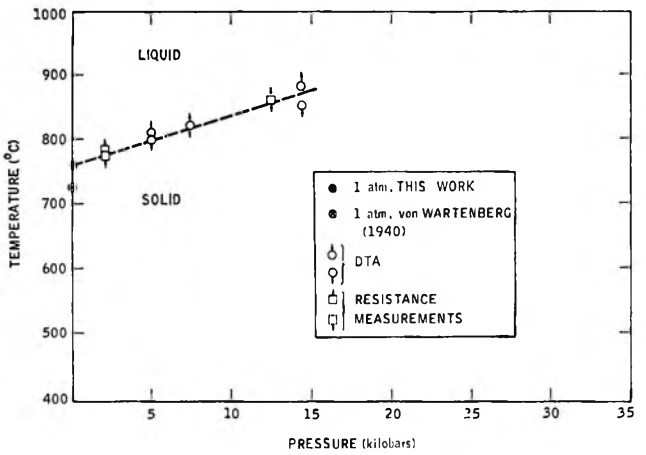

Figure 1. Pressure–temperature diagram for BiF_3.

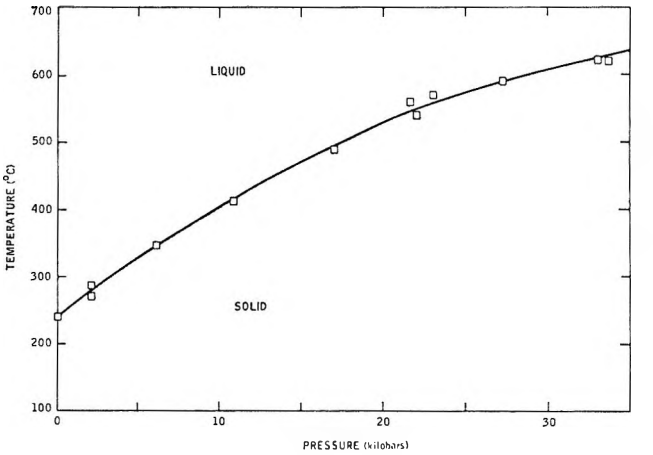

Figure 2. Pressure–temperature diagram for $BiCl_3$.

the third successive run on a sample. Presumably, this is due to reaction with the container. The melting point data at elevated pressures extrapolate to a melting point of 760° at zero pressure. The melting point under an atmosphere of argon was 755 ± 5°, which is higher than the melting point of 725° reported by von Wartenberg.[16] The initial slope of the melting temperature dependence upon pressure is given in Table I. Data for the entropy ΔS and volume ΔV of fusion of BiF_3 at 1 atm are not available so that an independent check of the slope by the Clausius–Clapeyron equation

$$(dT/dP)_{P=0} = 23.9\Delta V/\Delta S \qquad (1)$$

(where T is the melting temperature (°C) at a given pressure P expressed in kbars, ΔV and ΔS are the volume and entropy of fusion, respectively, in cm³ mole^{-1} and cal mole^{-1} deg^{-1}) cannot be made.

Solid BiF_3 was examined for phase transitions by the volume discontinuity and electrical resistance methods from room temperature to 700° at pressures up to 35 kbars. The $\alpha \rightleftarrows \beta$ phase transition at 200° and at atmospheric pressure reported by Hund and Fricke[17] was not detected by either method. The volume change for this transition may be too small to detect by our volumetric method. Below 400° the specific resistance of BiF_3 is so high that sample resistance exceeds the upper resistance limit of our cell and thus we would not be able to detect a phase change occurring below 400° by this resistometric method.

$BiCl_3$. The melting temperature as a function of pressure for $BiCl_3$ is shown in Figure 2 over the pressure range from 2 to 32 kbars. This pressure–temperature melting curve was determined by DTA and ac resistance methods. These two methods give melting points which are in good agreement and which extrapolate to the melting point at atmospheric pressure. The initial pressure dependence of the melting temperature is 15.5°/kbar. The melting curve is given up to 625° since, at temperatures above this, successive melting points on a given sample are not reproducible. This is probably due to reaction of the molten bismuth trichloride with the platinum dta cells. No polymorphic transitions were observed in $BiCl_3$ by either of the above methods from room temperature up to the melting point at pressures from 2 to 32 kbars.

$BiBr_3$. The pressure–temperature phase diagram for $BiBr_3$ to pressures up to 36 kbars is shown in Figure 3. The phase transitions were obtained by dta, alternating current resistance, and differential joule heating techniques. Again, reasonably good agreement is obtained when more than one method was used to determine a particular phase boundary. The

(16) H. von Wartenberg, *Z. Anorg. Allgem. Chem.*, **244**, 337 (1940).
(17) F. Hund and R. Fricke, *Z. Anorg. Allgem. Chem.*, **258**, 198 (1949).

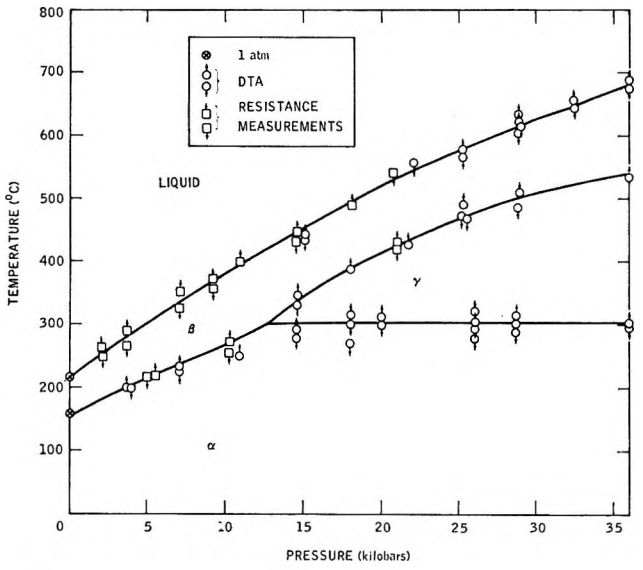

Figure 3. Pressure–temperature diagram for $BiBr_3$.

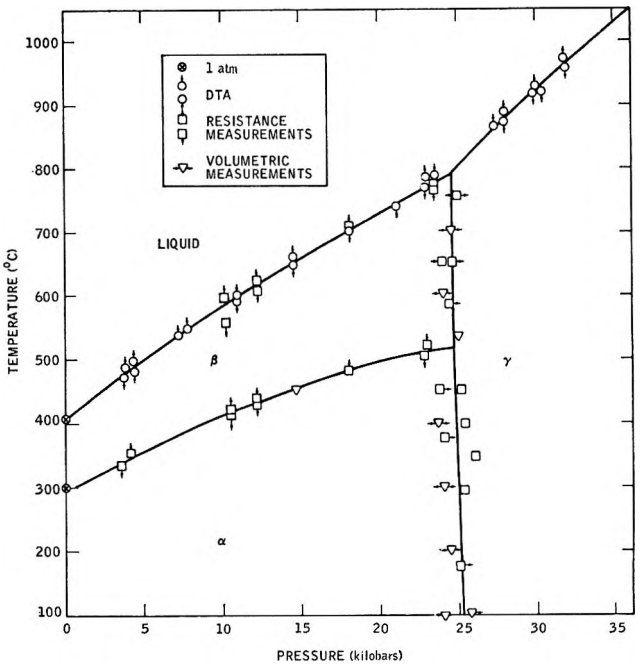

Figure 4. Pressure–temperature diagram for BiI_3.

melting point rises from 255° at a pressure of 2 kbars to 680° at a pressure of 36 kbars. The melting points at elevated pressure extrapolate to give a melting point of 215° at zero pressure which is in good agreement with the atmospheric melting point of 218.5°.[8] The pressure dependence of the melting temperature (dT/dP) is 16.6°/kbar. The $\alpha \rightleftarrows \beta$ transition reported at ambient pressure by Pushin[18] and by Wolten and Mayer[6a] was detected by dta and ac resistance methods. The temperature of this $\alpha \rightleftarrows \beta$ transition was determined as a function of pressure up to a temperature of 300° and at a pressure of 12.5 kbars. This pressure and temperature define the triple point between α and β phases and a newly discovered γ phase. This γ phase lies between α and β phases at pressures from 12.5 kbars up to 36 kbars, the highest pressure examined. Since the $\alpha \rightleftarrows \beta$ transition in $BiBr_3$ is detectable by thermal analysis,[8] then the ΔH for this transition is not equal to zero. Our data show that the temperature dependence dT/dP of the phase boundary between α and β is 12°/kbar. Therefore, from eq 1 the $\alpha \rightleftarrows \beta$ transition volume should not be equal to zero. Wolten and Mayer[6a] have examined $BiBr_3$ by X-ray diffraction at 1 atm but found no change in structure up to 195°. Wolten and Mayer's explanation is that the $\alpha \rightarrow \beta$ transition, which occurs with an enthalpy and volume change but without a change in structure type, could arise from free rotation of the molecules without a change in crystal symmetry. The $\alpha \rightleftarrows \gamma$ phase transition is also detectable by dta; however, the small size of the signal indicates that the heat of transition is small. The slope of this phase transition boundary dT/dP is zero and therefore from eq 1 ΔV for this transition is zero.

BiI_3. Bismuth triiodide was examined by the same experimental techniques as were used for $BiBr_3$. The pressure–temperature phase diagram for BiI_3 is shown in Figure 4. Zahner and Drickamer[19] examined BiI_3 by optical adsorption at pressures up to 75 kbars but failed to detect the $\alpha \rightleftarrows \gamma$ transition at 25 kbars shown in Figure 4. This phase transition proceeds with a large volume change (~5%) but is very sluggish at room temperature. This sluggishness at room temperature probably explains why Zahner and Drickamer failed to detect it. The transition shows up distinctly and reversibly at temperatures above 100° by the volume discontinuity and ac resistance methods. A typical example of the behavior of the electrical resistance of BiI_3 as a function of pressure at constant temperature is shown in Figure 5. The displacement between the compression and decompression cycles indicates hysteresis to the $\alpha \rightleftarrows \beta$ transition. The volume *vs.* pressure curve also exhibits a similar hysteresis effect. The $\alpha \rightleftarrows \beta$ phase transition appears to occur over a pressure interval of approximately 4 kbars, on both the compression and decompression cycles. Part of this pressure interval is due to the pressure differential along the length of the sample since the system is not hydrostatic. Part is attributed to sluggishness toward phase transformation from one solid phase to another. This behavior is exhibited by many substances and has been termed "pressure range of indifference" by Bridgman.[13] We have assumed the equilibrium pressure for the phase transformation to be the average of the pressures indicated for the compression and decompression cycles. Points midway between the onset and the completion of the phase

(18) N. A. Pushin, *Zh. Obshch. Khim.*, 18, 1599 (1948).

(19) J. C. Zahner and H. G. Drickamer, *J. Phys. Chem. Solids*, 11, 92 (1959).

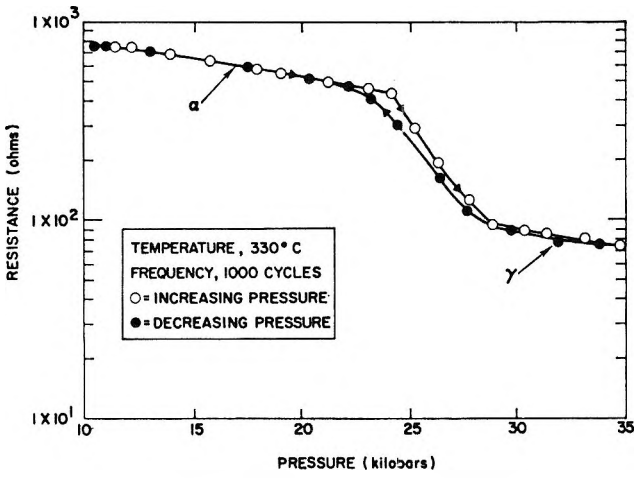

Figure 5. Electrical resistance of BiI_3 as a function of pressure at constant temperature.

transformation were taken as the transformation pressure for each cycle.

The existence of an $\alpha \rightleftarrows \beta$ transition in BiI_3 shown in Figure 4 was indicated in the phase diagram work on the Bi–BiI_3 system by Yosim, *et al.*,[8] although these authors could not unambiguously assign their thermal halts at 285 and 298° to definite phase transitions. No indication of a phase change in BiI_3 was found here which corresponds to the thermal halt at 285° in the Bi–BiI_3 system. However, it appears that the thermal arrest reported by Yosim, *et al.*,[8] at 298° corresponds to the $\alpha \rightleftarrows \beta$ transition in BiI_3 shown in Figure 4. This transition is not readily detected by thermal analysis but exhibits a discontinuity in the resistance *vs.* temperature curves. This is seen in Figure 6, which shows the electrical resistance of BiI_3 as a function of temperature at a constant pressure of 10.8 kbars. The $\alpha \rightleftarrows \beta$ transition occurs at 405° at this pressure. The $\beta \rightleftarrows$ liquid transition occurs over the temperature interval from 545 to 595°. The principal cause of this melting or freezing over such a wide interval is due to the pressure drop across the relatively long sample used in the resistance measurements. As stated above, this pressure drop may be of the order of 2–3 kbars. Since dT/dP for BiI_3 ($\beta \rightleftarrows$ l) is 17.5°/kbar (Table I), such a pressure differential might be expected to give a melting range of 35–55°. The dta method gives a sharper indication of the melting and freezing points at elevated pressures than the above resistance method since in the former case the salt sample is contained in a relatively short ampoule which is in direct contact with the thermocouple junction. Nevertheless, as shown in Figure 4, relatively good agreement is obtained between the two methods.

This resistance discontinuity in BiI_3 at the $\alpha \rightleftarrows \beta$ transition was found by Fischer[20] at atmospheric pressure but was attributed by him to a "premelting" phenomenon. However, our measurements indicate that this is a solid–solid phase transition. Rosztoczy

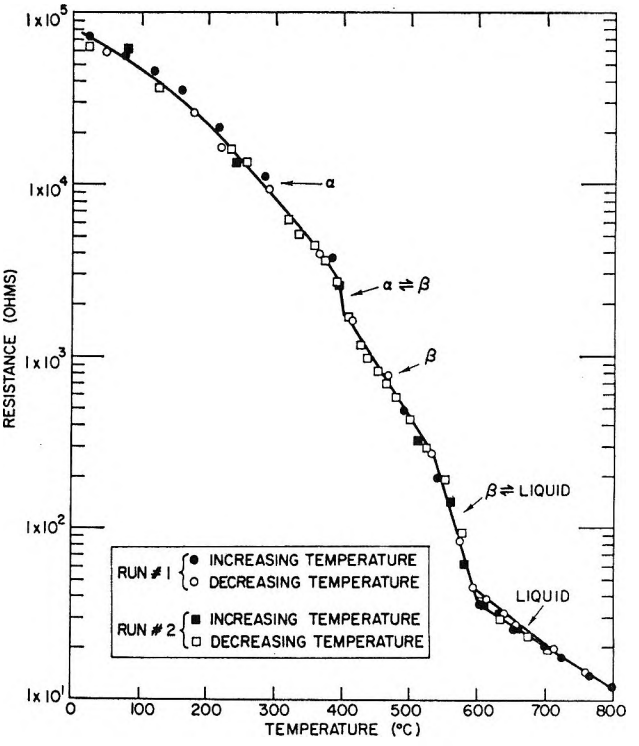

Figure 6. Electrical resistance of BiI_3 as a function of temperature at a constant pressure of 10.8 kbars.

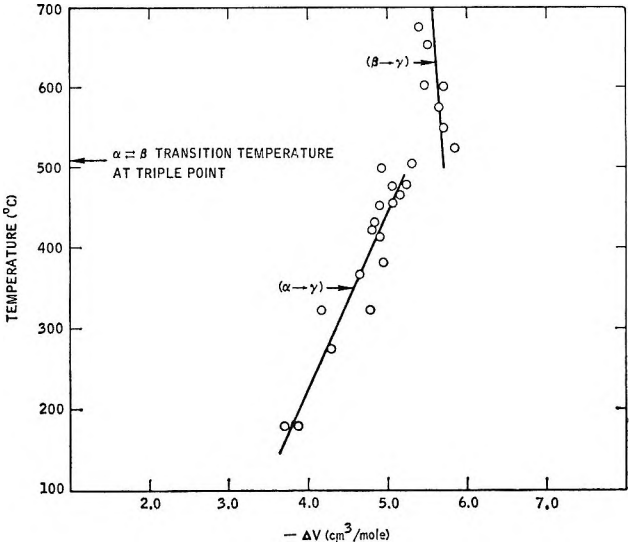

Figure 7. Transition volumes for the ($\alpha \rightarrow \gamma$) and ($\beta \rightarrow \gamma$) phase changes in BiI_3.

and Cubicciotti[21] and Cubicciotti and Eding[22] failed to find this $\alpha \rightleftarrows \beta$ transition in BiI_3 by thermal analysis[21] and by drop calorimetry.[22] The $\beta \rightleftarrows \gamma$ transition, like the $\alpha \rightleftarrows \gamma$ transition, was detected by both the volume discontinuity (Figure 5) and ac resistance techniques. The triple point for solid phases $\alpha \rightleftarrows \beta \rightleftarrows \gamma$ occurs at

(20) G. Fischer, *Helv. Phys. Acta*, **34**, 877 (1961).

(21) F. E. Rosztoczy and D. Cubicciotti, *J. Phys. Chem.*, **69**, 124 (1965).

(22) D. Cubicciotti and H. Eding, *ibid.*, **69**, 3621 (1965).

25.5 kbars and at 510°. The phase boundary slopes, dT/dP, for the phases in equilibrium around the triple point are: $\alpha \rightleftarrows \beta$, 5.5°/kbar; $\alpha \rightleftarrows \gamma$, −375°/kbar; and $\beta \rightleftarrows \gamma$, −1000°/kbar. The transition volumes for the $\alpha \rightleftarrows \gamma$ or $\beta \rightleftarrows \gamma$ transitions were measured from 175 to 675° by the volume discontinuity method of Bridgman.[13] The data points shown in Figure 7 represent an average of the transition volumes (ΔV_{tr}) obtained from the compression and decomposition processes at constant temperature. The discontinuity in the ΔV_{tr} *vs.* T curve at 510° is in agreement with resistance data which indicate a triple point at this temperature. The volume change for the $\alpha \rightleftarrows \beta$ transition was measured at one temperature only, 450°. These transition volumes were measured isothermally while varying the pressure. The results illustrated in Figure 4 show that the isotherm at 450° intersects this $\alpha \rightleftarrows \beta$ phase boundary at an acute angle. The detection or the measurement of ΔV of a transition when dT/dP is small is difficult to carry out isothermally. Nevertheless, the transition was carried out in this manner at 450°. The volume change for the $\alpha \rightarrow \beta$ transition determined by direct measurement is 0.1 cm³/mole with an estimated uncertainty of ± 0.1 cm³/mole. This is in fair agreement with $\Delta V(\alpha \rightarrow \beta)$ from $\Delta V(\beta \rightarrow \gamma) - \Delta V(\gamma \rightarrow \alpha)$ of 0.4 ± 0.4 cm³/mole. Thus the three independently measured transition volumes around the $\alpha \rightleftarrows \beta \rightleftarrows \gamma$ triple point are approximately additive. The slopes, dT/dP, of the boundaries between each of the three pairs of phases in equilibrium were also measured; thus the entropies, ΔS, of the three transitions can be calculated by use of eq 1. These values of ΔS calculated from ΔV and dT/dP are shown in Table II. The entropy changes around the triple point $\alpha \rightleftarrows \beta \rightleftarrows \gamma$ are thus additive within the experimental uncertainty of the measurement of the separate dT/dP and ΔV terms.

Table II: Thermodynamic Properties of Solid-Solid Phase Transitions in BiI_3

Phase change	dT/dP, deg/kbar	ΔV, cm³/mole	ΔS, eu
$\alpha \rightarrow \gamma$	−375	−5.3 ± 0.2	0.33
$\beta \rightarrow \gamma$	−1000	−5.7 ± 0.2	0.13
$\alpha \rightarrow \beta$	5.5	0.1 ± 0.1	0.43

Discussion

If data are available for ΔV and ΔS of fusion, then an independent check of the pressure dependence of the melting temperature dT/dP can be made by means of eq 1. Neither volumetric nor entropy data are available for the fusion of BiF_3. Data for the entropy of fusion are available for $BiCl_3$,[23] $BiBr_3$,[24,25] and BiI_3.[26] However, no direct determination of the volume of fusion of the bismuth trihalides has been reported. An indirect determination of ΔV_f is sometimes made from density of the liquid and of the solid phases at the melting point. Densities for the liquid salts $BiCl_3$, $BiBr_3$, and BiI_3 near their melting points have been determined by Cubicciotti and co-workers.[27-29] Data necessary to calculate the densities of the solid phases of $BiCl_3$, $BiBr_3$, and BiI_3 at their melting points are not available. Lattice parameters at 25° are available;[6] however, $BiBr_3$ and BiI_3 undergo phase transitions between room temperature and their melting points. Furthermore, the necessary thermal expansion data between 25° and the melting points are not available. It is noted that the densities of solid $BiCl_3$ and $BiBr_3$ calculated from the room temperature lattice parameter and space group assignments of Wolten and Mayer[6a] are less than the densities of the corresponding liquid salts at their melting points.[27,28] The densities of solid $BiCl_3$ and $BiBr_3$ calculated from Wolten and Mayer's data are 3.86 and 3.80 g/cm³, while the densities of the liquid salts at their melting points measured by Keneshea and Cubicciotti[27,28] are 3.94 and 4.72 g/cm³. From the slopes of the fusion curves, Figures 2 and 3, however, we see that the solids must be denser than the liquids.

On the other hand, if the experimentally determined[30] densities of 4.75 and 5.7 g/cm³ for $BiCl_3$ and $BiBr_3$, respectively, and 5.78 g/cm³ for $BiI_3(\alpha)$[6b] are compared with Cubicciotti's densities for these molten salts, then it is seen that an over-all volume increase of about 20% occurs in going from the solid at room temperature to the liquid state at its normal melting temperature.

The initial pressure dependence of the melting temperature $(dT/dP)_{P=0}$ and the entropy of fusion data available from the literature have been used to calculate the volume of fusion ΔV_f of $BiCl_3$, $BiBr_3(\beta)$, and $BiI_3(\beta)$ by eq 1. These are shown in Table I. The volume of the solid phase at the melting point was computed from density data of Cubicciotti, *et al.*,[27-29] and from the calculated values of ΔV_f, *i.e.*, $V_{solid} = V_{liquid} - \Delta V_{fusion}$. The ratios of molar volumes of liquid and solid $BiCl_3$, $BiBr_3$, and BiI_3 at their normal melting points are shown in Table I. These ratios for the bismuth halides are comparable to the ratios obtained for typical salts such as the alkali halides.[31]

Melting curves have commonly been reported in the form of the Simon[32] equation

(23) L. E. Topol, S. W. Mayer, and L. D. Ransom, *J. Phys. Chem.*, **64**, 862 (1960).
(24) L. E. Topol and L. D. Ransom, *ibid.*, **64**, 1339 (1960).
(25) D. Cubicciotti and H. Eding, *J. Chem. Eng. Data*, **12**, 548 (1967).
(26) D. Cubicciotti and H. Eding, *J. Phys. Chem.*, **69**, 3621 (1965).
(27) F. J. Keneshea, Jr., and D. Cubicciotti, *ibid.*, **62**, 843 (1958).
(28) F. J. Keneshea, Jr., and D. Cubicciotti, *ibid.*, **63**, 1112 (1959).
(29) F. J. Keneshea, Jr., and D. Cubicciotti, *ibid.*, **63**, 1472 (1959).
(30) O. Honigschmidt and L. Birckenbach, *Ber.*, **54B**, 1873 (1921).
(31) H. Spindler and F. Sauerwals, *Z. Anorg. Allgem. Chem.*, **335**, 267 (1965).
(32) F. E. Simon and G. Glatzel, *ibid.*, **178**, 309 (1929).

$$(P - P_0)/A = (T/T_0)^c - 1 \qquad (2)$$

where T is the melting temperature at pressure P, T_0 is the melting temperature at a triple point s ⇄ l ⇄ g or s ⇄ s′ ⇄ l, P_0 is the pressure at which $T = T_0$, and A and c are empirical constants. The Simon equation parameters were determined for each of the bismuth trihalides and are reported in Table III.

Table III: Parameters in the Simon Equation for the Melting Curves of the Bismuth Trihalides

Salt	T_0, °K	P_0, bars	A, bars	c
BiF_3	1030	0	130,000	1.01
$BiCl_3$	507	0	8,660	2.70
$BiBr_3$ (β)	492	0	14,400	1.85
BiI_3 (β)	681	0	17,700	1.95
BiI_3 (γ)	1073	25,000	16,800	2.38

Kraut and Kennedy[33,34] have recently proposed an equation relating the melting temperature T_m to the room-temperature compression, $-\Delta V/V_0$, of the solid phase in the form

$$T_m = T_m^0\left(1 + C\frac{\Delta V}{V_0}\right) \qquad (3)$$

where T_m^0 is the melting temperature at zero pressure and C is an empirical constant. Equation 3 gives a linear variation in T_m with $\Delta V/V_0$ for many simple substances such as metallic elements[34] and the alkali halides[35] over the pressure and temperature range for which melting and compression data are available. Vaidya and Gopal[35] have modified eq 3 so that the melting temperature of a high-pressure polymorph in equilibrium with the liquid is related to the temperature of the triple point and the compression of the high-pressure solid phase. The melting temperature of the bismuth trihalides at a given pressure have been plotted *vs.* the isothermal compression, $-\Delta V/V_0$, for the salt at this same pressure from compression data taken at 25°.[36] These data of T_m *vs.* $-\Delta V/V_0$ for the bismuth trihalides are shown in Figure 8. Only BiI_3 (γ) exhibits a linear relationship between T_m and $\Delta V/V_0$. The melting point data for the other bismuth trihalides exhibit an upward curvature similar to the data for helium and argon shown by Kraut and Kennedy.[34] The effects of ultrahigh pressures on liquids such as the bismuth trihalides may be complex and sufficiently large so that representation of the melting temperatures by an equation with only one adjustable parameter may not yield a linear relationship in T_m *vs.* $-\Delta V/V_0$ as was found in the case for the alkali metals and the alkali halides.

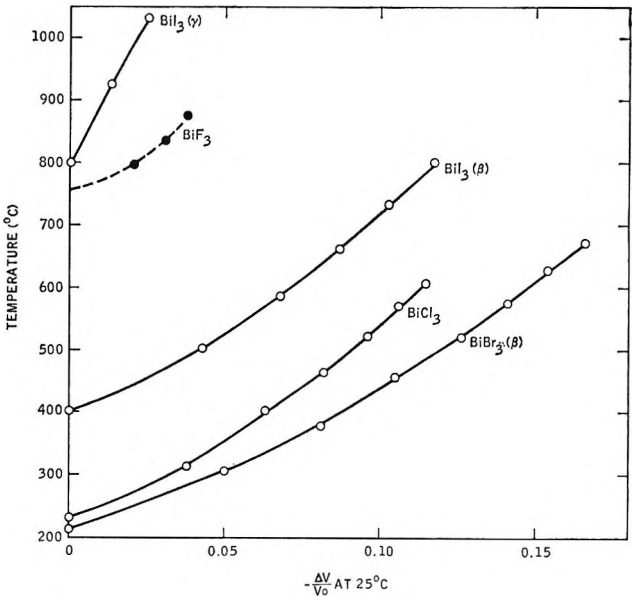

Figure 8. Melting temperature *vs.* compression ($-\Delta V/V_0$) for bismuth trihalides (Kennedy equation).

Summary and Conclusions

The pressure–temperature phase diagrams in Figures 1 through 4 outline the P–T boundaries for the liquid and various solid phases of the bismuth trihalides. No really satisfactory container was found for molten BiF_3 since not more than two or three reproducible melting points could be obtained with the containers employed. A similar problem was encountered with $BiCl_3$ at temperatures above ~650°. The melting points of the bismuth trihalides were found to rise as a function of pressure in a manner typical of a solid which expands during the melting process. The initial slopes of the melting curves (dT/dP) decrease in the order $BiI_3 > BiBr_3 > BiCl_3 > BiF_3$. This same order in dT/dP is observed for the halides of the alkali metals.[31] This sequence probably arises as a result of an increase in the volume of fusion with increasing atomic weight of the halogen. A direct measurement of the volume of fusion of the bismuth trihalides would be welcomed in order to check the consistency of the ΔS_f, dP/dT, and ΔV_f terms. An increase in complexity in the pressure–temperature diagrams is noted (Figures 1 through 4) as the atomic number of the halide increases. Additional structure data on the high-temperature and high-pressure polymorphs of $BiBr_3$ and BiI_3 would be useful toward a better understanding of these systems. We observe that the high-pressure (γ) form of BiI_3 can be retained in a metastable state if the temperature is

(33) E. A. Kraut and G. C. Kennedy, *Phys. Rev. Letters*, **16**, 608 (1966).

(34) E. A. Kraut and G. C. Kennedy, *Phys. Rev.*, **151**, 668 (1966).

(35) S. N. Vaidya and E. S. R. Gopal, *J. Phys. Chem. Solids*, **28**, 1074 (1967).

(36) A. J. Darnell and B. B. Owens, Abstracts, 150th National Meeting of the American Chemical Society, Atlantic City, N. J., Sept 1965, p 51V.

lowered and kept below −40° before the pressure is released to atmospheric. The γ form rapidly and spontaneously reverts to the α form with the evolution of heat when the temperature is raised to −30°. This metastability makes the γ form available for characterization studies at atmospheric pressure, if the temperature is kept below −30°.

Acknowledgment. The authors are indebted to Dr. S. J. Yosim for his continued interest and many helpful discussions during the course of this work.

Molecular Addition Compounds of Tin(IV) Chloride with Ethyl Esters of Dicarboxylic Acids in Benzene and Methylene Chloride

by Andrzej Kemula and Reynold T. Iwamoto

Department of Chemistry, University of Kansas, Lawrence, Kansas 66044 *(Received October 10, 1967)*

The acceptor–donor complexes of tin(IV) chloride with ethyl acetate, ethyl oxalate, ethyl malonate, ethyl succinate, ethyl glutarate, and ethyl adipate have been investigated. Ethyl acetate forms 1:1 and 1:2 $SnCl_4$–ester complexes, depending on the ratio of acceptor to donor; ethyl oxalate and ethyl malonate form five- and six-membered ring chelates, respectively; ethyl succinate is an intermediate case in which both chelated and monocoordinated species exist in solution; and ethyl glutarate and ethyl adipate do not form chelates but 1:1 and 2:1 $SnCl_4$–ester adducts, depending on the ratio of tin(IV) chloride to ester. Formation constants and ΔH and ΔS values were obtained for the complexes of ethyl oxalate and of ethyl malonate and approximate ΔH and ΔS values for the 1:1 complexes of ethyl succinate and of ethyl adipate.

Introduction

The Lewis-acid character of tin(IV) chloride was first investigated by Pfeiffer.[1] Since then over 300 addition compounds of tin(IV) chloride have been described.[2] Despite the large number of reports dealing with solid addition compounds, very little is known about the structure or behavior of the tin(IV) chloride adducts in solutions. Ulich, Hertel, and Nespital[3] have investigated solutions of tin(IV) chloride and ethers, ketones, and nitriles in benzene, utilizing a freezing-point-lowering technique and dielectric constant measurement. Brown and coworkers[4,5] have measured the formation constants of the tin(IV) chloride adducts of substituted benzonitriles, diisobutyl ketone, 9-fluorenone, and ethyl pivalate. Infrared spectral results were used. Myher and Russell[6] measured the formation constants of $SnCl_4$–monoester adducts using ultraviolet data, and Leclere and Duyckaerts[7] employed Raman spectroscopy to obtain the dissociation constant of the 1:2 $SnCl_4$–ethyl propionate complex. Clearly, there is need for further studies of the equilibria in solutions of tin(IV) chloride and Lewis bases. The results of a study of solutions of a series of ethyl esters of dicarboxylic acids and tin(IV) chloride in benzene and methylene chloride are presented in this paper. (Methylene chloride solutions were used in the nmr experiments.) This study was undertaken to obtain information on the physicochemical properties of the adducts of dicarboxylic esters with tin(IV) chloride and on the structure of these compounds in solution. The stoichiometry of each adduct was obtained from infrared and nmr measurements. The important equilibria were evaluated from infrared spectral data.

Experimental Section

Materials. The ethyl esters of acetic, propionic, oxalic, malonic, succinic, glutaric, and adipic acids used were of the highest purity available commercially. They were purified by drying over calcium hydride with subsequent fractional distillation. Refractive index values measured were all within 0.0003 of the literature values. Tin(IV) chloride, reagent grade, from Fisher

(1) P. Pfeiffer, *Ann. Chem.*, **376**, 285 (1910).

(2) I. R. Beattie, *Quart. Rev.* (London), **17**, 382 (1963).

(3) H. Ulich, E. Hertel, and W. Nespital, *Z. Phys. Chem.* (Frankfurt), **B17**, 21 (1932).

(4) T. L. Brown and M. Kubota, *J. Amer. Chem. Soc.*, **83**, 331 (1961).

(5) J. Laane and T. L. Brown, *Inorg. Chem.*, **3**, 148 (1964).

(6) J. J. Myher and K. E. Russell, *Can. J. Chem.*, **42**, 1555 (1964).

(7) G. Leclere and G. Duyckaerts, *Spectrochim. Acta*, **22**, 403 (1966).

Scientific Co., was used without further purification. Reagent grade benzene was dried and stored over sodium wire. Methylene chloride, reagent grade, was dried over calcium hydride and distilled.

Sample Preparation. Stock solutions of tin(IV) chloride in benzene and in methylene chloride were prepared in a dry bag. Appropriate volumes of these stock solutions were used to prepare solutions used in the experiments. Esters were measured out from 0.050- and 0.100-ml syringes. The concentrations of acceptor and of donor varied between 0.05 and 0.2 *M* for the formation constant measurements and between 0.1 and 1.5 *M* for other experiments.

Spectra. Nuclear magnetic resonance measurements were made with Varian spectrometers A-60 and A-60A, with TMS (tetramethylsilane $(CH_3)_4Si$) as the internal standard. The infrared studies were carried out with a Perkin-Elmer 421 spectrophotometer; liquid cells (0.10 mm) with NaCl windows were used. The instrument was always used in double-beam operation, with appropriate solvent in the reference beam. A heated liquid cell with BaF_2 windows (0.10 mm, Beckman FH-01) was used for the formation constant measurements. The temperature was controlled to within 0.2° by placing this cell in a water jacket (Beckman WJ-1) through which water of appropriate temperature was circulated from a constant-temperature bath. The temperature of the sample solution was monitored with an iron–constantan thermocouple placed in a hole drilled in the cell window. This enabled the thermocouple to be close to the solution without actually coming in contact with it. The thermocouple potential was measured with a Leeds & Northrup K-3 potentiometer. The spectrum from 1550 to 1900 cm^{-1} was recorded, *i.e.*, in the region where carbonyl stretching bands occur. At least six spectra were obtained for each solution, and the average absorption value was used for calculation. The chemical stability of solutions was checked by obtaining a spectrum immediately after preparation and 24 hr later. In all cases the spectra of freshly prepared solutions were reproduced within experimental error.

Analysis of Spectral Results. The coordination of a carbonyl group leads to the appearance of a new stretching band at lower frequency in the infrared spectrum.[2,8–10] The intensities of both the free carbonyl and the coordinated carbonyl bands have been shown to be proportional to the concentrations of the free and coordinated species in solution. Therefore, when enough acceptor is added to coordinate all available carbonyl sites, the band corresponding to the free carbonyl should disappear and the intensity of the band corresponding to the coordinated carbonyl should reach its maximum value. If the intensity of free or coordinated carbonyl band is plotted against the mole ratio of acceptor to donor in solution, breaks in the plot should occur at mole ratios corresponding to the stoichiometry of the adducts formed. Examples of such curves are shown in Figure 1 and 2.

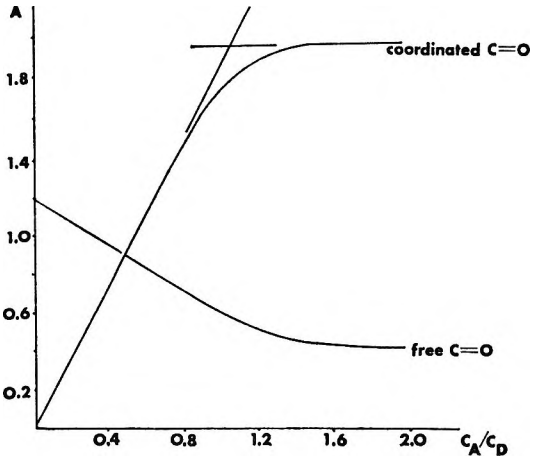

Figure 1. Dependence of the C=O absorbances of ethyl oxalate on the acceptor/donor ($SnCl_4$/ester) mole ratio: $SnCl_4$, 0–0.4 *M*; ester, 0.2 *M* in benzene.

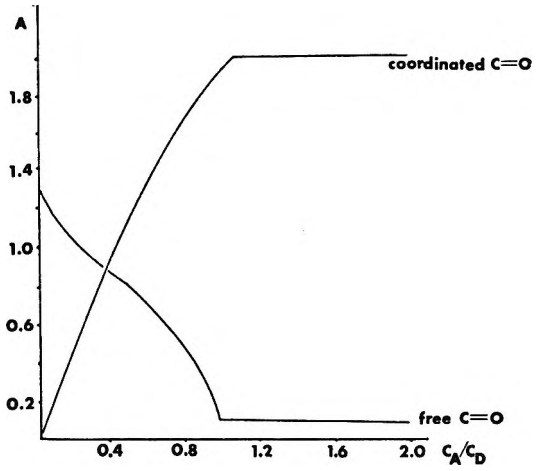

Figure 2. Dependence of the C=O absorbances of ethyl malonate on the acceptor/donor ($SnCl_4$/ester) mole ratio: $SnCl_4$, 0–0.4 *M*; ester, 0.2 *M* in benzene.

The formation constant and ΔH and ΔS values were obtained as follows. For each ester at each temperature studied a Beer's-law plot was obtained. Peak transmittances were recorded and converted to absorbances. The concentration of free ester in a solution of tin(IV) chloride and ester was read off the Beer's-law plot. The fact that free and coordinated carbonyl peaks do not overlap simplified the measurements considerably—the residual absorption due to the complexed carbonyl was negligible at the free carbonyl frequency. The formation constants for all of the 1:1 complexes were calculated using the expression

(8) M. F. Lappert, *J. Chem. Soc.*, 817 (1961).

(9) M. Zackrisson and I. Lindqvist, *J. Inorg. Nucl. Chem.*, **17**, 69 (1961).

(10) D. S. Bystrov and V. N. Filimonov, *Dokl. Acad. Nauk USSR*, **131**, 338 (1960).

$$K_{f(M^{-1})} = \frac{C_D - [D]}{[D]\{C_A - (C_D - [D])\}}$$

where C_A is the initial concentration of the acceptor, C_D is the initial concentration of the donor, and [D] is the concentration of free donor at equilibrium, determined experimentally as described. This expression gives the correct concentration constant for a 1:1 chelate but has to be modified to give the concentration formation constant for a 1:1 monocoordinated diethyl ester complex. The formation constants obtained for the 1:1 $SnCl_4$–ethyl succinate and 1:1 $SnCl_4$–ethyl adipate complexes using the above expression, therefore, are not correct (monocoordination prevails in these two cases). Sample calculations with the correct expression indicate the formation constants calculated with the above expression for these two cases to be too small by a factor of 10–16. However, the primary reason for obtaining the formation constants was to obtain ΔH and ΔS values which could be used to decide between chelate formation and monocoordination. The ΔH and ΔS values obtained with the formation constants calculated using the above expression have been estimated to be smaller by only two or three units and larger by only a few units, respectively, for the 1:1 complexes of ethyl succinate and of ethyl adipate. These ΔH and ΔS values, although approximate, should, therefore, serve to provide important supporting evidence for chelate or monocoordination. An attempt was made to measure the over-all formation constant for the 1:2 $SnCl_4$–ethyl acetate adduct at 25°, using the method described above for the 1:1 adducts. An excess of ester was added to force the formation of the 1:2 species. The expression

$$K_{f(M^{-2})} = \frac{{}^1/_2(C_D - [D])}{[D]^2\{C_A - {}^1/_2(C_D - [D])\}}$$

(symbols as noted above) was used to calculate the over-all formation constant. The second stepwise formation constant was then calculated from the first stepwise constant and the over-all constant.

Formation constants of 1:1 complexes at three or more temperatures were obtained, and ΔH and ΔS values were calculated from the $1/T$ dependence of log K. It should be noted that although the values listed for $K_{f(M^{-1})}$ are in units of M^{-1}, the values of ΔS were calculated[11] using K in units of (mol fraction)$^{-1}$.

After ΔH is obtained by the multiplication of the slope of the log K *vs.* $1/T$ plot by $-2.303R$, ΔS is obtained from the equation

$$\Delta S = \frac{\Delta H}{T} + 2.303R(\log K)$$

Nuclear magnetic resonance spectral studies provided important additional information. When an ester molecule participates in formation of an acceptor–donor complex, not only is a free electron pair on the carbonyl oxygen coordinated, but the electron distribution on the whole molecule undergoes a change. This change alters the environment of the protons in the molecule and causes usually a downfield shift of their peaks. The closer the proton is to the coordination site, the larger this downfield shift will be. The phenomenon of fast exchange prevents the instrument from "seeing" the peaks corresponding to both free and coordinated ester molecules. Instead, a peak is recorded whose position in the spectrum is the weighted average of all the species present in solution. The magnitude of the shift depends not only on the proximity of the proton to the coordination site, but also on the formation constant of the complex. In benzene, the formation of collision complexes between aromatic solvent molecules and polar solutes may cause selective shifts of the solute-proton signals to higher field. As this complicates the interpretation, methylene chloride was used as solvent for the nmr experiments described in this paper. Figure 3 shows a typical curve obtained when the chemical shifts of solute protons are plotted against the mole ratio of the acceptor to the donor in solution.

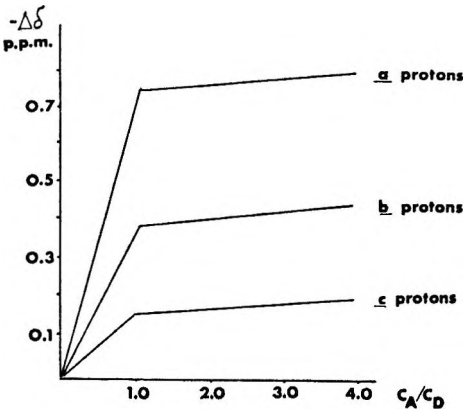

Figure 3. Downfield shifts of the protons of ethyl malonate caused by the addition of $SnCl_4$: $SnCl_4$, 0–1.2 M; ester, 0.3 M in methylene chloride. $\Delta\delta = \delta_{coord} - \delta_{free}$.

Results

The results of the infrared and nmr studies are given in Tables I–IV and Figures 1–3. Table V contains the formation constants and the ΔH and ΔS values.

Discussion

Although this study is mainly concerned with ethyl esters of dicarboxylic acids, an investigation of the interaction of tin(IV) chloride with the monoester ethyl acetate was carried out first to provide us with experimental background and some insight into the problems which would be encountered. The situation in the case of ethyl acetate is fairly simple; depending on the ratio of acceptor to donor, a 1:1 or 1:2 $SnCl_4$–ethyl acetate adduct is formed. The 1:1 adduct is quite

(11) G. C. Pimentel and A. L. McClellan, "The Hydrogen Bond," W. H. Freeman and Co., San Francisco, Calif., 1960, p 348.

Table I: Frequencies of Carbonyl Bands in Free Esters and 1:1 $SnCl_4$–Ester Adducts in Solution[a]

Ester	Free C=O, cm^{-1}	Coord C=O, cm^{-1}
Ethyl acetate	1735 vs	1625 vs
Ethyl oxalate	1740 s, 1765 s	1685 vs
Ethyl malonate	1740 s, 1760 s	1610 vw, 1670 vs
Ethyl succinate	1732 vs	1615 s, 1655 s
Ethyl glutarate	1730 vs	1630 vs, 1690 vw
Ethyl adipate	1728 vs	1615 vs

[a] vs, very strong; s, strong; vw, very weak.

Table II: Designations of Protons in Nuclear Magnetic Resonance Study

Ethyl acetate	$CH_3COOCH_2CH_3$ a b c
Ethyl oxalate	$CH_3CH_2OOCCOOCH_2CH_3$ c b b c
Ethyl malonate	$CH_3CH_2OOCCH_2COOCH_2CH_3$ c b a b c
Ethyl succinate	$CH_3CH_2OOCCH_2CH_2COOCH_2CH_3$ c b a a b c
Ethyl glutarate	$CH_3CH_2OOCCH_2CH_2CH_2COOCH_2CH_3$ c b a_1 a_2 a_1 b c
Ethyl adipate	$CH_3CH_2OOCCH_2CH_2CH_2CH_2COOCH_2CH_3$ c b a_1 a_2 a_2 a_1 b c

Table III: Chemical Shift (δ) Values in Free Ethyl Esters in Methylene Chloride, in Ppm (*vs.* TMS)

Ester	Protons a or a_1	a_2	b	c
Ethyl acetate	−1.98		−4.11	−1.22
Ethyl oxalate			−4.32	−1.35
Ethyl malonate	−3.34		−4.21	−1.27
Ethyl succinate	−2.58		−4.14	−1.23
Ethyl glutarate	−2.36	−2.02	−4.14	−1.23
Ethyl adipate	−2.31	−1.33	−4.12	−1.23

stable, whereas the 1:2 adduct is a weak complex, as evident from the two stepwise formation constants given in Table V. The formation constant, ΔH, and ΔS, for the 1:1 adduct, listed in Table V, are in good agreement with those obtained by Myher and Russell ($K_{f(M^{-1})} = 61$, $\Delta H = -10.5$ kcal/mol, and $\Delta S = -27.0$ cal/mol deg).[6] Because of the large uncertainty of the second formation constant, the ΔH and ΔS values for the formation of the 1:2 adduct were not calculated. One would expect these values to be roughly twice those for 1:1 coordination, or about −20.2 kcal/mol and −59.0 cal/mol deg, respectively. These estimated values are remarkably close to the values −21.0 kcal/mol and −58.6 cal/mol deg for ΔH and ΔS obtained by Myher and Russell.

Table IV: Downfield Shifts ($-\Delta\delta$) of Ester Protons upon Addition of Excess[a] Tin(IV) Chloride in Methylene Chloride, in Ppm (*vs.* TMS)

Ester	Protons a or a_1	a_2	b	c
Ethyl acetate	0.40		0.25	0.13
Ethyl oxalate			0.40	0.15
Ethyl malonate	0.78		0.43	0.20
Ethyl succinate	0.41		0.35	0.11
Ethyl glutarate	0.36	0.20	0.26	0.12
Ethyl adipate	0.34	0.14	0.24	0.12

[a] Excess tin(IV) chloride added to ensure coordination of all ester molecules. $\Delta\delta = \delta_{coord} - \delta_{free}$.

Ethyl Oxalate. The first serious attempt to establish the structure of the complexes of tin(IV) chloride with esters of dicarboxylic acids was made by Hieber and Reindl.[12] On the basis of calorimetric and vapor-pressure experiments, they assigned dimeric structures to the 1:1 complexes of tin(IV) chloride with diesters of oxalic, malonic, succinic, glutaric, and adipic acids in the solid state. Osipov, Artemova, Kogan, and Lysenko[13] corroborated these results (with the exception of the ethyl malonate complex, where they prefer a monocyclic configuration) with dipole moment and molecular weight measurements.

The infrared acceptor:donor mole ratio study summarized in Figure 1 indicates 1:1 stoichiometry for the $SnCl_4$–ethyl oxalate adduct in solution. The nmr studies (Table IV) provide evidence that the coordination is of the chelate type. When the effects of coordination on the b and c protons of ethyl acetate and ethyl oxalate are compared, it is clear that they are much larger in the latter ester. The difference may be explained by the fact that in the coordinated ethyl oxalate molecule the two deshielding effects add up, the deshielding through the carbonyl group closest to the protons in question and the simultaneous, though less pronounced, deshielding through the other carbonyl group, which is also coordinated to the same tin atom. It would be expected that this additive effect should be most pronounced for ethyl oxalate, as here the carbonyl groups are next to each other. The fact that the effect of coordination on the b and c protons is actually greater in the case of ethyl malonate, where there is a methylene group between the two carbonyls acting as a "barrier" to simultaneous deshielding, is not inconsistent with the explanation given above when the data in Table III are taken into consideration. In this table the chemical shifts of all protons in pure

(12) W. Hieber and E. Reindl, *Z. Elektrochem.*, 46, 559 (1940).

(13) O. A. Osipov, V. M. Artemova, V. A. Kogan, and Y. A. Lysenko, *Zh. Obshch. Khim.*, 32, 1368 (1962).

Table V: Equilibrium Constant, Enthalpy-, and Entropy-Change Values for 1:1 $SnCl_4$–Ester Adduct Formation in Benzene Solution

Ester	Temp, °C	$K_{f(M^{-1})}$	Av dev	ΔH, kcal/mol	ΔS, cal/mol deg
Ethyl acetate[a]	15	172.5	11.7	-10.1 ± 1.0	-29.6 ± 2.0
	25	93.5	3.4		
	35	55.5	2.1		
Ethyl oxalate	15	43.5	1.9	-16.2 ± 1.0	-52.8 ± 3.0
	25	18.5	1.7		
	35	7.0	0.5		
Ethyl malonate	25	769.0	58.4	-15.9 ± 1.6	-45.0 ± 4.0
	35	312.5	29.0		
	45	135.0	11.0		
Ethyl succinate	25	66[b]	4[b]	−8[b]	−24[b]
	35	41[b]	7[b]		
	45	24[b]	1[b]		
Ethyl adipate	15	91[b]	8[b]	−9[b]	−26[b]
	25	52[b]	3[b]		
	35	32[b]	2[b]		
	45	21[b]	2[b]		

[a] Second formation constant at 25°, $K^2_{f(M^{-1})} = 4.3$ (average deviation, 2.2); over-all formation constant for the 1:2 $SnCl_4$–ethyl acetate adduct, $K_{f(M^{-2})} = 400$. [b] See Experimental Section for the reliability of this value.

esters are recorded. The peaks of the b and c protons of ethyl oxalate are further downfield than those of any other ester. This situation with ethyl oxalate is due to the combined electron-withdrawing effect of two adjoining carbonyl groups, which deshields the alcohol group protons in ethyl oxalate more than those in other esters. The effect of tin(IV) chloride coordination to both carbonyl groups on the b and c protons is thus diminished by this initial downfield shift of the signals of the protons of the alcohol group in the pure ester. If the differences of chemical shifts of these protons in ethyl oxalate and ethyl malonate are taken as a measure of the deshielding due to the carbonyls being next to each other in ethyl oxalate (and separated by one methylene group in ethyl malonate) and then added to the coordination-caused downfield shift ($\Delta\delta$) of the peaks of the ethyl oxalate protons, we arrive at the results

b protons in free oxalate -4.32 ppm
b protons in free malonate $-(-4.21)$ ppm
-0.11 ppm

c protons -1.35 ppm
c protons $-(-1.27)$ ppm
-0.08 ppm

$\Delta\delta$ for the b protons in coordinated ethyl oxalate, corrected for the effect of adjacent carbonyl groups, thus is $-0.11 + (-0.40) = -0.51$ ppm, and $\Delta\delta$ for the c protons in coordinated ethyl oxalate, corrected for the effect of adjacent carbonyl groups, is $-0.08 + (-0.15) = -0.23$ ppm. The values for ethyl malonate are -0.43 and -0.20 ppm, respectively.

The 1:1 coordination of just one carbonyl group should result in downfield shifts of the peaks of the b and c protons of one alcohol group similar to those of the peaks of the b and c protons of coordinated ethyl acetate, while the other alcohol group of ethyl oxalate is affected much less. As the instrument cannot distinguish between the two sets of b and c protons but sees only their average, the resulting downfield shift for the signals of the protons of coordinated ethyl oxalate should be smaller than in the case of ethyl acetate. The data in Table IV indicate that this is not the case.

The entropy change on formation of tin(IV) chloride–ethyl oxalate 1:1 complex is -52.8 cal/mol deg (Table V), or about 8 cal/mol deg more positive than the entropy change on formation of the tin(IV) chloride–ethyl acetate 1:2 adduct.[6] This favorable entropy change is consistent with the formation of a chelated 1:1 complex between tin(IV) chloride and ethyl oxalate.[14] The ΔH of formation of the $SnCl_4$–oxalate adduct is -16.2 kcal/mol, which is much larger than the ΔH of formation of the $SnCl_4$–acetate 1:1 adduct (-10.1 kcal/mol). The difference in these ΔH values also is consistent with the two carbonyl groups interacting with one tin(IV) chloride molecule and forming a 1:1 chelate. For the ethyl oxalate case, it is clear that in benzene and methylene chloride the 1:1 $SnCl_4$–ester adduct is a chelate.

(14) G. Schwarzenbach, *Helv. Chim. Acta*, **35**, 2344 (1952).

Ethyl Malonate. The infrared mole ratio study of complex formation between tin(IV) chloride and ethyl malonate in benzene shows that a 1:1 adduct is formed (Figure 2). The disappearance of the free carbonyl band at a $C_A:C_D$ ratio of 1 indicates that the adduct formed is a chelate. The nmr measurements also provide evidence for chelation in the case of the 1:1 adduct. The methylene a protons of the malonate are deshielded upon formation of a complex much more than those of any other diester studied (Table IV), despite the fact that they are already deshielded in pure ester by electron-withdrawing action of the two neighboring carbonyl groups. In the chelate, the a protons undergo electron withdrawal (deshielding) by tin(IV) chloride from both sides directly and experience a much larger deshielding effect than from a single coordinated carbonyl. The argument for the b and c protons is analogous to that in the case of ethyl oxalate, except the effect, as expected, is smaller.

The entropy change on formation of 1:1 $SnCl_4$–malonate adduct is −45.0 cal/mol deg (Table V), or approximately 15 cal/mol deg more positive than the entropy change associated with the formation of 1:2 $SnCl_4$–ethyl acetate adduct. This favorable entropy change for the ethyl malonate case is consistent with formation of a 1:1 chelated complex. The much larger ΔH of formation of the tin(IV) chloride–ethyl malonate 1:1 complex (−15.9 kcal/mol) than that for the tin(IV) chloride–ethyl acetate 1:1 complex also indicates coordination of the two carbonyl groups in the malonate complex.

The above results all point to formation of a 1:1 chelated adduct between tin(IV) chloride and ethyl malonate in the solutions studied.

Ethyl Succinate. The ethyl succinate molecule has two methylene groups between the carbonyls. These groups not only lengthen the chain, but also give the molecule additional flexibility even when it is coordinated.

The infrared mole ratio study does not give results as clear-cut as in the case of ethyl malonate. A break in the free and coordinated C=O curves at the $C_A:C_D$ ratio equal to 1 can be distinguished; further addition of tin(IV) chloride leads to an increase in intensity of the complexed carbonyl band and a decrease in intensity of the free carbonyl band. This situation would seem to indicate that some of the succinate molecules are coordinated through one carbonyl only, rather than forming a chelate. In Table I it is shown that the coordinated C=O band at about 1680 cm^{-1} is due to the chelate-type structure (these bands are very strong only in oxalate and malonate complexes with tin(IV) chloride, where chelation has been shown to take place), whereas the band at about 1615 cm^{-1} is found in complexes where 1:1 monocoordination prevails ($SnCl_4$–ethyl acetate, $SnCl_4$–ethyl adipate). The tin(IV) chloride–ethyl succinate system is the only one in which these two bands have approximately the same intensity. The infrared information thus indicates the existence of both monocoordinated and chelated $SnCl_4$–succinate species in solution.

The nmr measurements show a sharp break at the acceptor:donor mole ratio of 1. This result does not exclude either of the possibilities discussed above. The downfield shift of the a methylene proton signals is much smaller than in the case of ethyl malonate, and the same holds true for the b- and c-proton signals. In the case of chelation the two methylene groups between the carbonyls form a much stronger barrier to mutual deshielding through both carbonyls and, consequently, the a groups are deshielded each through essentially one carbonyl only. In the case of monocoordination one methylene group (α to the coordinated carbonyl) is deshielded more than the other (β to the coordinated carbonyl). Owing to fast exchange the signals are averaged out and the resulting shift is smaller than expected. As both species have 1:1 stoichiometry, a sharp break is obtained at a mole ratio of 1.

The infrared results discussed above indicate that in the tin(IV) chloride–ethyl succinate system both chelated and monocoordinated species exist. The entropy-change experiments provide additional information on the distribution of these two coordinated species. For the formation of the monocoordinated complex the entropy change would be expected to be similar to the entropy change on formation of a tin(IV) chloride–ethyl acetate adduct, whereas the formation of a chelate should lead to an entropy change closer to that found for ethyl malonate. Table V shows that the former is the case. On the basis of these results it can be concluded that although probably some chelate species is formed in solution, the 1:1 monocoordinated complex prevails. The ΔH measurements are consistent with this conclusion, the value in the $SnCl_4$–succinate case being close to the value obtained for the $SnCl_4$–acetate 1:1 complex (Table V).

Ethyl Glutarate and Ethyl Adipate. Ethyl glutarate has three methylene groups between the carbonyls. This added length causes the two carbonyl groups to behave independently of each other. The infrared mole ratio method does not show sharply defined breaks; however, the band for the free carbonyl group disappears at the $SnCl_4$:ester ratio of 2:1, indicating that the two carbonyls are each coordinated by a molecule of tin(IV) chloride. The strong coordinated C=O band is at 1630 cm^{-1}, consistent with monocoordination, as discussed above.

The nmr measurements provide further evidence of monocoordination. The curves in the mole ratio study are diffuse, as expected, because of a number of possible species in solution and of the fast-exchange phenomenon, and the breaks are at the $C_A:C_D$ ratio of 2:1. Table IV shows that the a_1, b, and c protons of ethyl glutarate

undergo deshielding upon coordination to an extent very similar to those of the ethyl acetate protons under identical conditions. Both carbonyls of the glutarate molecule are coordinated, making it very similar to two 1:1 coordinated ethyl acetate molecules.

The infrared and nmr data obtained for the tin(IV) chloride–ethyl adipate case are analogous to those described for the case of ethyl acetate.

No values for ΔS and ΔH of formation of 1:1 tin(IV) chloride–ethyl glutarate adduct were obtained. From the results of the infrared and nmr studies, these values are expected to be similar to those for 1:1 tin(IV) chloride–ethyl adipate adduct. The ΔS value obtained for the formation of 1:1 tin(IV) chloride–ethyl adipate adduct is consistent with the conclusions reached on the basis of the mole ratio studies. It is very similar to the ΔS value obtained for the formation of tin(IV) chloride–ethyl acetate 1:1 adduct. The ΔH value obtained for the formation of 1:1 tin(IV) chloride–ethyl adipate complex is also in agreement with the formation of monocoordinated species.

The conclusion is thus reached that ethyl glutarate and ethyl adipate, although difunctional, do not form chelates with tin(IV) chloride. Instead, depending on the ratio of tin(IV) chloride to ester in solution, they form simple 1:1 and 2:1 adducts.

Chlorine Nuclear Quadrupole Resonance Study of Some Molecular Adducts of Phosphorus Oxychloride[1,2]

by Max T. Rogers and James A. Ryan

Department of Chemistry, Michigan State University, East Lansing, Michigan 48823 *(Received October 12, 1967)*

Several nuclear quadrupole resonance (nqr) absorption frequencies have been found for chlorine in the molecular adducts $SbCl_5 \cdot POCl_3$, $FeCl_3 \cdot POCl_3$, and $[TiCl_4 \cdot POCl_3]_2$; also, those for $SnCl_4 \cdot 2POCl_3$ have been reexamined at different temperatures than reported in the literature. From the known crystal structures of $SbCl_5 \cdot POCl_3$, $SnCl_4 \cdot 2POCl_3$, and $[TiCl_4 \cdot POCl_3]_2$, along with other available information, tentative assignments of the observed frequencies to specific chlorine atoms in the molecules of these adducts have been made and their electronic structures have been discussed. The temperature dependences of some of the frequencies were measured and have been discussed.

Introduction

Although charge-transfer type compounds have been studied extensively by spectroscopic, thermodynamic, and other physical methods, few have been investigated by nuclear quadrupole resonance (nqr) spectroscopy. In those studied,[3-7] most nqr absorption frequencies showed only negligible shifts on complex formation. In some cases frequency shifts in the direction opposite to that expected were observed and such shifts have been attributed to solid-state effects. Since the crystal structures of the complexes differ from those of the components, the effects of the crystal environment on the nqr frequencies will differ, may be in either direction, and may be larger than the effects due to changes in chemical bonding.

Rather large changes in the nqr frequencies for ^{35}Cl were observed[8] between the molecular adduct $SnCl_4 \cdot 2POCl_3$ and the components, $SnCl_4$ and $POCl_3$. It was thought that shifts of the ^{35}Cl nqr frequencies from those of the pure components might be large enough in a series of adducts of this type to provide significant information concerning chemical bonding. We have therefore prepared the adducts of $POCl_3$ with $SbCl_5$, $TiCl_4$, $FeCl_3$, and $SnCl_4$ and have obtained most of the

(1) This work was supported through a contract with the U. S. Atomic Energy Commission, and this is AEC Document No. COO-1385-19.

(2) This paper is abstracted from the Ph.D. thesis of J. A. Ryan, Michigan State University, 1967, and was presented at the 153rd National Meeting of the American Chemical Society, Miami Beach, Fla., April 10–14, 1967.

(3) D. Douglass, *J. Chem. Phys.*, **32**, 1882 (1960).

(4) H. Hooper, *ibid.*, **41**, 599 (1964).

(5) P. Cornil, J. Duchesne, M. Read, and R. Cahay, *Bull. Classe Sci. Acad. Roy. Belg.*, **50**, 235 (1964).

(6) V. Grechishkin and I. Kyuntsel, *Opt. Spectry.*, **16**, 87 (1964); *Fiz. Tverd. Tela*, **5**, 948 (1963); *Soviet Phys.-Solid State*, **5**, 694 (1963).

(7) H. Dehmelt, *J. Chem. Phys.*, **21**, 380 (1953).

(8) V. Biedenkapp and A. Weiss, *Z. Naturforsch.*, **19A**, 1518 (1964).

^{35}Cl nqr frequencies. From the known crystal structures and other available information, estimates of the solid-state effects have been made and the nqr frequencies have been assigned to specific chlorine atoms of the adducts. The shifts in nqr frequencies on complex formation have been related to the electronic structures of the adducts and to the acceptor strengths of the metal chlorides. Since this work was completed, a report of a study of both Sb and Cl resonances in $SbCl_5 \cdot POCl_3$ has appeared;[9] their experimental observations agree well with ours where they overlap.

Experimental Section

The resonances were detected with a frequency-modulated, externally quenched, superregenerative oscillator of the type described by Dean.[10] The frequency measurements were made in the usual manner[11] with an estimated accuracy of ±5 kHz. The signals were either displayed directly on an oscilloscope screen or recorded using 39-Hz frequency modulation and a Princeton Applied Research Model JB-4 lock-in amplifier. In most cases ^{37}Cl nqr absorptions were observed corresponding to the observed ^{35}Cl absorptions.

The frequency of one of the $SbCl_5 \cdot POCl_3$ lines was studied at room temperature, liquid nitrogen temperature, and several fixed intermediate temperatures provided by slush baths of carbon disulfide (165°K), ethyl acetate (190°K), and carbon tetrachloride (250°K).

In the cases of $SbCl_5 \cdot POCl_3$, $SnCl_4 \cdot 2POCl_3$, $TiCl_4 \cdot 2POCl_3$, and $[TiCl_4 \cdot POCl_3]$, the complexes were formed by mixing together stoichiometric quantities of the two reagents. They were purified by melting the resulting mixture, allowing all but the last few milliliters of liquid to solidify, and discarding the liquid residue; this process was repeated several times. $FeCl_3 \cdot POCl_3$ was made by the procedure of Gutmann and Baaz.[12]

Results

The chlorine quadrupole resonance frequencies observed in this work for the adducts at 77°K and at room temperature are listed in Table I along with values of the nqr frequencies for $SnCl_4$,[13] $POCl_3$,[13] and $SbCl_5$[14] reported in the literature. The temperature dependence of the frequency of the resonance at 27.327 MHz (77°K) for $SbCl_5 \cdot POCl_3$ is shown graphically in Figure 1.

The crystal structures of three of the complexes, $SbCl_5 \cdot POCl_3$, $SnCl_4 \cdot 2POCl_3$, and $[TiCl_4 \cdot POCl_3]_2$, have been determined,[15-17] and the configuration of the "molecule" of complex is shown in Figure 2 for each of these. The numbers assigned the various atoms are arbitrary and designate the various crystallographically nonequivalent positions in the unit cell; the same numbers are used in Table I to identify the frequencies whose assignments (see below) are based, in part, on

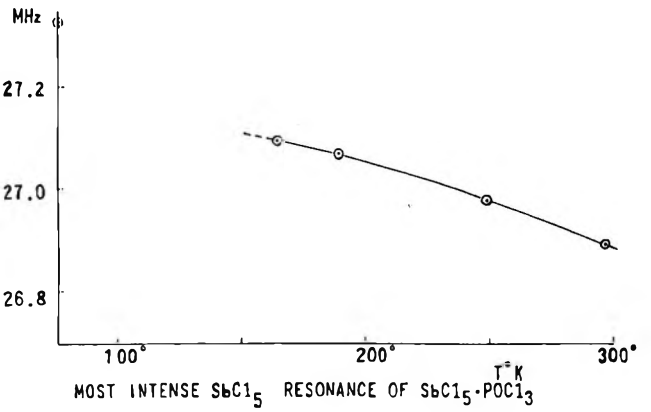

Figure 1. Temperature dependence of the most intense nqr absorption of $SbCl_5 \cdot POCl_3$.

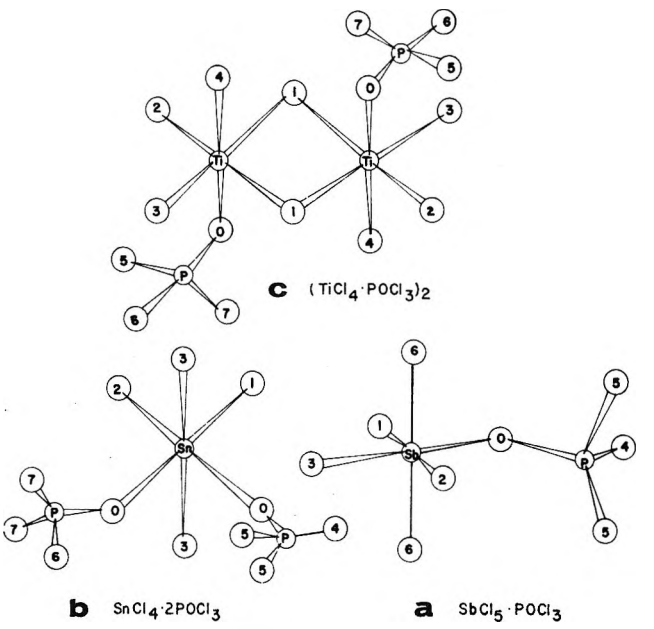

Figure 2. Molecular species in some adducts of phosphorus oxychloride: a, $SbCl_5 \cdot POCl_3$; b, $SnCl_4 \cdot 2POCl_3$; c, $[TiCl_4 \cdot POCl_3]_2$.

the calculated point-charge contributions to the measured coupling constant. The calculation of the point-charge contributions is discussed elsewhere,[2,18] and the results are tabulated in Table I for those compounds whose crystal structures have been determined.

(9) R. F. Schneider and J. V. Dilorenzo, Abstracts, 153rd National Meeting of the American Chemical Society, Miami Beach, Fla., April 10–14, 1967, L-134; also, private communications.

(10) C. Dean and M. Pollak, *Rev. Sci. Instr.*, **29**, 630 (1958).

(11) See, for example, T. Das and E. Hahn, "Nuclear Quadrupole Resonance Spectroscopy," Academic Press, New York, N. Y., 1958.

(12) V. Gutmann and M. Baaz, *Monatsh.*, **90**, 729 (1959).

(13) R. Livingston, *J. Phys. Chem.*, **57**, 496 (1953).

(14) D. McCall and H. Gutowsky, *J. Chem. Phys.*, **21**, 1300 (1953).

(15) C. Brändén and I. Lindqvist, *Acta Chem. Scand.*, **17**, 353 (1963).

(16) C. Brändén, *ibid.*, **17**, 759 (1963).

(17) C. Brändén and I. Lindqvist, *ibid.*, **14**, 726 (1960).

(18) J. A. Ryan and M. T. Rogers, unpublished results.

Discussion

Solid-State Effects. The observed shifts in ^{35}Cl nqr frequencies in going from pure components to adduct may be attributed to two rather different effects. The first, of primary interest to the chemist, is a transfer of electrons from the Lewis base ($POCl_3$) to the Lewis acid ($SnCl_4$, $TiCl_4$, $SbCl_5$, etc.) accompanied by formation of a new metal–oxygen bond, while the second is a solid-state effect due to the difference in lattice environments between adduct and pure components. The solid-state effect arises from intermolecular interactions in the solid, vibrational motions in the crystal and electric charges on the atoms.[19]

It is important for any discussion of the first effect to establish that the observed frequency shifts are not primarily solid-state effects, so we have attempted to evaluate these. The crystal structures[15-17] show that intermolecular bonding is not important in the adducts, and Bersohn[20] has shown that van der Waals interactions do not affect the field gradients at a quadrupolar nucleus to any great extent. Vibrational motions may be important but should be roughly the same for all chlorine atoms in the series of crystals studied here. The most important part of the solid-state effect should then be the contribution to the electric field gradient at a given chlorine nucleus by the charges on all the other atoms of the crystal. This point-charge contribution has been evaluated for each substance of known crystal structure and the calculated values for each chlorine atom are given in the right-hand column of Table I. Details of these calculations are presented elsewhere.[18] The Sternheimer antishielding factor[21] is not considered here because values are not available for these substances and there is some evidence that for compounds with bonds of large covalency the factor may not be too important.[22] In any case, these calculations have only been used in assigning the frequencies (see below), and the relative signs and magnitudes of the point-charge contributions are sufficient for this purpose. Also, our conclusions concerning chemical bonding in the adducts are not dependent on these calculated point-charge contributions.

Although it is not possible to determine the sign of the measured quadrupole coupling constant e^2Qq_{zz} (exptl) in a pure quadrupole resonance experiment, it can be concluded that the coupling constants in solids are negative for all chlorine atoms more positive than Cl^- by comparison with the known signs of coupling constants of chlorine compounds determined in microwave experiments. Therefore, all positive values of the point-charge contribution of $e^2Q\phi_{zz}$ will decrease the measured absorption frequency and all negative values will increase the measured absorption frequency.

Assignment of Frequencies. The number of different chlorine resonance frequencies observed (Table I) is the same as the number of crystallographically nonequivalent chlorine atoms in each case except that of $SnCl_4 \cdot 2POCl_3$. For the latter complex, four lines are predicted from the crystal structure[15] for chlorine bonded to phosphorus, but only two were observed by Biedenkapp and Weiss,[8] and we observed only two in agreement with their results; it is possible that the other two lines are actually present but cannot be distinguished in the complex absorption pattern or they may have disappeared as a result of a rapid reorientation of one of the $-PCl_3$ groups.

The formation of the new phosphorus–oxygen–metal bridge by donation of a lone pair of electrons from the oxygen of $POCl_3$ to the metal atom should lead to a decrease of electronic charge on the chlorine atoms bonded to phosphorus and a corresponding increase for those bonded to the metal. In agreement with this prediction, a set of lines is observed for each adduct at frequencies higher than pure $POCl_3$ and a second set with frequencies lower than in pure metal chloride, and these may then be assigned to the chlorine atoms of the adduct bonded to phosphorus and to metal, respectively. Finally, the nqr frequencies within each group may be assigned to specific chlorine atoms of the crystal structures if the point-charge contributions to the field gradients and the line intensities (Table I) are taken into account. The metal atoms in the complex are nearly octahedrally surrounded, and it is assumed that chlorine atoms *trans* to oxygen will experience a different field gradient from those *cis* to oxygen in the adduct.

It is not always possible to assign the frequencies unequivocally. For $SbCl_5 \cdot POCl_3$ there are four groups of chlorine atoms bonded to antimony (Cl(1), Cl(2), Cl(3), and Cl(6)) and the strongest line at 27.237 MHz is assigned to the two Cl(6) atoms on the basis of line intensity. The X-ray data for a number of oxygen adducts of $SbCl_5$ show[23] that the chlorine–antimony bond *trans* to the oxygen is always shorter (stronger) than the *cis* bonds. If this difference is attributed to the *trans* bond having slightly more double-bond character, then according to eq 1, we would expect the resonance frequency of a chlorine *trans* to the oxygen to be lower in frequency than those for the chlorines *cis* to the oxygen. In our case Cl(3) is *trans* to the oxygen and also has the shortest Sb–Cl bond distance (2.32 Å) so the line at 24.434 is assigned to Cl(3). On the basis of calculated point-charge contributions, the lines at 25.882 and 26.186 MHz are assigned to the Cl(1) and Cl(2) atoms, respectively.[24]

(19) C. Townes, "Handbuch der Physik," S. Flügge, Ed., Springer-Verlag, Berlin, 1958.

(20) R. Bersohn, *J. Appl. Phys. Suppl.*, **33**, 286 (1962).

(21) For discussion, see ref 11.

(22) R. Bersohn and R. Shulman, *J. Chem. Phys.*, **45**, 2298 (1966).

(23) C. Branden, A. Hansen, Y. Hermodsson, and I. Lindqvist, U. S. Department of Commerce, Office of Technical Services, AD265,316 (1961).

(24) The Sb–Cl(1) bond distance is somewhat longer than the other Sb–Cl bonds; this is due to weak intermolecular bonding (see ref 15).

Table I: Chlorine Nqr Absorption Frequencies and Coupling Constants for the Complexes and the Pure Components

Atom[a]	Absorption frequency, MHz	Temp, °K	e^2Qq/h, MHz	$e^2Q\phi_{zz}/h$, MHz (calcd)[f]
		$SbCl_5 \cdot POCl_3$		
Cl(1)	25.882	77	−51.644	
Cl(1)	25.370	297	−50.740	0.373
Cl(2)	26.186	77	−52.372	
Cl(2)	25.949	297	−51.898	−0.892
Cl(3)	24.434	77	−48.868	
Cl(3)	24.465	297	−48.930	0.280
Cl(4)	30.632	77	−61.264	−0.933
Cl(5)	30.565	77	−61.130	0.083
Cl(6)	27.327(s)[e]	77	−54.654	
Cl(6)	26.890	297	−53.780	−0.021
		$SnCl_4 \cdot 2POCl_3$[b]		
Cl(1)	19.807	77	−39.614	
Cl(1)	19.110	297	−38.220	−1.234
Cl(2)	19.035	77	−38.070	
Cl(2)	18.873	297	−37.746	−1.104
Cl(3)	21.462(s)	77	−42.292	
Cl(3)	20.945	297	−41.890	−1.146
Cl(4) or Cl(6)	30.213	77	−60.426	−0.990 or −0.857[g]
Cl(5) or Cl(7)	30.117	77	−60.134	−0.883 or 0.317
		$(TiCl_4 \cdot POCl_3)_7$		
Cl(5)	29.987	77	−59.974	0.515
Cl(6)	30.112	77	−60.224	0.273
Cl(7)	30.313	77	−60.626	−0.002
		$FeCl_3 \cdot POCl_3$		
(Cl of $POCl_3$)	30.263	77	−60.526	
		$SbCl_5$[c]		
Average	29.00	77	−58.00	
		$SnCl_4$[d]		
Average	24.095	77	−48.190	
		$POCl_3$[d]		
Average	28.961	77	−57.922	

[a] The numbering of atoms refers to Figure 2. [b] $SnCl_4 \cdot 2POCl_3$ resonance frequencies at 77°K are from Biedenkapp and Weiss.[8] [c] $SoCl_5$ frequencies at 77°K are from ref 9. All frequencies marked "average" are the average of several absorption frequencies belonging to chlorines which are chemically identical in an isolated molecule. [d] Frequencies for $SnCl_4$ and $POCl_3$ from Livingston.[12] [e] The intensity of the lines marked (s) is about twice that of the other lines in the same group of metal chloride absorption frequencies. [f] Point-charge contributions to the measured field gradient in MHz; ϕ_{zz} is the component of the tensor ϕ along the bond direction. The tensor ϕ represents the field gradient arising from point charges situated in the lattice. The Sternheimer antishielding factor has not been taken into account. [g] The two numbers refer to the two atoms in column one.

For the $SnCl_4 \cdot 2POCl_3$ complex, the strongest line at 21.462 MHz is again assigned to the two equivalent chlorine atoms Cl(3) of Figure 2(b) and the lowest frequency line at 19.035 MHz to Cl(2) which is bonded to tin with the longest Sn–Cl distance, 2.36 Å. The point-charge contributions are large and negative for Cl(1), Cl(2), and Cl(3), and so do not alter these assignments. The final assignments are listed in Table I where the numbering of chlorine atoms corresponds to Figure 2.

Electronic Structures of the Adducts. The measured chlorine quadrupole coupling constants may be related to various parameters describing the chemical bonds to chlorine by the relationship[11]

$$\rho = e^2Qq(\text{exptl})/e^2qQ(\text{at}) = 1 - I - \pi - (\alpha - \delta) \quad (1)$$

where ρ is the ratio of the observed coupling constant to that for atomic chlorine. If this ratio for a chlorine atom of the $-PCl_3$ group of the adduct (ρ_1) is now compared with that for pure $POCl_3$(ρ_2), we obtain a difference

$$\Delta\rho = \rho_1 - \rho_2 = -\Delta I - \Delta\pi - \Delta(\alpha - \delta) \quad (2)$$

In these equations, I is the fractional ionic character of a given P–Cl bond, π is the π-character, and α and δ are the fractional s and d hybridizations for the bond. Since the bond lengths and bond angles for the $-PCl_3$

group of the adduct are close to those reported[25] for pure gaseous $POCl_3$, the values of π, δ, and α are probably similar and the frequency shift can then be related to the change ΔI in ionic character of the bond. Values of ρ and of $\Delta I(=-\Delta\rho)$ obtained on this assumption are given in Table II for the complexes studied (the sign denotes the direction of charge transfer). These have been computed using average chlorine resonance frequencies in those cases where the chlorine atoms of $POCl_3$ give rise to several lines.

Table II: Values of the *p*-Electron Defect ρ for Chlorine Atoms Bonded to Phosphorus and the Derived Values for the Change in Ionicity ΔI on Complex Formation

Compound	ρ	ΔI
Chlorine Atoms of $-PCl_3$ Group		
$SbCl_5 \cdot POCl_3$	0.556	−0.028
$[TiCl_4 \cdot POCl_3]_2$	0.548	−0.020
$FeCl_3 \cdot POCl_3$	0.551	−0.023
$SnCl_4 \cdot 2POCl_3$	0.549	−0.021
$POCl_3$	0.528	...
Chlorine Atoms of MCl_n Group		
$SbCl_5 \cdot POCl_3$ [Cl *cis* to oxygen (av)]	0.486	0.051
$SbCl_5 \cdot POCl_3$ [Cl *trans* to oxygen]	0.445	0.092
$SnCl_4 \cdot 2POCl_3$ [Cl *cis* to both oxygen atoms (av)]	0.391	0.048
$SnCl_4 \cdot 2POCl_3$ [Cl *trans* one oxygen atom]	0.354	0.085
$SnCl_4$ [av]	0.439	...
$SbCl_5$ [av]	0.529	...

In going from free $POCl_3$ to adduct, the chlorine resonance frequency should change and this change should be proportional to the strength of the metal–oxygen bond formed. Since this bond in the adduct is formed by transfer of charge from $POCl_3$ to the Lewis acid ($SbCl_5$, $TiCl_4$, etc.), the stronger the bond the greater will be the transfer of charge and the greater the expected decrease in ionicity of the P–Cl bond and increase in ionicity of the M–Cl bond. The increase in chlorine resonance frequency for the chlorine atoms bonded to phosphorus and the decrease for chlorine atoms bonded to metal (compared to the $POCl_3$ and MCl_n frequencies) should both be larger for a larger transfer of charge and stronger M–O bond formed. These differences should then provide an order of strengths for the Lewis acids relative (in this case) to the base $POCl_3$.

The quantity ΔI may be interpreted as the fraction of an electronic charge transferred from chlorine to phosphorus on forming the complex and the order of Lewis acid strengths obtained in $SbCl_5 > FeCl_3 > SnCl_4 > TiCl_4$. This ordering is the same as found by chemical methods.[26]

It is similarly possible to obtain values of ΔI by comparing the coupling constants for the chlorine atoms bonded to the metal in the adduct and pure metal chlorides. In the case of $SnCl_4 \cdot 2POCl_3$, two types of chlorine atoms may be distinguished, the two Cl(3) atoms which are *cis* to both oxygen atoms and the remaining two atoms Cl(1) and Cl(2) each of which is *trans* to one of the oxygen atoms. Since two groups of absorption frequencies are found (Table I), we will associate them with the two different classes of chlorine atom in agreement also with the observed line intensities. We may compute a value of $\Delta\rho$ for each group and find $\Delta\rho$ (Cl(1) and Cl(2)) $= -0.085$ and $\Delta\rho$ (Cl(3)) $= -0.048$. It is clear from the $\Delta\rho$ values found that a transfer of charge from tin to chlorine has taken place on adduct formation, and the values suggest a smaller increase in ionic character for the Sn–Cl(3) bond ($\Delta I = +0.048$) than for the Sn–Cl(2) [or Cl(1)] bond for which $\Delta I = +0.085$. Similarly, if the averages of the observed chlorine frequencies at 77°K for chlorine atoms of the $-SbCl_5$ group *cis* and *trans* to oxygen in $SbCl_5 \cdot POCl_3$ are used along with the average for $SbCl_5$ itself, values of $\Delta\rho(=-\Delta I)$ of +0.043 and +0.084 are calculated, respectively. Again, the increase in ionic character is smaller for the chlorine atoms *cis* to oxygen in the adduct.

Temperature Dependence of the Nqr Lines. The chlorine nqr lines observed at 77°K for those chlorine atoms bonded to metal in the adduct remain, with nearly unchanged intensity, on warming to room temperature (Table I), while the resonances for chlorine atoms of the $-PCl_3$ groups disappear somewhat below room temperature. A similar "fade-out" of chlorine resonances has been reported[27] for a number of compounds (CH_2Cl_2, CH_3CCl_3, etc.) known to undergo internal rotations above a certain temperature in the solid phase. A similar mechanism may operate here and the disappearance of the $-PCl_3$ chlorine resonances could result from internal rotation of the $-PCl_3$ group about its (approximate) threefold axis. This view is supported by the unusually large X-ray temperature factors found[15,17] for the chlorine atoms bonded to phosphorus in $SbCl_5 \cdot POCl_3$ and $[TiCl_4 \cdot POCl_3]_2$ and by the large average temperature factor reported[16] for $SnCl_4 \cdot 2POCl_3$. Further, the temperature dependence of the 27.327-MHz line of $SbCl_5 \cdot POCl_3$ (Figure 1) suggests that a phase transition of some type occurs between 77 and 165°K. The fact that only two resonances are observed for $POCl_3$ in $SnCl_4 \cdot 2POCl_3$, whereas four are expected on the basis of the crystal structure (see Figure 2), could then be explained by assuming a lower barrier hindering rotation in one $-PCl_3$ group so that even at 77°K the resonances for that set would be lost while those for the second set

(25) G. Badgley and R. Livingston, *J. Am. Chem. Soc.*, **76**, 261 (1954).

(26) V. Gutmann, U. S. Department of Commerce, Office of Technical Services, PB Rept. 152,848 (1960), and private communication.

(27) H. S. Gutowsky and D. McCall, *J. Chem. Phys.*, **32**, 548 (1960).

would only disappear at higher temperatures. Some preliminary measurements on $TiCl_4 \cdot 2POCl_3$, which is isomorphous[28] with $SnCl_4 \cdot 2POCl_3$, seem to indicate that all four expected resonances for chlorine bonded to phosphorus are present.

Acknowledgment. The assistance of Dr. V. Nagarajan and Mr. Michael Buckley in some of the experimental work is gratefully acknowledged.

(28) C. Brändén, *Acta Chem. Scand.*, **16**, 1806 (1962).

Excess Properties of Some Aromatic–Alicyclic Systems. III. Analysis of H^E and V^E Data in Terms of the Theory of Flory[1]

by G. C. Benson and Jaswant Singh[2]

Division of Pure Chemistry, National Research Council of Canada, Ottawa, Canada *(Received October 23, 1967)*

The Flory theory of nonpolar solutions is used to analyze previously published data for the thermodynamic properties of a number of aromatic–alicyclic systems. Values of the excess enthalpy and excess volume can be correlated fairly well by the theory.

Introduction

Part I[3] of this series presented the results of measurements of molar excess enthalpies (H^E) and molar excess volumes (V^E) at 25° for eight binary aromatic–alicyclic systems formed by mixing either benzene or toluene with cyclopentane, cyclohexane, cycloheptane, and cyclooctane. The data were examined[4] from the point of view of the Scatchard–Hildebrand equation,[5] the quasi-lattice theory of Barker,[6] and the Prigogine corresponding states average potential model.[7] Although each of these approaches provided some basis for analysis of the results, none was particularly satisfactory.

Recently Flory[8] has developed a statistical theory for mixtures of nonpolar molecules differing in size, which should be quite suitable for describing the properties of aromatic–alicyclic systems. The few calculations for benzene–cyclohexane carried out by Abe and Flory[9] support this view, and the theoretical estimates of the excess volumes of an equimolar mixture are in excellent agreement with the experimental results over a range of temperatures.

The present paper describes the analysis of H^E and V^E data from ref 3 in terms of Flory's theory. It thus provides a more extensive examination of the applicability of the theory to aromatic–alicyclic systems.

Flory's Theory of Binary Mixtures

This section summarizes the equations of the Flory theory which are needed for the subsequent application. With a few minor exceptions, Flory's notation has been followed closely; reference should be made to the original paper[8] for details of the derivations.

A molecule is considered to be made up of segments (isometric portions), the effective number being r. Each segment has s intermolecular contact sites capable of interacting with neighboring sites. In the liquid state, the volume per mole of segments is denoted by v, and the corresponding "hard-core" or "characteristic" volume by v^*. The molar values of these are indicated by

$$\mathrm{v} = rv \tag{1}$$

and

$$\mathrm{v}^* = rv^* \tag{2}$$

respectively. The reduced volume of a mole of segments is

$$\tilde{v} = v/v^* = \mathrm{v}/\mathrm{v}^* \tag{3}$$

(1) Issued as Nationa Research Council No. 10070.

(2) National Research Council of Canada Postdoctorate Fellow 1965–1967.

(3) A. E. P. Watson, I. A. McLure, J. E. Bennett, and G. C. Benson, *J. Phys. Chem.*, **69**, 2753 (1965).

(4) I. A. McLure, J. E. Bennett, A. E. P. Watson, and G. C. Benson, *ibid.*, **69**, 2759 (1965).

(5) J. H. Hildebrand and R. L. Scott, "Regular Solutions," Prentice-Hall Inc., Englewood Cliffs, N. J., 1962, Chapter 7.

(6) J. A. Barker, *J. Chem. Phys.*, **20**, 1526 (1952)

(7) I. Prigogine, "The Molecular Theory of Solutions," North Holland Publishing Co., Amsterdam, 1957, Chapters 10, 11.

(8) P. J. Flory, *J. Amer. Chem. Soc.*, **87**, 1833 (1965).

(9) A. Abe and P. J. Flory, *ibid.*, **87**, 1838 (1965); see also P. J. Flory and A. Abe, *ibid.*, **86**, 3563 (1964).

and can be calculated from the coefficient of thermal expansion (α) using the expression

$$\tilde{v} = [(1 + {}^4/_3\alpha T)/(1 + \alpha T)]^3 \quad (4)$$

At zero pressure, the reduced volume and reduced temperature ($\tilde{T}$) are related by the equation of state

$$\tilde{T} = (\tilde{v}^{1/3} - 1)/\tilde{v}^{4/3} \quad (5)$$

This is the central equation of Flory's theory. The characteristic temperature T^* and pressure p^* are obtained from the relations

$$T^* = T/\tilde{T} \quad (6)$$

and

$$p^* = \gamma T\tilde{v}^2 \quad (7)$$

where

$$\gamma = \alpha/\beta \quad (8)$$

is the thermal pressure coefficient and β is the isothermal compressibility.

It can be shown that the reduced temperature of a mixture of two species of molecules (indicated by subscripts 1 and 2) at mole fraction x_1 is given by

$$\tilde{T} = (\phi_1 p^*_1 \tilde{T}_1 + \phi_2 p^*_2 \tilde{T}_2)/(\phi_1 p^*_1 + \phi_2 p^*_2 - \phi_1\theta_2 X_{12}) \quad (9)$$

where the segment fractions ϕ_1 and ϕ_2 are defined by

$$\phi_2 = 1 - \phi_1 = x_2/\left(x_2 + x_1\left(\frac{r_1}{r_2}\right)\right) \quad (10)$$

and the site fraction θ_2 by

$$\theta_2 = \phi_2/\left(\phi_2 + \phi_1\left(\frac{s_1}{s_2}\right)\right) \quad (11)$$

The molar excess enthalpy, excess volume, and residual[10] entropy of the mixture are

$$H^E = x_1 p^*_1 v^*_1(\tilde{v}_1^{-1} - \tilde{v}^{-1}) + x_2 p^*_2 v^*_2(\tilde{v}_2^{-1} - \tilde{v}^{-1}) + x_1 v^*_1 \theta_2 X_{12}\tilde{v}^{-1} \quad (12)$$

$$V^E = (x_1 v^*_1 + x_2 v^*_2)(\tilde{v} - \phi_1\tilde{v}_1 - \phi_2\tilde{v}_2) \quad (13)$$

and

$$S^R = -3\left[\frac{x_1 p^*_1 v^*_1}{T^*_1}\ln\left(\frac{\tilde{v}_1^{1/3} - 1}{\tilde{v}^{1/3} - 1}\right) + \frac{x_2 p^*_2 v^*_2}{T^*_2}\ln\left(\frac{\tilde{v}_2^{1/3} - 1}{\tilde{v}^{1/3} - 1}\right)\right] \quad (14)$$

In eq 9 and 12, X_{12} is a constant characterizing the difference in the energy of interaction between sites on neighboring molecules of species 1 and 2, from the average of the interactions in the pure component liquids.

Treatment of Data for Aromatic–Alicyclic Systems

The geometric parameters r and s enter the equations for the excess properties of mixtures only as the ratios r_1/r_2 and s_1/s_2. Since the same hard core volume is adopted for segments of both species, it follows from eq 2 that

$$\frac{r_1}{r_2} = \frac{v^*_1}{v^*_2} \quad (15)$$

Abe and Flory[9] assumed that the numbers of contact sites on the benzene and cyclohexane molecules were proportional to the surface areas of spheres having the same core volumes, and deduced that

$$\frac{s_1}{s_2} = \left(\frac{v^*_2}{v^*_1}\right)^{1/3} \quad (16)$$

These relations will be used for the eight systems considered here.

The values of the properties of the component liquids are summarized in Table I where corresponding values of the characteristic volumes, temperatures, and pressures are also given.

Table I:[a] Parameters for the Pure Liquids at 25°

	v,[b] cm³ mol⁻¹	$10^3\alpha$, deg⁻¹	$10^6\beta$, atm⁻¹	v^*, cm³ mol⁻¹	T^*, deg K	p^*, J cm⁻³
C_6H_6	89.43	1.217[c,d]	98.12[e]	69.30	4720	624.1
C_7H_8	106.84	1.071[c]	95.0[f]	84.65	5040	542.5
C_5H_{10}	94.74	1.325[c]	135.1[g]	72.28	4531	509.0
C_6H_{12}	108.85	1.217[c]	115.5[e]	84.34	4720	530.2
C_7H_{14}	121.62	1.00[c]	98.0[h]	97.48	5231	479.9
C_8H_{16}	134.96	0.99[c]	81.2[i]	108.34	5260	571.5

[a] Data for α and β are the same as given in ref 4, except for correction of printing errors. [b] Based on density values from ref 3. [c] American Petroleum Institute, Research Project 44, Carnegie Press, Pittsburgh, Pa., 1953, and later revisions. [d] S. E. Wood and A. E. Austin, *J. Amer. Chem. Soc.*, **67**, 480 (1945). [e] G. A. Holder and E. Whalley, *Trans. Faraday Soc.*, **58**, 2095 (1962). [f] B. Jacobson, *Acta Chem. Scand.*, **6**, 1485 (1952). [g] A. Weissler, *J. Amer. Chem. Soc.*, **71**, 419 (1949). [h] Estimated by interpolation of data for the other cycloparaffins. [i] E. Butta, *Ric. Sci.*, **26**, 3643 (1956).

Evaluation of the excess enthalpy and volume of a binary mixture from eq 12 and 13 requires, in addition to data for the pure component liquids, a knowledge of the interaction energy X_{12}. This quantity was treated by Abe and Flory[9] as an adjustable parameter and its value was chosen to fit H^E in an equimolar solution. In the present investigation, we have calculated X_{12} from the individual values of H^E and V^E over the full concentration range. The results for benzene and toluene systems are shown in Figures 1 and 2, respec-

(10) It should be noted that Flory employs the term *residual* to indicate the normal thermodynamic function for mixing exclusive of the combinatorial term. This differs from earlier usage by J. S. Rowlinson in "Liquids and Liquid Mixtures," Butterworth and Co., Ltd., London, 1959.

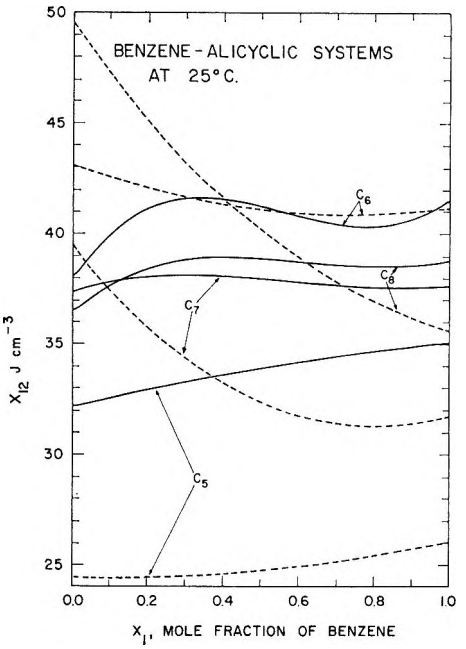

Figure 1. Variation of parameter X_{12} for benzene systems: solid curves, values determined from H^E; broken curves, determined from V^E. Curves are labeled with number of carbon atoms in cycloparaffin.

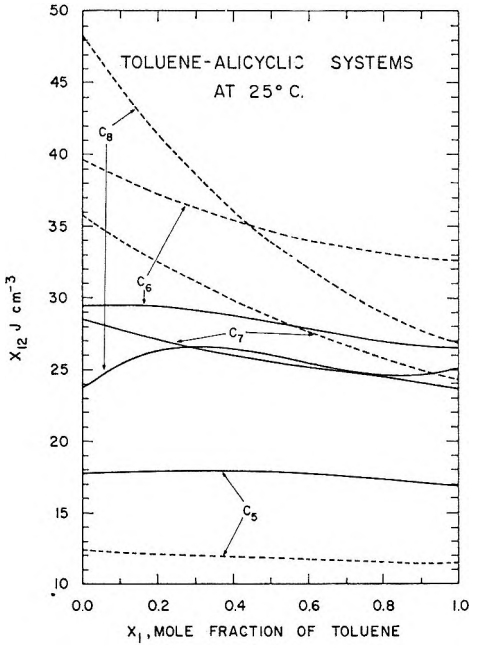

Figure 2. Variation of parameter X_{12} for toluene systems: solid curves, values determined from H^E; broken curves, from V^E. Curves are labeled with number of carbon atoms in cycloparaffin.

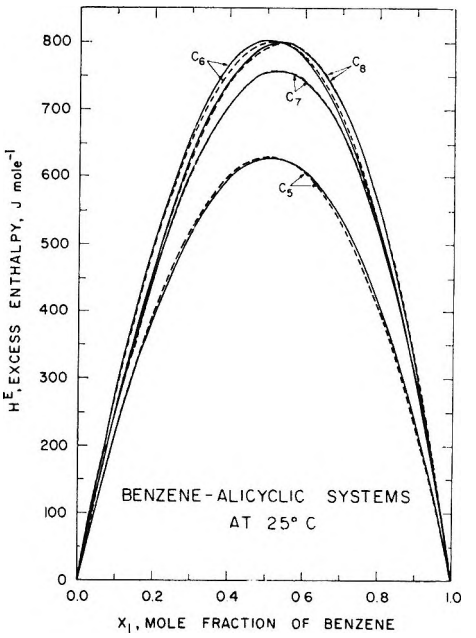

Figure 3. Excess enthalpies of benzene systems: solid curves, based on experimental results from ref 3; broken curves, calculated from eq 12 with X_{12} from second column of Table II. Curves are labeled with number of carbon atoms in cycloparaffin.

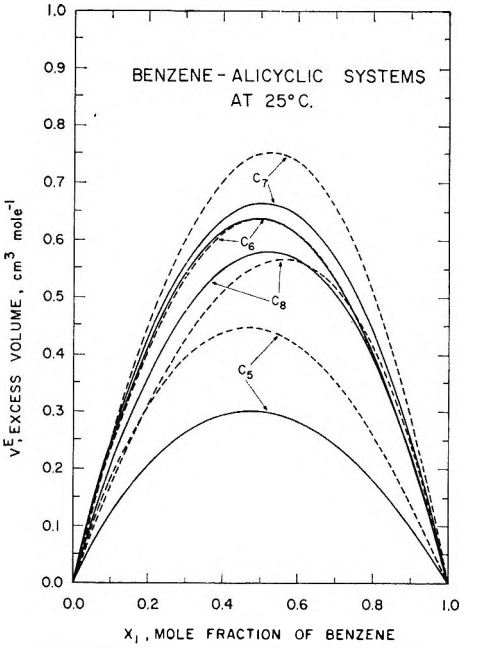

Figure 4. Excess volumes of benzene systems: solid curves, based on experimental results from ref 3; broken curves, calculated from eq 13 with X_{12} from second column of Table II. Curves are labeled with number of carbon atoms in cycloparaffin.

tively. It is clear from these that, in general, different values of X_{12} are required to fit H^E at each concentration. Also, at any one concentration, different values of X_{12} are determined from the fit of H^E and of V^E, values of X_{12} obtained from V^E generally show a somewhat wider variation with concentration. The relative positions of the curves in Figures 1 and 2 show an interesting parallel between the variation of X_{12} for the benzene and toluene systems. The benzene–cyclohexane system conforms most nearly to the behavior required by the Flory theory, but even in this case there is an over-all spread of about 5 J cm^{-3} in the values of X_{12}.

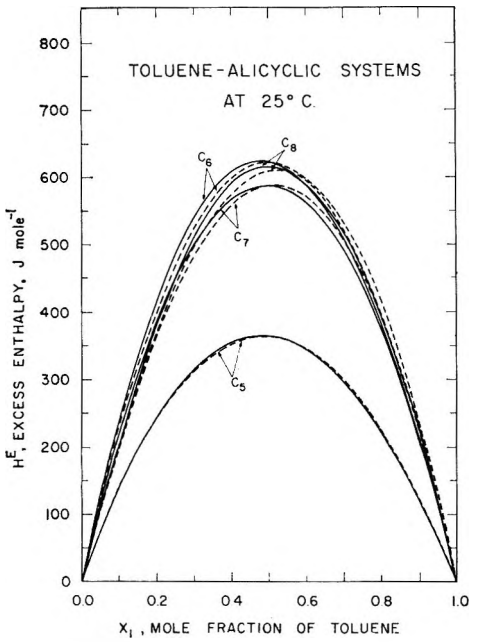

Figure 5. Excess enthalpies of toluene systems: solid curves, based on experimental results from ref 3; broken curves, calculated from eq 12 with X_{12} from second column of Table II. Curves are labeled with number of carbon atoms in cycloparaffin.

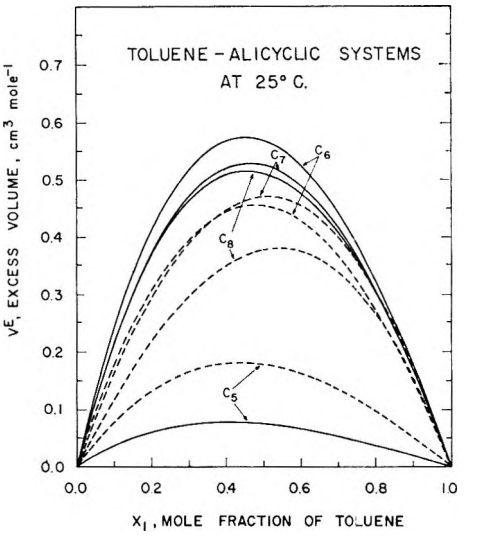

Figure 6. Excess volumes of toluene systems: solid curves, based on experimental results from ref 3; broken curves, calculated from eq 13 with X_{12} from second column of Table II. Curves are labeled with number of carbon atoms in cycloparaffin.

The values of X_{12} giving the best (least-squares) fit either of the experimental H^E data or of the experimental V^E data were determined by minimizing either the integral

$$\sigma_H^2(X_{12}) = \int_0^1 (H^E_{\text{exptl}} - H^E_{\text{Flory}}(X_{12}))^2 \, dx_1 \quad (17)$$

or the integral

$$\sigma_V^2(X_{12}) = \int_0^1 (V^E_{\text{exptl}} - V^E_{\text{Flory}}(X_{12}))^2 \, dx_1 \quad (18)$$

In the case of the fit of H^E_{exptl}, the resulting X_{12} was used to calculate V^E_{Flory}, and, alternatively, X_{12} determined from V^E_{exptl} was used to calculate H^E_{Flory}. These computations are summarized in Table II where X_{12}, σ_H, and σ_V are given for the two ways of fitting the experimental data. In general the use of H^E_{exptl} to determine X_{12} leads to a better agreement between theoretical and experimental values. This is not surprising since as noted by Abe and Flory,[9] X_{12} is an energy parameter which enters the formula for V^E only implicitly through the reduced temperature $\tilde{T}$ of the mixture: thus it appears more logical to determine its value from the enthalpy, which is an explicit function of X_{12}, as well as depending on it through $\tilde{T}$. Figures 3–6 compare the experimental values of H^E and V^E (solid curves) with those calculated from eq 12 and 13 (broken curves) using the X_{12} values based on the fit of H^E (as given in the second column of Table II).

Assuming that the combinatorial entropy of mixing is ideal, the excess Gibbs free energy can be calculated from the relation

$$G^E = H^E - TS^R \quad (19)$$

The broken curves in Figures 7 and 8 were computed in this way. Experimental data for three of the systems[11-13] are shown as solid curves. In these cases the theoretical values of G^E are 1.5 to 2 times larger than observed experimentally.[14]

Considering the very simple equation of state on which the Flory theory is based, the properties of the

Table II: Values of X_{12} Determined from Least-Square Fit of H^E and of V^E

	Fit of H^E data			Fit of V^E data		
System	X_{12}, J cm^{-3}	σ_H, J mol^{-1}	σ_V, cm^3 mol^{-1}	X_{12}, J cm^{-3}	σ_H, J mol^{-1}	σ_V, cm^3 mol^{-1}
C_6H_6–C_5H_{10}	33.84	7.4	0.105	24.76	123.8	0.003
C_6H_6–C_6H_{12}	41.02	6.9	0.005	41.25	7.6	0.005
C_6H_6–C_7H_{14}	37.87	3.0	0.061	32.69	76.7	0.016
C_6H_6–C_8H_{16}	38.68	3.4	0.030	40.02	20.8	0.026
C_7H_8–C_5H_{10}	17.69	3.1	0.076	11.80	91.1	0.002
C_7H_8–C_6H_{12}	28.25	12.7	0.089	34.94	109.4	0.017
C_7H_8–C_7H_{14}	25.53	13.9	0.049	28.79	56.8	0.027
C_7H_8–C_8H_{16}	25.68	12.0	0.108	33.89	144.1	0.046

(11) G. Scatchard, S. E. Wood, and J. M. Mochel, *J. Phys. Chem.*, **43**, 119 (1939).

(12) R. W. Hermsen and J. M. Prausnitz, *Chem. Eng. Sci.*, **18**, 485 (1963).

(13) T. Katayama, E. K. Sung, and E. N. Lightfoot, *A.I.Ch.E. J.*, **11**, 924 (1965).

(14) The Barker theory, as applied in ref 4, also led to values of G^E which were too large; the discrepancies (not reported previously) were similar in magnitude to those noted above.

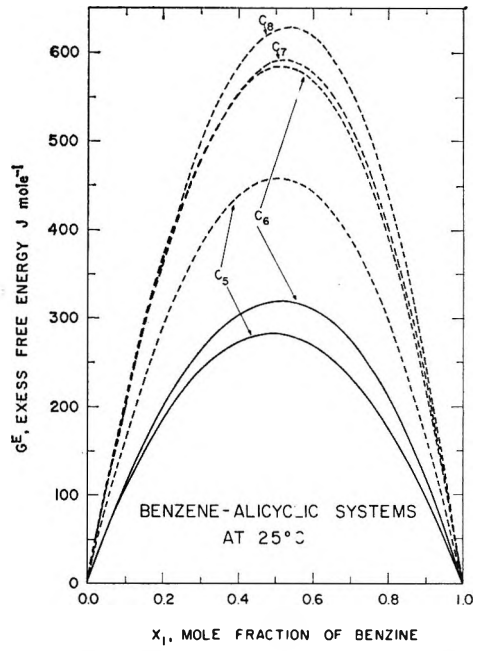

Figure 7. Excess Gibbs free energy of benzene systems: solid curves, based on experimental results from ref 10 and 11; broken curves, calculated from eq 14 and 19 with X_{12} from second column of Table II. Curves are labeled with number of carbon atoms in cycloparaffin.

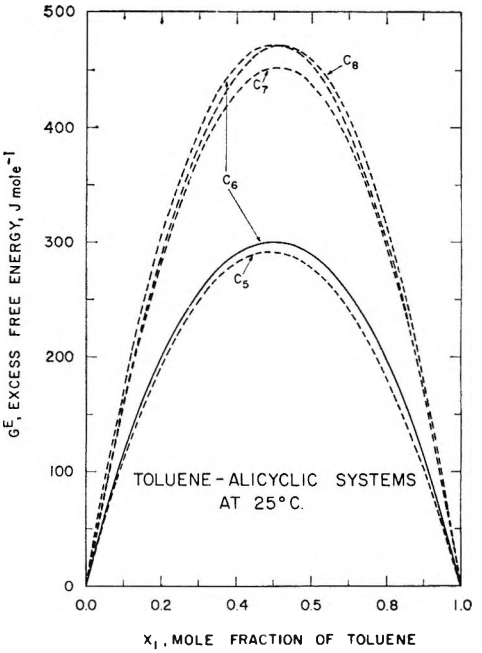

Figure 8. Excess Gibbs free energy of toluene systems: solid curve, based on experimental results from ref 12; broken curves, calculated from eqs 14 and 19 with X_{12} from second column of Table II. Curves are labeled with number of carbon atoms in cycloparaffin.

aromatic–alicyclic systems considered in this paper are correlated fairly well by it. Abe and Flory[9] have discussed the dependence of the theoretical values on the precision of the data for the pure component liquids. Of the present set of systems, undoubtedly the values of the properties of benzene and cyclohexane are the most accurate: possibly, some of the discrepancies between theory and experiment may be attributed to inaccuracies of data for the other liquids.

Acknowledgment. The authors wish to thank Mr. A. Potworowski for computational assistance.

Solution Kinetics *via* Fluorescence Quenching—Transient and Solvent Effects

by J. Q. Umberger

Holmdel, New Jersey 07733 *(Received October 23, 1967)*

The Smoluchowski–Sveshnikoff diffusion treatment is modified in accordance with new experimental data particularly for high concentrations of quencher. The data indicate that proton transfer from the solvent to the photoexcited dye, in polarized association with the quencher, might be the quantum event leading to quenching of uranin.

Introduction

The Smoluchowski[1] treatment of collision processes in solution was generalized by Umberger and La Mer[2]—following Debye[3]—for diffusion in a potential field as in the case of ions. In applying this Fick's law calculation to their fluorescence-quenching measurements, Umberger and La Mer included the transient by which Sveshnikoff[4] rationalized departures from Stern–Volmer kinetics. At the suggestion of Kimball, however, the subsequent coworkers[5-7] of La Mer abandoned the transient. Later, in a theoretical paper, Kimball and Collins[8] reconsidered and generalized Smoluchowski's boundary condition; this vindicated transient diffusion for fluorescence quenching, in general, and the original Smoluchowski boundary condition for rapid quenching, in particular.

The above diffusion treatments emphasize the influence of solvent viscosity and dielectric strength, but Umberger[9,10] has recently shown that solvent proticity, or H-bond donor strength, also can influence fluorescence quenching. The general equation of Collins and Kimball has proven unwieldy in interpreting solvent and transient effects;[11,12] thus simpler boundary condition and equation are presented and tested against new quenching data.

Theory

Calculation of the Quenching Constant, k_q°, for Low Concentration of Quencher. In the calculation of Sveshnikoff,[4] the excited dye molecule is made the center of diffusion, but the calculation is easier when the quencher is made the center—provided the individual quencher molecules are far apart.

At the photostationary state, the average concentration, N, of excited dye molecules at distance r from the central quencher is independent of time, *i.e.*

$$\frac{\partial N}{\partial t} = 0 = D\nabla\cdot\frac{\overrightarrow{\partial N}}{\partial r} - \frac{N}{\tau_0} + \text{constant} \qquad (1)$$

excess of in-diffusing over out-diffusing excited dye molecules/cc sec; loss of excited dye molecules by fluorescence/cc sec; formation of excited dye molecules by light absorption/cc sec

or

$$0 = \frac{D}{r}\frac{\mathrm{d}^2(rN)}{\mathrm{d}r^2} - \frac{N}{\tau_0} + \frac{N_0}{\tau_0} \qquad (2)$$

The boundary conditions are: (a) when $r = \infty$, $N = N_0$, where N_0 is the concentration of excited dye molecules in the absence of quencher; (b) when $r = R$, $N = aN_0$, where a is a constant less than unity. Quenching starts at this center-to-center distance between dye and quencher: $R = r_d + r_q + \delta$, *i.e.*, R exceeds, by small amount δ, the sum of the radii of dye and quencher.

The solution of eq 2 with boundary conditions (a) and (b) is

$$N = N_0\left[1 - (1-a)\frac{R}{r}\exp\left(\frac{R-r}{\sqrt{\tau_0 D}}\right)\right] \qquad (3)$$

$$\left.\frac{\mathrm{d}N}{\mathrm{d}r}\right]_R = (1-a)\frac{N_0}{R}\left[1 + \frac{R}{\sqrt{\tau_0 D}}\right] \qquad (4)$$

Equations 3 and 4 apply when $r \geqq R$. It is assumed that quenching occurs within the spherical shell of thickness δ and volume $v = 4\pi R^2\delta$, *i.e.*, between $r = R$ and $r = R - \delta$. The shell is assumed sufficiently thin that the concentration of excited dye molecules within is maintained at aN_0 by the diffusion

(1) M. V. Smoluchowski, *Ann. Physik*, **48**, 1103 (1915); *Z. Physik. Chem.*, **92**, 129 (1917).

(2) J. Q. Umberger and V. K. La Mer, *J. Am. Chem. Soc.*, **67**, 1099 (1945).

(3) P. Debye, *Trans. Electrochem. Soc.*, **82**, 265 (1942).

(4) B. Sveshnikoff, *Acta Physicochim. U.R.S.S.*, **3**, 257 (1935).

(5) B. Williamson and V. K. La Mer, *J. Am. Chem. Soc.*, **70**, 717 (1948).

(6) K. C. Hodges and V. K. La Mer, *ibid.*, **70**, 722 (1948).

(7) J. C. Rowell and V. K. La Mer, *ibid.*, **73**, 1630 (1951).

(8) F. C. Collins and G. E. Kimball, *J. Colloid Sci.*, **4**, 425 (1949); **5**, 499 (1950); *Ind. Eng. Chem.*, **41**, 2551 (1949).

(9) (a) J. Q. Umberger, *J. Phys. Chem.*, **71**, 2054 (1967); (b) *ibid.*, **71**, 4588 (1967).

(10) (a) J. Q. Umberger, *Phot. Sci. Eng.*, **11**, 385 (1967); (b) *ibid.*, **11**, 392 (1967).

(11) (a) R. M. Noyes, *J. Am. Chem. Soc.*, **86**, 4529 (1964); (b) *ibid.*, **79**, 551 (1957); (c) *J. Phys. Chem.*, **69**, 3182 (1965); (d) *Progr. Reaction Kinetics*, **1**, 131 (1961).

(12) W. R. Ware and J. S. Novros, *J. Phys. Chem.*, **70**, 3246 (1966).

$$0 = 4\pi R^2 D \left.\frac{dN}{dr}\right]_R - \frac{aN_0 v}{\tau_0} - \frac{aN_0 v}{\tau_q} + \frac{N_0 v}{\tau_0} \quad (5)$$

diffusion of excited dye molecules into the shell; loss of excited dye molecules from the shell by fluorescence; loss of excited dye molecules from the shell by quenching; formation of excited dye molecules in the shell by light absorption

The effect of possible association between quencher and dye, prior to excitation, is considered later.

The quenching constant at low concentration of quencher is $k_q^\circ = av\tau_0/\tau_q$, where τ_q is the average time required for quenching of excited dye molecules within the shell. On inserting the value of a obtained by eliminating $dN/dr]_R$ from eq 4 and 5, k_q° becomes

$$k_q^\circ = \frac{[4\pi R\tau_0 D(1 + R/\sqrt{\tau_0 D}) + v]}{1 + [4\pi R\tau_0 D(1 + R/\sqrt{\tau_0 D}) + v]\tau_q/(\tau_0 v)} \quad (6)$$

The three terms in the numerator of eq 6, *viz.*, $4\pi R\tau_0 D$, $4\pi R^2\sqrt{\tau_0 D}$, and v, depend, respectively, on the first power, the one-half power, and the zeroth power of the diffusion constant D. These terms might be regarded as arising, respectively, when dye and quencher are originally far apart, at medium distance requiring less diffusion for quenching, and in the quenching shell requiring no diffusion. This last term represents static quenching.

Equation 6 can be simplified if v is small and if τ_q is replaced by δ/k, where k is the specific quenching rate of Collins and Kimball[8]

$$k_q^\circ = \frac{4\pi R\tau_0 D(1 + R/\sqrt{\tau_0 D})}{1 + (1 + R/\sqrt{\tau_0 D})D/kR} \quad (7)$$

Equation 7 can be confirmed by the alternate calculation where the excited dye molecule is made the center of diffusion. The correct expression for the quencher flux, Φ_m, is[8]

$$\Phi_m = 4\pi R^2 D\left(\frac{\partial C}{\partial r}\right)_R = 4\pi D C_0\left[R - \beta + \frac{(R-\beta)^2}{\beta} e^{Dt/\beta^2}\,\mathrm{erfc}\frac{\sqrt{Dt}}{\beta}\right]$$

This, when employed in the Sveshnikoff-type calculation, yields

$$I/I_0 = \frac{1}{\tau_0}\int_0^\infty \exp\left\{-(t/\tau_0) - 4\pi D C_0 \int \times \left[R - \beta + \frac{(R-\beta)^2}{\beta} e^{Dt/\beta^2}\,\mathrm{erfc}\frac{\sqrt{Dt}}{\beta}\right]dt\right\}dt \quad (8)$$

where the symbols are those of Collins and Kimball. Equation 8 can be integrated at low concentrations of quencher, C_0, for then the complicated exponential can be simply expanded. In this way, eq 9 is ultimately obtained.

$$k_q^\circ = 4\pi R^2 k\tau_0\left[1 - \frac{kR}{D}\left(\frac{\sqrt{\tau_0 D}}{R} - \frac{\tau_0 D}{\beta R} \cdots\right)\right] \quad (9)$$

When rearranged and expanded, eq 7 can be placed in a form agreeing exactly with eq 9.

Calculation of the Quenching Constant, k_q, for Any Concentration of Quencher. Though eq 8 must be integrated exactly to obtain k_q for all, including high, concentrations of quencher, a good approximation for moderate concentrations is obtained if the following expression is employed for C as a function of time and distance from the central excited dye molecule

$$C = C_0\left[1 - (1-a)\frac{R}{r}\left(1 - \mathrm{erf}\frac{r-R}{\sqrt{4Dt}}\right)\right] \quad (10)$$

In eq 10 when $r = R$, $C = aC_0$; when $r = \infty$, $C = C_0$; when $t = \infty$, $C = C_0[1 - (1-a)R/r]$; when $t = 0$, $C = C_0$ except at $r = R$. These represent the boundary conditions for actual quenching except that the initial concentration of quencher within the thin quenching shell at $r = R$ actually should be C_0 rather than aC_0. This difference can be allowed for if, on excitation, the central dye molecule is assumed to react instantaneously with a fraction, $(1 - a)$, of the original amount of quencher, vC_0, in the shell. In other words, very rapid static quenching is assumed to reduce the quencher concentration in the shell to aN_0 before significant diffusion occurs. With eq 10 and corrected boundary condition at $r = R$, Sveshnikoff's method of calculation now yields

$$I_0[1 - (1-a)vC_0]/I = (1 + \alpha\tau_0)\delta \quad (11)$$

where $\alpha = 4\pi RDN_A[Q](1-a)/1000$; $1/\delta = 1 - 2\gamma e^{\gamma^2}\left[\sqrt{\pi}/2 - \int_0^\gamma e^{-z^2}\,dz\right]$; $\gamma = (R/\sqrt{\pi D})\alpha/(\alpha + 1/\tau_0)^{1/2}$; [Q] = concentration of quencher in moles per liter; N_A = Avogadro's constant.

At low concentrations of quencher, eq 11 correctly reduces to an expression for k_q° identical with eq 6. At somewhat higher concentrations of quencher and when v is small, eq 11 can be expanded in a form useful for interpreting experimental data

$$k_q/k_q^\circ = 1 + \frac{\frac{\pi-2}{\pi} + \frac{\sqrt{g}}{2}}{(1+\sqrt{g})^2}(k_q^\circ[Q]) + \frac{\frac{(\pi-3)}{\pi} - \frac{g}{8}}{(1+\sqrt{g})^3}(k_q[Q])^2 \quad (12)$$

where the dimensionless parameter $g = \tau_0 D/R^2$. This predicts an almost linear plot of k_q/k_q° *vs.* $k_q^\circ[Q]$ with slope $[(\pi-2)/\pi + \sqrt{g}/2]/(1+\sqrt{g})^2$. There should, however, be slight downward curvature as predicted from the small negative value of the second derivative, $[2(\pi-3)/\pi - g/4]/(1+\sqrt{g})^3$, and from the requirement that k_q must approach the value $4\pi R^2 k\tau_0$ at large

Table I: k_q *vs.* Solvent Proticity for Fluorescein Dianion (Uranin)

Solvent	Relative viscosity[a] at 25°	Dielectric constant at 25°	k_q[b] (iodide quenching) at 27°	k_q[b] (aniline quenching) at 27°	H-bond donor strength[a]
Water	17.1 sec	79	15	28	Strong
Methanol	13.4	33	1.5	19	Med. strong
Ethanol	24.1	24	...	10	Medium
Dimethyl-formamide (DMF)	16.2	38	0.0	5	Weak

[a] Drainage time of pure solvent through vacuum-jacketed glass capillary. [b] $k_q = ((I_0/I) - 1)/[Q]$ l./mole: I_0 is fluorescence of 10^{-5} *M* uranin in 90% organic solvent + 10% H_2O by volume; I is fluorescence of same but 0.10 *M* in KI or 0.05 *M* in aniline; materials were analytical reagent where available.

concentrations of quencher. The slope of the plot should be greater than predicted by eq 12 if the quenching shell thickness, δ, becomes appreciable compared with R, then

$$k_q/k_q^\circ = 1 + \left[\frac{\frac{\pi - 2}{\pi} + \frac{\sqrt{g}}{2}}{(1 + \sqrt{g})^2} + \frac{\frac{\delta}{R}}{g + \sqrt{g}}\right] k_q^\circ [Q] \qquad (13)$$

Experimental Section

In measuring the effect of transient diffusion on quenching, k_q was determined for: (a) 10^{-6} *M* fluorescein with NaOH added to about pH 12 and employing aniline hydrochloride (plus NaOH to neutralize to pH 12) as quencher in 0.02, 0.04, 0.08, and 0.16 *M* concentrations; (b) 10^{-5} *M* fluorescein in presence of 0.002 *M* $HClO_4$ and employing KI as quencher in 0.02, 0.04, 0.08, and 0.16 *M* concentrations; and (c) 10^{-6} *M* fluorescein with NaOH added to pH 12 and employing KI as quencher in 0.02, 0.04, 0.08, and 0.16 *M* concentrations. Since (c) involves reactants both of which are charged, the ionic strength was kept constant and high by adding KNO_3 to make total salt including KI equal to 1.16 *M*. These dye concentrations were low enough to make the correction for fluorescence reabsorption, first reported by Umberger and La Mer,[2] relatively insignificant. The average data for (a), (b), and (c) are plotted in Figure 1. The excitation wavelengths were: (a) 480 mμ; (b) 410, 425, and 430 mμ in different runs: and (c) 480 mμ. The fluorescence intensities were read at: (a) 535 and 570 mμ in different runs; (b) 520, 550, and 570 mμ in different runs; and (c) 535 and 570 mμ in different runs.

Solvents with similar viscosities and dielectric constants but with differing H-bond donor strengths were tested for effect on quenching constant. In Table I are listed such solvents, their relevant properties, and fluorescence quenching constants in a mixture of 9 parts of solvent and 1 part of water.

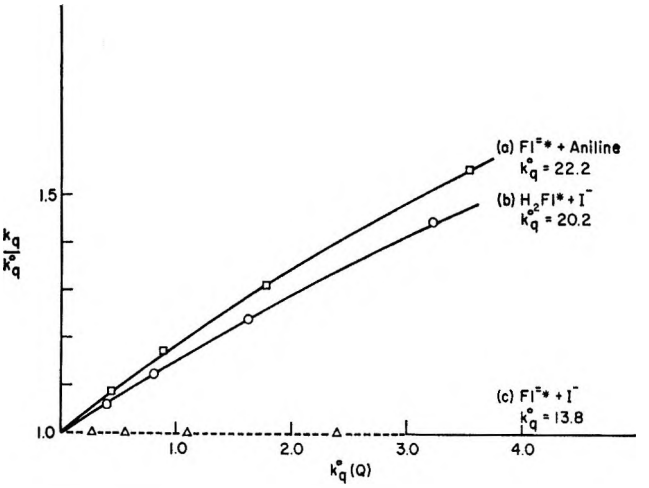

Figure 1. Transient diffusion—increase of k_q with the concentration, (Q), of quencher.

All measurements of fluorescence intensity were made with the Aminco-Bowman Spectrofluorometer No. 4-8202. Unless otherwise specified, the excitation wavelength was 480 mμ for fluorescein dianion in alkaline solution and the fluorescence intensity was read at 575 mμ. On this machine, the fluorescence intensity could be measured with a precision of ±1% if special means were employed to place the fluorescence cell in precisely the same position every time and if the gradual decrease in brightness of the light source was corrected for by reading I_0 immediately before and after reading I. Thus quenching constants could be determined with a precision of about ±2% at constant temperature. Since quenching has low activation energy and is thus relatively insensitive to temperature change, the measurements were made at room temperature, 27 ± 1.5°. From the known temperature coefficient[5] of 2.3% deg^{-1} for k_q, temperature variation added error of ±3.5%. Combining these errors in root-mean-square fashion yields probable precision of ±4%, *e.g.*, k_q = 20.0 ± 0.8. The errors in solution preparation normally were relatively insignificant.

Table II: Comparison of Quenching Equations with Data of Figure 1

Curve	Initial slope	Calcd slope	$g = \tau_0 D/R^2$	τ_0, nsec	D^6, cm²/sec	R^6, Å	δ, Å
a	0.183	0.124 (eq 12)	7.5	4.4	1.4×10^{-5}	9.1	~0
a	0.183	0.189 (eq 13)	4.2	4.4	1.4×10^{-5}	12.1	~3
b	0.148	0.138 (eq 12)	5.5	3.1[a]	$\sim 1.4 \times 10^{-5}$	8.9	~0
c	0.0	Equations 12 and 13 fail in presence of ionic forces					

[a] Measured for neutral fluorescein in water *via* subnanosecond phase fluorometer.[9]

Discussion

Transient Diffusion Effects. Previous workers[11,12] have employed the Collins–Kimball[8] expression, $\Phi_m \cong 4\pi DC_0(R - \beta)\,[1 + (R - \beta)/\sqrt{\pi Dt}]$, for the quencher flux toward a central fluorescent molecule. This is accurate only when $Dt/\beta^2 \gg 1$, but in the present experiments $Dt/\beta^2 \leqq 1$ for times up to ~1 nsec; for solvents more viscous than water, the solvent for Figure 1 data, the above approximation becomes even poorer. This lessens the transient—as evinced in the factor $(R - \beta)$—and contributes to the failure of previously published equations to account fully[11d] for the observed increase in k_q with increase in quencher concentration. The new eq 12, which is not so restricted to large time, fits the data of curve b, Figure 1, as indicated in Table II. Curve a has greater slope, *i.e.*, greater transient-diffusion quenching, than curve b, but eq 13 with a quenching shell thickness of $\delta \cong 3$ Å provides nice fit. Curve c coincides with the abscissa axis, because k_q was observed to be independent of quencher concentration; electrostatic repulsion apparently reduces the concentration of iodide ion (I^-) in the immediate vicinity of fluorescein dianion (Fl^{2-}) to a value close to the steady-state diffusion value. It should be noted that prior to constructing Figure 1, the values of k_q° for curves a, b, and c were determined by plotting k_q *vs.* [Q] and extrapolating to [Q] = 0. The probable precision of k_q° is ±4%.

An oversized quenching sphere, *e.g.*, with 3-Å shell thickness as above, can rationalize very large dependence of k_q on quencher concentration. This is preferred over rationalization by complex formation between quencher and dye prior to excitation, because spectrophotometric absorption curves indicate no such complexing. In the event that the oversized-sphere model is replaced by a complexation, which is so "loose" in the ground state as to cause insignificant change in absorption spectrum, the term $(\delta/R)/(g + \sqrt{g})$ in eq 13 is replaced by K/k_q°, where K is the molar association constant. With normal R value of 9.1 Å, a K value of 1.3 yields correct slope of k_q/k_q° *vs.* k_q°[Q] for Fl^{2-} quenched by aniline. This corresponds to about 11% of the dye ions being associated with aniline prior to excitation.

Solvent Effects. From the data of Table I it appears that reaction of uranin, or fluorescein dianion, with polarizable quenchers is encouraged in protic solvents and slowed in the aprotic solvent dimethylformamide. Thus proton transfer from the solvent to excited uranin, polarized by the quencher, might contribute to quenching in this symmetrical dye. Solvent proticity has previously been observed to encourage internal quenching in erythrosin[9]—where the iodine is part of the molecule—as it apparently does in uranin in collision with iodide ion. This suggests the interaction between quencher and excited dye is an instantaneous electric field effect, *i.e.*, a polarization of one molecule by the time-varying dipole of the other, not requiring conjugative linkage. Such interaction seems more physical than chemical consistent with the observed absence of chemical change during quenching. Jette, *et al.*,[13] were early in observing dependence of dye fluorescence quenching on polarizability of quencher but did not correlate with solvent properties.

Quenching by aniline, as well as by iodide ion, and absence of oxygen effect argue against a triplet mechanism.[12] Rowell and La Mer's[7] finding that sterically crowded dimethylmesidine is very active as quencher appears inconsistent with a radical mechanism involving complete transfer of an electron from quencher to dye, but it is consistent with the more physical polarization view since dimethylmesidine has higher electronic polarizability[14] than either aniline or mesidine. Rollefson and Stoughton[15] raised some questions about electron transfer theories of dye fluorescence quenching. Brackman[16a] rationalized fluorescence quenching *via* "complex resonance;" today, this might be described as a charge-transfer complexation between polarizable or "soft"[16b] Lewis acid and base. This could contribute to the later stages of quenching when partial desolvation of the reactants could encourage π-orbital overlap; it might be more characteristic of aniline than of iodide quenching.

The proposed protonic quenching mechanism is exemplified in Figure 2 by inductive interaction of a

(13) E. Jette, W. West, and R. H. Müller, *Proc. Roy. Soc.* (London), **A121**, 294, 299 (1928).

(14) C. E. Ingham and G. C. Hampson, *J. Chem. Soc.*, 985 (1939).

(15) G. K. Rollefson and R. W. Stoughton, *J. Am. Chem. Soc.*, **63**, 1517 (1941).

(16) (a) W. Brackman, *Rec. Trav. Chim.*, **68**, 147 (1949); (b) R. G. Pearson, *J. Am. Chem. Soc.*, **85**, 3533 (1963); *Chem. Eng. News*, May 31, 90 (1965).

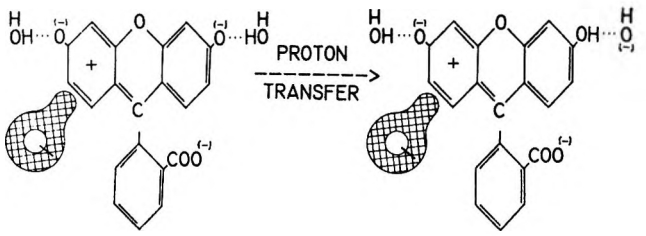

Figure 2. Proposed critical complex of fluorescent dye and polarizable quencher in protic solvent.

polarizable quencher and an excited fluorescein dianion in the protic solvent, water. Delocalization is represented by migration of orbital vacancy[9] shown as positive charge in the figure. Under the influence of the instantaneous electric field of the quencher, the positive hole can be attracted to the quencher, as shown, because of the high polarizability of the S_1 excited state of the dye relative to the S_0 ground state.[9]

H-bridging between protic solvent and auxochrome of a symmetrical dye, in the ground state, prepares the molecular geometry for quenching by rapid proton transfer. Such protic solvent effects are allowed for in the above quenching equations by τ_q, the average time required for quenching in the shell, or the k of Collins and Kimball. The data of Hodges and La Mer[6] with eq 6 yield $\tau_q/\tau_0 \cong 0.1$ for aqueous uranin quenched by aniline; *i.e.*, the average time required for quenching in the 3-Å shell is roughly $^1/_{10}$ that required for fluorescence. The unusually low quenching constants found by Hodges and La Mer[6] in methyl, ethyl, and propyl alcohol solutions free from water suggest τ_q/τ_0 is about 0.3 due to the lesser proticity of these solvents compared with water;[9] in essentially aprotic solvents, *e.g.*, dimethylformamide, τ_q/τ_0 becomes even greater.

Nature of the Dye Excited Singlet State. The polarizability and auxochrome reactivity—inferred from fluorescence quenching and internal conversion data[9,10]—are consistent with the view that resonance stabilization in S_1 is weak relative to that in S_0. S_0 has symmetric wave function $\psi(S_0) \simeq A + \mu M + B$ representing the resonance interaction of structures (A) $\bar{Q}=\overset{(+)}{X}-\bar{Q} \leftrightarrow$ (M) $\bar{Q}-\overset{(+)}{X}-\bar{Q} \leftrightarrow$ (B) $\bar{Q}-X=\overset{(+)}{Q}$, where X symbolizes the center and Q the auxochromic ends of the dye. S_1 has antisymmetric wave function $\psi(S_1) \simeq A-B$; exclusion of the middle structure (M), by symmetry selection rule,[17] lessens the resonance interaction between mirror-image structures A and B. Thus S_1 offers only minimal resonance-energy opposition to polarization and, depending on the direction of the perturbing electric field, might readily be converted to either of structures A and B; these have increased basicity, due to the electron pair "localized" at one end, and encourage protonation by the solvent, internal-conversion to similarly-protonated "hot" ground state,[9a] and ultimate "cooling" by deprotonation. The above valence-bond rationalization is supported also by its success in relating dye color to structure.[17,18]

Particularly significant is the correspondence between the intuitive rule of Lewis,[19] that the main absorption wave length is always greater as the fraction of the positive charge on the auxochromes is greater, and the more formal statement that the smaller the weighting coefficient μ, above, the smaller is the resonance depression of S_0 below S_1 in energy. The exclusion of structure M from S_1 is supported by measurements of absorption and fluorescence in meso-substituted oxacarbocyanines;[10b] such data indicate the *meso* or middle position is less positive in S_1 than in S_0. Thus *meso*-substituents have increased basicity in S_1; for *o*-hydroxybenzophenones this apparently promotes intramolecular proton transfer, *i.e.*, from *o*-hydroxy group to *meso*-carbonyl oxygen, and internal conversion to similarly protonated "hot" ground state. Loss of fluorescence in sterically crowded dyes now appears to result from (a) minimal resonance-energy opposition to certain skeletal deformations in S_1 and (b) radiationless transition to similarly deformed "hot" ground states.

(17) W. E. Moffitt, *Proc. Phys. Soc.*, **63A**, Part 7, No. 267, 700 (1950).

(18) L. G. S. Brooker and W. T. Simpson, *Ann. Rev. Phys. Chem.*, **2**, 124 (1951).

(19) G. N. Lewis, *J. Am. Chem. Soc.*, **67**, 770 (1945).

Reduction Potentials of Complex Ions. The Tris(pyridine-2-aldoxime)iron(III)–Tris(pyridine-2-aldoxime)iron(II) System[1]

by George I. H. Hanania, Dennis H. Irvine, and Fahd R. Shurayh

Department of Chemistry, American University of Beirut, Beirut, Lebanon *(Received October 24, 1967)*

The reduction potential E for the tris(pyridine-2-aldoxime)iron(III)–tris(pyridine-2-aldoxime)iron(II) couple has been measured potentiometrically in dilute aqueous solution within the ranges of pH 6.0–7.5, ionic strength 0.085–0.015 M, temperature 14.5–33.2°. The data on the variation of E with pH are consistent with the assumption of one protonation equilibrium involving the iron(II) complex. At 25.0° and $I = 0$ the thermodynamic pH-independent reduction potential is $E_i^\circ = 0.348 \pm 0.001$ V with $\Delta H^\circ = -20.7 \pm 0.5$ kcal/mole and $\Delta S^\circ = -42.6 \pm 1.6$ eu. The equilibrium between the above redox couple and the hexacyanoferrate(III)–hexacyanoferrate(II) redox couple was investigated by a direct spectrophotometric method yielding $K_i^\circ = 0.9 \pm 0.1$ with $\Delta H^\circ = -5.2 \pm 1.3$ kcal/mole and $\Delta S^\circ = -18 \pm 5$ eu at 25.0° and $I = 0$. The large uncertainty in these results reflects the limited precision with which the equilibrium constant could be measured. These thermodynamic quantities are also calculated, with higher precision, from the known data on the two redox couples involved. The tris(pyridine-2-aldoxime)iron(III–II) system is examined in relation to analogous iron complexes of neutral organic nitrogen ligands and also to inorganic anionic complexes of the hexacyanoferrate type.

In a preceding comparison of thermodynamic data on redox cell reactions in aqueous solutions[2] it was noted that there are wide variations in reduction potential for a series of analogous iron complexes. Thus the tris(*o*-phenanthroline)- and tris(dipyridyl)iron(III)–(II) couples have reduction potentials of about 1.1 V, whereas for the tris(4,7-dihydroxyorthophenanthroline)iron(III–II) couple the value is −0.1 V when all six hydroxyl groups are ionized. This shows the profound influence of the electrostatic environment of the metal on its oxidation–reduction potential. Moreover, the data show that the effect appears primarily as a change in exothermicity and, to a lesser extent, as a change in entropy for the cell reaction.

The tris(pyridine-2-aldoxime) complex of iron is similar to the dipyridyl and phenanthroline complexes in being a low-spin octahedral complex in which iron is bonded to six nitrogen atoms. It differs however in having three polar oxime –OH groups. The system can therefore be used for a detailed study of the effect of acidic side groups in a ligand on the reduction potential of the chelate. The converse effect, *viz.*, the influence of the metal on the thermodynamics of ionization of the oxime side groups in this system, has already been examined.[3] In that case, pK of the oxime group was found to decrease from 10.22 in the free ligand to 7.13 in the complex, although the charges involved are the same in both cases. This 1000-fold increase in acid strength paralleled a decrease of 6 kcal/mole in the endothermicity of ionization.

In this paper, we report a potentiometric study of the reduction potential of the tris(pyridine-2-aldoxime)-iron(III–II) couple covering ranges of pH, ionic strength, and temperature. Since this potential is close to that of the hexacyanoferrate(III–II) couple, the equilibrium between the two systems was also investigated by an independent spectrophotometric method. A preliminary account of the work has been reported.[4]

Theory

Pyridine-2-aldoxime (PH) forms well-defined ferrous and ferric complexes in aqueous solution. In each case the complex undergoes three successive ionizations

$$Fe(P_3H_3)^{2+} \rightleftharpoons \rightleftharpoons \rightleftharpoons Fe(P_3)^- \quad (1)$$

$$Fe(P_3H_3)^{3+} \rightleftharpoons \rightleftharpoons \rightleftharpoons Fe(P_3)^0 \quad (2)$$

It is known[3] that for the iron(II) complex, in eq 1, p$K_1 <$ 3, p$K_2 = 3.4$, and p$K_3 = 7.1$, and that for the iron(III) complex, in eq 2, pK_1 and p$K_2 < 3$ while p$K_3 = 3.5$.

Since measurements on these systems were largely confined to the range of optimum stability of both complexes, pH 6.0–7.5, the only prototropic equilibrium involved is the third oxime ionization of the iron(II) complex

$$Fe(P_3H)^0 = Fe(P_3)^- + H^+ \quad (3)$$

The Redox Reaction. The parent cell reaction for the

(1) Work supported by an Arts and Sciences research grant from the American University of Beirut.

(2) G. I. H. Hanania, D. H. Irvine, W. A. Eaton, and P. George, *J. Phys. Chem.*, 71, 2022 (1967).

(3) G. I. H. Hanania and D. H. Irvine, *J. Chem. Soc.*, 2745 (1962).

(4) G. I. H. Hanania, D. H. Irvine, M. S. Michaelides, and F. R. Shurayh, "Proceedings of the 9th International Conference on Coordination Chemistry," W. Schneider, Ed., Verlag Helvetica Chimica Acta, Basel, Switzerland, 1966, p 224.

tris(pyridine-2-aldoxime)iron(III–II) redox couple *vs.* standard hydrogen electrode is

$$Fe(P_3)^0 + {}^1/_2H_2 = Fe(P_3)^- + H^+ \quad (4)$$

where the charges of 0 and −1 are the result of three oxime ionizations in the oxidant and reductant ions, respectively. The reductant ion is also involved in the prototropic equilibrium of eq 3. All other ionization and ion association equilibria are assumed to make negligible contributions to the measured free energy change within the experimental range of conditions. On this basis, the measured reduction potential E (defined at given pH, ionic strength I, and temperature T, for equal total molar concentrations of oxidant and reductant) will vary with pH and I in accordance with the relation

$$E = E^\circ_i + \frac{RT}{F} \ln (1 + (h/K_3)) + \frac{RT}{F} \ln (y_O/y_R) \quad (5)$$

where E°_i is the thermodynamic pH-independent reduction potential of the couple in eq 4 relative to s.h.e., K_3 the appropriate value of the ionization constant for eq 3, h the hydrogen ion activity in the solution computed on the assumption that the measured pH = $-\log h$, and y_O and y_R are the mean molar activity coefficients of free oxidant and reductant ions, respectively. At given finite ionic strength, it is convenient to calculate from the measured reduction potential E the pH-independent value E_i which is the reduction potential for the parent couple in eq 4. Thus defining

$$E_i = E^\circ_i + \frac{RT}{F} \ln (y_O/y_R) \quad (6)$$

it follows from eq 5 that

$$E_i = E - \frac{RT}{F} (\ln 1 + (h/K_3)) \quad (7)$$

The ionic strength variation of E_i follows readily from eq 6 using an extended Debye–Hückel relation for activity coefficients with the mean distance of closest approach of ions taken to be about 7 Å

$$E_i = E^\circ_i + cI^{1/2}/(1 + 2.3I^{1/2}) \quad (8)$$

Here the parameter $c = 2.303ART/F$ and is seen to include the Debye–Hückel term A which is defined as $A = 1.825 \times 10^6 (\rho_0/\epsilon^3T^3)^{1/2}$, ρ_0 being the density and ϵ the dielectric constant of the solvent at temperature T°K. For water at 25.0°, $A = 0.510$, and since $RT/F = 59.17$ mV, it follows that $c = 30.2$ mV.

Reaction between Tris(pyridine-2-aldoxime)iron(II) and Hexacyanoferrate(III). This reaction, an electron exchange between two redox couples, is represented by the equilibrium

$$Fe(P_3)^- + Fe(CN)_6^{3-} = Fe(P_3)^0 + Fe(CN)_6^{4-} \quad (9)$$

where both systems are in their fully ionized forms. The thermodynamic pH-independent equilibrium constant K°_i is defined in terms of activities, and the measured equilibrium constant K is defined in terms of the total molar concentrations of all species for each reactant and product in eq 9. K varies with pH, ionic strength, and temperature. At constant temperature, within the range of our experiments (pH 6.0–7.5, and concentrations about 10^{-4} M), the hexacyanoferrate system is not appreciably influenced by protonation or ion association equilibria,[5] and the only variation of K arises as a result of the ionization in eq 3. Thus, at finite ionic strength, one can calculate from the measured equilibrium constant K the corresponding value for the pH-independent constant K_i which refers to the equilibrium in eq 9. The relation is simply

$$K_i = K(1 + (h/K_3)) \quad (10)$$

The dependence of K_i on ionic strength is readily shown to be given by

$$\log K_i = \log K^\circ_i + 6AI^{1/2}/(1 + 2.9I^{1/2}) \quad (11)$$

where the mean distance of closest approach in the Debye–Hückel expression is taken at nearly 9 Å in this system. The term A was defined above. The mean enthalpy change for the reaction in eq 9 is obtained from the temperature variation of the calculated K_i values at low ionic strength, and as a first approximation this is taken to be equal to the thermodynamic quantity ΔH°.

The above experimentally determined values of K°_i and ΔH° can now be compared with the derived values which are calculated from the thermodynamic quantities for the two redox couples involved. Thus

$$\Delta G^\circ(\text{eq 9}) = \Delta G^\circ(\text{hexacyanoferrate}) - \Delta G^\circ(\text{eq 4}) \quad (12)$$

from which it follows at 25.0° that

$$0.05916 \log K^\circ_i = E^\circ(\text{hexacyanoferrate}) - E^\circ_i(\text{eq 4}) \quad (13)$$

where the reduction potentials are in volts.

Experimental Section

Reagents and Materials. Pyridine-2-aldoxime was purchased from Light & Co., Colnbrook, England, and recrystallized to constant melting point, 113°. All other chemicals were of AnalaR grade. The purity of the salt $Fe(NH_4)_2(SO_4)_2 \cdot 6H_2O$ as determined by titration against $KMnO_4$ was 99.9%, and that of $Fe(NH_4)(SO_4)_2 \cdot 12H_2O$ titrated against $SnCl_2$ was 98.6%; in both cases allowance was made for this in the weighing

(5) W. A. Eaton, P. George, and G. I. H. Hanania, *J. Phys. Chem.*, 71, 2016 (1967).

of samples. $K_3Fe(CN)_6$ as used in the equilibrium experiments was taken from a freshly opened bottle without further purification. Buffer solutions were prepared from appropriate mixtures of 0.05 *M* NaOH and NaH_2PO_4, adjusted to the required ionic strength by dilution and/or addition of NaCl (*vide infra*).

The iron(II) complex of pyridine-2-aldoxime formed immediately when a 0.1 *M* solution of the latter was added to a solution of ferrous ammonium sulfate containing an equivalent amount of $HClO_4$, the ligand to metal ratio being 280. The stock solution so made, usually about 10^{-3} *M*, was diluted in the appropriate buffer to give the required concentration. These solutions were fairly stable. For the iron(III) complex, ligand was added to a solution of ferric ammonium sulfate containing 3 equiv of $HClO_4$/equiv of Fe, and 4 min was allowed for complete formation. No buffer was added in order to give the maximum ligand to metal ratio of 480. Nevertheless, these solutions were not so stable. Consequently, fresh solutions of both complexes were made up for each experiment, as were all other solutions except buffers. Deionized glass redistilled water was used in making all the solutions.

Measurement of Reduction Potential. Reduction potentials were measured in a thermostated two-compartment cell with an agar-saturated KCl bridge. The reference half-cell was a selected commercial saturated calomel electrode constantly equilibrated in saturated KCl, while the other contained 14.0 ml of an equimolar mixture of the ferrous and ferric complexes, usually of concentration 2.50×10^{-4} *M* each. One gold and one rhodium metal electrode dipped into this solution, and purified nitrogen was bubbled into the mixture to effect mixing. Potentials were read to 0.1 mV on a Radiometer PHM 4 potentiometer. pH was then measured using the same solution and apparatus with a thermostated electrode assembly. In both cases, temperature was controlled to $\pm 0.05°$ or better. NBS standards were used in calibrating the pH scale.[6]

Potentials were read at 1-min intervals for about 10 min. A rise of 1–2 mV was usually observed in the first few minutes followed by a slow decay. Linear extrapolation from this region to zero time (involving no more than 2 mV) yielded emf values which were taken to be the redox potentials corresponding to the moment of mixing. The gold and rhodium electrodes gave concordant results and were used in preference to platinum which had a slower response and gave readings which were higher but not consistent.

The reversibility of the system was tested using molar ratios of oxidant to reductant varying from 1:4 to 4:1 at constant total ionic strength; the measured emf's yielded a reduction potential constant within 0.5 mV. The effect of concentration was also tested over the range 1.0×10^{-4} to 5.0×10^{-4} *M* and gave reduction potentials constant within 0.5 mV.

For every experiment, at given ionic strength, pH, and temperature, two or three independent measurements of reduction potential were made. Reproducibility varied between 0.3 and 1.0 mV depending on conditions.

Determination of Equilibrium Constant. The equilibrium between the tris(pyridine-2-aldoxime)iron(III–II) and the hexacyanoferrate(III–II) systems was investigated spectrophotometrically. It was found convenient to prepare the various equilibrium mixtures by adding the tris(pyridine-2-aldoxime)iron(II) complex to a solution of hexacyanoferrate(III) in buffer under the required conditions. The reverse approach, starting with the iron(III) complex and hexacyanoferrate(II), proved unsatisfactory possibly owing to the instability of the iron(III) complex. Measurements were made at 515 mμ where the iron(II) complex has a strong absorption maximum while the iron(III) complex has weak absorption (at pH 7.0, ϵ 10,000 and 2450 M^{-1} cm^{-1}, respectively); the corresponding absorption by hexacyanoferrate(II) is negligible, and for hexacyanoferrate(III) ϵ is 16 M^{-1} cm^{-1}.

For every experiment, three of four mixtures were prepared containing 1.00×10^{-4} *M* iron(II) complex and concentrations of hexacyanoferrate(III) varying from 1.00×10^{-4} to 3.00×10^{-4} *M*. Absorbancies at 515 mμ were read on a Unicam SP 500 spectrophotometer with a thermostated cell compartment. It was found that the absorbancy increased perceptibly with time (averaging about 0.005 unit/min); readings were therefore taken at rapid intervals up to about 3 min, and the value corresponding to the moment of mixing was obtained by extrapolation. The effect was smaller at lower ferricyanide concentrations and at lower ionic strengths. As a further check, the absorbancy of the solution containing only iron(II) complex was measured independently, and that for the iron(III) complex was obtained from a series of independent measurements on solutions containing progressively increasing molar ratios of ligand to iron. This latter value is pH independent, whereas the corresponding value for the iron(II) complex varied with pH in accordance with the ionization in eq 3.

The measured equilibrium constant K is defined in terms of the total molar concentrations of the species in eq 9. It can readily be shown that if A_1 is the absorbancy of a given equilibrium mixture, A_2 that of the iron(II) complex, and A_3 that of the iron(III) complex, all under the same conditions, then

$$K = c(A_2 - A_1)^2/\{(A_1 - A_3) \times [f(A_2 - A_3) - c(A_2 - A_1)]\} \quad (14)$$

where c is the initial molar concentration of the iron(II) complex, and f is the initial ferricyanide concentration.

(6) R. G. Bates, "Determination of pH," John Wiley and Sons, Inc., New York, N. Y., 1964, p 123.

Equation 14 was used in calculating K. In theory, the only variation in K at constant temperature and ionic strength arises from the ionization in eq 3, and on this basis one calculates the pH-independent equilibrium constant K_i using eq 10. K was determined from the measured absorbancies corresponding to between 40 and 75% reaction; beyond this a tailing was observed, K values tending to rise with increasing ferricyanide concentration. This, together with the uncertainty in the extrapolation of absorbancies to zero time, leads to uncertainty in K estimated at no less than $\pm 5\%$.

Ionic Strength. For every experiment, the total molar ionic strength was computed from the contributions of the phosphate buffer, acid, and salts in the solution. In redox experiments, buffer ions contributed about 80% of the total. Since stock solutions of the iron salts were made in the presence of $HClO_4$, these solutions invariably caused a lowering of the pH of phosphate buffers, the effect being more pronounced at higher pH and at lower ionic strengths. Calculation of buffer contribution had to take this effect into account and was therefore based on the measured pH of the final reaction mixture. Other contributing ions include NH_4^+, SO_4^{2-}, ClO_4^-, and $Fe(P_3)^-$. Independent conductivity measurements also showed that under our experimental conditions enough KCl diffuses from the salt bridge to contribute about 0.001 M. Thus in a typical redox experiment: I = 0.42 (buffer) + 0.007 (other ions) + 0.001 (bridge) = 0.050 M.

In the equilibrium experiments, where measurements were spectrophotometric, the solutions were more dilute than in redox (potentiometric) experiments. Buffer contributions were accordingly higher, over 90% of total, and pH effects were smaller. Salt ions include NH_4^+, SO_4^{2-}, ClO_4^-, and $Fe(P_3)^-$, as well as K^+, $Fe(CN)_6^{4-}$, and $Fe(CN)_6^{3-}$. Since hexacyanoferrate ions were about 10^{-4} M, ion association was neglected.[5] Thus in a typical equilibrium experiment: I = 0.048 (buffer) + 0.001 (other ions) + 0.001 (hexacyanoferrates) = 0.050 M.

Results

The Redox Reaction. Following the above procedure, the reduction potential for the tris(pyridine-2-aldoxime) iron(III–II) system was measured over ranges of pH, ionic strength, and temperature. Table I summarizes the results obtained at 25.0° and I = 0.050 M, within the pH range 6.0–7.5, and gives the pH-independent reduction potential E_i calculated in each case using eq 7. The constancy of E_i, 352.8 ± 0.7 mV, confirms the validity of the assumption that the redox reaction involves one prototropic equilibrium, that of the third oxime ionization of the iron(II) complex (eq 3).

The variation of E with ionic strength at 25.0° and within the range 0.085–0.015 M is summarized in Table II, which also gives the calculated values of E_i.

Table I: Effect of pH on the Reduction Potential E for the Tris(pyridine-2-aldoxime)iron(III–II) Couple at 25.0° and I = 0.050 M[a]

pH	E, mV	E_i, mV (eq 7)
6.05	412.0	351.9
6.25	403.5	354.0
6.45	392.0	352.1
6.50	390.0	352.4
6.70	383.0	353.9
6.85	375.0	351.6
6.96	373.5	353.8
7.20	366.0	353.0
7.30	363.5	352.7
7.45	360.5	352.4
	Mean	352.8 ± 0.7 mV

[a] E (mV) = 244.5 + measured potential *vs.* saturated calomel electrode, the uncertainty being about ±0.5 mV. Corresponding values for the pH-independent reduction potential E_i are calculated from eq 7 taking $K_3 = 9.5 \times 10^{-8}$.[3]

The dependence of E_i on ionic strength is in accord with the Debye–Hückel function of eq 8; this enables the calculation of the corresponding thermodynamic reduction potential $E°_i$. It may be concluded from these results that the mean value at 25.0° is $E°_i$ = 0.348 ± 0.001 V.

Table II: Effect of Ionic Strength on the pH-Independent Reduction Potential E_i for the Tris(pyridine-2-aldoxime)iron(III–II) Couple at 25.0°[a]

I, M	pH	E, mV	10^8K_3, (ref 3)	E_i, mV (eq 7)	$E°_i$, mV (eq 8)
0.085	6.83	378.0	10	354.6	349.4
0.050	[b]	[b]	[b]	352.8	348.4
0.035	6.98	371.5	8.9	351.5	347.6
0.025	7.00	370.0	8.7	350.4	347.0
0.015	6.69	381.5	8.5	350.1	347.3
				Mean	347.9 ± 0.8 mV

[a] E(mV) = 244.5 + measured potential *vs.* saturated calomel electrode, the uncertainty being ±0.5 mV. E_i is calculated from E using eq 7. The thermodynamic reduction potential $E°_i$ is calculated from E_i using eq 8. [b] See Table I.

The reduction potential E was also measured at several temperatures between 14.5 and 33.2°, all at constant ionic strength 0.050 M. The results are given in Table III together with the corresponding calculated values of E_i at every temperature. The plot of E_i against temperature shows slight curvature; around 25° the slope $dE_i/dT = (-1.85 \pm 0.07) \times 10^{-3}$ V/deg which may, as an approximation, be assumed to be the value at zero ionic strength $dE°_i/dT$. On this basis,

Table III: Effect of Temperature on the Reduction Potential E for the Tris(pyridine-2-aldoxime)iron(III–II) Couple at $I = 0.050\ M$[a]

Temp, °C	pH	E, mV	$10^8 K_3$ (ref 3)	E_i, mV (eq 7)
14.5	6.88	391.5	9.1	368.7
16.5	6.90	387.0	9.2	365.4
18.7	6.90	384.0	9.3	362.4
22.2	6.97	376.0	9.4	356.7
25.0	[c]	[c]	[c]	352.8
27.7	6.96	366.0	9.7	346.4
32.5	6.85	361.5	9.9	338.2
33.2	6.87	360.0	9.9	337.2

[a] E(mV) = $E°(H_2, sce)$[b] + measured potential *vs.* saturated calomel electrode, the uncertainty being about 0.5 mV. Corresponding values for the pH-independent reduction potential E_i are calculated from eq 7. [b] Values taken from ref 6, p 278. [c] See Table I.

at 25.0°, $\Delta H° = -20.7 \pm 0.5$ kcal/mole and $\Delta S° = -42.6 \pm 1.6$ eu for the cell reaction given in eq 4.

The Equilibrium with Hexacyanoferrate. The equilibrium constant K for the reaction between tris(pyridine-2-aldoxime)iron(II) and hexacyanoferrate(III), eq 9, was measured over ranges of ionic strength and temperature, and the pH-independent constant K_i was computed in each case by applying eq 10 and using the known value of K_3.[3] The results are shown in Table IV. The dependence of K_i on ionic strength is in accord with the Debye–Hückel function of eq 11; this enables the calculation of the thermodynamic equilibrium constant $K°_i$ at zero ionic strength, yielding a mean value at 25.0° of $K°_i = 0.85 \pm 0.08$. Consideration of uncertainties requires that the result be taken as 0.9 ± 0.1 and no better.

The enthalpy change for the above reaction was obtained from the K_i values at $I = 0.030\ M$ which were determined at three temperatures, also in Table IV. The mean value of ΔH is found to be -5.2 ± 1.3 kcal/mole which is assumed to be approximately $\Delta H°$. Consequently, the entropy change for the above reaction is $\Delta S° = -18 \pm 5$ eu. The wide limits of uncertainty in these results are unavoidable because of the limited precision with which K could be measured.

Table IV: Effect of pH, Ionic Strength and Temperature on the Measured Equilibrium Constant K for the Reaction in Eq 9[a]

Temp, °C	I, M	pH	K (eq 14)	$10^8 K_3$ (ref 3)	K_i (eq 10)	$K°_i$ (eq 11)
25.0	0.050	6.96	1.20	9.5	2.59	1.00
25.0	0.030	6.02	0.17	8.8	2.02	0.90
25.0	0.030	7.08	0.90	8.8	1.75	0.78
25.0	0.030	7.40	1.16	8.8	1.69	0.75
25.0	0.015	6.80	0.60	8.4	1.73	0.92
25.0	0.010	6.90	0.57	8.2	1.45	0.84
25.0	0.008	7.02	0.58	8.1	1.26	0.77
20.0	0.030	6.95	0.92	8.7	2.10	0.94
30.0	0.030	6.98	0.72	9.0	1.56	0.69

[a] Corresponding values of K_i, the pH-independent constant, are calculated using eq 10. The thermodynamic equilibrium constant $K°_i$ is calculated from K_i using eq 11. The uncertainty in K is about 5% and in K_i about 8%. The mean value of $K°_i$ at 25.0° is 0.85 ± 0.08.

An indirect but nevertheless more precise estimate of the above data can be obtained from the known thermodynamic parameters of the two redox couples involved. These are: the tris(pyridine-2-aldoxime)-iron(III–II) system for which $E°_i = 0.348 \pm 0.001$ V, $\Delta H° = -20.7 \pm 0.5$ kcal/mole, and $\Delta S° = -42.6 \pm 1.6$ eu (this paper); and the hexacyanoferrate(III–II) system for which $E° = 0.355 \pm 0.001$ V, $\Delta H° = -26.7 \pm 0.3$ kcal/mole, and $\Delta S° = -62.1 \pm 1.0$ eu.[2] Using eq 13 we obtain for the equilibrium in eq 9: $K°_i = 1.3 \pm 0.1$, $\Delta H° = -6.0 \pm 0.8$ kcal/mole, and $\Delta S° = -19.6 \pm 2.8$ eu.

Discussion

In the present work the standard reduction potential $E°_i$ of the tris(pyridine-2-aldoxime)iron(III–II) couple was found to be 0.348 ± 0.001 V. This refers to the fully ionized oxidant and reductant species in eq 4 and is thus the pH-independent value at pH >7.5, at 25.0° and $I = 0$. Since the potentiometric determination of E involved the use of a salt bridge, this result will be subject to the uncertainties of liquid junction potential, namely, that any residual junction potential in the experimental cell, in the region of very low ionic strength, is either insignificantly small or is virtually constant but indeterminate. A similar assumption was made in the hexacyanoferrate case.[2]

The above result is of particular interest when one considers the close structural similarity which the pyridine-2-aldoxime system bears to the dipyridyl and phenanthroline complexes of iron, the latter being octahedral N-heterocyclic complexes with standard reduction potentials over 1.1 V. It may appear at first sight that the organic N-ligand pyridine-2-aldoxime acts more like the inorganic anionic ligands F^- and CN^- which lower the Fe(III–II) reduction potential by preferentially stabilizing the Fe(III) state, although there is no structural relation whatever between the two types of complexes.

However, for strict comparison with other nitrogen ligands, account must be taken of the various oxime ionizations in the pyridine-2-aldoxime complexes of iron. One can write a hypothetical cell reaction involving only the neutral (completely unionized) ligand PH

$$Fe(P_3H_3)^{3+} + {}^1/_2H_2 = Fe(P_3H_3)^{2+} + H^+ \qquad (15)$$

with a pH-independent reduction potential E_{ii}. This equilibrium refers to a hypothetical situation in ex-

tremely acidic solution. It can be shown that E_{ii} is related to the corresponding reduction potential E_i of the cell reaction in eq 4, which involves only the completely ionized ligand P^-, by the equation

$$E_{ii} = E_i + \frac{RT}{F} \ln \left\{ \left(\frac{1 + (h/K_3) + (h^2/K_3K_2) + (h^3/K_3K_2K_1)}{1 + (h/K_3') + (h^2/K_3'K_2') + (h^3/K_3'K_2'K_1')} \right) \Big/ \left(\frac{1 + (K_1/h) + (K_1K_2/h^2) + (K_1K_2K_3/h^3)}{1 + (K_1'/h) + (K_1'K_2'/h^2) + (K_1'K_2'K_3'/h^3)} \right) \right\} \quad (16)$$

where K_1, K_2, K_3 are the successive acid ionization constants of the three oxime groups in the iron(II) complex, and K_1', K_2', K_3' are the corresponding ionization constants for the iron(III) complex; h is the hydrogen ion activity. It is known[3] that $K_3 = 10^{-7}$, $K_2 = 4 \times 10^{-4}$, $K_1' \sim 10^{-1}$ (say), and $K_3' = 3 \times 10^{-4}$. Assuming now that in the iron(III) complex the first two ionizations bear the same relationship to the third as obtains in the case of the iron(II) complex, we may take $K_2' \sim 1$, and $K_1' \sim 10^2$. Substitution into eq 16 gives $E_{ii} \sim 1$ V at $h = 1$, a value which is of the right order for neutral ligands of this type. On this basis it may be concluded that the observed value of $E_i \sim 0.35$ V is merely the thermodynamic consequence of the difference between the total free energy of ionization of the three oxime groups in the oxidant ($\Delta G'_{123}$) and reductant (ΔG_{123}) ions. In fact, the relation is simply

$$\Delta G_{ii} - \Delta G_i = \Delta G_{123} - \Delta G'_{123} = -16 \text{ kcal/mole} \quad (17)$$

where ΔG_{ii} refers to the hypothetical cell reaction in eq 15, and ΔG_i to eq 4.

The assumption that the neutral bidentate ligand PH is thermodynamically equivalent to phenanthroline and dipyridyl cannot be strictly valid because of the expected influence of the polar oxime side groups. However, insofar as the analogy applies to a first approximation, the change in enthalpy for the hypothetical cell reaction in eq 15 would be of the order -30 kcal/mole. The experimentally determined value for the cell reaction involving fully ionized oximes is -21 kcal/mole (this paper). On this basis, the total enthalpy of oxime ionizations in the oxidant would be more exothermic than that of the reductant by about 9 kcal/mole. Qualitatively this is, of course, to be expected in view of the higher positive charge on the former, but the data are not available to test it.

Further indication of the above comes from a consideration of ionic entropies. Thus for the cell reaction in eq 4

$$\bar{S}^\circ(R) - \bar{S}^\circ(O) = \Delta S^\circ + {}^1/_2 S^\circ(H_2) - \bar{S}^\circ(H^+) = -27 \text{ eu} \quad (18)$$

where $\bar{S}^\circ(R)$ and $\bar{S}^\circ(O)$ are the partial molal entropies of the reductant and oxidant ions, respectively, $\bar{S}^\circ(H_2) = 31.2$ eu and $\bar{S}^\circ(H^+) = 0$ (practical scale). The corresponding values for complexes with neutral organic ligands, where the positive charge is buried within a rigid aromatic shell, are much smaller and in some cases nearly zero.[2] Clearly the complex with oximate anionic ligand is unlike the regular organic complexes in its charge distribution and solvent interaction effects; and, since the various oxime ionization entropies are mostly unknown, one cannot predict the extent to which the hypothetical complex with PH as ligand would approach the properties of the regular complexes of dipyridyl and its analogs.

On the other hand, it can be shown that the complex with oximate anionic ligand is also unlike the inorganic cyanide complexes of iron. From eq 3 and 4 we deduce that $\bar{S}^\circ(Fe^{II}P_3H^0) - \bar{S}^\circ(Fe^{III}P_3^0) = 3$ eu; that is, the ionic entropy of oxidant Fe(III) complex and of protonated reductant Fe(II) complex, both carrying the same (zero) over-all charge, are nearly equal. This contrasts markedly with the behavior of hexacyanoferrate and tetracyanodipyridyliron(III–II) systems where the corresponding differences are, respectively, -26 and -20 eu. Thus, unlike inorganic oxy anions and other anionic complexes, the protonated tris(pyridine-2-aldoximate)iron(II) ion does not appear to have an abnormally low partial molal entropy relative to its unprotonated conjugate, the oxidant ion.[7] Unfortunately the data are not available for comparison with dipyridyl and other neutral organic systems. Further investigations of systems of this type would be fruitful.

Another interesting feature of the tris(pyridine-2-aldoxime)iron(III–II) system is the closeness of its reduction potential to that of the hexacyanoferrate-(III–II) system. This coincidence enabled us to study, by an independent spectrophotometric method, the equilibrium between these two redox couples. The results provide an opportunity for testing internal agreement among three interdependent equilibria. Some difficulty was, however, encountered in obtaining reproducible data as all spectrophotometric measurements had to be taken as a function of time and then extrapolated. Aquatization of $Fe(CN)_6^{4-}$ can be ruled out as the cause of instability since the equilibrium was unaffected by addition of excess CN^-. Interaction between the ligand pyridine-2-aldoxime, present in large excess in the reacting mixture, with hexacyanoferrate ions was shown not to occur. The iron(II) complex of pyridine-2-aldoxime is stable but the iron(III) complex is much less stable. It is possible that the very favorable free energy of binding Fe^{3+} to $Fe(CN)^{4-}$ enhances the instability and thus accounts for the observed rise in

(7) P. George, G. I. H. Hanania, and D. H. Irvine, *Rec. Trav. Chim.*, 75, 759 (1956).

absorbancy with time. Furthermore, the observed pH dependence of the reaction (eq 10) was found to be limited to the range of pH >6.0, thus indicating that other protonation equilibria may be involved in more acidic solutions.

Considering the above limitations and taking results only from the narrow range of optimum conditions, the thermodynamic equilibrium constant for the reaction in eq 9 was $K°_i = 0.9 \pm 0.1$ with $\Delta H° = -5.2 \pm 1.3$ kcal/mole and $\Delta S° = -18 \pm 5$ eu. The wide limits of uncertainty in these results preclude their use in calculating indirectly thermodynamic data for the tris(pyridine-2-aldoxime)iron(III–II) couple. The reverse calculation is more meaningful. Thus, taking the data for the above couple as determined experimentally (this paper) together with the data for the hexacyanoferrate(III–II) couple as determined experimentally by a similar method[2] yields for the reaction in eq 9 the following calculated values: $K°_i = 1.3 \pm 0.1$, $\Delta H° = -6.0 \pm 0.8$ kcal/mole, $\Delta S° = -19.6 \pm 2.8$ eu. It is noteworthy that although there is an apparent discrepancy between the measured and calculated values of $K°_i$, the enthalpies and entropies are well within limits of uncertainty. The equilibrium constant is clearly very close to unity. In a sense then, the two redox couples are equivalent. However, whereas pyridine-2-aldoxime complexes have the advantage of small charge and no ion association complications, the hexacyanoferrates have other advantages over the other ligand—they are considerably more stable as complex ions over a wide pH range and are also free from protonation equilibria at pH >5.

Mean Activity Coefficient of Polyelectrolytes. VIII. Osmotic and Activity Coefficients of Polystyrenesulfonates of Various Gegenions[1]

by Norio Ise and Tsuneo Okubo

Department of Polymer Chemistry, Kyoto University, Kyoto, Japan

Accepted and Transmitted by The Faraday Society (July 25, 1967)

The osmotic and mean activity coefficients of polystyrenesulfonates of various gegenions were investigated by means of the isopiestic vapor-pressure measurements. The order of the magnitude of the activity coefficient was $H^+ > Li^+ > Na^+ > K^+$, $Ca^{2+} > Ba^{2+}$, and $N^+(n\text{-}C_4H_9) > N^+(n\text{-}C_3H_7) > N^+(C_2H_5)_4 > N^+(CH_3)_4 > N^+(CH_3)_3CH_2C_6H_5 > NH_4^+$. This relative order was accounted for in terms of the structural effects of the ions on water. It was inferred that the polystyrenesulfonate ion acted as a fairly strong structure former because of the benzene ring. The structure-forming tendency of the polysulfonate ion was suggested to be enhanced with increasing concentration, in contrast with the structural influences of simple ions which are so far considered concentration independent.

As is well recognized, the mean activity coefficient of electrolytes is a most basic and most important quantity for understanding the thermodynamic properties of the solutions. (In the present work, the mean activity coefficient is discussed, which should not be confused with the single-ion activity coefficient.) For low molecular weight electrolytes, systematic study, experimental and theoretical, on this quantity has been conducted thoroughly, as far as dilute aqueous solutions of 1–1 type electrolytes are concerned. In the field of high molecular weight electrolytes, however, there is very little information concerning the activity coefficient, the only published data being those measured in aqueous media in this laboratory.[2-7] Thus, it is strongly hoped to extend the experimental work to other polyelectrolyte systems. In the present paper, we report the results obtained for various salts of a polystyrenesulfonic acid (PSt) in the binary aqueous solutions. The main purpose of this work is to study

(1) Part VII: H. Matsui, N. Ise, and T. Okubo, *J. Phys. Chem.*, submitted for publication.

(2) N. Ise and T. Okubo, *ibid.*, **65**, 4102 (1965).

(3) N. Ise and T. Okubo, *ibid.*, **70**, 1930 (1966).

(4) N. Ise and T. Okubo, *ibid.*, **70**, 2400 (1966).

(5) N. Ise and T. Okubo, *ibid.*, **71**, 1287 (1967).

(6) N. Ise and T. Okubo, *ibid.*, **71**, 1886 (1967).

(7) T. Okubo, N. Ise, and F. Matsui, *J. Am. Chem. Soc.*, **89**, 3697 (1967).

the specificity of gegenions on the osmotic and activity coefficients of the polyelectrolyte. In the previous work,[6] the activity coefficients of alkali metal salts of a polyvinylsulfuric acid were found to be in the same order as Gurney's empirical rule[8] predicts. Since this rule was originally found for uniunivalent simple electrolytes, mainly for alkali halides, the observed concordance was considered rather surprising and it was tempting to ascribe this result to the low charge density of the polyelectrolyte used. Thus, the measurements are now extended to polystyrenesulfonates having a high charge density. This polyelectrolyte is a strong acid and stable in the acid form, unlike the polyvinyl sulfate, which can easily undergo saponification at low pH's. Therefore H^+ can now be included in the series of gegenions.

Experimental Section

Sodium polystyrenesulfonate (NaPSt) of a degree of polymerization of 2500 was a gift from the Dow Chemical Co., Midland, Mich. A solution of the NaPSt was passed through a column of cation- and anion-exchange resins to the acid form. Then the aqueous solutions of various salts of PSt such as Li-, Na-, K-, Ca-, Ba-, NH_4-, $N(CH_3)_4$-, $N(C_2H_5)_4$-, $N(n\text{-}C_3H_7)_4$-, $N(n\text{-}C_4H_9)_4$-, and $N(CH_3)_3(CH_2C_6H_5)$PSt were prepared by neutralization with aqueous solutions of the corresponding hydroxides.

Osmotic and activity coefficients were determined by the isopiestic vapor-pressure measurements at 25 ± 0.005° with an apparatus employed earlier.[7] The reference electrolyte was potassium chloride. The experimental error of the present isopiestic measurements was at highest 1.0% of the concentration value, which was estimated from the duplicate or repeated runs. This order of error was considered gratifying in the light of rather large uncertainty inherent in the determination of polyelectrolyte concentration.

Results and Discussion

The concentrations at isopiestic equilibrium are given in Table I. The osmotic and activity coefficients for the polystyrenesulfonates were tabulated in Table II. The practical osmotic coefficients of the polysalts (φ_z) were evaluated by using the relation

$$\varphi_z = 2m_{KCl}\varphi_{KCl}/(z/z_g + 1)(m/z) \quad (1)$$

where m_{KCl} is the molality of reference potassium chloride solution, m the concentration of the polysalts (equiv/1000 g of water), z the stoichiometric valency of the macroion, Z_g the valency of gegenions, and φ_{KCl} the osmotic coefficient of KCl at m_{KCl}. It should be noted that the osmotic coefficient dealt with in the present paper is the one defined on the basis of the stoichiometric number of ions, not of the free ions. The φ_{KCl} values were obtained from literature.[9] The activity coefficients of polystyrenesulfonates, γ^*, were calculated from the osmotic coefficient by using the Gibbs–Duhem equation

$$\ln(\gamma_1^*/\gamma_2^*) = \varphi_{z1} - \varphi_{z2} + 2\int_{m_1}^{m_2}[(1-\varphi_z)/\sqrt{m}]\,d\sqrt{m} \quad (2)$$

where the suffixes 1 and 2 of the coefficients refer to concentrations m_1 and m_2, respectively. This relative values of the activity coefficient thus determined was conveniently standardized at infinite dilution. The assumptions involved were that the mean activity coefficients of the various salts of PSt have the same value at infinite dilution, *i.e.*, γ_0^*, and that the cube-root rule concerning the polymer concentration dependence of the activity coefficient was valid down to infinite dilution. The activity coefficient given in Table II, (γ^*/γ_0^*), was thus obtained.

The osmotic coefficient observed is, in most cases, found to increase with increasing concentration, as seen from Table II. Furthermore, the osmotic coefficient is influenced sensitively by the gegenions. The activity coefficient is generally found to decrease with increasing concentration and increase through a minimum. We note here that the trend of decreasing of the activity coefficient is representable by the cube-root rule, which has been found to hold for some polyelectrolytes,[3-7] but the range of fit of the rule is confined to lower concentrations for the polystyrenesulfonates, because strong solvent–solute interaction exists in the present cases, as will be shown. The magnitude of the activity coefficient is in the order

$$H^+ > Li^+ > Na^+ > K^+ \quad (A)$$

$$Ca^{2+} > Ba^{2+} \quad (B)$$

and

$$N^+(n\text{-}C_4H_9)_4 > N^+(n\text{-}C_3H_7)_4 > N^+(C_2H_5)_4 > N^+(CH_3)_4 > N^+(CH_3)_3CH_2C_6H_5 > NH_4^+ \quad (C)$$

One explanation for this specificity would be possible in terms of the specific way in which the structure of water may be altered by the ions, as suggested by Frank.[10] It has been shown that the concepts of the structural salting-out and salting-in can explain the positions of activity coefficient–concentration curves, if the relative strengths of the influences are postulated. Specifically the salting-out results in the high-lying curves, whereas the salting-in results in the low-lying ones. If one accepts this interpretation, it would be possible to infer the most important structural factor from the experimentally found orders: A, B,

(8) R. W. Gurney, "Ionic Processes in Solution," McGraw-Hill Book Co., Inc., New York, N. Y., 1953, Chapter 16.

(9) R. A. Robinson and R. H. Stokes, "Electrolytes Solutions," Butterworth and Co. Ltd., London, 1959, pp 476, 481.

(10) H. S. Frank, *J. Phys. Chem.*, **67**, 1554 (1963); *Z. Physik. Chem.*, **228**, 364 (1965).

Table I: Concentrations of Isopiestic Solutions of Potassium Chloride and Polystyrenesulfonates at 25°

HPSt		LiPSt		NaPSt	
m_{KCl}, m	m, equiv/1000 g	m_{KCl}, m	m, equiv/1000 g	m_{KCl}, m	m, equiv/1000 g
0.152	0.360	0.0841	0.217	0.0460	0.143
0.213	0.469	0.0851	0.225	0.0492	0.157
0.271	0.572	0.109	0.285	0.0637	0.198
0.344	0.649	0.115	0.303	0.0817	0.250
0.555	0.848	0.154	0.377	0.0926	0.291
0.868	1.07	0.160	0.395	0.104	0.320
1.85	1.66	0.232	0.503	0.115	0.334
		0.297	0.582	0.148	0.419
		0.370	0.673	0.160	0.440
		0.411	0.709	0.249	0.587
		0.562	0.850	0.414	0.801
		0.815	1.05	0.424	0.832
		0.979	1.18	0.565	0.996
		1.48	1.48	0.580	1.01
		1.85	1.74	0.815	1.23
		3.23	2.19	0.880	1.29
				1.85	1.99

NH_4PSt		$N(CH_3)_4PSt$		$N(C_2H_5)_4PSt$	
m_{KCl}, m	m, equiv/1000 g	m_{KCl}, m	m, equiv/1000 g	m_{KCl}, m	m, equiv/1000 g
0.0417	0.115	0.0560	0.187	0.0468	0.130
0.0516	0.159	0.0689	0.219	0.0516	0.157
0.0595	0.190	0.0752	0.241	0.0595	0.180
0.0851	0.259	0.0892	0.272	0.0851	0.243
0.109	0.324	0.113	0.327	0.109	0.305
0.115	0.337	0.123	0.354	0.115	0.315
0.154	0.422	0.144	0.402	0.154	0.394
0.160	0.437	0.180	0.473	0.160	0.409
0.232	0.548	0.269	0.616	0.232	0.523
0.253	0.590	0.321	0.684	0.297	0.613
0.297	0.661	0.472	0.859	0.370	0.710
0.370	0.757	0.493	0.889	0.411	0.756
0.411	0.811	0.779	1.18	0.562	0.907
0.562	0.990	1.85	1.83	0.815	1.09
0.815	1.28			0.979	1.23
0.979	1.40			1.48	1.49
1.48	1.85			1.85	1.67
1.85	2.07			3.23	2.11
3.23	2.59				

KPSt		CaPSt		BaPSt	
m_{KCl}, m	m, equiv/1000 g	m_{KCl}, m	m, equiv/1000 g	m_{KCl}, m	m, equiv/1000 g
0.0460	0.154	0.0349	0.177	0.0447	0.242
0.0492	0.170	0.0369	0.189	0.0560	0.271
0.0637	0.214	0.0464	0.226	0.0689	0.308
0.0817	0.269	0.0470	0.236	0.0752	0.348
0.0926	0.304	0.0523	0.256	0.0892	0.395
0.104	0.331	0.0592	0.282	0.113	0.484
0.148	0.439	0.0661	0.311	0.123	0.551
0.249	0.623	0.0731	0.339	0.144	0.672
0.253	0.621	0.0901	0.397	0.180	0.864
0.269	0.677	0.113	0.505	0.269	1.19
0.280	0.683	0.124	0.552	0.321	1.40
0.411	0.908	0.154	0.638	0.411	1.58
0.424	0.899	0.274	0.912	0.472	1.80
0.580	1.12	0.682	1.45	0.493	1.88
0.815	1.39	1.58	2.11	0.779	2.61
0.880	1.47			1.85	3.45
1.85	2.34				

$N(n\text{-}C_3H_7)_4PSt$		$N(n\text{-}C_4H_9)_4PSt$		$N(CH_3)_3CH_2C_6H_5PSt$	
m_{KCl}, m	m, equiv/1000 g	m_{KCl}, m	m, equiv/1000 g	m_{KCl}, m	m, equiv/1000 g
0.0695	0.156	0.0817	0.156	0.0349	0.122
0.0841	0.197	0.0841	0.167	0.0369	0.129
0.115	0.265	0.0926	0.190	0.0464	0.154
0.160	0.349	0.104	0.216	0.0470	0.158
0.232	0.450	0.115	0.228	0.0523	0.172
0.297	0.536	0.148	0.293	0.0592	0.192
0.370	0.623	0.160	0.304	0.0661	0.211
0.411	0.673	0.249	0.413	0.0731	0.229
0.562	0.780	0.253	0.415	0.0901	0.267
0.815	0.978	0.269	0.468	0.113	0.346
0.979	1.09	0.280	0.462	0.124	0.379
1.48	1.38	0.411	0.603	0.154	0.454
1.85	1.52	0.424	0.604	0.274	0.706
3.23	1.91	0.565	0.721	0.682	1.29
		0.580	0.737	1.58	1.96
		0.815	0.911		
		0.880	0.945		

and C. As is duly supported by the partial molal entropy data,[11] the structure-forming tendency decreases in the order $H^+ > Li^+ > Na^+ > K^+$. The hydronium ion is the strongest structure former in this series. Also Ca^{2+} has a smaller entropy value than Ba^{2+}. For the aliphatic organic cations, the more carbon atoms surrounding the nitrogen, the more hydrophobic and stronger structure former these cations will be.[12] In other words, the strength of the structure-forming tendency is in the order: $N^+(n\text{-}C_4H_9)_4 > N^+(n\text{-}C_3H_7)_4 > N^+(C_2H_5)_4 > N^+(CH_3)_4 > NH_4^+$. Then, the polystyrenesulfonate ion would be expected to salt-out hydronium, calcium, and tetrabutylammonium ions most strongly, in the respective series, and potassium, barium, and ammonium ions most weakly, provided that this effect outweighs the self-salting-in of cation by cation and of anion by anion. In other words, the polystyrenesulfonate ion would have to be either a strong structure breaker or a structure former of a mode incompatible with the cations. The first possibility may be excluded from further consideration, since the polystyrenesulfonate ion has a large hydrocarbon tail (benzene ring), which would promote the water structure.[13] The partial molal entropy of HSO_3^- is reported to be +32.6 eu

(11) Reference 8, p 267.

(12) H. S. Frank and W. Y. Wen, *Discussions Faraday Soc.*, **24**, 133 (1957).

(13) G. Némethy and H. A. Scheraga, *J. Chem. Phys.*, **36**, 3401 (1962).

Table II: Osmotic and Activity Coefficients of Polystyrenesulfonates at 25°

	m, equiv/1000 g	HPSt φ_z	HPSt log (γ^*/γ_0^*)	LiPSt φ_z	LiPSt log (γ^*/γ_0^*)	NaPSt φ_z	NaPSt log (γ^*/γ_0^*)
1	0.2					0.604	−0.503
2	0.3			0.705	−0.437	0.600	−0.577
3	0.4	0.786	0.001	0.747	−0.464	0.648	−0.602
4	0.5	0.841	0.002	0.830	−0.439	0.709	−0.604
5	0.6	0.918	0.015	0.921	−0.405	0.780	−0.595
6	0.7	1.01	0.050	1.01	−0.362	0.828	−0.576
7	0.8	1.12	0.101	1.12	−0.314	0.902	−0.551
8	0.9	1.23	0.159	1.22	−0.260	0.960	−0.536
9	1.0	1.35	0.223	1.32	−0.207	1.03	−0.506
10	1.2	1.57	0.344	1.52	−0.097	1.16	−0.434
11	1.4	1.78	0.471	1.70	0.018	1.29	−0.368
12	1.6	1.97	0.612	1.85	0.134	1.42	−0.289
13	1.8			2.00	0.242	1.55	−0.221
14	2.0			2.38	0.396	1.69	−0.129

	KPSt φ_z	KPSt log (γ^*/γ_0^*)	CaPSt φ_z	CaPSt log (γ^*/γ_0^*)	BaPSt φ_z	BaPSt log (γ^*/γ_0^*)
1	0.552	−0.601				
2	0.566	−0.680	0.800	−0.239	0.833	−0.302
3	0.602	−0.714	0.828	−0.250	0.820	−0.323
4	0.651	−0.714	0.850	−0.263	0.804	−0.335
5	0.699	−0.730	0.880	−0.265	0.794	−0.367
6	0.744	−0.726	0.936	−0.249	0.792	−0.392
7	0.794	−0.720	1.00	−0.217	0.792	−0.413
8	0.834	−0.717	1.08	−0.173	0.792	−0.421
9	0.880	−0.702	1.16	−0.125	0.800	−0.421
10	0.96	−0.668	1.35	−0.006	0.822	−0.427
11	1.05	−0.629	1.61	0.131	0.834	−0.433
12	1.14	−0.589	1.88	0.293	0.924	−0.412
13	1.23	−0.552	2.18	0.479	0.946	−0.382
14	1.32	−0.512	2.50	0.685	1.04	−0.370

(on a scale of zero for a proton),[11] comparable with +26.4 eu for NH_4^+, which is believed not to alter greatly the water structure.[14] Thus, we may expect that the structural influence of the polystyrenesulfonate ion is determined by that of the benzene ring. In other words, this ion is structure forming. It would furthermore be accepted that the water structure around the inorganic cations is different from that in the vicinity of polystyrenesulfonate ion.[15] Also, the organic cations tend to enhance the cage-like structure, whereas the polystyrenesulfonate ion may interact with OH groups in water molecules through the intermediary of π electrons of the benzene ring,[16,17] so that the orientation of water molecules in contact with the benzene ring is largely restricted. Thus the polystyrenesulfonate ion influences water structure in a different way from the other inorganic and organic cations.

In the light of the interaction between OH groups and π electrons just mentioned, it may be inferred that the aromatic hydrocarbons are weaker structure formers than the aliphatic ones.[13] Therefore, the relative position of trimethylbenzylammonium ion and tetramethylammonium ion, in the observed order, can be accounted for by the structural factor of the benzene ring in the former, which would cause a less efficient salting-out (or a more efficient salting-in) between the cation and polyanion.

It would then be interesting to compare the polystyrenesulfonate ion with other macro- and simple anions in relation to their structural influences. Figure 1 shows the osmotic coefficients of sodium polystyrenesulfonate (NaPSt), sodium polyethylenesulfonate (NaPES), and sodium polyacrylate (NaPAA). (The osmotic coefficient can be more conveniently used for comparison between polyelectrolytes and simple electrolytes than the activity coefficient of the solute, since γ_0^*, the limiting value of the activity coefficient, cannot uniquely be determined for polyelectrolytes at present.[2]) The data of NaPES have been obtained in this

(14) P. M. Vollmar, *J. Chem. Phys.*, **39**, 2236 (1963).

(15) W.-Y. Wen, S. Saito, and C. Lee, *J. Phys. Chem.*, **70**, 1244 (1966).

(16) I. M. Goldman and R. O. Crisler, *J. Org. Chem.*, **23**, 751 (1958).

(17) M. Oki and H. Iwamura, *Bull. Chem. Soc. Japan*, **33**, 717 (1960).

	NH_4PSt		$N(CH_3)_4PSt$		$N(C_2H_5)_4PSt$	
	φ_z	$\log(\gamma^*/\gamma_0^*)$	φ_z	$\log(\gamma^*/\gamma_0^*)$	φ_z	$\log(\gamma^*/\gamma_0^*)$
1	0.593	−0.851	0.594	−0.429	0.632	−0.393
2	0.622	−0.904	0.621	−0.481	0.670	−0.448
3	0.654	−0.936	0.633	−0.511	0.733	−0.462
4	0.711	−0.939	0.709	−0.516	0.784	−0.458
5	0.785	−0.927	0.788	−0.515	0.864	−0.429
6	0.842	−0.916	0.864	−0.493	0.932	−0.410
7	0.905	−0.898	0.940	−0.462	1.01	−0.379
8	1.00	−0.877	1.01	−0.432	1.11	−0.337
9	1.02	−0.849	1.06	−0.401	1.20	−0.283
10	1.11	−0.801	1.21	−0.335	1.41	−0.181
11	1.22	−0.738	1.37	−0.228	1.65	−0.040
12	1.82	−0.672	1.57	−0.118	1.92	0.130
13	1.92	−0.618	1.81	0.013	2.23	0.321
14	1.61	−0.570			2.60	0.522

	$N(n\text{-}C_3H_7)_4PS$		$N(n\text{-}C_4H_9)_4PSt$		$N(CH_3)_3CH_2C_6H_5PSt$	
	φ_z	$\log(\gamma^*/\gamma_0^*)$	φ_z	$\log(\gamma^*/\gamma_0^*)$	φ_z	$\log(\gamma^*/\gamma_0^*)$
1	0.790	−0.352	0.900	−0.325	0.582	−0.471
2	0.824	−0.392	0.962	−0.322	0.613	−0.530
3	0.888	−0.373	1.03	−0.284	0.610	−0.579
4	0.958	−0.339	1.12	−0.243	0.638	−0.606
5	1.05	−0.301	1.24	−0.177	0.672	−0.620
6	1.15	−0.255	1.34	−0.099	0.705	−0.623
7	1.27	−0.178	1.47	−0.027	0.742	−0.632
8	1.38	−0.113	1.60	0.050	0.780	−0.637
9	1.50	−0.044			0.818	−0.630
10	1.74	0.088			0.894	−0.602
11	2.01	0.262			1.00	−0.549
12	2.32	0.534			1.14	−0.480
13	2.72	1.02			1.29	−0.401

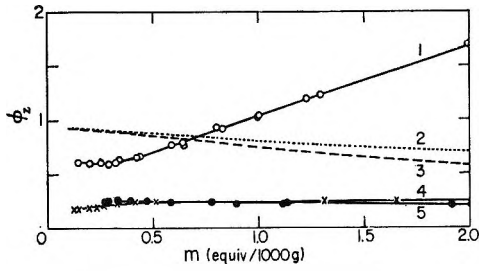

Figure 1. Osmotic coefficients of aqueous solutions of polystyrenesulfonate, polyethylenesulfonate, polyacrylate, and ethylbenzenesulfonates at 25°: (1) sodium polystyrenesulfonate, (2) lithium ethylbenzenesulfonate, (3) sodium ethylbenzenesulfonate, (4) sodium polyacrylate, and (5) sodium polyethylenesulfonate.

laboratory,[18] and those of NaPAA have been calculated from published values of the osmotic coefficient defined on the basis of the number of free ions.[5] These three macroions have approximately the same (linear) charge density. It is seen from Figure 1 that the osmotic coefficient is strongly influenced by the nature of the macroions. According to the structural explanation mentioned above, the experimental results show that the salting-out effect between polystyrenesulfonate ions and sodium ions is stronger than between polyethylenesulfonate ions and sodium ions. It is reasonable to ascribe the difference to the hydrocarbon tail (*i.e.*, benzene ring) present in the polystyrenesulfonate ion, which has a structure-forming tendency as mentioned above, since the sodium ion can be considered a structure former. The relative position of the osmotic coefficients of NaPAA and NaPES at higher concentrations can be accounted for by the stronger structure-forming nature of the former, which is supported by the smaller entropy value for CH_3COO^- (about 15 eu[6]) than that for HSO_3^- (about 32 eu).

Further remarks appear necessary with regard to differences between macroions and simple ions. In Figure 1, the osmotic coefficients of sodium and lithium salts of *p*-ethylbenzenesulfonic acid (EBS)[19] are presented. The coefficient of LiEBS is larger than that of NaEBS. This indicates either the structure-

(18) N. Ise and K. Asai, *J. Phys. Chem.*, in press.
(19) S. Lindenbaum and G. E. Boyd, *ibid.*, 71, 581 (1967).

breaking nature of ethylbenzenesulfonate ion or the presence of an ordered structure around this ion, which is formed in an incompatible way with that around the cation. Clearly the second possibility is acceptable, since this is in accord with the previously concluded structural influence of polystyrenesulfonate ion. However, the osmotic coefficient of NaPSt increases with increasing concentration, whereas that of NaEBS decreases; accordingly, a crossing appears. It is believed that the structural influence of the polyanion sharply varies with concentration, whereas that of the simple anion does not. We propose that the polyanion becomes progressively structure forming with rising concentration. This would be plausible because two benzene rings in the polystyrenesulfonate ion (probably neighboring ones) could fix water molecules by hydrogen bonding involving π electrons in a cooperative manner. Such a sandwich-type structure could be more easily formed at higher concentrations than at lower ones, as a consequence of concentration dependence of the chain configuration. The fact that the structural effects of NaEBS and also of NaPES are concentration insensitive can be accounted for by the above interpretation: for NaEBS, the hydrogen bond is not strong enough to link two benzene rings of independent molecules through the intermediary of water molecules; and NaPES lacks the benzene ring. It is to be remarked that the structure-forming nature of polystyrenesulfonate ion was also concluded from the solubility measurement.[20]

The argument presented in the above paragraphs has been based on the structure concepts which have been originally developed for simple electrolytes. If it can be regarded as successful also in the case of polyelectrolytes, it should be noted that the *ad hoc* postulates, *e.g.*, gegenion association by macroions, have been unnecessary, at least as far as the osmotic and activity coefficients and polystyrenesulfonates are concerned. Though the association does really take place, our results show that the structural factor is of primary importance.

Acknowledgment. The sodium polystyrenesulfonate was kindly furnished from the Dow Chemical Co., Midland, Mich., by courtesy of Drs. W. N. Vanderkooi and J. C. Moore.

(20) J. Steigman and J. L. Lando; *J. Phys. Chem.*, 69, 2895 (1965).

Mean Activity Coefficient of Polyelectrolytes. IX. Activity Coefficients of Polyethylenesulfonates of Various Gegenions[1]

by Norio Ise and Kiyotsugu Asai

Department of Polymer Chemistry, Kyoto University, Kyoto, Japan *(Received October 30, 1967)*

The osmotic and activity coefficients of polyethylenesulfonates of various gegenions in aqueous media have been determined at 25° by means of isopiestic vapor pressure measurements. The polysalts of inorganic gegenions such as H^+, Li^+, Na^+, and K^+ have comparatively small osmotic coefficients. The activity coefficients of these salts decrease linearly with the cube root of polymer concentration, up to about 1 equiv/1000 g of water and decrease in the order H > Li > Na > K. The osmotic coefficients of tetraalkylammonium salts have large values and increase with increasing concentration. The magnitude of the activity coefficient is in the order $N(n\text{-}C_4H_9)_4 > N(n\text{-}C_3H_7)_4 > N(C_2H_5)_4 > N(CH_3)_4 > N(CH_3)_3CH_2C_6H_5 > NH_4$. These relative orders are the same as the ones found for polystyrenesulfonates and are accounted for in terms of the structural effects of the ions on water. It is inferred that the polyethylenesulfonate ion is a structure former.

Introduction

In a previous paper, the (mean) activity coefficients of polystyrenesulfonates of various gegenions have been determined by the isopiestic vapor pressure measurements.[2] The mean activity coefficient to be discussed in the present work should be carefully distinguished from the single-ion activity coefficient having no sound thermodynamic basis. The results have shown that the polystyrenesulfonate ions could

(1) Presented at the 16th Symposium of Polymer Sciences, Fukota, Japan, Oct 1967.

(2) N. Ise and T. Okubo, *J. Phys. Chem.*, 72, 1361 (1968).

form an ordered structure of water. This ability has been ascribed to the presence of benzene rings. In order to study whether this conclusion is of general validity, we extend the measurements to polyethylenesulfonate. This material lacks the benzene ring, so one might expect much weaker solvent–solute interaction than in the polystyrenesulfonate case.

Another purpose of this work is to investigate the specificity of various gegenions in the osmotic and activity coefficients. In previous publications, the specificity of gegenions observed for polystyrenesulfonates[2] and polyvinyl sulfates[3] could successfully be accounted for in terms of the structural influences of the ions on water.[4-6] Though the explanation appears to be reasonable, it is not yet cogent enough to lead us to the recognition of the basic similarity between polyelectrolyte and simple electrolyte solutions, since the structural factor of the ions was found originally for simple electrolyte solutions. Thus it is interesting to accumulate further experimental data for various polyelectrolyte systems.

Experimental Section

Sodium polyethylenesulfonate (NaPES) was a gift from the Hercules Powder Co., Wilmington, Del. The degree of polymerization was 770 by viscometry. An aqueous solution of this salt was passed through a column of cation- and anion-exchange resins to the acid form. Then the aqueous solutions of various salts, such as Li-, Na-, K-, NH_4-, $N(CH_3)_4$-, $N(C_2H_5)_4$-, $N(n\text{-}C_3H_7)_4$-, $N(n\text{-}C_4H_9)_4$-, and $N(CH_3)_3(CH_2C_6H_5)$PES, were prepared by neutralization with aqueous solutions of the corresponding hydroxides (reagent grade). The elementary analyses of the final products showed that the sodium contents were within the range of the experimental error. The analyses indicated that the lithium, potassium, tetraethylammonium, and tetrabutylammonium salts were hydrated with 0.78, 0.39, 8.8, and 9.3 molecules of water/base molecule, respectively. Taking into account these hydration numbers, the degree of sulfonation was determined as 0.99.

Osmotic and activity coefficients were determined by the isopiestic equilibration method at 25 ± 0.005° with an apparatus described before.[7] The reference electrolyte was potassium chloride. The experimental error of the present measurements was, at the highest, 2% of the concentration value.

Results and Discussion

The measured concentrations of the solutions of PES salts and potassium chloride in isopiestic equilibria are listed in Table I.

The practical osmotic coefficient of the polyelectrolyte (ϕ_z) was calculated by the condition of the equal solvent vapor pressure, *i.e.*

$$\phi_z = 2m_{KCl}\phi_{KCl}/(Z/Z_{2g} + 1)(m/Z) \qquad (1)$$

Table I: Isopiestic Concentrations of Potassium Chloride and Polyethylenesulfonates at 25°[a]

m_{KCl}	H	Li	m_{KCl}	Na	m_{KCl}	K
0.0309	0.286	0.288	0.0337	0.268	0.0455	0.432
0.0362	0.306	0.311	0.0391	0.288	0.0634	0.594
0.0461	0.340	0.354	0.0437	0.333	0.0837	0.790
0.0502	0.360	0.374	0.0523	0.397	0.134	1.35
0.0587	0.404	0.419	0.0611	0.469	0.173	1.79
0.0715	0.472	0.488	0.0747	0.586	0.245	2.69
0.0914	0.574	0.602	0.0988	0.777	0.365	4.16
0.117	0.698	0.736	0.106	0.894	0.584	6.09
0.147	0.827	0.878	0.129	1.12		
0.224	1.13	1.19	0.138	1.13		
0.299	1.40	1.51	0.213	1.91		
0.557	2.07	2.25	0.226	2.04		
0.896	2.78	3.08	0.350	3.35		
			0.451	3.84		

m_{KCl}	NH_4	$N(CH_3)_3$-$CH_2C_6H_5$	$N(CH_3)_4$	$N(C_2H_5)_4$	$N(n\text{-}C_3H_7)_4$	$N(n\text{-}C_4H_9)_4$
0.0732	0.274	0.205	0.204	0.202	0.195	0.185
0.177	0.592	0.285	0.374	0.357	0.334	0.304
0.239	0.763	0.502	0.482	0.456	0.410	0.382
0.386	1.09	0.716	0.669	0.626	0.549	0.515
0.520	1.33	0.885	0.817	0.756	0.659	0.622
1.20	1.91	1.45	1.31	1.20	1.04	1.02
1.42	2.03	1.58	1.43	1.32	1.14	1.13

[a] m_{KCl} is in molality; polysulfonate concentration is in equiv/1000 g of water.

where m_{KCl} is the molality of the reference potassium chloride solution, m is the concentration of polyethylenesulfonate (equiv/1000 g of water), Z is the stoichiometric valency of the macroion, Z_{2g} is the valency of gegenion, and ϕ_{KCl} is the practical osmotic coefficient of potassium chloride solution. The activity coefficients of the polyelectrolytes (γ^*) were calculated by using the Gibbs–Duhem equation

$$\ln(\gamma_1^*/\gamma_2^*) = \phi_{z1} - \phi_{z2} + 2\int_{m_1}^{m_2} [(1 - \phi_z)/\sqrt{m}]\, d\sqrt{m} \qquad (2)$$

where the subscripts 1 and 2 correspond to m_1 and m_2, respectively.

The osmotic coefficients of various polyethylenesulfonates are given in Figures 1A and 1B. Evidently, the ϕ_z values of the sulfonates having inorganic gegenions are small compared to those of salts of organic cations. In the concentration range studied, ϕ_z of KPES is smaller than 0.2, whereas the coefficient ex-

(3) N. Ise and T. Okubo, *J. Phys. Chem.*, 71, 1886 (1967).

(4) H. S. Frank and W. Y. Wen, *Discussion Faraday Soc.*, 24, 133 (1957).

(5) H. S. Frank, *J. Phys. Chem.*, 67, 1554 (1963).

(6) H. S. Frank, *Z. Phys. Chem.* (Leipzig), 228, 364 (1965).

(7) T. Okubo, N. Ise, and F. Matsui, *J. Amer. Chem. Soc.*, 89, 3697 (1967).

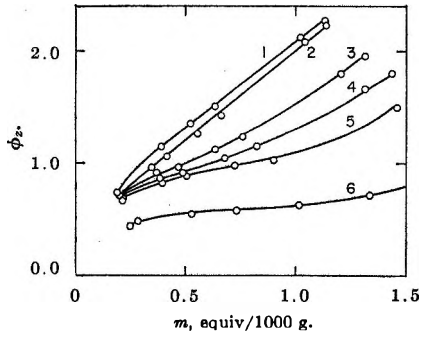

Figure 1A. Osmotic coefficients of aqueous solutions of polyethylenesulfonates at 25°: 1, $N(n\text{-}C_4H_9)_4$; 2, $N(n\text{-}C_3H_7)_4$; 3, $N(C_2H_5)_4$; 4, $N(CH_3)_4$; 5, $N(CH_3)_3CH_2C_6H_5$; 6, NH_4.

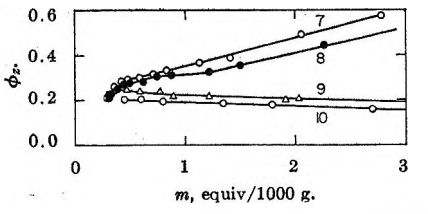

Figure 1B. Osmotic coefficients of aqueous solutions of polyethylenesulfonates at 25°: 7, H; 8, Li; 9, Na; 10, K.

ceeds over unity frequently for organic cations. Furthermore, the osmotic coefficient increases with increasing polymer concentration, except for the sodium and potassium cases.

For H-, Li-, Na-, and KPES, the relative value of the activity coefficient (γ_1^*/γ_2^*) obtained by eq 2 was standardized to γ_0^* at infinite dilution by using the cube-root relation, as before.[3] The final results denoted by γ^*/γ_0^* are given in Figure 2 as a function of the cube root of polymer concentration. Clearly the cube-root rule is valid for these salts at low concentrations. The slopes of the straight lines are -1.0_3, -1.0_9, -1.2_5, and -1.3_2, for H-, Li-, Na-, and KPES, respectively. The activity coefficient is seen to be in the order

$$H^+ > Li^+ > Na^+ > K^+ \qquad (A)$$

This order is the same as found for H_2O–polystyrenesulfonate. As for the alkali metal ions, the same order was found for polyvinyl sulfate in water.[3] The slope values are found to be larger than those observed previously for lithium-, sodium-, and potassium polyvinyl sulfate (ranging from -0.60 to -0.97[3]). This difference is, however, in accord with our previous finding[8] that the magnitude increases with increasing (linear) charge density of the macroion, since the degree of esterification of the polyvinyl sulfate was only 0.227 whereas the degree of sulfonation of the PES almost 1.0. From Figure 2, the upper bound of the range of fit of the rule is about 1 equiv/1000 g of water for all salts. It should be remarked that this value is approximately equal to the ones reported for sodium

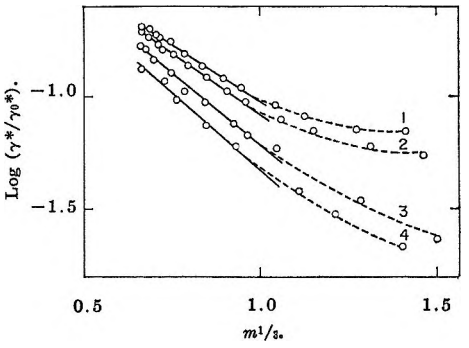

Figure 2. Activity coefficients of polyethylenesulfonic acid and its alkali salts as a function of the cube-root of polymer concentration at 25°: 1, H; 2, Li; 3, Na; 4, K.

polyacrylate[9] and polyethylenimine salt[10] but is much larger than that observed for simple electrolytes (*e.g.*, 0.10 mol/l. for NaCl[11]). Furthermore, the upper bound for the PES is much higher than that observed for polystyrenesulfonates (0.3 equiv/1000 g of water). The reason for this is the strong solvent–solute interaction in the latter case, as mentioned above.

For polyethylenesulfonates of organic gegenions, on the other hand, the activity coefficient increases with increasing concentration. In other words, the cube-root rule does not apply for these salts in the concentration range studied. As a consequence, the standardization could not be carried out at infinite dilution by using the cube-root relationship. Thus the activity coefficient was expediently standardized at 0.2 equiv/1000 g of water and was denoted as $\gamma^*/\gamma_{0.2}^*$. Figure 3 is the graphical presentation of the activity coefficient thus determined. The activity coefficient is seen to be in the order

$$N^+(n\text{-}C_4H_9)_4 > N^+(n\text{-}C_3H_7)_4 > N^+(C_2H_5)_4 > N^+(CH_3)_4 > N^+(CH_3)_3CH_2C_6H_5 > NH_4^+ \qquad (B)$$

We note here that an ambiguity is associated with the order because of the absence of experimental data in the more dilute region. In the light of the osmotic coefficient data given in Figures 1A and 1B, however, the subsequent discussion appears to be meaningful. Furthermore, it should be remembered that the activity coefficients of polystyrenesulfonates[2] decrease in the same order as found in the present work.

According to the theory of structural influences of ions,[4-6] the salting out between ions causes large osmotic and activity coefficients, whereas the salting in causes small ones. Thus the data given in Figures 1A and 1B indicate that the salting-in effect is strong in the

(8) N. Ise and T. Okubo, *J. Phys. Chem.*, **69**, 1930 (1966).
(9) N. Ise and T. Okubo, *ibid.*, **71**, 1287 (1967).
(10) N. Ise and T. Okubo, *ibid.*, **70**, 2400 (1966).
(11) H. S. Frank and P. T. Thompson, "The Structure of Electrolytic Solutions," W. J. Hamer, Ed., John Wiley and Sons, New York, N. Y., 1959.

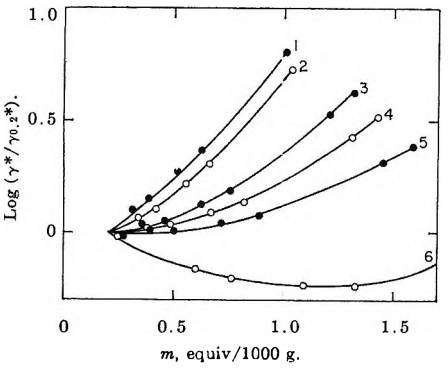

Figure 3. Activity coefficients of polyethylenesulfonates having large organic gegenions at 25°: 1, $N(n\text{-}C_4H_9)_4$; 2, $N(n\text{-}C_3H_7)_4$; 3, $N(C_2H_5)_4$; 4, $N(CH_3)_4$; 5, $N(CH_3)_3CH_2C_6H_5$; 6, NH_4.

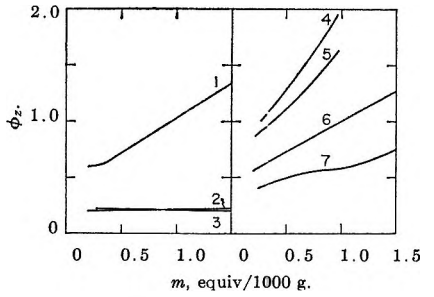

Figure 4. Osmotic coefficients of aqueous solutions of polystyrenesulfonates, polyethylenesulfonates, and polyacrylates at 25°. 1, sodium polystyrenesulfonate; 2, sodium polyacrylate; 3, sodium polyethylenesulfonate; 4, tetrabutylammonium polyethylenesulfonate; 5, tetrabutylammonium polystyrenesulfonate; 6, ammonium polystyrenesulfonate; 7, ammonium polyethylenesulfonate.

cases of inorganic gegenions, whereas the salting-out effect is predominant for the PES having organic gegenions. Since the inorganic cations under consideration are structure forming in the order $H^+ > Li^+ > Na^+ > K^+$,[12] the experimental data suggest that the PES ion should be also a structure former of a mode compatible to that of these gegenions.[13] Because the PES anion does not contain benzene rings, it is not structure producing to the same extent as the PSt ion. However, in view of the ionic entropy value of HSO_3^- (+32.6 eu[12]) being close to that of NH_4^- (+26.4 eu[12]), which is considered not to alter the water structure much,[14] the PES ion can be regarded as a structure former. Furthermore, it would be admitted that the sulfonate group of the PES ion and the inorganic cations immobilize water molecules around themselves by the electrostatic action so that they make a similar water structure and, accordingly, can strongly salt in each other. The stronger salting-in effect in the PES systems than in the PSt cases is understandable in the light of hydrophobic nature of the benzene ring in PSt ions and is clearly demonstrated in Figure 4 (left). It is seen that sodium polyacrylate having hydrophilic carboxylate groups also exhibits a marked salting-in effect.

Unlike the inorganic cation, the organic gegenions are hydrophobic and tend to make the "cage-like" structure of water.[4] Thus the mode of structure making by these large gegenions is incompatible with that by the PES ion. Furthermore, the structure-making tendency is enhanced with increasing numbers of carbon atoms around nitrogen.[5] Thus the PES anion salts out tetrabutylammonium ion most strongly, as is shown in Figure 1A. The relatively weak salting-out effect in the trimethylbenzylammonium case, as demonstrated in Figure 1A, can be accounted for by the less strong structure-making ability of the aromatic (benzene) group than an aliphatic one.[15] The weakest effect for the ammonium salt is due to the inability of this gegenion to alter the water structure.

Comparison between the alkylammonium polyethylenesulfonate and polystyrenesulfonate invites some comments. We note that these two kinds of macroions and also the tetraalkylammonium ions being considered are structure formers. The mode of structure formation by these gegenions is less incompatible with that of the PSt anion than that of the PES anion because of the hydrophobicity of the former anion. Accordingly, a weaker salting-in (or stronger salting-out) effect can be expected in the PES cases. This is substantiated experimentally as shown in Figure 4 (right). (Compare curves 4 and 5.) For ammonium salts, on the other hand, the relative order of ϕ_z is reversed (curves 6 and 7); NH_4PSt has larger ϕ_z than NH_4PES. Since the ammonium ion has little influence on water structure, as mentioned above, and the PSt anion is a stronger structure former than the PES anion, the ammonium ion may be expected to salt out the PSt ion more strongly than the PES ion.

Acknowledgments. The sodium polyethylenesulfonate was kindly furnished from the Hercules Powder Co., Wilmington, Del., by courtesy of Dr. D. S. Breslow.

(12) R. W. Gurney, "Ionic Processes in Solution," McGraw-Hill Book Co., Inc., New York, N. Y., 1953, Chapter 16.

(13) W.-Y. Wen, S. Saito, and C. Lee, *J. Phys. Chem.*, **70**, 1244 (1966).

(14) P. M. Vollmar, *J. Chem. Phys.*, **39**, 2236 (1963).

(15) G. Némethy and H. A. Scheraga, *ibid.*, **36**, 3401 (1962).

Mean Activity Coefficient of Polyelectrolytes. X. Activity Coefficients of Polyphosphates of Various Gegenions[1]

by Norio Ise and Tsuneo Okubo

Department of Polymer Chemistry, Kyoto University, Kyoto, Japan *(Received August 29, 1967)*

The osmotic and (mean) activity coefficients of polyphosphates (PP) of various gegenions in aqueous media have been determined at 25° by means of the isopiestic vapor pressure measurements. The osmotic coefficients of Li-, Na-, and KPP are comparatively small and concentration insensitive, whereas those of $N(n\text{-}C_4H_9)_4$-, $N(n\text{-}C_3H_7)_4$-, $N(C_2H_5)_4$-, $N(CH_3)_4$-, and $N(CH_3)_3CH_2C_6H_5$PP are large and increase with increasing concentration. The activity coefficients of the polyphosphates decrease linearly with the cube root of polymer concentration, up to 0.5 equiv/1000 g of water. The order of the magnitude of the activity coefficient is $N(n\text{-}C_4H_9)_4 > N(n\text{-}C_3H_7)_4 > N(C_2H_5)_4 > N(CH_3)_4 > N(CH_3)_3CH_2C_6H_5$ and Li > Na > K. These relative orders are accounted for in terms of the structural influences of the ions on water. It is inferred that the polyphosphate ion is a structure former, with a mode incompatible to that of sodium ions. The degree of incompatibility is suggested to be intermediate between that of sodium polystyrenesulfonate and sodium polyethylenesulfonate or polyacrylate, owing to a charge-transfer-type interaction of the phosphate group with water molecules. Finally a discrepancy is pointed out between the order of the observed osmotic coefficients and that of the degree of gegenion association. This is interpreted as implying that the solvent–solute interaction is more important than the gegenion association.

Introduction

The systematic study of the (mean) activity coefficients of polyelectrolytes in aqueous solutions is being intensively conducted in this laboratory.[2] So far our attention has been paid to organic polyelectrolytes. In this communication, the measurements are extended to various salts of a polyphosphate, which is an inorganic material. A variety of properties of its solution have been studied by many authors, but the activity coefficient has never been discussed. Thus the osmotic and activity coefficients of polyphosphates are now determined by using the isopiestic equilibration method, and the specificity of gegenions on these coefficients is studied.

Experimental Section

The sodium polyphosphate (NaPP) was a gift from the Monsanto Company, St. Louis, Mo. Its number-average degree of polymerization was 600 in osmometry.[3] A stock solution of NaPP was prepared using conductivity water and was purified by passing through a column containing cation- and anion-exchange resins. The polyacid solution thus obtained was neutralized by the aid of conductometric titration with an aqueous solution of reagent grade LiOH, NaOH, KOH, $(CH_3)_4NOH$ (TMAOH), $(C_2H_5)_4NOH$ (TEAOH), $(n\text{-}C_3H_7)_4NOH$ (TPAOH), $(n\text{-}C_4H_9)NOH$ (TBAOH) or $(CH_3)_3CH_2C_6H_5NOH$ (TMBAOH). The polymer concentration was determined by the titration data.

The isopiestic measurements were carried out at 25 ± 0.005° by using an apparatus described before.[4] The experimental procedures were also reported previously.[4] The maximum inaccuracy of the present measurements was 2% of the concentration values. Usually 72 hr was necessary to attain the isopiestic equilibrium, and several successive experiments were made with the same solution. In order to examine whether degradation can occur during the equilibration time, the viscosity measurements of a carefully stored solution of NaPP were undertaken at a 30-day interval. The results show that the reduced viscosity stayed constant within 3%. From this we concluded that the degradation is practically negligible. Furthermore, we assumed that this applied also to others than the sodium salt. Degradation in the acid form, however, proceeds easily. Thus the neutralization with various alkali solutions was completed within a period as short as possible. It is believed, however, that this is not a source of serious error in our measurements, because the activity coefficient is rather insensitive toward molecular weight like some other thermodynamic properties of polyelectrolytes.

Results and Discussion

The measured concentrations of the isopiestic solutions of the polyphosphate and potassium chloride (reference electrolyte) are given in Table I.

(1) Presented at the 16th Symposium of Polymer Sciences, Fukuoka, Japan, Oct 1967.

(2) In the present work, the mean activity coefficients of polyelectrolytes are being dealt with, which should not be confused with the single-ion activity coefficients of any ionic species.

(3) The measurement was done by using a stock solution of the potassium salt which was prepared as described in the text and employed for the isopiestic experiments.

(4) T. Okubo, N. Ise, and F. Matsui, *J. Amer. Chem. Soc.*, **89**, 3697 (1967).

Table I: Concentrations of the Isopiestic Solutions of Potassium Chloride and Polyphosphates at 25°[a]

m_{KCl}	Li	Na	K	$N(CH_3)_4$	$N(C_2H_5)_4$	$N(n\text{-}C_3H_7)_4$	$N(n\text{-}C_4H_9)_4$	$N(CH_3)_3(CH_2C_6H_5)$
0.0344	0.127	0.126	0.128	...	...	...	...	...
0.0384	0.142	0.142	0.147	...	...	...	...	...
0.0458	0.172	0.178	0.188	...	0.156	...	...	0.154
0.0541	0.207	0.217	0.232	0.178	0.177	0.164	...	0.176
0.0678	0.263	0.282	0.305	0.214	0.210	0.193	0.177	0.213
0.0879	0.348	0.378	...	0.263	0.256	0.230	0.208	0.265
0.103	0.406	0.438	0.446	0.306	0.289	0.259	0.242	0.300
0.143	0.555	0.613	0.593	0.409	0.379	0.340	0.317	0.405
0.198	0.761	0.862	0.838	0.531	0.481	0.428	0.392	0.535
0.244	0.915	1.05	1.01	0.636	0.580	0.520	0.481	0.656
0.351	1.27	1.53	1.48	0.841	0.764	0.673	0.625	0.901
0.529	1.87	2.31	2.28	1.14	1.00	0.885	0.820	1.24
1.12	...	...	...	1.87	1.63	1.40	1.35	2.15

[a] m_{KCl} is in molality; polyphosphate concentration is in equiv/1000 g of water.

The practical osmotic coefficient of the polyelectrolyte (ϕ_z) was calculated by the condition of equal solvent vapor pressure, as previously described.[5] The osmotic coefficients of potassium chloride solutions were taken from the literature.[6] The ϕ_z values of various polyphosphates are presented in Figures 1 and 2. It is seen that polyphosphates having metal ions as gegenions have generally much smaller osmotic coefficients than those of organic gegenions. Furthermore, the coefficients of LiPP, KPP, and NaPP are almost concentration independent in the studied range of concentration and do not change markedly with gegenions. On the other hand, as seen from Figure 2, the ϕ_z values of polyphosphates of organic gegenions increase with increasing concentration and vary remarkably with gegenions.

The activity coefficient (γ^*) was calculated using the Gibbs–Duhem relation, as reported previously.[5] The assumptions involved in the calculation[7] were: first, the cube-root rule holds down to infinite dilution; and second, the polyphosphates have the same activity coefficient γ_0^* at infinite dilution, irrespective of the gegenions. The results are plotted against the cube root of polymer concentration in Figure 3. It is seen that the cube-root rule is valid at low concentrations. The upper bound of the range of fit of the rule is about 0.5 equiv/1000 g of water. The slopes are −1.21, −1.33, −1.42, −3.06, −0.18, −0.45, −0.61, and −0.70 for Li-, Na-, K-, TBA-, TPA-, TEA-, TMA-, and TMBAPP, respectively. As was mentioned in a previous paper,[5] the cube-root rule is related to the local regular distribution of ions, which is caused mainly by the electrostatic interaction. When the nonelectrostatic interaction is strong enough, the rule does not hold, or the range of fit shifts toward lower concentrations. For example, in polystyrenesulfonate solution,[8] in which the strong solvent–solute interaction owing to the benzene ring exists, the rule is

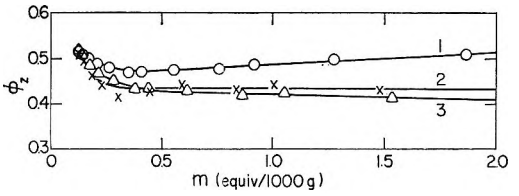

Figure 1. Osmotic coefficients of aqueous solutions of lithium, potassium, and sodium polyphosphates (25°): 1, LiPP; 2, KPP; 3, NaPP.

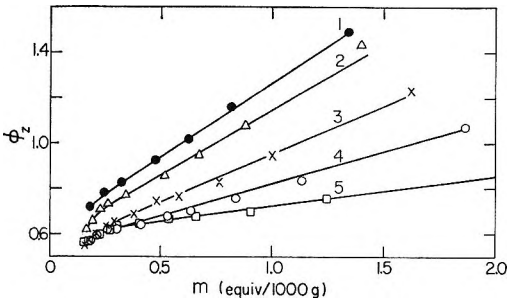

Figure 2. Osmotic coefficients of aqueous solutions of tetrabutylammonium, tetrapropylammonium, tetraethylammonium, tetramethylammonium, and trimethylbenzylammonium polyphosphates (25°): 1, TBAPP; 2, TPAPP; 3, TEAPP; 4, TMAPP, 5, TMBAPP.

valid up to $m = 0.3$. Sodium polyacrylate and polyethylenimine salt, on the other hand, showed a long straight segment of the cube-root plot up to $m \approx 1$, in which the solvent–solute interaction is much weaker than in the polystyrenesulfonate cases.[5,9] From

(5) N. Ise and T. Okubo, *J. Phys. Chem.*, **71**, 1287 (1967).

(6) R. A. Robinson and R. H. Stokes, "Electrolyte Solutions," Butterworth and Co. Ltd., London, 1959, pp 476, 481.

(7) For earlier references on the cube-root rule and for the γ_0^* problem, see N. Ise and T. Okubo, *J. Phys. Chem.*, **71**, 1886 (1967).

(8) N. Ise and T. Okubo, *ibid.*, **72**, 1361 (1968).

(9) N. Ise and T. Okubo, *ibid.*, **70**, 2400 (1966).

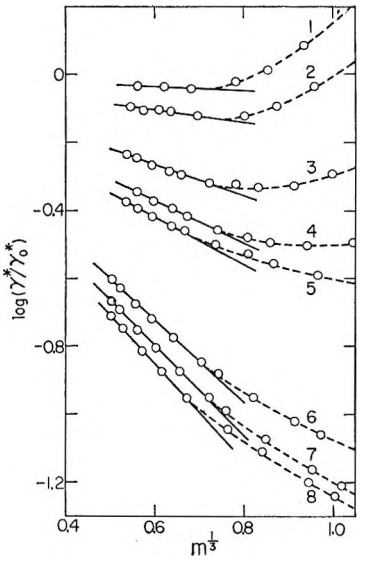

Figure 3. Activity coefficients of polyphosphates in aqueous solutions as a function of the cube root of polymer concentration (25°): 1, TBAPP; 2, TPAPP; 3, TEAPP; 4, TMAPP; 5, TMBAPP; 6, LiPP; 7, NaPP; 8, KPP.

these data it is inferred that the solvent–solute interaction in the polyphosphate solutions is intermediate between the polyacrylate and the polystyrenesulfonate. This matter will be discussed again in the latter part of this paper.

Figure 3 shows that the activity coefficients of the polyphosphates decrease in the order

$$\text{Li} > \text{Na} > \text{K} \qquad \text{(A)}$$

and

$$\text{TBA} > \text{TPA} > \text{TEA} > \text{TMA} > \text{TMBA} \qquad \text{(B)}$$

These orders were already found for polystyrenesulfonates[8] and polyethylenesulfonates.[10] Figure 3 also shows that the activity coefficients of the alkali polyphosphates are smaller than those of the organic salts. According to the existing theories of structural influences of ions on water,[11-14] the structural salting-out effect is more preponderant for the organic salts than for the alkali salts. The alkali metal ions can immobilize water molecules, owing to the electrostatic interaction, and hence can be regarded as structure formers. Similarly, the polyphosphate ion can form an ordered structure as a consequence of the intense electric field around the charged site. Therefore, it is also a structure former. This is in line with the fairly large hydration number of the polyphosphate ion as found by Conway, *et al.*[15] Thus we may expect strong salting-in effect between the metal ion and the polyphosphate ion. It is believed, on the other hand, that the tetraalkylammonium ions have a tendency of forming cage-like water structure around themselves.[11] The incompatibleness of the modes of structure formation causes a strong salting-out effect between the organic gegenions and polyphosphate ion, as was earlier suggested for low molecular weight fluorides by Wen, *et al.*[14]

Next we compare structural influences of various macroions. The existing data show that the osmotic coefficient of sodium salts decreases in the order

$$\text{polystyrenesulfonate}^{8} > \text{polyphosphate} > \text{polyacrylate}^{5} \approx \text{polyethylenesulfonate}^{10} \qquad \text{(C)}$$

Since the polystyrenesulfonate anion has large hydrocarbon parts, an ordered water structure would be formed around this macroion in a way incompatible to that of sodium ion. Thus this macroion would salt out sodium ion strongly. Therefore the ϕ_z is large.[16] The polyacrylate ion can be regarded as a structure former, in the light of the ionic entropy value of CH_3COO^- (+15.0 eu[17]). Similarly, the polyethylenesulfonate ion was also concluded to be a structure former.[10] The mode of water structure around these two macroions is believed to be compatible with that of sodium ions. Thus the salting-in effect is strong for sodium polyacrylate and sodium polyethylenesulfonate, so that small ϕ_z values are observed. It is possible now to conclude that the degree of the incompatibility for sodium polyphosphate is intermediate between two extremes, namely polystyrenesulfonate and polyethylenesulfonate. In this respect, it may be suggested that the polystyrenesulfonate can interact with water molecules through the intermediary of π-electrons of the benzene ring, whereas the polyethylenesulfonate cannot. The situation is the same as found for sodium naphthalenesulfonate and sodium butane-1-sulfonate.[18] Then it is tempting to suggest further that the polyphosphate can interact with water molecules more weakly than the polystyrene, and the polyacrylate interacts as weakly as the polyethylenesulfonate. Though no conclusive proof is available at present, we suggest that the charge-transfer interaction might be a factor determining the observed order (C). Since the charge-transfer interaction can be described by the ionization potential to the first approximation,[19]

(10) N. Ise and K. Asai, *J. Phys. Chem.*, **72**, 1366 (1968).

(11) H. S. Frank and W.-Y. Wen, *Discussion Faraday Soc.*, **24**, 133 (1957).

(12) H. S. Frank, *J. Phys. Chem.*, **67**, 1554 (1965).

(13) H. S. Frank, *Z. Physik. Chem.* (Leipzig), **228**, 364 (1965).

(14) W.-Y. Wen, S. Saito, and C. Lee, *J. Phys. Chem.*, **70**, 1244 (1966).

(15) B. E. Conway, J. E. Desnoyers, and A. C. Smith, *Phil. Trans. Roy. Soc. London*, **256**, 389 (1964).

(16) The structural influences can be discussed in terms of the osmotic coefficient, instead of the activity coefficient. When comparison of various polyelectrolytes is sought, the use of the osmotic coefficient is convenient because the activity coefficient at infinite dilution (γ_0^*) varies from polyelectrolyte to polyelectrolyte. For the γ_0^* problem, see ref 17.

(17) N. Ise and T. Okubo, *J. Phys. Chem.*, **71**, 1886, 4588 (1967).

(18) Z. Yoshida, E. Ōsawa, and R. Oda, *ibid.*, **68**, 2895 (1964).

(19) R. S. Mulliken, *J. Amer. Chem. Soc.*, **74**, 811 (1952); *J. Phys. Chem.*, **56**, 801 (1952).

cur experimental data indicate that the phosphate group has a lower ionization potential than the acrylate group, which would enable the former to form a stronger charge-transfer-type hydrogen bond.[20] Anyway, the mode of the immobilization of water molecules due to the electrostatic forces, which may occur in the cases of simple ions such as metal, carboxylate, or sulfate ions, can be altered by the hydrogen bond formation to the largest extent for the polystyrenesulfonate and to a lesser extent for the polyphosphate. The order of the incompatibility series mentioned above, therefore, can be understood. Also, this explanation is in line with the conclusion in the previous paragraph which was derived on the solvent–solute interaction from the cube-root relationship.

Finally, mention should be made of the gegenion association. This phenomenon has been studied by many authors, since it is characteristic of polyelectrolytes. Experimental data[21] show that the extent of gegenion association by polyphosphate ions decreases in the order

$$\text{Li} > \text{Na} > \text{K} > \text{Cs} \qquad \text{(D)}$$

We may expect that the larger the extent the smaller the number of free gegenions and hence the smaller the ϕ_z value. Therefore, ϕ_z should decrease in the order Cs > K > Na > Li. This is evidently contrary to the observed order Li > Na ≈ K, as shown in Figure 1. This contradiction tells us that the solvent–solute interaction is at least as important as the gegenion association. It appears that a similar conclusion was earlier obtained from the viscometric results.[22] Further, it would be interesting to recall that the ϕ_z value of the polystyrenesulfonate is about ten times larger than that of the polyethylenesulfonate at a given concentration. It seems that such a large difference cannot be explained in terms of the specificity of macroions in the gegenion association phenomenon only. Recently, furthermore, the ϕ_z values have been reported of NaH_2PO_4, $Na_4P_2O_7$, and $Na_5P_3O_{10}$,[23] which are reproduced in Figure 4. The ϕ_z value becomes small as the molecular weight of the polyphosphate increases. According to the transference experiments,[24] on the other hand, the degrees of sodium ion association are 0, 0.021, 0.29, and 0.71 for NaH_2PO_4, $Na_4P_2O_7$, $Na_5P_3O_{10}$, and NaPP, respectively. Therefore, the order of ϕ_z is in agreement with that of the degree of association. However, though the effective number of charges of the sodium polyphosphate should be one-half as many as that of $Na_5P_3O_{10}$, the ϕ_z value of the former is not correspondingly small. These facts strengthen the conclusion mentioned above on the preponderance of the solvent–solute interaction over the gegenion association, though hitherto the contrary appears to be believed to be the case.

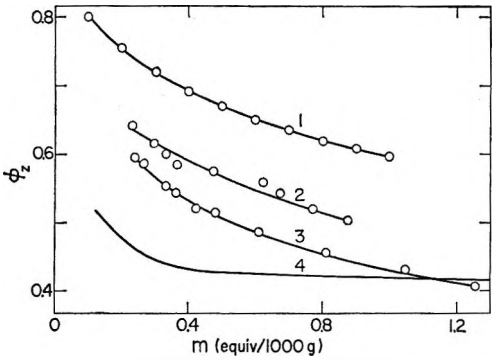

Figure 4. Osmotic coefficients of aqueous solutions of low and high molecular weight polyphosphates (25°): 1, NaH_2PO_4; 2, $Na_4P_2O_7$; 3, $Na_5P_3O_{10}$; 4, NaPP.

Acknowledgment. The authors gratefully acknowledge the encouragement received from Professor Ichiro Sakurada. One of the authors (N. I.) expresses his sincere thanks to Professor Z. Yoshida, Department of Synthetic Chemistry of Kyoto University, for his illuminating suggestion on the hydrogen bond formation between the π base and the proton acceptor. The sodium polyphosphate was kindly furnished from the Monsanto Company, St. Louis, Mo., by courtesy of Dr. E. J. Griffith.

(20) It is not clear presently whether the hydrogen bond is due to π-electrons of the unsaturated bond or to the lone electron pair of phosphorus or carbon atom. Because of a lack of the measurement of the ionization potential of phosphate, our inference mentioned in the text cannot be judged at present either.

(21) U. P. Strauss and P. D. Ross, *J. Amer. Chem. Soc.*, 81, 5295 (1959).

(22) U. P. Strauss, D. Woodside, and P. Wineman, *J. Phys. Chem.*, 61, 1353 (1957).

(23) G. Miller and A. S. Porter, *Trans. Faraday Soc.*, 63, 335 (1967).

(24) F. T. Wall and R. H. Doremus, *J. Amer. Chem. Soc.*, 76, 868 (1954).

Metal–Ammonia Solutions. III. Spectroscopy of Quaternary Ammonium Radicals

by R. K. Quinn and J. J. Lagowski

Department of Chemistry, The University of Texas, Austin, Texas 78712 *(Received October 30, 1967)*

Techniques for the electrolytic generation and the spectroscopic characterization of quaternary ammonium radicals in liquid ammonia have been developed. The spectra of seven tetraalkylammonium radicals in liquid ammonia have been examined in the range 200–2500 mμ. The effects of concentration and temperature, as well as dissolved salts, upon the spectra have been examined. These data indicate that the absorbing species is the same in each case and has the same characteristics as the absorbing species present in metal–ammonia solutions. The implications of these results with respect to the current theories of metal–ammonia solutions are discussed.

Introduction

The addition of active metals to liquid ammonia yields solutions whose physical properties are apparently independent of the identity of the metal; the properties of dilute solutions ($<5 \times 10^{-3}$ *M*) are attributed to the "solvated electron,"[1] a species that is still poorly defined despite the considerable data that have been gathered on these systems. Two basic models for the solvated electron have been used to interpret the properties of these solutions. In the "cavity" model,[2-5] the electron is trapped in a cavity created in the bulk solvent; the system is stabilized by the orientation of the ammonia dipoles on the periphery of the cavity. The "expanded-metal" model[6-8] is conceptually related to the "cavity" model in that the electron in question occupies an "expanded orbital" defined by the hydrogen atoms of the first solvent sphere about the cation.

The transmission spectra of several alkali metal solutions in the concentration range 10^{-1} to 10^{-3} *M* indicate the presence of a single intense band at approximately 1500 mμ.[9-11] The band maximum shifts to lower energies with an increase in temperature and to higher energies if sodium iodide is added to sodium–ammonia solutions. Similar results were obtained for dilute solutions of alkali and alkaline earth metals in liquid deuterioammonia.[12] According to the description of the two models for the negative species present in metal–ammonia solutions, the "cavity" model suggests that the energy for the transition should be essentially independent of the identity of the metal cation. The energy of transition based on the "expanded-metal" model should show a more marked dependence on the size of the cation. However, the variation in the size of the alkali and alkaline earth metal ions may not be sufficient to allow discrimination between the two models.

The electrolysis of quaternary ammonium salts in liquid ammonia produces blue solutions[13-15] which have chemical properties similar to those of the metal–ammonia solutions[16-18] as well as comparable oxidation potentials.[19,20] These observations suggested that a spectroscopic study of the cathodic products formed in the electrolysis of tetraalkylammonium salts in liquid ammonia might aid in understanding the nature of metal–ammonia solutions because of the possibility of varying the size of the cation associated with the electron in these solutions.

Experimental Section

Tetraalkylammonium salts, the purest available commercially, were dried *in vacuo* at 100°, recrystallized from anhydrous liquid ammonia, heated again *in vacuo* at 100°, and stored in a helium-filled drybox the at-

(1) C. A. Kraus, *J. Franklin Inst.*, **212**, 537 (1931).
(2) R. A. Ogg, *J. Am. Chem. Soc.*, **68**, 155 (1946).
(3) R. A. Ogg, *J. Chem. Phys.*, **14**, 144 (1946).
(4) R. A. Ogg, *ibid.*, **14**, 295 (1946).
(5) J. Jortner, *ibid.*, **30**, 839 (1959).
(6) E. Becker, R. H. Lindquist, and B. J. Alder, *ibid.*, **25**, 971 (1956).
(7) E. Arnold and A. Patterson, Jr., *ibid.*, **41**, 3089 (1964).
(8) H. M. McConnell and C. H. Holm, *ibid.*, **26**, 1517 (1957).
(9) M. Gold and W. L. Jolly, *Inorg. Chem.*, **1**, 818 (1962).
(10) C. J. Hallada and W. L. Jolly, *ibid.*, **2**, 1076 (1963).
(11) R. C. Douthit and J. L. Dye, *J. Am. Chem. Soc.*, **82**, 4472 (1960).
(12) D. F. Burow and J. J. Lagowski, Advances in Chemistry Series, No. 50, American Chemical Society, Washington, D. C., 1965, p 125.
(13) W. Palmaer, *Z. Elektrochem.*, **8**, 729 (1902).
(14) H. H. Schlubach, *Ber.*, **53B**, 1689 (1920).
(15) H. H. Schlubach and F. Ballauf, *ibid.*, **54B**, 2811 (1921).
(16) H. H. Schlubach and G. V. Zwehl, *ibid.*, **56B**, 1889 (1923).
(17) H. H. Schlubach and H. Miedel, *ibid.*, **65B**, 1892 (1923).
(18) S. Goldschmidt and F. Nagel, *ibid.*, **64B**, 1744 (1931).
(19) G. S. Forbes and C. E. Norton, *J. Am. Chem. Soc.*, **48**, 3233 (1926).
(20) H. A. Laitinen and C. J. Nyman, *ibid.*, **70**, 3002 (1948).

mosphere of which was equilibrated with Na–K liquid alloy.[21]

Preliminary studies of the spectra of electrolytically generated tetraalkylammonium radicals were made using a modified version of an apparatus described previously.[12] The results of these experiments indicated the desirability of modifying several of the design features of the original optical cell to increase the reliability of the data. Accordingly, a multicompartmented dewar vessel (Figure 1) was constructed. The winch mechanism used to introduce solids into the cell has been described[12] previously. The outer vacuum jacket was continually evacuated with an oil diffusion pump backed by a mechanical pump; under these conditions condensation did not form on the optical windows. The electrolytic–optical cell was attached to the vacuum jacket by means of an O-ring joint which permitted ready access to the tri-compartmented Pyrex electrolysis cell carrying a fused quartz optical cell; this feature was indispensible in the early experiments. The electrode compartments (A and B) were separated by medium porosity frits from an intermediate compartment (C) which was used as a salt bridge. The optical cell was attached to the cathode compartment with graded seals.

The large extinction coefficient ($\epsilon \simeq 4 \times 10^4$) of the broad absorption band characteristic of metal–ammonia solutions[9–12] and the very intense solvent bands for liquid ammonia in the region of interest[12] required that the optical path length be ≤ 0.5 mm for best results; the path length of the cell (Figure 2) used in these experiments was 0.421 mm. The platinum gauze cathode was positioned to permit the electrolysis products to diffuse rapidly into the light path.

The entire dewar system was permanently installed in the cell compartment of a Beckman DK-2 ratio-recording spectrophotometer. The optical quartz windows were secured to ground-glass flanges on the dewar vacuum jacket with picein sealing compound and transmitted both the sample and reference beams of the spectrometer. The outer dewar jacket, O-ring, and inner electrolytic–optical cell were oriented to allow the sample beam to pass through the inner optical cell while the reference beam passed through the evacuated portion of the dewar.

The reaction vessel was cleaned by a special rinsing procedure[12] which involved keeping a sodium–ammonia aging solution in the vessel for several hours as the key step. Qualitatively, ammonia solutions of tetraalkylammonium radicals appear to be less stable than those of the alkali metals. However, there was no appreciable decomposition in the time required to determine the spectrum of a given system. If the absorbance at a given wavelength decreased by less than 0.025 unit in the time required to record the spectrum from 200 to 2500 mμ, the spectrum was considered acceptable since the region of particular

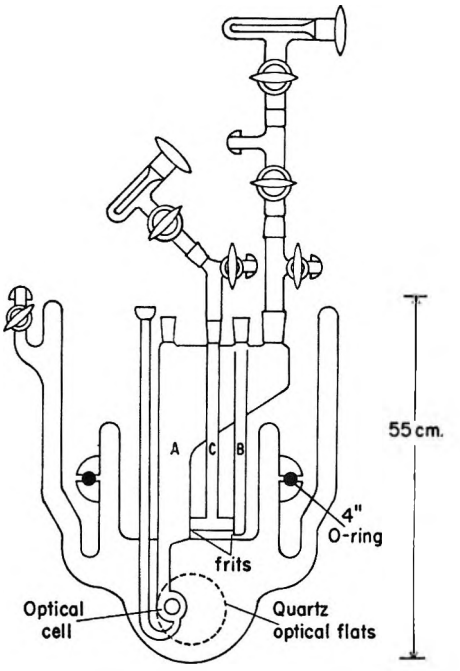

Figure 1. A schematic diagram of the electrolytic–optical dewar system. An "unfolded" cross section of the cell is shown for ease of description.

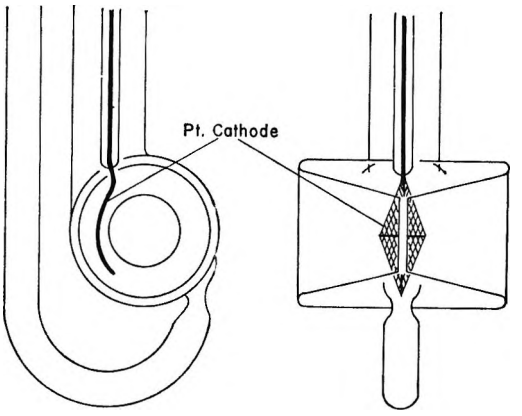

Figure 2. Quartz optical cell with platinum cathode in position.

interest (800–2000 mμ) required only a fraction of the total scan time. The concentration of the absorbing species was determined coulometrically using a graphical integration method accurate to within ±0.005 coulomb.[22]

Results and Discussion

Spectral measurements on the rate of diffusion of the electrolytically generated species indicated that diffusion had virtually ceased about 10–12 min after the electrolysis was terminated. After this time slow de-

(21) D. F. Burow, Ph.D. Dissertation, The University of Texas, 1966.

(22) R. K. Quinn, Ph.D. Dissertation, The University of Texas, 1967.

composition of the radical was observed as reflected by a decrease of <0.025 absorbance unit/hr at the band maximum. Metal–ammonia solutions decompose to form metal amide and hydrogen in the presence of platinum,[23] and by analogy, a similar reaction would be expected for ammonium radicals.

$$NR_4\cdot + NH_3 \longrightarrow NR_4^+ + NH_2^- + {}^1/_2H_2 \quad (1)$$

However, the decomposition of the cathodically generated species in the presence of platinum is not as important as the procedure used to clean the cell; a much higher rate of decomposition is observed if the apparatus is only rinsed with anhydrous ammonia. Quaternary ammonium ions are unstable in the presence of amide ions at the boiling point of liquid ammonia.[24] If the decomposition of the cathodically generated species corresponds to the process shown in eq 1, the decrease in absorbance is equivalent to the formation of less than 10^{-5} mole/l. of NH_2^- per hour, an amount which could not be detected spectrophotometrically[25] with the apparatus used in this investigation. Decomposition of the quaternary ammonium ions by NH_2^- arising from eq 1 should be significant under these conditions.

Electrolysis of concentrated ammonium chloride solutions maintained at −78 to −80° for several hours produced large quantities of hydrogen and nitrogen as verified by mass spectroscopy. Previous attempts to produce hydrogen-substituted ammonium radicals were also unsuccessful.[14,15,26,27] Quaternary ammonium salts containing an aromatic group did not yield blue solutions after electrolysis for several hours, in agreement with the results of other investigators.[14,15]

The spectra of the blue solutions formed in the electrolysis of seven tetraalkylammonium salts were determined at 200–2500 mμ. A single broad band with a maximum at 1440 ± 4 mμ at −70° was observed in all cases (Figure 3). The band parameters were the same within experimental error for all the radicals studied in the concentration range 2–200 × 10^{-5} *M* (Table I). Although the bands appear symmetrical with respect to wavelength, they are asymmetrical on an energy scale. Calculation of the extinction coefficients of the radicals based on the number of coulombs of electricity passed through the cell gave an average extinction coefficient of 4 ± 1 × 10^4 l. mole^{-1} cm^{-1}. Using the approximation method suggested by Dunn,[26] a value of 0.65 ± 0.06 was obtained for the oscillator strength of the species giving rise to the transition. An increase in wavelength of the absorbance maximum with increasing concentration (1–100 × 10^{-3} *M*) for solutions of alkali metals in ammonia has been reported;[9,11] however, this dependence was not observed for more dilute (5–50 × 10^{-5} *M*) metal–deuterioammonia solutions.[12] The spectra of quaternary ammonium radicals throughout the concentration range (2–200 × 10^{-5} *M*) studied show a random scattering of λ_{max} that is within the error

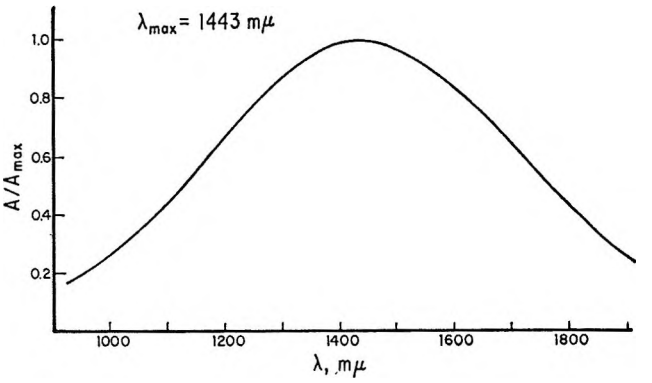

Figure 3. The absorption spectrum (normalized) of 3.48 × 10^{-4} *M* tetraethylammonium radical at −70°.

Table I: Position of Absorption Maxima of Quaternary Ammonium Radicals in Ammonia at −70°

$NR_4\cdot$	λ_{max}, mμ	$\bar{\nu}_{max}$, cm^{-1}	$W_{h/2}$, mμ
$N(Me)_4$	1445	6920	653
$N(Et)_3Me$	1438	6954	627
$N(Et)_4$	1443	6930	644
$N(Et)_3Pr^n$	1437	6959	660
$N(Pr^n)_4$	1434	6974	629
$N(Bu^n)_4$	1434	6974	660
$N(Me)_3$dodecyl	1446	6916	655
Average	1440 ± 4	6944 ± 21	647 ± 12

of the experiments, indicating that there is no dependence of the band position on the concentration.

Previous investigations of metal–ammonia solutions indicate a perturbation of the spectrum in the presence of alkali metal halides.[9–12,27] Since all the quaternary ammonium radicals were generated electrolytically from solutions of their respective salts, it should be possible to observe these effects in the experiments reported here. However, the position and the shape of the band for all the tetraalkylammonium radicals studied were unaltered as the concentration of tetraalkylammonium salt was varied in the range 1–1000 × 10^{-4} *M*.

The effect of temperature on the absorption band was studied using a solution of 2.85 × 10^{-4} *M* tetraethylammonium radical, generated in the presence of 0.03 *M* $(C_2H_5)_4NBr$, in the temperature range −33 to −73°. The band maximum moves to longer wavelengths as the temperature increases. The linear relationship

(23) G. W. Watt, G. D. Barnett, and L. Vaska, *Ind. Eng. Chem.*, **46**, 1022 (1954).

(24) W. L. Jolly, *J. Am. Chem. Soc.*, **77**, 4958 (1955).

(25) R. E. Cuthrell and J. J. Lagowski, *J. Phys. Chem.*, **71**, 1298 (1967).

(26) T. M. Dunn, "Modern Coordination Chemistry," J. Lewis and R. G. Wilkins, Ed., Interscience Publishers Inc., New York, N. Y., 1960, p 276.

(27) H. C. Clark, A. Horsfield, and M. C. R. Symons, *J. Chem. Soc.*, 2478 (1959).

between temperature and position of the band maximum (Figure 4) gives a temperature coefficient of 2.7 ± 0.4 mμ deg^{-1} (−12.7 ± 2.0 cm^{-1} deg^{-1}). Temperature coefficients of −9.1,[28] −9.7,[11] −12.7,[9] and −12.0[22] cm^{-1} deg^{-1} have been reported for solutions of alkali metals in liquid ammonia. Analysis of the spectrum of the tetraethylammonium radical at several temperatures indicates that the band width at half-height (647 ± 12 mμ) varies in a random manner with temperature. Thus, the shape of the band for the electrolytically generated species appears to be independent of the temperature. Electrolytically generated alkali metal solutions in the same concentration range show a single band with a maximum centered between 1430 and 1454 mμ, with an average width at half-height of 639 mμ, and an average extinction coefficient of 4.8 × 10^4 l. mole^{-1} cm^{-1}.[22] Thus it appears that the species giving rise to the spectral transition in solutions of tetraalkylammonium radicals is the same as that in metal–ammonia solutions, *i.e.*, the "solvated electron."

The most outstanding feature of the spectra of liquid ammonia solutions of tetraalkylammonium radicals is the constancy of the position of the absorption band at 1440 mμ throughout the range of cation size studied (Figure 5). An estimate of the volumes for the symmetrical and nearly symmetrical tetraalkylammonium ions was obtained by assuming that the alkyl branches were in the least sterically hindered conformation; this procedure gives a result which represents the minimum volume that the tetraalkylammonium cations could occupy. Spectral data for dilute solutions of the alkali and alkaline earth metals are also included in Figure 5; the volumes of the corresponding cations have been calculated from Pauling's ionic radii.[28] Errors in the calculation of the volumes introduced by these approximations are relatively unimportant in view of the fact that no significant variation in the position of the absorption band was observed from the smallest alkali metal ion to the largest tetraalkylammonium ion. The slope of the line shown in Figure 5, which was obtained from a least-squares analysis, is indistinguishable from zero within experimental error. Of special interest are the results obtained with solutions containing dodecyltrimethylammonium cations; the band maximum for this species was observed at 1446 mμ. Elworthy[29] has described the shape of the solvated trimethyloctylammonium ion in aqueous solution as a prolate ellipsoid with a major axis of 9 Å and a minor axis of 3.6 Å, yielding an approximate volume of 500 Å^3. In the case of dodecyltrimethylammonium cation, the major axis, at least, would have to be longer than that for trimethyloctylammonium ion, leading to a larger volume for the former species. Thus, one of the tetraalkylammonium cations used in this investigation must be unsymmetrical with respect to the center of positive charge.

Basically, two models for the monomer species have been suggested: (a) an electrostatic association of the solvated electron and a solvated cation,[30] and (b) the "expanded-metal" model.[6-8] It has been suggested that the monomer in the "expanded-metal" model is in equilibrium with solvated electrons (M = M$^+$ + e$^-$, K = 0.03 at −33°).[6] Although in metal–ammonia solutions the concentration of the monomer is negligibly small in dilute solutions (*i.e.*, a total metal concentration of 1 × 10^{-3} M), in the presence of a large excess of cation the concentration of monomer should increase. Under the conditions of our experiments (*e.g.*, 0.1 M MX and 1 × 10^{-3} M solvated electrons) and assuming that the value of the constant reported[6] for the equilib-

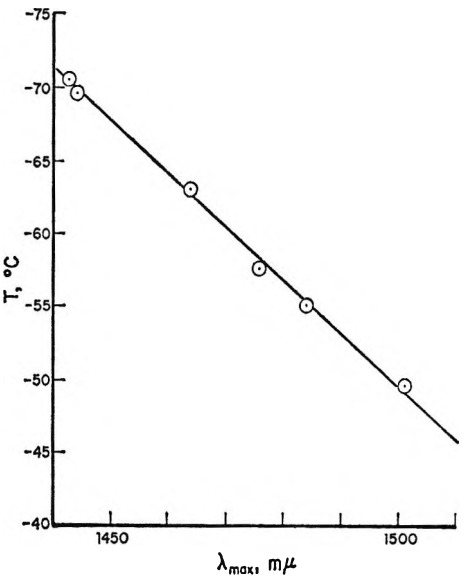

Figure 4. The temperature dependence of the position of the band maximum for 2.85 × 10^{-4} M $(C_2H_5)_4N\cdot$ in liquid ammonia.

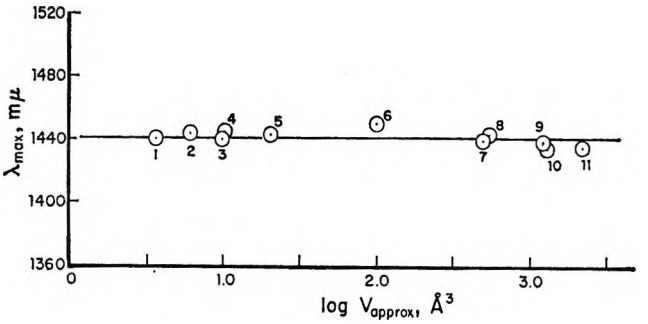

Figure 5. The position of the absorption maximum in solutions containing the solvated electron associated with cations of various sizes: 1, Na^+; 2, Sr^{2+}; 3, K^+; 4, Ba^{2+}; 5, Cs^+; 6, $N(CH_3)_4^+$; 7, NEt_3Me^+; 8, NEt_4^+; 9, NEt_3Pr^+; 10, NPr_4^+; 11, NBu_4^+.

(28) L. Pauling, "The Nature of the Chemical Bond," 3rd ed, Cornell University Press, Ithaca, N. Y., 1960, p 514.

(29) P. H. Elworthy, *J. Chem. Soc.*, 388 (1963).

(30) M. Gold, W. L. Jolly, and K. S. Pitzer, *J. Am. Chem. Soc.*, 84, 2264 (1962).

rium between monomers and solvated electrons for the alkali metals is essentially the same for tetraalkylammonium cations, some solutions should have contained at least 60% of the electrons as monomers. Moreover, the monomers, if they are formed containing tetraalkylammonium cations, should contain cations with widely differing geometrical requirements which should be reflected in the spectra of these solutions.

Making the reasonable assumption that our solutions contain a significant fraction of electrons as NR_4 monomers, the spectral data suggest that in the relatively dilute concentration range (2–200 $\times$ 10^{-5} M) the solvated electron is not associated with the solvated cationic species in solution in the manner required by the "expanded-metal" model.[6-8] Rather the results seem to favor the "cavity model"[2-5] in which the trapped electron is electrostatically associated with the solvated cations present,[30] much as is any ammonia solution containing charged species.[31]

Acknowledgment. We gratefully acknowledge the financial support of the Robert A. Welch Foundation and the National Science Foundation.

(31) V. F. Hnizda and C. A. Kraus, *J. Am. Chem. Soc.*, 71, 1565 (1949).

A Temperature-Jump Study of the Kinetics of the Formation of the Monosulfato Complex of Iron(III)

by Francesco Paolo Cavasino

Institute of Physical Chemistry, University of Palermo, Palermo, Italy

Accepted and Transmitted by The Faraday Society (May 25, 1967)

The rate of formation of the monosulfato complex of iron(III) has been studied in acidic aqueous solution at 25° and ionic strength of 1.2 and 2.0 M and in the temperature range of 7–33° at ionic strength 0.5 M. Over the range of acidity studied at $\mu = 0.5$ M ($0.01\ M \leqslant [H^+] \leqslant 0.41\ M$), the complex formation occurs significantly *via* two paths: *i.e.*, an acid-independent path and a second path dependent on the reciprocal of the hydrogen ion concentration. The investigations performed at ionic strength of 1.2 and 2.0 M over a wider acidity range have shown that an additional path dependent on $[H^+]$ also contributes to the complex formation at higher acidities. Activation parameters for the formation and dissociation of $FeSO_4^+$ lead one to consider Fe^{3+} and SO_4^{2-}, rather than $FeOH^{2+}$ and HSO_4^-, as the reactants in the acid-independent path. The results are in agreement with the view that the elimination of a water molecule coordinated to the metal ion is the rate-determining step in all cases, even though for the reaction of Fe^{3+} with SO_4^{2-} the water elimination rate may be probably somewhat enhanced.

Introduction

In a previous paper[1] concerning the mechanism of iron(III) complex formation it was observed that in the case of the formation of $FeSO_4^+$ there was a discrepancy between the experimental data of Wendt and Strehlow[2] and those obtained by Davis and Smith.[3] In fact, according to the latter investigators the formation of the $FeSO_4^+$ complex would occur only *via* an acid-independent path, while Wendt and Strehlow also observed the contribution of a second reaction path dependent on the reciprocal of the hydrogen ion concentration. As was previously pointed out,[1] this discrepancy is not explained by taking into account the different range of acidity in which the two groups of investigators worked. Therefore, we have considered that it was suitable to reexamine the kinetics of formation of this complex over a wide range of acidity and temperature.

Experimental Procedure[4]

A stock acidified solution of $Fe(ClO_4)_3$ was prepared from Fluka reagent grade salt and perchloric acid, using doubly distilled water. The metal ion concentration was determined by complexometric titration with disodium EDTA.[5] The perchloric acid content

(1) F. Accascina, F. P. Cavasino, and S. D'Alessandro, *J. Phys. Chem.*, 71, 2474 (1967).

(2) H. Wendt and H. Strehlow, *Z. Elektrochem.*, 66, 228 (1962).

(3) G. G. Davis and W. MacF. Smith, *Can. J. Chem.*, 40, 1836 (1962).

(4) The experimental part of this work was performed at the Max Planck Institut für Physikalische Chemie, Göttingen, West Germany.

(5) A. I. Vogel, "A Text-book of Quantitative Inorganic Analysis," 3rd ed, Longmans, Green and Co., London, 1964, p 444.

was determined as described by Milburn and Vosburgh.[6]

Stock solutions of sodium sulfate and sodium perchlorate were prepared by dissolving the appropriate weight of very pure Fluka salts (Na_2SO_4 and $NaClO_4 \cdot H_2O$) in doubly distilled water. Anhydrous sodium sulfate was dried for 4 hr at 130° before weighing.

Each solution examined was prepared by mixing fixed amounts of the stock solutions of sodium sulfate and iron(III) perchlorate. The ionic strength and the hydrogen ion concentration were adjusted to the desired value with the stock sodium perchlorate solution and standard perchloric acid, respectively. The pH measurements were made with a Radiometer 22 pH meter.

The kinetic experiments were performed on the temperature-jump apparatus used previously[7] at the wavelength of 320 mμ. The kinetics were studied at an ionic strength of 0.5 *M* in the temperature range 7–33°. Further investigations were carried out at 25° and an ionic strength of 1.2 and 2.0 *M*. These temperature values indicate the final temperature reached after the temperature jump of 6°.

All the sample solutions showed a single relaxation effect in the time range 0.05–20 μsec. Since blank solutions containing only iron(III) perchlorate at the same conditions of concentration, ionic strength, and pH gave no relaxation in the same range of time, the observed relaxation time should be related to the metal-complexing reaction. A second relaxation effect was also observed at longer times ($\gtrsim$0.5 sec) with sample solutions at pH >1.6. This relaxation was also exhibited by the corresponding blank solutions. This longer relaxation, which would be ascribed very probably to the dimerization reaction of $FeOH^{2+}$,[8] did not interfere with the evaluation of the relaxation time related to the complexations.

Calculations

According to the general mechanism previously suggested for the formation of complexes of iron(III) with monodentate ligands,[1] the formation of $FeSO_4^+$ in aqueous solution may be considered to occur as follows

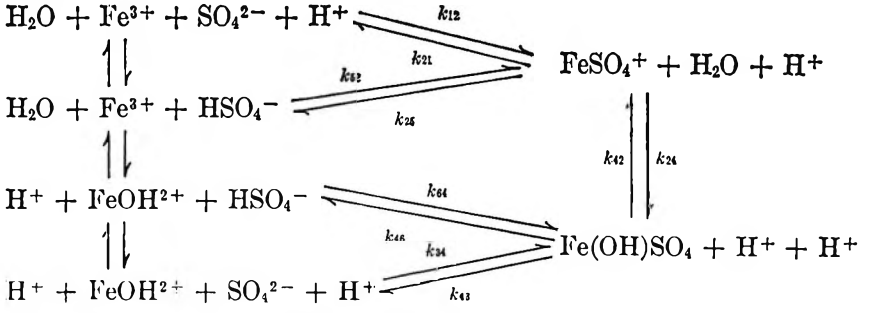

with $K_C = k_{12}/k_{21}$; $K_C K_H = k_{52}/k_{25}$; $K_C K_i/K_{OH} = k_{34}/k_{43}$; $K_C K_H K_i/K_{OH} = k_{64}/k_{46}$ (K_C is the formation constant of $FeSO_4^+$, K_H is the dissociation constant for the acid HSO_4^-, K_{OH} is the equilibrium constant for the first hydrolysis of ferric ion, and $K_i = k_{24}/k_{42}$ is the equilibrium constant for the hydrolysis of $FeSO_4^+$).

Such a reaction scheme would lead to a spectrum of relaxation times. However, since the protolytic reactions (vertical steps) will be associated with very short relaxation times, which hence would not be observed, only one relaxation time related to the slower metal-complex formation reactions should be expected to be found. A single relaxation effect was, in fact, found experimentally over the time range examined (2×10^{-5} to 5×10^{-2} sec).

Assuming that the intermediate $Fe(OH)SO_4$ is in a steady state, the usual rate expression for the formation of $FeSO_4^+$ is given by (charges are omitted for simplicity; the SO_4^{2-} anion is indicated by A)

$$\frac{d(FeA)}{dt} = k_{12}(Fe)(A) + k_{52}(Fe)(HA) + k_{64}(FeOH)(HA) + k_{34}(FeOH)(A) - k_{21}(FeA) - k_{25}(FeA)(H) - k_{46}K_i(FeA) - k_{43}(K_i/K_w)(OH)(FeA) \quad (1)$$

where K_w is the ionic product of water.

The rate equation valid in the neighborhood of equilibrium can be obtained by using the equations

$$\Delta[FeA] + [FeA] = (FeA); \quad \Delta[Fe] + [Fe] = (Fe); \text{ etc.} \quad (2)$$

and the conservation relations

$$\Delta[Fe] + \Delta[FeOH] + \Delta[FeA] = 0; \quad (\Delta[Fe(OH)A] \approx 0)$$
$$\Delta[A] + \Delta[HA] + \Delta[FeA] = 0 \quad (3)$$
$$\Delta[H] + \Delta[HA] = \Delta[FeOH]; \quad (\Delta[OH] \approx 0)$$

where the brackets indicate the equilibrium concentration and Δ[] indicates the deviation of the concentration of a given ion from its equilibrium value.

After substitution of eq 2 and 3 into eq 1 and appropriate expansion, noting that $\Delta[]\Delta[] \approx 0$, $k_{12}[Fe]$-

(6) R. M. Milburn and W. C. Vosburgh, *J. Amer. Chem. Soc.*, **77**, 1352 (1955).

(7) F. P. Cavasino, *Ric. Sci. Rend.*, **A8**, 1120 (1965).

(8) H. Wendt, *Z. Elektrochem.*, **66**, 235 (1962).

[A] = k_{21}[FeA], etc., for the other equilibrium conditions, the following rate equation is obtained

$$\frac{d\Delta[FeA]}{dt} = -\frac{\Delta[FeA]}{\tau}$$

with

$$\frac{1}{\tau} = \left\{\frac{k_{52}[H]}{K_H}(1+\beta) + k_{34}\frac{K_{OH}}{[H]}(1+\delta) + k_{12} + k_{64}\frac{K_{OH}}{K_H}(1+\eta)\right\}B \quad (4)$$

where τ is the relaxation time and

$$B = \frac{[Fe]}{1+\gamma} + \frac{[A]}{1+\alpha} + \frac{1}{K_C}$$

where $\gamma = \Delta[HA]/\Delta[A]$ and $\alpha = \Delta[FeOH]/\Delta[Fe]$. The γ and α factors can be evaluated with the use of eq 3 and the expressions

$$K_{OH}\Delta[Fe] = [H]\Delta[FeOH] + [FeOH]\Delta[H]$$

$$K_H\Delta[HA] = [H]\Delta[A] + [A]\Delta[H]$$

The result is

$$\gamma = \frac{[H]\{[H] + K_{OH} + [FeOH]\} + K_{OH}[A]}{K_H\{[H] + K_{OH} + [FeOH] + [HA]\}}$$

$$\alpha = \frac{K_{OH}\{[H] + K_H + [A] + [Fe]\}}{[H]\{[H] + K_H + [A]\} + K_H[FeOH]}$$

The quantities β, δ, and η depend on the equilibrium concentrations of the various chemical species and are negligible with respect to unity under the conditions of the experiments. Therefore, eq 4 can be rewritten as

$$1/\tau B = (k_{52}[H]/K_H) + (k_{34}K_{OH}/[H]) + k \quad (5)$$

where

$$k = k_{12} + (k_{64}K_{OH}/K_H) \quad (6)$$

Equation 5 is analogous to that reported in the previous paper (with (H) = [H]).[1]

Results and Discussion

The total concentration of iron and of sulfate, indicated by $(Fe)_T$ and $(SO_4)_T$, respectively, together with the equilibrium hydrogen ion concentration, $[H^+]$, and the relaxation time, τ, at ionic strength 0.5 *M* and various temperatures are reported in Table I. The experimental data at 25° and ionic strength 1.2 and 2.0 *M* are assembled in Table II. The relaxation time has been evaluated by the plot of the logarithm of the oscilloscope amplitude *vs.* time. The relaxation times reported are the mean of four runs and are affected by a maximum error of about ±7%. The hydrogen ion concentrations listed in Table I were calculated from pH measurements using activity coefficients evaluated by the equation of Wenger and coworkers.[9] The hydrogen ion concentration of Table II was assumed equal to the stoichiometric concentration of perchloric acid.

Table I: Kinetic Data for $FeSO_4^+$ Formation[a]

$10^3(Fe)_T$, *M*	$10^3(SO_4)_T$, *M*	$10^3[H^+]$, *M*	$10^2\tau$, sec
	Temp = 33°		
1.50	0.75	11.4	1.97
2.00	0.75	13.1	1.98
3.00	2.50	15.1	1.87
2.00	0.75	19.4	2.94
1.00	0.75	22.3	3.69
2.00	1.00	27.4	4.40
1.50	0.75	39.6	5.08
2.50	1.00	51.0	6.09
2.50	1.00	90.8	10.3
3.50	2.00	415	20.8
	Temp = 25°		
2.00	1.50	9.7	2.80
1.50	0.75	11.4	4.17
2.00	0.75	13.0	4.10
3.00	2.50	15.1	3.76
2.00	1.00	15.7	4.41
2.00	0.75	19.3	6.10
1.00	0.75	22.2	6.80
2.00	1.00	27.3	8.14
1.50	0.75	39.4	11.0
2.50	1.00	50.8	12.3
2.00	0.75	61.2	14.3
2.50	1.00	90.4	18.3
2.00	1.00	101	18.3
3.50	2.00	413	31.6
	Temp = 15°		
1.50	0.75	11.3	10.2
2.00	0.75	13.0	11.7
3.00	2.50	14.9	10.0
2.00	0.75	19.2	16.3
1.00	0.75	22.1	17.1
2.00	1.00	27.2	21.0
1.50	0.75	39.3	25.5
2.50	1.00	50.6	31.8
2.50	1.00	90.1	46.2
2.00	1.00	101	41.9
3.50	2.00	411	72.7
	Temp = 7°		
1.50	0.75	11.3	23.9
2.00	0.75	12.9	26.6
3.00	2.50	14.9	26.1
2.00	0.75	19.2	41.3
1.00	0.75	22.0	45.0
2.00	1.00	27.1	48.4
3.00	2.00	29.9	41.6
1.50	0.75	39.1	53.6
2.00	0.75	60.6	71.3
2.50	1.00	89.6	99.3
3.50	2.00	409	143

[a] μ = 0.5 *M*.

(9) P. E. Wenger, D. Monnier, and I. Kapetanidis, *Helv. Chim. Acta*, **40**, 1456 (1957).

Table II: Kinetic Data for $FeSO_4^+$ Formation[a]

$10^3(Fe)_T$, M	$10^3(SO_4)_T$, M	$10^3[H^+]$, M	$10^3\tau$, sec	$10^{-3}(1/\tau B)$, M^{-1} sec^{-1}
		$\mu = 1.2\ M$		
1.50	0.75	8.1	4.26	25.7
2.00	0.75	9.5	4.94	21.4
2.00	0.75	12.0	6.64	15.9
2.00	1.00	20.8	9.24	11.4
2.00	1.00	30.3	11.8	9.06
2.00	1.00	39.7	14.3	7.58
2.50	1.00	77.9	20.1	5.49
3.50	2.00	380	31.8	3.76
4.50	3.00	554	34.5	3.47
4.50	3.00	757	35.0	3.50
5.00	3.00	946	35.0	3.55
5.00	3.00	1055	34.0	3.66
5.00	3.00	1155	33.7	3.71
		$\mu = 2.0\ M$		
1.50	0.75	11.0	7.31	12.8
2.00	0.75	15.0	9.37	9.66
2.00	1.00	23.0	11.9	7.58
2.00	1.00	33.0	14.9	6.12
2.00	1.00	63.0	20.6	4.56
3.00	1.50	231	29.3	3.34
3.50	1.50	405	31.2	3.23
5.00	3.00	765	30.0	3.38
5.00	3.00	1100	29.5	3.52
5.00	3.00	1500	28.5	3.69
5.00	3.00	2000	27.2	3.91

[a] Temp = 25°.

Table III: Equilibrium Constants

Temp, °C	K_C, M^{-1}	10^2K_H, M	10^3K_{OH}, M	$10^2K_{OH}/K_H$
		$\mu = 0.5\ M$		
7	115	6.50	0.60	0.93
15	149	5.40	1.02	1.89
25	205	4.33	1.87	4.32
33	260	3.59	2.96	8.24
		$\mu = 1.2\ M$		
25	132	6.70	1.55	2.31
		$\mu = 2.0\ M$		
25	110	8.32	1.41	1.69

Table IV: Rate Constants for $FeSO_4^+$ Formation

Temp, °C	μ, M	$10^{-3}k$,[a] M^{-1} sec^{-1}	$10^{-4}k_{34}$, M^{-1} sec^{-1}	k_{52}, M^{-1} sec^{-1}
7	0.5	0.70 ± 0.06[b]	6.0 ± 0.2	...
15	0.5	1.7 ± 0.2	11.2 ± 0.3	...
25	0.5	4.6 ± 0.6[c]	23.1 ± 0.6	...
33	0.5	10 ± 1	36.5 ± 0.9	...
25	1.2	3.0 ± 0.3	11.4 ± 0.4	~38
25	2.0	2.8 ± 0.2	7.8 ± 0.3	51 ± 8

[a] $k = k_{12} + (k_{34}K_{OH}/K_H)$. [b] $k \simeq k_{12}$. [c] k_{12} would be ranging from $\sim 3.5 \times 10^3$ to $4.6 \times 10^3\ M^{-1}$ sec^{-1}. See text.

The equilibrium constants used for the evaluation of the equilibrium concentrations and of the quantity B of eq 5 are reported in Table III. The formation constant for the complex, K_C, and the dissociation constant for the bisulfate ion, K_H, at ionic strength 0.5 M and different temperatures were obtained by interpolating the experimental values of Davis and Smith.[3] The K_H values at 25° and ionic strengths 1.2 and 2.0 M were calculated using the expression given by Reynolds and Fukushima.[10] The K_C values under the same experimental conditions were obtained by the interpolation of Mattoo's data.[11] The equilibrium constant for the hydrolysis of ferric ion, K_{OH}, was evaluated by the Milburn expression and by setting $\Delta H = 10.4$ kcal mol^{-1}.[12]

Since the plot of $1/\tau B$ *vs.* $1/[H^+]$ (Figure 1) is linear at the four temperatures examined and ionic strength 0.5 M over the hydrogen ion concentration range covered, it is possible to deduce that the term $k_{52}[H^+]/K_H$ is negligible with respect to other terms (see eq 5). Therefore, the slope and the intercept of the straight lines obtained would yield $k_{34}K_{OH}$ and k, respectively (Table IV).

The observed dependence of the rate on the reciprocal of the hydrogen ion concentration and the estimated value of k_{34} at 25° ($k_{34} = 2.31 \times 10^5\ M^{-1}$ sec^{-1} at $\mu =$ 0.5 M; see Table IV) are in good agreement with those found by Wendt and Strehlow[2] at the same temperature and $\mu = 0.075\ M$ ($k_{34} = 2.4 \times 10^5\ M^{-1}$ sec^{-1}), despite the different ionic strength.

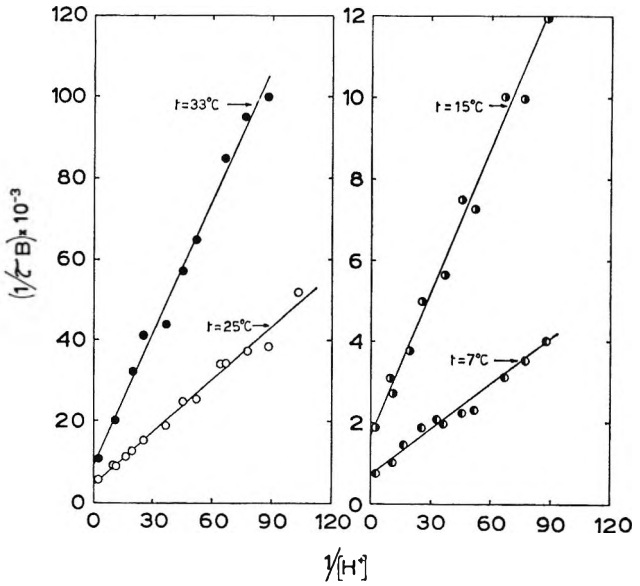

Figure 1. $1/\tau B$ *vs.* $1/[H^+]$ plot at various temperatures and ionic strength 0.5 M.

(10) W. L. Reynolds and S. Fukushima, *Inorg. Chem.*, **2**, 176 (1963).
(11) B. N. Mattoo, *Z. Physik. Chem.* (Frankfurt), **19**, 156 (1959).
(12) R. M. Milburn, *J. Amer. Chem. Soc.*, **79**, 537 (1957).

In order to attempt the evaluation of the rate constant k_{52}, we have performed further studies at higher acidity.

As was previously pointed out,[1] the behavior of $1/\tau B$ as a function of the hydrogen ion concentration would show, according to eq 5, a minimum at a certain $[H^+]$ value, which depends on the dissociation constant, K_H, for the acid ligand

$$[H^+]_{min} = \left(\frac{k_{34}K_{OH}}{k_{52}}K_H\right)^{1/2} \quad (7)$$

Table II shows very clearly the occurrence of the minimum at $[H^+] \simeq 0.40\ M$ for the measurements at $\mu = 2.0\ M$. At ionic strength 1.2 M the minimum also appears, although less clearly, at $[H^+] \simeq 0.55\ M$.[13]

These results show that an additional term dependent on $[H^+]$ must be taken into account at high acidities, as expected from the reaction mechanism proposed.

In these two systems in which the occurrence of the minimum has been observed, it has been possible, therefore, to evaluate all the three rate constants: k, k_{52}, and k_{34} (Table IV). Figure 2 shows the agreement between the theoretical curve (see eq 5) made by using the estimated values of k, k_{52}, and k_{34} at $\mu = 2.0\ M$ and the experimental points, and also the contribution of the three terms of eq 5 to the $1/\tau B$ value.

As was shown in the previous paper[1] (*cf.* also ref 14), the rate constants for the reaction of Fe^{3+} with the univalent anions Cl^-, Br^-, and CNS^- vary from 9.4 to 127 M^{-1} sec^{-1} at 25° and $\mu = 0.4 - 1.7\ M$.[15-18] The values of the rate constant estimated in this work for the reaction between Fe^{3+} and HSO_4^- at 25° and $\mu = 1.2$ and 2.0 M fall within this range and would, therefore, provide further support to the suggestion[1,14] that the loss of a coordinated water molecule is the rate-determining step in these reactions.

It remains now to attempt the evaluation of the rate constants k_{12} and k_{64}, which are involved in the acid-independent term k (see eq 6).

Owing to the higher value of the equilibrium constant for the formation of the ion pair between $FeOH^{2+}$ and SO_4^{2-},[1] the rate constant, k_{34}, for the reaction of $FeOH^{2+}$ with the bivalent anion SO_4^{2-} must be higher than that, k_{64}, for the reaction between the same cation and the univalent anion HSO_4^-.[1] However, if it is assumed that $k_{12} \ll k_{64}K_{OH}/K_H$, and if the rate constant k_{64} is then calculated by the resulting expression $k = k_{64}K_{OH}/K_H$ (see eq 6) at the four temperatures investigated at $\mu = 0.5\ M$, it turns out that, at temperatures below about 10°, the calculated values of k_{64} would be larger than those of k_{34}. This casts doubt on the assumption that $k_{12} \ll k_{64}K_{OH}/K_H$. Furthermore, the temperature dependence of k_{64} would yield a value of 2.3 (±1.4) kcal mol^{-1} for the heat of activation, which is too low compared with those for analogous reactions which are higher than 9 kcal mol^{-1} [11] (*cf.* also

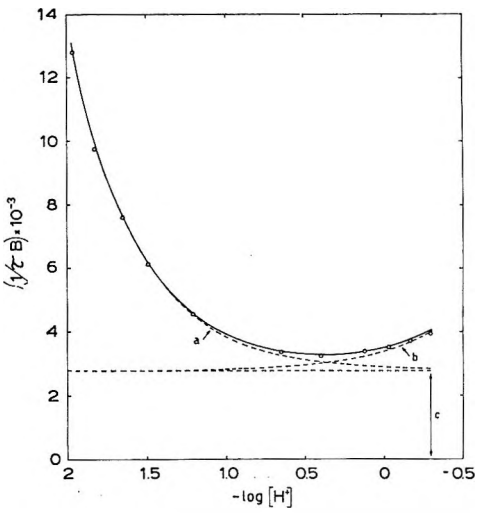

Figure 2. Comparison between the predicted variation of $1/\tau B$ as a function of $-\log [H^+]$ (full line) and experimental values (O) at $\mu = 2.0\ M$ and 25°: a represents the contribution of $k_{34}K_{OH}/[H^+]$; b represents the contribution of $k_{52}[H^+]/K_H$; c represents the acid-independent term $k = k_{12} + (k_{64}K_{OH}/K_H)$.

Table V). We must then conclude that it is not correct to identify k with $k_{64}K_{OH}/K_H$, as was previously done.[1,14] Therefore, the value of k_{64} reported in the previous studies[1,14] for the reaction of $FeOH^{2+}$ with HSO_4^- must be considered incorrect. We now note that the rate constants for the reaction of $FeOH^{2+}$ with various univalent anions so far studied[1,14,18] range only from 1×10^4 to $2.6 \times 10^4\ M^{-1}$ sec^{-1} at 25° and ionic strength 0.4–1.7 M. If we assume that in the case of the $FeOH^{2+}$ and HSO_4^- reaction the value of k_{64} at 25° and $\mu = 0.5\ M$ falls also in the same range, the term $k_{64}K_{OH}/K_H$ should range from 4.3×10^2 to $11 \times 10^2\ M^{-1}$ sec^{-1} and, therefore, the extent of its contribution should be at most equal to ~25% of the k value. The value of k_{12} would then lie in the range 3.5×10^3 to $4.6 \times 10^3\ M^{-1}$ sec^{-1} at 25° and $\mu = 0.5\ M$ (Table IV).

Since the K_{OH}/K_H ratio decreases quite rapidly as

(13) It may be noted that the $[H^+]_{min}$ value shifts at higher acidities when the ionic strength is decreased.

(14) D. Seewald and N. Sutin, *Inorg. Chem.*, **2**, 643 (1963).

(15) With Cl^-, $k_{12} = 9.4\ M^{-1}$ sec^{-1} at $\mu = 1.0\ M$; with Br^-, $k_{12} = 20\ M^{-1}$ sec^{-1} at $\mu = 1.7\ M$ and 22°; with CNS^-, $k_{12} = 127\ M^{-1}$ sec^{-1} at $\mu = 0.4\ M$.

(16) Bauer and Smith[17] made equilibrium and kinetic studies on the iron(III)–oxalate system, obtaining results which are different from those found by Moorhead and Sutin.[18] In fact, according to Bauer and Smith, significant amounts of the protonated complex $FeHC_2O_4^{2+}$ are present in acidic aqueous solutions, unlike the observations of Moorhead and Sutin. Moreover, great differences were found in the values of the rate constant for the acid-independent path. The rate constant for the acid-dependent path (*i.e.*, for the reaction of Fe^{3+} with the univalent bioxalate anion $HC_2O_4^-$) was estimated by Moorhead and Sutin to be equal to 860 M^{-1} sec^{-1} at 25° and $\mu = 1.0\ M$, while Bauer and Smith found a value of 1440 M^{-1} sec^{-1} at $\mu = 0.5\ M$ and the same temperature.

(17) R. F. Bauer and W. MacF. Smith, *Can. J. Chem.*, **43**, 2755 (1965); *ibid.*, **43**, 2763 (1965).

(18) E. G. Moorhead and N. Sutin, *Inorg. Chem.*, **5**, 1866 (1966).

Table V: Activation Parameters for the Formation of Monocomplexes of Iron(III)[a]

Reaction	μ, M	$\Delta H_f^{\pm}$, kcal mol^{-1}	$\Delta S_f^{\pm}$, cal deg^{-1} mol^{-1}	Ref
$FeOH^{2+} + HF$	0.5	10	−8	1, 19
$FeOH^{2+} + HN_3$	0.1	9	−10	1
$FeOH^{2+} + CNS^-$	0.4	10	−7.6	1, 20
$FeOH^{2+} + Cl^-$	1.0	13	4	1, 21
$FeOH^{2+} + SO_4^{2-}$	0.5	11.3	4	This work
$Fe^{3+} + HF$	0.5	8.7	−24	1, 19
$Fe^{3+} + CNS^-$	0.4	13	−5	1, 20
$Fe^{3+} + Cl^-$	1.0	16.6	2	1, 21
$Fe^{3+} + SO_4^{2-}$	0.5	14.3–16.6	6–14	This work

[a] Temp = 25°.

the temperature decreases (see Table III), the $k_{64}K_{OH}/K_H$ contribution will be larger at 33°, while it is reasonable to think that at 7° it will be very small and within the limits of the experimental errors in k. We may therefore assume, as a good approximation, that $k \simeq k_{12}$ at the temperature of 7° (Table IV).

If k_{12} is identified with k at the four temperatures examined at $\mu = 0.5\ M$, the temperature dependence of k_{12} yields a heat and an entropy of activation equal to 16.6 ± 1.5 kcal mol^{-1} and 14 ± 5 cal deg^{-1} mol^{-1}, respectively. If k_{12}, according to what has been said above, is assumed equal to 75% of k at 25° (*i.e.*, $k_{12} = 3.5 \times 10^3\ M^{-1}$ sec^{-1}), the estimated heat and entropy of activation are 14.3 kcal mol^{-1} and 6 cal deg^{-1} mol^{-1}, respectively. These activation parameters and those for the reaction of $FeOH^{2+}$ with SO_4^{2-}, obtained from the temperature dependence of k_{34}, are compared in Table V with the corresponding quantities for the formation of other monocomplexes of iron(III).[1,19-21]

As was previously shown,[1,22] because of the contribution from the heat and entropy of the ion-pair formation in the first step of the reactions, the experimental activation parameters for the reaction involving a given cation are expected to increase differentially with the negative charge on the ligand, $\Delta S_f^{\pm}$ increasing more than $\Delta H_f^{\pm}$. It can be seen (Table V) that the activation parameters estimated in this work are really higher than those for the reactions involving CNS^- or uncharged ligands. The comparison with the activation parameters for the reaction of Fe^{3+} and $FeOH^{2+}$ with Cl^- shows some discrepancy, which may be probably attributed to the fact that the kinetic studies on the $FeCl^{2+}$ formation were carried out at higher ionic strength. Thus the activation parameters obtained in this work would not be in disagreement with the view that the rate of iron(III) complex formation is controlled by the rate of loss of a coordinated water molecule from the cation.[1,14]

Further confirmation that the value of k estimated in this work has to be practically attributed to the rate constant k_{12} for the Fe^{3+} and SO_4^{2-} reaction may be obtained by comparing the activation parameters for the dissociation (aquation) of $FeSO_4^+$ with those for other iron(III) complex dissociations (Table VI). They have been evaluated, when not previously reported in literature, by means of the appropriate thermodynamic quantities (ΔS and ΔH) and the formation activation parameters.

Although the dissociation activation parameters depend to some extent on the nature of the ligand, it may be seen that, in the case of the complexes previously studied, the dissociation activation parameters for the pathways involving $FeOH^{2+}$ in the transition state are significantly higher than those for the pathways involving Fe^{3+}. In the case of the dissociation of $FeSO_4^+$ the activation parameters for the acid-independent path ($\Delta H_d^{\pm} = 11$ kcal mol^{-1}, $\Delta S_d^{\pm} = -15$ cal deg^{-1} mol^{-1}) are less than those for the pathways involving $FeOH^{2+}$ and similar to the corresponding quantities for other dissociation reactions which involve the Fe^{3+} ion in the transition state. Since the transition state must be the same for both the complex dissociation and formation reactions, it seems reasonable to consider correct the conclusion that $k \simeq k_{12}$.

The rate constant k_{12} estimated in this work at 25° (see Table IV) appears to be too high compared with those for the analogous reactions with the univalent anions Cl^-, Br^-, HSO_4^-, and CNS^-,[15] even though the enhancement in the rate due to the increase in the ligand charge is taken into account.[23,24] Moreover, it would be smaller than expected on the basis of the increased ligand charge if it is compared with the rate constant for the reaction of Fe^{3+} with bioxalate anion.[16] On the other hand, the latter rate constant is markedly higher than those found at least in the case of the anions with the same charge Cl^-, Br^-, and HSO_4^-.

For the present, it is indeed hard to give some explanation for the enhancement of the rate with the bioxalate and sulfate ions. However, in view of the above considerations on the formation and dissociation activation parameters, in the case of the sulfate ion a possible simple explanation is that because of the higher charge on the anion the ion pair between Fe^{3+} and SO_4^{2-} may be more stable than would be predicted on the basis of the simple electrostatic model for which

(19) D. Pouli and W. MacF. Smith, *Can. J. Chem.*, **38**, 567 (1960).

(20) J. F. Below, Jr., R. E. Connick, and C. P. Coppel, *J. Amer. Chem. Soc.*, **80**, 2961 (1958).

(21) R. E. Connick and C. P. Coppel, *ibid.*, **81**, 6389 (1959).

(22) F. P. Cavasino, *J. Phys. Chem.*, **69**, 4380 (1965).

(23) Assuming the Fuoss equation[1,22,24] may be used at $\mu = 0.5\ M$, it can be calculated that the equilibrium constant for the formation of the ion pair between Fe^{3+} and SO_4^{2-} is about eight times higher than that for the ion pair between the same cation and univalent anions at 25° and $\mu = 0.5\ M$.

(24) R. M. Fuoss, *J. Amer. Chem. Soc.*, **80**, 5059 (1958).

Table VI: Activation Parameters for the Dissociation of Monocomplexes of Iron(III)[a]

Species involved in the transition state[b]	μ, M	$\Delta H_d^{\ddagger}$[c]	$\Delta S_d^{\ddagger}$[d]	Species involved in the transition state[b]	$\Delta H_d^{\ddagger}$[c]	$\Delta S_d^{\ddagger}$[d]	Ref
Fe^{3+}, HF	0.4	9	−32	$FeOH^{2+}$, HF	20	5	19
Fe^{3+}, HN_3	0.1	...	...	$FeOH^{2+}$, HN_3	17	3	1
Fe^{3+}, Cl^-	1.0	11	−21	$FeOH^{2+}$, Cl^-	17	2	20
Fe^{3+}, CNS^-	0.4	15	−10	$FeOH^{2+}$, CNS^-	22	10	20, 21
Fe^{3+}, SO_4^{2-}	0.5	11	−15	$FeOH^{2+}$, SO_4^{2-}	16	−3	This work

[a] Temp = 25°. [b] Coordination and solvation water is omitted. [c] Unit, kcal mol^{-1}. [d] Unit, cal deg^{-1} mol^{-1}.

Fuoss equation[24] is valid. Bearing in mind[1] that $k_{12} = K_0 k^*$ (K_0 is the ion-pair association constant and k^* is the first-order rate constant for a coordinated water elimination), the greater stability of the ion pair would lead to an increase either in the only K_0 value or in the values of both K_0 and k^*, and, consequently, to an enhancement in the reaction rate.[25] The rate-determining step for the reaction of Fe^{3+} with SO_4^{2-} would still be, however, the loss of a water molecule coordinated to the metal ion.

Other possibilities, which may be taken into account, are an "inner hydrolysis" of the ion pair between Fe^{3+} and SO_4^{2-} or an S_{N2} mechanism for water substitution. But the assumption of any of these mechanisms involves some difficulties. For an "inner hydrolysis" one would expect a similar transition state as for the reaction $FeOH^{2+}$ and HSO_4^- ("outer hydrolysis"). This reaction, however, was excluded on the basis of the above arguments.[26] On the other hand, S_{N2} mechanism should be more likely with coordination shells which have some space left for attack of the ligand. As compared to Mg^{2+}, Ca^{2+}, and some bivalent transition ions, for which ligand independence has been established,[7,22,27] the coordination shell of Fe^{3+} should be more highly closed, so that a mechanism in which the loss of a water molecule from the inner coordination sphere is the rate-limiting step seems to be more likely.

Acknowledgment. The author wishes to thank Professor Manfred Eigen for the kind hospitality in his laboratory and the Max Planck Institut für Physikalische Chemie, Göttingen, West Germany, for the financial support during his stay there.

(25) An enhancement in the rate of formation of complexes of cobalt(II) with highly charged anions, *i.e.*, $HP_2O_7^{3-}$ and $HP_3O_{14}^{4-}$, was also observed by G. G. Hammes and M. L. Morrel, *J. Amer. Chem. Soc.*, 86, 1497 (1964).

(26) It needs to be pointed out that in the case of the complexes FeF^{2+} and FeN_3^{2+}, the activation parameters for the dissociation reaction *via* the acid-independent path are not able to establish whether the $FeOH^{2+}$ ion involved in the transition state comes from the reactants $FeOH^{2+}$ and the neutral acids or from the reactants Fe^{3+} and the corresponding anions whose ion pairs undergo an "inner hydrolysis." However, according to previous suggestions [1,14] the first case seems to occur.

(27) M. Eigen and L. De Maeyer in "Technique of Organic Chemistry," Vol. VIII, 2nd ed, S. L. Friess, E. S. Lewis, and A. Weissberger, Ed., Interscience Publishers, Inc., New York, N. Y., 1963, Part 2, p 895.

NOTES

Chemistry of Crystalline Aluminosilicates. IV. Factors Affecting the Formation of Zeolites X and B[1]

by George T. Kerr

Research Department, Central Research Division Laboratory, Mobil Research and Development Corporation, Princeton, New Jersey 08540 *(Received September 25, 1967)*

The effects of a number of variables on the kinetics of crystal growth of zeolite A were previously reported.[2] Zeolite A is a truly synthetic substance, with no naturally occurring counterpart, and is readily prepared free of other zeolitic impurities. Zeolites X[3] and B[4] have essentially the same composition but differ markedly in their respective crystal structures. As a consequence of their having similar compositions, these zeolites can be prepared from reaction mixtures of the same over-all composition. Subtle changes in the preparation of the reaction mixtures determine which zeolite crystallizes from the mixture. A study of the nature of these techniques and their effects is the subject of this communication.

Experimental Section

Reagents and Apparatus. Reagent grade sodium metasilicate nonahydrate and sodium aluminate (34.6 wt % Na_2O and 41.0 wt % Al_2O_3) were used. Distilled water was used throughout these studies. The apparatus was described previously.[2]

Synthesis of the Zeolites. The same quantities of reagents were used for synthesizing zeolites X and B: 83.8 g of sodium silicate, 18.3 g of sodium aluminate, and 400 ml of water.

Without Seeding. Zeolite X was prepared by adding a boiling solution of the sodium silicate in 250 ml of water, stirring as rapidly as possible (preferably in 5 sec or less), to a boiling solution of the sodium aluminate in 150 ml of water. Stirring was continued for 1–2 min to give a smooth, creamy gel and then was terminated. The resulting crystalline product, obtained after 3–4 hr at reflux temperature, was at least 10% more crystalline than a reference Linde 13X molecular sieve sample, as shown by sorptive-capacity measurements and X-ray diffraction analysis.

Seeding. Zeolite X formation can be successfully seeded with a special seed material that is obtained by halting a standard zeolite X preparation after a reaction time of about 3.5 hr. At that point the solid phase of the reaction mixture consists of about 75% zeolite X and 25% amorphous sodium aluminosilicate. In a typical experiment, sufficient special seed was placed in the sodium silicate solution, used in a standard zeolite X preparation, to yield approximately 10–15% zeolite X in the initial solid phase of the reaction mixture. Crystallization was complete in 3.25 hr to yield a zeolite X that was free of zeolite B. This crystallization was completed in about 0.8 of the time required for the nonseeded preparations.

Still more effective seeding can be achieved by saturating boiling solutions of reagents with seed material prior to formation of the amorphous substrate and by adding seed to the reaction mixture. Using this technique with 10–15% zeolite X in the initial solid phase, the crystallization was complete in about 2.75 hr. The greater effectiveness of seed material in preparations of zeolite X suggests that the initial aqueous phase of the reaction mixture has a deleterious effect on zeolite X crystals; perhaps silica and/or alumina are preferentially dissolved from the crystals to alter at least a portion of the crystal surfaces that serve as nucleation or growth sites.

Zeolite B was prepared by slowly adding, over a 25–35-sec period, a boiling solution of the sodium silicate in 100 ml of water to a boiling solution of the sodium aluminate in 300 ml of water. Stirring was used during the mixing of reagent solutions and throughout the ensuing crystallization. After about 4.5 hr at reflux temperature, zeolite B was obtained free of any detectable amount of crystalline impurity.

Deviations from the standard procedures for preparing zeolites X and B generally lead to the formation of mixtures of these zeolites. The most important, most easily controlled deviation is in the rate of combining the reagent solutions: combining times of 10–20 sec lead to mixtures of X and B.

Sampling. The sampling technique used for obtaining rate data on zeolite growth was described previously.[2]

Analysis. After many measurements it was found that the best zeolite X samples prepared in this laboratory sorbed 0.185 g of cyclohexane per g of activated sample at 20 mm and 0.315 g of water per g of activated sample at 12 mm. Zeolite B sorbs no cyclohex-

(1) For part III, see G. T. Kerr, *Inorg. Chem.*, **5**, 1539 (1966).

(2) G. T. Kerr, *J. Phys. Chem.*, **70**, 1047 (1966).

(3) D. W. Breck, W. G. Eversole, and R. M. Milton, *J. Amer. Chem. Soc.*, **78**, 2338 (1956).

(4) R. M. Milton, U. S. Patent 3,008,803 (1961).

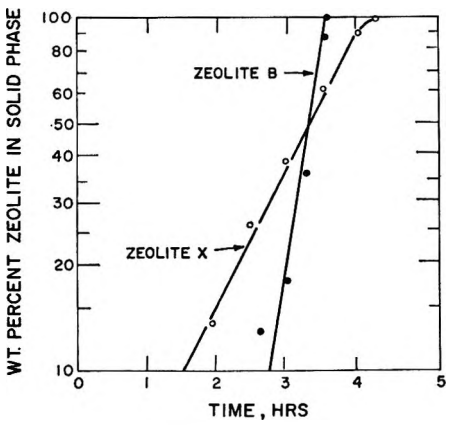

Figure 1. The growth of zeolites X and B.

ane, but does sorb 0.200 g of water per g of activated sample at 12 mm. The weight per cent zeolite X in the solid activated samples was determined from the cyclohexane sorptive capacities of the samples. When zeolite B was the only crystalline substance present in the samples, as shown by X-ray diffraction analysis, the weight per cent of zeolite present was determined from the water sorptive capacities. In those samples shown by X-ray diffraction to contain both zeolites, the zeolite B content was determined by correcting the samples' water-sorptive capacities for the water sorbed by the zeolite X present, the latter being determined by cyclohexane sorption.

Results and Discussion

In Figure 1 are shown typical growth curves for the formation of zeolites X and B. These results show that the rates of formation of these zeolites follow the same law as for zeolite A[2]

$$\frac{dZ}{dt} = KZ$$

where Z is the weight per cent of zeolite in the solid phase at time t, and K is a constant. Numerous experiments have shown that solution concentration, volume, and temperature have the same qualitative effect on the formation of zeolites X and B as was observed for zeolite A.

Table I: Formation of Zeolite X–Zeolite B Mixtures

Time, hr	Wt % in solid phase	
	X	B
0	19.5	...
0.50	20.4	...
1.25	23.6	...
1.50	21.8	...
1.75	27.0	...
2.00	28.8	12.5
2.50	33.0	61.0
3.00	32.4	68.5
3.50	30.3	73.0

Because of its faster growth rate, the presence of traces of zeolite B in samples of zeolite X used as seed has the effect shown in Table I. In this experiment zeolite X seed containing 10% zeolite B was added to a system designed to optimize zeolite X formation. Zeolite X nucleates more readily than B, but grows at a much slower rate. Thus in any system in which both can form, zeolite X will almost certainly be present, because it nucleates more rapidly. However, zeolite B will predominate because of its faster growth rate once started.

The observations made above may explain why phillipsite, a zeolite closely related to zeolite B, always predominates in natural deposits of faujasite, a natural zeolite X.

Aliphatic Semidiones. IX. Hyperfine Splittings by Nitrogen Atoms Attached to a Paramagnetic Center[1]

by Glen A. Russell, John McDonnell, and Charles Myers

Department of Chemistry, Iowa State University, Ames, Iowa 50010
(Received September 5, 1967)

The Karplus–Fraenkel equation[2] applied to a nitrogen hyperfine splitting takes the form of eq 1 where X_i are atoms bonded to nitrogen.[3] Estimates of Q_{CN}^{N} have in

$$a^{N} = Q_{N}^{N}\rho_{N} + \sum_{i} Q_{X_i N}^{N}\rho_{X_i} \qquad (1)$$

general been small and usually between ±2 G.[3-6] We previously investigated some cases possessing a π system in which the carbon atom bonded to nitrogen had a high π-electron density. We concluded that our empirical spin densities possibly demanded a value of Q_{CN}^{N} in the range of 14 G.[6a] We have now submitted this parameter to direct experimental observation and find that a value approaching zero is indeed demanded.

As a model compound we prepared semidione radical anion **1** by base-catalyzed oxidation of 3-quinuclidinone.[7] The observed hyperfine splittings of 1.6 G (2 hydrogens) and 0.8 G (2 hydrogens) are consistent with

(1) This work was supported by a grant from the National Science Foundation, Grant No. GP-6402X.

(2) M. Karplus and G. K. Fraenkel, *J. Chem. Phys.*, **35**, 1312 (1961).

(3) E. W. Stone and A. H. Maki, *ibid.*, **39**, 1635 (1963).

(4) B. L. Barton and G. K. Fraenkel, *ibid.*, **41**, 1455 (1964).

(5) P. T. Cottrell and P. H. Rieger, *Mol. Phys.*, **12**, 149 (1967).

(6) For reviews of pertinent data, see (a) E. T. Strom, G. A. Russell, and R. Konaka, *J. Chem. Phys.*, **42**, 2033 (1965); (b) J. Q. Adams, J. W. Nicksic, and J. R. Thomas, *ibid.*, **45**, 654 (1966).

(7) G. A. Russell and E. T. Strom, *J. Amer. Chem. Soc.*, **86**, 744 (1964).

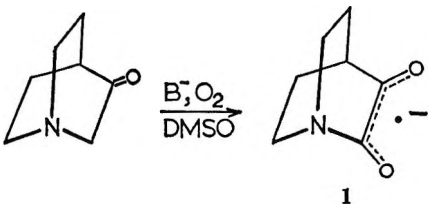

1

the long-range W-plan splitting expected in this azabicyclooctane semidione.[8] No hyperfine splitting by the nitrogen atom was observed, even though our line widths were quite small (200-mG line width). Since the carbonyl carbon atoms of a *cis*-semidione have a ρ_C value of 0.25–0.35,[9] and a^N must be less than 0.1 G in structure **1**, we conclude that $Q_{CN}{}^N$ is $<|0.4|$ G. It should be noted that in structure **1** the geometry places the nitrogen lone pair in the nodal plane of the π system and $\rho_\pi{}^N$ is zero.

We have previously commented that $Q_{CO}{}^O$ must be zero, or nearly so.[10] From the reported spectra of alkylnitroxides it can be concluded that $Q_{NC}{}^C$ must be quite small.[11] It has been shown that $Q_{ON}{}^N$ is less than 1 G for diaryl nitroxides.[12] In di-*t*-butylketyl the value of a^C for the quaternary carbon atoms is less than 0.5 G[10,13] and it would appear that $Q_{CC'}{}^{C'}$ is less than 1 G.[14]

Further evidence indicating that $Q_{CN}{}^N$ must be a small number is furnished by the observed values of a^N for structures 2 and 3, formed by reduction of N,N′-dimethylalloxan in dimethyl sulfoxide solution by the enolate anion of propiophenone[15] and dimethylparabanic acid in acetonitrile electrolytically.

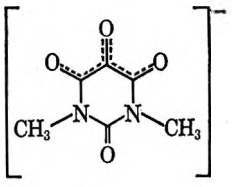

2

$a^N = 0.50$ G

$a_{CH_3}{}^H = 0.30$ G

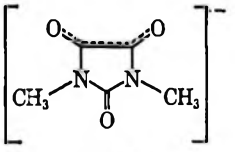

3

$a^N = 1.66$ G

$a_{CH_3}{}^H = 0.11$ G

The ratios of a^N/a^H for structures **2** and **3** show a serious deviation from the value of ~1 often observed for radicals containing the N-methyl group.[16] It seems certain that structure **3** has the largest $\rho_\pi{}^N$ but the smallest $a_{CH_3}{}^H$. This appears to be analogous to di-*t*-butylketyl (**4**) and di-*t*-butylsemidione (**5**). Here also the largest $a_{CH_3}{}^H$ is associated with the lowest $\rho_\pi{}^C$.

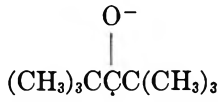

4

$a^H = 0.12$ G

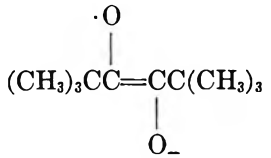

5

$a^H = 0.34$ G

Obviously hyperfine splitting by the hydrogen atoms in structures **2–5** involves more than simple C–H or C–CH_3 hyperconjugation. The sign reversal in $a_{CH_3}{}^H$ between the di-*t*-butylnitroxide and 2,4,6-tri-*t*-butylphenoxy radical is in agreement with the existence of at least two mechanisms of interactions for radicals similar to structures **4** and **5**.[17] Multiple mechanisms apparently also apply to structures **2** and **3**.

(8) G. A. Russell and K.-Y. Chang, *J. Amer. Chem. Soc.*, **87**, 4381 (1965); G. A. Russell, G. Holland, and K.-Y. Chang, *ibid.*, **89**, 6629 (1967).

(9) G. A. Russell and R. D. Stephens, *J. Phys. Chem.*, **70**, 1320 (1966); G. A. Russell, E. T. Strom, E. R. Talaty, and S. A. Weiner, *J. Amer. Chem. Soc.*, **88**, 1998 (1966).

(10) G. A. Russell and G. R. Underwood, *J. Phys. Chem.*, **72**, 1074 (1968).

(11) H. Lemaire, A. Rassat, P. Servos-Gavin, and G. Berthier, *J. Chim. Phys.*, 1247 (1962); H. Lemaire, R. Ramasseul, and A. Rassat, *Mol. Phys.*, **8**, 557 (1964); see, however, R. H. Heller and D. H. Geske, *J. Org. Chem.*, **31**, 4249 (1966), who indicate $Q_{NC}{}^C > 7.5$ G.

(12) P. B. Ayscough and F. P. Sargent, *J. Chem. Soc.*, *B* 907 (1966).

(13) N. Hirota and S. J. Weissman, *J. Amer. Chem. Soc.*, **82**, 4424 (1960).

(14) On the other hand, $a_{CH_3}{}^C$ for ethyl radical is 13.6 G: R. W. Fessenden, *J. Phys. Chem.*, **71**, 74 (1967). In biacetyl radical anion $a_{CH_3}{}^C$ is 4.5 G and a value of $Q_{CC'}{}^{C'}$ of 14 to 18 G is indicated.[10]

(15) G. A. Russell and M. C. Young, *J. Amer. Chem. Soc.*, **88**, 2007 (1966).

(16) K. Kuwata and D. H. Geske, *ibid.*, **86**, 2101 (1964); W. M. Tolles, D. W. Moore, and W. E. Thun, *ibid.*, **88**, 3476 (1966); S. F. Nelsen, *ibid.*, **88**, 5666 (1967).

(17) K. H. Hausser, H. Brunner, and J. C. Jochims, *Mol. Phys.*, **10**, 253 (1966).

On the Kinetics of Color Development in the Landolt ("Iodine Clock") Reaction

by John A. Church and Sanford A. Dreskin

Princeton Laboratory, American Can Company, Princeton, New Jersey 08540 *(Received September 25, 1967)*

Although the Landolt "clock" reaction of iodate, bisulfite, and starch has been the subject of numerous studies,[1] essentially nothing is known of the rapidity with which color develops in the solution when free iodine suddenly appears at the end of the induction period. This striking phenomenon, owing to the formation of the deep blue iodine–iodide–amylose complex, is usually described as instantaneous, although Landolt[1b] observed that it was noticeably slower when the induction period was long.

Herein we report the results of a study of the kinetics of this transition, the rate of which we have determined photometrically with an oscilloscope. The occurrence of minimum transition ("fall") times is explained, and

(1) (a) H. Landolt, *Chem. Ber.*, **18**, 249 (1885); (b) *ibid.*, **19**, 1317 (1886); (c) J. Eggert, *Helv. Chim. Acta*, **32**, 629 (1949); (d) E. Abel, *Monatsh. Chem.*, **81**, 1029 (1950); (e) C. H. Sorum, F. S. Charlton, J. A. Neptune, and J. O. Edwards, *J. Amer. Chem. Soc.*, **74**, 219 (1952); (f) J. Eggert and T. Rohr, *Helv. Chim. Acta*, **36**, 855 (1953); (g) T. Pinter and V. Hankonyi, *Chem. Ber.*, **90**, 746 (1957); (h) H. v. Euler and H. Hasselquist, *Z. Naturforsch.*, **12b**, 600 (1957).

an analysis is given to account for the sigmoid shape of the curves of transmitted light intensity *vs.* time which were observed. In addition, the relationship between initial reagent concentrations and the induction period is further clarified.

The series of reactions in this system may be represented as

$$IO_3^- + 3HSO_3^- \longrightarrow I^- + 3SO_4^{2-} + 3H^+ \quad (1)$$

$$IO_3^- + 5I^- + 6H^+ \longrightarrow 3I_2 + 3H_2O \quad (2)$$

$$I_2 + HSO_3^- + H_2O \longrightarrow 2I^- + SO_4^{2-} + 3H^+ \quad (3)$$

$$xI_2 + yI^- + \text{amylose} \rightleftharpoons \text{blue complex} \quad (4)$$

Due to the rapidity of (3), the concentration of the blue complex remains essentially zero until the bisulfite nears exhaustion; at some low value of bisulfite concentration, the rate of iodine generation by (2) begins to exceed the rate of its consumption by (3) and the concentration of the complex consequently increases. Under proper conditions the solution undergoes an abrupt transition from nearly clear to nearly opaque, provided that the light path is on the order of a few centimeters.

Experimental Section

Solutions were prepared with distilled water, reagent grade potassium iodate, Fisher Certified sodium bisulfite, and filtered soluble starch solution (prepared by briefly boiling a suspension of Fisher ACS soluble starch). The starch concentration was 0.044 g/100 ml, dry basis, which calculation showed provided sufficient amylose to ensure the adherence of the solutions to Beer's law down to extremely low values of per cent transmission.[2] Solutions were always used promptly.

To initiate the reaction, 1.00 ml of bisulfite solution was quickly added with a small syringe to 29.0 ml of starch–iodate solution in a 3-cm Brice-Phoenix T-101 cell, with efficient magnetic stirring which was always continued until a few seconds before the transition was expected to occur. The light source was a 70-mW He–Ne laser emitting at 6328 Å, which is close to the wavelength of maximum absorption by iodine–iodide–amylose complexes.[2] The beam was passed through the cell, then through a neutral density filter of absorbance 4.3, and onto an RCA 7102 photomultiplier tube. The tube output was fed into an oscilloscope, the sweep circuit of which was set to trigger when a small decrease in output was sensed. Linearity of response of the system was checked with additional filters.

The total Δy recorded on the oscilloscope-trace photographs, from the original level until apparent equilibrium was reached (corresponding, in all cases, to apparent opacity), was taken as the original intensity, I_0. The fall time was defined as the time required for the intensity to drop to I_0/e, measured from the point of first appreciable decrease in intensity (usually the left edge of the oscilloscope graticule). Figure 1 shows a typical trace, with the original intensity indicated by a separate trace.

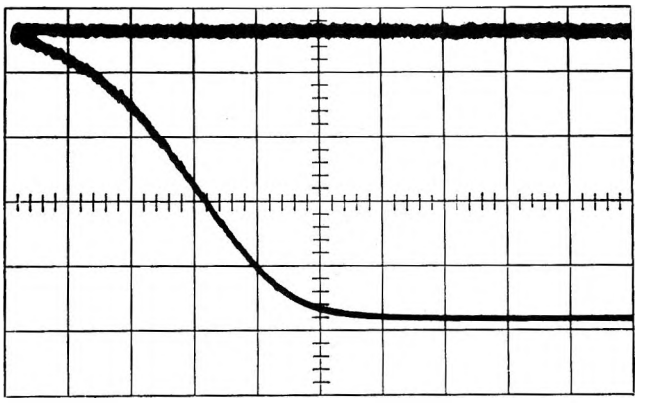

Figure 1. Oscilloscope trace: initial [KIO_3] = 0.0374 *M*, initial [$NaHSO_3$] = 0.0093 *M*. One large scale division equals 0.0005 sec.

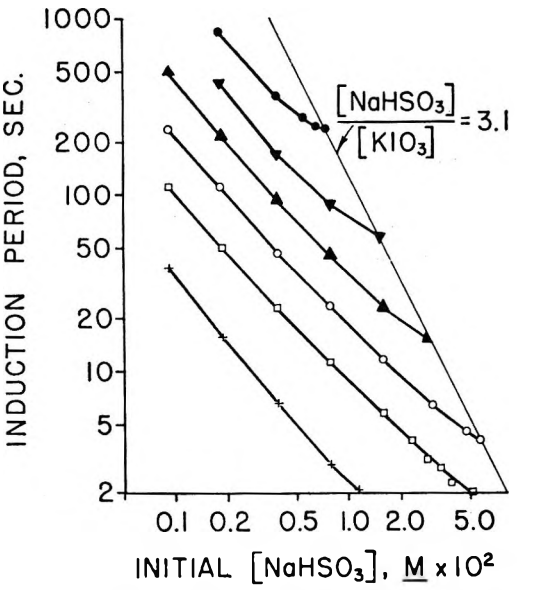

Figure 2. Induction period *vs.* initial [$NaHSO_3$] at constant initial [KIO_3]; initial [KIO_3]: ●, 0.00234 *M*; ▼, 0.00467 *M*; ▲, 0.00934 *M*; ○, 0.0187 *M*; □, 0.0374 *M*; +, 0.149 *M*.

All measurements were made at 23 ± 0.5°. Temperature changes due to the reaction were inappreciable.

Induction periods were separately determined with a stopwatch. They were not measurably changed by passage of the laser beam through the solution.

Results

Kinetics of The Induction Period. The dependence of the induction period on the initial[3] bisulfite concen-

(2) R. R. Baldwin, R. S. Bear, and R. E. Rundle, *J. Amer. Chem. Soc.*, **66**, 111 (1944).

(3) "Initial concentration" refers to the concentration immediately after mixing the two solutions.

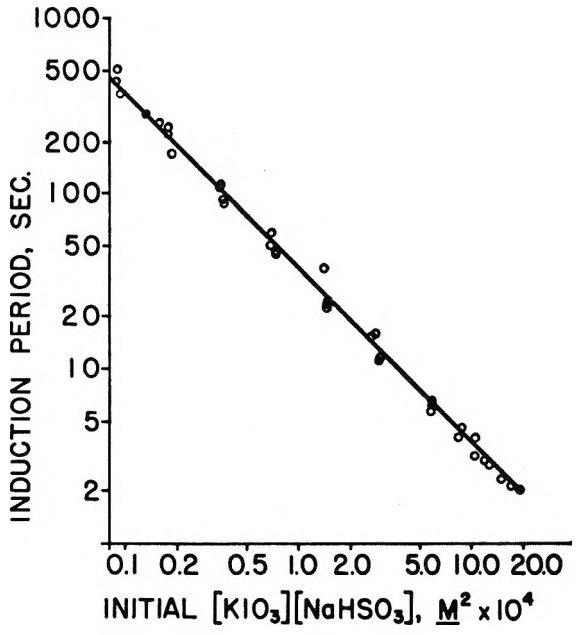

Figure 3. Induction period *vs.* initial $[KIO_3][NaHSO_3]$.

tration (corrected for assay of the bisulfite) at constant initial iodate concentrations is shown in Figure 2. When the mole ratio of bisulfite to iodate exceeded 3.1:1, the bisulfite was in excess, and consequently the color never developed. The slight excess of this value over theory (3.0:1) may have been due to consumption of a small amount of bisulfite by dissolved oxygen.

The logarithm of the induction period is linearly related to the logarithm of the product of the initial iodate and bisulfite concentrations, as shown in Figure 3. As the slope of the straight line (least squares) was −1.00, the rate law reduces to the form

$$P = \frac{0.0037 \text{ sec mol}^2 \text{ l.}^{-2}}{[KIO_3][NaHSO_3]} \quad (5)$$

where P is the induction period at 23°. To our knowledge, this simple relationship has not been shown previously.

Kinetics of Fall Times. The fall time at initial concentrations of iodate and bisulfite giving a 0.002-sec fall time was found to be essentially independent of starch concentration over a 50-fold range (0.02–1.00 g/100 ml). This indicates that reaction 4 is not rate controlling with respect to the kinetics of the fall time in this region of starch concentration and must, therefore, be relatively rapid.

The dependence of the fall time (at constant initial iodate and starch concentrations) upon initial bisulfite concentration is shown in Figure 4. The reason for the minima in these curves is discussed below.

The right-hand limbs of the curves in Figure 4 for initial $[KIO_3]$ equal to 0.00467 and 0.00934 M have been carried very close to the equivalence point. The right-hand limb for the curve with initial $[KIO_3]$

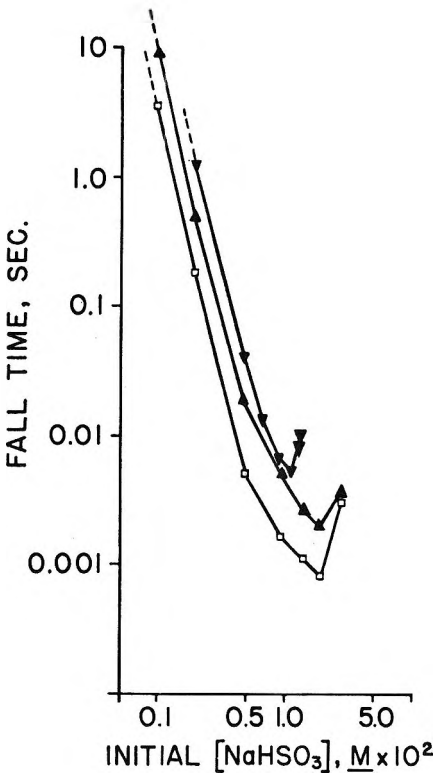

Figure 4. Fall time *vs.* initial $[NaHSO_3]$ at constant initial $[KIO_3]$; initial $[KIO_3]$: ▼, 0.00467 M; ▲, 0.00934 M; □, 0.0374 M.

equal to 0.0374 M would continue to initial $[NaHSO_3]$ of about 0.112 M, but the induction period becomes inconveniently short (less than 3 sec) at initial $[NaHSO_3] > 0.03$ M.

Discussion

Minimum Fall Times. The minima in Figure 4 may be explained as follows. At low initial bisulfite concentrations, $[I^-]$ and $[H^+]$ are necessarily low at the end of the induction period, as relatively small amounts have been generated by reactions 1 and 3; therefore reaction 2, and hence the transition, is slow, because its rate is (approximately) given by[4]

$$-d[IO_3^-]/dt = k[IO_3^-][I^-]^2[H^+]^2 = {}^1/_3 d[I_2]/dt \quad (6)$$

Apparently, as the initial bisulfite concentration is increased, the product of $[I^-]^2$ and $[H^+]^2$ increases faster than $[IO_3^-]$ decreases (at the end of the induction period), leading to more rapid generation of I_2 and therefore progressively shorter fall times. However, the fall times should ultimately increase again at high initial bisulfite concentrations because $[IO_3^-]$ remaining at the end of the induction period must eventually approach zero as the equivalence mole ratio (3:1) is approached; this must lead, eventually, to slower generation of I_2 by reaction 2 and hence a slower transition. More succinctly, $k[IO_3^-][I^-]^2[H^+]^2$ must

(4) K. J. Morgan, *J. Chem. Soc.*, 1865 (1951).

approach zero as $[IO_3^-]$ approaches zero, because $[I^-]^2[H^+]^2$ cannot become arbitrarily large.

Shape Of Intensity–Time Curves. We advance the following simplified analysis to account for the sigmoid shape of the intensity–time curves. Let (2) and (3) be written

$$A \xrightarrow{k_1} B \quad (7)$$

$$B + C \xrightarrow{k_2} D \quad (8)$$

Let x be the concentration of B (I_2) generated by (7) at a time t after $t = 0$, the point of onset of color development. Let y be the concentration of B consumed by eq 8 at time t; then the net concentration of B available for reaction with iodide and amylose at time t is $x - y$. The various concentrations are summarized by Table I; it is assumed that C (HSO_3^-) is consumed only by eq 8. Especially when the fall time is short, the approximation that $x \ll A_0$ during the transition period

Table I

	[A]	[B]	[C]	[D]
$t = 0$	A_0	0	C_0	D_0
$t = t$	$A_0 - x$	$x - y$	$C_0 - y$	$D_0 + y$

is justified; *i.e.*, the concentrations of iodate, iodide, and hydrogen ions are not appreciably changed during this short interval. Therefore

$$dx/dt = k_1(A_0 - x) \cong k_1A_0 \quad (9)$$

or

$$x = k_1A_0t \quad (10)$$

since $x = 0$ at $t = 0$. If a first-order rate law is assumed, as an approximation, to describe the decrease in [C] with time, then

$$-d(C_0 - y)/dt = k_c(C_0 - y) \quad (11)$$

where k_c is not the same as k_2. This leads directly to

$$C_0 - y = C_0e^{-k_ct} \quad (12)$$

Therefore

$$x - y = k_1A_0t - C_0(1 - e^{-k_ct}) \quad (13)$$

If Beer's law is assumed to be obeyed, then

$$I = I_0e^{-Kl(x-y)} \quad (14)$$

where I is the intensity of beam emerging from the cell at time t, I_0 is the intensity of beam emerging from cell at $t = 0$, K is the molar absorption coefficient of the iodine–iodide–amylose complex, l is the cell length, and the assumption is made that amylose and iodide are in excess. The complete expression relating I to t is therefore

$$I = I_0e^{-Kl[k_1A_0t - C_0(1-e^{-k_ct})]} \quad (15)$$

Since $dx/dt = dy/dt$ at $t = 0$, we have $k_1A_0 = k_cC_0$, and if we assume appropriate values for any three of these constants, the fourth is fixed by this relationship.

To test eq 15, the following values of the constants were assumed: $K = 10^5$ l. cm^{-1} mol^{-1}; $l = 3$ cm; $k_1 = 1$ sec^{-1}; $A_0 = 10^{-3}$ mol l.$^{-1}$; $k_c = 10^2$ sec^{-1} (fixing C_0 at 10^{-5} mol l.$^{-1}$). Equation 15 then generated a sigmoid curve of I *vs.* t similar to Figure 1, with a fall time of 0.0095 sec.

Acknowledgment. The authors gratefully acknowledge the loan of photomultiplier tubes from J. Langone and F. Fry. We also wish to thank M. R. Church for translational assistance and the American Can Company for permission to publish this work.

Complete Proton and Naturally Occurring ^{33}S Hyperfine Splittings in the Thianthrene Cation Radical

by H. J. Shine[1]

Department of Chemistry, Texas Technological College, Lubbock, Texas 79409

and Paul D. Sullivan

Department of Chemistry, University of Waterloo, Waterloo, Ontario, Canada *(Received September 28, 1967)*

The thianthrene cation radical in sulfuric acid has been the subject of several investigations,[2-5] and the five-line esr spectrum has been attributed to splitting by the four equivalent protons in the 2, 3, 7, and 8 positions. No other spin interactions have been reported, although lines of low intensity were detected in the wings and body of the spectrum and assigned to other radicals.[3] These lines have escaped detection in later studies.[4] In this paper we wish to report the investigation of the thianthrene cation radical in the aluminum chloride–nitromethane system.[6]

The spectra obtained are shown in Figures 1 and 2. Figure 1 shows the complete proton hyperfine spectrum, obtained by working with dilute solutions. Splitting

(1) Support by the Directorate of Chemical Sciences, Air Force Office of Scientific Research, Grant AF-AFOSR-975-66, is gratefully acknowledged.

(2) J. E. Wertz and J. Vivo, *J. Chem. Phys.*, **23**, 2193 (1955).

(3) A. Fava, P. B. Sogo, and M. Calvin, *J. Am. Chem. Soc.*, **79**, 1078 (1957).

(4) H. J. Shine and L. Piette, *ibid.*, **84**, 4798 (1962).

(5) E. A. C. Lucken, *Theoret. Chim. Acta* (Berlin), **1**, 397 (1963).

(6) W. F. Forbes and P. D. Sullivan, *J. Am. Chem. Soc.*, **88**, 2826 (1966).

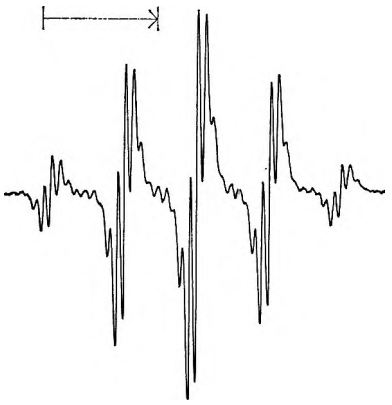

Figure 1. The esr spectrum of a dilute solution of thianthrene in nitromethane containing aluminum chloride at −51°. The scale mark represents 2 G and the direction of increasing field. A JES-3BX spectrometer with 100-kc modulation was used.

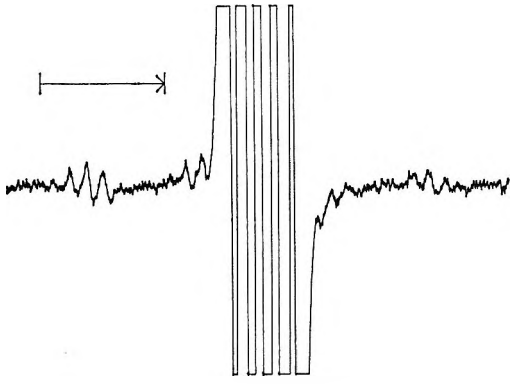

Figure 2. The esr spectrum of a concentrated solution of thianthrene in nitromethane containing aluminum chloride at −51°, recorded under conditions of high signal gain. The scale mark represents 10 G and the direction of increasing field.

of the major lines (a = 1.28 G) into the smaller quintet (a = 0.135 G) is attributable to the 1, 4, 6, and 9 protons. This resolution has not been achieved hitherto in work with sulfuric acid solutions. The experimental value of 0.135 G for the splitting constant is close to that obtained by Lucken (0.14 G) using MacLachlan's method for the p-orbital model.[5] The agreement in values is fortuitous, however, since the calculated major splitting constant (0.75 G) for this model is much smaller than observed. Further small lines are observed between the main lines in Figure 1. These are presumably due to naturally occurring ^{13}C, but we have not interpreted them in detail.

Figure 2 shows the spectrum obtained with concentrated solutions under high gain conditions. A group of lines is observed on either side of the main signal. Other lines of low intensity are seen close to the outermost lines of the main signal. These observations are undoubtedly similar to those made by Fava, Sogo, and Calvin[3] with sulfuric acid solutions, but contrary to the earlier workers we interpret these lines as due to coupling with naturally abundant ^{33}S.

Naturally occurring ^{33}S splittings have been observed in the inorganic radicals $[ON(SO_3)_2^{-2}]$,[7] SO_2^-,[8] SO_3^-,[9] and H_2S^-.[10] A radical formed by the irradiation of ^{33}S-enriched 2,4,6-tri-*t*-butylthiophenol gave a ^{33}S splitting constant of 14.75 G.[11] To the best of our knowledge no previous reports of naturally occurring ^{33}S splitting constants in organic radicals have appeared.

The ^{33}S spectrum (Figure 2) consists of four groups of lines due to those radicals (*ca.* 1.5%) containing one ^{33}S nucleus (natural abundance ≅0.75%) with nuclear spin of $^3/_2$. The positions and intensities of the lines agree well with this interpretation, and the magnitude of the splitting constant (9.15 G) is consistent with other work.[11] The lines due to the ^{33}S nucleus are broader at high field than at low, which enables us to consider the sign of the splitting constant.

Following Fraenkel,[12] an expression for the line width variations for the lines due to the ^{33}S splitting can be written in the form of eq 1, where $\Delta(\tilde{m})$ is the half-width, A, B, and C are constants, and $\tilde{m}_S$ is defined as positive on the high-field side of the spectrum.

$$\Delta(\tilde{m}) = A + B\tilde{m}_S + C\tilde{m}_S^2 \qquad (1)$$

Since the high-field lines are broader than the low-field ones, the sign of B is positive. Using the condition that the local spin density is not too small compared with the spin densities on nearest-neighbor atoms (supported by m.o. calculations), we can express B as in eq 2. In this expression, α is a positive constant, ζ is

$$B = \alpha\zeta\epsilon_s\rho g^{(0)} \qquad (2)$$

related to γ_S and will be positive, ρ_S is the local spin density on sulfur and is assumed (supported by m.o. calculations) positive, and $g^{(0)} = \sqrt{6}\,(2g_3 - (g_1 + g_2))$ and is assumed to be negative.[13] Therefore, ϵ_S must be negative and since $\epsilon_S = -\tilde{a}_S/|\tilde{a}_S|$, the sign of a must be positive. Investigations of substituted thianthrenes also show improved resolution and evidence of ^{33}S splittings in CH_3NO_2-$AlCl_3$, and work is continuing along these lines.

(7) J. J. Windle and A. K. Wiersema, *J. Chem. Phys.*, **39**, 1139 (1963).

(8) P. W. Atkins, A. Horsfield, and M. C. R. Symons, *J. Chem. Soc.*, 5220 (1964).

(9) G. W. Chantry, A. Horsfield, J. R. Morton, and D. H. Whiffen, *Mol. Phys.*, **5**, 233 (1962).

(10) J. E. Bennett, B. Mile, and A. Thomas, *Chem. Commun.*, 182 (1966).

(11) W. Rundel and K. Scheffler, *Angew. Chem. Intern. Ed.*, **4**, 243 (1965).

(12) G. K. Fraenkel, *J. Phys. Chem.*, 71, 139 (1967).

(13) The assumption that $g^{(0)}$ is negative should be treated with reservation since there is evidence that the neutral molecule is bent. Further work will be required to evaluate the g tensor and verify the sign of $g^{(0)}$.

Acknowledgments. We wish to express our appreciation to Professor W. F. Forbes, University of Waterloo, for the generous use of esr facilities. P. D. S. wishes to thank the National Research Council of Canada for a studentship.

Small Tunneling Effect in the Electron Paramagnetic Resonance Spectrum of Cu^{2+}–CaO at 1.2°K

by R. E. Coffman, D. L. Lyle, and D. R. Mattison

Chemistry Department, Augsburg College, Minneapolis, Minnesota 55404 *(Received October 6, 1967)*

Recently, several papers have reported detection of a tunneling effect in the low-temperature epr spectrum of Cu^{2+} $(3d)^9$ and Sc^{2+} $(3d)^1$, present as substitutional impurities in high-symmetry crystals.[1,2] We wish to report our conclusions concerning the tunneling splitting in Cu^{2+}–CaO at 1.2°K. Some information on the epr spectrum of Cu^{2+}–CaO *vs.* temperature has been published earlier.[3] We have repeated these measurements in order to see if there is any similarity in the angular dependence of the absorption lines at 1.2°K to. that found in Cu^{2+}–MgO at 1.2°K.[1] We have studied the angular dependence of the Cu^{2+}–CaO single-crystal resonances in the (100) and (110) planes at 77 and 1.2°K. We found different types of spectra in each temperature range, as we expected, but the liquid helium temperature spectrum shows that the three tetragonal distorted-state functions interact weakly by way of an interference (tunneling) effect.

Single crystals of copper-doped calcium oxide were obtained from Semielements, Inc. and from W. N. C. Spicer, Ltd. Measurements in the (100) plane at 1.2°K showed a single absorption peak (A) and a set of four resolved hfs peaks (B) (Figure 1, top). The absorption peaks in the [110] direction indicate a considerably distorted and broadened line shape which becomes too broad to be detected for $\mathbf{H}_0$ parallel to a [100] crystal direction. The [110]-direction line shape resembles the spectrum of Cu^{2+} in a glass for which A corresponds to $g_\perp$ and B corresponds to $g_{||}$.[4] Line A is found to be nearly isotropic, but line B is definitely anisotropic. The (100)-plane angular dependence of the peaks of these lines is plotted in Figure 2. If we assume a frozen out Jahn–Teller distortion, as was previously done[3] for a compressed octahedron having $g_{||} = 2$ and $g_\perp = 2 + 6u$ ($u = |\lambda|/\Delta = 0.0552$ cm^{-1}, where λ is the spin–orbit coupling parameter and Δ is the crystal field splitting), then the (100)-plane resonances would consist of three lines at the g values

$$g_1 = g_\perp \tag{1a}$$

$$g_2 = g_{||} \cos^2\theta + g_\perp \sin^2\theta \tag{1b}$$

$$g_3 = g_{||} \sin^2\theta + g_\perp \cos^2\theta \tag{1c}$$

where θ is the angle between $\mathbf{H}_0$ and a [100] axis. The experimental points in Figure 2 are curiously similar to eq 1, but the crossover predicted by eq 1b and 1c was definitely not found, a point which was carefully checked. Moreover, we proved that line A is a Cu^{2+} resonance by measuring the (110)-plane angular dependence, in which plane it could be resolved into four hfs lines (Figure 1, middle). Thus there are at least two strong resonances in the (100) plane (disregarding hfs), but the resonances, which are of the 1 ion/unit cell type do not obey eq 1.

The tunneling effect, when large, transforms the behavior of the ground state of a Cu^{2+} ion so that the

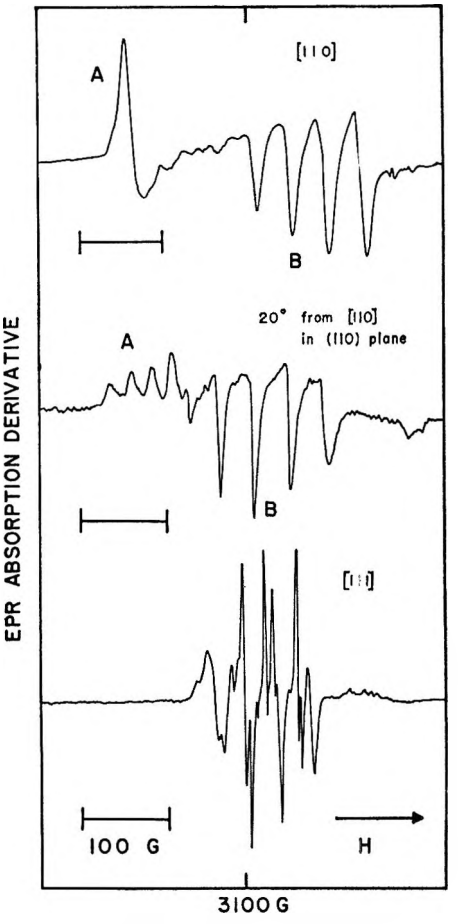

Figure 1. Electron paramagnetic resonance absorption derivative spectra of single crystal Cu^{2+}–CaO at 1.2°K. The bottom two traces were measured at 9.606 GHz. The top trace, which was measured at 9.272 GHz, has been shifted upfield by the factor 9.606/9.272.

(1) R. E. Coffman, *Phys. Letters*, **19**, 475 (1965); **21**, 381 (1966).
(2) U. T. Höchli and T. L. Estle, *Phys. Rev. Letters*, **18**, 128 (1967).
(3) W. Low and J. T. Suss, *Phys. Letters*, **7**, 310 (1963).
(4) W. B. Lewis, M. Alei, and L. O. Morgan, *J. Chem. Phys.*, **44**, 2409 (1966).

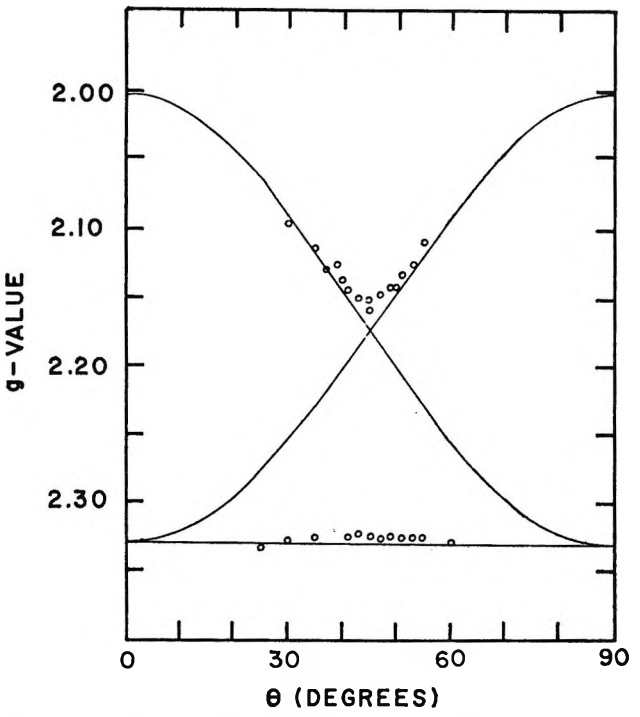

Figure 2. Experimental and calculated g values *vs.* angle of $\mathbf{H}_0$ from the [100] direction in a (100) plane. Calculated g value are for frozen out compressed octahedra.

three transitions of eq 1 are replaced by an isotropic and two anisotropic transitions having g values[1,5]

$$g_1 = 2 + 4u \tag{2a}$$

$$g_{2,3} = 2 + 4u \pm 2u[1 - 3(l^2m^2 + m^2n^2 + n^2l^2)]^{1/2} \tag{2b}$$

where l–n are the direction cosines of $\mathbf{H}_0$ with respect to the crystalline [100] axes. These equations represent transitions within a Kramers' doublet and quartet separated by a tunneling splitting, the magnitude of which we denote by $3V$. The symmetry of this spectrum is of the 1 ion/unit cell type. Spectra of this type have been observed for Cu^{2+}–MgO and Sc^{2+}–CaF_2 in which cases the tunneling splitting is evidently quite large,[1,2] since for both only the ground state Kramers' quartet can be observed at 1.2°K, but the excited state doublets have been observed for Sc^{2+}–CaF_2 at higher temperatures.[6] Now suppose that we could vary the magnitude of the tunneling effect. Then as $3V$ varies from 10 cm^{-1}, for example, to 0 cm^{-1}, we expect to find some type of transformation of the spectrum by which the g values of eq 2 transform into eq 1. So we asked the following question. If V were very small, would the resonances resemble eq 1 in some way while still exhibiting the 1 ion/unit cell property? In order to answer this question, we programmed an eigenvalue, eigenvector, g value, and absorption-intensity calculation which numerically reproduced eq 1 and 2 for limits $V = 0$ and $V > 1$ cm^{-1}, respectively, using[3] $u = 0.0552$ cm^{-1}.

The method of calculation is as follows. A basis set of four spin–orbit functions may be used to describe the paramagnetic ground state of the Cu^{2+} ion in octahedral (sixfold coordinated) or slightly distorted (near octahedral) symmetry[5,7]

$$\Phi^i = \Gamma_8{}^i(e_g) + (3/2)^{1/2}u\Gamma_8{}^i(t_{2g}) \tag{3}$$

where i = a, b, c, and d. Using this basis set having fixed (z axis) quantization, we construct three sets of two functions each, representing the ground-state Kramers' doublets for compressed octahedra having compression axes along the crystallographic x, y, or z axes

$$\Phi^-{}_{qn} = \left(\cos\frac{\phi}{2}\Phi^c + \sin\frac{\phi}{2}\Phi^a\right)\chi_{qn} \tag{4a}$$

$$\Phi^+{}_{qn} = \left(\cos\frac{\phi}{2}\Phi^d + \sin\frac{\phi}{2}\Phi^b\right)\chi_{qn} \tag{4b}$$

where $\phi = 0, (\pm 4\pi/3)$ for the distortion direction index $q = z, x,$ or y. The tunneling effect, which we represent by an operator $\hat{V}$, arises when the vibrational functions $\chi_{zn}, \chi_{yn}, \chi_{zn}$ (vibrational quantum number n) are not orthogonal. $\hat{V}$ is then diagonal[8] within these symmetrized linear combinations of eq 4 (in which we neglect certain small overlap terms necessary for proper normalization[9])

$$\Psi^\pm{}_{1n} = \frac{1}{\sqrt{3}}[\Phi^\pm{}_{xn} + \Phi^\pm{}_{yn} + \Phi^\pm{}_{zn}] \tag{5a}$$

$$\Psi^\pm{}_{2n} = \frac{1}{\sqrt{6}}[2\Phi^\pm{}_{zn} - \Phi^\pm{}_{xn} - \Phi^\pm{}_{yn}] \tag{5b}$$

$$\Psi^\pm{}_{3n} = \frac{1}{\sqrt{2}}[\Phi^\pm{}_{xn} - \Phi^\pm{}_{yn}] \tag{5c}$$

We then solved this problem by matrix diagonalization

$$[\hat{V} + \beta\mathbf{H}_0\cdot(\mathbf{L} + 2\mathbf{S})]\Psi_i = E_i\Psi_i \tag{6}$$

where Ψ_i is a linear combination of the functions (5), and E_i is its energy eigenvalue. Having found the eigenvectors and eigenvalues, we computed the g values and intrinsic intensities using V as an adjustable parameter

$$g_{ij} = (E_i - E_j)/\beta\mathbf{H}_0 \tag{7}$$

$$I_{ij} = |\langle\Psi_i|\beta\mathbf{H}_1\cdot(\mathbf{L} + 2\mathbf{S})|\Psi_j\rangle|^2 \tag{8}$$

In eq 7 we used $\mathbf{H}_0 = 3000$ G and the microwave magnetic field $\mathbf{H}_1$ perpendicular to $\mathbf{H}_0$. The necessary approximations which we make in eq 7 in order to

(5) R. E. Coffman, in *J. Chem. Phys.* in press.
(6) U. Höchli, *Phys. Rev.*, 162, 262 (1967).
(7) C. J. Ballhausen, "Introduction to Ligand Field Theory," McGraw-Hill Book Co., Inc., 1962, p 120.
(8) I. B. Bersuker, *Soviet Phys. JETP*, 16, 933 (1963).
(9) I. B. Bersuker, *ibid.*, 17, 836 (1963).

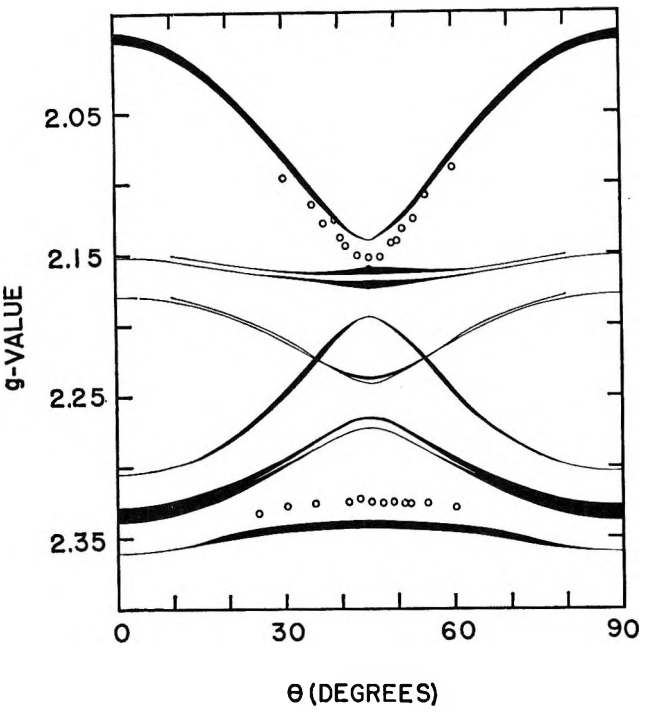

Figure 3. Experimental and calculated g values *vs.* θ as in Figure 2. Calculated g values are for a tunneling splitting of 0.006 cm^{-1}. The thickness of the lines is proportional to the epr absorption intensity.

easily compute the g values is that the experimental g values are not much different from those for an experiment in which $\mathbf{H}_0$ is held constant and the klystron frequency is varied. This is a good approximation, provided both the zero field splittings and the nonlinearity of the energy levels is small, a set of conditions which are well satisfied for the values of the parameters which we have found to be of greatest interest. We were pleased to find that the g values and intensities, when plotted *vs.* V for $\mathbf{H}_0$ parallel to [100] exhibited precisely the discontinuous transition found by O'Brien.[10] (See Figure 3a in that paper).

The results for $V = 0.002$ cm^{-1} are given in Figure 3, in which are also given some experimental g values determined at 1.2°K. The calculated $g(\theta)$ values exhibit a qualitative resemblance to both eq 1 and 2, owing to the small value of V which permits strong mixing between the doublet and quartet states. The shape of the experimental absorption curves in the (100) plane indicates a considerably distorted and broadened paramagnetic absorption, as we verified by numerical integration, so that the derivatives in Figure 1 (top and middle tracings) demark the lower- and upper-field boundaries of $\chi''(H)$, for each value of the nuclear-spin quantum number. We see that the envelope of the predicted (100)-plane transitions follows the experimental points quite closely. The line-broadening effects may be due to crystal strains, since the behavior observed here is generally similar to the results of strain effect studies.[11,12] The random distribution of such strains may explain why Figure 1 (top) resembles the epr absorption derivative of Cu^{2+} in a glass. These strains are least effective as a line broadening mechanism for $\mathbf{H}_0$ parallel to [111]; the multiplicity of hfs lines for this direction (Figure 1, bottom) agrees with the general results of our calculation for the (100) plane as in Figure 3, which predicts a relatively large number of transitions of various intensities for a tunneling splitting of 0.006 cm^{-1}.

We conclude that the epr spectrum of Cu^{2+}–CaO at 1.2°K exhibits a small tunneling splitting of 0.006 cm^{-1} (sign undetermined), and that the results of interference between the eigenstates of the three types of tetragonal distortions are directly evident in the epr spectrum. The tetragonal distortions are compressions rather than elongations of the CuO_6 octahedron, as has also been determined from the line width behavior.[3] The calculations indicate that the 1.2°K spectrum should be strongly frequency dependent.

Acknowledgment. We are indebted to Professor John Wertz of the University of Minnesota for the use of his laboratory facilities, and we acknowledge the assistance of Mr. Dean Gulden in programming the Pillsbury time-shared computer. This work was supported, in part, by the Research Corp. under a Frederick Gardner Cottrell Grant and by the Solid State Sciences Division, Air Force Office of Scientific Research under Grant 200-66. R. E. C. wishes to thank Dr. U. Höchli for a preprint.

(10) M. C. M. O'Brien, *Proc. Roy. Soc.* (London), **A281**, 323 (1964)
(11) E. R. Feher, *Phys. Rev.*, **136**, A145 (1964).
(12) E. B. Tucker, *ibid.*, **143**, 264 (1966).

The Radiolysis of Liquid Nitrous Oxide[1]

by M. G. Robinson and G. R. Freeman

Department of Chemistry, University of Alberta, Edmonton, Alberta, Canada *(Received October 30, 1967)*

During the course of recent investigations of the effect of nitrous oxide on the radiolysis of liquid hydrocarbons, an estimate of the yield of nitrogen from the "direct radiolysis" of nitrous oxide in the liquid phase was required. Accordingly, the radiolysis of pure liquid nitrous oxide and of nitrous oxide–cyclopentane solutions were investigated and the results are reported here.

Experimental Section

Matheson research grade nitrous oxide was purified

(1) This project was partially supported by the Defence Research Board of Canada.

by freeze–pump–thaw and distillation cycles in a vacuum system.

Phillips research grade cyclopentane was purified by treatment with concentrated sulfuric acid, thoroughly washed with water, then dried with magnesium sulfate and distilled over lithium aluminum hydride.

Two-gram samples, contained in 2.5-ml Pyrex cells, were prepared by standard vacuum techniques. Great care was required to thoroughly remove nitrogen and oxygen from the samples.

The liquid samples, maintained at 185°K by methanol slush, were irradiated in a ^{60}Co Gammacell-220. The dose rate was determined with the Fricke dosimeter, making the appropriate electron density corrections. The dose rate was 5×10^{17} eV/min g of N_2O and the highest dose used was 1×10^{19} eV/g of N_2O.

The product gases noncondensable at 77°K were collected by vacuum distillation, measured in a McLeod–Toepler apparatus, and analyzed with a CEC (21-614) mass spectrometer.

Nitrogen dioxide was measured after conversion to nitrite.

$$2NO_2 + 2OH^- \longrightarrow NO_2^- + NO_3^- + H_2O \quad (1)$$

Frozen nitrous oxide samples were broken in a 1-l. evacuated jar that contained 20 ml of 0.025 *M* sodium hydroxide. After equilibration, the nitrite concentration was measured spectrophotometrically at 520 mμ, using the α-naphthylamine–sulfanilic acid reagent.[2] Unirradiated samples were run as blanks.

Results and Discussion

Pure Nitrous Oxide. The yields of nitrogen and oxygen from liquid nitrous oxide irradiated at 185°K were $G(N_2) = 12.9 \pm 0.2$ and $G(O_2) = 2.6 \pm 0.1$, independent of dose over the range 1–5 $\times 10^{18}$ eV/g. At 1×10^{19} eV/g, $G(NO_2) = 5.0 \pm 0.2$. The overall stoichiometry may be represented by

$$6N_2O \xrightarrow{\sim\sim} 5N_2 + 2NO_2 + O_2 \quad (2)$$

which is the same as that found for the vapor phase radiolysis of nitrous oxide at 298°K and 600 torr.[3] In fact, the low-temperature liquid phase yields are quite similar to those that have been reported for the vapor phase at room temperature.[3,4]

The following mechanism is not unique in its ability to explain the results, but it is based upon reactions that have been proposed to occur in the vapor phase radiolysis,[3-5] photolysis,[6-8] and pyrolysis[9,10] of nitrous oxide. The listed *G* values are those that would be consistent with the present results and the *W* value of gaseous nitrous oxide (32.9 eV[11]).

	G	
$N_2O \xrightarrow{\sim\sim} N_2O^+ + e^-$	3.0	(3)
$\xrightarrow{\sim\sim} N_2O^*$	6.4	(4)
$e^- + N_2O \longrightarrow N_2O^-$	3.0	(5)
$N_2O^- \longrightarrow N_2 + O^-$	3.0	(6)
$O^- + N_2O \longrightarrow N_2 + O_2^-$	0.5	(7)
$\longrightarrow NO + NO^-$	3.0	(8)
$N_2O^+ + O_2^-(NO^-) \longrightarrow N_2O^* + O_2(NO)$	3.0	(9)
$N_2O^* \longrightarrow N_2 + O$	9.4	(10)
$O + O + M \longrightarrow O_2 + M$	4.7	(11)
$2NO + O_2 \longrightarrow 2NO_2$	5.0	(12)

Reactions 7 and 8 have been observed to occur in a mass spectrometer.[12]

Reaction 13 has a large rate constant[13] and probably occurs to an appreciable extent at higher doses. How-

$$O + NO_2 \longrightarrow O_2 + NO \quad (13)$$

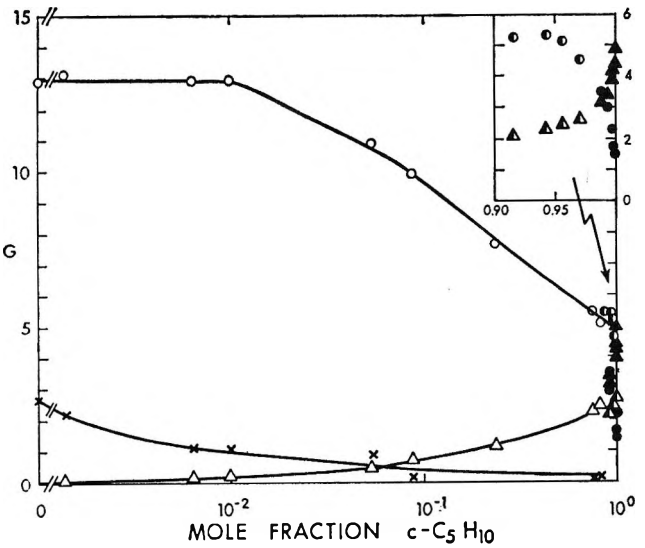

Figure 1. Product yields from nitrous oxide–hydrocarbon solutions. Cyclopentane solute: N_2 (○), O_2 (×) and H_2 (△) at 185°K; N_2 (●) and H_2 (▲) at 300°K. Cyclohexane solute: N_2 (◐) and H_2 (▲) at 300°K.

(2) "Methods for the Determination of Toxic Substances in Air," 16.1 (1961), International Union of Pure and Applied Chemistry, Butterworth and Co. Ltd., London, 1962.

(3) T. F. Jones and T. J. Sworski, *J. Phys. Chem.*, **70**, 1546 (1966).

(4) G. R. A. Johnson, *J. Inorg. Nucl. Chem.*, **24**, 461 (1962).

(5) W. J. Holtslander and G. R. Freeman, *Can. J. Chem.*, **45**, 1661 (1967).

(6) W. A. Noyes, Jr., *J. Chem. Phys.*, **5**, 807 (1937).

(7) M. Zelikoff and L. M. Aschenbrand, *ibid.*, **22**, 1680, 1685 (1954).

(8) (a) J. P. Doering and B. H. Mahan in "Chemical Reactions in the Lower and Upper Atmosphere," Stanford Research Institute Symposium, Interscience Publishers, Inc., New York, N. Y., 1961, p 327; (b) *J. Chem. Phys.*, **36**, 1682 (1962).

(9) H. S. Johnson, *ibid.*, **19**, 663 (1951), and references therein.

(10) L. Friedman and J. Bigeleisen, *J. Am. Chem. Soc.*, **75**, 2215 (1953), and references therein.

(11) G. G. Meisels, *J. Chem. Phys.*, **41**, 51 (1964).

(12) B. P. Burtt and J. Henis, *ibid.*, **41**, 1510 (1964).

(13) C. A. Barth in "Chemical Reactions in the Lower and Upper Atmosphere," Stanford Research Institute Symposium, Interscience Publishers, Inc., New York, N. Y., 1961, p 303.

ever, it would not alter the product yields, but would merely decrease the extent of reaction 11.

Reactions 14 and 15 are highly exothermic,[14] but are

$$O(^3P) + N_2O \longrightarrow N_2 + O_2 + 79 \text{ kcal/mole} \quad (14)$$

$$\longrightarrow 2NO + 36 \text{ kcal/mole} \quad (15)$$

apparently too slow[8a,15] to occur to an appreciable extent in the present system. However, the equivalent reactions involving excited oxygen atoms could occur.[8a,16] Inclusion of appreciable contributions from reactions 10′, 14′, and 15′, in such a way as to fit the

$$N_2O^* \longrightarrow N_2 + O^* \quad (10')$$

$$O^* + N_2O \longrightarrow N_2 + O_2 \quad (14')$$

$$\longrightarrow 2NO \quad (15')$$

observed product yields, simply entails decreasing the estimated yields of reactions 4, 10, and 11 and increasing the estimated value of k_7/k_8. This would bring the value of k_7/k_8 closer to the value 1.2 estimated for the gas-phase radiolysis of nitrous oxide at room temperature.[17] Of course, there is no reason why the ratio should have the same value under the two different sets of conditions.

Nitrous Oxide–Cyclopentane Solutions. Oxygen atoms react readily with hydrocarbons,[18] so the addition of cyclopentane to nitrous oxide would be expected to decrease $G(O_2)$, as observed (Figure 1). The nitrogen yield decreased only at cyclopentane concentrations greater than 10^{-2} mole fraction (Figure 1), and the decrease was due mainly to the effect of dilution.

In Figure 1, moving from the extreme right to the left, the abrupt rise in nitrogen and decrease in hydrogen yield are due to the nitrous oxide scavenging the electrons generated in the hydrocarbon. These effects are discussed elsewhere.[19] However, it should be noted that the results obtained at 185°K for cyclopentane flow smoothly into those obtained at 300°K for both cyclopentane and cyclohexane (Figure 1), so the effect of temperature on the electron scavenging reactions is small.

The hydrogen yields can be expressed as $g(H_2) = G(H_2)/\epsilon_{C_5H_{10}}$, where $\epsilon_{C_5H_{10}}$ is the electron fraction of cyclopentane in the solution. The value of $g(H_2)$ increases as the value of $\epsilon_{C_5H_{10}}$ decreases below about 0.5 and reaches a plateau of $g(H_2) = 15$ for $\epsilon_{C_5H_{10}} < 0.010$. This behavior indicates that energy transfer occurs from nitrous oxide to cyclopentane

$$N_2O^{**} + C_5H_{10} \longrightarrow N_2O + C_5H_{10}^{**} \quad (16)$$

$$C_5H_{10}^{**} \longrightarrow H_2 + \text{products} \quad (17)$$

Furthermore, the results can be used to show that $G(N_2O^{**}) \approx 0.5$ and that if $k_{16} \approx 10^{10}$ l./mole sec, then $k_{18} \approx 10^9$ sec^{-1}.

$$N_2O^{**} \longrightarrow \text{decomposition or deactivation} \quad (18)$$

(14) Calculated from data in F. T. Wall, "Chemical Thermodynamics," 2nd ed, W. H. Freeman & Co., San Francisco, Calif., 1965, pp 54, 61.
(15) H. W. Ford and N. Endow, *J. Chem. Phys.*, **27**, 1156 (1957).
(16) R. J. Cvetanovic, *ibid.*, **39**, 1902 (1963).
(17) J. M. Warman, *Nature*, **213**, 381 (1967).
(18) H. W. Ford and N. Endow, *J. Chem. Phys.*, **27**, 1277 (1957).
(19) M. G. Robinson and G. R. Freeman, *ibid.*, in press.

Influence of the Solvent Structure on Ion-Pair Association

by Filippo Conti, Pietro Delogu, and Gianfranco Pistoia

Istituto di Chimica Fisica, Università di Roma, Rome, Italy

Accepted and Transmitted by The Faraday Society (July 21, 1967)

Many authors have pointed out the influence of the solvent on the values of ion-pair association constants (K_A). In particular, Kay,[1] in studying some salts of tetraalkylammonium in methyl alcohol, obtained values of K_A higher than those expected on the basis of Bjerrum–Fuoss theory.[2] The author explains this behavior with the hypothesis that the ion-pair association process is affected by the particular structure of the alcohol.

In order to have a better understanding of this ion–solvent interaction mechanism, we studied the behavior of alkylammonium salts in binary mixtures of methyl alcohol with solvents capable of affecting its structure in different ways. In this paper we report some results obtained for tetraethylammonium perchlorate in methanol–carbon tetrachloride and methanol–pyridine mixtures.

Experimental Section

The methanol, pyridine, and carbon tetrachloride (Erba RP products) were purified with the methods of Hartley,[3] Kraus,[4] and Fuoss,[5] respectively. The tetraethylammonium perchlorate (Erba RS product) was crystallized twice with *n*-butyl alcohol and dried under high vacuum at 150°.

The apparatus and technique used for the conductivity measurements have been described before.[6]

The values of the physical constants for the system

(1) R. Kay, C. Zawoyski, and D. F. Evans, *J. Phys. Chem.*, **69**, 4208 (1965).
(2) N. Bjerrum, *Kgl. Danske Videnskab. Selskab, Mat. Fys. Medd.*, **7**, No. 9 (1926); R. Fuoss and C. Kraus, *J. Am. Chem. Soc.*, **55**, 1019 (1933).
(3) H. Hartley and H. Raikes, *J. Chem. Soc.*, 524 (1925).
(4) W. Luder and C. Kraus, *J. Am. Chem. Soc.*, **69**, 2481 (1947).
(5) H. Sadek and R. Fuoss, *ibid.*, **76**, 5897 (1954).
(6) F. Accascina, A. D'Aprano, and R. Fuoss, *ibid.*, **81**, 1058 (1959).

CH_3OH–CCl_4 were interpolated by the data of Sadek and Fuoss,[5] while for the CH_3OH–C_5H_5N system they were determined by the techniques used in this institute.[7]

The nmr measurements were made with a Varian A-60 spectrometer at a temperature of 29 ± 1°. The values reported (in cps from benzene as external reference) represent the average of several measurements made at every concentration, the reproducibility of which was always within ±0.5 cps. The values have been corrected for the differences in susceptibilities of the different solutions.

Results and Discussion

Table I gives the physical constant values of the mixtures (d, η, and D).

Table I: Properties of Solvents

No.	% MeOH	D	100η	d
		CH_3OH–CCl_4		
1	100.00	32.63	0.5445	0.7866
2	89.65	31.05	0.5675	0.8301
3	82.95	29.98	0.5843	0.8606
4	74.96	28.52	0.6070	0.9005
5	73.07	28.15	0.6125	0.9104
6	62.26	25.80	0.6480	0.9720
7	43.60	20.46	0.7220	1.0997
8	38.22	18.60	0.7462	1.1432
		CH_3OH–C_5H_5N		
9	95.27	31.8	0.5559	0.7956
10	83.44	30.9	0.5854	0.8167
11	69.77	29.2	0.6198	0.8422
12	46.51	25.7	0.6772	0.8872
13	21.14	19.8	0.7561	0.9366
14	0.00	12.3	0.8827	0.9780

The experimental data obtained were analyzed with Fuoss' equation,[8] which holds good for associated electrolytes

$$\Lambda = \Lambda_0 - S\sqrt{c\gamma} + Ec\gamma \log c\gamma + Jc\gamma - K_A c\gamma f^2\Lambda - F\Lambda_0 c \quad (1)$$

where γ is the fraction of salt present as free ions and F is the Einstein coefficient $(5\varphi/2)C$, where φ is volume fraction of solute.

The calculations were made with an IBM 7040 computer according to the program developed by Kay.[9] The value of 0.5 for the coefficient F was obtained according to Kay.[10]

The values of the concentrations c (equiv/l.) and of the equivalent conductivities Λ (ohm^{-1} cm^2 equiv^{-1}) are given in Table II.

Table III shows the derived constants (Λ_0, K_A, J, and a_J) and σ_Λ (average of the percentage differences between the experimental values and those computed with eq 1).

Table II: Conductance of Tetraethylammonium Perchlorate at 25°

10^4c	Λ	10^4c	Λ	10^4c	Λ
		CH_3OH–CCl_4			
No. 1		No. 2		No. 3	
3.003	125.318	5.600	115.615	3.569	112.848
6.419	121.946	10.340	111.774	8.126	108.340
8.955	119.979	15.225	108.656	12.335	105.202
11.190	118.471	18.954	106.646	16.543	102.624
11.869	118.048	24.564	104.025	21.551	100.003
14.517	116.441				
16.520	115.385				
17.469	114.883				
No. 4		No. 5		No. 6	
3.794	106.526	4.616	103.812	4.277	94.289
7.550	102.393	8.372	99.960	11.486	86.882
11.915	98.796	11.841	97.137	14.286	84.744
16.676	95.691	15.842	94.476	17.582	82.595
21.693	92.974	19.444	92.435		
No. 7		No. 8			
4.335	72.809	2.958	67.951		
8.533	66.721	5.536	62.487		
12.037	63.068	8.340	58.320		
14.669	60.814	11.277	55.107		
		14.255	52.522		
		CH_3OH–C_5H_5N			
No. 9		No. 10		No. 11	
4.789	114.886	3.831	103.936	4.010	94.522
10.120	110.839	7.419	100.995	11.689	88.953
13.589	108.778	10.749	98.846	15.431	87.009
17.395	106.826	13.821	97.152	18.880	85.468
21.492	105.001	17.042	95.598		
No. 12		No. 13			
3.717	84.817	4.127	79.967		
7.537	80.688	7.923	75.402		
11.135	77.859	11.917	72.035		
14.317	75.818	15.356	69.752		
17.482	74.092	18.942	67.777		

The value of Λ_0 for Et_4NClO_4 in CH_3OH (131.39 ± 0.09) is in agreement with the sum of the ion mobilities: $\Lambda_0^+ = 60.5$,[1] $\Lambda_0^- = 71.0$.[11]

Figure 1 shows the curves for the dilution shifts of the alcoholic protons. In the case of the mixture CH_3OH–CCl_4, the shift trend is diamagnetic, but, in the case of the mixture CH_3OH–C_5H_5N, it is paramagnetic. The same figure also shows the curve for the system CH_3OH–$ClCH_2CH_2Cl$. Since pyridine and *sym*-dichloro-

(7) F. Accascina, S. Petrucci, and S. Schiavo, *Sci. Tec.*, **2**, 27 (1958).

(8) R. Fuoss and F. Accascina, "Electrolytic Conductance," Interscience Publishers, Inc., New York, N. Y., 1959, p 234.

(9) R. Kay, *J. Am. Chem. Soc.*, **82**, 2099 (1960).

(10) D. F. Evans, C. Zawoyski, and R. Kay, *J. Phys. Chem.*, **69**, 3878 (1965).

(11) J. Prue and P. Sherrington, *Trans. Faraday Soc.*, **57**, 1795 (1961).

Table III: Derived Constants

No.	A_0	a	K_A	J	σA
		CH_3OH–CCl_4			
1	131.39 ± 0.09	4.6 ± 1.5	41 ± 7	2175	0.009
2	124.70 ± 0.02	3.8 ± 0.2	47 ± 1	2089	0.001
3	120.10 ± 0.03	4.1 ± 0.3	59 ± 2	2333	0.004
4	114.73 ± 0.06	5.5 ± 0.7	89 ± 4	3151	0.008
5	113.12 ± 0.07	5.7 ± 0.7	94 ± 5	3285	0.006
6	103.88 ± 0.09	3.4 ± 0.7	111 ± 7	2695	0.009
7	86.16 ± 0.04	2.4 ± 0.1	285 ± 4	3485	0.004
8	81.4 ± 0.1	3.7 ± 0.5	560 ± 15	5895	0.02
		CH_3OH–C_5H_5N			
9	122.57 ± 0.02	4.6 ± 0.2	41 ± 1	2275	0.002
10	110.45 ± 0.01	3.7 ± 0.2	36 ± 1	2178	0.002
11	101.48 ± 0.01	4.3 ± 0.1	45.6 ± 0.5	2920	0.01
12	93.40 ± 0.06	4.8 ± 0.3	99 ± 5	5318	0.008
13	90.8 ± 0.1	5.1 ± 0.4	156 ± 10	7407	0.02

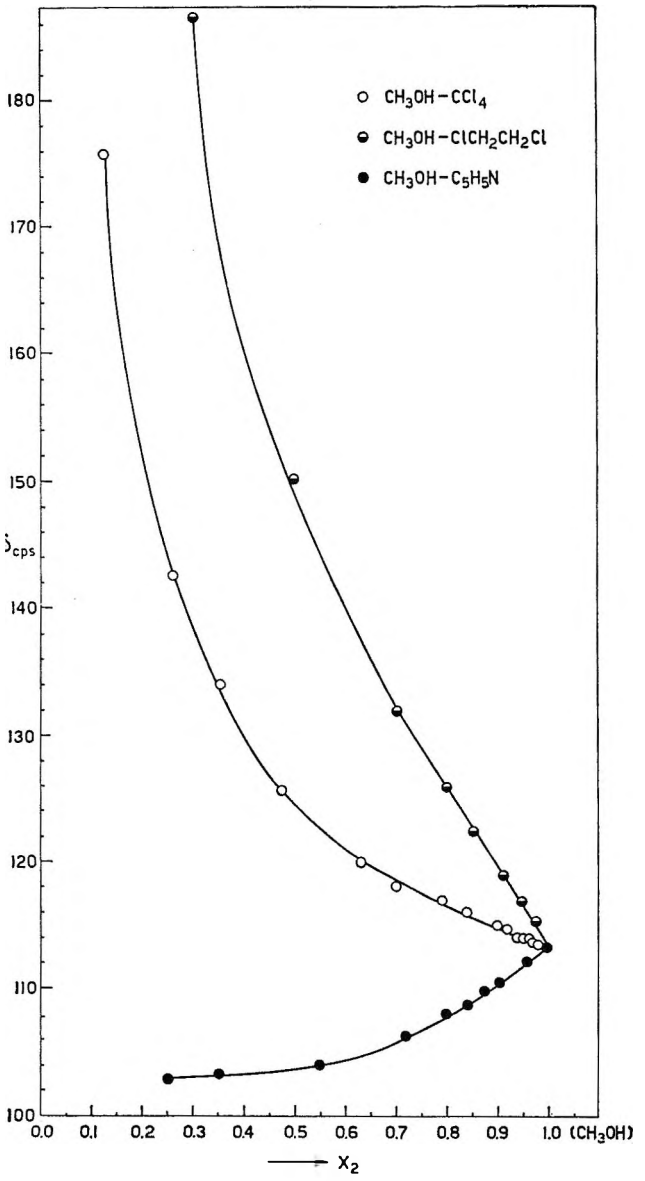

Figure 1. Dilution shift of hydroxylic proton resonance of CH_3OH in different solvents.

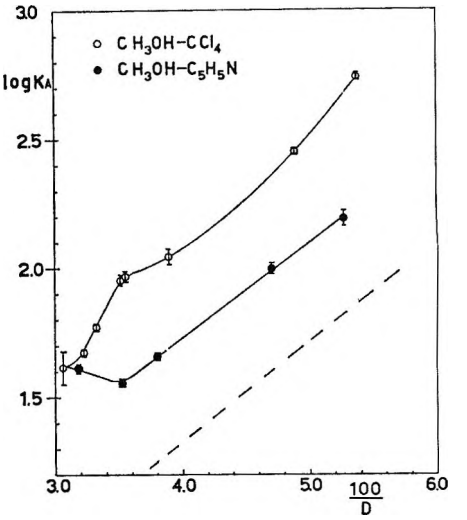

Figure 2. Dependence of association constants on dielectric constant: dotted line, association constants computed by eq 2 with a = 6.4 Å.

ethane have very similar dielectric constants, the different behavior observed is evidently attributable to the methanol–pyridine intermolecular association.

The nonlinearity of $\log K_A$ as a function of $1/D$ (Figure 2) reveals the existence of strong interactions between the solvent and the electrolyte, showing areas in which the slope of the curves abruptly varies.

In both systems the curves lie above the theoretical straight line of the equation

$$K_A = \frac{4\pi N a_K^3}{3000} e^{e^2/a_K DkT} \qquad (2)$$

for which the crystallographic value of a = 6.4 has been used. Therefore, it is necessary to introduce into eq 2 Gilkerson's term E_s,[12] defined as a difference between the energies of ion–solvent interaction and that of ion pair–solvent interaction ($E_s = (E_+ + E_-) - E_\pm$). Then eq 2 becomes

$$K_A = \frac{4\pi N a_K^3}{3000} e^{(e^2/a_K DkT) - (E_s/kT)} \qquad (3)$$

Since the experimental values found are always larger than those calculated with (2), this seems to indicate that the term E_s/kT is negative in the range of D examined ($E_\pm > E_+ + E_-$). On the other hand, the trend of the curves would lead one to assume that, contrary to what happens for many systems, E_s does not remain constant with the variation in the composition of the solvent, except in the system CH_3OH–C_5H_5N for $D < 28$. In particular, in the two systems studied, there would be initially a ΔE_s of opposite sign, producing in the system CH_3OH–CCl_4 a sharp increase of K_A and in the system CH_3OH–C_5H_5N an initial decrease. This should be related to the different effect of CCl_4

(12) W. Gilkerson, *J. Chem. Phys.*, **25**, 1199 (1956).

and C_5H_5N on the methanol structures. The first solvent, in fact, may act only as an inert diluent, whereas the second forms a strong H bond (ΔH = −3.88 kcal/mole)[13] as shown by the dilution shifts. As D decreases, the curves tend to become more regular. It seems that, over a certain concentration, the alcohol structures which could affect the association process of the ions would undergo less marked variations, exerting an influence almost constant in the system CH_3OH–C_5H_5N and less noticeably in the system CH_3OH–CCl_4.

For the latter, the value of a_K (distance of closest approach of the two ions), deducible from the average slope of the first part of the curve (log K_A)/(1/D) (2.5 Å), is considerably below the sum of the crystallographic radii (6.4 Å). However, over a certain value of D, the average value of a_K is comparable with the theoretical one. On the other hand, the curve is very similar to the one observed by Sadek and Fuoss for Bu_4NBr in the same solvent mixture.[5] For the system CH_3OH–C_5H_5N, in the first part of the curve there would actually be a negative a_K, whereas in the second part its value (6.6 Å) is in excellent agreement with the crystallographic datum.

The results so far obtained do not yet allow an ion–solvent interaction mechanism to be proposed. For a more thorough study of the behavior of electrolytes of this type, further measurements are needed in various solvent mixtures.

(13) E. Becker, *Spectrochim. Acta*, 17, 436 (1961).

COMMUNICATIONS TO THE EDITOR

Estimation of Bond Dissociation Energies of N–H Bonds by Correlation with HT Yields from Recoil Tritium Abstraction[1]

Sir: The yield of HT from the reactions of energetic tritium atoms with C–H bonds has been shown to depend strongly upon the nature of the C–H bond involved and to correlate very well with the bond dissociation energies of saturated hydrocarbons.[2–4] We have now carried out a similar series of reactions with several compounds containing N–H bonds and have again observed an excellent correlation for the yield of reaction 1 with the known bond dissociation energies. As with the C–H correlation, the HT yield under controlled conditions of energetic tritium reaction can be employed for the estimation of unknown or uncertain bond dissociation energies.[5]

$$T^* + H\text{—}N\langle \longrightarrow HT + \cdot N\langle \qquad (1)$$

Experimental investigations of the reactions of recoil tritium atoms with N–H bonds are effectively limited to the abstraction process, since the lability of typical N–H bonds ensures rapid isotopic exchange between ⟩NH (and ⟩NT) and other exchangeable materials present, including especially –OH (and –OT). Consequently, our experiments have been almost exclusively concerned with the determination of HT yields. However, when both C–H and N–H positions are present in the target molecule, the former have been masked by deuteration,[6] and the radio gas chromatographic measurements have involved the separation of HT and DT.[4,7]

The experiments have been conducted in the presence of 3.5 cm of O_2 and a large excess of N_2, ensuring that the moderation and scavenging properties of the medium are essentially constant for each molecule measured. Some hydrocarbon molecules have been included for calibration and comparison with the data of Tachikawa for N_2–O_2 systems.[4] Yield data are summarized in Table I and displayed graphically in Figure 1. The correlation previously obtained for hydrocarbons is also shown in Figure 1 for convenient comparison.[4]

The data for N–H bonds show a correlation similar to, but slightly displaced from, the C–H correlation line. However, the bond dissociation energies of N–H bonds are neither numerous nor very accurately known,[8] and the two correlations agree within the rather large

(1) This research was supported by AEC Contract No. AT-(11-1)-34, Agreement No. 126.

(2) W. Breckenridge, J. W. Root, and F. S. Rowland, *J. Chem. Phys.*, 39, 2374 (1963).

(3) J. W. Root, W. Breckenridge, and F. S. Rowland, *ibid.*, 43, 3694 (1965).

(4) E. Tachikawa, Ph.D. Thesis, University of California, Irvine, Calif., 1967.

(5) J. W. Root and F. S. Rowland, *J. Phys. Chem.*, 68, 1226 (1964).

(6) Experimental measurements have shown that substitution of deuterium in one position has a negligible effect on abstraction from neighboring positions. See ref 4.

(7) J. K. Lee, E. K. C. Lee, B. Musgrave, Y.-N. Tang, J. W. Root, and F. S. Rowland, *Anal. Chem.*, 34, 741 (1962).

(8) J. A. Kerr, *Chem. Rev.*, 66, 456 (1966).

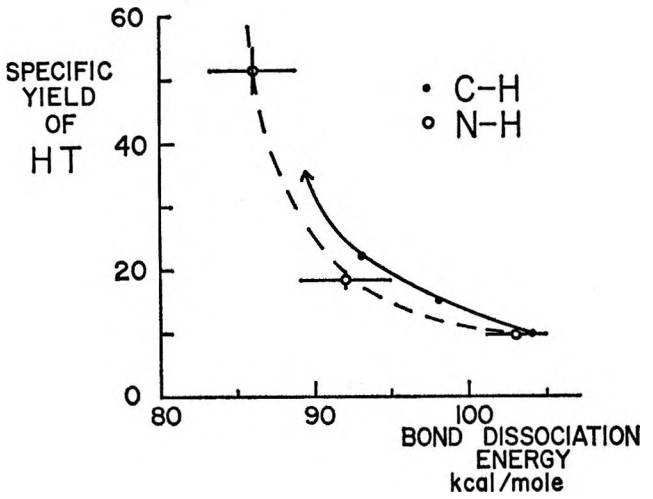

Figure 1.

Table I: Relative HT Yields from Different C–H and N–H Bonds in Recoil Tritium Reactions[a]

RH	Specific yield of HT[b]	Bond dissociation energy[a]
CH_4	9.9	104
C_2H_6	15.3	98
c-C_3H_{10}	22	93
NH_3	9.5	103 ± 2
CD_3NH_2	18 ± 1	92 ± 3
$(CD_3)_2NH$	51 ± 4	86 ± 3

[a] Sample composition: N_2, 60–70 cm; O_2, 3.5 cm; He^3, 1 cm; RH, 5–10 cm. [b] Yield per C–H or N–H bond under equivalent experimental conditions.

experimental error. Certainly, one can conclude that the mechanism of abstraction is quite similar from both C–H and N–H bonds, involving in each case those factors that are important in controlling the bond dissociation energy. Further testing of the correlation and improvement of its accuracy requires experiments with many additional N–H bonds to determine both standard HT yields from recoil tritium reactions and the values of the corresponding bond dissociation energies.

DEPARTMENT OF CHEMISTRY
UNIVERSITY OF CALIFORNIA
IRVINE, CALIFORNIA 92664

T. TOMINAGA
F. S. ROWLAND

RECEIVED JANUARY 2, 1968

X-Ray Evidence for Residual Water in Calcined Divalent Cation Faujasite-Type Zeolites

Sir: There have been several reports that directly or indirectly support the thesis that divalent cation faujasite-type zeolites activated at 500° or below contain residual water.[1-5] When alkaline earth X and Y zeolites were heated from 500 to 1000°, Pickert, Rabo, Dempsey, and Schomaker found weight losses ranging from 1.04% for MgX to 0.25% for BaY.[1] As they point out, this weight loss could represent the removal of residual water and/or the loss of water formed by the condensation of zeolitic hydroxyl groups. Recently, Ward presented infrared evidence for the formation of pyridinium ions in divalent cation Y zeolites.[2] He attributes their formation to the reaction of pyridine with acidic hydrogen resulting from the hydrolysis of residual water molecules attached to cations

$$M(OH_2)^{2+} \longrightarrow M(OH)^{+} + H^{+}$$

In addition, he found that pyridinium ion concentration increases with decreasing cation radius, which is consistent with his hydrolysis model and the weight loss data of Pickert, *et al.*[1]

We have recently obtained evidence concerning the coordination of the residual water oxygen from single-crystal X-ray studies of vacuum-activated CaX, SrX,[6] and nickel(II)-exchanged natural faujasite, NiFj.[7] These zeolites were evacuated for 8–16 hr at 400° and 10^{-6} torr and sealed, without exposure, in capillaries; then counter X-ray data were collected at room temperature. The structures were solved using conventional Fourier, difference Fourier, and least-squares techniques. A CaX difference map[6] indicated scattering matter in SII′ (see footnote of Table I for a description of the site nomenclature), which was assigned to calcium ion, Ca3, based upon the Ca3–O2 (framework oxygen) distance of 2.28(7) Å. This new cation site is 0.03 Å from the plane of the supercage six-ring and 0.74 Å from the position a calcium ion would take in SII. Additional scattering matter found in the SII′ region was assigned to oxygen, Ow, and attributed to a residual water molecule. The Ca3–Ow and Ca2 (calcium ion in a SI′ site)–Ow distances, 2.34 (12) and 2.64 (8) Å, respectively, are the main bases for this assignment. Since the Ow peak on the difference map is small and less than twice the background level, the following facts are given to support this assignment.

1. Including Ow with partial occupancy in the model drops the refined weighted R from 0.083 to 0.079. Applying a linear hypothesis test,[8] we find that the

(1) P. E. Pickert, J. A. Rabo, E. Dempsey, and V. Schomaker, *Proc. Intern. Congr. Catalysis, 3rd, Amsterdam, 1964*, 1, 714 (1965).

(2) J. W. Ward, presented at the 41st National Colloid Symposium, Buffalo, N. Y., June 1967.

(3) C. L. Angell and P. C. Schaffer, *J. Phys. Chem.*, 70, 1413 (1966).

(4) J. L. Carter, P. J. Lucchesi, and D. J. C. Yates, *ibid.*, 68, 1385 (1964).

(5) E. Dempsey, Research Department, Mobil Research and Development Corp., Princeton, N. J., unpublished research.

(6) D. H. Olson, unpublished research.

(7) D. H. Olson, in preparation.

(8) W. C. Hamilton, *Acta Cryst.*, 18, 502 (1965).

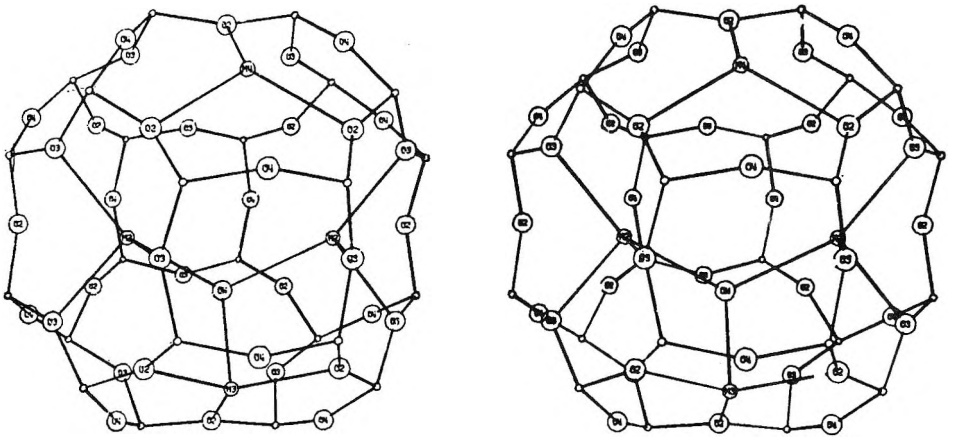

Figure 1. Stereoscopic drawing of a sodalite cage in a faujasite-type structure showing the coordination of a residual water oxygen. Oxygens O2 and O4 are members of the supercage six-ring and oxygens O2 and O3 are members of the hexagonal prism six-ring.

Ow scattering matter can be included in the model at the 0.005 significance level.

2. The refined population parameter for Ow is 5.5 times its standard deviation.

3. The population parameter for the calcium ion in SII′ is roughly equal to that for Ow, implying simultaneous occupancy of the SII′ site and the formation of a Ca3–Ow bond (this agreement of occupancy factors for Ow and metal cation in SII′ is also observed in SrX[6] and NiFj[7]). In fact, the presence of residual water oxygen in site SII′ is the most logical explanation for the ~0.7-Å movement of metal ions from SII to SII′.

Table I: Summary of Nonframework Atom Sites[a]

Atom type	Site	CaX No./u.c.[c]	SrX No./u.c.	NiFj No./u.c.
Cation (M1)	SI	7.5 (5)	11.2 (3)	10.6 (1)
Cation (M2)	SI′	17.3 (6)	7.0 (6)	3.2 (3) + 1.9 (6)[b]
Cation (M3)	SII′	9.0 (10)	4.2 (8)	1.9 (6)
Cation (M4)	SII	17.3 (6)	19.5 (6)	6.4 (2)
Ow	SII′	10.5 (19)	5.4 (15)	1.9 (15)

[a] The site designations used here are those introduced by Pickert, *et al.*[1] SI is in the center of the hexagonal prism; SI′ is adjacent to SI, and in the sodalite cage, SII′ is in the sodalite cage adjacent to the supercage six-ring and SII is in the supercage adjacent to SII′. Except for site SI, the sites define a region in crystal space and not a definite point. [b] There are two site SI′ peaks assigned to nickel ions. The smaller is 2.0 Å from Ow scattering matter.[7] [c] u.c. = unit cell.

Evidence for residual water, Ow in SII′, was also found in SrX and NiFj, although in these cases the occupancy factors were lower (Table I). In these two structures, the population parameters for Ow and M3 were adjusted by computing a succession of difference maps.

The position and coordination of the residual water oxygen, Ow, is shown in Figure 1.[9] In addition to its coordination to M3 cations, Ow is coordinated to cations in SI′ with M–O distances of 2.64 (8), 2.67 (8), and 2.0 (3) Å in CaX, SrX, and NiFj, respectively. The Ow and M2 population parameters (Table I) indicate that an average of 1.6, 1.3, and 1.0 such bonds per Ow occur in these three zeolites when evacuated as described earlier. The multiple coordination of Ow explains its retention following the relatively severe dehydrating conditions. The multiple coordination would also promote the hydrolysis reaction which Ward[2] has shown to occur. The M3 cation is tetrahedrally coordinated by Ow and three framework oxygens of the supercage six-ring. Further support for this coordination is afforded by the uv diffuse reflectance work of Williams, who found evidence for tetrahedrally coordinated cobalt in a cobalt-exchanged zeolite X heated at 400° in flowing N_2.[10]

Thus divalent cation faujasite-type zeolites, as well as the trivalent rare earth forms,[11] retain water oxygens at 400° or above. This residual water no doubt influences the cation distribution.[5] The monovalent analogs of these zeolites dehydrate much more readily,[1,2,5] as would be predicted from the lower cation charge density.

Acknowledgment. Several helpful discussions with E. Dempsey of this laboratory are gratefully acknowledged.

(9) Computer drawn using ORTEP. C. K. Johnson, ORTEP, Oak Ridge National Laboratory, Oak Ridge, Tenn., 1964.

(10) C. J. Williams, unpublished research carried out at Mobil Research and Development Corp., Princeton, N. J.

(11) D. H. Olson, G. T. Kokotailo, and J. F. Charnell, presented at the 41st National Colloid Symposium, Buffalo, N. Y., June 1967.

MOBIL RESEARCH AND DEVELOPMENT CORPORATION
PRINCETON, NEW JERSEY 08540
D. H. OLSON

RECEIVED JANUARY 12, 1968

Production of $N_2(A^3\Sigma)$ and $CO(a^3\pi)$ by $Hg(^1P_1)$ Photosensitization; Pressure Dependence of 2537-Å Emission[1]

Sir: The pressure dependence of emission at 2537 Å when N_2 or CO undergo $Hg(^1P_1)$ photosensitization provides compelling evidence for the excitation of these species to their respective $A^3\Sigma$ and $a^3\pi$ states.

Excitation of Hg to its $^3P_1$ state by energy transfer from $N_2(A^3\Sigma)$ has been proposed[2] to account for the observed 2537-Å emission when Hg vapor is exposed to active nitrogen; kinetic studies[3] have confirmed this proposal. Emission at 2537 Å from the $Hg(^1P_1)$ photosensitization of N_2 or CO has been detected[4] spectrographically, and the possibility of the generation of $N_2(A^3\Sigma)$ and $CO(a^3\pi)$ by energy transfer from $Hg(^1P_1)$ has been inferred from this observation. The observed chemistry of CO under $Hg(^1P_1)$ photosensitization has been interpreted[5] in terms of $CO(a^3\pi)$.

We have studied the pressure dependence of 2537-Å emission under the conditions of both $Hg(^1P_1)$ and $Hg(^3P_1)$ photosensitization. A 2-in. diameter, flat-spiral, low-pressure mercury resonance lamp (Hanovia Corp.) fabricated of Suprasil quartz provided 2537- and 1849-Å radiation. Isolation of λ 1849 Å was effected by using an LiF window which was freshly irradiated with 2-Mrad doses of ^{60}Co γ rays. A Corning 7910 filter was used to isolate the 2537-Å line. Emission at 2537 Å was measured at right angles to the incident beam by means of a Jarrell–Ash 0.5-m Ebert monochromator, EMI 6255 B photomultiplier, and Tektronix 535 A oscilloscope with photographic recording.

The quenching by N_2 or CO of λ 2537-Å fluorescence produced by irradiation at this wavelength obeyed the Stern–Volmer relationship over the pressure range 10^{-3} to 700 torr. From the ratio of the slopes of these plots, the ratio of quenching rate constants, $k_Q^{CO}/k_Q^{N_2} = 23$, was calculated, in excellent agreement with the ratio of the accepted values of these constants.[6] The observed emission of λ 2537 Å from incident λ 1849 Å in the presence of N_2[7] or CO, corrected for the measured quenching of λ 2537 Å under identical conditions, is analyzed below. The analogous emission at 2537 Å in the presence of Ne or He was negligible.

Equation A is readily derived from the mechanism[8]

$$Hg(^1S_0) + h\nu(1849\ \text{Å}) \longrightarrow Hg(^1P_1) \qquad (I^{1849})$$

$$Hg(^1P_1) + N_2(X^1\Sigma) \longrightarrow Hg(^1S_0) + N_2(A^3\Sigma) \qquad (k_1)$$

$$Hg(^1P_1) \longrightarrow Hg(^1S_0) + h\nu(1849\ \text{Å}) \qquad (k_f^{1849})$$

$$N_2(A^3\Sigma) + Hg(^1S_0) \longrightarrow N_2(X^1\Sigma) + Hg(^3P_1) \qquad (k_2)$$

$$Hg(^3P_1) \longrightarrow Hg(^1S_0) + h\nu(2537\ \text{Å}) \qquad (k_f^{2537})$$

$$\frac{1}{I^{2537}_{\text{emission}}} = \frac{1}{I^{1849}(\text{Hg})} + \frac{k_f^{1849}}{k_1 I^{1849}(\text{Hg})(\text{N}_2)} \qquad (A)$$

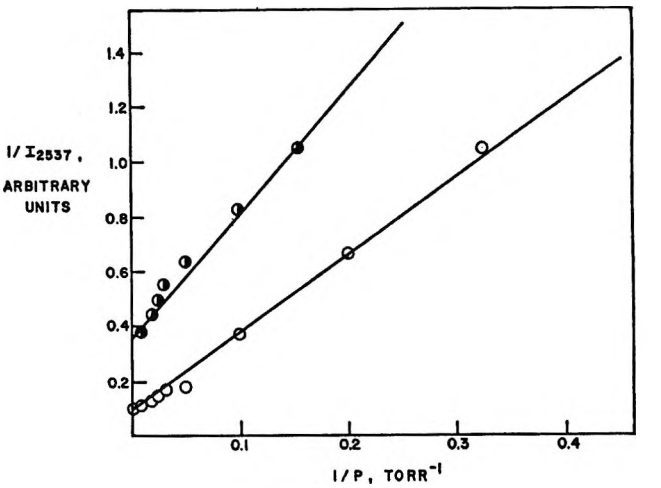

Figure 1. Plot of 2537-Å emission data in the form of eq A: ○, N_2; ◑, CO.

An analogous set of equations can be written for CO. Agreement of the data for N_2 and CO with eq A is demonstrated in Figure 1. The value of slope/intercept of these plots, k_f^{1849}/k_1, is 27 for N_2 and 13 for CO. Although the significance of k_f^{1849} is complicated by imprisonment of radiation, it can be concluded that the energy-transfer process represented by k_1 is of similar efficiency for N_2 and CO.

(1) Supported by the Air Force Office of Scientific Research under Contracts AF-AFOSR-765-65 and 765-67.

(2) W. R. Brennen and G. B. Kistiakowsky, *J. Chem. Phys.*, **44**, 2695 (1966).

(3) R. A. Young and G. A. St. John, *ibid.*, in press.

(4) T. A. Gover and H. G. Bryant, *J. Phys. Chem.*, **70**, 2070 (1966).

(5) G. Liuti, S. Dondes, and P. Harteck, *J. Chem. Phys.*, **44**, 4051 (1966).

(6) J. G. Calvert and J. N. Pitts, Jr., "Photochemistry," John Wiley and Sons, Inc., New York, N. Y., 1966, p 74.

(7) We have also found that quenching of $Hg(^1P_1)$ fluorescence by N_2 follows the Stern–Volmer relationship.

(8) Radiative and wall decay of $N_2(A^3\Sigma)$ is assumed to be negligible over the range of conditions.

DEPARTMENT OF CHEMISTRY
BOSTON UNIVERSITY
BOSTON, MASSACHUSETTS 02215

A. GRANZOW
M. Z. HOFFMAN
N. N. LICHTIN
S. K. WASON

RECEIVED JANUARY 23, 1968

Reactions of Tetranitromethane with Hydroxide Ion and Nitrite Ion

Sir: For some time we have been studying the reactions of tetranitromethane (TNM) with hydroxide ion and nitrite ion. The quantitative conversion of TNM to nitroform with nitrite ion has already been reported.[1]

(1) D. J. Glover, J. C. Dacons, D. V. Sickman, M. E. Hill, and M. J. Kamlet, U. S. Patent 3,125,606 (March 17, 1964).

We have obtained kinetic data for the reaction of TNM with hydroxide ion and nitrite ion which will be reported in a later communication. During this study in dioxane–water mixtures (the solvent varied from water to dioxane–water mixtures), it became evident that with insufficiently purified dioxane, an immediate reaction was occurring which could be explained by reaction with peroxides present in the dioxane. By adding a known amount of hydrogen peroxide (1.5×10^{-4} M final) an immediate reaction occurred producing equivalent quantities of nitroform ion (1.5×10^{-4} M) and nitrite ion (1.6×10^{-4} M). The solution was initially 9.2×10^{-4} M in TNM and 0.1 M in potassium bicarbonate.

In a recent report in this journal,[2] it was stated that TNM was found not to react with either nitrite or peroxide alone or with both together at pH 5 or above. The results with nitrite ion are contrary with the findings in this laboratory as reported in ref 1. It is not at all obvious why Bielski and Allen[2] did not observe the reactions with peroxide. Their experiments involved hydrogen peroxide of the order of 10^{-5} M and TNM of the order of 10^{-3} M. As shown above, nitroform would be produced equivalent to 10^{-5} M at a pH corresponding to that with bicarbonate ion. The actual rate constant found by Hoffsommer[3] for the reaction with hydroperoxide ion was 1.44×10^3 l./mole sec, in water.

The results of the kinetic study of TNM with base in dioxane are illustrated by the data in Figure 1. That the autocatalytic reaction is due to nitrite ion is clearly shown. Nitrite ion was added initially and the slow reaction is absent. When nitrite ion was not added, the other products were nitrate ion equivalent to the nitroform produced and nitrite ion equivalent to four times the TNM not going to nitroform. That this latter reaction also gives rise to carbonate ion was shown by Schmidt.[4] Carbonate ion and nitrate ion in the present study were shown not to affect the reaction. The rate constant for the reaction of TNM with nitrite ion was found by interpolation to 0.46 l./mole-hr at 24° and explains why Bielski and Allen[2] observed no reaction with nitrite ion. With nitrite ion 10^{-5} M and TNM 10^{-3} M, a yield of nitroform of 5×10^{-9} M would be expected which could not be detected under their conditions.

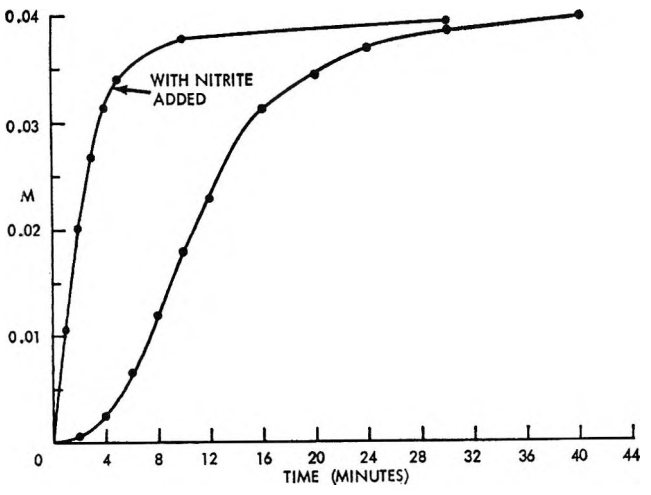

Figure 1. Formation of nitroform from TNM by reaction with hydroxide in dioxane–water.

In our study, when the base concentration was sufficiently low and the nitrite ion sufficiently high, only nitroform, nitrate ion, and nitrite ion were produced, confirming the catalytic nature of nitrite ion.

The reactions studied in our kinetic investigation were

$$C(NO_2)_4 + 6OH^- \longrightarrow CO_3^{2-} + 4NO_2^- + 3H_2O \quad (1)$$

$$C(NO_2)_4 + 2OH^- \longrightarrow C(NO_2)_3^- + NO_3^- + H_2O \quad (2)$$

$$C(NO_2)_4 + NO_2^- \longrightarrow C(NO_2)_3^- + N_2O_4 \quad (3)$$

$$N_2O_4 + 2OH^- \longrightarrow NO_2^- + NO_3^- + H_2O \quad (4)$$

The product N_2O_4, although not identified, explains the results most satisfactorily.

(2) B. H. J. Bielski and A. O. Allen, *J. Phys. Chem.*, **71**, 4544 (1967).

(3) A detailed kinetic study of the reaction of TNM with various peroxides has been reported by J. C. Hoffsommer, Doctoral Thesis, George Washington University, 1964. The results of this study are also planned for a future communication.

(4) E. Schmidt, *Ber.*, **52B**, 400 (1919).

U. S. NAVAL ORDNANCE LABORATORY
CHEMISTRY RESEARCH DEPARTMENT
ADVANCED CHEMISTRY DIVISION
WHITE OAK, SILVER SPRING, MARYLAND
DONALD J. GLOVER

RECEIVED FEBRUARY 5, 1968

Homogeneous Periodic Reactions

Sir: Two reactions are known which oscillate and which have been reported to take place in a homogeneous phase. One is the reaction between hydrogen peroxide and periodate in acid solution,[1] and the other is the series of cool flames observed in hydrocarbon oxidations.[2] The reason for the oscillatory behavior of cool flames appears to be that one of the rate-determining reactions has a negative temperature coefficient,[3] and as the temperature rises, the reaction dies out, restarting again when the system cools.

We have performed experiments[4] at 60° on the reac-

(1) W. C. Bray, *J. Amer. Chem. Soc.*, **43**, 1262 (1921).

(2) B. Lewis and G. von Elbe, "Combustion, Flames and Explosions of Gases," 2nd ed, Academic Press Inc., New York, N. Y., 1961.

(3) J. H. Knox in "Photochemistry and Reaction Kinetics," P. G. Ashmore, F. S. Dainton, and T. M. Sugden, Ed., Cambridge University Press, Cambridge, England, 1967.

(4) We are indebted to Mr. R. I. McLean for assistance with these experiments and to Mr. V. A. LoDato for helpful discussions.

tion of periodate with hydrogen peroxide [B.D.H. 0.5% acetanilide inhibitor] using glass beads to facilitate agitation and confirmed the periodic evolution of oxygen discovered by Caulkins and Bray,[1] under similar concentration conditions. We found that the *exclusion of daylight* from the system *suppressed the oscillations* (so did the addition of liquid mercury). Our sample of hydrogen peroxide decomposed monotonically at 60°, unlike some samples previously described,[5] and *the rate of decomposition doubled when daylight was excluded!* It seems likely that an excited state of acetanilide is a better inhibitor than the ground state. In our view, the peroxide–periodate oxidation can no longer be considered as an example of a homogeneous oscillating reaction—the mechanism is very complex, and subtle heterogeneous[5] and photochemical effects are present.

Bak[6] discusses the possibility that the Master equation can have imaginary eigenvalues, leading to a permanently oscillatory behavior, and, more realistically, that the Master equation should have complex eigenvalues which will lead *via* damped oscillations to final equilibrium. However, if the individual elementary processes are microscopically reversible (which is necessary if a final equilibrium is to be attained), a transformation can always be found which symmetries the Master equation for an isolated system, so that the eigenvalues are necessarily real.[4] Consequently, a periodic reaction cannot occur in the homogeneous phase in a thermodynamically closed system.

(5) F. O. Rice and O. M. Reiff, *J. Phys. Chem.*, **31**, 1352 (1927).

(6) T. A. Bak, "Contributions to the Theory of Chemical Kinetics," W. A. Benjamin, Inc., New York, N. Y., 1963.

C.R.E.S.S.
YORK UNIVERSITY
TORONTO, CANADA

D. H. SHAW
H. O. PRITCHARD

RECEIVED FEBRUARY 29, 1968